Investigations of Upper Atmospheric Phenomena over Mid-Latitudes during Daytime

A thesis submitted in partial fulfilment of
the requirements for the degree of

Doctor of Philosophy
by

Kshitiz Upadhyay
(Roll No.: 19330010)

under the guidance of

Prof. Duggirala Pallamraju
Space and Atmospheric Sciences Division
Physical Research Laboratory, Ahmedabad, India

Discipline of Physics
Indian Institute of Technology, Gandhinagar, India
2024

Dedicated to my family

Declaration

I, Kshitiz Upadhyay, hereby declare that this written submission represents my ideas in my own words, and where others' ideas or words have been included, I have adequately cited and referenced the original sources. I also declare that I have adhered to all principles of academic honesty and integrity and have not misrepresented or fabricated or falsified any idea/data/fact/source in my submission. I understand that any violation of the above can cause disciplinary action by the Institute and can also evoke penal action from the sources which have thus not been properly cited or from whom proper permission has not been taken when needed.

Kshitiz Upadhyay

(Roll no. 19330010)

Date: 7 August 2024

Certificate

It is certified that the work contained in the thesis entitled "**Investigations of Upper Atmospheric Phenomena over Mid-Latitudes during Daytime**" by Mr. Kshitiz Upadhyay (Roll no. 19330010), has been carried out under my supervision and this work has not been submitted elsewhere for any degree, or diploma.

(**Prof. Duggirala Pallamraju**)
Thesis Supervisor
Space and Atmospheric Sciences Division
Physical Research Laboratory
Unit of Department of Space, Government of India
Ahmedabad-380009, Gujarat, India.

Date: 7 August 2024

Acknowledgements

My journey during this doctoral work at the Physical Research Laboratory (PRL), Ahmedabad, has been an enriching experience, made possible by the support and guidance of many individuals who supported me directly and indirectly. I am pleased to take this opportunity to convey my heartfelt thanks for all the support and encouragement I have received.

First and foremost, with due respect, I would like to extend my deepest gratitude to my thesis supervisor, Prof. Duggirala Pallamraju, for his insightful guidance, countless support, and encouragement throughout this research journey. His broad knowledge in the field of space weather and aeronomy greatly enriched my understanding of the field. His unwavering dedication, enormous patience, and steady character have always inspired me on a personal level. I am deeply thankful to have such a mentor who consistently inspired me during my setbacks and guided me through challenges. This thesis would not have been possible without his steadfast support, and I will forever remain deeply indebted to him. I would like to extend my sincere gratitude to Shri Bhuvaneswari Ma'am, Ananth, and Samba for their homely and gracious welcome. I am so thankful for all the dishes full of sweetness that the Ma'am provided by preparing herself, which contributed to truly unforgettable moments in this journey.

I am highly obliged to my Doctoral Studies Committee (DSC) members: Prof. Dibyendu Chakrabarty, Dr. Mudit Srivastava, and Dr. Brajesh Kumar, for evaluating my progress reports and providing their valuable suggestions and critical comments throughout these years. All the continuous feedback from my DSC members deeply benefited my research work. My special thanks to Prof. D. Chakrabarty for his encouraging feedback and critical questions during my seminars to improve the scientific outcomes.

My sincere thanks to the Department of Space, Government of India, for providing me with all kinds of support during my research work. I thank Prof. Anil Bhardwaj, the Director of PRL; Prof. P Janardhan, former Dean; Prof. D. Pallamraju, present Dean; Mr. Deekshitulu, former Registrar; and Prof. R. D. Deshpande, present Registrar, for providing me the necessary facilities to carry out my thesis work. I also thank Dr. Bhushit Vaishnav, Head of Academic Services, for helping me in all academic matters since my joining. I also thank all the academic committee members for their critical evaluation and input during review seminars. I thank all the PRL faculties for providing me with exposure to various

research works at PRL. I also thank them for teaching various courses, such as research methodology and statistical Methods, during my coursework at PRL. I extend my thanks to Prof. Rajat Moona, the Director of IIT Gandhinagar, Dr. Nithin George, Dean, and the academic and administrative personnel of IITGN for their support and efficient help on all official and academic matters.

I am grateful to Dr. Nishtha Anilkumar and members of the library for their support and cooperation. I express my appreciation to all the members of the PRL computer center, particularly Mr. Jigarbhai, Hitendra ji, and Alok ji, for providing different software for data analysis, excellent computational and internet facilities without interruption. I thank the members of Canteen and CMD for continuously providing the necessary facilities to smoothly carry out the research work. I also thank Dr. Samir Dani, Dr. Shital Patel, and other staff members of PRL Dispensary for their support during my illness.

I sincerely thank the faculty members of the Space & Atmospheric Sciences Division: Prof. L. K. Sahu, Prof. Som Kumar Sharma, Dr. Harish Gadhavi, Dr. R. P. Singh, Dr. T. A. Rajesh, Dr. A. Guharay, and Dr. Narendra Ojha for giving me the detailed exposure and discussion in several subjects during the early phase of my research work. I also thank Prof. S. Ramachandran, Dr. K. Venkatesh, and Mr. S. Venkataramani for their discussions and guidance. I also thank Sneha di, Aryan, and Hemangi for their extended help with any office work. I thank my SPASC colleagues, Anil, Aditya, Rahul, Jacob, Aniket, Abhishek, Maanyash, Mr. Atul Manke, Mr. Mitesh, Mr. T. K. Sunil Kumar, Mr. Malaidevan, and Vishnu for creating a lively environment.

I am grateful to the Scientific Committee on Solar-Terrestrial Physics (SCOSTEP) for selecting me under the SCOSTEP Visiting Scholar (SVS) program and providing foreign travel support to visit the Institute for Space-Earth Environmental Research (ISEE), Nagoya University, Japan. I would like to thank Prof. Kazuo Shiokawa for his guidance and discussions during my research work at ISEE and for the visit to the MU radar observatory, Shigaraki, which gave me a memorable experience. I thank Prof. Yuichi Otsuka for the discussions I had on radar data. I also sincerely thank Miho-san for all the academic and administrative support during my stay at ISEE. I also thank Dr. Sandeep, Dr. Pankaj, and Dr. Shreedevi for their help and support in Nagoya.

The GLobal airglOW Model (GLOW) model used in this study was made available through the NCAR website at https://www2.hao.ucar.edu/modeling/glow. I acknowledge Dr. Stanley Solomon for

providing the same. World Data Center for Geomagnetism, Kyoto, and CEDAR Madrigal Databases host the data of geomagnetic indices, incoherent scatter radar (ISR), DMSP, and GPS-TEC used in this study. These databases are duly acknowledged.

I am thankful for everyone in my group of optical aeronomy lab, including my present/former laboratory colleagues, Pradip, Shashank, Pankaj, Mohit, Chithra, Subir, Sovan, Sunil, Dupinder, Komal, Dheeraj, and Narayan for a lively atmosphere, where I got the opportunity to learn about the techniques of optical instruments. I am happy to have my seniors Subir, Sovan, and Sunil for their wonderful company and helping me during my scientific work. I spent a joyful time with them playing games, having various discussions on endless things during the tea breaks, and dining excursions. The insightful conversations with them and my junior (Komal) helped me to learn a lot about their research topics.

My special thanks to all my sweet batchmates Ajayeta, Bharathi, Bijoy, Birendra, Gourav, Jiban, Neha, Rithvik, Santunu, Satyam, Saumya, Saurabh, Swagatika, Tanya, Vardaan, Vineet, and Yogesh. The time spent together on various occasions is unforgettable.

This section remains incomplete without mentioning my wonderful seniors and loving juniors in PRL: Kuldeep, Ankit, Sovan, Suman, Subarna, Sunil, Yogesh, Deepak, Madhu, Sandeep, Meghna, Monika, Anshika, Dipak, Sarika, Daya, Arijit, Supriya, Kamran, Dharmendra, Mansi, Akanksha, Malika, Haritha, Kiran, Aakash, Sandip, Ankita, Shivam, Harsh, and many more, who made my stay pleasant and lively, both at hostel and campus. I thank them for their wonderful company and experience by organizing friendly and fun-filled activities in the hostel, after-dinner walks, games, etc.

I am thankful to my teachers, Dr. Avinash Agarwal and Dr. V. P. Singh, Dept. of Physics, Bareilly College, Bareilly, for their invaluable teaching and encouragement.

Last, but not the least, I am immensely thankful to my parents for their invaluable and selfless support and encouragement, which have kept me inspired at every step. I am forever grateful to Vibhu, Kishu, Shanu, Didi, and Jija ji for their affection, care, and unwavering support. The willingness of my family to help me in any situation has always been a source of motivation. No matter how I express it, words cannot fully convey the depth of my gratitude and love for them.

Kshitiz Upadhyay

Abstract

The Earth's mid-latitude region is an intermediate area – poleward of the equatorial anomaly crests and equatorward of the auroral oval, typically between ±30° and ±60° latitude. The mid-latitude region is generally within the closed magnetic field lines during geomagnetic quiet times and serves as a transition region between the dynamics of the plasmasphere and magnetosphere. The upper atmosphere (UA) over mid-latitudes undergoes several dynamical changes due to interactions between magnetosphere-ionosphere (M-I) and ionosphere-thermosphere that are enhanced during geomagnetic storms. Being sandwiched between low and high-latitude regions, perturbations in atmospheric dynamics over these latitudes also modulate the mid-latitude dynamics. Some of the phenomena that occur during geomagnetic storms in the mid-latitude UA are storm-enhanced densities (SED) and stable auroral red (SAR) arcs. Such processes extend both in the temporal and spatial domains. So far, optical investigations of such effects have been mainly confined to nighttime observations, as the presence of scattered sunlight during the day poses a great challenge in optical investigations. However, for a comprehensive understanding of various coupling of space weather effects in mid-latitudes, daytime investigations are essential. Therefore, the present thesis focuses primarily on investigating the dynamics of mid-latitude UA during daytime conditions.

This thesis uses the atomic oxygen (OI) 630.0 nm (red line) airglow emissions during the daytime as the primary dataset to understand these processes in both temporal and spatial domains. Due to their sensitivity to ionospheric-thermospheric variations, these emissions act as a good tracer for investigating the dynamic processes occurring in the UA. These optical data were retrieved using a ground-based high-resolution imaging Echelle spectrograph (HIRISE) from Boston (42.36°N, 71.05°W), a mid-latitude location. During geomagnetic storms, the plasmapause can approach the magnetic latitude (≈ 52°N) of the observational location, presenting an opportunity for the investigation of plasmasphere-ionosphere coupling effects in the UA. For a comprehensive investigation, this study also comprises the measurements of ionospheric parameters from a collocated incoherent scatter radar (ISR) and digisonde (located at Millstone Hill; 42.64°N, 71.50°W), GPS total electron content, and satellite-borne instruments. In addition, a physics-based model, GLOW, and the WINDII empirical model (WEM) have also been used to estimate the intensity of red line emissions, which are further compared with the HIRISE measured emission intensities.

The measured brightness was found to be larger at different local times during the periods of geomagnetic disturbances, as compared to the model calculated emissions. Further investigations were carried out to identify the cause of such enhancements in the measured emission intensity. The analyses reveal a considerable increase in the electron density, Ne, and electron temperatures, Te, at altitudes above 400 km, play the dominant role in accounting for the larger emission magnitudes through dissociative recombination and photoelectron impact production mechanisms. Volume emission rates (VER) of OI 630.0 nm emissions, as a function of altitude, were calculated using the GLOW model. Contrary to the typical origin altitude of 230 km of red line emission, the increased emissions were found to peak and correlate with the topside plasma variations in association with the high-altitude ionospheric perturbations. We further examined the source of enhancement in the ionospheric parameters causing larger emissions during the daytime. The significant factors increasing the topside Ne and Te were identified as the eastward electric field and soft-particle precipitation because of the magnetosphere-ionosphere and plasmasphere-ionosphere couplings during daytime.

During the main phase of the storm, the expansion of the high-latitude two-cell convection pattern providing the daytime electric field was inferred from the variation in the rate of change of the TEC index (ROTI), reaching mid-latitudes over the North American sector. On the other hand, the larger Te magnitudes were caused by the additional heat deposition from the downward precipitating electron heat flux in the mid-latitude ionosphere. In addition to their impact on red line emissions, we further quantitively estimated their variation using the measured emission intensity and through forward modeling. An analytic expression was also presented between the calculated electron heat flux and electron temperature variations for daytime conditions. Based on the investigations of nighttime SAR arc conjunction events from 2012-2019, the calculated electron heat flux was found to vary with solar activity variation. Moreover, the further calculated model VER profiles suggested the solar activity dependence in the variation of the peak height of SAR arc emission. It was found that the peak altitude of the SAR arc could also exist below 300 km during low solar activity periods, whereas most of the studies in the past considered the peak altitude at around 400-450 km altitudes.

Furthermore, for occasions with no drastic variation in the measured emission intensities, we investigated the quiet-time thermospheric variations in terms of gravity wave (GW) dynamics over mid-latitudes using large field-of-view data from HIRISE. Systematic measurements of daytime red line emissions on clear all-sky days during 2005-2007 were investigated, wherein GW scale sizes in the meridional direction were obtained. Interestingly, the estimated scale

sizes indicate a positive relationship with auroral activity, even during quiet periods. Therefore, these results bring out new insights into the dynamics of the UA over mid-latitudes for both geomagnetically quiet and disturbed periods during daytime conditions.

Keywords: Mid-latitude ionosphere, daytime OI 630.0 nm emissions, storm enhanced density, Stable Auroral Red (SAR) arcs, electron temperature enhancement, electron heat flux precipitation, magnetosphere-plasmasphere-ionosphere coupling, space weather.

Contents

Abstract ..... **v**
Contents ..... **ix**
List of Figures ..... **xiii**
List of Tables ..... **xxiii**
Introduction **1**
1.1 Structure of the Earth's magnetosphere and ionosphere 3
1.1.1 Plasmasphere, particle motion, and adiabatic invariants 4
1.1.2 Ring current and geomagnetic storms 7
1.1.2 Ionospheric D, E, and F-region 10
1.2 High and mid-latitude phenomena due to magnetosphere-ionosphere coupling 15
1.2.1 Aurora 15
1.2.2 Field-aligned currents and High-latitude two-cell pattern 17
1.2.3 Subauroral ion drifts and polarization streams 20
1.2.4 Storm-enhanced density over mid-latitudes 22
1.2.5 Stable auroral red arcs 29
1.2.6 Strong Thermal Emission Velocity Enhancement 33
1.3 Role of Optical emissions in the study of ionospheric phenomena 35
1.4 Summary 37
1.5 Objective of the thesis 37
1.6 Structure of the thesis 38
Experimental datasets, models, techniques, and data analysis **39**
2.1 Introduction 39
2.2 Daytime atomic Oxygen 630.0 nm (red line) emission 41
2.2.1 Production mechanisms of daytime OI 630.0 nm emission 42
2.3 Daytime optical measurements 45
2.3.1 High-Resolution Imaging Spectrograph using Echelle grating (HIRISE) 48
2.3.2 Daytime airglow emission extraction procedure 52
2.3.3 Comparison of dayglow extraction method with previous approaches 56
2.4 Radio measurements 58
2.4.1 Digisonde 59
2.4.2 Millstone Hill Incoherent Scatter Radar 60
2.4.3 Total electron content (TEC) data (Rate of change of TEC index (ROTI)) 62
2.4.4 Plasma measurements on-board Defense Meteorological Satellite Program (DMSP) ... 65
2.5 Geomagnetic and solar activity indices 65

2.6 Estimation of Dayglow Emissions Using Models 66
2.6.1 GLOW model 67
2.6.2 WINDII empirical model (WEM) 68
2.7 Spectral Analysis Techniques Used 69
2.7.1 Fourier Series 69
2.7.2 Fourier Transform 70
2.7.3 Lomb-Scargle analysis 72
2.8 Summary 77
Response of mid-latitude ionosphere observed during daytime SED 79
3.1 Introduction 79
3.2 Datasets used 80
3.3 Results and discussions 81
3.3.1 Ionospheric variations 85
3.3.2 SED Plume formation on 9 November 2004 88
3.3.3 Influence of magnetospheric convection on the F-region ionosphere 90
3.3.4 Role of Electric field during SED 92
3.3.5 Altitude Variation of 630.0 nm using volume emission rate profiles 95
3.3.6 Small-scale fluctuation in 630.0 nm Dayglow and TEC 98
3.4 Summary 99
Daytime SAR arcs in red line emission 101
4.1 Introduction 101
4.2 Datasets used 105
4.3 Results and discussions 106
4.3.1 Observations of optical and ionospheric signature of SAR arcs in daytime 106
4.3.2 Dayside signature of SAR 109
4.3.3 Impact of increased electron temperature on 630.0 nm production 112
4.3.4 Estimation of electron temperature using forward modeling 115
4.4 Summary 119
Estimation of electron heat flux at ionospheric altitude during SAR arcs 121
5.1 Introduction 121
5.1.1 Electron thermal balance equation and the electron heat flux in upper F-region 123
5.2 Datasets used 126
5.3 Results and discussions 126
5.3.1 Observations of enhanced 630.0 nm emission and electron temperature 126
5.3.2 Determination of electron heat flux during daytime observation of SAR arc 138
5.3.3 Determination and variation of electron heat flux during nighttime SAR arc 142
5.4 Summary 153

Effect of geomagnetic activity on gravity wave dynamics over mid-latitudes 157
6.1 Introduction 157
6.2 Datasets used 161
6.3 Results and Discussions.....161
6.3.1 Meridional scale-size calculation 164
6.3.2 Seasonal variation in calculated scale sizes 166
6.4 Summary.....174
Summary and Future Scope 177
7.1 Summary.....177
7.2 Future Scope.....182
References.....185
List of Publications 205

List of Figures

Figure 1. 1: Schematic of Geocentric solar ecliptic (GSE) coordinate systems for Sun-Earth system. 2

Figure 1. 2: a) Structure of Earth's magnetosphere along with its various components, **b)** the typical radiation belt structure in the inner magnetosphere (After Regi, 2016). 3

Figure 1. 3: (a) Schematic representation of a magnetically trapped charged particle in the magnetosphere (Tascione, 1988). **(b)** Different particle motions (from left to right): gyro, bounce and drift due to first M, second J, and third Φ adiabatic invariants, respectively. (Kivelson & Russell, 1995). The gyro and drift motions are depicted for electrons, the motion is oppositely directed for ions. 5

Figure 1. 4: A schematic of dayside magnetic reconnection process and again in nightside for southward directed IMF Bz along with magnetic field and plasma convection (Tsurutani et al., 2003). 8

Figure 1. 5: A schematic of Dst-index is shown to identify the magnetic storms. Panel (a) shows a magnetic storm caused by a CME (mostly occur during solar maximum). Panel (b) shows a magnetic storm caused by a CIR. 'SO' stands for storm onset. (Tsurutani, 2000). 9

Figure 1. 6: A schematic diagram of Russell-McPherron effect showing the maximum possibility of southward Bz during spring equinox for negative IMF polarity and during fall equinox for positive IMF polarity (Zhao & Zong, 2012). 10

Figure 1. 7: Neutral temperature profile of the atmosphere for day and nighttime and during different solar activities. From Doornbos (2012). 11

Figure 1. 8: International Quiet Solar Year (IQSY) daytime plasma and neutral composition. Helium distribution is from a nighttime measurement. (Adapted from Kelley, 2009). 12

Figure 1. 9: Day and nighttime Ionospheric electron density profile during low and high solar activity (Courtesy: Hargreaves, 1992) 13

Figure 1. 10: Different regions of aurora are shown: (1) the equatorward boundary as a white outer ring, (2) the auroral oval as a shaded transparent region, and (3) the location of auroral observation (Sigernes et al., 2011). 16

Figure 1. 11: Satellite observation of OI 1356 Å obtained during 1911–2048 UT (1411–1548 LT) shows the presence of aurora over Boston, a mid-latitude region, during local daytime (Pallamraju & Chakrabarti, 2005). 17

Figure 1. 12: a) The schematic of combined FACs and ionospheric current systems. (Le at al., 2010), and **b)** High-latitude two-cell plasma convection pattern and associated plasma drift in the northern hemisphere for southward IMF Bz and IMF By=0 (Kelley & Heelis, 1989). 18

Figure 1. 13: Schematic representation of changes in convection-cell pattern under different conditions of IMF By component and when IMF Bz is southward. Adapted from Kelley, 2009. 20

Figure 1. 14: Schematic showing the Connection between the region-1 and region-2 FAC and sub-auroral ion drifts (SAID) / sub auroral polarization stream (SAPS) (Mishin & Burke, 2005). 21

Figure 1. 15: A scatter plot showing larger friction heating at larger ion convection velocity observed between 450 km and 550 km altitude at 57° magnetic latitude. (From Yeh & Foster, 1990). 22

Figure 1. 16: An effect of positive ionospheric storm during local daytime is shown in maximum electron density (NmF2) during a period of geomagnetic storm. The positive phase is observed at mid-latitude location of WALLOPS ISLAND (northern hemisphere) and HOBART (southern hemisphere). Mendillo & Narvaez, (2010). 23

Figure 1. 17: The Vertical components of the plasma drifts over mid-latitudes are shown from left to right for an electric field (E; eastward), neutral wind (un; equatorward), and vertical gravitational forces (F; downward) from left to right. I represent the magnetic inclination angle. (Jee, 2023). 24

Figure 1. 18: The top left figure shows the plasmasphere image taken from IMAGE EUV satellite. The bottom figure shows the ionospheric SED using TEC data over North American sector. The boundary of SED plume (thick red lines) matches with the boundaries of plasmaspheric plume, shown in top right panel. (Foster et al., 2002). 25

Figure 1. 19: Earth's Magnetosphere showing the general form of the convective flow in the equatorial plane and the dawn-dusk direction (Brice, 1967). 26

Figure 1. 20: Two dimensional TEC maps showing SED during different geomagnetic storms, superposed with convection pattern as solid and dashed black lines. Dotted line in each panel represents the terminator. The formation of SED plume and tongue-of-ionization (TOI) can be seen in panel (b) and (d) respectively (Zou et al., 2014). 27

Figure 1. 21: a) A schematic representation of latitudinally narrow SAR arc in the equatorward of high-latitude aurora (Kozyra et al., 1997), **b)** An observation of mid-latitude nighttime SAR arc at Millstone Hill using OI 630.0 nm emission. The bright aurora is shown at the top of the image. (Courtesy: Buimaging.com) 28

Figure 1. 22: SAR arc emissions are generated at the foot-points of closed field lines in the overlapping region of the ring current and plasmasphere encircling the Earth, as shown by the schematic of the inner magnetosphere (Kozyra et al., 1987). 30

Figure 1. 23: The energy transfer processes of different mechanism responsible for the formation of SAR arcs are shown (Kozyra et al., 1997). 31

Figure 1. 24: Nighttime observations of SAR arc during a geomagnetic storm on 2 October 2013 over Millstone Hill. SAR arc can be seen having small-scale structures in the zonal direction. After Mendillo et al., 2016a. 32

Figure 1. 25: Seasonal occurrence rates of SAR arcs based on nighttime observations made during the period of 1985–2013 (Mendillo & Wroten, 2019). 33

Figure 1. 26: (a) Observations of STEVE arc by Citizen scientist along with the green picket fence on 8 May 2016 over North America. **(b)** All-sky-imager observations of STEVE equatorward to high-latitude auroral activity. **(c)** Simultaneously detected STEVE in the southern hemisphere using satellite measurements. After Nishimura et al. 2019. 34

Figure 1. 27: Satellite measured SAID signatures are shown in conjunction with a STEVE event on 25 July 2016 by shaded region. (MacDonald et al., 2018). 35

Figure 2. 1: The observational location of Boston over North American longitudes is shown by a blue dot, indicating where OI 630.0 nm emissions were being observed by HIRISE. The red vertical bar represents the meridional extent covered by the HIRISE field-of-view (FOV). 41

Figure 2. 2: The peak emission altitude variation for three 630.0 nm dayglow production mechanisms is shown for geomagnetically quiet (solid) and disturbed periods (dashed) at solar zenith angle of 50°. The green, cyan, and red lines represent the profile of DR, PEI, and PD production mechanisms, respectively (Culot et al., 2005). 45

Figure 2. 3: Schematic diagram of High-Resolution Imaging Spectrograph using Echelle grating (HIRISE) used to obtain the OI 630.0 nm emissions during daytime (Pallamraju et al., 2002)... 47

Figure 2. 4: Comparison of chromatic aberration: (a) Lateral chromatic aberration for different wavelengths due to different focal lengths. (b) Use of achromatic doublet to solve the lateral chromatic aberration simultaneously focusing different wavelengths at one point. (After Brady & Legge, 2009.) 49

Figure 2. 5: The incidence angle (α) and diffraction angle (β) are shown in relation to the blaze angle (θ_B). GN is the normal to the horizontal grating surface and FN is the facet normal. (From Palmer, 2020). 50

Figure 2. 6: A sample image of the daytime sky spectrum observed by HIRISE on 23 March 2008 over Boston. The x-axis represents the wavelength information, while the spatial information is represented on y-axis. 51

Figure 2. 7: The intricacies involved in the data analysis procedure are depicted. Panel (a) shows the blue-sky spectrum obtained using a 6300 Å region. Panel (b) shows the need for matching the continuum regions on either side of the emission wavelength. (c) Scaled solar and blue-sky spectra after the least-squares matching at the continuum regions on either side of the emission line of interest at 6300.3 Å. (d) Atmospheric contribution around the 6300 Å region, obtained by subtracting the solar spectrum from the blue-sky spectrum shown in the above panel. Error (±1) bars are also shown. The one at the 6300 Å region consists of both the dayglow and the contribution due to Ring Effect, while the next one consists of only Ring Effect. The difference of area under these two curves yields the contribution due to dayglow at that time. This scaling is repeated for every data sample to obtain a diurnal behavior of the dayglow variability. (Pallamraju et al., 2002). 53

Figure 2. 8: Example of a complex spectral observation: (a) Scaled bright reference, (b) twilight data, and (c) their difference. The Fraunhofer lines are indicated by H, K, and L, where the cluster of Fe

and Mg emission lines exist at L. The false inverted Fraunhofer feature caused by cluster of Fe and Mg lines during rationing method can be seen in the residual spectrum. (Swift et al., 1990.) 57

Figure 2. 9: Two ISR antenna at Millstone Hill: a) The 68-meter zenith antenna, b) 46-meter steerable antenna (also known as MISA), and c) lower elevation limit for MISA in the azimuth direction. (Credit: Madrigal Database at Millstone Hill). 60

Figure 2. 10: A Doppler shifted incoherent scatter spectrum is shown. (After Evans, 1969). 62

Figure 2. 11: A schematic representation of ionospheric thin shell geometry. 63

Figure 2. 12: A comparison of evenly and unevenly spaced data by FFT and Lomb-Scargle (L-S): The left column shows sample data composed of three known frequencies (0.03, 0.10, and 0.12 Hz). The top panel displays the full signal with equally spaced data points. Subsequent panels show unevenly spaced data by randomly removing 10-40% of the original data points. The middle and right columns represent the frequencies obtained by FFT and L-S analysis, respectively. The observed frequency with the maximum normalized power is indicated by f. The horizontal lines in the right column indicate the False Alarm Level (90% confidence limit) for the significant periods. 76

Figure 3. 1: the panels (a)–(c) show the variations in Dst-index, IMF-Bz component, and 3-hourly Kp-index values for the duration of the observation period (7–9 Nov 2004). The horizontal arrows represent the daytime (6–18 LT) on each day. The strong geomagnetic disturbances of kp = 9- can be seen on 8 November (1 UT) and 9 November (20 UT); LT = UT-5 hr. 82

Figure 3. 2: the diurnal variation in OI 630.0 nm dayglow emission intensity (along with ±1σ values) as measured by hirise (red dots) over zenith (FOV ≈ 6°), estimated by glow-model estimates blue asterisks), and by WEM predictions (black dashed line) are shown. Panels (a)–(c) show the variations corresponding to 7, 8, and 9 November 2004. Panel (d) shows the zoomed-in plot of dayglow variation for 9 November during 14–17 LT at a higher data cadence of ~4 min. 83

Figure 3. 3: the left two columns show the local time variation of altitude profiles of Te (top), Ti (middle) and Ne (bottom), as measured by the Millstone Hill ISR on 8 and 9 November 2004. The third column shows the comparison of these parameters at 15:04 LT, which is the time of major geomagnetic disturbance observed on the 9 November 2004. 84

Figure 3. 4: the GPS-TEC temporal variation in the mid-latitude range 45°–55° MLAT within 90°W to 60°W geographic longitude. Different lines represent the TEC variation for different magnetic latitudes separated by 1° in the range of 45°N–55°N. The black dashed lines represent the two quiet days before (5–6 Nov) and after (13–14 Nov) the storm day (9 November), while the solid red lines correspond to the variation on the storm day. A clear enhancement in TEC in the 45°–55°N MLAT range can be seen in evening hours (15–17 LT), which illustrates the "dusk effect." 87

Figure 3. 5: the TEC maps involving 5-min integration during the period of observed enhancement in dayglow that is, 20–21 UT (15–16 LT) on 9 November 2004. White star indicates the observation location, Boston (42.36°N, 71.05°W). The black arrow at 20 UT (15 LT) signals the onset of enhanced density plume. 88

Figure 3. 6: (left) the 2D TEC map for 9 Nov obtained by integrating the TEC for a half hour duration (20:00–20:30 UT). The white arrow represents the direction of motion of sed plume, which is sunward. The white star indicates the observation location, Boston. **(right)** the SED plume connected with the tongue of ionization (TOI) across the polar cap through ionospheric equipotential contours of the high latitude convection pattern at 22:55-23:00 UT during a geomagnetic storm 23 April 2012 (after Zou et al., 2014)..... 89

Figure 3. 7: ROTI maps over north america on 9 November 2004 during 19–22 UT at half an hour interval. The white star symbol represents the observation location, Boston. 91

Figure 3. 8: (a) the enlarged ROTI map (with changed colorbar to highlight the variation) upto 20°W showing the ground track of DMSP-F14 (red line) at 21.08 UT (16.08 LT). The two white dashed line represent the 40° and 60° N MLAT which intersect the dmsp pass at P1 and P2. (b) DMSP observed horizontal ion velocities (positive is sunward) between P1 and P2 region (black dashed line). This region can be seen having fast plasma flow (~1 km-s^{-1}) in sunward direction. 92

Figure 3. 9: a schematic representing the induced plasma drifts in vertically up direction due to the eastward electric field in daytime. 93

Figure 3. 10: a measured upward ion drift (positive upward) by ISR at 325 km altitude reaching up to 300 m-s^{-1} at around 15 LT on 9 November 2004. 94

Figure 3. 11: the effect of purely zonal motion (case-a), poleward (case-b), and equatorward (case-c) convective flow has been sown by model simulations during 2-hour interval period in the left side. The corresponding variation in altitude profile of electron density for different cases (a, b, and c) has been shown in the right side. After Heelis et al., (2009). 95

Figure 3. 12: (a) the OI 630.0 nm volume emission rates (VER) as a function of time, as estimated by the GLOW model using as inputs the ISR measured Ne, Te, and Ti data. The one-dimensional plot of VER on 9 November in panel (b) clearly shows a shift in peak emissions to higher altitudes (up to 420 km) during 15–16 LT (thick red lines)..... 96

Figure 3. 13: the HIRISE observed dayglow (top row), GLOW estimated dayglow (middle row), and TEC (bottom row) are shown. The 3-hr running average was taken (dashed line) and the residuals thus obtained (with zero mean) are also shown in these panels. The left column shows the diurnal profile of these parameters, middle column shows the variation of these parameters near one hour of major disturbances (15–16 LT ± 0.5 hr), and the right column shows the presence of periodicity of about 30 min in both dayglow (observed, estimated) and TEC for the same period. 98

Figure 4. 1: examples of SAR arcs seen at Millstone Hill, Westford, MA. Each panel shows unwrapped all-sky images at millstone hill captured between 05:00-06:00 UT (LT=UT-5 hr) on the night of 28 December 2003. The OI 630.0 nm (red line) and 557.7 nm (green line) emissions are represented in top panels (a and b), and bottom panels (c and d), respectively. For each image, N and E represents the geographic north and east directions, respectively. The bright northern most part in each image is aurora (marked by dashed arrow), whereas, to the equatorward of aurora, a SAR arc is seen in the red line (solid arrow), which is clearly absent in the green line emission, representing their spectral purity. From optical aeronomy at Boston university (buimaging.com). 102

Figure 4. 2: observation of SAR arc during nighttime over Millstone Hill on 1 June 2013 (left column) along with the latitudinal variation of DMSP measured ionospheric ion density (Ni) and electron temperature (Te) (right column). The enhanced Te peak corresponds to the region of SAR arc. After Martinis et al. (2019). 103

Figure 4. 3: locations of Te enhancements (≥ 5000 k) at the lowest subauroral latitudes (represented by L value) versus local time, as observed from all DMSP passes on 26–27 Sep 2011. Different symbols indicate the different satellites and the hemisphere where the observations were made. The in-situ measured Te peak between L=2-4 and 06-18 LT suggest the presence of SAR in dayside. After mendillo et al., 2013. 104

Figure 4. 4: the daytime OI 630.0 nm airglow emissions on geomagnetically quiet (a, b) and disturbed (c, d) days are shown: HIRISE measurements (red filled circles with ±1σ uncertainties), WEM estimates (black dashed line), and GLOW estimates (blue asterisks). The measured and estimated emissions match well during quiet conditions. The enhancements in measured emissions on 7 December 2006 (panel c), are due to a stable auroral red arc event observed during the daytime for the first time. 106

Figure 4. 5: digisonde obtained NmF2 comparison for each day shown in Figure-4.4, representing the largest enhancement in densities on 14 December 2006 as reflected in HIRISE measured and GLOW estimated larger emission intensities. 107

Figure 4. 6: millstone hill ISR measured electron temperature (Te) profiles on 7 and 14 December 2006 in the altitude range 100–600 km. Increased values of Te can be noted on 7 December during similar interval of measured larger emissions, marked by the white-dashed lines. 108

Figure 4. 7: the dynamics explorer (DE)-2 spacecraft observed precipitating electrons in the lowest energy channels in dayside during 22:48 UT and 22:51 UT. (Adapted from Kozyra et al., 1997.) 109

Figure 4. 8: a) DMSP measured Te and Ni latitudinal variations are shown in top and bottom panel, respectively between 45°–70°N magnetic latitude range near 16.4 UT (11.4 LT) at ~850 km altitude. The dashed vertical lines correspond to 54°–55°N MLAT, overlapping with the latitudinal location of Boston (54.35°N MLAT). A peak in te close to the equatorward boundary of mid-latitude trough (bottom panel) can be seen. **B)** the latitudinal Te variation for all dayside DMSP passes covering 30° and 70°N MLAT range is shown, which reveals a region of enhanced Te between 50° and 60°N MLAT globally. White filled-circle line represents the temporal movement of Te peak, reaching below 54°N MLAT (dotted line) during the observational period between 17 to 19 UT. 110

Figure 4. 9: latitudinal variation of equatorward boundary of ionospheric trough in 40-70°N MLAT range using dmsp measured Ne. Dashed line marks the observation magnetic latitude. The vertical arrows represent the temporal movement of trough. 111

Figure 4. 10: a comparison of digisonde Ne obtained output of GLOW model with the output obtained after providing first 'ISR Ne only' and then 'ISR Ne, Te both'. The HIRISE observed dayglow emissions are also overplotted (red dots). 113

Figure 4. 11: ISR measured averaged Te in the altitude range of 520–540 km (Te_high_alt) and 320–340 km altitude (Te_low_alt) is shown by blue dots in top and bottom panels, respectively, along with the 630.0 nm emissions on 7 December 2006. The green-asterisks represent the interpolated emissions with respect to the times of ISR measurement. In the top panel, a strong positive

correlation of 0.76 can be seen between Te_high_alt and dayglow during 12.6 and 14.2 LT, while the emissions were strongly anti-correlated with bottomside Te during the same period (bottom panel)..... 114

Figure 4. 12: the left plot shows the IRI predicted usual Te profiles in 100-650 km altitude range on 7 Dec 2006, while the right plot shows the forward modeling (FM) obtained Te at each altitude above 200 km. Larger Te values obtained by FM can be seen clearly at higher altitudes, which were absent in those predicted by the IRI. 116

Figure 4. 13: in top panel, HIRISE (red dots) and GLOW (blue asterisks) emissions are shown. The green-asterisks present the GLOW emissions obtained after performing the forward modeling (FM). The right-side y-axis shows the FM estimated Te (sky-blue dots) in GLOW model to match the model estimates with the observed emissions during the period of 12.5–14.75 LT. The bottom panel compares the fm estimated Te with ISR_Te_high and ISR_Te_low. It is clearly evident that electron temperature values were larger corresponding to that measured by HIRISE than that of ISR. 117

Figure 4. 14: other days showing larger brightness of HIRISE measured OI 630.0 nm emissions than the modeled brightness at different local times (indicated by dashed-black vertical arrow), similar to 7 December 2006. 118

Figure 5. 1: a) a flow chart representing the process of downward heat flux responsible for the formation of SAR arcs. **B)** a typical thermal electron maxwellian distribution within a SAR arc region. The shaded region represents the population of thermal electrons responsible for SAR arc emissions. (Adapted from Kozyra et al., 1997). 122

Figure 5. 2: 630.0 nm dayglow temporal variations are shown for four days. Bottom and top x-axes represent the local and universal time (LT=UT-5 hr). The red-color shows the HIRISE measured dayglow emissions over Boston, black line and blue color represents the WEM and GLOW estimates, respectively. The panel-a (30 October 2006) shows a geomagnetically quiet day with daily average, <Kp>=2 and maximum Kp (Max_kp) during daytime hours as 2+. Panels-(b,c,d) show three disturbed days with <Kp> and Max_kp ≥ 3 and 3+, respectively. The F10.7 for each of the days is also shown. Larger measured emissions by HIRISE on 20 February and 10 November 2006 are due to SAR arcs in the daytime. 127

Figure 5. 3: panels a and b show ground-tracks of three different DMSP passes on 20 February2006 and 10 November 2006, respectively, with dayglow observation location, Boston indicated by red star. The panels-c,e,g show the latitudinal Te variation for three passes on 20 February (shown in panel-a) in 20-70° N MLAT range. Similarly, panels-d,f,h represent Te variation on 10 November. The times of dmsp pass over ~52° N MLAT (marked by dashed vertical line) are indicated next to each Te profile. The black-solid line shows the polynomial fits for each Te variations. A sharp Te peak can be seen at 17.34 UT corresponding to observed enhancement in dayglow on 20 February near 13 LT (18 UT) and another Te peak on 10 November from 12.80-14.89 UT, in conjunction with the observed emission brightness duration around 7.2-10 LT (12.2-15 UT). 129

Figure 5. 4: similar to Figure-5.3 but for 630.0 nm daytime airglow emission observations on 24 November 2006. 130

Figure 5. 5: the left columns show four disturbed days of dayglow observation, similar to Figure-5.2c and 2d. The middle column shows respective DMSP measured latitudinal Te variation for two

different passes- one during the time of observed enhancement in 630.0 nm emissions (red-color) and other just before/after this duration (black-color). The dotted-black and red-dashed arrow corresponds to the MLATs of observation of enhanced emission and maximum in Te in 40-60° MLAT range for the first pass. For each profile, a polynomial fit was performed in the 40-60° MLAT range to show Te peak clearly. The right column shows the corresponding DMSP ground-tracks. The poleward shift or disappearance of Te peak can be seen before/after the duration of observed enhancement in emissions by black-colored Te variation. 132

Figure 5. 6: a) diurnal variations in GPS-TEC for all days listed in Table-5.1. The vertical lines correspond to the time of observed increase in the 630.0 nm emission brightness on each day. A clear reduction with no remarkable increase in plasma density can be seen during the period of enhanced emissions on these days, which rules out the in the observed increase in brightness due to the topside density variation **b)** dmsp measured latitudinal Ne variations between 20-70°N MLAT range corresponding to the time of peak Te occurrence for each day. The dashed line corresponds to the MLAT of observational location, while squares represent the location of Te peak for each latitudinal Ne. 134

Figure 5. 7: emission rates obtained by forward modeling (FM) are shown by blue-asterisks for all days listed in Table-5.1. FM was performed during the period when HIRISE observed emissions were larger than the model estimates. The FM estimated emissions match well with the HIRISE observed emissions. The right-side y-axis shows the FM estimated maximum Te (in 200-650 km) required to produce higher magnitudes of $O(^1D)$ emissions that match with the observed emissions. 136

Figure 5. 8: van allen probe (VAP)- B (left) and VAP A (right) data from HOPE and EMFSIS instruments is shown. The location of the plasmapause associates with enhanced fluxes in the O, He and H ion species during ~08:00 - 08:20 UT. The field lines data obtained by both probes connect to region of SAR arc being measured by the Millstone Hill ASI (shaded blue region). After Gallardo-Lacourt et al., 2021. 137

Figure 5. 9: an example of forward modeling (FM) obtained Te profile to estimate the electron heat flux at 300 and 500 km altitudes. 139

Figure 5. 10: the estimated heat-flux at 300 (blue dots) and 500 km (red-dots) altitudes using the FM computed Te profiles. The solid-blue line represents the best polynomial fit (φ_{fit}) through the measured data points. The obtained relation has been used to calculate the heat flux associated with dmsp peak Te as shown by green dashed line. A non-linear behavior between the estimated heat flux and Te can be seen. 140

Figure 5. 11: ASI captured nocturnal 630.0 nm image at Gakona on 4 November 2019 (a), along with DMSP-F15 measured electron density (b), ion velocity (c), and electron temperature (d) are shown. Panel-(e) represents the nighttime red line emission intensity observed at Athabasca close to the footprint of DMSP satellite. The Gakona station is marked by black dot at the center of the image. DMSP pass is shown by black dashed line crossing the SAR arc at 13:24:50 UT mapped to altitude of 400 km. The SAR arc emission intensity can be seen aligned directly with the Te peak indicated by red vertical dashed line. After Inaba et al., 2021. 142

Figure 5. 12: the hemispherical electron flux obtained from GLOW model (square symbol) and by using the Maxwellian Distribution Function (black dashed curve) at nearly same characteristic energy (e_m = 0.41 ev), marked by dotted vertical line. Red and blue color indicates the variations corresponding to high and low solar activity periods i.e., 2015 (HSA) and 2018 (LSA), respectively. 145

Figure 5. 13: a) in-situ measured electron density (Ne), and **b)** electron temperature (Te) variations (black dots) in conjunction with each SAR arc observation between the year 2012 and 2020 for solar cycle-24 are shown with respect to solar activity index F10.7 (red open circles). A direct and inverse relation of electron density and electron temperature enhancements with solar flux can be seen. Panel **c)** shows the strong dependence of measured SAR arc intensity with respect to simultaneous electron temperature measurements with a correlation coefficient of 0.72. 146

Figure 5. 14: a) the estimated electron heat flux at 650 km altitude using measured SAR arc emissions and corresponding Te enhancement is shown. The red and blue dots indicate the variations in the obtained electron heat flux during HSA and LSA periods, respectively. Panel **b)** shows the estimated heat flux (black dots) variation with solar flux F10.7 (red open circles). The positive correlation of 0.7 between heat flux and F10.7 suggest the strong dependence of downward energy input with solar activity..... 147

Figure 5. 15: a) the estimated heat flux does not show any correlation with respect to in-situ measured electron density (Ne) at ~800 km altitude. **B)** the heat flux has a strong positive correlation with the estimated ionospheric Ne at 650 km altitude obtained by using Maxwellian energy distribution function. This indicates the major influence of ambient electron densities in governing the magnitude of downward heat flux. 149

Figure 5. 16: a) the modeled volume emission rates (VER; photons cm^{-3} sec^{-1}) for typical OI 630.0 nm nightglow (without heat flux) and sar arc case (with heat flux) are shown by open and filled dots respectively. Red and blue color indicates the solar activity maximum and minimum durations, as represented by F10.7 index, respectively. Both profiles were derived at nearly same characteristic energy (e_m=0.41 ev). The variation in VER profile for SAR arc case can be seen due to additional heat input, as compared to the typical nightglow profile. **B)** the variation in peak altitude of modeled SAR arc emissions with respect to solar activity variation is shown. During low periods of solar activity, SAR arc emissions can originate at lower heights as compared with HSA. 151

Figure 6. 1: the three classes of atmospheric waves are shown. The waves can oscillate in three different directions. The variation of magnitudes is not to scale. (after Beer, 1974) 158

Figure 6. 2: an illustration of a mountain wave (Lee wave) depicting an internal gravity wave generated by airflow over a mountain range. (after Andrews, 2010)..... 159

Figure 6. 3: schematic representation of internal gravity waves with downward phase propagation and instantaneous velocity vectors. Energy flow is obliquely upward. (Kelley, 2009)..... 160

Figure 6. 4: diurnal and spatial variation of 630.0 nm airglow emission intensities during daytime is shown on a geomagnetically quiet day of 05 March 2006 (<kp>=0+). The noon time missing data is due to the saturation of CCD. 162

Figure 6. 5: a) the 15-minute averaged spatial variation of 630.0 emission intensity in meridional direction at 14.88 LT is shown by a red solid line on 05 March 2006. The 350 km running average is shown by a black dashed line. The residual (difference between running average and dayglow) is shown by a blue dash-dot line. **B)** the Lomb-Scargle periodogram analysis of the residual is shown by the solid blue line. The horizontal dashed line represents the 90% false alarm limit (FAL). The significant scale sizes with normalized power spectral density (PSD) above FAL are shown by blue dots..... 163

Figure 6. 6: the diurnal variation of valid scale sizes as obtained from the spectral analysis on 05 March 2006 is shown by gray dots. The red dots indicate the corresponding scale sizes with maximum (PSD) at a given time. 164

Figure 6. 7: the calculated scale size with maximum PSD above 90% FAL for each day during data availability from 2005-2007 is shown by a gray dash with respect to local time. The data is binned at one hour time resolution. The red dots indicate the average of scale sizes at individual times. 165

Figure 6. 8: the calculated scale sizes binned at 1-hour temporal resolution with respect to local time are shown by red filled dots (connected by dashed line) on a quiet day 01 October 2005, with daily averaged kp=3–. The corresponding AE index variation at the same time intervals is shown by blue-filled squares (connected by a dotted line). The AE values are shown on the right-side y-axis. A correlation coefficient (cc) of 0.84 can be seen between the calculated scale size and AE index variation. 166

Figure 6. 9: the variation of the correlation coefficient between GW meridional scale size and AE index is shown with respect to the day of the year (DOY) during 2005-2007. The filled (open) circles represent the variation on quiet (disturbed) days. The solid blue line is the non-linear fit to the quiet time values, given by Equation-6.3. The blue curve indicates a semi-annual variation in the influence of the AE index on gravity wave dynamics at mid-latitudes. 167

Figure 6. 10: the vertical scale sizes were calculated over a low-latitude location, ahmedabad (23°N, 72.5°E), under quiet times during 2012-2014. The top panel shows the daily averaged scale size values by black dots. The red diamonds show their monthly mean. The bottom panel shows the number of days with data availability for each month during these two years. A semi-annual variation in vertical scale sizes can be seen by the red-dashed curve in the top panel (Mandal & Pallamraju, 2020). 169

Figure 6. 11: a comparison of semi-annual variation obtained for vertical scale sizes (λ_z) and correlation-coefficient between λ_y and AE-index, from equations-6.3 and 6.4 is shown by red-dashed and solid blue curves, respectively, with respect to the day of the year. 172

Figure 6. 12: the distribution of the occurrence frequency during disturbed periods with AL index less than -135 nT, based on 20 years of datasets is shown by black squares (adapted from Ahn & Moon, 2003). The non-linear fit f_2 to the monthly data points is shown by black dotted curve. The correlation fit f_1 is also overplotted by solid blue curve. No significant difference can be seen between the maxima of these two curves, which lie near day 100 and 275 during the spring and fall equinox, respectively. 173

Figure 7. 1: a schematic illustration of the work discussed in the thesis chapters over mid-latitudes during daytime conditions. 178

List of Tables

Table 1. 1: Characteristic time scales for the three types of trapped-particle motion. 7

Table 2. 1: Characteristics of HIRISE. Specifications of each optical components are given. After Pallamraju et al. (2002). 51

Table 3. 1: Change in the ionospheric parameters obtained using altitude profiles from ISR and GLOW during 15-16 LT. 97

Table 4. 1: The corresponding characteristics of daytime O(^{1}D) emission enhancement shown in Figure-4.14, similar to 7 December 2006. 119

Table 5. 1: The observed characteristics of daytime O(^{1}D) emission enhancement measured by HIRISE and DMSP measured peak Te variations. 133

Table 5. 2: Event list of SAR arc conjunction events during years of Solar Cycle-24 observed by previous studies. 143

Table 5. 3: Variation in the measured and estimated parameters for the two SAR arc events shown in Figure-5.16a. 152

Chapter: 1

Introduction

Earth's atmosphere is a fascinating and dynamic system composed of several layers characterized by varying temperatures, pressures, and gas compositions. Near the Earth's surface, the troposphere contains a mixture of gases, primarily nitrogen (78%) and oxygen (21%), along with trace amounts of gases such as argon, carbon dioxide, and water vapor. As altitude increases, the stratosphere, located above the troposphere, contains higher ozone concentrations. This stratospheric ozone protects us by absorbing harmful ultraviolet rays from the Sun. Higher still, the mesosphere and thermosphere contain progressively fewer molecules, primarily lighter gases such as helium, hydrogen, and oxygen atoms.

One important region of the atmosphere is the ionosphere, which is a part of the thermosphere. The ionosphere contains charged particles created when solar and cosmic radiation ionize atmospheric gases. This layer is crucial for radio communications because it reflects and refracts radio waves, allowing them to travel great distances. The ionosphere also interacts with Earth's magnetic or geomagnetic field, which extends from the Earth's interior into space. This interaction helps to form phenomena like auroras, which are beautiful light displays near the polar regions caused by the collision of charged particles from the solar wind with the atmosphere. Each layer of the atmosphere is vital in supporting life on Earth and enabling various technologies. The connection between the ionosphere and the geomagnetic field adds another layer of complexity and importance to studying the upper atmosphere.

Earth's magnetic field can be approximated to be dipolar in nature. The magnetic field lines are almost horizontal over low latitudes and are inclined at high latitudes. The strength of the geomagnetic field is measured in nanoteslas (nT) and varies from ~3.0 x 10^4 nT over the equator to ~6.5 x 10^4 nT over the poles. The magnetic flux density at a distance *r* from Earth's surface decreases in accordance with $1/r^3$. The geomagnetic field is surrounded by a vast region known as the *magnetosphere*, which extends over a large volume in space. Various solar

activities during the Sun's 11-year solar cycle significantly influence the Earth's magnetosphere and atmosphere.

Sun's upper atmosphere, known as the corona, releases huge amounts of charged particles through the solar wind. This solar wind is embedded with the Sun's magnetic field, also known as an interplanetary magnetic field, which is 'frozen-in' to the plasma because of very high electrical conductivity. This interplanetary magnetic field extends out to our solar system. Solar wind speed is supersonic due to heating, compression, and subsequent expansion combination among the solar wind charged particles. The Earth's magnetosphere is continuously bombarded by the solar wind particles. While most of this plasma is deflected by the edges of the magnetosphere, some can penetrate and cause disturbances in the regions of Earth's magnetosphere and the upper atmosphere. The two major solar drivers that can significantly disturb the geospace are Coronal Mass Ejections (CMEs) and Corotating Interaction Regions (CIRs). The strength of CMEs varies during different phases of the solar cycle, and the geo-effectiveness of CIRs is more dominant during the solar cycle minimum. These eruptions are so strong that when they emanate from the Sun, they carry the interplanetary magnetic field (IMF) along with them. IMF consists of three vector components, $\overrightarrow{B_x}$, $\overrightarrow{B_y}$, and $\overrightarrow{B_z}$, where X-axis points towards the Sun from the center of Earth, Z-axis is perpendicular to the ecliptic plane, and Y-axis is orthogonal to X & Z- axis in the Geocentric Solar Ecliptic coordinate system (GSE), as shown by a schematic diagram in Figure-1.1. Therefore, the magnitude of total interplanetary magnetic field (B) is defined as:

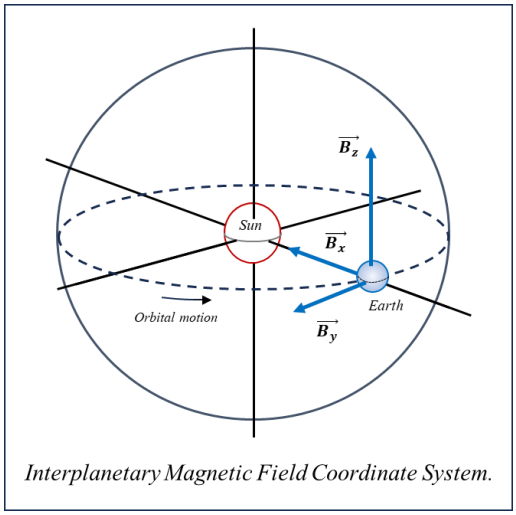

Figure 1.1: *Schematic of Geocentric solar ecliptic (GSE) coordinate systems for Sun-Earth system.*

$$B = \sqrt{B_x^2 + B_y^2 + B_z^2} \tag{1.1}$$

The polarity of the IMF Bz component determines the nature of the coupling between the interplanetary magnetic field and the geomagnetic field. For the negative value of *Bz* or its southward orientation with respect to the northward geomagnetic field, magnetic reconnection

occurs. Due to the magnetic reconnection, a large amount of energy is injected into the Earth's magnetosphere, which increases the strength of ring current particles, which causes geomagnetic storms. The Earth's magnetosphere, ring current, and other respective terminologies have been described in subsequent sections.

1.1 Structure of the Earth's magnetosphere and ionosphere

Earth's magnetosphere is a vast structure that extends up to 10-15 of Earth's radii (R_E, 1 R_E = 6371 km) on the dayside and several hundreds of Earth's radii on the night side. The magnetosphere can be divided into several parts, such as bow shock, magnetosheath, magnetopause, magnetotail, plasmasphere, radiation belts, and magnetospheric currents. Figure-1.2a shows various components of the magnetosphere as discussed below:

Earth's magnetosphere works like a solid object in the way of solar wind. The solar wind-charged particles are not able to penetrate the magnetosphere and are deflected from the top and below it to the night side, forming a bowshock (Fairfield, 1971), shown by the dotted line in Figure-1.2a. Bowshock is the outermost layer of the magnetosphere. It is a transition region where the density, pressure, temperature, and Mach number change abruptly. At bowshock,

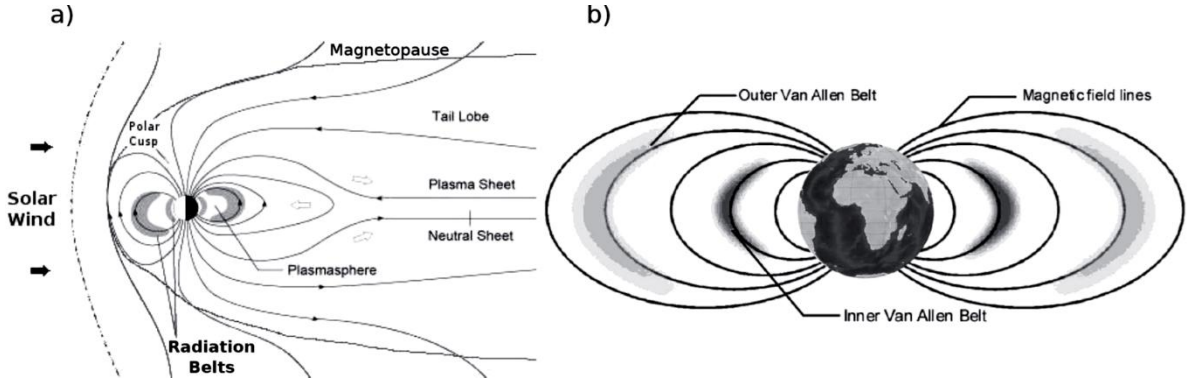

Figure 1. 2: a) *Structure of Earth's magnetosphere along with its various components,* ***b)*** *the typical radiation belt structure in the inner magnetosphere (After Regi, 2016).*

solar wind supersonic speed is reduced to subsonic, resulting in a decrease in Mach number. After bowshock, **magnetopause** (Safrankova et al., 2002) is the boundary of the magnetosphere located at 10-15 R_E in dayside, which was first introduced by Chapman and Ferraro (1933). At the magnetopause region, the pressure exerted by the solar wind is balanced

by the inside geomagnetic field line pressure. Magnetopause separates the geomagnetic field from the solar wind (Russell, 2003). The region between magnetopause and bow shock is known as **magnetosheath**. When the solar wind reaches bowshock, a small amount of plasma enters the magnetosheath. The solar wind speed is reduced to subsonic in this region, resulting in an increase in their thermal energy. The magnetosphere is extended into the nightside of the Earth, forming a long tail known as **magnetotail** (Nishida, 2000). This magnetotail is extended into an anti-sunward direction up to a distance of 30-300 R_E.

1.1.1 Plasmasphere, particle motion, and adiabatic invariants

The innermost region of Earth's magnetosphere is the **plasmasphere**, which is in the form of a toroidal shape encircling the Earth and consists of closed magnetic field lines, i.e., both feet of magnetic field lines connect to the ground on either side of the hemispheres, as shown in Figure-1.2a. The outermost boundary of the plasmasphere is called the **plasmapause,** extending from L = 2.5 to 5.5 in the equatorial plane (Carpenter & Anderson, 1992). The L-value was given by Mcllwain (1961) as:

$$\mathrm{r} = L\,cos^2\theta \tag{1.2}$$

where, θ is the magnetic latitude, and r is the distance from the Earth's surface where a particular magnetic field line will cross the geomagnetic equator in terms of Earth's radii, R_E. For example, the magnetic latitude (θ) of 45°, 60°, and 67.1° will correspond to L= 2, 4, and 6.6, respectively.

As the plasmasphere is tied with the Earth via closed field lines, it corotates along with it. The corotation electric field, E_R, in the equatorial region can be defined as (Kivelson & Russell, 1995):

$$E_R = \left(\frac{B_0}{L^3}\right) L R_E \omega \tag{1.3}$$

where, B_0 is the strength of the magnetic field in the equatorial plane, and ω represents the Earth's angular rotation frequency of about 7.3 x 10^{-5} sec^{-1}. Therefore, this corotation electric field, pointing in the Earthward direction, forces the cold plasma to corotate inside the plasmasphere with the angular velocity of Earth (Carpenter, 1966). The plasmasphere contains dense (around 1-1000 electrons-cc^{-1}) and cold plasma or low-energy (~1-2 electron-Volts, eV)

particles (Lemaire & Gringauz, 1998). The plasmasphere is composed of electrons and positive ions (mainly protons, H^+, ~90% other than He^+ and O^+), and the magnitude of plasma densities can cover a range of several orders (Goldstein, 2007). At heights greater than plasmapause, the plasma density decreases sharply (~1 electrons-cc^{-1}) in the magnetosphere, forming "the Carpenter Knee" (Carpenter, 1963), and this tenuous region can be referred to as the outer magnetosphere.

Based on the characteristics of particles in the plasmasphere, it is also known to form the radiation belts region. The region of radiation belts, also known as Van Allen radiation belts (Van Allen & Frank, 1959), is highly dynamic. There are two radiation belts: The outer and Inner, as shown by a schematic diagram in Figure-1.2b. The outer radiation belt lies around L=3-6 R_E and is known as the electron radiation belt, while the Inner radiation belt, also called the proton belt, lies typically between L=1.5-2 R_E.

The outer radiation belt is majorly composed of Solar wind and magnetospheric plasma, which mostly contain relativistic electrons with energies greater than 1 MeV and make up a large portion of the radiation belt, while protons may be expelled through processes such as Coulomb collisions with electrons. The dynamics of the outer belt are largely governed by geomagnetic disturbances (Baker et al., 1994; Shprits et al., 2008). The proton flux is anticorrelated with solar flux and shows changes with the solar cycle (Miyoshi et al., 2000). The inner belt,

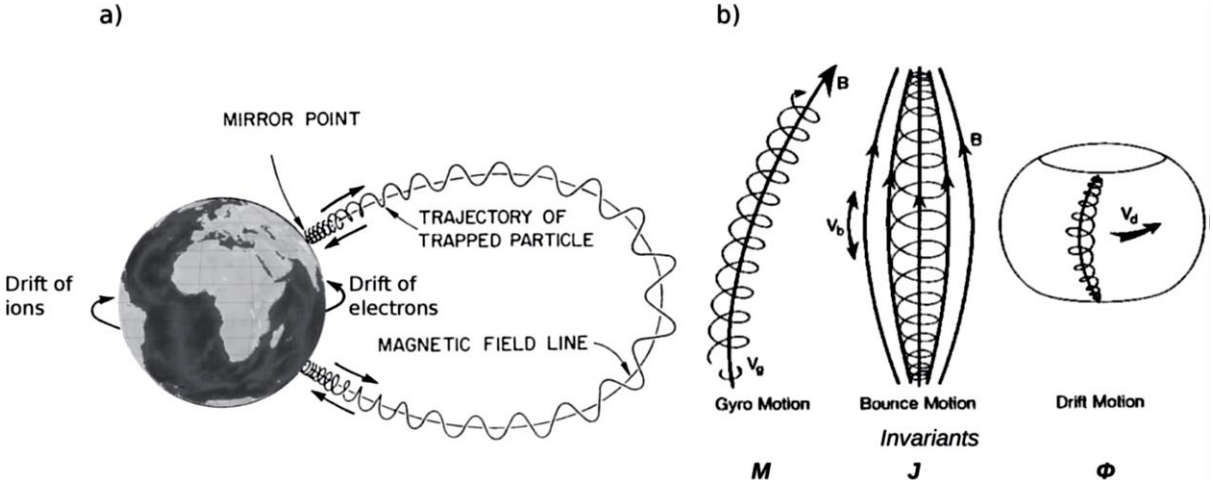

Figure 1. 3: (a) *Schematic representation of a magnetically trapped charged particle in the magnetosphere (Tascione, 1988).* ***(b)*** *Different particle motions (from left to right): gyro, bounce and drift due to first M, second J, and third Φ adiabatic invariants, respectively. (Kivelson & Russell, 1995). The gyro and drift motions are depicted for electrons, the motion is oppositely directed for ions.*

surrounded by the outer radiation belt, has majorly protons of energy 100 MeV and electrons of 10-100 KeV. The innermost region of the proton belt (L < 1.8) is relatively stable, and the variations in flux can be found during disturbed conditions. These radiation belt regions comprising energetic charged particles with energies from keV to MeV can also be detrimental to the low earth orbit (LEO) satellites (Singh et al., 2010). The empty gap between the outer and inner belt (around 2<L<3) is known as the 'safe slot' or 'slot region' and separates the two radiation belts. The 'slot region' is formed due to the scattering of electrons due to wave-particle interaction in the plasmasphere (Meredith et al., 2007).

In the closed magnetic field lines region, particles are trapped and guided by the geomagnetic field, where the energy of trapped particles remains conserved under adiabatic conditions (Figure-1.3a). These trapped particles undergo three different kinds of motion: a) gyromotion (v_g) due to a magnetic field, b) bounce-back motion (v_b) along the field line or grad-B drift, and c) drift motion (v_d) across the field lines or curvature drift, as shown in Figure-1.3b. Each motion follows specific frequencies which are distinctly separated from each other (Roederer, 1970). The local geomagnetic field, $\vec{B}$, exerts a Lorentz force on the relativistic charged particles and makes them rotate around the field line with cyclotron frequency as:

$$f = qB/2\pi m_0\gamma \tag{1.4}$$

where, γ is defined as $1/\sqrt{(1-(v/c)^2)}$, q, v, and m_0 is the charge, rest mass, and velocity of the particle, respectively, and c is the speed of light. Thus, the most rapid gyro motion of the particle is defined by the cyclotron frequency (f), and the velocity of the guiding center is indicated by (v_g). The magnetic moment (M) generated due to this gyro motion is conserved and known as the *first adiabatic invariant*, which is given by,

$$M = p_\perp^2/2m_0B \tag{1.5}$$

Here, $p_\perp$ represents the projection of relativistic particle momentum ($\vec{p}$) in the perpendicular direction to $\vec{B}$. Additionally, if the parallel component (i.e., $p_{//}$) of $\vec{p}$ to $\vec{B}$ over the magnetic equator is non-zero, then the particle also starts motion along the field line from the equator to poles or higher latitudes. The ratio of perpendicular to parallel component of particle velocity or momentum defines the *pitch angle,* α, as $\alpha = \tan^{-1}(v_\perp/v_\parallel)$. Since the strength of the geomagnetic field is larger near the poles than the equator, the $p_\parallel$ component reduces as the particle moves towards the footprint of the field line and slowly becomes zero. In this case,

only *the* $p_{\perp}$ component acts on the particle, and thus, the motion is reversed at this point to an equatorward direction. This point, where the $p_{\perp}$ component dominates and $p_{\parallel}$ becomes minimal, is known as *the mirror point*, with the energy being conserved. At mirror points, the pitch angle α reaches 90°. Therefore, the particle keeps moving back and forth between two mirror points in both hemispheres, where the feet of field lines are connected to the ground, and the motion is referred to as *bounce motion*. During bounce-back motion, the quantity $J = \oint p_{\parallel} ds$ remains conserved and is known as the *second adiabatic invariant*, where *s* signifies the distance of footprint of a magnetic field line from the equator along the curved path. Under the dipolar approximation, the strength of the geomagnetic field in the equatorial plane increases radially earthward. This induces the azimuthal (or curvature) drift motion to the guiding center of the charged particle from one field line to other, where the magnetic flux Φ, known as *third adiabatic invariant,* remains conserved under the drift shell during such motion.

Type of Particle Motion	Adiabatic Invariant	Conserved quantity	Electron period (second)	Proton period (second)
Gyro	First	M	10^{-3} to 10^{-4}	10^{-1} to 10^{-2}
Bounce-back	Second	J	0.1	1
Drift	Third	Φ	100-1000	100

Table 1. 1: *Characteristic time scales for the three types of trapped-particle motion.*

These different particle motions with their characteristic time scales (for both electrons and protons) and corresponding adiabatic invariants have been summarized in Table-1.1.

1.1.2 Ring current and geomagnetic storms

The motion of charged particles around Earth is oppositely directed for oppositely charged particles. Protons follow a westward drift, while electrons drift eastward, resulting in the formation of a net westward electric current, known as the *ring current,* which flows in the region of around L= 1.5 - 5 R_E. As mentioned, the trapped charged particles follow three different kinds of motions due to the geomagnetic field; the current density is defined by the electric current per unit cross-section area. By the conservation of the first adiabatic invariant,

the current density (J) becomes equal to the sum of individual currents due to gyromotion, bounce-back motion, and the curvature drift as given below:

$$\boldsymbol{J} = \frac{\boldsymbol{B}}{B^2} \times \left[\nabla P_{\perp} + \frac{P_{\parallel} - P_{\perp}}{B^2}(\boldsymbol{B}.\nabla)\boldsymbol{B}\right] \tag{1.6}$$

where, $P_{\parallel}$ and $P_{\perp}$ represents the parallel and perpendicular components of plasma pressure, respectively, which are given as:

$$P_{\perp} = \int \frac{1}{2} m v^2 f(\boldsymbol{v}) sin^2\alpha \, d\boldsymbol{p} \tag{1.7}$$

and

$$P_{\parallel} = \int m v^2 f(\boldsymbol{v}) cos^2\alpha \, d\boldsymbol{p} \tag{1.8}$$

where, f and α represent the phase space density and pitch angle, respectively. The gyromotion of charged particles is represented by the first term on the right-hand side in Equation-1.6, also known as *diamagnetic current*. For the case of ring current, this first term, i.e., the diamagnetic current, dominates over the second term of Equation-1.6, which consequently results in the westward (eastward) flow of ring current in the outer (inner) region (Lui et al., 1987).

The ring current strengthens during the southward component of IMF B_z (Kokubun, 1972). The interaction of southward-directed IMF (B_z<0) with the northward geomagnetic field causes the magnetic reconnection, wherein closed field lines at magnetopause in dayside reconnect with the interplanetary magnetic field and are dragged in the anti-sunward direction along with

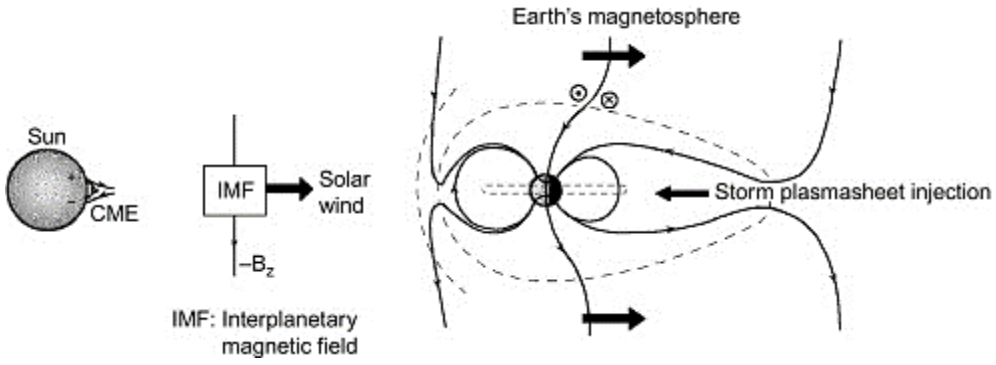

Figure 1. 4: *A schematic of dayside magnetic reconnection process and again in nightside for southward directed IMF Bz along with magnetic field and plasma convection (Tsurutani et al., 2003).*

the solar wind and again reconnect in the night side (Dungey, 1961). This process of breaking of field lines and then reconnecting is known as magnetic reconnection, as shown in Figure-1.4. The magnetic reconnection allows the transfer of solar wind energy, mass, and momentum and the direct entry of charged particles of solar wind origin inside the magnetosphere, and more plasma is accumulated in the inner magnetosphere (Dessler & Parker, 1959; Sckopke, 1966). As the particles in the ring current are enhanced and gain more kinetic energy, this results in the intensification of the ring current and decreases the horizontal component (H-component) of the magnetic field on the surface (Egeland & Burke, 2012). The depression in the Earth's magnetic field during prolonged southward IMF B_z (~few hours) is known as geomagnetic storm.

The observation of storm phenomena suggests that there are three phases of the storm. These phases are the a) initial phase, b) main phase, and c) recovery phase, as shown in Figure-1.5. The Dst index (Disturbance storm time index) is developed to measure the strength of magnetic disturbance (Sugiura, 1963), which is formalized by using the speed and density of solar wind along with the IMF B_z component (Burton et al., 1975). During the initial phase, Dst shows increased magnetic strength, which is known as the storm sudden commencement (SSC), and this phase can last from a few minutes to a few hours. When B_z turns southward, the main phase of the storm begins, and Dst shows a depression. The Dst index turns towards greater negative values during the main phase of the storm. The larger the negative value of Dst, the larger the severity of the storm. As the IMF B_z turns northward again and the intensified ring current starts to decay, the recovery phase starts, and Dst starts increasing again from its minimum value to the

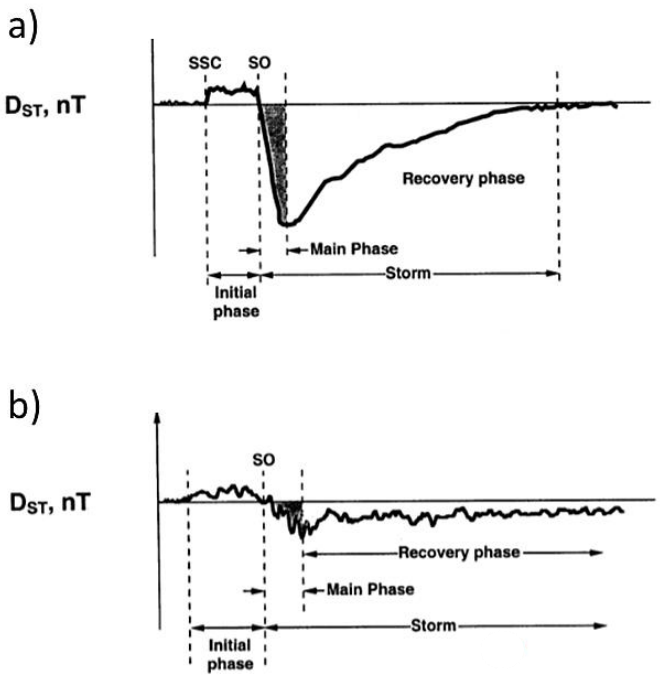

Figure 1. 5: *A schematic of Dst-index is shown to identify the magnetic storms. Panel (a) shows a magnetic storm caused by a CME (mostly occur during solar maximum). Panel (b) shows a magnetic storm caused by a CIR. 'SO' stands for storm onset. (Tsurutani, 2000).*

quiet time values. The recovery phase lasts around one to six days. A typical nomenclature has been classified to define the strength of geomagnetic storm by different ranges of minimum Dst-index (Dst_{min}) as below-

(i) quiet to mild storm (-30 nT > Dst_{min} > -50 nT)

(ii) moderate storm (-50 nT > Dst_{min} > -100 nT)

(iii) intense storm (-100 nT > Dst_{min} > -250 nT)

(iv) super storm (Dst_{min} < -250 nT)

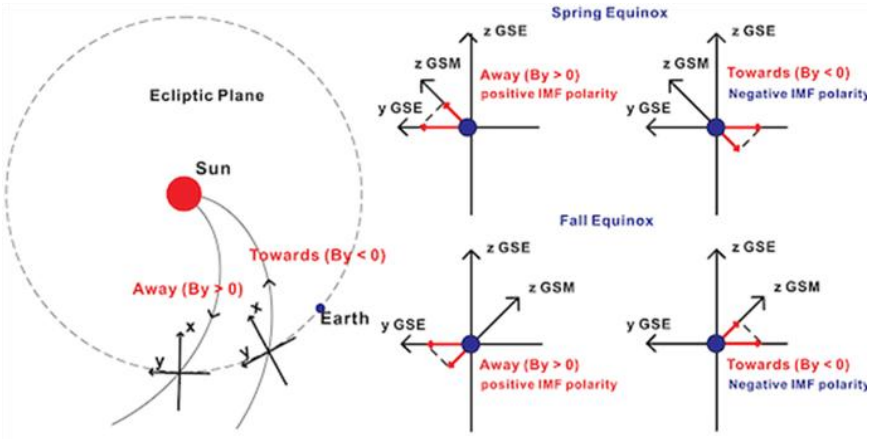

Figure 1. 6: *A schematic diagram of Russell-McPherron effect showing the maximum possibility of southward Bz during spring equinox for negative IMF polarity and during fall equinox for positive IMF polarity (Zhao & Zong, 2012).*

A semi-annual variation has been observed in the geomagnetic activity, which is maximum around spring and fall equinoxes. This variation is also known as the Russell-McPherron (R-M) effect (1973). The R-M effect defines the variation in geomagnetic activity on the basis of IMF B_z polarity. Figure-1.6 shows the dependence of southward IMF with the sunward/anti-sunward direction of the IMF Bx component. According to this hypothesis, intense activity can occur during the fall equinox for the anti-sunward direction of IMF and during the spring equinox for the sunward direction of IMF (B_x > 0).

1.1.2 Ionospheric D, E, and F-region

The upper atmosphere of Earth starts from around 80-90 km and goes up to 1000 km from the surface (depending on solar activity) and contains both neutral and ionized species. The neutral portion of the upper atmosphere is called *the thermosphere*, in which the neutral temperature increases with altitude because of the absorption of solar extreme ultraviolet (EUV) radiation by atoms and molecules and reaches from around 700 K to greater than 1000 K from low to high solar activity, respectively (Figure-1.7). Since the absorption cross-section of neutral species for solar EUV radiation is greater, hence these EUV photons get absorbed in the upper atmosphere at various wavelengths, and the ionization processes can be described as:

$$X + h\nu \rightarrow X^{+} + e\text{-}$$

where, X indicates a particular species (e.g., Oxygen atom (O), Hydrogen atom (H), Nitrogen molecule (N_2), etc.), h is Planck's constant, and ν is the frequency of solar photon. The photon energy ($h\nu$) should be greater than the ionizing potential of species X for the process of photoionization to occur. There exists a *turbopause* at around 100 km altitude. Below and above the turbopause, regions are homogeneously mixed (because of turbulent mixing) and

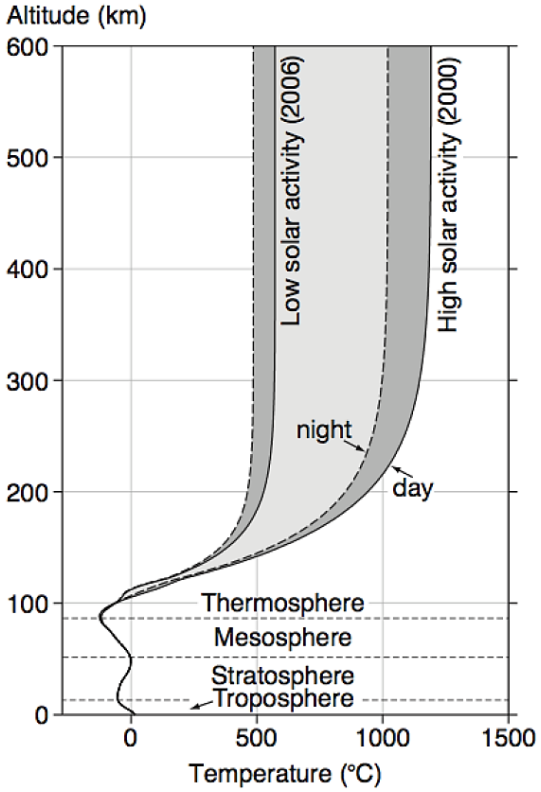

Figure 1. 7: *Neutral temperature profile of the atmosphere for day and nighttime and during different solar activities. From Doornbos (2012).*

inhomogeneous in nature (i.e., molecular diffusion governs the altitudinal distribution), respectively. Above turbopause in the thermosphere, the density of each neutral species decreases with altitude according to the following Equation-

$$n(X) = n_0(X)e^{-z/H} \tag{1.9}$$

where, n is the number density of the species, n_0 defines the density at a reference altitude, z is height, and H is the *scale height,* defined as $H(X) = k_B T/m_X g$; where, k_B is Boltzmann's constant, T is temperature, m_X is the atomic or molecular mass of 'X' and g is the acceleration due to gravity.

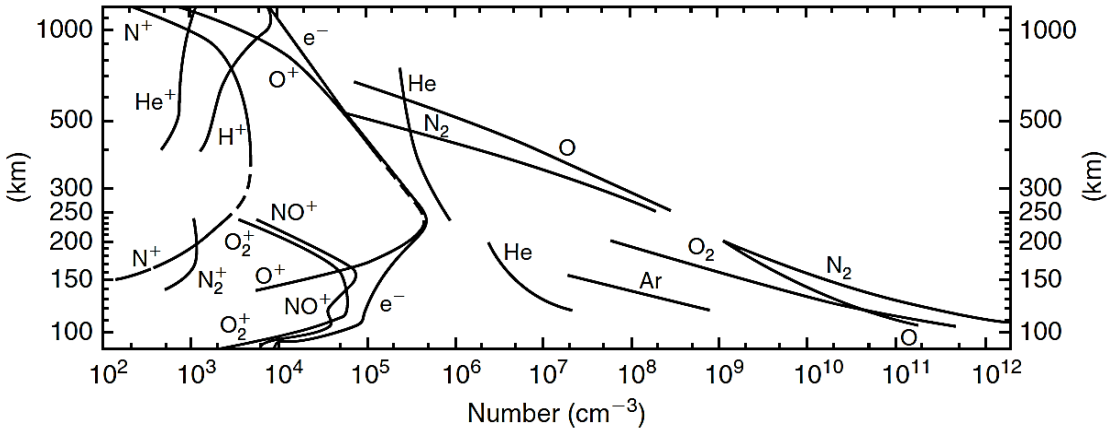

Figure 1. 8: *International Quiet Solar Year (IQSY) daytime plasma and neutral composition. Helium distribution is from a nighttime measurement. (Adapted from Kelley, 2009).*

Earth's *ionosphere* is a partially ionized region of the upper atmosphere and contains a high density of plasma in the form of charged particles (i.e., electrons and ions). The ionospheric plasma coexists with the thermosphere, i.e., the region of neutral atmosphere. The number density of neutrals (N_n) is three orders larger than the plasma density, and the various compositions of neutral and plasma densities are shown in Figure-1.8. In the ionosphere, the electron densities, Ne, and ion densities, Ni, are nearly equal to each other, resulting in a nearly zero net electrical charge density, and this feature of plasma, i.e., Ne ≈ Ni, is known as *quasi-neutrality*. The solar wind and magnetospheric plasma also follow quasi-neutrality; however, in this case, plasmas are completely ionized without having any neutrals, which is not the case in the Earth's upper atmosphere. Earth's ionosphere begins at a height of around 60 km and extends up to 1000 km. The plasmasphere is known to be the extension of the ionosphere beyond 1000 km. Therefore, the top of the ionosphere acts as a base of the plasmasphere. Under quiet solar conditions, the typical magnetic field lines at plasmapause map down to the

geomagnetic latitude of around 60° at the surface of the Earth. At mid-latitudes, the ionospheric plasma can reach the conjugate ionosphere or the inner radiation belt region due to ionospheric outflow following the field lines or may become trapped in the plasmasphere (Walt, 1994; Hultqvist et al., 1999).

Based on the vertical stratification and composition of neutral constituents (O, N_2) in the Earth's atmosphere, the ionosphere has been categorized into different regions, namely, D-region (60-90 km), E-region (between 90 - 130 km), and F-region (above 130 km). On occasions, the F-layer can be further split into two regions, F1 and F2, where the F2-layer covers an altitude range of about 180–400 km. During nighttime, D and F1 regions disappear due to the unavailability of ionizing solar radiation, and the densities in the E-region are also reduced. The Figure-1.9 shows the vertical structure of electron density over mid-latitudes. The maximum electron density in the ionosphere (NmF_2) exists at the peak height of the F2 layer (also called hmF_2), and as we go towards higher altitudes, the plasma density decreases. The maximum value of electron density in the ionosphere is of the order of about 10^6 cm^{-3}. Also, during the daytime, the NmF_2 is approximately proportional to the thermospheric O/N_2 ratio (Rishbeth & Barron, 1960; Pirog, 2006). The O/N_2 is the ratio of vertical column densities of Oxygen atom to Nitrogen molecule, where $[N_2]$ is calculated at a standard depth of 10^{17} cm^{-2} with respect to the solar zenith angle.

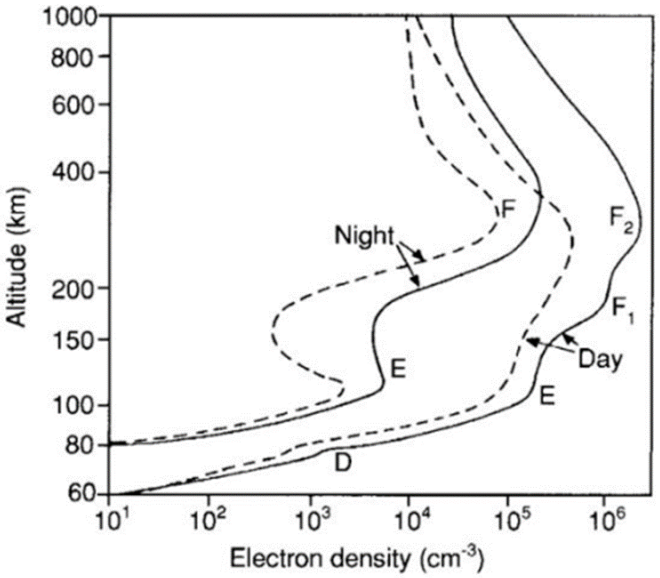

Figure 1. 9: *Day and nighttime Ionospheric electron density profile during low and high solar activity (Courtesy: Hargreaves, 1992)*

In the D region, the major sources of ionization are the Lyman-alpha line of solar chromospheric hydrogen (λ = 121.5 nm), hard x-rays from the Sun (λ = 0.2 - 0.8 nm), and cosmic rays, while during storm times, the precipitation of energetic particles of solar wind origin also ionizes the atmosphere. In the E-region, the Lyman-alpha line and soft x-rays (λ = 30 - 100 nm) cause the ionization of major species of O_2 and N_2 molecules. Therefore, the most abundant species are NO^+ and O_2^+ in the D and E regions and are quickly lost by ion-electron

dissociative recombination. The degree of ionization does not reach beyond the value of $N_e/N_n \approx 10^{-10}$ in the D-region. In the F1 region, solar X-rays in the wavelength range of 1-10 nm ionize all species, and EUV radiations in the wavelength range of 80-102.7 nm cause ionization of molecular oxygen, causing the maximum density in the F2 layer. The degree of ionization in the E and F2 layers has a value $Ne/Nn \approx 3 \times 10^{-8}$ and $\approx 10^{-3}$, respectively. Both ions and electrons show different kinds of motion in the D, E, and F regions (Rishbeth & Garriott, 1969; Rishbeth, 1997). If ν_{in}, ν_{en} are ion-neutrals collision frequency, electrons-neutral collision frequency, and ω_i, ω_e are ion and electron gyro-frequencies, respectively, then, for different ionospheric regions, we get-

$$\begin{aligned} \mathrm{D-region:}\ \frac{\nu_{in}}{\omega_i} &\gg 1 \ \text{and}\ \frac{\nu_{en}}{\omega_e} \gg 1 \\ \mathrm{E-region:}\ \frac{\nu_{in}}{\omega_i} &> 1 \ \text{and}\ \frac{\nu_{en}}{\omega_e} \ll 1 \\ \mathrm{F-region:}\ \frac{\nu_{in}}{\omega_i} &\ll 1 \ \text{and}\ \frac{\nu_{en}}{\omega_e} < 1 \end{aligned} \qquad (1.10)$$

A relation between the plasma frequency (f_p) and electron density is given as $f = 9 \times 10^{-3}\ N_e^{1/2}$ where f_p is in Megahertz (MHz) and N_e is in cm^{-3}. For example, as the maximum electron density in the ionosphere is of the order of 10^6 cm^{-3}, therefore the maximum plasma frequency is $(f_p)_{max} \approx 10$ MHz. The total integrated electron density in a given column of a unit cross-section area in the ionosphere is known as the ionospheric total electron content (TEC). The unit of TEC is defined as TECU (total electron content unit), and 1 TECU = 10^{12} electrons/cm^2. The ionospheric region above the peak of the F-layer contributes to approximately 80% of the TEC available in the ionosphere and is referred to as the topside ionosphere (Bilitza, 2009). The region below the F-layer peak is usually known as the bottomside ionosphere and typically corresponds to lower altitudes up to about 300-350 km. In the bottomside ionosphere, as the neutral densities are larger, higher ion-neutral collision frequencies reduce the chemical lifetime of an ion. These ions are expected to follow the ambient photochemical equilibrium (equilibrium between the production and chemical loss of individual ions). Meanwhile, for the topside ionosphere, the timespan of an ion is enhanced compared to its horizontal or vertical transport time. For a condition of a chemical lifetime much greater than the vertical transport time of plasma, similar to the topside ionosphere, the diffusive equilibrium is valid, and therefore, Ne varies exponentially with respect to height in the topside ionosphere. A general continuity equation for the density N of electrons or ions can be defined as:

$$\frac{\partial N}{\partial t} = q - L(N) - \vec{\nabla}.\left(N\vec{V}\right) \quad (1.11)$$

In the above Equation-1.11, the first term 'q' on the right-hand side indicates the local production of ionization, the middle term '*L(N)*' represents the loss term mainly due to recombination and charge exchange reactions, while the third term '$\vec{\nabla}.(N\vec{V})$' represents the transport due to different mechanisms such as advection and ambipolar diffusion. In the D, E, and F1 regions (typically in the bottomside ionosphere), production (*q)* is much greater than transport ($\vec{\nabla}.(N\vec{V})$) due to strong solar radiation. Since recombination and other loss processes (L) are also significant at these altitudes, the electron density is primarily controlled by local photochemical balance ($q \approx L$). Thus, local production dominates in this photochemical regime during the day, while transport remains less effective (i.e., $\vec{\nabla}.(N\vec{V}) << q, L$). While, in the F2-region (topside ionosphere), photoionization decreases with altitude and recombination processes are slow ($q << L$). As a result, transport dominates (i.e., $\vec{\nabla}.(N\vec{V}) >> q, L$) and acts as a primary factor in redistributing the plasma. The mid-latitude ionosphere is strongly influenced by the magnetosphere or plasmasphere (inner-magnetosphere) in the form of electrodynamic magnetosphere-ionosphere (M-I) coupling. During storm times, the horizontal transport of plasma in the mid-latitude ionosphere also gets influenced by the imposition of storm-time electric fields, which drive $E \times B$ drifts. These drifts transport plasma perpendicular to both the electric and geomagnetic fields, leading to various phenomena in the mid-latitude ionosphere, as discussed below. Therefore, the study of such ionospheric phenomena at mid-latitudes serves as a good proxy for the investigation of underlying mechanisms in the plasmasphere and/or magnetosphere.

1.2 High and mid-latitude phenomena due to magnetosphere-ionosphere coupling

1.2.1 Aurora

The high-energy protons and electrons of solar wind and/or magnetospheric origin are precipitated in the Earth's high latitude upper atmosphere due to the open field lines and deposit energy by exciting and ionizing the thermospheric species. As the excited atoms or molecules in high latitude upper atmosphere come to their ground states, they emit photons. This

magnificent display of light emitted by the excitation of auroral species due to the precipitation of energetic electrons is referred to as *Aurora*. The visibility of aurora depends on the energy of precipitating particles and takes place in an oval-shaped region at high latitudes (Akasofu, 1981). The energies of precipitating electrons regulate the lowest altitude of energy deposition and corresponding ionization of species. The electrons with energies of keV range can penetrate the E-region heights or even lower, while low energetic electrons (a few eV) mostly deposit their energy above the peak of the F-layer. The most common species that are excited by such particle precipitation are atomic oxygen and N_2. The excited N_2 molecule produces blue line emissions at 391.4, 427.8, and 470.9 nm below 90 km. The atomic oxygen excitation causes green line (557.7 nm) and red line (630.0 nm) auroral emissions in the E-region (near 120 km) and F-region (near 250 km or higher), respectively. While several other emissions also take place in Aurora, the green line emission in Aurora is most intense due to the high energy of precipitated particles penetrating the E-region.

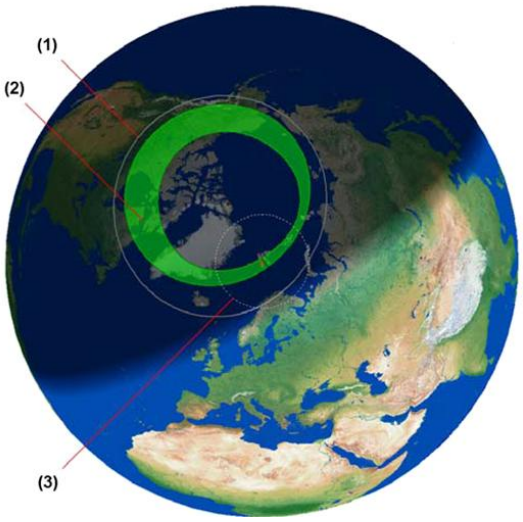

Figure 1. 10: *Different regions of aurora are shown: (1) the equatorward boundary as a white outer ring, (2) the auroral oval as a shaded transparent region, and (3) the location of auroral observation (Sigernes et al., 2011).*

The auroras formed in the northern and southern polar regions are known as *aurora borealis* and *aurora australis*, respectively. The region over which auroras are formed is called *auroral oval*, as shown in Figure-1.10. During geomagnetic storms, solar wind couples very strongly with the magnetosphere, and with an increase in solar wind dynamic pressure, the auroral oval also becomes larger, expanding to mid-latitudes. During high geomagnetic activity, the outer boundary of the auroral oval may also reach around 55° magnetic latitude on the dayside, as shown in Figure-1.11. Figure-1.11 shows around ten times an increase in the intensity of atomic oxygen emission at 135.6 nm wavelength (indicating an intense aurora) over mid-latitude locations than their surrounding regions. These intense emissions, as shown in red, depict the aurora reaching over Boston in the afternoon period (1411–1548 LT) (Pallamraju &

Chakrabarti, 2005). As IMF turns northward, the strength of coupling is reduced, and thus, the size of the auroral oval gets smaller along with the poleward motion of the outer boundary. Such expansion of the auroral oval and further shrinking in size is also shown to affect and reduce the strength of the ring current (Ebihara & Fok, 2004).

The poleward region or inner boundary of the auroral oval is known as the *polar cap*, which is a region of open field lines, i.e., only one foot of the magnetic field line is on the ground, and the other gets swept away anti-sunward with the solar wind and extends in the night side, forming the *tail lobes* (northern lobe and southern lobe in the northern and southern hemisphere, respectively). During nightside reconnection, electrons and/or ions trapped in open field lines are accelerated sunward and precipitated in the polar regions. Therefore, sometimes, the soft precipitation of less energetic electrons (~500 eV) in the polar cap is referred to as *polar rain*. Since both hemispheres contain open field lines, the entry of polar rain is defined by the IMF Bx component. The precipitation will happen in the northern polar cap for IMF Bx > 0 and in the southern polar cap for IMF Bx < 0.

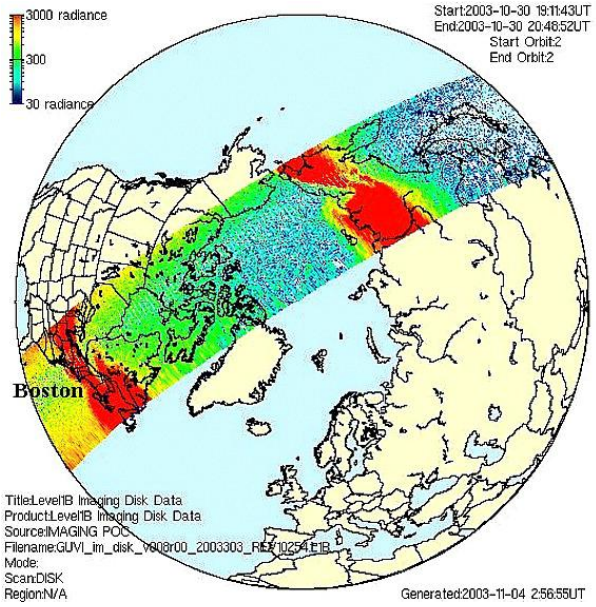

Figure 1. 11: *Satellite observation of OI 1356 Å obtained during 1911–2048 UT (1411–1548 LT) shows the presence of aurora over Boston, a mid-latitude region, during local daytime (Pallamraju & Chakrabarti, 2005).*

1.2.2 Field-aligned currents and High-latitude two-cell pattern

Geomagnetic field lines are equipotential and similar to electric wires. These lines act as good electric conductors, allowing plasma motion through them. A region of the magnetosphere structure acts as a current source and regulates the auroral circuit. This structure also drives a downward current flow along the field line in the polar ionosphere and is known as field-

aligned current (FAC) or Birkeland current. The field-aligned currents (FACs) or Birkeland currents connect the magnetosphere with the Earth's high-latitude upper atmosphere, resulting in magnetosphere-ionosphere coupling. FACs are also an important source of magnetic field in space, which intensifies during geomagnetic storms. Although electrons or ions can both generate FACs, the major charge carriers of FACs are supposed to be electrons that flow along the field line, and therefore, FACs play an important role in transporting the energy between the magnetosphere and the ionosphere. The transport of magnetic flux from the magnetotail region on the night side to the dipolar region and then to the dayside magnetopause over the poles is known as *magnetospheric convection* (Tanaka, 2007). In the process of magnetospheric convection, plasma and magnetic flux are also transported from nightside to dayside.

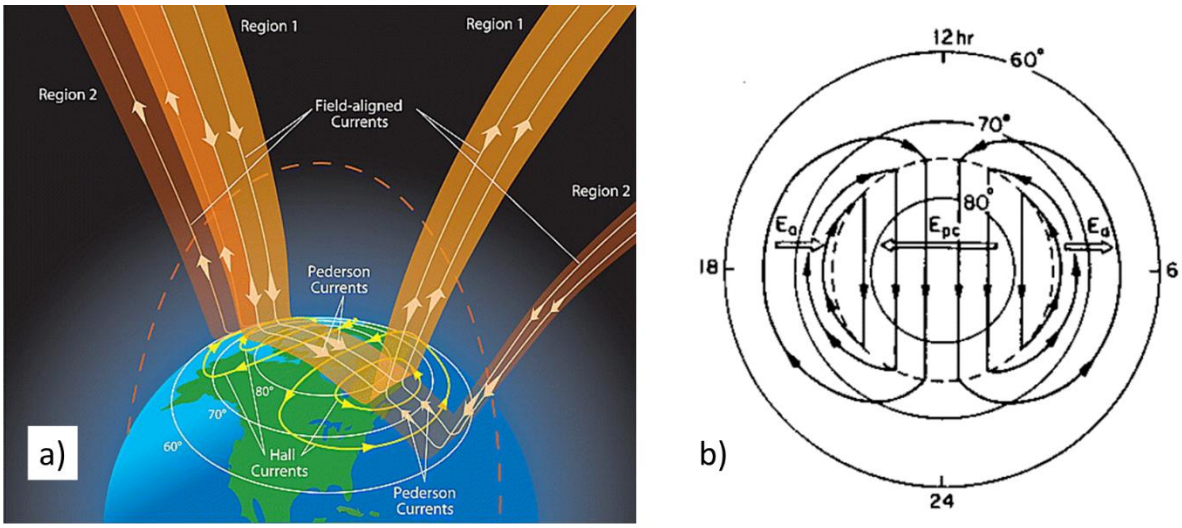

Figure 1. 12: a) *The schematic of combined FACs and ionospheric current systems. (Le at al., 2010), and* ***b)*** *High-latitude two-cell plasma convection pattern and associated plasma drift in the northern hemisphere for southward IMF Bz and IMF By=0 (Kelley & Heelis, 1989).*

FACs are defined as region-1 (R1) and region-2 (R2) currents located in poleward and equatorward directions of the auroral oval, respectively, as shown in Figure-1.12(a). The region-1 current enters from the dawnside and exits from the dusk side, while the region-2 current flows in a similar way but with opposite polarities. Downward FAC flows horizontally through the ionospheric E-region (known as the Pedersen current), where ion-neutral collision frequency is much larger than ion gyro-frequency, i.e., $\nu_{in} \gg \Omega_{in}$ and again flows as upward FAC towards the source, making a single current circuit. Therefore, the ionosphere serves as a medium for the closure of the path to connect the downward FAC with the upward FAC, and

a potential difference is created. The flow of these currents gives rise to convective electrojets, called auroral electrojets, and energy is deposited in the auroral ionosphere from the magnetospheric region. Therefore, a potential difference of magnetospheric origin across the field lines maps to a potential difference along the field lines in the ionosphere and can accelerate the charged particles from magnetospheric heights to the ionosphere and can also take plasma away from the ionosphere to the magnetosphere as ionospheric outflow (Welling et al., 2015). The downward FACs are associated with precipitating electrons, and a similar mechanism of accelerated particles into the ionosphere can be considered for particle precipitation in the case of aurora (Kamide & Akasofu, 1976).

The direction of the electric field between FACs is from inflow to outflow, which generates a two-cell convection pattern at high latitudes. Therefore, the electric field by region-1 FAC is directed from dawn to dusk in the polar cap region where plasma is transported from noon to midnight, i.e., anti-sunward across the polar cap, as shown in Figure-1.12(b). The electric field generated by region-2 FAC is in the opposite direction to the convection electric field from dawn to dusk and thus fully/partially shields the inner magnetospheric region from magnetospheric convection. Therefore, the electric field produced by this region-2 FAC is known as the *shielding electric field*. During periods of weakened convection field (dawn-to-dusk) and no significant perturbation in the region-2 FACs, *overshielding* may occur (Spiro et al.,1988; Peymirat et al., 2000). It has been shown that the overshielding occurs during the northward turning of prolonged IMF Bz component and can exist for ~ 10-20 minutes (Spiro et al.,1988; Fejer et al., 1990). For a prolonged southward IMF Bz during geomagnetic storms, the solar wind induces a convection electric field ($E= -V_{SW} \times B_{IMF}$) in the magnetosphere in the dawn-to-dusk direction. Following the open field lines, this convection field gets mapped to the high-latitude ionosphere by region-1 FACs. Although the shielding electric field also strengthens, this convection field of magnetospheric origin dominates and penetrates promptly to low and mid-latitude regions, being directed eastward in the dayside and westward in the nightside, and known as prompt penetration of electric field (Kelley et al., 2003; Kikuchi et al., 2008). The Figure-1.12(b) represents a cell pattern for southward IMF ($B_z < 0$) and IMF $B_y=0$. It can be seen that the cell pattern is a closed circuit. Thus, the plasma is transported horizontally from dayside to nightside over the polar cap region via horizontal FACs and returns to dayside by flowing through the lower-latitude regions of the cell pattern on the dawn and dusk sides. This process of transporting the plasma is known as *ionospheric convection* (Weimer, 2005), which follows magnetospheric convection. The positive and negative values

of IMF create a tilt in the cell pattern with respect to the noon-midnight meridian, as shown in Figure-1.13. The latitudes away in the equatorward edge of the high-latitude two-cell pattern or the auroral oval region are referred to as the subauroral latitudes (~40°–60° in both hemispheres). These are closed field line regions where a corotation electric field exists.

1.2.3 Subauroral ion drifts and polarization streams

Sub auroral ion drift (SAID) is a latitudinally narrow region (~1° width) located on the dusk-midnight side, where rapid plasma flow is observed in the sunward or westward direction, with a speed of ~ 1-2 km-s^{-1} or greater during geomagnetically disturbed periods (Spiro et al., 1978). Previously, SAID was also known as *Polarization Jet* in the subauroral ionosphere (Galperin et al., 1974). The region of formation of SAID is the presence of a strong electric field (≳ 350

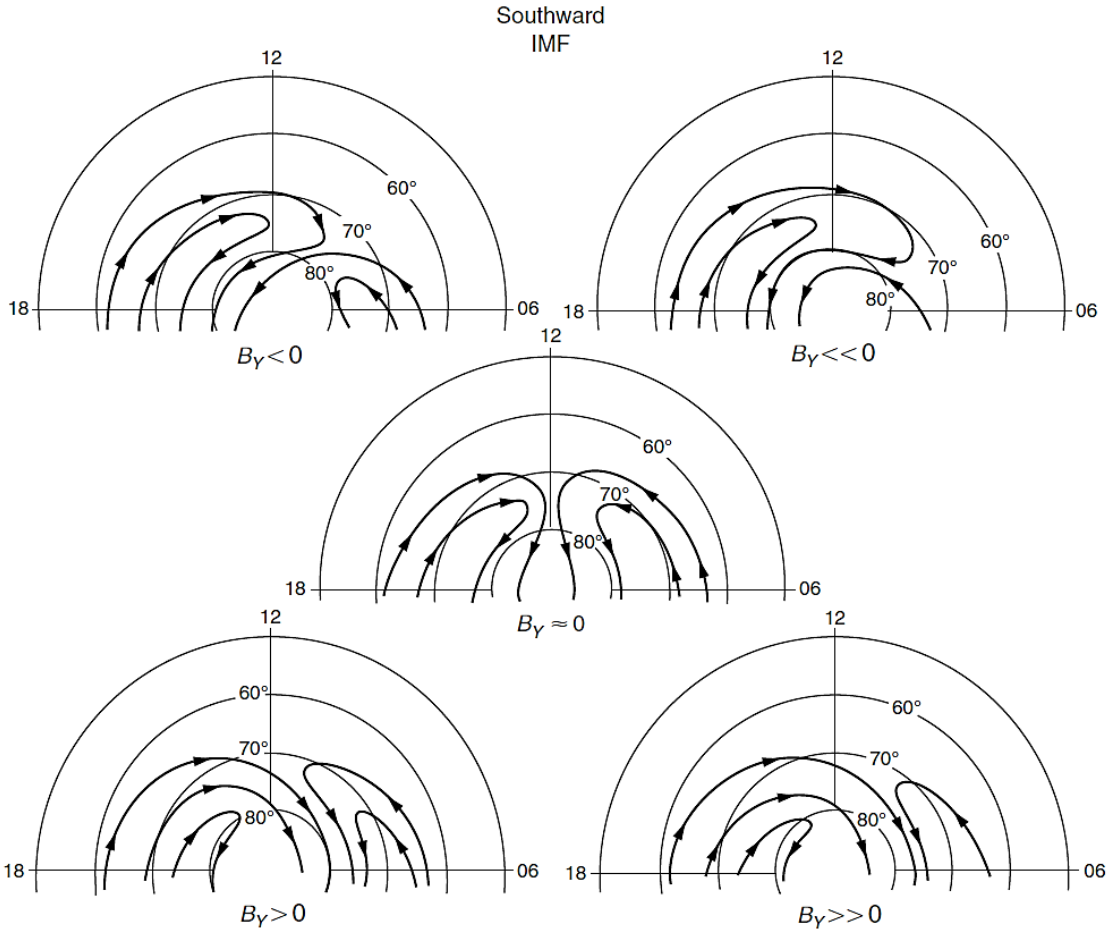

Figure 1. 13: *Schematic representation of changes in convection-cell pattern under different conditions of IMF By component and when IMF Bz is southward. Adapted from Kelley, 2009.*

mV-m^{-1}) at altitudes of around 500-1500 km in the subauroral region, which is in a poleward direction driven by Pedersen current closure (Smiddy et al., 1977; Maynard, 1978; Karlsson et al., 1998). These SAIDs are found to form in the fixed magnetic local time, MLT, regime of about 18 to 02 MLT i.e., dusk to pre-midnight region, and the magnetic latitude range, MLAT, of about 50°-70° MLAT in mid-latitude ionosphere (Spiro et al., 1979; Karlsson et al., 1998), and also to be associated with downward FACs (Rich et al., 1980). Therefore, the intense poleward electric field provided by the region-2 FACs located equatorward of the auroral oval supports the scenario of SAID formation (Southwood & Wolf, 1978; Anderson et al., 1993). Adding to the nomenclature of SAID, a new term, *sub auroral polarization stream* (SAPS), was introduced by Foster and Burke (2002). SAPS was shown to consist of both the above features of intense electric field due to FACs and the associated rapid sunward plasma flow similar to SAID and simultaneously referred to as *SAPS electric field*. Similar SAPS characteristics were described to be wider than SAID, with a few degrees of latitudinal width (Yeh et al., 1991). SAPS were found to be formed due to the closure of FACs at low latitudes as a consequence of M-I coupling, similar to SAID formation, and gaining the average westward flow velocity by about one km-s^{-1} in a latitudinal range of 3-5° (Foster & Vo, 2002). A rough schematic of SAID and SAPS is depicted in Figure-1.14.

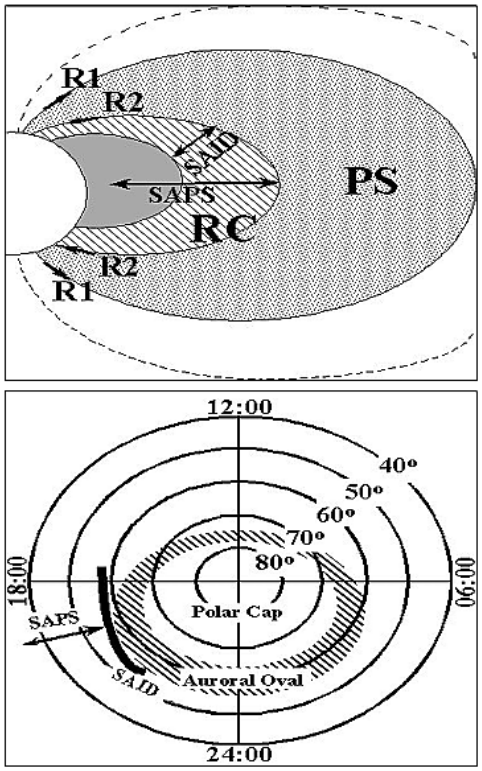

Figure 1. 14: *Schematic showing the Connection between the region-1 and region-2 FAC and sub-auroral ion drifts (SAID) / sub auroral polarization stream (SAPS) (Mishin & Burke, 2005).*

As SAPS passes through the low conductivity region, the rapid flow of plasma in the SAPS channel causes frictional or collisional heating due to frequent ion-neutral collisions. The Figure-1.15 shows a scatter plot between the ion convection velocity and temperature of ions near a zonally elongated convection channel observed at mid-latitudes during local evening hours. The rise in ion temperature at larger velocities indicates frictional heating. This increased

heating in the ionosphere increases the rate of ion-neutral interchange through O^+ ions and nitrogen molecules due to the rapid movement of ions. The NO^+, thus formed from the ion-neutral interchange, undergoes faster recombination with electrons and further reduces the conductivities in the ionospheric F-region at subauroral latitudes. Such heating is also responsible for ion outflow through FACs along the field lines and greatly reduces plasma density in the ionospheric F-region.

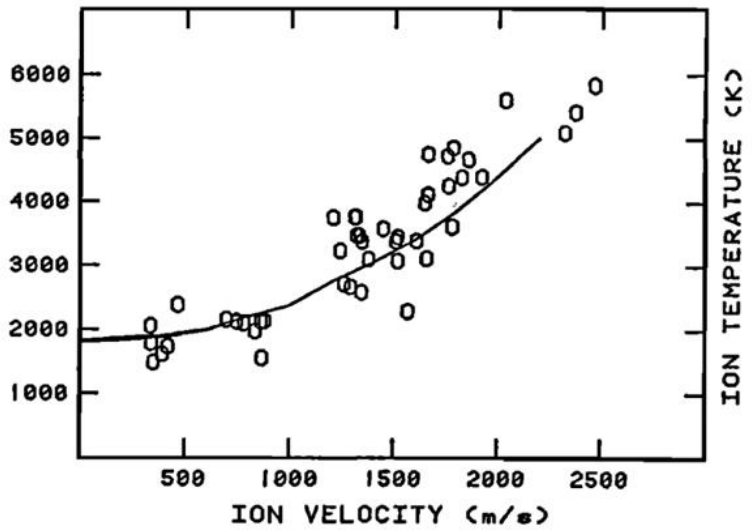

Figure 1. 15: *A scatter plot showing larger friction heating at larger ion convection velocity observed between 450 km and 550 km altitude at 57° magnetic latitude. (From Yeh & Foster, 1990).*

This large depression in F-region plasma density causes the formation of *the mid-latitude ionospheric trough*, which can have a latitudinal span of about 5°–10° (Voiculescu et al., 2010), 10°–15° (Liu & Xiong, 2020) or greater, depending on geomagnetic activity. Therefore, the mechanism of such strong plasma flow in the SAPS region, causing frictional heating and consequently reducing the plasma density and conductivity, was suggested by Anderson et al. (1993). Such rapid sunward flow has also been observed in the magnetosphere (Rowland & Wygant, 1998), which also thus appears to be related to SAPS in the mid-latitude ionosphere through the field lines. Studies have also shown that SAPS has a significant impact on the space weather (e.g., Coster & Foster, 2007).

1.2.4 Storm-enhanced density over mid-latitudes

As a consequence of geomagnetic storms, the density and composition of the ionosphere often change drastically and can last for several days. For large disturbances, the plasma density in the ionosphere often increases or decreases significantly from its typical quiet time values. Such increases/decreases in electron concentrations are called *ionospheric storms* (Fuller-Rowell et al., 1997; Prölss, 1995, 1997; Buonsanto, 1999). The first review on ionospheric storms was presented by Obayashi (1964) as a result of magnetosphere-ionosphere coupling. There is further characterization of storms as positive and negative. Positive ionospheric storms are referred to an increase in electron density, while negative ionospheric storms are referred to a decrease in electron density and show local time dependence (e.g., Balan and Rao, 1990; Mayr et al., 1978; Prölss, 1995; Rishbeth, 1998; Tsagouri et al., 2000).

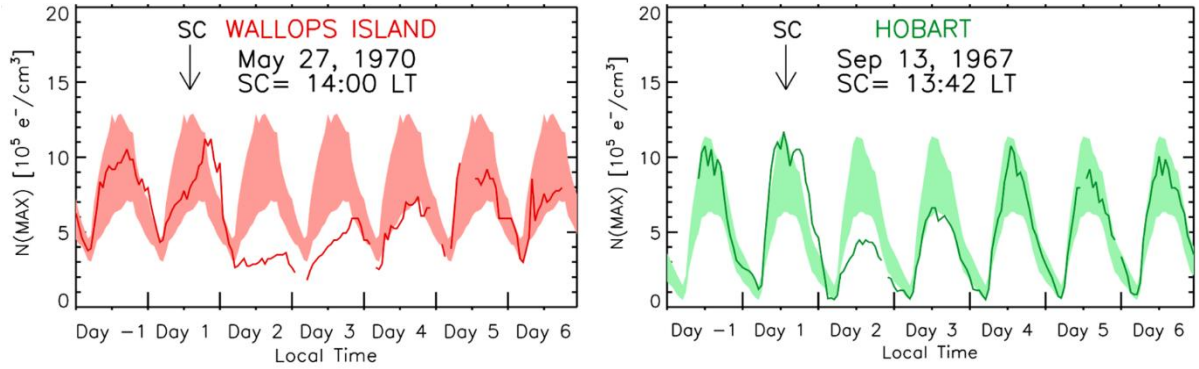

Figure 1. 16: *An effect of positive ionospheric storm during local daytime is shown in maximum electron density (NmF2) during a period of geomagnetic storm. The positive phase is observed at mid-latitude location of WALLOPS ISLAND (northern hemisphere) and HOBART (southern hemisphere). Mendillo & Narvaez, (2010).*

These ionospheric storms have been investigated extensively with various ionospheric parameters, such as using NmF_2 (Prolss, 1995), TEC (Mendillo, 2006), and satellite measurements of thermosphere parameters (Prolss & Von Zahn, 1974). The negative ionospheric storms are found to have a good correlation with thermospheric O/N_2 density variations, and the reduced NmF_2 during negative storms was found to exist with a simultaneous reduction in O/N_2 density at around 290 km (Mayr et al., 1978; Prölss, 1991; Prölss& Craven, 1998). The negative phase is mainly attributed to composition changes by atmospheric disturbances, causing an enhancement in $[N_2]$ (Prolss et al., 1988; de Abreu et al.,

2010), whereas the positive storm phase is suggested to be due to composition changes (Field et al., 1998) along with the wind perturbations (e.g., Balan et al., 2010).

Positive ionospheric storms over mid-latitude have been suggested due to the expansion of high-latitude convection electric fields towards lower latitudes or equatorward (e.g., Foster, 1993; Heelis et al., 2009). However, with geomagnetic disturbances beginning in the local daytime, negative storms over mid-latitudes have been shown to occur during the preceding night (Prölss, 1993). The Figure-1.16 shows an example of positive ionospheric storm at northern (Wallops Island) and southern (Hobart, Tasmania) mid-latitude locations during the sudden commencement (SC) of a geomagnetic storm. Kelley et al. (2004) showed the effect of a prompt penetration of a strong eastward electric field to build a positive phase at mid-latitudes during local daytime. Such electric fields provide the vertical $E \times B$ plasma drift, which uplifts the ionospheric layer to higher heights and thereby increases the densities as the recombination process is small at higher altitudes. The vertical plasma drift in the mid-latitude ionosphere, where magnetic field lines are tilted, is determined by the interplay between convection electric field, thermospheric wind, and ambipolar diffusion. Therefore, the role of electric field and/or winds to provide a vertical plasma drift can be given as (Schunk & Nagy, 2009):

$$u_{iz} = \frac{E}{B} cosI + u_n \, sinI \, cosI - D_a sin^2 I \left(\frac{1}{n_i} \frac{\partial n_i}{\partial z} + \frac{1}{T_p} \frac{\partial T_p}{\partial z} + \frac{1}{H_p} \right) \qquad (1.12)$$

where, subscript i is for ions, E is the eastward electric field, B is magnetic field, I is the inclination angle, u_n is meridional neutral wind velocity, z is height, T_p is plasma temperature

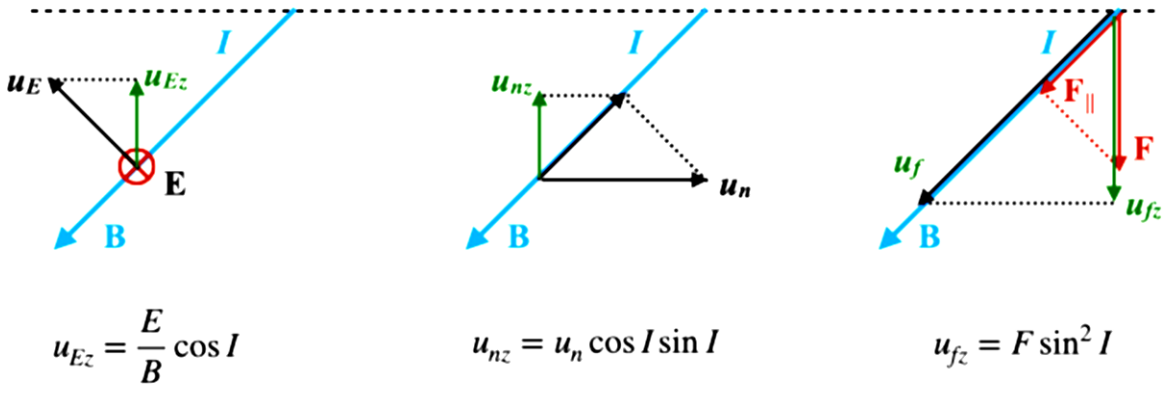

Figure 1. 17: *The Vertical components of the plasma drifts over mid-latitudes are shown from left to right for an electric field (E; eastward), neutral wind (un; equatorward), and vertical gravitational forces (F; downward) from left to right. I represent the magnetic inclination angle. (Jee, 2023).*

(average of ion and electron temperature), n_i is ion density, $D_a = 2kTp/m_i\nu_i$ is the ambipolar diffusion coefficient (ν_i is the momentum transfer collision frequency for ions and neutrals). $H_p = 2kT_p/m_ig$ is the plasma scale height.

The Figure-1.17 shows a schematic to illustrate the effect of eastward electric field, equatorward neutral wind, and vertical forces with downward gravitational acceleration g on the vertical plasma drift components for the tilted magnetic field with inclination I in the mid-latitude ionosphere. Therefore, over mid-latitudes, $E \times B$ drift has both horizontal and vertical

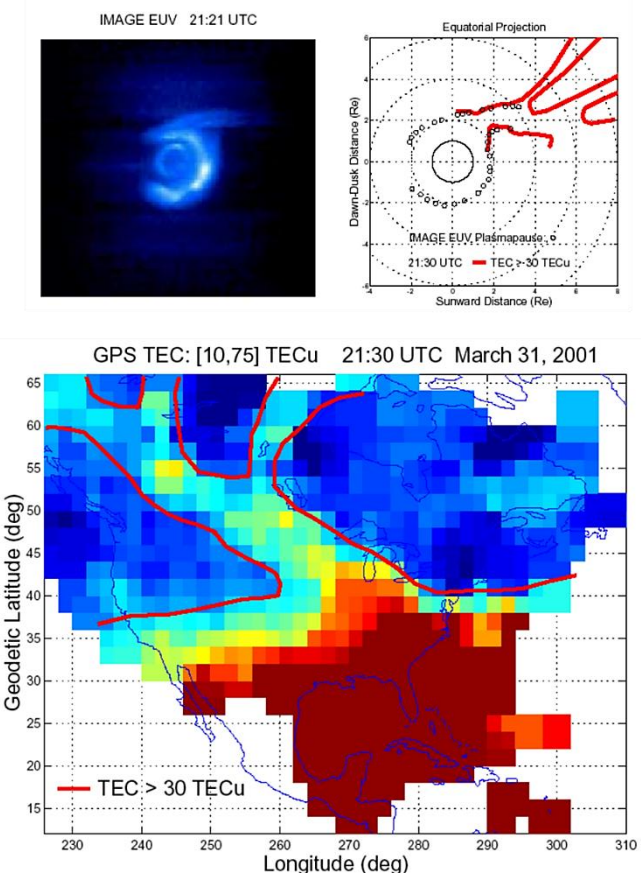

Figure 1. 18: *The top left figure shows the plasmasphere image taken from IMAGE EUV satellite. The bottom figure shows the ionospheric SED using TEC data over North American sector. The boundary of SED plume (thick red lines) matches with the boundaries of plasmaspheric plume, shown in top right panel. (Foster et al., 2002).*

components, which can amplify during storm time, and penetration of a stronger daytime eastward electric field may strengthen the upward component over the horizontal component, resulting in the uplift of the ionospheric layer to higher heights.

During the phase of positive ionospheric storm, a region of electron density enhancement often occurs over mid-latitudes, which is known as the *storm-enhanced density* (SED) (Foster, 1993). Sometimes, this region of enhanced density plasma can enter the polar cap region at high latitudes, forming a structure of tongue-of-ionization (TOI). Foster (1993) suggested that SEDs extend in the westward and poleward directions towards higher latitudes, thus forming a plume, also known as a *SED plume*. The density enhancements in SEDs over a large scale are primarily observed during nighttime or after evening hours using the TEC data. The SED plume is also found to be the ionospheric projection of the plasmaspheric plume (i.e., the erosion of outer layers of dusk side plasmasphere in sunward direction) in the equatorial region, as shown in Figure-1.18 (Foster et al., 2002). The plasmaspheric plume shown in the top left of Figure-1.18, coincident with the ionospheric plume shown by the TEC map in the bottom panel, was observed by the IMAGE EUV satellite. The same equatorial projection of ionospheric SED mapped to the plasmasphere is represented in the top right panel and can be seen to coincide with the plasmaspheric plume motion in a sunward direction.

So far, studies have suggested that the westward and poleward plasma motion during SED is accompanied by large sunward convection flows due to SAPS (Foster & Burke, 2002; Foster & Vo, 2002), which are related to region-2 FACs and maps to mid-latitude ionospheric trough. This westward and poleward flow of plasma can be understood from the interaction of corotating plasma motion over mid-latitudes with the sunward flow of plasma at high latitudes due to magnetospheric convection. The Figure-1.19 represents the general form of convective flow in the equatorial plane, with Earth at the center, noon or Sun to the left, and dawn at the top side of the figure. The solid lines depict the plasma flow in a sunward direction under the magnetospheric convection V_{sw} x B_{IMF}. The closed region around Earth represents the

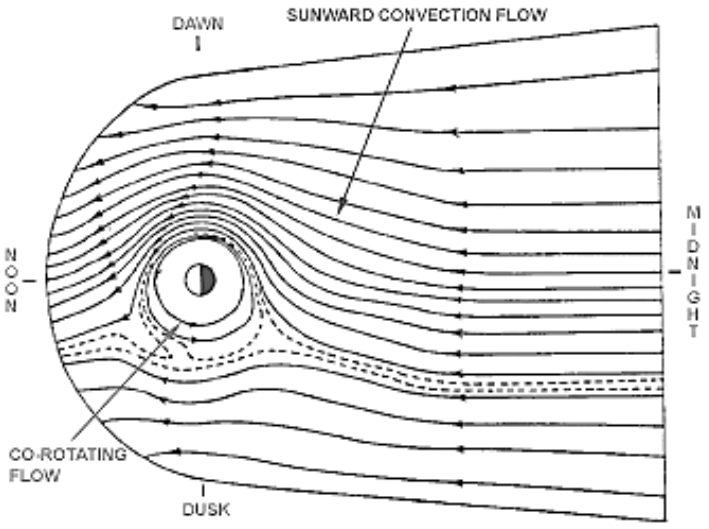

Figure 1. 19: *Earth's Magnetosphere showing the general form of the convective flow in the equatorial plane and the dawn-dusk direction (Brice, 1967).*

corotating plasma flow in an anti-sunward direction at the dusk side. During geomagnetic storms, the strong sunward flow due to magnetospheric convection at high latitudes expands to mid-latitudes and dominates over the corotating flow. By the interaction of these two oppositely directed plasma flows in the dusk side, the corotating plasma velocity reduces, and more plasma is accumulated, and since the storm-induced magnetospheric convection is stronger, it carries this dusk-side accumulated plasma along with it in the sunward direction, as shown by dashed lines. Therefore, a sunward flow of ionospheric SED or plasmaspheric plume is generated and, being fixed in local time (i.e., near dusk side), the enhancement in density during SED is also referred to as the *dusk effect*. This effect can also be noticed in Figure-1.20, where the x-axis is magnetic local time, MLT, along with the formation of the

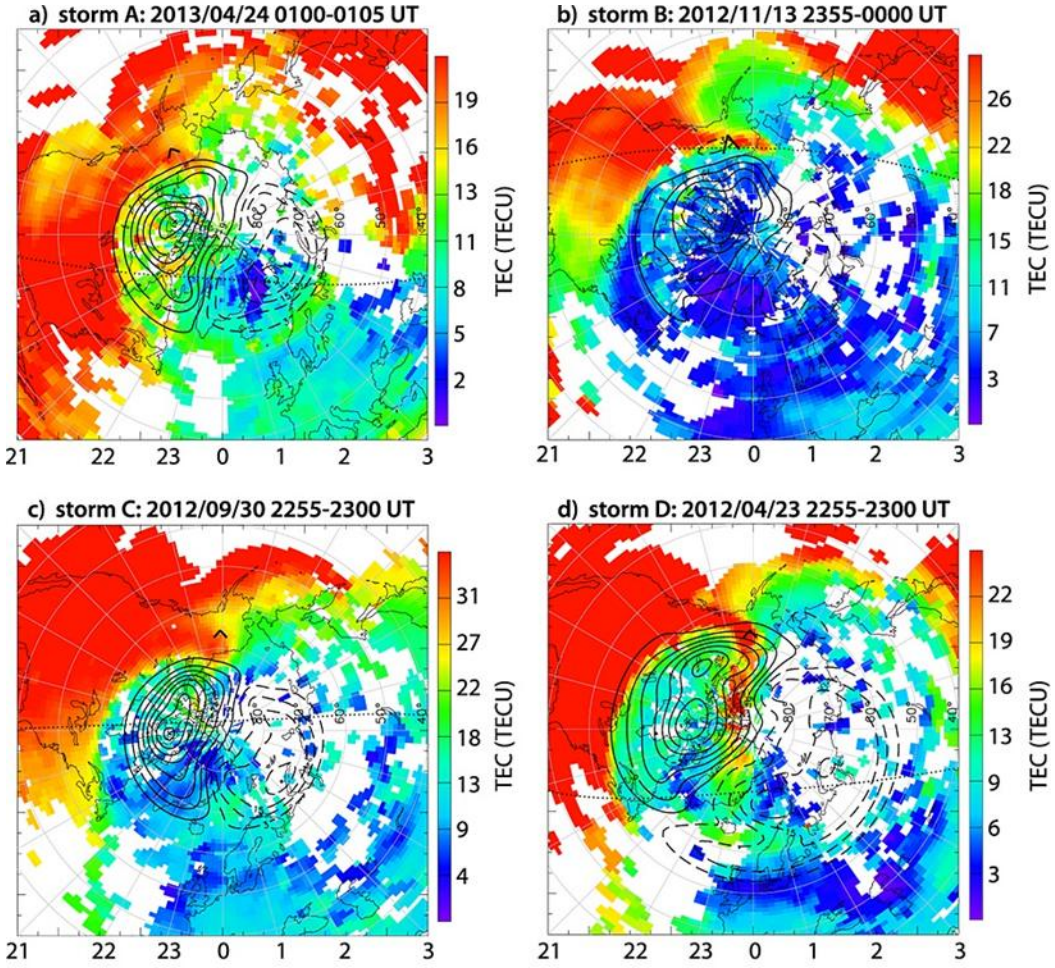

Figure 1. 20: *Two dimensional TEC maps showing SED during different geomagnetic storms, superposed with convection pattern as solid and dashed black lines. Dotted line in each panel represents the terminator. The formation of SED plume and tongue-of-ionization (TOI) can be seen in panel (b) and (d) respectively (Zou et al., 2014).*

SED plume and its evolution to TOI. The behavior of the high latitude 2-cell pattern is also shown for each SED case using black curved lines.

The panels (a-d) in Figure-1.20 show large-scale 2-dimensional geographical maps of TEC at specific time intervals during different geomagnetic storms. A large region of enhanced plasma density can be seen between the 21-23 MLT period (i.e., in the dusk to the pre-midnight region) for each storm, which is the storm-enhanced density region. Panel b shows a narrow-confined structure moving towards higher latitudes, called the SED plume, while panel d shows the evolution of SED into tongue-of-ionization entering the polar cap region at high latitudes following the low latitudes of the convection cell. From each panel in Figure-1.20, it can be seen that SEDs are associated with steep density gradients, especially between the poleward region of the SED and the equatorward wall of the trough. Such steep gradients are shown to affect radio communication and navigation systems (e.g., Doherty et al., 2004; Coster & Skone, 2009; Sun et al., 2013). Large electron densities during SEDs are also suggested as a cause that can affect ion upflow fluxes (e.g., Foster et al., 2005; Zou et al., 2013; Heelis, 2016). The dayside reconnection has also been found to be affected significantly due to an important role played by the plasmaspheric plume in the magnetosphere (Borovsky & Denton, 2008; Walsh et al., 2014). This connection between SED plumes in the ionosphere and plasmaspheric plumes suggests an important influence of magnetosphere- plasmasphere- ionosphere coupling over mid-latitudes and further requires a three-dimensional approach to understand the plasma

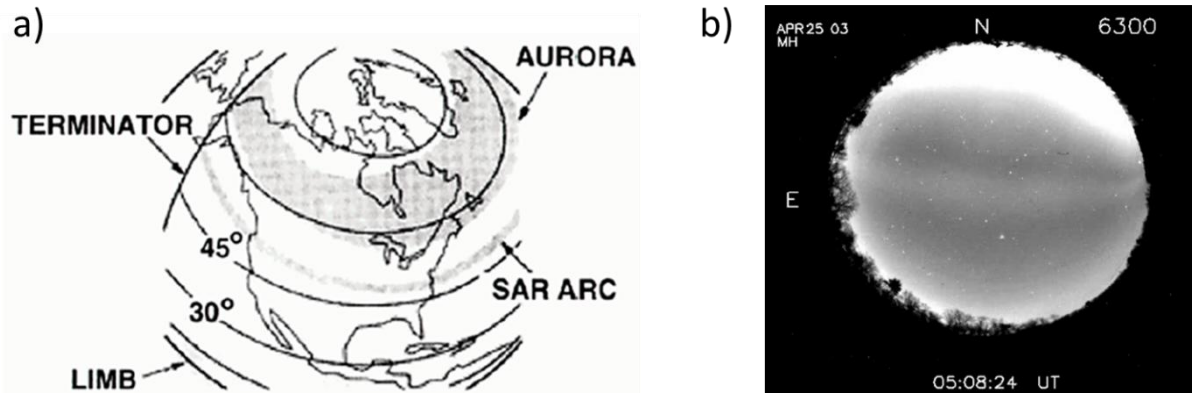

Figure 1. 21: a) *A schematic representation of latitudinally narrow SAR arc in the equatorward of high-latitude aurora (Kozyra et al., 1997),* ***b)*** *An observation of mid-latitude nighttime SAR arc at Millstone Hill using OI 630.0 nm emission. The bright aurora is shown at the top of the image. (Courtesy: Buimaging.com)*

distribution due to M-I coupling effects. Therefore, investigations of SED phenomena during geomagnetic disturbances continue to attract significant attention from researchers.

1.2.5 Stable auroral red arcs

In addition to the high-latitude auroral emissions, another form of optical emission was observed situated equatorward of the aurora in the mid-latitude ionosphere and termed as *stable auroral red arcs* (SAR arcs) (Barbier, 1958), as shown by a schematic in panel (a) of Figure-1.21. From earlier studies, it was found that these arcs can persist for hours up to ~10 hours or more over a location. The Dynamic Explorer-1 polar spacecraft revealed a long-lived nighttime SAR arc for 28 continuous hours (Craven et al., 1982). Hence, the term *stable* was coined. SAR arc emissions are monochromatic atomic oxygen red line emission (630.0 nm wavelength), extending approximately 100° zonally but with a latitudinally narrow width of around 1-3° (Kozyra et al., 1997). The peak altitude of SAR arc emission was suggested to be around 400 km by Roach and Roach (1963). Being dominated by red line emissions and due to the absence of other emissions, such as 557.7 nm, SAR arcs are referred to as 'spectrally pure.' As in terms of brightness, the auroral emissions are known to be very intense and can be seen with the naked eye, whereas the SAR arc emissions are subvisual and much fainter (around 10-20 times) than the visible red aurora (Chamberlain, 1995). The panel (b) of Figure-1.21 demonstrates a SAR arc at 630.0 nm wavelength during the night of 25 April 2003, which was observed using an all-sky imager over Millstone Hill. In the north of the image, the bright region indicates the aurora, and close to the center of the image, a comparatively less bright region of the SAR arc aligned in an east-west direction and located equatorward of the aurora can be seen.

SAR arcs are found to be formed due to the transfer of energy by low-energy particles (less than around 10 eV) from the magnetosphere. It was postulated that during geomagnetic disturbances, when plasmapause and ring current regions overlap, the cold particles at the plasmapause boundary undergo coulomb collisions with the hot and high-energy ring current ions and generate energy. This energy is then conducted down to the low-temperature region of the topside ionosphere following the closed field lines and heats the ambient electrons in the F-region. Lobzin and Pavlov (1999) suggested that electron temperature enhancement in the SAR arc region strongly depends on the downward heat flux, which is responsible for the additional heating of the electron gas. Therefore, the main ionospheric signature of SAR arc

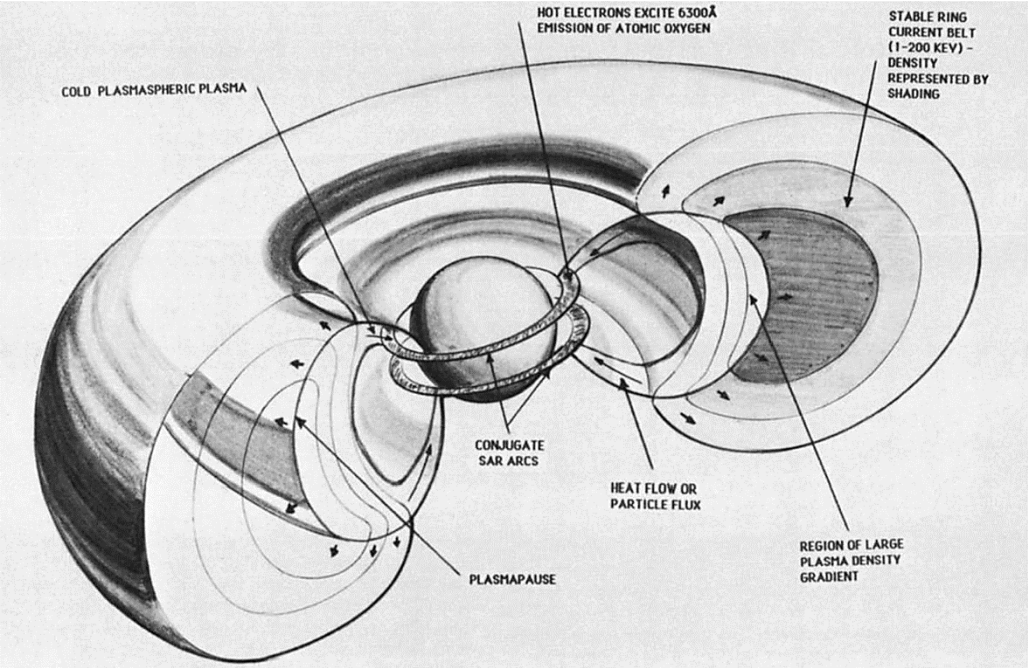

Figure 1. 22: *SAR arc emissions are generated at the foot-points of closed field lines in the overlapping region of the ring current and plasmasphere encircling the Earth, as shown by the schematic of the inner magnetosphere (Kozyra et al., 1987).*

generation is the elevated electron temperature (>3000 K) in the region of their formation (Rees & Roble, 1975) and the collision of these heated electrons with ambient oxygen atoms. This additional energy results in the excitation of the O(^{1}D) state to produce the 630.0 nm emission, the characteristic of a SAR arc. This downward flow of energy was also considered to reach the ionospheric foot-points connected in both the northern and southern hemispheres and thus 'Conjugate SAR arcs' were expected to occur simultaneously. Figure-1.22 depicts a schematic representation of the plasmasphere to show the overlap region of the ring current with the outer boundary of the plasmasphere. The two toroidal rings in each hemisphere can be seen encircling the Earth. SAR arcs occur at these foot-points of closed field lines threading the overlap region and thus indicate the conjugate SAR arc formation. Recently, the property of SAR arcs being a conjugate phenomenon was also demonstrated in both hemispheres using ground-based observations and shown to have seasonal variability due to differences in magnetospheric forcing in respective hemispheres (Martinis et al., 2019). The transfer of energy of several eV to produce SAR arc emission was considered in the form of precipitating electrons (or electron heat flux), and various mechanisms were proposed to understand the process of energy transfer from near plasmapause region to the ionosphere (Kozyra et al., 1997

and references therein). These authors primarily suggested three possible mechanisms for the deposition of electron heat flux: a) Coulomb collision between cold electrons of plasmasphere and energetic ions in the ring current region and the subsequent energy transferred to ionosphere via heat conduction (e.g., Cole, 1965), b) Landau damping of electromagnetic ion cyclotron (EMIC) waves to the thermal plasmaspheric electron with the energy transfer as a precipitation of low-energy particle flux (Cornwall et al., 1971), and c) kinetic Alfven waves (KAWs), which has a parallel electric field to the $\vec{B}$ can accelerate cold electrons in the plasmasphere to ionospheric heights (Hasegawa & Mima, 1978). The mechanisms of different theories suggested for energy transfer are illustrated by a schematic in Figure-1.23, wherein the shaded region represents the overlap region of the outer boundary of the plasmasphere with the inner ring current region. Although all proposed mechanisms are based on the interaction of cold plasmaspheric particles with hot ring current ions, the major candidate source still remains unknown as there is no study on the relative contribution of these mechanisms and no quantitative evaluation of the high-altitude energy source of a SAR arc. However, the theory of Coulomb collision indicating heat conduction along the geomagnetic field lines is widely accepted as a plausible source for SAR arc formation (e.g., Kozyra et al. 1987, 1993; Prölss, 2006; Inaba et al., 2021) and the brightness of SAR arc depends on the amount of heat conducted along the field lines. For such case of energy deposition in the ionosphere, the steady state heat conduction equation for the electron gas can be given as:

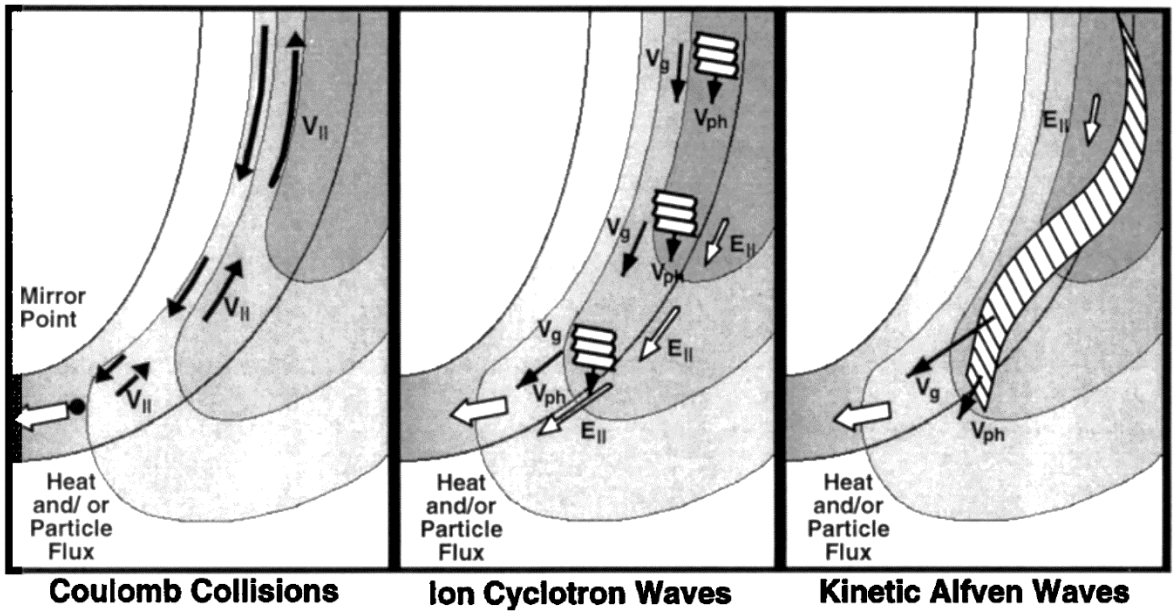

Figure 1. 23: *The energy transfer processes of different mechanism responsible for the formation of SAR arcs are shown (Kozyra et al., 1997).*

$$-\frac{d}{dz}\left[K^e(z,T_e)\frac{dT_e}{dz}\right] = \Sigma Q_e(z) - \Sigma L_e(z,T_e) \tag{1.13}$$

where, z is the height, $K^e(z,T_e)$ is electron thermal conductivity, T_e is electron temperature and Q_e, L_e indicates the total heating from local (solar radiation) and non-local (electron heat flux) sources and energy loss from various sources, such as (i) elastic/inelastic collisions of e- with neutrals, (ii) Coulomb collisions of *e*- with ions, oxygen atoms (O) to produce O(^{1}D) state, and (iii) Coulomb collisions of e- with O exciting the fine structure of O(^{3}P). Therefore, the loss process of thermal electrons (e^-*) with oxygen atoms to produce O(^{1}D) state by Coulomb collisions acts as the source of SAR arc emission (Rees & Roble, 1975), and therefore the production mechanism for SAR arc emission is:

$$\begin{aligned} O + e^-* &\rightarrow O^* + e^- \\ O^* &\rightarrow O + h\nu\,(630.0\,nm) \end{aligned} \tag{1.14}$$

As the downward deposition of heat from the inner magnetosphere creates heating in the topside ionosphere and increases the temperature of electrons, several studies have reported such electron temperature enhancement using observations from various instruments (e.g., Foster et al., 1994; Mendillo et al., 2013; Martinis et al., 2019). It has been found that the heating occurs primarily in the reduced density region of the mid-latitude ionospheric trough, where the foot of field lines at the plasmapause region connect to the subauroral ionosphere. Therefore, apart from being dominated by red line emissions, the other two important conditions to distinguish a SAR arc are- (i) Elevated electron temperature (Te>3000 K), Rees

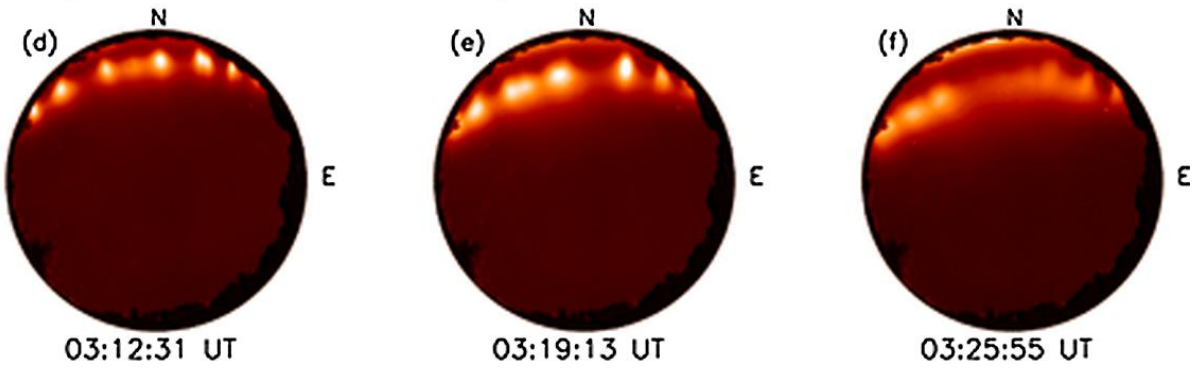

Figure 1. 24: *Nighttime observations of SAR arc during a geomagnetic storm on 2 October 2013 over Millstone Hill. SAR arc can be seen having small-scale structures in the zonal direction. After Mendillo et al., 2016a.*

and Roble (1975), and (ii) reduced electron density (Ne) (Foster et al., 1994) in the region of their formation (Baumgardner et al., 2013).

In addition, some other SAR arc characteristics in terms of brightness, longevity, and occurrence have also been studied, wherein small zonal structures were found within a SAR arc, as shown in Figure-1.24 (Mendillo et al., 2016a). These authors also presented evidence of a long-lived SAR arc lasting for five consecutive days. Also, from the nighttime observations of SAR arcs, it is found that SAR arcs mostly occur during the equinox months followed by the winter months, as shown in Figure-1.25, where the seasonal occurrence rates of SAR arcs over Millstone Hill during 1985–2013 are shown (Mendillo & Wroten, 2019). Baumgardner et al. (2007) found the average value of SAR arc brightness during nighttime in the range of around ~500±270 Rayleigh, as observed over Millstone Hill for the period of 1983 to 2006. A SAR arc was reported during the initial phase of the storm, which occurred due to the inward movement of the ring current (Shiokawa et al., 2013). Based on the statistical analysis of nighttime SAR arc detachments, it was found that as the auroral oval contracts in size and moves further poleward after the end of the main phase, the SAR arc gets detached from the oval and thus is suggested to occur at the beginning of the recovery phase (Takagi et al., 2018). Therefore, the overlap between the ring-current and outer boundary of the plasmasphere during geomagnetic disturbances plays a crucial role in affecting the thermal balance in the mid-latitude ionosphere. Hence, being associated with the downward electron heat flux from the inner magnetosphere and connected with the plasmapause region, SAR arcs become direct optical evidence of magnetosphere-ionosphere coupling in the mid-latitude ionosphere.

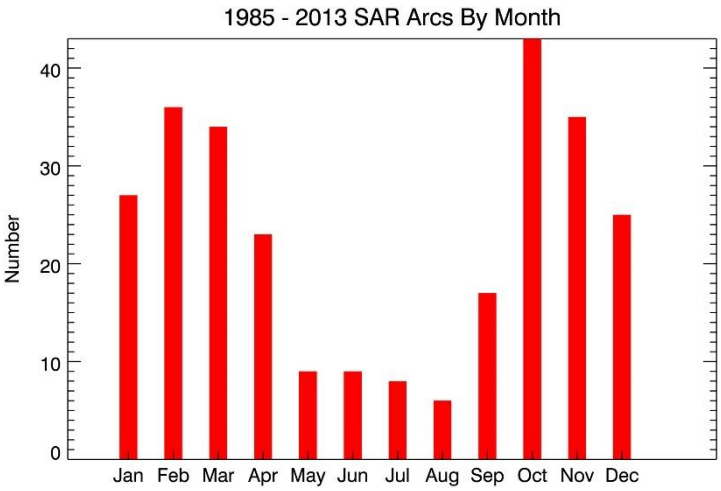

Figure 1. 25: *Seasonal occurrence rates of SAR arcs based on nighttime observations made during the period of 1985–2013 (Mendillo & Wroten, 2019).*

1.2.6 Strong Thermal Emission Velocity Enhancement

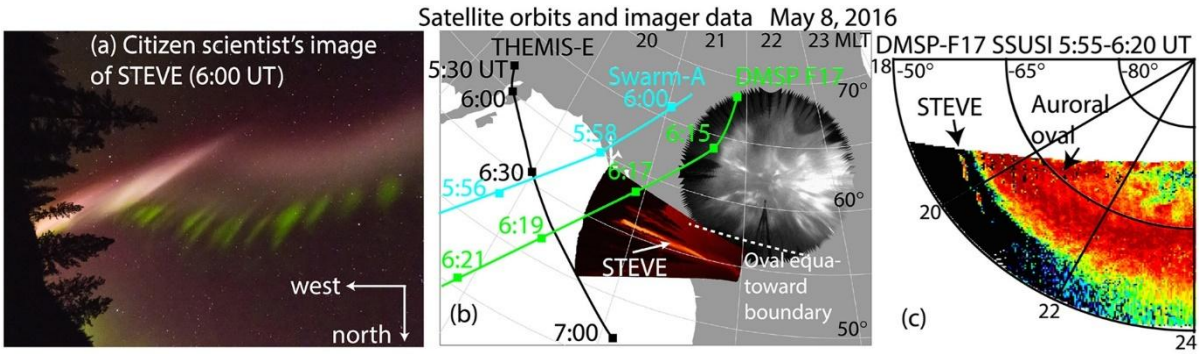

Figure 1. 26: (a) *Observations of STEVE arc by Citizen scientist along with the green picket fence on 8 May 2016 over North America.* ***(b)*** *All-sky-imager observations of STEVE equatorward to high-latitude auroral activity.* ***(c)*** *Simultaneously detected STEVE in the southern hemisphere using satellite measurements. After Nishimura et al. 2019.*

Strong thermal emission velocity enhancement (STEVE) is a mid-latitude phenomenon that was recently discovered and first reported by MacDonald et al. (2018). Furthermore, these authors also reported a green emission feature in the form of a picket fence in addition, called a green line picket fence structure, which is sometimes observed and sometimes not observed along with the STEVE. STEVE is formed equatorward of the auroral oval and is elongated thousands of kilometers (km) zonally with a latitudinal width of about a few 10s of km. A photo of a purplish ribbon-like structure of STEVE along with the green picket fence structure is shown in Figure-1.26(a), and the panels-b, c shows the observed position of STEVE through various instruments to be located equatorward of the auroral oval (Nishimura et al., 2019). The red emission, along with an excess of blue emissions through the excitation of O atom and N_2^+ ion, gives SETVE a purplish color (Mende & Turner, 2019). During an event, both features of STEVE and picket fence were observed simultaneously along similar magnetic field lines. Their height distribution revealed that STEVE used to occur at high altitude F-region (about 130-270 km). In comparison, picket fence occurs in the E-region ionosphere ranging from around 95 to 150 km altitude (Archer et al., 2019). The investigation of the generation mechanism of recently observed STEVE and picket fence emissions suggested that STEVE emissions are associated with a rapid plasma flow of SAID and collocated near the poleward boundary of the ionospheric trough, as shown in Figure-1.27, while the picket fence was attributed to high energy electron precipitation (~10 keV) and upward FACs (Nishimura et al., 2019). STEVE is also found to be following the preceding SAR arc (Chu et al., 2019; Martinis

et al., 2021), and the transition of a SAR arc into STEVE is currently a topic of discussion. Therefore, STEVE phenomena become different from the mid-latitudes SAR arcs, which are monochromatic red line emissions and are generated by soft particle precipitation with energies of few electron volts. Therefore, the frictional heating by subauroral ion drift or SAID is an important factor in the formation of STEVE, and these emissions are said to be the optical manifestation of SAID in the mid-latitude ionosphere (MacDonald et al., 2018).

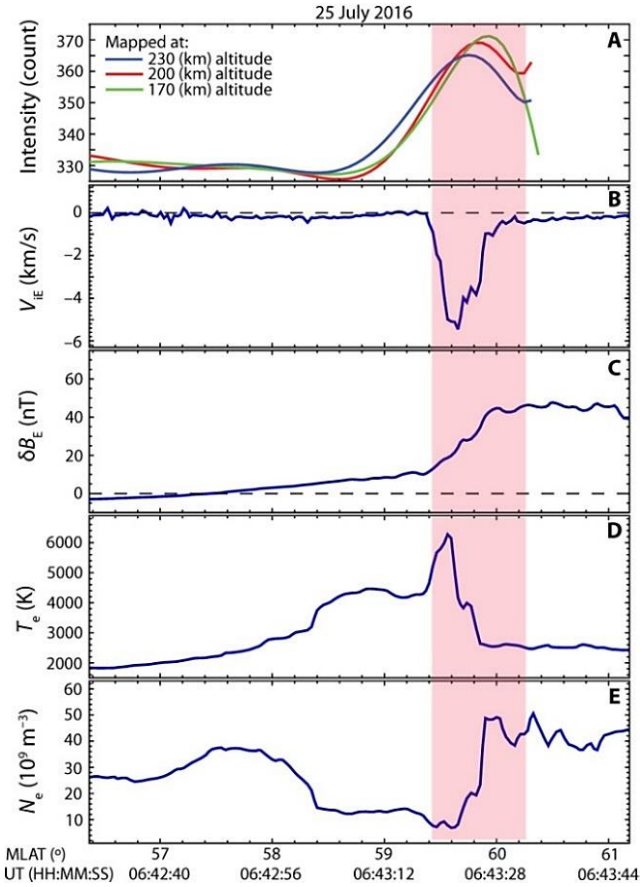

Figure 1. 27: *Satellite measured SAID signatures are shown in conjunction with a STEVE event on 25 July 2016 by shaded region. (MacDonald et al., 2018).*

1.3 Role of Optical emissions in the study of ionospheric phenomena

As discussed, the optical structures at mid-latitudes are associated with different morphologies and dynamics as compared to those at high latitudes. However, the behavior of optical emissions observed over mid- and high-latitudes is strongly linked to magnetosphere-ionosphere coupling. These optical emissions also reflect the variations in local ionospheric

dynamics during geomagnetically disturbed periods and thus become good tracers to investigate the Earth's upper atmosphere. Apart from such auroral or subauroral emissions, which are localized phenomena and occur over specific latitudes, there is another form of optical emissions, which is omnipresent around the globe and is referred to as *airglow*. Airglow emissions are produced due to the absorption of solar radiation by the neutrals in the upper atmosphere and various photochemical reactions that take place within those altitude regions (Chamberlain, 1961). Different atmospheric species produce different airglow emissions at different altitudes in the upper atmosphere and are associated with characteristics emissions, such as yellow line emission from Sodium atom at 589.3 nm wavelength, OH-band emissions, Nitrogen ion (N_2^+) emission at 427.8 nm, N(^{2}D) emission at 520.0 nm, atomic oxygen green line (557.7 nm) and red line (630.0 nm) emissions due to O(^{1}S) and O(^{1}D) states, respectively, 777.4 nm emission by the excited state O(3p^{5}P), 135.6 nm emissions due to O(3s^{5}S) state among others.

For the investigation of upper atmospheric science, these emissions have been used by numerous researchers. The high latitude upper atmospheric phenomenon of proton precipitation was first discovered by the optical spectroscopy method (Vegabd, 1939). These thermospheric emissions have also been used to measure the thermosphere winds and neutral temperature (e.g., Gurubaran et al., 1995; Shiokawa et al., 2003a). The measured hydroxyl airglow emissions were used to derive the mesospheric rotational temperatures (e.g., López-González et al., 2007; Singh & Pallamraju 2015, 2016, 2017). By using the airglow emissions at 630.0 nm wavelength, features of high-latitude cusp and first signatures of aurora during daytime over mid-latitudes were reported (Pallamraju et al., 2004; Pallamraju & Chakrabarti, 2005; Pallamraju et al., 2011). Apart from this, the upper atmosphere dynamics monitored from daytime optical measurements revealed several new insights, such as the existence of wind circulation during stratospheric sudden warming events (Laskar & Pallamraju, 2014), the existence of latitudinal variation in as small as 3° separation in longitude in the equatorial electrodynamical processes (Karan & Pallamraju, 2017) among others. As various optical phenomena over mid and high latitudes are attributed to the M-I coupling, these emissions also provide a wealth of information about the number flux and deposition of energy in the ionosphere and contribute to the characteristic energies of precipitating particles. Therefore, the direct spectral measurements of optical airglow/auroral emissions have become an important means of investigating atmospheric dynamics and energy.

1.4 Summary

In this chapter, various components of Earth's magnetosphere and ionosphere were discussed. It was introduced that the magnetosphere is largely disturbed by its interaction with the interplanetary magnetic field of solar wind origin. The perturbations generated in the magnetosphere during geomagnetically disturbed periods have a significant influence on the mid and high-latitude upper atmosphere, such as changes in dynamics, currents, and charged particle content of the ionosphere, among others. The ionosphere over mid-latitudes, which is inherently coupled with the plasmasphere through the closed geomagnetic field lines, also undergoes several dramatic changes, and several large-scale space weather phenomena occur in the mid-latitude upper atmosphere as a consequence of this magnetosphere-ionosphere coupling. It was also discussed that some of these phenomena manifest as large-scale optical structures in the mid-latitude ionosphere. Thus, studies of the temporal behavior of these optical emissions can offer valuable insights into understanding the upper atmospheric phenomena and the response to geomagnetic storms and sub-storms caused during space weather disturbances.

1.5 Objective of the thesis

During geomagnetic disturbances, the upper atmosphere at mid-latitudes shows highly dynamic changes as a consequence of magnetosphere-ionosphere coupling, and high to mid-latitude coupling, and the response of mid-latitude upper atmosphere has long been the subject of great interest. Various phenomena at mid-latitudes are typically studied under nighttime conditions. Therefore, the primary objective of this study is to investigate several of the upper atmospheric phenomena and the consequences of different coupling processes over mid-latitudes during daytime conditions. This has been achieved through the analysis of the atomic oxygen 630.0 nm daytime airglow emissions as a primary dataset during different geophysical conditions, varying from periods of severe geomagnetic activities to quiet time periods. Some of the questions that have been addressed are as follows:

a) What are the optical consequences of storm-enhanced densities?

b) Can SAR arc be observed during daytime? If so, what will the role of thermal enhancements be in producing daytime SAR arcs?

c) How can an electron heat flux be quantified using 630.0 nm emissions for daytime SAR arcs?

d) Apart from the dramatic ionospheric changes during geomagnetic disturbances, how do the thermospheric neutral dynamics vary in the mid-latitude upper atmosphere during quiet times?

1.6 Structure of the thesis

Chapter 1 introduces the various constituents of the magnetosphere-ionosphere and thermosphere-ionosphere systems. M-I coupling effects over the mid-latitude ionosphere, as seen in different mid-latitude phenomena, are also described.

Chapter 2 consists of information on the instrument used for obtaining the 630.0 nm emissions during daytime, along with other complementary datasets. Some of the analysis techniques used in this work are also briefly described. The novelty of the daytime airglow extraction technique used in this study, along with the production mechanisms, is also described.

Chapter 3 presents the behavior of atomic oxygen 630.0 nm emission during a main phase of the geomagnetic storm over mid-latitudes.

Chapters 4 and 5 present the role of electron temperature in atomic oxygen 630.0 nm emission, focusing on thermal enhancements under daytime conditions and the variation of electron heat flux responsible for thermal electron heating during the recovery phase.

Chapter 6 presents the change in neutral dynamics for the periods of geomagnetically quiet activities.

Chapter 7 provides the summary of the thesis work along with the future plan.

Chapter: 2

Experimental datasets, models, techniques, and data analysis

2.1 Introduction

As discussed in Chapter 1, various phenomena in the mid-latitude upper atmosphere such as SED, SAR arcs, and other consequences of magnetosphere-ionosphere coupling, occur during both day and night and are associated with various emissions. The scientific objective of this study is to investigate the response of the mid-latitude upper atmosphere (UA) by optical means for both geomagnetically quiet and disturbed periods. Remote sensing techniques enable a thorough investigation of the Earth's upper atmosphere and involve two types: active and passive. Active remote sensing consists of transmitting a probing electromagnetic wave into a medium and detecting the scattered or reflected signals, with RADAR (RAdio Detection And Ranging) and LIDAR (Light Detection And Ranging) being common examples. In contrast, passive remote sensing records naturally occurring radiation within the medium, without disturbing the medium by any external signal. Emissions in the electromagnetic spectrum occur in ultra-violet, visible, near-infrared, and infrared wavelengths due to ambient photochemical and chemiluminescent processes. These emissions are called ‘Airglow’ and are an efficient tracer of the behavior of the medium in the upper atmosphere altitudes from where they originate. Different techniques, such as photometry, spectrometry, or interferometry of these naturally occurring airglow emissions, are employed to derive various physical parameters for passive remote sensing of the UA.

Optical techniques provide important information on the neutral parameters of the upper atmosphere, such as temperature, winds, and atmospheric gravity waves. While several studies have been conducted using optical methods during nighttime (e.g., Ejiri et al., 2003; Gurubaran & Sridharan, 1993; Kosch et al., 2007; Kubota et al., 2000; Lakshmi Narayanan et al., 2010;

Makela et al., 2001, 2004, 2013; Martinis et al., 2010; Mendillo et al., 1997, 2001; Mukherjee et al., 2006; Narayanan et al., 2013; Otsuka et al., 2002; Pedersen et al., 2010; Singh & Pallamraju, 2016; Shepherd et al., 1980, 1995, 1997; Shiokawa et al., 2003b, 2006, 2009; Sridharan et al., 1993a; Taylor et al., 1995), studies on the daytime upper atmospheric dynamics have been quite sparse.

The ground-based dayglow measurements are much more challenging than nightglow due to the strong solar scattered continuum in the background, whose brightness is of the order of Mega-Rayleigh $Å^{-1}$ (10^6 R). Dayglow intensities are of the order of kilo-Rayleigh (10^3 R) [1 Rayleigh (R) = $10^6/4\pi$ photons cm^{-2} s^{-1} sr^{-1}]. Few attempts have been made earlier for dayglow studies but with limited success (e.g., Bens et al., 1965). In a system using a triple Fabry-Pérot etalon, Barmore (1977) resolved the OI 630.0 nm emission and concluded that the measured temperatures closely matched those obtained from the incoherent scatter radar. Cocks and Jacka (1979) determined the wind velocity and temperature in the thermosphere using OI 630.0 nm emissions with a high-resolution dual Fabry-Pérot etalon system. Narayanan et al. (1989) and Sridharan et al. (1992) introduced a method for isolating dayglow emission intensities from the solar scattered background using a pressure-tuned low-resolution Fabry-Pérot etalon and a temperature-tuned narrow-band interference filter. They used a radial chopper to differentiate between line emissions and background and an automated data processing system. The method allowed extraction of OI 630.0 nm emissions, with simplified optical alignment through a single etalon setup. Further, Pallam Raju et al. (1996) used a dual mask system divided into 12 equal segments to separate the OI 630.0 nm emission region from the background continuum. Out of these, the most successful have been the dayglow photometry, as described in Narayanan et al. (1989), Sridharan et al., 1993, 1998, Pallamraju et al., 1996 and Pallamraju, 1996, and spectrography (Chakrabarti et al., 2001; Pallamraju et al., 2000, 2002, 2013). These are reviewed by Pallamraju (1996) and Chakrabarti (1998). Several insightful results on low, equatorial, and high latitudes have been obtained using these techniques (e.g., Pallam Raju et al., 1995; Sridharan et al., 1995; Pallamraju & Sridharan, 1998a; Pallam Raju & Sridharan, 1998b; Chakrabarty et al., 2005).

In this work, results obtained from mid-latitudes will be presented. This work primarily involves passive methods and the analysis of atomic oxygen 630.0 nm daytime airglow emissions. Radio and magnetic measurements and model outputs have also been utilized as complementary datasets to substantiate the findings. The daytime 630.0 nm airglow emissions were obtained using a ground-based High-Resolution Imaging Spectrograph with an Echelle

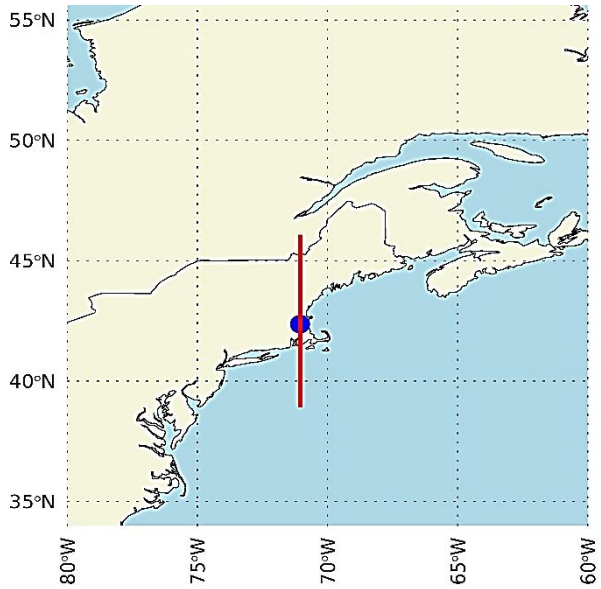

Figure 2. 1: *The observational location of Boston over North American longitudes is shown by a blue dot, indicating where OI 630.0 nm emissions were being observed by HIRISE. The red vertical bar represents the meridional extent covered by the HIRISE field-of-view (FOV).*

grating (HIRISE) from Boston (42.36° N, 71.05° W), a mid-latitude location, as indicated by the map shown in Figure-2.1. The red vertical line represents the geographic latitude range covered by the large field-of-view (~140° angle, ~39° to 46° N) of HIRISE. This chapter describes the HIRISE instrument and methods used for the image processing and extraction of OI 630.0 nm emissions during daytime. This chapter also describes some other datasets, and models used in this study.

2.2 Daytime atomic Oxygen 630.0 nm (red line) emission

Optical airglow emissions during daytime, also called dayglow, occur because of various photochemical reactions involving the ambient neutral and plasma densities. As the Sun's radiation interacts with atmospheric atoms and molecules like nitrogen and oxygen, these species absorb sunlight and ionize, and undergo various reactions with other neutrals and ionized species. Under certain circumstances, they get excited to their higher energy states and, on their deexcitation, release energy as a photon, contributing to the daytime airglow. Different excited species emit photons in various wavelengths varying from ultraviolet to infrared due to

different production mechanisms that are operative at their respective altitudes of origin. As the ambient neutral and plasma densities are affected by the geophysical conditions, this leads to the variation in the airglow emission intensities. Therefore, variabilities in dayglow emissions serve as a good tracer for understanding the atmospheric dynamics at their altitude of origin. As mentioned earlier, the work presented in this thesis is based on the variabilities of 630.0 nm emission, peaking at around 230 km, produced by the oxygen atoms. The following sections discuss the production mechanism of daytime 630.0 nm emissions and the emission extraction procedure for the HIRISE obtained sky spectrum.

2.2.1 Production mechanisms of daytime OI 630.0 nm emission

The atomic oxygen (OI) red line emissions at 630.0 nm wavelength are formed by the radiative de-excitation of the O(^{1}D) state to the ground state O(^{3}P) (Torr & Torr, 1982). The transition of the O(^{1}D) to O(^{3}P) state is forbidden, with a lifetime of about 110 seconds. The metastable state O(^{1}D) leading to 630.0 nm emission is produced mainly by the photoelectron impact, photodissociation, and dissociative recombination mechanisms during daytime (Solomon & Abreu, 1989), as below:

a) Photoelectron impact (PEI) excitation of oxygen atom:

Excitation of O(^{3}P) to the O(^{1}D) state requires 1.96 eV energy. When a photoelectron (e_{ph}) or thermally heated electron (e^*) carries energy greater than the required excitation energy of 1.96 eV, its collision with the ambient oxygen atom results in the transfer of required energy and produces the O(^{1}D) state.

$$O + e_{ph}^{*} \xrightarrow{> 1.96\ eV} O(^1D) + e_{ph} \tag{2.1}$$

The role of thermally heated electrons is important for auroral/subauroral emissions, apart from airglow emissions due to particle precipitation (Wickwar & Kofman, 1984). A brief review of thermal electrons is presented by Mantas and Carlson, 1991. As the neutral density of oxygen atoms ($[O]$) varies with altitude (z), the associated total production rate for this mechanism (P_{PEI}) can be calculated as below:

$$P_{PEI}^{630.0}(z) = [O(z)] \int \sigma_{1_D}(E)\, \phi(E,z)\, dE \tag{2.2}$$

where, $\sigma_{1_D}(E)$ is the excitation cross section, given by Doering (1992), and the photoelectron flux for a given energy *E* is represented by ϕ *(E, z)* as a function of altitude (*z*).

b) Photodissociation (PD) of molecular oxygen:

The dissociation of molecular oxygen (O_2) by the solar photons in the wavelength regions extending from 135-175 nm leads to the production of the O(^{1}D) state. This continuum lying in the wavelength range 135-175 nm is known as the *Schumann–Runge continuum*.

$$O_2 + h\nu \xrightarrow{135-170\ nm} O + O(^1D) \tag{2.3}$$

The production rate of the PD mechanism (P_{PD}) for varying densities of molecular oxygen (O_2) with altitude (*z*) is given as:

$$P_{PD}^{630.0}(z) = [O_2(z)] \int_{135-170\ nm} \sigma_{sr}(\lambda)\, I(\lambda,z)\, d\lambda \tag{2.4}$$

where σ_{sr} is the photodissociation cross sections (Torr et al., 1980) and *I (λ, z)* represent the attenuation in solar flux with height in the given wavelength range.

c) Dissociative recombination (DR) of molecular oxygen ion:

The molecular oxygen ion (O_2^+) is formed by the charge exchange between the O^+ ion and the O_2 molecule as:

$$O_2 + O^+ \xrightarrow{k_1} O_2^+ + O \tag{2.5}$$

where, $k_1 = 1.95 \times 10^{-7}\ (Te/300)^{-0.70}$ is the rate coefficient ($cm^3\ s^{-1}$) (Mostefaoui et al., 1999). Tthe O_2^+ thus formed recombines dissociatively with the ambient thermal electrons (e_{th}) to produce the O(^{1}D) state.

$$O_2^+ + e \rightarrow O(^1D) + O \tag{2.6}$$

At a given altitude, z, for electron density, *Ne(z),* and molecular oxygen ion density of $[O_2^+(z)]$, the production rate for the DR mechanism (P_{DR}) is given as:

$$P_{DR}^{630.0}(z) = \beta_2 k_2 [O_2^+(z)]\, N_e(z) \tag{2.7}$$

where, β_2 and k_2 are the efficiency and reaction rate coefficients (Guberman, 1988).

The transition of the excited O(^{1}D) state, formed by the aforementioned production mechanisms, to the ground state O(^{3}P) can occur either by (i) collisional deactivation as:

$$O(^1D) + A \rightarrow A + O(^3P) \tag{2.8}$$

(where, A represents the species N_2, O_2, O, or e_{th}) or (ii) radiative transition as:

$$O(^1D) \rightarrow O(^3P) + h\nu \tag{2.9}$$

Therefore, the radiative transition as above results in the formation of 630.0 nm red line emission.

From the consideration of the above source mechanisms, the following expression can be used to calculate the total production rate (P_{total}) of O(^{1}D):

$$P_{total}\big(O(^1D)\big) = P_{PEI} + P_{PD} + P_{DR} \tag{2.10}$$

Similarly, the quenching rate, Q, by loss mechanisms can be expressed as:

$$Q = \frac{A_{10}}{(A_{10} + A_{11} + k_6[N_2] + k_7[O_2] + k_8[O] + k_9[e])} \tag{2.11}$$

where, k_i are the reaction rate coefficients and A_i represents the Einstein's transition probabilities (Solomon & Abreu, 1989; Witasse et al., 1999). Therefore, the total volume emission rate (VER; photons cm^{-3} s^{-1}) of atomic oxygen O(^{1}D) state can be given as:

$$VER_{O(^1D)} = Q \times P_{total}[O(^1D)] \tag{2.12}$$

The above three different production mechanisms show that the total production of the O(^{1}D) state depends on the densities of ambient electrons, atomic oxygen, and oxygen molecules. Also, all these mechanisms peak at different altitudes, and the relative contribution of all three production mechanisms is shown in Figure-2.2. For geomagnetically quiet periods, the impact of the PEI mechanism peaks at lower heights (below 150 km), while the contribution of the DR mechanism is more significant in the 230-250 km altitude range. Out of the three production mechanisms, the PEI and PD have a major impact due to variations in solar flux and solar zenith angle, whereas, DR mechanism involves the contribution from electron density variations and shows temporal behavior in addition to that of the solar zenith angle variation. The PEI and PD mechanisms contribute significantly (by around 60-70%) to the total production of 630.0 nm emissions during the daytime, and the contribution from the DR mechanism accounts for around 20-30% (Hays et al., 1978; Pallamraju et al., 1996). As the electron densities vary more rapidly over a small-time scale than the solar flux on any given day, almost all the small time-scale features in the OI 630.0 nm dayglow emission intensity variation can be attributed to those of electron densities.

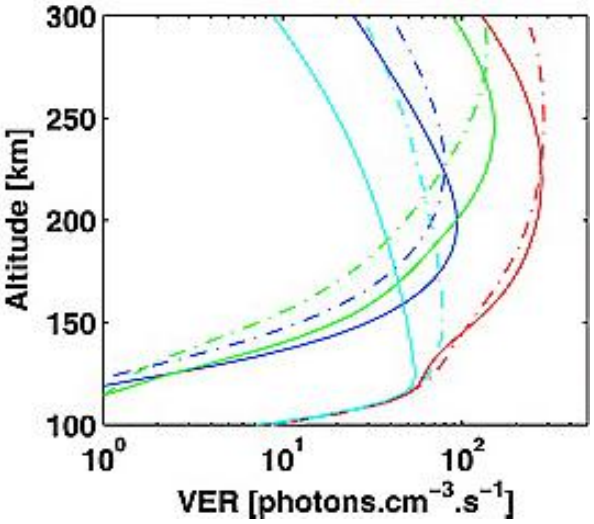

Figure 2.2: *The peak emission altitude variation for three 630.0 nm dayglow production mechanisms is shown for geomagnetically quiet (solid) and disturbed periods (dashed) at solar zenith angle of 50°. The green, cyan, and red lines represent the profile of DR, PEI, and PD production mechanisms, respectively (Culot et al., 2005).*

2.3 Daytime optical measurements

As discussed, the variabilities in airglow emissions are associated with changes in neutral and plasma densities, and provide information on the dynamics in the upper atmosphere. Also, information on upper atmospheric compositional changes, rotational temperatures, winds, and

more can be obtained using optical emissions. The remote sensing techniques utilizing optical methods are primarily based on photometry, interferometry, and spectrometry for performing optical observations. Since the beginning of optical observations, most ground-based airglow emissions observations are limited to nighttime conditions (Chamberlain, 1961). With time, the advancements in technology enabled the observations of these nightglow emissions with better spectral and temporal resolutions (Hernandez & Roble, 1976; Kulkarni, 1976; Hays & Sharp, 1973; Hays et al., 1978; Shepherd, 1979; Mendillo & Baumgardner, 1982; Meriwether et al., 1986; Sridharan et al., 1991; Shiokawa et al., 1999; Chakrabarty et al., 2001; Meriwether, 2006).

Observing airglow emissions during the daytime, is highly challenging due to the strong solar continuum in the background. However, attempts were made to obtain the dayglow emissions, but the results were inconclusive. The first attempt to measure dayglow was performed in a balloon-borne experiment by Wallace (1961) but was unsuccessful. Later, their technique used a high-resolution spectrograph but could not resolve the Fraunhofer absorption features (Wallace & McElroy, 1966). Since the dayglow emissions are unpolarized, Noxon (1968) used a polarimetry technique to measure the dayglow. However, the difficulty of background intensity could not be resolved, leading to a lack of systematic observations. Later, subsequent studies managed to obtain 630.0 nm dayglow emissions, which used the combinations of Fabry-Perot (FP) etalons of both low and high resolutions (Barmore, 1977; Cocks et al., 1980). Although these techniques were successful in obtaining the dayglow, no systematic studies of upper atmospheric processes could be carried out as they struggled with maintaining the temperature of FP etalons. Therefore, an innovative technique of dayglow photometry was developed, which used a pressure-tuned low-resolution FP etalon for temperature stability and a unique optical mask system to differentiate the solar background (Narayanan et al., 1989; Sridharan et al., 1992a). This technique became successful in carrying out the observations of dayglow emissions in both a systematic and continuous manner (Pallam Raju et al., 1996; Pallamraju, 1996). This optical mask system was further modified to develop a multiwavelength dayglow photometer (Sridharan et al., 1998). Therefore, these developments of dayglow photometer and multiwavelength dayglow photometer led to several new and insightful results for daytime conditions covering from whole low and equatorial latitudes to high latitude regions (e.g., Sridharan et al., 1991, 1992b, 1993a, 1995; Pallam Raju et al., 1996; Pallamraju and Sridharan, 1998a, 1998b). With the help of such daytime optical measurements and investigations, a breakthrough came in the field of daytime optical aeronomy.

The WIND Imaging Interferometer (WINDII) onboard the Upper Atmosphere Research Satellite (UARS) provided the opportunity to study airglow and auroral emissions under daytime conditions from a global perspective (Shepherd et al., 1993a). Additionally, by using an echelle grating in combination with a Charge-Coupled Device (CCD) and interference filter, a spectrograph called the High Throughput Imaging Echelle Spectrograph (HiTISE) was developed to study nightglow emissions (Chakrabarti et al., 2001). Further, a potentially capable variant of HiTISE for dayglow observations, named HIRISE (High-Resolution Imaging Spectrograph using Echelle grating), was developed by employing the echelle grating to obtain a high-resolution daytime spectrum (Pallamraju et al., 2002).

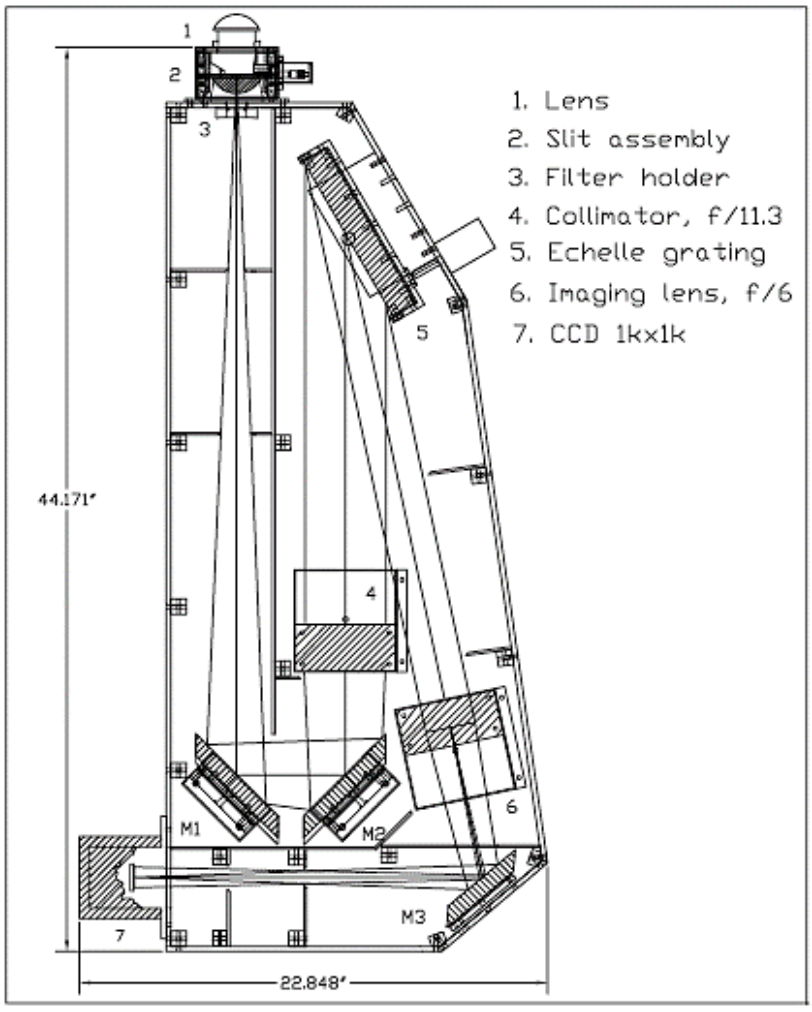

Figure 2. 3: *Schematic diagram of High-Resolution Imaging Spectrograph using Echelle grating (HIRISE) used to obtain the OI 630.0 nm emissions during daytime (Pallamraju et al., 2002).*

This thesis primarily uses the ground-based observations of daytime 630.0 nm airglow emission as the principal dataset obtained from HIRISE to investigate the daytime upper

atmosphere over mid-latitudes. The HIRISE was operational from 2003 to 2008. Therefore, the OI 630.0 nm dayglow observations investigated in this study correspond to the duration of decreasing phase of solar cycle-23. The red line emission data obtained from HIRISE have yielded several new and first kind of results in the mid-latitude upper atmosphere during daytime conditions, which are discussed in subsequent chapters. The details of the HIRISE and its technical specifications are discussed below.

2.3.1 High-Resolution Imaging Spectrograph using Echelle grating (HIRISE)

HIRISE is a high-resolution long slit spectrograph that used echelle grating and interference filter to obtain the observations of OI 630.0 nm dayglow emissions, as shown by the schematic in Figure-2.3 (Pallamraju et al., 2002). The various components and functioning of HIRISE to obtain the sky spectrum can be described briefly as below:

i) objective lens
ii) slit assembly
iii) interference filter
iv) collimator lens (f/11.3)
v) echelle grating
vi) imaging lens (f/6)
vii) CCD

Firstly, the light enters from the *objective lens* located at the top of the instrument. The field-of-view of HIRISE can be changed from 8° (zenith) up to 180° (all sky) by changing the objective lens. A slit (40 mm length) along with a field lens and an interference filter (of about 100 Å FWHM; FWHM: Full width at half maximum) is placed right behind the objective lens. The interference filter is used for order separation, and therefore, it allows only a narrow range of wavelengths to pass through. A field lens placed behind the slit reduces the divergence of the light entered. The two plane mirrors, *M1* and *M2*, redirect the incident beams to fall on a *collimator lens* (f/11). The collimator used here is an apochromat and is used to minimize the chromatic aberrations. A depiction of chromatic aberration is illustrated in Figure-2.4.

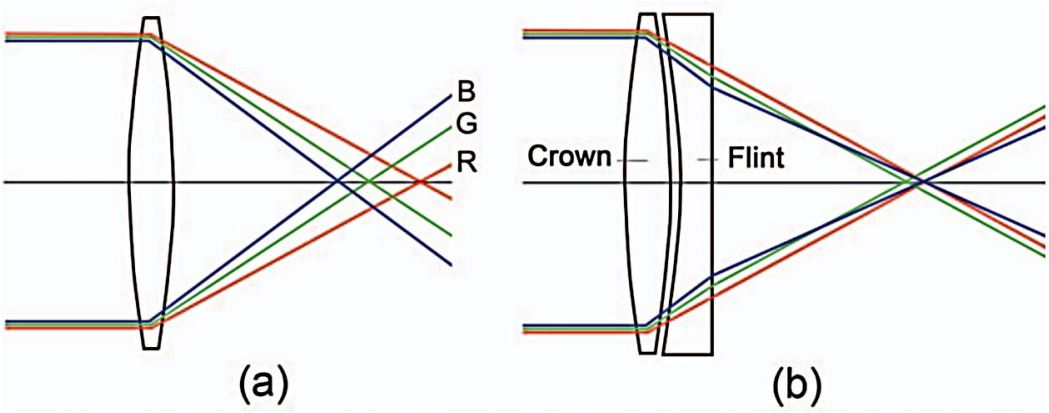

Figure 2. 4: *Comparison of chromatic aberration: (a) Lateral chromatic aberration for different wavelengths due to different focal lengths. (b) Use of achromatic doublet to solve the lateral chromatic aberration simultaneously focusing different wavelengths at one point. (After Brady & Legge, 2009.)*

This collimated beam now falls on the *echelle grating*, which is the key element of the instrument. The grating disperses the light into its components and can be expressed by the *grating equation*, given as-

$$n\lambda = d(sin\alpha + sin\beta) \tag{2.13}$$

where, n is diffraction order, λ is the wavelength of light, d is the groove spacing, α is the angle of incidence, and β is the angle of diffraction. For HIRISE, the angle between α and β is 12°.

After falling onto the grating, the light gets diffracted for different wavelengths at different orders, as described by the Equation-2.13. The angular dispersion of light for a given angle of incidence can be obtained by differentiating the Equation-2.13 and is given as-

$$\frac{d\beta}{d\lambda} = \frac{n}{dcos(\beta)} \tag{2.14}$$

Using Equation-2.13, the above Equation-2.14 becomes:

$$\frac{d\beta}{d\lambda} = \frac{(sin\alpha + sin\beta)}{\lambda\cos(\beta)} \tag{2.15}$$

Therefore, a high angular dispersion can be obtained for large values of incidence and diffraction angles (α and β), and a small groove spacing (d). The grating used by HIRISE has a groove density of 98.6 lines mm^{-1}, and a blaze angle of 63.5° and operates at high orders (n ≈25-45). Blaze angle represents the angle between the face of the groove and the grating surface, as shown by the schematic in Figure-2.5. The gratings that operate at high values of α and β are known as echelle gratings and provide a higher resolution spectrum as they correspond to higher orders.

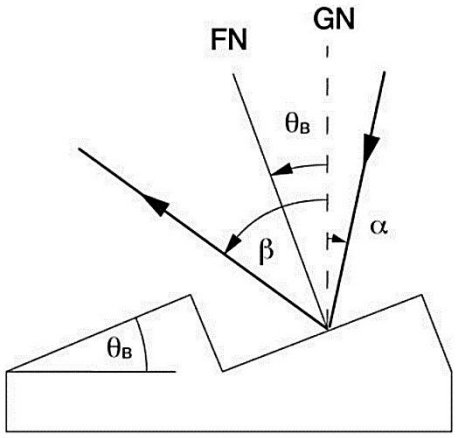

Figure 2. 5: *The incidence angle (α) and diffraction angle (β) are shown in relation to the blaze angle (θ_B). GN is the normal to the horizontal grating surface and FN is the facet normal. (From Palmer, 2020).*

This diffracted light from grating now passes through an *imaging lens* (*f* /6), which is another apochromatic lens of focal length 600 mm. Since the *f* /6 lens is smaller in focal length than *f* /11, it reduces the size of the beam by approximately a factor of 2. The light from the camera lens is folded by mirror *M3* and is imaged on a 24 mm wide (1024×1024 pixels) *CCD chip*. The dispersion arrived at by HIRISE is 0.004 nm $pixel^{-1}$. The pixel size of CCD is around 3x larger than the diffraction limit of the lenses (9.2 μm at 6500 Å). However, as will be shown in section 2.3.2, the dispersion and resolutions arrived at by HIRISE is sufficient to extract the daytime airglow emissions. As the dispersion limit is much better than the pixel size, a suitable modification with a smaller pixel size CCD and with small modification to the optics design led to the development of a Multiwavelength Imaging Spectrograph using Echelle-grating (MISE; Pallamraju et al., 2013).

The CCD chip has a large spectral range varying from 390.0 nm to 800.0 nm. When the light is illuminated, each pixel in the CCD acts like a small bucket that gathers electrons. The amount of light (brightness) hitting each pixel determines how many electrons are accumulated in that pixel. Brighter light causes more electrons to be accumulated, resulting in a region of brighter pixels. These accumulated electrons are then counted by the computer processing to create a digital representation of the image. Therefore, the brightness values are converted to electron counts or data numbers (DN) as a two-dimensional array, and an image of a high-resolution sky spectrum is obtained. A sample image obtained by HIRISE is shown in Figure-2.6.

Different pixels in the image obtained from the CCD correspond to different positions in the sky (FOV ~140°). Bright areas of the image have a high number of counts, while dark areas have low counts. The pixels on the image have a wavelength and spatial information along the *x*- and *y*- axis, respectively. Dark vertical lines in the image represent the Fraunhofer absorption lines. The primary features of the HIRISE instrument are summarized in Table-2.1.

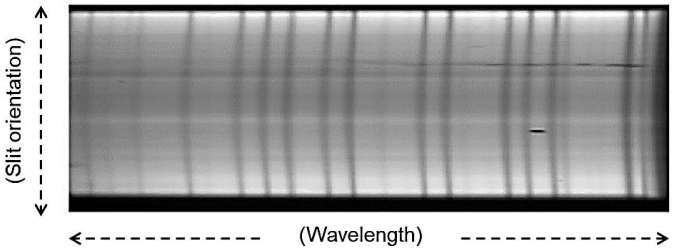

Figure 2. 6: *A sample image of the daytime sky spectrum observed by HIRISE on 23 March 2008 over Boston. The x-axis represents the wavelength information, while the spatial information is represented on y-axis.*

Slit length	40 mm	
Slit width	0.040–3.0 mm	
Throughput (AΩ)	3.1229×10^{-4} cm^2	
Collimator	f = 1130 mm	(F/11) apochromat
Grating	98.6 lines mm^{-1}	100 mm x 200 mm
Angle between α and β	12°	
Camera lens	f = 600 mm	(F/6) apochromat
Estimated Optical Transmission τ	0.16875	
		Quantum efficiency $q(\lambda)$: 0.8 e- ph^{-1}
		λ range: 3900-8000 Å
Detector	Thinned 1024 × 1024 pixels	Dark signal: 0.1 e- s^{-1} pixel^{-1}
	SITe CCD	Read noise: 6 e- RMS
		Gain, g: 2.656 e- DN^{-1}
		Pixel size: 0.024 mm
No. of rows (n_{rows})	110 for 8-pixel binning along the slit	
Dispersion (d)	0.04 Å pixel^{-1}	at 5893 Å
Resolution	0.12 Å	at 5893 Å

Table 2. 1: *Characteristics of HIRISE. Specifications of each optical components are given. After Pallamraju et al. (2002)*

2.3.2 Daytime airglow emission extraction procedure

The HIRISE observed sky spectrum was compared with the solar spectrum (Solar Atlas BASS2000; http://bass2000.obspm.fr/solar_spect.php) in wavelengths and continuum regions around the desired dayglow emission (here 630.0 nm) region, as shown in Figure-2.7. The comparison of two spectra leads to the wavelength information corresponding to different pixels on the x-axis of the image, and the location of 630.0 nm emission is achieved. The best possible match of the above two spectra is attained by a least-squares technique, wherein the continuum regions around the emissions region are considered. As normalized solar spectrum is used, a scaling array or continuum values are obtained (panels 1b and 1c in Figure-2.7). The presence of atmospheric emissions (airglow), the depth of atmospheric absorptions (Telluric lines), and atmospheric scattering (Ring effect; Grainger & Ring, 1962) make the sky spectrum different from the solar spectrum. The Ring effect is found to be due to rotational Raman scattering and exists in all Fraunhofer absorption regions (Conde et al., 1992; Pallamraju et al., 2000). Remember that any instrumental solar and sky spectra are not the 'true' spectra but the result of convolution with the instrument's function, affecting the observed spectra and blending the true spectral features. Therefore, the scaled solar spectrum is then subtracted from the sky spectrum to obtain the difference between them and to remove the solar background. It is to be noted that the absorption line at 630.0 nm dayglow region is not telluric; the atmospheric contribution at 630.0 nm will consist of contributions from the optical emissions and scattering (Ring effect). The atmospheric contribution from the Fraunhofer absorption region separated by just ~ 0.035 nm (corresponding to Scandium) is also not a telluric line, and thus, the atmospheric contribution at this wavelength corresponds to the Ring effect alone (panel 1d of the Figure-2.7).

A critical need is to appropriately account for the ring account with regard to its wavelength and solar zenith angle dependence, which can otherwise lead to overestimating 630.0 nm emission intensities. An approach given by Pallamraju et al. (2000) was used to remove the contribution from the ring account, wherein it has been shown that the scattering contribution in two neighboring absorption regions of equivalent absorption line strengths (normalized depth × width) is equal. Therefore, the two neighboring lines, the oxygen Fraunhofer line (630.03 nm) and the Scandium Fraunhofer line (630.06 nm), were used to calculate the ratio factor (f) as follows:

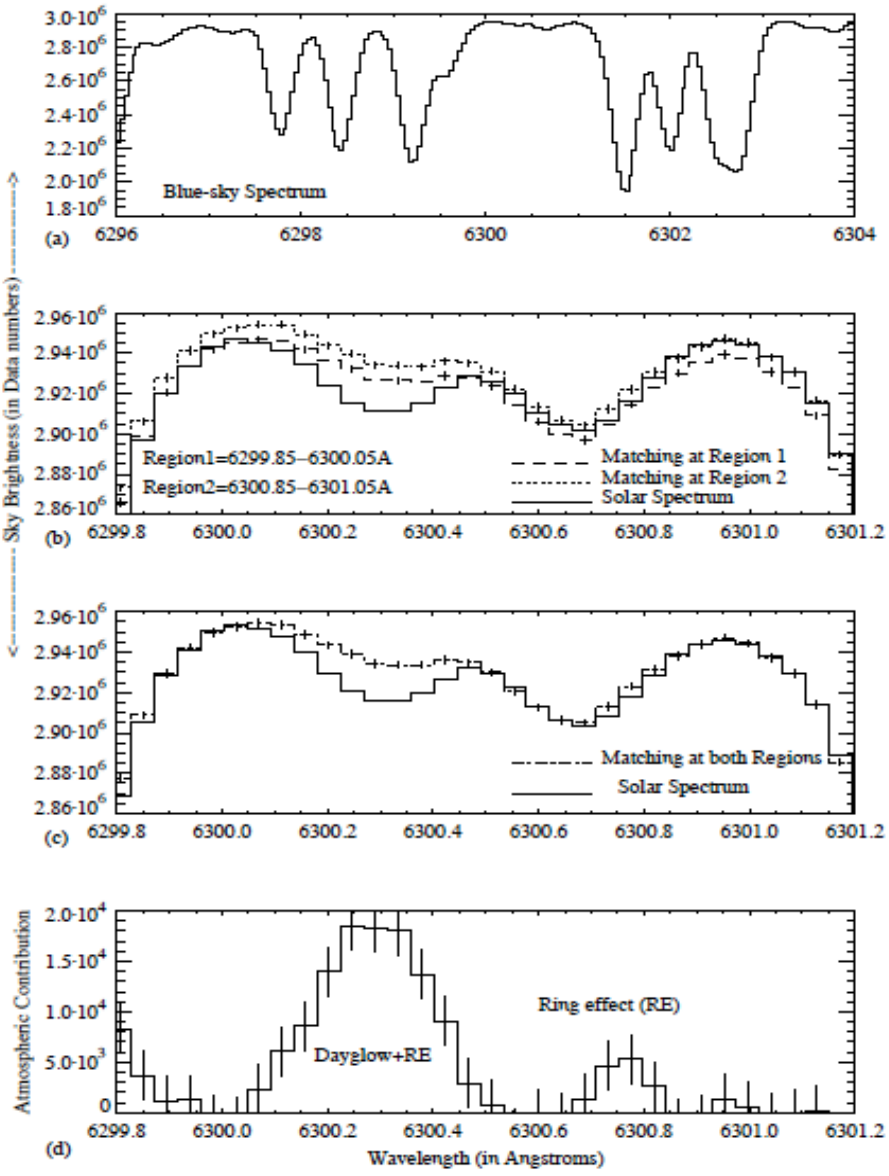

Figure 2. 7: *The intricacies involved in the data analysis procedure are depicted. Panel (a) shows the blue-sky spectrum obtained using a 6300 Å region. Panel (b) shows the need for matching the continuum regions on either side of the emission wavelength. (c) Scaled solar and blue-sky spectra after the least-squares matching at the continuum regions on either side of the emission line of interest at 6300.3 Å. (d) Atmospheric contribution around the 6300 Å region, obtained by subtracting the solar spectrum from the blue-sky spectrum shown in the above panel. Error (±1) bars are also shown. The one at the 6300 Å region consists of both the dayglow and the contribution due to Ring Effect, while the next one consists of only Ring Effect. The difference of area under these two curves yields the contribution due to dayglow at that time. This scaling is repeated for every data sample to obtain a diurnal behavior of the dayglow variability. (Pallamraju et al., 2002).*

$$f = \frac{(I_{c1} - I_{d1}) \times \lambda_{\omega 1}}{(I_{c2} - I_{d2}) \times \lambda_{\omega 2}} \tag{2.16}$$

where, I_{c1} and I_{d1} represent the intensity at the continuum level and the depth of the oxygen line, respectively, while $\lambda_{\omega 1}$ is the half-width of the oxygen Fraunhofer line centered at 630.03 nm. I_{c2}, I_{d2}, and $\lambda_{\omega 2}$ represent the same but for the neighboring scandium line at 630.06 nm. The ratio factor (f) scales the amount of scattering contribution from the scandium line to be considered for the oxygen line. Therefore, the only contribution from dayglow emission at 630.0 nm wavelength is given as:

$$Dayglow = \left[(Area)_{region-1}\right] - \left[(Area)_{region-2}\right] \times f \tag{2.17}$$

where, $Area_{region\text{-}1}$ and $Area_{region\text{-}2}$ represent the area under the curve of the oxygen line (containing both dayglow and scattering) and the area under the curve of the scandium line (containing scattering only). The difference in contributions between the airglow region (630.0 nm) and the neighboring spectral regions (630.07 nm), as above, accounts for the scattering contribution and yields the contribution of the dayglow alone. This well-established technique for extracting dayglow has been extensively documented in the literature (Pallamraju et al., 2013). Repeating the procedure for different-different images at different local times can retrieve the dayglow throughout a given day.

Since the measured intensity from HIRISE images is in the form of counts, the corresponding emission magnitudes in the Rayleigh unit can be estimated as:

$$N(\lambda) = B(\lambda) \times S(\lambda) \times t \tag{2.18}$$

where, $N(\lambda)$ is the number of photons registered on CCD, $B(\lambda)$ is dayglow emission intensity (in Rayleigh), $S(\lambda)$ is the sensitivity (DN s^{-1} R^{-1}) of the instrument, and t is the integration time (seconds). For a pixel on CCD, the sensitivity (Å) is given by Pallamraju et al. (2002) and can be expressed as:

$$S_{pixel} = (10^6 / 4\pi) \times Q(\lambda) \times \tau(\lambda) \times A \times \Omega / n_{rows}$$

where, $Q(\lambda)$ is *the overall* efficiency of the CCD detector ($Q(\lambda) = \text{quantum efficiency q}(\lambda) / \text{gain, g}$), $\tau(\lambda)$ is the optical efficiency of the instrument, A is the area of the slit, Ω is the solid angle made by sky on the slit, d is the dispersion in nm $pixel^{-1}$ and

n_{rows} represents the number of rows obtained after on-chip binning in the spatial direction. Thus, using the specifications of the instrument as mentioned in Table-2.1, the sensitivity of HIRISE was calculated as (Pallamraju et al., 2002):

$$S_{pixel} = 4.6 \times 10^{-4} \left(\text{DN Å R}^{-1}\,\text{s}^{-1}\right) \tag{2.19}$$

Therefore, the emission intensity can be changed from counts to Rayleigh units using the above sensitivity term in Equation-2.18.

Since the emission intensities are retrieved from CCD images, which are known to have different types of uncertainties, such as dark noise, readout noise, and digitization noise. In the case of airglow emission, as the count observations are larger, the digitization noise becomes insignificant. Therefore, the standard deviation (σ) for the case of CCD counts, where airglow photons follow the Poisson distribution, can be given as $\sqrt{mean}$, and the signal-to-noise ratio (SNR) is given as:

$$SNR = \frac{S}{\sqrt{(S+B)+D+R}} \tag{2.20}$$

where, S is signal strength, B is background, D is the dark noise, and R is the readout noise, respectively. The uncertainty in measurement is the reciprocal of SNR. Also, in the case of dayglow emissions, the readout and dark noise values are dominated by the strong signal and background strength, rendering them negligible. The SNR for daytime OI 630.0 nm airglow emissions thus becomes:

$$SNR = \frac{S}{\sqrt{(S+B)}} \tag{2.21}$$

Therefore, considering the parameters outlined in the CEDAR tutorial (Pallamraju, 2003), along with co-adding, binning, and averaging, the SNR for daytime OI 630.0 nm emissions was calculated. The resulting SNR typically varies from 2 to 27, according to variation in local time (essentially, the solar zenith angle).

The Interactive Data Language (IDL) programming language was used to perform the abovementioned procedure for obtaining the dayglow emission intensities. Sperate codes were developed to perform the different parts of the dayglow extraction procedure at 630.0 nm

wavelength and obtain the corresponding emission intensities. Also, as stated earlier, HIRISE can image different parts of the sky in the meridional direction (y-axis) by adjusting the FOV from 8° (essentially used for zenith) to 180° (all-sky). Therefore, the data from HIRISE includes both the zenith and all-sky measurements of OI 630.0 nm emissions at different times of data availability and is used accordingly.

2.3.3 Comparison of dayglow extraction method with previous approaches

The Ring effect tends to fill in the Fraunhofer valley of absorption lines; an innovative and efficient emission extraction method needs to be employed to account for this effect properly. Attempts were made to resolve the issue of scattering when the technique of dayglow observations was evolving. Broadfoot and Hunten (1966) analyzed the N_2^+ emissions during twilight, wherein a spectrometer was used over a short-spectrum region. They assumed that the scattering contribution remains the same with respect to the solar zenith angle for Fraunhofer lines. Therefore, a singly scattered K-absorption line was used to scale the background solar spectrum with the N_2^+ spectrum, and a direct difference was taken to observe the N_2^+ emissions. Also, their approach used different spectral widths for two regions: 8 Å spectral width region (3911-3917 Å) for their emission region of interest while 30 Å width (3920-3950 A) as background region, which is ~4 times larger than the emission region and not identical. A similar method was used for twilight time Ca+ emissions using the K-absorption line by Broadfoot (1967). Due to the selection of a single K-absorption line for scaling and different equivalent widths, the scattering issue was not resolved, leading to a substantial error in the measured intensities. Therefore, the *direct differencing technique* of sky and solar spectra resulted in a considerable deviation in the measured emission intensities. This method faces challenges due to changes in wavelength and amplitude of the atmospheric continuum with time. If the emission line is far from the normalization region, these changes can distort the results, particularly in valleys of the Fraunhofer structure, where atmospheric emissions often occur. Additionally, variations in brightness with time can create false signals in the residual spectrum, resulting in an inverted Fraunhofer structure in such analysis.

Another approach, such as the *rationing method*, was used by performing the scaling at finite wavelength points of solar spectra with sky spectra to observe the NO_2 absorption line (Noxon et al., 1979). For the scattering contribution, Noxon suggested that, since the filling in of

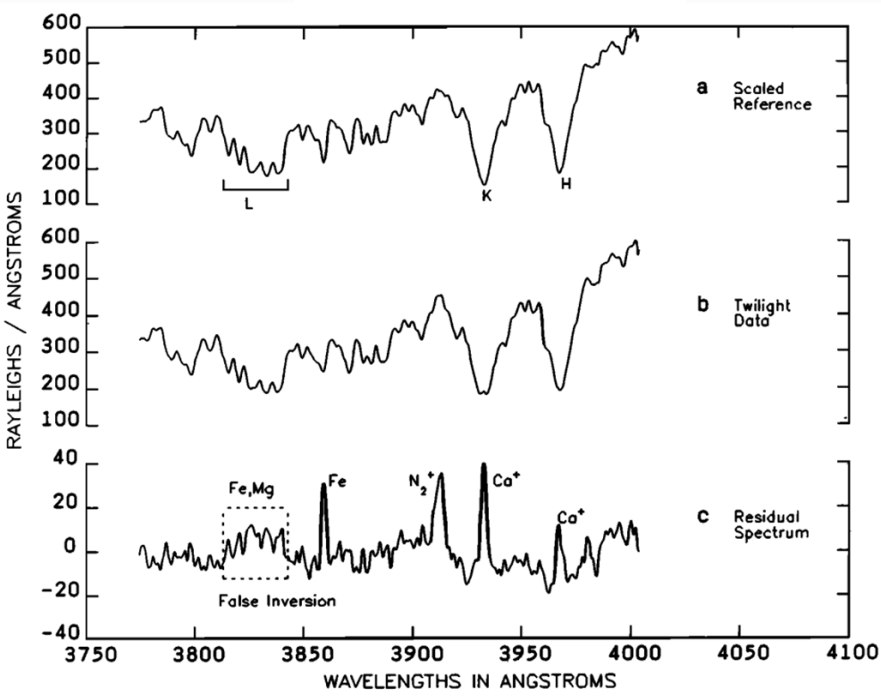

Figure 2. 8: *Example of a complex spectral observation: (a) Scaled bright reference, (b) twilight data, and (c) their difference. The Fraunhofer lines are indicated by H, K, and L, where the cluster of Fe and Mg emission lines exist at L. The false inverted Fraunhofer feature caused by cluster of Fe and Mg lines during rationing method can be seen in the residual spectrum. (Swift et al., 1990.)*

Fraunhofer lines may differ between the twilight and background spectra, using a single scattered line for the spectral ratio may result in incomplete removal of the Fraunhofer structure. Noxon used a method of estimating the slope and intensity of the continuum at several finite wavelength points and iteratively adjusted until the Fraunhofer signature was eliminated from the ratio. The same procedure was then followed by Tepley et al., 1981. Although the desired emission line was observed by the rationing method, the atmospheric continuum could not be obliterated, and the Fraunhofer structure at other wavelengths in the remainder of the spectrum was still present, which led to the difficulty in using this method. This process also considers the wavelength points at desired emission regions for scaling, which essentially varies with time. This method can also not be applied for two nearby emissions regions (e.g., a cluster of Fel and Mgl lines near 383 nm; Moore et al., 1966), and the rationing method for such cases will result in increased Fraunhofer structure in the remainder of the spectrum. An example of *false inversion of the Fraunhofer feature* is shown in Figure-2.8 (Swift et al., 1990). Such subtraction methods faced difficulty while observing

an emission feature closer to Fraunhofer absorptions, and the problem also arose in the case of molecular bands having emissions wavelengths that are closer to one another. Therefore, such measurements were found to be needing an improvement for proper consideration as an airglow extraction procedure.

However, in case of dayglow extraction by HIRISE, three distinctly different continuum regions were selected at multiple wavelength regions to perform the scaling of two spectra. Those investigations led to a comprehensive understanding of the behavior of the Ring effect (Pallamraju et al., 2000). The dayglow extraction procedure discussed in section 2.3.2 also considers different continuum regions around the wavelength of interest. The technique includes two subtraction methods: firstly, the difference between correctly scaled solar spectra and sky spectra at the continuum (*Subtraction-1*), and secondly, the difference of two neighboring regions (region-1 & 2) of equivalent identical width to properly account for the scattering contribution (*Subtraction-2*). Thus, in continuation with the nomenclature used in past literature, this method can be dubbed the "*double-subtraction*" method.

Based on this technique and systematic dayglow emission observations, various results from low to high latitudes, such as low-latitude electrodynamical effects on OI 6300 Å dayglow (Pallamraju et al., 2004; Das et al., 2010), ground-based measurements of daytime aurora using 630.0 nm emission over Boston (Pallamraju & Chakrabarti, 2005), observations of daytime auroral arc and high latitude cusps using 630.0 nm emissions (e.g., Pallamraju et al., 2001, 2004, 2011, 2020), among others have been obtained in the recent past and thus demonstrates the accuracy and validity of the aforementioned dayglow extraction procedure.

2.4 Radio measurements

As discussed, the OI 630.0 nm airglow emissions act as a good tracer for studying thermospheric variations. In order to study the upper atmosphere as a whole, a comprehensive understanding of ionospheric processes and plasma is also required. Therefore, apart from the optical daytime airglow emissions, that is used as a primary dataset, additional complementary datasets have also been utilized in this thesis work to verify further and supplement the findings. These are mentioned below:

2.4.1 Digisonde

Since, the variations in electron density significantly have an influence on the variation of OI 630.0 nm emissions, consequently the vertical electron density profiles are also investigated in this study. This work uses the electron density profiles retrieved from collocated Millstone Hill-based digisonde (monostatic, pulsed digital ionosonde), which records the ionograms routinely. These digisonde data were obtained from the Digital Ionogram DataBase (DIDBase; https://giro.uml.edu/didbase/), using the Global Ionosphere Radio Observatory (GIRO) portal. The vertical electron density profiles were frequently available during the data availability period of HIRISE emissions, which enabled further investigation of the ionosphere for day-to-day variation.

The Millstone Hill Digisonde transmits high frequency (HF) radio waves toward the ionosphere, typically from 1 to 20 MHz range. It is an example of an active remote sensing method. It is based on the basic principle of total reflection of transmitted waves, which differs from the scattering concept used by ISR. The characteristic plasma frequency (f_p) and electron density (N_e) are related to each other by the following relation:

$$f_p^2 = \frac{N_e e^2}{4\pi\epsilon_o m} = 80.5\, N_e \tag{2.22}$$

where, f_p is in Hz and N_e is in m^{-3}, e is the charge of the electron, m is the electron mass, and ϵ_o is the permittivity of free space. The plasma refractive index depends on Ne and affects the radio wave propagation. The plasma refractive index (n) for an incident HF radio wave of angular frequency, ω, can be defined as:

$$n^2 = 1 - \frac{\omega_p^2}{\omega^2} \tag{2.23}$$

where, ω_p is the angular frequency of the plasma, given by $\omega_p = 2\,\pi\, f_p$. At altitudes where $\omega_p > \omega$ (from Equation-2.23), the refractive index becomes imaginary, causing radio waves to be absorbed.

Conversely, at altitudes where $\omega_p = \omega$, radio waves are reflected. This reflected echo is received by the antenna at the receiving end of the digisonde. The time delay between the transmitted signal and the received echo provides information about the height of the reflecting layer. Since

the maximum Ne is available at the peak height of the F-region, the plasma refractive index at a particular frequency decrease and becomes zero at this height. Consequently, information on electron density variation can be obtained up to the F-region peak height using the ionosonde

2.4.2 Millstone Hill Incoherent Scatter Radar

For the plasma variations in the ionosphere above the peak of the ionosphere, a co-located Millstone Hill-based Incoherent Scatter Radar (ISR) is used, as the digisonde described above is not suitable. ISR is located at 42.64°N and 71.50°W; Invariant or magnetic latitude (MLAT) ≈ 53°N. It is located near the plasmapause and the mid-latitude trough and has a great potential for the studies of M-I coupling processes. The ISR measurements of height-resolved basic ionospheric state variables, i.e., electron density (Ne), electron temperature (Te), and ion temperature (Ti), have been used primarily for a detailed investigation of ionospheric properties and dynamics. Among these parameters, the altitude variation in electron densities and temperatures can also significantly affect the altitude profiles of OI 630.0 nm emissions, as seen by production mechanisms, and thus is also of significance in this thesis work, as this feature is used to arrive at some of the results.

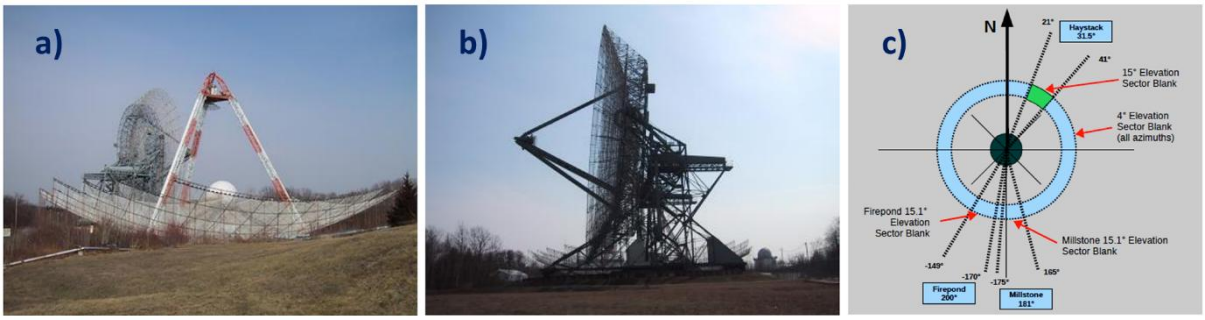

Figure 2. 9: *Two ISR antenna at Millstone Hill: a) The 68-meter zenith antenna, b) 46-meter steerable antenna (also known as MISA), and c) lower elevation limit for MISA in the azimuth direction. (Credit: Madrigal Database at Millstone Hill; http://millstonehill.haystack.mit.edu/).*

Millstone Hill has two types of ISRs: i) a 46-meter fully steerable antenna (MISA; Millstone Hill Steerable Antenna), and ii) a 68-meter fixed zenith antenna, as shown by panel-a and panel-b in Figure-2.9. The location where MISA can map is shown in panel-c of Figure-2.9. The various ionospheric parameters from these antennas are available online and have been

accessed from the CEDAR MADRIGAL database (http://cedar.openmadrigal.org/), which is managed by MIT Haystack Observatory (https://www.haystack.mit.edu/geospace/). MISA is primarily used as an ultra-high frequency (UHF; 300 MHz to 3GHz range) radar antenna, which has a line-of-sight propagation and allows ionospheric observations over a latitude span with down to 4-degree elevation, providing horizontal gradients along with the vertical structure. The fixed zenith antenna operates at 440 MHz for use in a vertically up direction with the facility's UHF transmitter with an elevation greater than 87 degrees. These instruments measure the ionospheric parameters from around 90 to 1000 km altitude range with a height resolution of hundreds of meters.

Millstone Hill ISR operates on a scheduled basis, and most experiments use both antennas. However, at a particular time, only one mode is operational. In this regard, different codes have been assigned for different experiments and are mentioned by an instrument code *kinst*. Thus, the three ISR operational modes are: i) a *combination of the Zenith and MISA antennas*, *ii) the MISA antenna*, and iii) the *zenith antenna*, corresponding to kinst codes 30, 31, and 32, respectively. The ISR data is measured at different time intervals using single-pulse and alternating codes. Single-pulse codes do not use any modulation in the transmitted signal with the typical pulse length of 480 µs and range resolution of 72 km. For longer pulse lengths, the SNR becomes larger and is often used for low elevations. On the other hand, the alternating code pulses use phase modulation for better range resolution. The typical pulse length and the range resolution (in the E-region) is 480 µs and around 4.5 km. The parameter mdtyp is used to identify the individual measurement as single-pulse or alternating code, where mdtyp = 115 is for single-pulse, and mdtyp = 97 denotes the alternating code. In this work, measurements from the zenith antenna using alternating-code data have been used. A typical density calculation by ISR in the 90-400 km range is defined as:

$$\text{Density}_{(beofre\ temp\ coresction)} = \text{Calfac(i)} * \left[\frac{S}{N}\right](\text{i}) * \text{Systemp} * \text{R(i)} ** 2/\text{Xmtr_power}$$

where, *Calfac* is the radar calibration factor, *S/N* is SNR, *Systmp* is the system temperature (K), *R* is range (km), *Xmtr_power* is the transmitter peak power (MW), and *i* is the range index. More details about the ISR measurement techniques, output, and error messages can be found at http://www.haystack.mit.edu.

The principle used by ISR is based on the process of *Thomson scattering (incoherent scattering)*, which states that the electromagnetic energy (light or radio wave) is scattered by

the electrons according to their classical radius. ISRs transmit high-power radio waves, and a partially coherent beam, scattered via electrons, is received. The scattered signal follows the Bragg's condition given as:

$$\overrightarrow{k} = \overrightarrow{k_i} - \overrightarrow{k_s}$$

where, $\overrightarrow{k_i}$ and $\overrightarrow{k_s}$ are the incident and scattered wave vectors, respectively, while $\overrightarrow{k}$ is the resultant wave vector in the medium.

The electrons in the ionosphere remain close to the ions; however, being heavier in mass, ions do not readily get excited by the transmitted energy of radio waves and do not re-radiate the signal. Therefore, as a transmitted beam interferes with the electrons, which are in motion at different speeds due to ambient ionospheric dynamics, the re-radiated beam would be Doppler-shifted in accordance with the mean thermal velocity of the electrons (Gordon, 1958). A characterization of the Doppler shifted wave is shown in Figure-2.10. In case of no net plasma drift and zero currents flow relative to the radar, the scattered spectrum will be symmetric and centered at the radar frequency, as shown in Figure-2.10. However, in the presence of currents, one peak will have higher power than the other, and for the equal drift velocity of electrons and ions, a net plasma drift will produce a Doppler shift in the whole spectrum (Evans, 1969). Detection of re-radiated waves by the electrons is possible by large bandwidths; therefore, a powerful radar system is required. The number of reflected waves will be larger for a large number of electrons available in the medium, resulting in an increased echo at the receiver. Therefore, electron density can be determined by the receiver using the measured profiles of total scattered power.

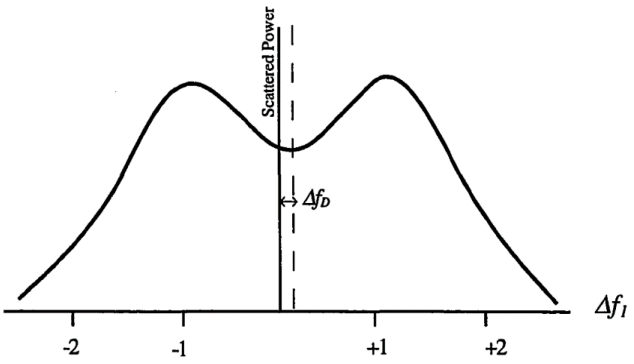

Figure 2. 10: *A Doppler shifted incoherent scatter spectrum is shown. (After Evans, 1969).*

2.4.3 Total electron content (TEC) data (Rate of change of TEC index (ROTI))

As discussed in Chapter 1, various mid-latitude phenomena are related to the variation in plasma density over a large spatial scale. Therefore, in the context of large-scale ionospheric behavior, TEC data from worldwide distributed GNSS (global navigation satellite system) receivers is also utilized in this study. TEC is the integrated number of electrons available in a column of the unit cross-sectional area between the ground receiver and satellite position and represented in the unit of *TECu*, where 1 *TECu* = 10^{16} electrons-m^{-2}. Therefore, for each slant path between satellite and receiver, the line-of-sight TEC or slant TEC (*sTEC*) can be given as:

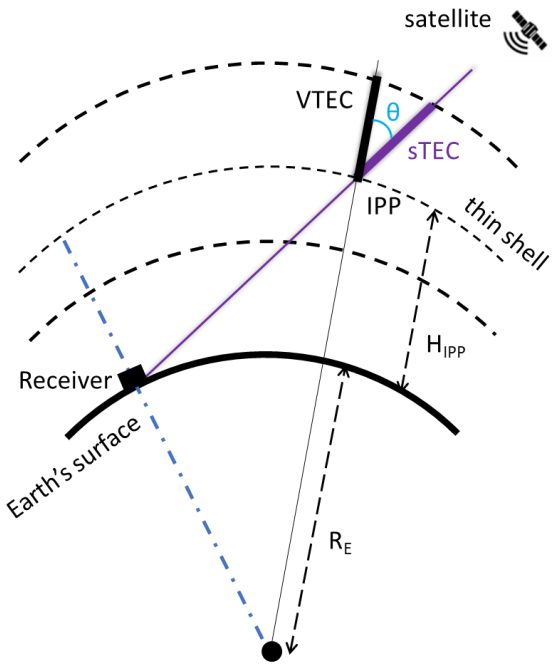

Figure 2. 11: *A schematic representation of ionospheric thin shell geometry.*

$$sTEC = \int_{r}^{s} N_e(l)\, dl$$

where, *r* and *s* denote the positions of receiver and satellite, respectively, *dl* is the line element along the path of signal from receiver to satellite, and *Ne(l)* represents the electron density along the path of the signal. The *sTEC* can also be calculated using the group delay measurements of signal's travel time from satellite to the receiver by the following expression:

$$sTEC \equiv \frac{f_1^2 . f_2^2}{40.3\,(f_1^2 - f_2^2)} . (P_1 - P_2) + TEC_{bias} \qquad (2.24)$$

where, *f1* (=1575.42 MHz) and *f2* (=1227.60 MHz) are the two L-band carrier frequencies at L1 and L2 transmitted by the GPS, respectively, while *P1*, *P2* are the pseudoranges of *L1* and *L2*. The term TEC_{bias} indicates the bias correction term for both satellite and receiver. The slant TEC is converted to vertical TEC (*VTEC*) by assuming the ionosphere as a thin cell positioned at *an ionospheric pierce-point* (IPP; Klobuchar, 1996; Rama Rao et al., 2006), as shown by the schematic in Figure-2.11, and thus can be given as:

$$VTEC = sTEC * cos\left(sin^{-1}\left(\frac{R_E \cos\theta}{R_E + H_{IPP}}\right)\right)$$

where, R_E is the Earth's radius, H_{IPP} = 350 km is the height of the ionospheric pierce point from the Earth's surface, and θ (in radians) is the elevation angle between the satellite position and the GPS receiver. In addition to the ionosphere, the plasmasphere also influences radio wave propagation between the satellite and the receiver, affecting the delay of the received signal. However, the effects of the plasmasphere are expected to be small in comparison to the delay caused by the ionosphere.

In this work, the rate of change of TEC of index (ROTI; Pi et al., 1997) is also examined in addition to the TEC measurements, which is defined as the standard deviation of TEC rate of change over 5 minutes and can be derived as:

$$\text{ROTI} = \sqrt{< ROT^2 > - < ROT >^2)} \tag{2.25}$$

where, *ROT* is the *rate of change of TEC*. The first and second term on right side of Equation-2.25 represents the average of the square of ROT and the square of the average value of ROT parameter, respectively. The ROT can be obtained as:

$$\text{ROT} = \frac{sTEC(t + dt) - sTEC(t)}{dt} \tag{2.26}$$

where, *t* is the time of TEC measurement, and *dt* is the time interval between two sTEC values. The unit of ROTI is given as TECU/min. The spatial resolution of the two-dimensional maps used for TEC and ROTI data is 0.5° × 0.5° in the geographic latitude-longitude grid, with a temporal resolution of 5 minutes. Also, the TEC data from a single co-located GPS station, Westford (USA) (71.4° W, 42.6° N, GPS code = WES2), has been used. The GNSS-TEC software developed by Seemala and Valladares (2011) is used to estimate the TEC while appropriately accounting for receiver biases. Only data from satellites with an elevation angle greater than 30° are considered to reduce multipath errors from different satellites. Detailed information on data processing is described by Rideout and Coster (2006).

The daily TEC data files for specific GPS stations can be obtained from the CDDIS archive (https://cddis.nasa.gov/archive/gnss/data/daily). Combined worldwide TEC data from all

stations can be accessed using the CEDAR Madrigal database (http://cedar.openmadrigal.org/list).

2.4.4 Plasma measurements on-board Defense Meteorological Satellite Program (DMSP)

The in-situ measured plasma parameters were investigated as obtained from the Defense Meteorological Satellite Program (DMSP) to understand the topside ionospheric variations. DMSP has had multiple satellites launched since the 1960s. DMSP are sun-synchronous polar-orbiting satellites that are aligned dawn-dusk with an inclination of around 98°. The orbital altitude and orbital period of DMSP are around 840 km and 101 minutes, respectively. The DMSP satellites are equipped with comprehensive onboard instruments, which include the Special Sensor J/4 (SSJ/4) to measure the auroral energy particle precipitation, Special Sensor for Ion and Electron Scintillation (SSIES) to measure the topside ionospheric plasma parameters at DMSP altitude, such as ambient electron density, temperatures, and ion velocities, among others. The energy range to detect suprathermal electrons by DMSP is from 30 eV to 30 keV (Greenspan et al., 1986; Rich & Hairston, 1994). DMSP also consists of an SSM (Special Sensor Microwave Imager) instrument that measures geomagnetic fluctuations. The total ion densities, including the hydrogen ion and oxygen ions densities, are measured by RPA (Retarding Potential Analyzer), and the electron temperature and densities are measured by EP (Electron Langmuir Probe).

This work investigated the measurements of various ionospheric parameters, such as electron temperature, electron densities, and ion velocities, among others, with 4-s resolution at around 840 km altitude for all dayside passes of different DMSP satellites. The DMSP data can be accessed using the Madrigal CEDAR Database (http://cedar.openmadrigal.org/).

2.5 Geomagnetic and solar activity indices

The Dst and Kp index indicates the strength of a geomagnetic storm. Measurements of the Dst index, which are based on the perturbation in the horizontal component of the magnetic field at the Earth's surface, are available at hourly intervals. The Kp-index is a three-hourly planetary index widely used to characterize the severity of geomagnetic storms. Kp-values range from 0-

9, wherein Kp = 0 to Kp < 3 are considered to be geomagnetically quiet days, while Kp ≥ 3 indicate geomagnetically disturbed periods. The higher values of Kp, reaching 9, indicate a greater severity of the storm. The values of these Dst and Kp indices are obtained from the World Data Center, Kyoto (WDC Kyoto, http://wdc.kugi.kyoto-u.ac.jp/).

In addition to the Dst and Kp geomagnetic index, the AE (Auroral Electrojet) indices are also used. The AE index measures the global strength of auroral electrojet activity in the polar regions, as introduced by Davis and Sugiura (1966). The AE index is the difference between the auroral upper (AU) and auroral lower (AL) envelopes, which are associated with the eastward and westward electrojet currents over auroral latitudes, respectively. The stronger eastward (westward) electrojet intensifies the magnitudes of the AU (AL) index. Therefore, the AE index (AE=AU-AL) represents the total maximum electrojet current and serves as a good proxy for identifying sub-storm activity. This work obtained the AE index data using the NASA CDAWeb facility (https://cdaweb.sci.gsfc.nasa.gov/index.html/).

The solar radio flux received on the ground at 10.7 cm wavelength, also termed the F10.7 index, is generated from the outer part of the solar atmosphere, i.e., a region between the upper chromosphere and lower corona. The ground-based measurements of these solar flux values are represented in terms of solar flux units (sfu, 1 sfu = 10^{22} $Wm^{-2}Hz^{-1}$) and have been found to show good agreement with the variation in sunspot numbers on the Sun's surface (Floyd et al., 2005). Also, the EUV emissions affecting the Earth's upper atmosphere correlate well with the F10.7 index. For this reason, the F10.7 index has been used as a good proxy to identify solar activity variations and their effect on the ionosphere-thermosphere system. The daily averaged data of solar flux F10.7 index used in this study is obtained from http://omniweb.gsfc.nasa.gov.

2.6 Estimation of Dayglow Emissions Using Models

Apart from HIRISE measured red line dayglow emissions, a physics-based model- GLOW (Solomon, 2017) and an empirical model- WINDII empirical model (WEM; Shepherd & Cho, 2021) are also used to estimate the OI 630.0 nm dayglow emission intensities for comparison with the calculated emissions and the measured emissions for different geophysical conditions.

2.6.1 GLOW model

The Global Airglow (GLOW; Solomon et al., 1988; Solomon & Abreu, 1989; Bailey et al., 2002) model is a single-column model and calculates the vertical profile or volume emission rates (VER; photons cm^{-3} s^{-1}) of optical emissions in the upper atmosphere at different wavelengths (Solomon, 2017). In this work, the vertical profiles of daytime 630.0 nm airglow emissions and corresponding column-integrated 630.0 nm emission intensities have been considered, which can be produced by solar radiation, particle precipitation, and photochemical reactions, as discussed earlier. To consider the effect of photoionization due to solar radiation, GLOW takes the Solar EUV inputs from the EUV for Aeronomic Calculations (EUVAC) model (Richards et al., 1994). For the impact ionization from precipitating electrons, GLOW implements the Monte Carlo two-stream electron transport algorithm given by A. F. Nagy and P. M. Banks (Nagy & Banks, 1970; Banks & Nagy, 1970) to model the electron transport through the atmosphere. GLOW considers 650 km height as the top of the atmosphere and the altitude profiles of airglow emissions are calculated by considering the variation of neutral atmospheric composition from Naval Research Laboratory Mass Spectrometer Incoherent Scatter (NRLMSIS-00; Picone et al., 2002) and the variations of ionospheric electron/ion densities and temperatures as provided by International Reference Ionosphere model (IRI-90; Bilitza et al., 1990).

As discussed in the DR production mechanism, the variation in electron density plays a significant role in determining the OI 630.0 nm emission variabilities. Various factors, such as the solar EUV flux, winds, and solar flares, can affect electron densities at varying times (from minutes to hours). However, the variation in neutral compositions is gradual. Since GLOW uses IRI-calculated electron densities, a climatological model, the calculated values during the disturbed periods may be inadequate to reflect the true ionospheric changes. Therefore, in this work, the IRI-calculated electron density profiles are replaced with the measured electron density profiles by ISR/digisonde to improve the accuracy of the model-estimated emissions. The analyses are carried out at each altitude in the defined altitude range from ~ 80 to 650 km by considering all the production and loss mechanisms of OI 630.0 nm dayglow emissions. As GLOW is a single-column model, it needs to be run iteratively at different local times and solar zenith angles for a given location to obtain the VER throughout the day.

Therefore, the one-dimensional altitude profiles of daytime 630.0 nm emission rates due to incident solar radiation and incident particles on the ionosphere are estimated using the GLOW model. Further, these profiles were vertically integrated to obtain the column-integrated values of 630.0 nm emissions and were compared with those measured by HIRISE during various geomagnetically quiet and disturbed conditions. GLOW model source code (version 0.982) used in the study is publicly available at https://www2.hao.ucar.edu/modeling/glow/code.

2.6.2 WINDII empirical model (WEM)

The solar flux is known to affect the intensities of OI 630.0 nm dayglow emissions (e.g., Solomon & Abreu, 1989; Pallamraju et al., 2010, 2020). Therefore, daily varying solar flux gives rise to day-to-day variability in these emission magnitudes. By using the OI 630.0 nm dayglow measurements from the Wind Imaging Interferometer (WINDII) on board the Upper Atmosphere Research Satellite (UARS) obtained during 1992-1996, an empirical model was derived by Shepherd and Cho (2021), known as the WINDII empirical model (WEM).

The WEM parameterized the total column integrated emission rate (I) of 630.0 nm dayglow emissions can be represented solely in terms of Solar Flux ($F10.7$) and solar zenith angle (χ) as below:

$$\ln(I) = 5.237 + 0.212 * Cos^2\chi + 1.664 * Cos^{0.5}\chi + 0.072 * (lnF10.7)^2 \quad (2.27)$$

where, I is in Rayleigh (R), χ in degrees, and $F10.7$ is in sfu. The WEM output averages out several time dependent temporal variations brought in due to neutral or electrodynamic changes in the upper atmosphere and predicts the broad systematic diurnal variation in OI 630.0 nm dayglow as a function of solar zenith angle and solar flux for a given day. The 630.0 nm dayglow emissions obtained from WEM have been found to match well with the measured 630.0 nm dayglow intensities from Hyderabad during geomagnetically quiet periods (Pallamraju et al., 2020) and have also, in turn, served to validate the WEM predictions (Shepherd & Cho, 2021). Thus , WEM predicted OI 630.0 nm dayglow emissions are also used in this study by providing the solar flux and SZA as inputs to the Equation-2.27.

2.7 Spectral Analysis Techniques Used

Spectral analysis techniques help in decomposing the data based on their frequency content, by transforming it from the time domain into the frequency domain and help in examining constituent frequencies and their amplitudes. This transformation reveals insights not apparent in the time domain, particularly for complex signals with overlapping frequencies. In the previous sections, different datasets and measurement techniques were discussed. Various methods (e.g., Fourier transform, Lomb-Scargle analysis, wavelet transform, Hilbert transform, etc.) can be used to perform the spectral analysis of such data sets depending on the scientific requirements. Different spectral analysis techniques have their advantages and disadvantages. In this work, following spectral analyses methods have been used.

2.7.1 Fourier Series

The French mathematician J. Fourier demonstrated that any periodic function can be broken down into an infinite series of sinusoidal components. This concept is fundamental in signal processing and allows the analysis and reconstruction of complex periodic signals using their frequency components.

Therefore, by using this concept, any periodic function $f(t)$ with the time period, T, and angular frequency, ω_0, ($\omega_0 = 2\pi/T$) can be written by using sine and cosine functions, or alternatively, using complex exponentials. The general form of a Fourier Series for function $f(t)$ is given by:

$$f(t) = a_0 + \sum_{n=1}^{\infty} \left(a_n \cos\left(\frac{\pi n t}{T}\right) + b_n \sin\left(\frac{\pi n t}{T}\right) \right)$$

$$\Rightarrow f(t) = a_0 + \sum_{n=1}^{\infty} (a_n \cos(n\omega_0 t) + b_n \sin(n\omega_0 t)) \tag{2.28}$$

where, a_0 represents the average value of the function over one period, while a_n and b_n are the Fourier coefficients, which determine the amplitude of the cosine and sine components, respectively. Due to the orthogonal property of sine and cosine functions, the Fourier coefficients a_n and b_n can be calculated independently using the integrals of the function $f(t)$ over one period T, which are defined as:

$$a_0 = \frac{1}{2T}\int_{-T}^{T} f(t)dt \tag{2.29}$$

$$a_n = \frac{1}{2T}\int_{-T}^{T} f(t)\cos(n\omega_0 t)\,dt \tag{2.30}$$

$$b_n = \frac{1}{2T}\int_{-T}^{T} f(t)\sin(n\omega_0 t)\,dt \tag{2.31}$$

These integrals are computed over a single period of the function, enabling the extraction of the frequency components that constitute the original signal. Using values of a_n and b_n in the above Fourier Series, we get:

$$f(t) = a_0 + \sum_{n=1}^{\infty}(a_n^2 + b_n^2)^{1/2}\left[\frac{a_n}{(a_n^2 + b_n^2)^{1/2}}\cos n\omega_0 t + \frac{b_n}{(a_n^2 + b_n^2)^{1/2}}\sin n\omega_0 t\right] \tag{2.32}$$

By considering the amplitude $(A_n) = (a_n^2 + b_n^2)^{1/2}$, phase angle $(\delta_n) = \arctan(-b_n/a_n)$, and $\cos\delta_n = a_n/(a_n^2 + b_n^2)^{1/2}$, the *Amplitude-phase form* of Equation-2.32 can be given as:

$$f(t) = a_0 + \sum_{n=1}^{\infty} A_n \cos(n\omega_0 t + \delta_n) \tag{2.33}$$

where, A_0, A_1… and $\omega_0, 2\omega_0$… are referred to frequency and amplitude spectrum of function *f (t)*. Since the powers are obtained as discrete frequencies, the resulting spectrum is known as a *discrete spectrum*.

2.7.2 Fourier Transform

The Fourier Transform (FT) is the cornerstone of spectral analysis, converting time-domain signals into their constituent frequencies. The Discrete Fourier Transform (DFT) and its computationally efficient counterpart, the Fast Fourier Transform (FFT), are widely used to analyze data with equal spacing. These transforms represent the signal in the frequency domain, showing the amplitude and phase of each frequency component. Though the Fourier series is applied to periodic functions with a finite period *T*, the Fourier transform provides a continuous spectrum for periodic or aperiodic signals and converts the dataset from time to frequency

domain. The Fourier transform for function *f (t)* over the entire real line, $t \in (-\infty, \infty)$ and is given as:

$$F(\omega) = \int_{-\infty}^{\infty} f(t) e^{-i\omega t}\, dt \tag{2.34}$$

This integral transform provides a continuous spectrum *F(ω)*, representing the signal's frequency content. As the integral is taken over all times, i.e., from $-\infty$ to ∞, the time information corresponding to the frequency occurrence is lost. Also, the power of frequency obtained by the integral will be larger if *f (t)* has a stronger amplitude component at time *t*. If the signal does not contain any stronger amplitude or the amplitude is zero with time-period *t*, the power will also become lower or zero. The inverse Fourier Transform, which reconstructs the time-domain signal from its frequency components, is defined as:

$$f(t) = \frac{1}{2\pi} \int_{-\infty}^{\infty} F(\omega) e^{i\omega t}\, d\omega \tag{2.35}$$

As $T \to \infty$, the sum in the Fourier Series approaches an integral, leading to the Fourier Transform definition:

$$\lim_{T\to\infty} \sum_{n=-\infty}^{\infty} c_n e^{i\frac{2\pi n t}{T}} = \frac{1}{2\pi} \int_{-\infty}^{\infty} F(\omega) e^{i\omega t}\, d\omega$$

The Fourier transform of natural experimental observations, which are discrete, is known as *Discrete Fourier Transform* (DFT), and are defined as:

$$f(\omega_k) = \frac{1}{N} \sum_{k=0}^{N-1} f(t_k)\, e^{-i\omega_k t_k}\, dt \tag{2.36}$$

where, $f(t_k)$ is a 1-D continuous function. Therefore, the inverse DFT can be given as:

$$f(t_k) = \frac{1}{N} \sum_{k=0}^{N-1} f(\omega_k)\, e^{-i\omega_k t_k}\, d\omega \tag{2.37}$$

For a given signal of length N, DFT performs approximately N^2 complex operations. It can be noticed that DFT is designed for discrete-time signals and assumes that the input signal is

periodic. It transforms a finite sequence of equally spaced signal samples into a series of coefficients representing complex sinusoidal components. However, in the case of dayglow emissions observations, various factors, such as different sky conditions, cloud cover, saturation of CCD at local noon, etc., can make the observations unequally spaced in time. Also, many other geophysical observations are not equally spaced in time. Therefore, this limitation of DFT in the case of irregularly spaced data is avoided by using the Lomb Scargle spectral analysis, as discussed below.

2.7.3 Lomb-Scargle analysis

The Lomb-Scargle periodogram is used to analyze the unevenly spaced time series data, as in the case of geophysical observations and other irregularly sampled data. It was developed independently by Nicholas R. Lomb (1976) and Jeffrey D. Scargle (1982), and the term periodogram stands for spectral power as a function of frequency. The Lomb-Scargle periodogram addresses the limitations of traditional Fourier analysis when dealing with non-uniformly sampled data.

For an arbitrarily sampled observations, $X(t_j)$; j = 1, 2, …, N_0), the classical periodogram (Deeming, 1975) is given as:

$$P_X(\omega) = \frac{1}{N_0}|DFT\ (\omega)|^2$$

$$= \frac{1}{N_0}\left|\sum_{j=0}^{N_0} X(t_j)\, e^{-i\omega t_j}\right|^2$$

$$= \frac{1}{N_0}\left|\left(\sum_j X_j \cos\omega t_j\right)^2 + \left(\sum_j X_j \sin\omega t_j\right)^2\right| \quad (2.38)$$

The above periodogram can be calculated for any value of ω. For a sinusoidal component of frequency ω_o, the power will become stronger near $\omega = \omega_o$ due to the same phase of the factors X_j and $e^{-i\omega t_j}$, while at other frequencies, the power will be reduced due to the opposite phase. Another analogous form of the above Equation-2.38 with the same statistical properties was derived by Scargle (1982) as:

$$P_X(\omega) = \frac{1}{2}\left\{\frac{\left[\sum_j X_j \cos\omega(t_j-\tau)\right]^2}{\sum_j \cos^2\omega(t_j-\tau)} + \frac{\left[\sum_j X_j \sin\omega(t_j-\tau)\right]^2}{\sum_j \sin^2\omega(t_j-\tau)}\right\} \quad (2.39)$$

where, the *time offset parameter* (τ) is calculated to align the phase of the sinusoidal model with the data optimally, thereby making the periodogram invariant to shifts in the time axis, and is given as:

$$\tau = \frac{1}{2\omega}\tan^{-1}\left(\frac{\sum_j \sin\ (2\omega t_{j)}}{\sum_j \cos\ (2\omega t_j)}\right) \quad (2.40)$$

The above periodogram given by Equation-2.39 has simple statistical behavior and is equivalent to the least square fitting of sine and cosine functions to the data (Scargle, 1982). Therefore, this modified form is preferred over the classical periodogram. With the help of τ, the periodogram's power spectrum remains unchanged if the time series data are shifted uniformly in time. Therefore, if all data points at time t_i are shifted by a constant value Δt (e.g., from t_i to $t_i + \Delta t$), the periodogram's power spectrum $P_X(\omega)$ will not change, and this property is known as the *time translation invariance*. Horne and Baliunas (1986) presented that the modified periodogram (Equation-2.39) must be normalized by σ^2, i.e., the total variance of the data.

The uncertainty in the frequency is given as (Horne & Baliunas,1986):

$$\delta\omega = \frac{3\pi\sigma_N}{2\sqrt{N_o}TA} \quad (2.41)$$

where, T is the total length of the dataset, A is amplitude, and $\sigma_N$is the standard deviation of the noise obtained after the signal is subtracted.

Therefore, the normalized Lomb-Scargle periodogram has several benefits over the Fourier transforms, such as the use of τ keeps the periodogram due to the time shifting, the form is equivalent to the least square fitting of sine & cosines, and in the case of only noisy data, the periodogram will follow an exponential probability distribution (Horne & Baliunas, 1986).

2.7.3.1 The False Alarm Probability

False alarm probability (FAP) is the probability that the highest peak in the periodogram exceeds a given threshold purely due to noise. A lower FAP indicates a higher confidence that the detected signal is real. The periodogram's peak power values follow an exponential distribution for large datasets. If z is the observed peak power in a periodogram, the FAP can be estimated as:

$$\text{FAP} \approx 1 - (1 - e^{-z})^{N_i} \tag{2.42}$$

where, N_i is the number of independent sampled frequencies (trials) in the periodogram. Thus, in such a case, the probability of each independent frequency to be less than z becomes $1 - e^{-z}$. Therefore, FAP helps in distinguishing proper signals from false detections caused by random fluctuations, and each power value below FAP is considered statistically insignificant.

2.7.3.2 The Significant Power Level

The significant power level corresponds to a specific FAP. It is the power level that a peak must exceed to be considered significant at a given confidence level. The common significance levels are 1%, 0.1%, and 0.01%, corresponding to the FAP values of 0.01, 0.001, and 0.0001, respectively. For a given FAP, the corresponding power level z can be found by solving:

$$z = -\ln\left(1 - (1 - FAP)^{1/N_i}\right) \tag{2.43}$$

Therefore, for example, if a periodic signal is detected in a noisy dataset and the FAP of the dataset is defined as 0.01 (1%) and if z = 10. Then, for such a case, it can be understood that any peak in the periodogram exceeding this power level is statistically significant at the 1% level, i.e., that there is only a 1% chance that this peak is due to random noise and thus represents the obtained significant power corresponding to the 99% confidence level.

Therefore, the *significant power level* is the threshold power above which peaks in the periodogram are considered statistically significant, and indicate a high likelihood that the periodic signal obtained is accurate.

2.7.3.3 The Number of Independent Frequencies

The *Number of Independent Frequencies* (N_i) in Lomb-Scargle analysis is a concept used to determine the statistical significance of peaks in a periodogram. It represents the number of effectively independent frequencies at which the periodogram is evaluated. In statistical terms, when evaluating the periodogram at multiple frequencies, each frequency at which the periodogram is computed can be viewed as an independent trial. These frequencies can range from 2π/T to *Nyquist Frequency* for a total time interval T. The Nyquist frequency is mentioned as half the sampling rate for evenly spaced data and sets the upper limit for the frequencies that can be resolved with the given data spacing. However, due to the nature of the data and the analysis method, not all frequencies are completely independent.

The factors, including the total number of data points, sampling rate, range of frequencies, Nyquist Frequency, and the time intervals between observations, affect the Number of Independent Frequencies. Therefore, to obtain the correct value of N_i, Horne and Baliunas (1986) performed simulations over large unevenly spaced data and found a relation as a function of N_o value, as given below:

$$N_i = -6.362 + 1.193\, N_o + 0.00098\, N_o^2 \tag{2.44}$$

Therefore, N_i reflects the number of effectively independent trials conducted in the frequency domain analysis, and its accurate estimation ensures reliable calculation of the FAP.

Figure-2.12 illustrates a comparison between FFT and Lomb-Scargle analysis. The left column presents datasets with three known frequencies (0.03 Hz, 0.10 Hz, and 0.12 Hz). The top panel displays the original signal sampled at equal time intervals (100% data retention). The subsequent panels in the left column show the same signal with 10% to 40% of data points randomly removed, indicated as *NaN*.

For each dataset configuration, both the FFT and Lomb-Scargle (L-S) periodograms were computed. The results of these analyses are depicted in the middle and right columns, respectively, where *f* denotes the detected frequency corresponding to the maximum power. Dashed horizontal lines in the right column panels represent the FAL to assess the significance of different frequency components.

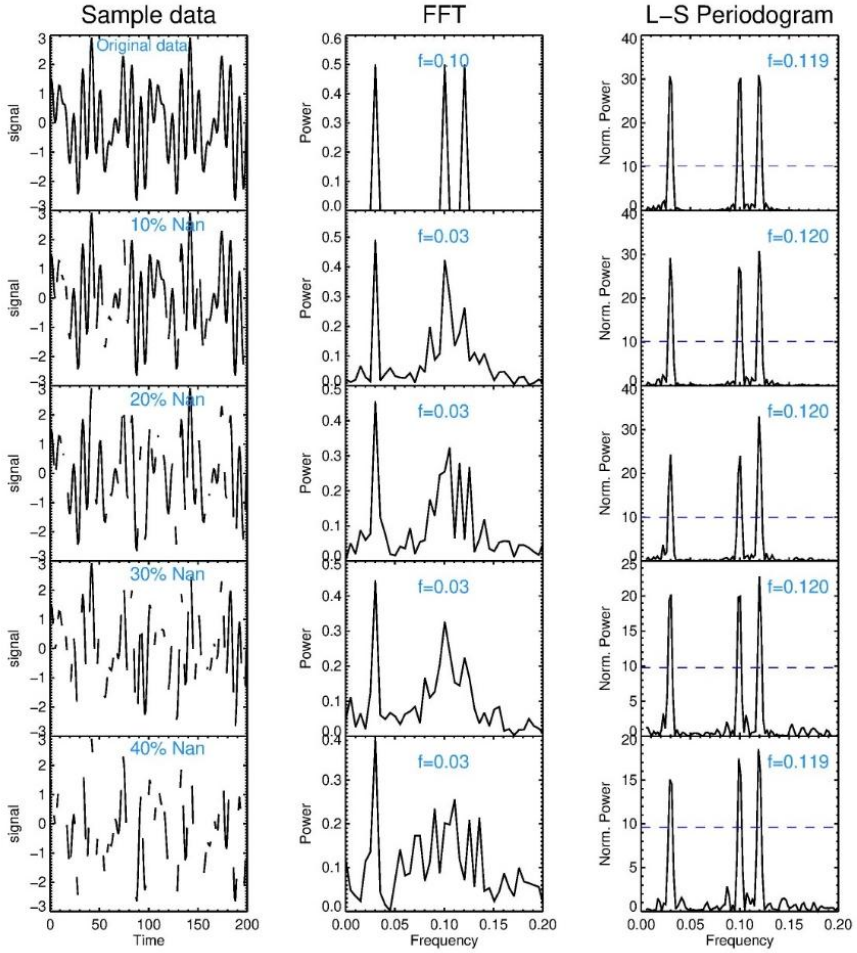

Figure 2. 12: *A comparison of evenly and unevenly spaced data by FFT and Lomb-Scargle (L-S): The left column shows sample data composed of three known frequencies (0.03, 0.10, and 0.12 Hz). The top panel displays the full signal with equally spaced data points. Subsequent panels show unevenly spaced data by randomly removing 10-40% of the original data points. The middle and right columns represent the frequencies obtained by FFT and L-S analysis, respectively. The observed frequency with the maximum normalized power is indicated by f. The horizontal lines in the right column indicate the False Alarm Level (90% confidence limit) for the significant periods.*

In the case of the dataset with 100% equally spaced samples, both FFT and L-S methods accurately identified the known frequencies. However, for datasets with missing or irregularly spaced data, FFT failed to detect all frequencies reliably, and only found the lowest frequency at 0.03 Hz having maximum power. Conversely, while the L-S periodogram exhibited variations in power estimates compared to the original case (top panel), however, it successfully identified the frequencies above the FAL in case of missing data also. This demonstrates the advantage of Lomb-Scargle analysis over FFT in analyzing irregularly spaced

data. Therefore, in this study, Lomb-Scargle analyses has been used to determine the periodicities and wave numbers under varying conditions

2.8 Summary

In this chapter, various data sets and techniques used in the study have been presented. It includes an in-depth presentation of the daytime OI 630.0 nm optical emissions, used as a primary dataset in this study, and elaborates on their production mechanisms. A detailed description of the HIRISE, which facilitated the daytime OI 630.0 nm optical observations over Boston, is included. Further, the procedure used to extract dayglow emissions from the sky spectrum obtained by HIRISE is explained in detail. The chapter also presents the estimation of 630.0 nm dayglow emissions through two different models: a physics-based model, GLOW, and an empirical model, WEM. Further, in addition to the ground-based optical measurements, additional datasets relevant to this study, including ISR data, digisonde measurements, GPS-TEC data, DMSP satellite observation, solar flux indices, and Dst indices, among others are presented in this chapter. Furthermore, the chapter details the various spectral analysis techniques applied in this research, such as the Fourier Transform and Lomb-Scargle analysis, which were used to identify periodicities and wave numbers in different datasets. The application of these techniques has yielded several new findings in the upper atmosphere under daytime conditions. These results will be detailed in the following chapters.

Chapter: 3

Response of mid-latitude ionosphere observed during daytime SED

3.1 Introduction

During geomagnetic storms, the mid-latitude upper atmosphere undergoes dramatic changes in terms of neutral compositions, ionospheric plasma variations, electrodynamics, and other physical processes. As a consequence, the electron densities in the ionosphere are also significantly affected during storms, showing an increase or decrease than their quiet-time values, and are generally referred to as positive and negative ionospheric storm effects, respectively, as discussed earlier (section-1.4). The positive ionospheric storms are produced by the prompt penetration of electric field or equatorward winds during daytime (e.g., Prölss, 1993, Balan et al., 2009), whereas negative ionospheric storms occur mostly due to the variation in neutral composition (Seaton, 1956) and through the motion of ionospheric trough from high and mid-latitudes to lower latitudes (Mendillo et al., 1974). Apart from the above usual positive phase, a further enhancement in the electron density is sometimes observed during the early stages of a geomagnetic storm over mid-latitudes and is known as the storm-enhanced density (SED) (Foster, 1993). SED is a large-scale phenomenon associated with the enhancement in TEC and increased plasma flow in the sunward direction. Due to the sunward convection, SEDs form a narrowly-confined plume kind of structure directed in the north-west direction (e.g., Coster et al., 2007). Additionally, SED plume also sometimes contributes to the formation of the tongue of ionization (TOI), wherein the enhanced density plasma is transported into polar cap region from mid-latitudes along the noon-midnight meridian (e.g., Foster et al., 2005; Q.-H. Zhang et al., 2013). The SED plume observed in the subauroral ionosphere is also indicated as a projection of plasmaspheric plume when mapped along the geomagnetic field lines in the magnetosphere region (Foster et al., 2002). Various physical mechanisms have been suggested to understand the formation of SED, such as the expansion

of high latitude convection cell towards lower latitudes (Foster, 1993), midnight to noon-side flow of plasma under magnetospheric sunward convection (Kelley et al., 2004), and due to the interaction of subauroral polarization electric field with the mid-latitude ionosphere (Foster et al., 2007). Despite different proposed mechanisms, the vertical $E \times B$ drift provided by the storm time electric field appears to have a significant role in the SED formation (e.g., Heelis et al., 2009; Thomas et al., 2013). The effects of SEDs are typically observed as an increase in TEC and/or the increased ionospheric electron densities due to the interconnection with overlying magnetosphere. Such enhancement in the electron content during disturbed times may significantly affect the radio-wave propagation (e.g., Coster and Skone, 2009; Sun et al., 2013).

SEDs are primarily studied by using various ground-based and space-borne data sets, such as TEC (e.g., Coster & Skone, 2009; Thomas et al., 2013), and ionospheric data from ISR (e.g., Foster et al., 2005; Zou et al., 2013, 2014), among others. However, there has been no report on the impact on optical emissions of this mid-latitude phenomenon during daytime, to the best of our knowledge. In this work, the atomic oxygen 630.0 nm dayglow emissions have been used as a primary dataset. The results indicate a sudden anomalous enhancement in the intensity of O(^{1}D) dayglow emissions over Boston around dusk for about an hour during a super-geomagnetic storm occurred between 7–9-November 2004, as observed by HIRISE. This sudden enhancement in dayglow emissions is investigated as a possible signature of SED phenomena over mid-latitudes during daytime using complementary observations from multiple instruments including ISR, TEC, and DMSP. Further, the GLOW model estimated column integrated daytime OI 630.0 nm emissions show a good match with those observed by the HIRISE.

3.2 Datasets used

The daytime observations presented and discussed here make the use of HIRISE measured OI 630.0 nm airglow intensity along with the GLOW and WEM model estimates, ISR measured vertical profiles of electron density and electron temperature, GPS TEC, and DMSP in-situ measurements, as discussed in detail in Chapter 2. Below is the brief description of specific parameters used during the period of interest 7–9-November 2004.

The OI 630.0 nm (red line) daytime airglow emissions are the primary optical data used in this study and have been obtained using a HIRISE from Boston, as discussed in section-2.3. The daytime red line airglow observations presented here were carried out during 7–9-November 2004 centered around the zenith having the HIRISE field of view (FOV) of about 6°. In addition to HIRISE measurements, GLOW and WEM estimated emissions are also used.

The Millstone Hill ISR data have been used to provide more information on the variation of ionospheric parameters during the observed anomalous enhancement in the brightness of red line dayglow emissions. The Millstone Hill ISR was operating in the ionospheric mode on 8 and 9-November 2004 wherein, altitude profiles of electron density (Ne) and electron/ion temperature (Te/Ti), among other ionospheric parameters corresponding to zenith were considered. Since, ISR data were not available on 7 November 2004, the variation in electron density data is obtained from the Millstone Hill based digisonde at a data cadence of 15 min.

As SED is usually generated in the lower mid-latitude regions (Foster, 1993), the TEC maps over the North American continent are considered to examine its large-scale spatial variation and temporal evolution during the observation period. The specific variation in diurnal TEC over Boston is also analyzed using TEC data from a collocated GPS station, Westford. To obtain the information on plasma convection velocities in mid-latitude ionosphere, DMSP data were utilized at ~840 km altitude.

3.3 Results and discussions

As described in Section-2.2, the OI 630.0 nm dayglow emissions typically peak at around 230 km altitude and are produced by PD, PE, and DR mechanisms. Though, PD and PE production mechanisms are dominant contributors to daytime 630.0 nm emissions and are solely dependent on solar flux and solar zenith angle, the DR mechanism depends on the densities of electrons and O_2^+ ions. Therefore, DR becomes important in defining any small-scale temporal features in the variability of daytime OI 630.0 nm emission caused by the electron density variations (greater than ~12 min; Brunt-Väisälä period). The typical altitude of maximum electron density during the day lies near 230-250 km during geomagnetically quiet times. During storms, perturbations in the electric field and/or winds can take the plasma to higher (lower) altitudes, resulting in a decrease (increase) in the electron density in the bottomside

ionosphere. Therefore, if the electron density near 230-250 km altitude decreases, the intensity of OI 630.0 nm emissions can be considered to decrease simultaneously.

Figure-3.1 shows the evolution of geomagnetic activity during the 7–9 November 2004 as indicated by (a) Dst, (b) interplanetary magnetic field (IMF) Bz component, and (c) Kp indices. The solar flux on these days varied in the range from 120 to 140 sfu (1sfu = 10^{-22} Wm^{-2} Hz^{-1}). A strong full halo coronal mass ejection (CME) occurred on 7 November 2004 at 1726 UT (Local Time, LT = UT-5 hr, marked by horizontal arrows), as observed by SOHO/LASCO. The interaction of CME sheath plasma with magnetopause caused a huge perturbation in the Earth's magnetic field. A storm sudden commencement was observed on 7 November 2004 at around 19 UT (14 LT), as indicated by the Dst reaching +60 nT shown in Figure 3.1a, followed by the onset of the main phase of the storm with the Dst minimum dropping to around −370 nT at 6 UT (1 LT) on 8 November 2004, making this event into a category of superstorm. Another major disturbance was noted on 9 November 2004, when a sudden strong negative excursion in IMF Bz at 20 UT (15 LT), as shown in Figure 3.1b, caused a large decrease in the induced magnetic field on the ground with the Dst again dropping down to a value of around −210 nT. From Figure 3.1c, it can be noted that the maximum value of Kp-index was 9- during 2–4 UT on 8 November 2004 and 18–20 UT (13–15 LT) on 9 November 2004, indicating the severity of the storm. The IMF Bz was −12 nT at 20 UT (15 LT) and

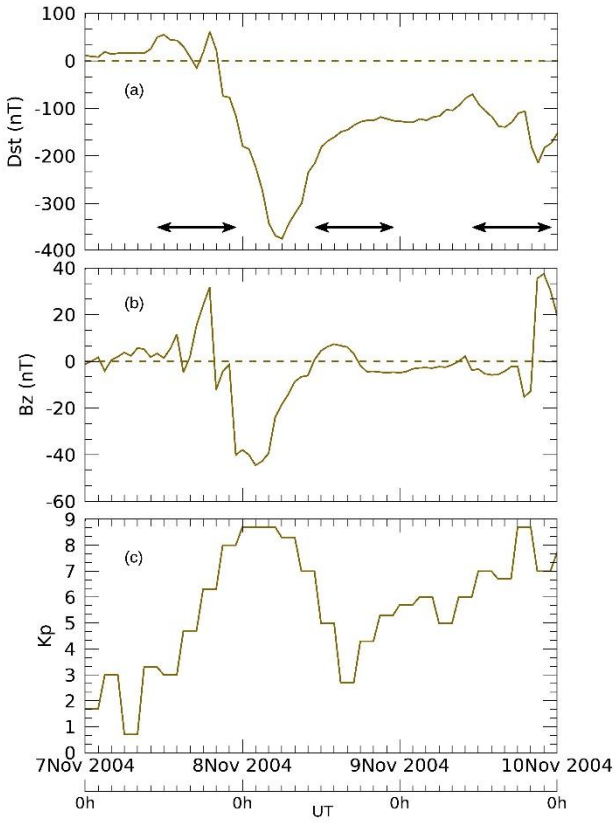

Figure 3. 1: *The panels (a)–(c) show the variations in Dst-index, IMF- Bz component, and 3-hourly Kp-index values for the duration of the observation period (7–9 November 2004). The horizontal arrows represent the daytime (6–18 LT) on each day. The strong geomagnetic disturbances of Kp = 9- can be seen on 8 November (1 UT) and 9 November (20 UT); LT = UT-5 hr.*

turned to 35 nT after an hour at 21 UT (16 LT) on 9 November 2004. This northward turning of the IMF Bz after 21 UT on 9 November reduced the geoeffectiveness of the storm.

The variations in OI 630.0 nm emissions during the local daytime over Boston for the given period are shown in Figure-3.2. The three panels (a)–(c) in Figure 3.2 show the HIRISE measured O(^{1}D) dayglow emissions in Rayleighs (red dots) along with ±1σ values for 7, 8, and 9 November 2004. On 9 November, due to larger signal strength near 15 LT, the dayglow variations were reanalyzed at a slightly higher data cadence (~4 min, exposure: 200 s) for a specific period of 14–17 LT, as shown in Figure 3.2d. The missing data before 10 LT and during 14–16.2 LT on 7 and 8 November are due to the presence of clouds in the field of view of HIRISE. The noon time dayglow data were not available, as the presence of direct sunlight overhead causes saturation in HIRISE's detector. The WEM O(^{1}D) emission estimates for all the days corresponding to their solar flux values are also shown in Figure-3.2 as a black dashed line along with the observed O(^{1}D) emissions. It may be noted that on 8 and 9 November the measured values match well with those of WEM until 13.5 LT. On 7 November, the measurements show larger values than the WEM

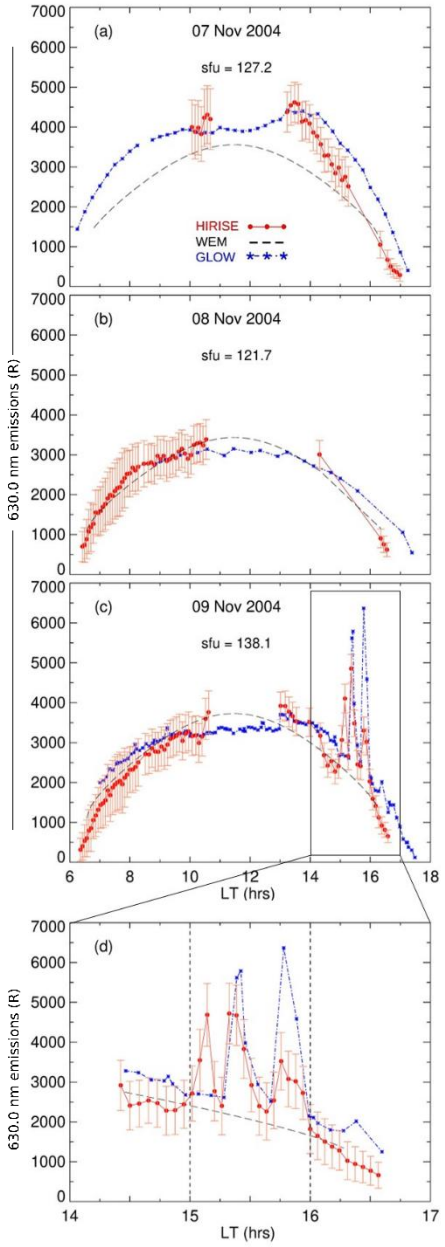

Figure 3. 2: *The Diurnal variation in OI 630.0 nm dayglow emission intensity (along with ±1σ values) as measured by HIRISE (red dots) over zenith (FOV ≈ 6°), estimated by GLOW-model estimates blue asterisks), and by WEM predictions (black dashed line) are shown. Panels (a)–(c) show the variations corresponding to 7, 8, and 9 November 2004. Panel (d) shows the zoomed-in plot of dayglow variation for 9 November during 14–17 LT at a higher data cadence of ~4 min.*

estimates. Such differences can occur if the electron densities are larger on this geomagnetically disturbed day. Therefore, on this day, the measured electron densities were considered from a collocated digisonde and corresponding ionic composition, as predicted by the IRI model for the given values of measured electron density, as inputs to the GLOW model. The resulting output is shown in Figure-3.2 as the line joining blue asterisks. It can be noted that the GLOW model output matches better with the measurements as compared to the WEM estimates, indicating that, indeed the larger electron densities on this day contributed significantly in increasing the red line dayglow emission intensities. The agreement is not perfect, however, which could be due to approximations in the estimation of the altitude profile of electron density above peak F2 height of the F-region. Incidentally, as also mentioned above, on 8 and 9 November, Millstone Hill ISR data were available, so altitude profiles of the

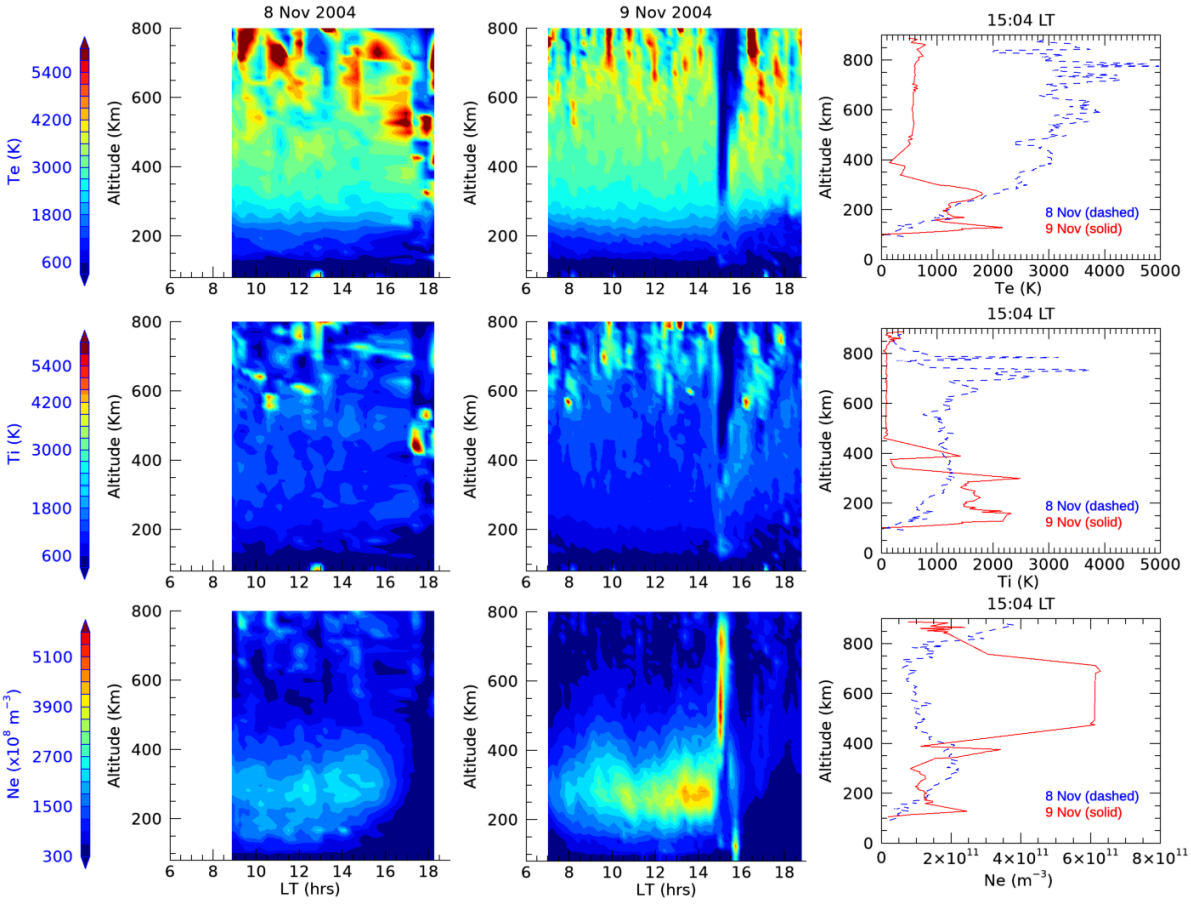

Figure 3. 3: *The left two columns show the local time variation of altitude profiles of Te (top), Ti (middle) and Ne (bottom), as measured by the Millstone Hill ISR on 8 and 9 November 2004. The third column shows the comparison of these parameters at 15:04 LT, which is the time of major geomagnetic disturbance observed on the 9 November 2004.*

measured plasma parameters in the range of 90–800 km have been used as inputs into the GLOW model. It can be seen that, on all these days the GLOW model estimates match well with the HIRISE measured emissions, except during 13.5–16 LT on 9 November 2004, when sharp excursions are seen in both the measured and estimated emissions (although with some differences in magnitudes). The ISR data used corresponds to the mean azimuth and elevation angles of 178° and 88°, which are very close to the zenith of the HIRISE field-of-view. Nevertheless, there could be a mismatch in the co-volume corresponding to both these measurements, which can contribute to the small differences in the magnitudes of HIRISE measured and estimated emissions using ISR data. A clear enhanced emission peak intensity of around 2.5 kR in the O(^{1}D) dayglow emissions is observed near the dusk time (at ~15 LT) for about an hour. Note that there are three peaks, I, II, and III, in the HIRISE observations at 15.16, 15.37, and 15.78 LT, respectively. The model emissions match with the measurements at two peaks (II and III). Thus, the observations present an anomalous enhancement in the observed 630.0 nm dayglow intensity during storm-time that was caused by a significant increase in electron density at altitudes above 300 km. To better understand the variation, the corresponding associated ionospheric features with their diurnal variation are also presented, which show a clear relationship with storm enhanced electron density over mid-latitudes.

3.3.1 Ionospheric variations

To identify the cause of observed enhancements in the dayglow emissions on 9 November 2004, the vertical profiles of Ne, Te, and Ti measured by the ISR zenith radar beam were investigated (Figure-3.3). Figure 3.3 shows the comparison of these profiles between 8 and 9 November in the altitude range of 100–800 km as a function of time. The top, middle and the bottom rows show the variations of Te, Ti, and Ne, respectively. The left two columns show the diurnal variation of all profiles (Te, Ti, and Ne) on 8 and 9 November 2004. The rightmost column shows the comparison in these parameters between these two days at around 15 LT when large enhancements were observed in the OI 630.0 nm dayglow measurements (shown in Figure-3.2d). By observing the altitude profile of electron temperature (Te), it is evident that during the period of enhanced emissions on 9 November, Te experienced a reduction of over 2000 K above 300 km within the F-region, in contrast to 8 November, while ion temperature displayed an increase of approximately 700 K limited to the lower F-region. However, both the

Te and Ti was reduced drastically in the topside ionosphere (above 400 km) on 9 November in comparison to that on 8 November between 15-16 LT. Previous studies have demonstrated that energetic particle precipitation (<200 eV) has the potential to elevate ionospheric electron temperature by 1000 K or higher (e.g., Seo et al., 1997). However, the electron temperature recorded on 9 November was approximately 700 K only, suggesting the absence of any low-energy particle precipitation effects. The electron density on 9 November was reduced by around 1.2 times in the bottomside ionosphere (200-400 km height), while it was increased by around 4-5 times at higher heights (400-700 km) contrary to 8 November. Considering that, an upward shift of the peak altitude of ionospheric F-region to above 400 km was identified. Therefore, the enhancement in the electron density in the topside ionosphere probably led to the increased cooling rate of the electrons and resulting in the low electron temperatures accordingly. Also, the OI 630.0 nm dayglow emission intensity variations are shown to be in accordance with those of F-region electron density over low and high latitude regions (Pallamraju et al., 1996, 2004, 2010). In addition, the SAR arcs phenomena in mid-latitude ionosphere can also cause enhancements in the OI 630.0 nm emission intensities due to an increased electron temperature at around 400 km altitudes. Therefore, to further rule out this possibility, an average of Ne, Te, and Ti in the range of 200–450 km altitude was considered on 9 November 2004 and it was found that at 15 LT, there was a sharp reduction in the average variation of Ne and Te, but an increase in Ti (~2000 K). The average electron and ion temperature decreased and increased around 2 times, respectively, in the bottomside ionosphere. In the lower ionosphere, ions are heated mainly through Ion-neutral collisions, leading to increased Ti. However, in the topside ionosphere, the neutral density decreases significantly, reducing the frequency of electron-ion collisions. Where the neutral densities are sufficient at a given altitude, ions can lose energy via charge exchange with neutrals, thereby contributing to reduction in Ti. Also, as mentioned above, the Te was reduced significantly at each altitude above ~300 km, and unlike electron temperature, ion temperatures do not play any role in the production of 630.0 nm emission rates (e.g., Torr et al., 1976; Alge et al., 1983). Therefore, any effect of decreased electron temperature cannot be considered in the observed enhancement of dayglow emissions during this time interval and the observed increase in emissions is thus inferred to be directly caused by the enhancements in electron densities in the ionosphere above 400 km. A sudden enhancement in the electron density at higher altitudes, reduced electron temperature and an increase in hmF_2 associated with strong sunward convection, are some of the characteristics of the mid-latitude phenomenon SED (Foster et al., 2005; Yuan et al., 2009; Zou et al., 2014 and references therein). Since, in past studies,

GPS-TEC data were used primarily to study the SED over the mid-latitudes (e.g., Foster, 2008; Zou et al., 2014), a comparison is made on TEC variation between the storm day 9 November 2004 and other neighboring quiet days (5–6 November, 13–14 November) as obtained in the 45°N to 55°N magnetic latitude (MLAT) and 90°W to 60°W geographic longitude (GLON) range with respect to local time. The longitudinal average of TEC over 90°-60° W at each degree magnetic latitude from 45° to 55°N is shown in Figure-3.4. The black dash-dot lines show the variations in TEC on the four quiet days, while the solid red lines represent the TEC variations on disturbed day 9 November 2004. Until 10 LT, the temporal variation in TEC on 9 November (solid red), was almost similar to those seen on the quiet days but was lower than those on the quiet days during 10 to 15 LT. Nonetheless, after 15 LT, a sharp rise in TEC at each magnetic latitude between 45-55°N is observed, clearly opposed to the quiet days' TEC variations. The TEC on quiet days follow the typical local production pattern owing to the ionization by solar EUV radiation from noon to evening hours, however, the sudden increase

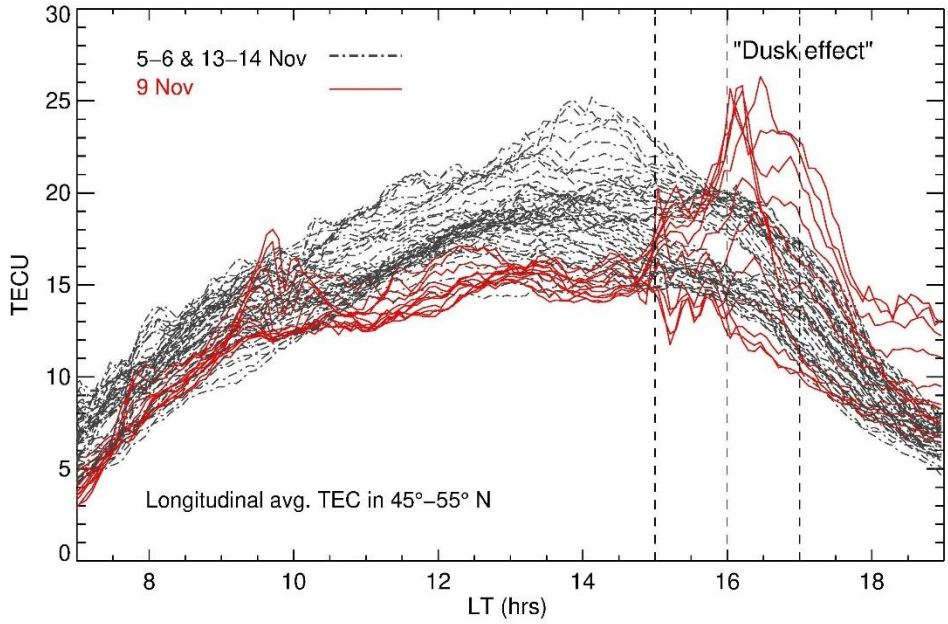

Figure 3. 4: *The GPS-TEC temporal variation in the mid-latitude range 45°–55° MLAT within 90°W to 60°W geographic longitude. Different lines represent the TEC variation for different magnetic latitudes separated by 1° in the range of 45°N–55°N. The black dashed lines represent the two quiet days before (5–6 November) and after (13–14 November) the storm day (9 November), while the solid red lines correspond to the variation on the storm day. A clear enhancement in TEC in the 45°–55°N MLAT range can be seen in evening hours (15–17 LT), which illustrates the "dusk effect."*

in TEC on 9 November during dusk hours is due to the storm onset and sudden southward turning of IMF Bz component. This storm enhanced TEC over mid-latitude during the dusk hours has been referred to as the "dusk effect" (Evans, 1970; Mendillo et al., 1970) and is attributed to be due to the presence of SED. Such enhancements in TEC during storm time SEDs have been shown to follow the various ranges of increase from ~1.4 to 5.5 times in comparison to their quiet time values (Zou et al., 2014). Here, the TEC on 9 November 2004 shows an increase of around 1.25 times as compared to the other quiet days, which is close to the lower end of the range of 1.4 times reported by Zou et al. (2014).

Therefore, the GPS-TEC and Millstone Hill ISR data together affirm the observed anomalous enhancements in the dayglow brightness to be a consequence of storm enhanced density phenomena over mid-latitudes.

3.3.2 SED Plume formation on 9 November 2004

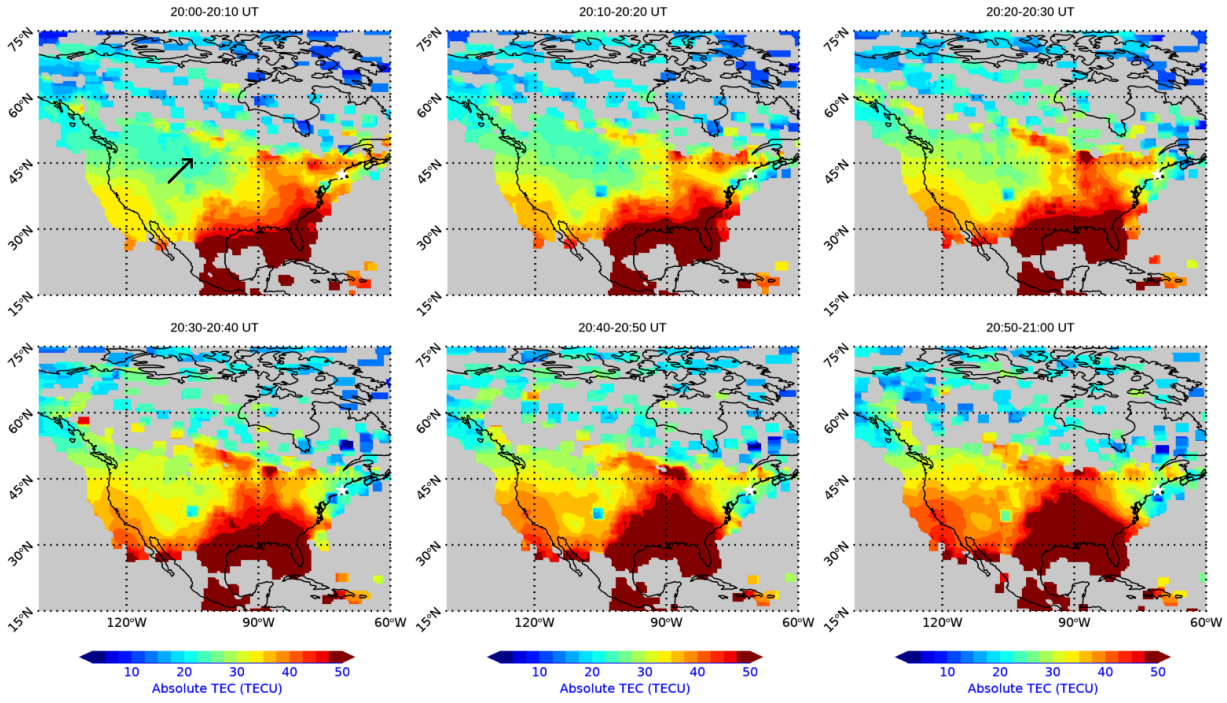

Figure 3. 5: *The TEC maps involving 5-min integration during the period of observed enhancement in dayglow that is, 20–21 UT (15–16 LT) on 9 November 2004. White star indicates the observation location, Boston (42.36°N, 71.05°W). The black arrow at 20 UT (15 LT) signals the onset of enhanced density plume.*

As the enhancement in TEC and electron density in the overhead ionosphere were clearly observed during the SED on 9 November, to identify the large-scale variations, the absolute TEC over North America during the observation period were examined using two-dimensional TEC maps. The TEC maps involving 5-min integration during the period of observed enhancement in the dayglow i.e., 15–16 LT (20–21 UT) are shown in Figure-3.5 on 9 November 2004. From the top panel in Figure-3.5, a narrow and poleward extending plasma flow channel in the sunward or westward direction at 20 UT, marked by an arrow, can be seen emerging as an enhanced density plume over Boston (white star). The time-evolution of this SED plume is clearly visible from the top panel during different local times. Additionally, the bottom row of Figure-3.5 not only shows the presence of SED plume, but also clearly depicts a broadly distributed enhancement in TEC with time in the mid-latitude ionosphere. Due to sparse GPS receivers at high latitudes, TEC maps do not contain enough data points at those latitudes. Therefore, to present a comprehensive view of the SED structure formed over mid-latitudes, the TEC data during the interval 20:00–20:30 UT (15:00–15:30 LT) is integrated, as shown in the left side of Figure-3.6 (note the different colorbar that used in Figure-3.5). From Figure-3.6 (left-side), it becomes more evident that the observation location, marked by the

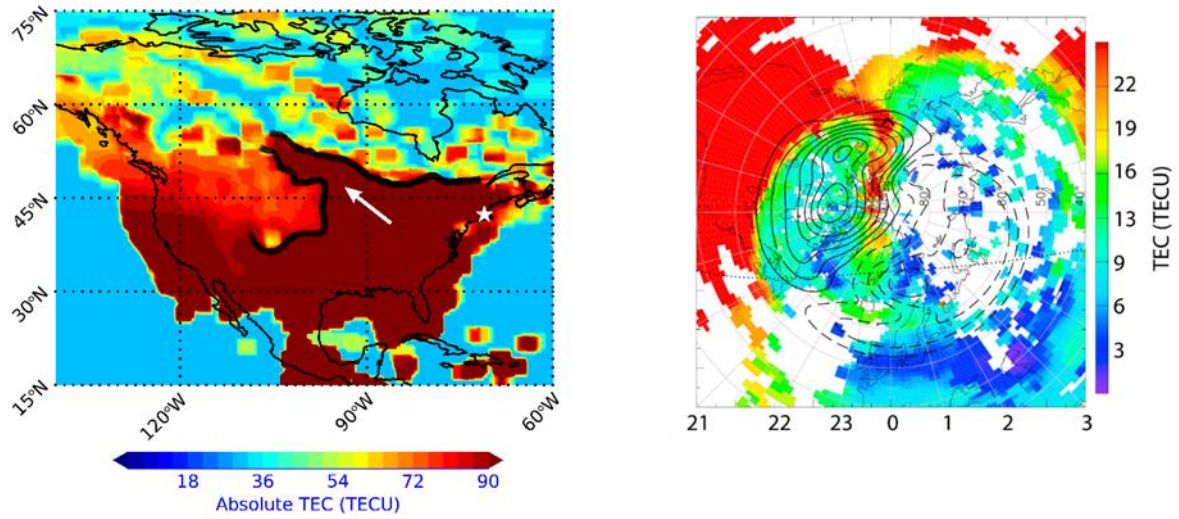

Figure 3. 6: (Left) *The 2D TEC map for 9 Nov obtained by integrating the TEC for a half hour duration (20:00–20:30 UT). The white arrow represents the direction of motion of SED plume, which is sunward. The white star indicates the observation location, Boston.* ***(Right)*** *The SED plume connected with the Tongue of Ionization (TOI) across the polar cap through ionospheric equipotential contours of the high latitude convection pattern at 22:55-23:00 UT during a geomagnetic storm 23 April 2012 (After Zou et al., 2014).*

white star symbol, is located amidst the increased plasma density region due to the SED structure. A sharp gradient in the SED plume is indicated by white arrow and thick black lines. Such plume is considered to be the ionospheric signature of the dusk side erosion of the outer layers of the plasmasphere due to the strong SAPS (subauroral polarization streams) electric fields imposed by the expanded high latitude convection pattern (Foster et al., 2004). Under the effect of a high latitude convection pattern, the SED plume was also found to clearly evolve as a tongue of ionization in the dayside across the cusp region by Zou et al., 2014, as shown in the right side of Figure-3.6.

3.3.3 Influence of magnetospheric convection on the F-region ionosphere

To interpret the effect of high-mid latitude coupling, the variation in the rate of change of TEC index (ROTI) over North America on 9 November 2004 was investigated during 14–17 LT (19-22 UT) and is shown in Figure-3.7 at 30 minutes time interval. The ROTI variations show that as the storm progressed, the convection cell expanded equatorward and reached to the mid-latitude region. During the period of 15–16 LT, a large increase in ROTI extending over all longitudes of North America and reaching the observation location (Boston; white star) at 15 LT (20 UT) can be seen which remained persistent over there for one hour duration till 16 LT (21 UT). It is important to note that this rapid expansion of convection pattern from high to mid-latitudes was in association with the southward (negative) IMF Bz duration from 20 to 21 UT (15–16 LT) and was thereby present over the observational field of view for an hour. After 21 UT, the region of enhanced ROTI moved poleward due to the northward turning of IMF Bz. This enhanced region from 15 to 16 LT manifests the expansion of equatorward boundary of high latitude two cell pattern to lower latitudes, which is associated with the SAPS electric fields. SAPS have strong plasma flow having velocities of about a few 100-1000s m-s^{-1} in the sunward direction at subauroral latitudes and have a latitudinal width of several degrees (Erickson et al., 2011; Foster & Burke, 2002). SAPS have been found to take the plasma in sunward and poleward direction during SED from the nightside region (Foster et al., 2002, 2004). Therefore, it is concluded that the observed enhancement in TEC is due to the transport of plasma convected from the post-dusk sector to the dayside under the strong sunward magnetospheric convection. Although the plasma convection in subauroral ionosphere is visible from the TEC maps from Figure-3.5, to examine the zonal velocities of plasma flow,

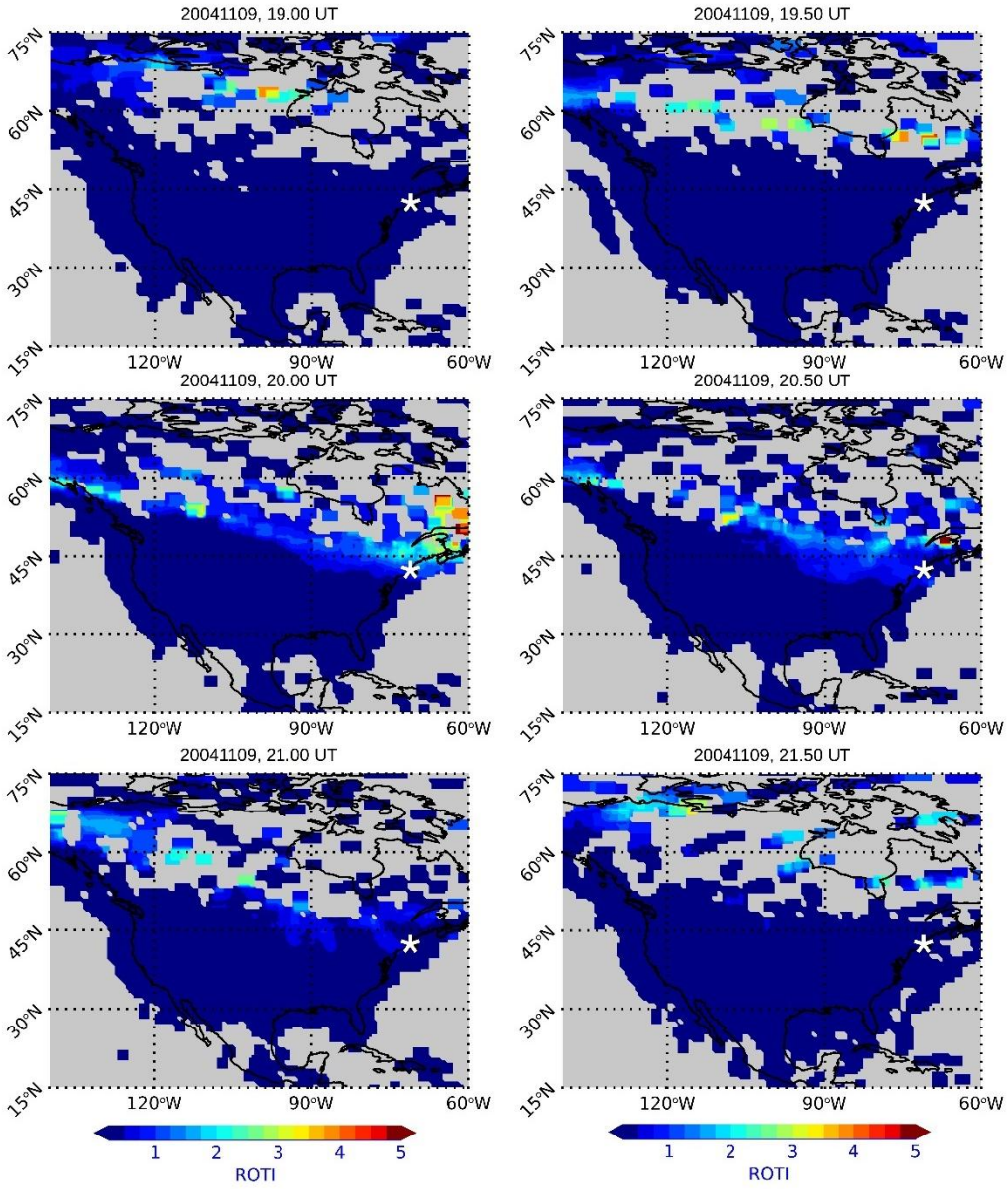

Figure 3. 7: *ROTI maps over North America on 9 November 2004 during 19–22 UT at half an hour interval. The white star symbol represents the observation location, Boston.*

the DMSP ion drift data during 20–21 UT were utilized. The Figure-3.8a represents the ROTI variation at 21.08 UT (16.08 LT) over the enlarged map, wherein the closest DMSP-F14 pass was observed at 21.09 UT (16.09 LT) as shown by thick red line. The two dashed white lines indicate the mid-latitude region between 60°N and 40°N MLAT which intersect the F14 pass at point P1 and P2, respectively. From Figure-3.8b, a fast horizontal ion drift (Vy) can be seen as measured by the F14 satellite with the velocities reaching around 1 km-s^{-1} in the sunward direction between P1 and P2 region (marked by a black dashed line). Such a strong sunward flow of plasma in dayside with a latitudinal width of several degrees clearly signifies the presence of a SAPS electric field in the mid-latitude ionosphere. These westward SAPS flows

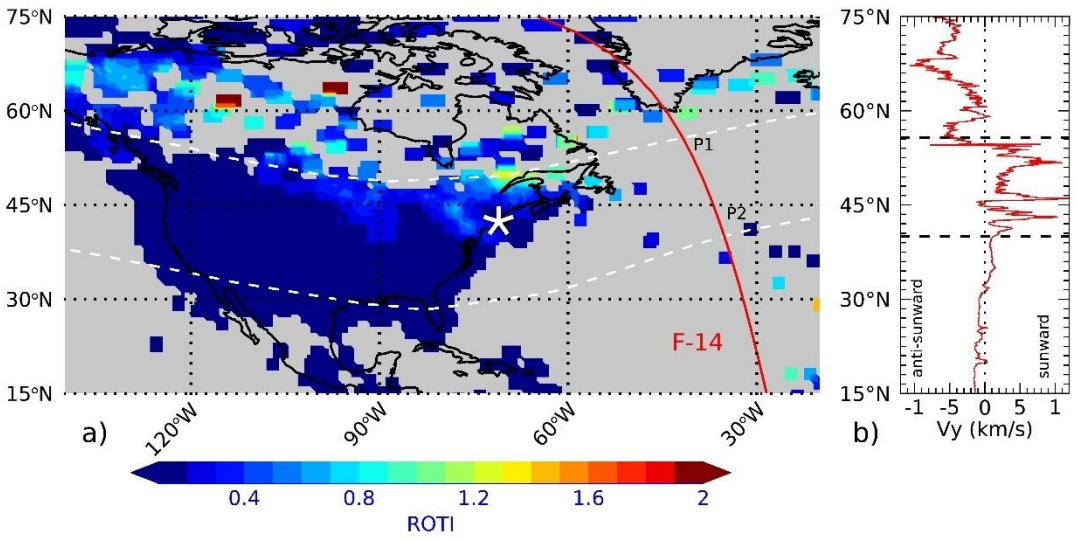

Figure 3. 8: *(a) The enlarged ROTI map (with changed colorbar to highlight the variation) upto 20°W showing the ground track of DMSP-F14 (red line) at 21.08 UT (16.08 LT). The two white dashed line represent the 40° and 60° N MLAT which intersect the DMSP pass at P1 and P2. (b) DMSP observed horizontal ion velocities (positive is sunward) between P1 and P2 region (black dashed line). This region can be seen having fast plasma flow (~1 km-s^{-1}) in sunward direction.*

are in opposition to the corotation flows over mid-latitudes which are in an anti-sunward direction, therefore the stagnation region generated by the interaction of these two oppositely directed plasma flows resulted in the plasma build-up in the form of a plume by following the convection patterns. Since, the sunward flow of plasma in dayside must have a poleward component for the completion of 2-cell pattern, which is also an inherent characteristic of convection cell potential distributions and is seen directly during the observations of convection velocity (Heelis, 1984). Therefore, the sunward and poleward motion of increased plasma density seen in Figure-3.6 was found to be due to the effect of the SAPS electric field driven by the expanded high-latitude convection to mid-latitudes.

3.3.4 Role of Electric field during SED

From the consideration of altitude variation of Ne, Te, and Ti (Figure-3.3), it is seen that on 8 November, these parameters do not show any abnormal behavior. However, on 9 November, a striking change from the general temporal behavior is observed for around 1 hour near dusk in each parameter. As seen from Ne profiles, the F region maximum electron density (NmF_2) was found to be 2.3×10^{11} m^{-3} at 15 LT on 8 November and 6.28×10^{11} m^{-3} on 9 November around

the same local time, indicating an enhancement by a factor of about 2.7. An elevated height of hmF_2 caused an enhancement in the electron density at higher altitudes by reducing the chemical loss rates due to the less collisions at those altitudes. The F-region peak promptly shifted upward from 250–300 km range to 450–550 km altitude in about 15 min around 15 LT during the onset of the main phase of the storm on 9 November. Usually during daytime, the eastward electric field penetration and/or equatorward neutral winds act as two important possible mechanisms for the uplift of ionospheric plasma layer (e.g., Yuan et al., 2003, Prölss, 1993, 1997, Lu et al., 2001, Balan et al., 2009). However, as the effect of winds on the F-layer height is expected to be gradual in nature in comparison to the sudden enhancement observed in this case, the role of eastward electric field has been investigated. To uplift the ionospheric F-layer vertically during daytime, a zonal electric field in the eastward direction is required, with the vertical velocity (V) of plasma as:

$$V = \frac{\vec{E} \times \vec{B} \cos(I)}{\left|\vec{B}\right|^2} \tag{3.1}$$

where, $\vec{E}$ is the electric field, $\vec{B}$ is the magnetic field, and I is the magnetic dip angle of the geomagnetic field. A schematic is shown in Figure-3.9 to understand the induced plasma drifts by an eastward electric field over mid-latitude where geomagnetic field lines are tilted. The x-axis indicates the north-south plane from low to high latitudes, while the y-axis denotes the altitude. The thick black tilted line represents the magnetic field line and I is the magnetic inclination or dip angle (~68°) of Boston at around 450 km altitude. The red dot corresponds to the direction of an eastward electric field out of the plane. Therefore, in the presence of an eastward electric field, a vertically tilted $E \times B$ drift perpendicular to the magnetic field is produced, as shown by the red arrow, having a E/B cos(I) component (U_c = E/B) in the vertical direction. For a strong electric field imposed during geomagnetic storms, this vertical

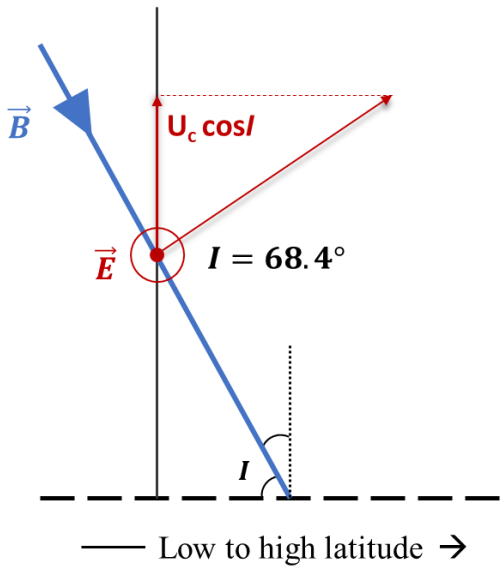

Figure 3. 9: *A schematic representing the induced plasma drifts in vertically up direction due to the Eastward Electric field in daytime.*

projection dominates and carries the plasma in the upward direction as opposed to downward field aligned flow due to the vertical forces (gravity and pressure gradient) resulting in a positive vertical drift. As discussed above, the expanded convection favored the SAPS electric field in the overhead ionosphere, which consequently provided the vertical $E \times B$ drift in the ionosphere. Therefore, such a rapid increase in the plasma height was driven by the penetration of zonal eastward electric field during the daytime. Also, from the simultaneous measurements by ISR, a strong eastward electric field of ~10 mV-m^{-1} was detected at 15 LT on 9 November 2004, which was the strongest on that day. As from Equation-3.1, when the electric fields are stronger, this could give rise to larger vertical ion drifts. Therefore, the ISR measured vertical drift velocities of plasma in the ionosphere at 325 km altitude were compared between 8 and 9 November 2004, as shown in Figure-3.10. The vertical drifts reaching 200-300 ms^{-1} for about half an hour during 15 -16 LT can be clearly seen on 9 November. Ion temperatures are generally lower than the electron temperatures in the F-region due to their heavier mass, but on 9 November, the thermal conduction among fast moving ions due to strong upward drift most likely caused an increase in the ion temperatures, as seen earlier in the rightmost column of Figure-3.3. Therefore, the observed ion drifts were found to support the effect of larger electric fields on the uplift of the ionosphere. Such uplifts over mid-latitude have also been observed on several occasions (e.g., Foster et al., 2005, Yuan et al., 2009).

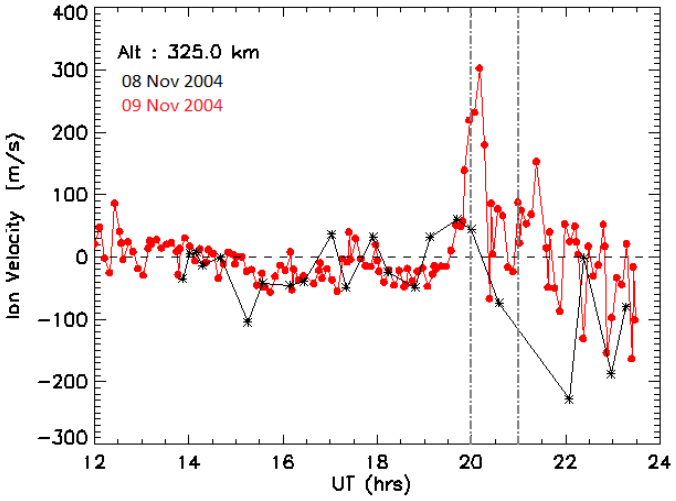

Figure 3. 10: *A measured upward ion drift (positive upward) by ISR at 325 km altitude reaching up to 300 m-s^{-1} at around 15 LT on 9 November 2004.*

To understand the mechanism of the upward movement of plasma due to the electric field, a physical explanation has been suggested by Heelis et al. (2009), as shown in Figure-3.11. The left side in case (a) demonstrates the simple corotation convective flow without any additional electric field component wherein, the corresponding hmF_2 variation of electron density (right panel) shows typical height variation of F-region during the two-hour period. The simulated effect of additional zonal electric field with poleward plasma motion is shown in case (b). It

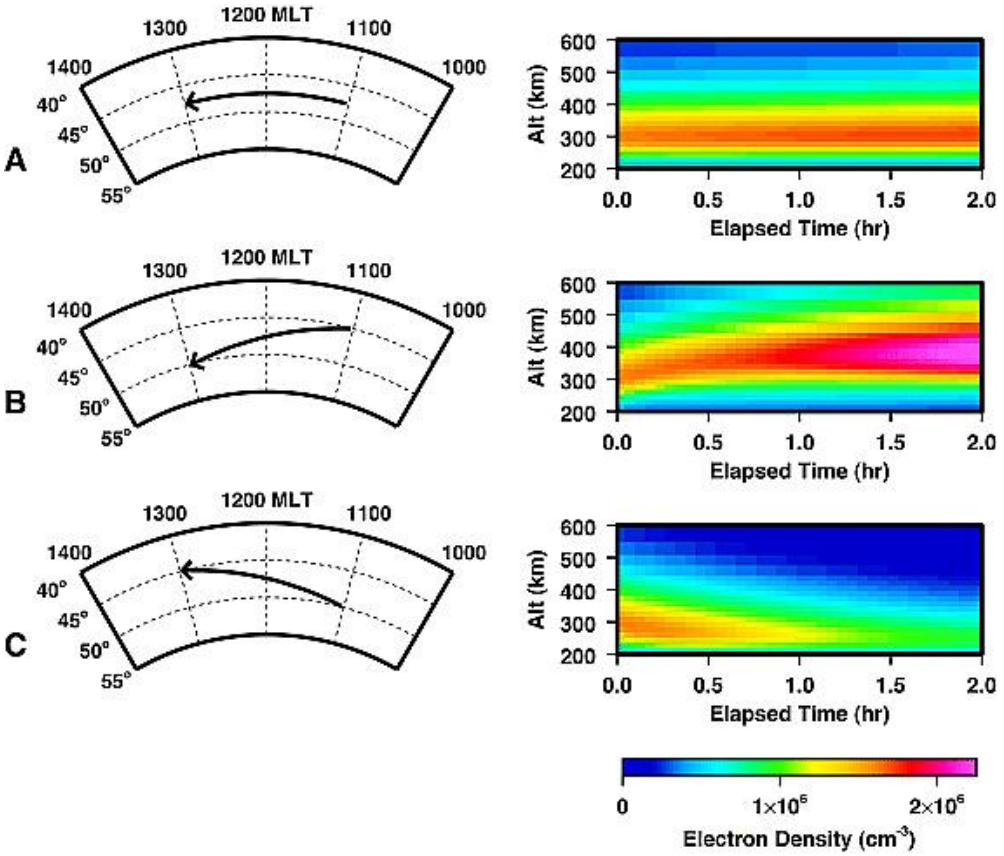

Figure 3. 11: *The effect of purely zonal motion (case-A), poleward (case-B), and equatorward (case-C) convective flow has been sown by model simulations during 2-hour interval period in the left side. The corresponding variation in altitude profile of electron density for different cases (A, B, and C) has been shown in the right side. After Heelis et al., (2009).*

can be seen that during the poleward movement from 11 to 13 LT, the plasma height increases simultaneously with an increase in the plasma density. Therefore, from Ne variation in Figure-3.3, the shift in hmF_2 to higher altitudes by around 200 km is inferred to be due to the SAPS electric field in subauroral ionosphere which provided the strong $E \times B$ drift, causing an increase in the peak height of the F-region and also resulting in enhanced red line dayglow emissions.

3.3.5 Altitude Variation of 630.0 nm using volume emission rate profiles

Although the unusual variations in electron density, electron/ion temperatures have been investigated in earlier studies, the ionospheric behavior during the SED and its effects on 630.0

nm VER profile during daytime are not studied to date. Therefore, to investigate the altitudinal effects of ionospheric parameters on 630.0 nm dayglow emissions for 8 and 9 November, the ISR measured Ne, Te, Ti profiles were provided to the GLOW model as inputs. The GLOW estimated volume emission rates as a function of altitude and local time for 8 and 9 November are shown in Figure-3.12a. To highlight the variation explicitly, Figure-3.12b shows the line plot of VER as a function of altitude for the two days at different times. The dashed blue and thin red lines show the VER variation on 8 and 9 November, respectively and the variations in VER during the observed period of dayglow enhancements i.e., 15-16 LT on 9 November is represented by thick red lines. It is clearly seen that during 15-16 LT the emissions were further enhanced by around 1.5 times than the maximum peak production of ~200 photons-cm^{-2}-sec^{-1}. Additionally, the peak emission altitude of dayglow emission was shifted to higher heights of about 400 km, similar to the hmF_2 variation shown in Figure-3.3. It is important to note that the dissociative recombination mechanism of O_2^+ follows a two-stage process. Initially, there is a charge exchange between O^+ and O_2 resulting in the formation of O_2^+. In the current

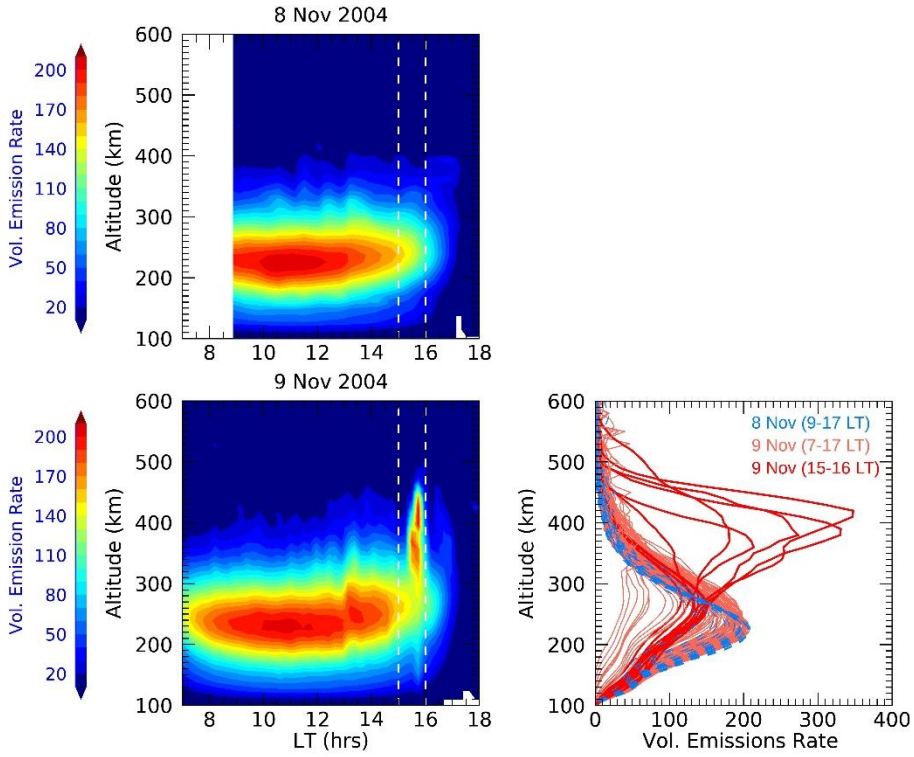

Figure 3. 12: *(a) The OI 630.0 nm volume emission rates (VER) as a function of time, as estimated by the GLOW model using as inputs the ISR measured Ne, Te, and Ti data. The one-dimensional plot of VER on 9 November in panel (b) clearly shows a shift in peak emissions to higher altitudes (up to 420 km) during 15–16 LT (thick red lines).*

scenario, where Ne concentrations were increased at higher heights, charge conservation necessitates a corresponding rise in O^+ concentrations. These increased densities of O^+ and Ne by the power of 2, compensate more than adequately for the reduction in O_2, which decreased by a factor of 1/e over a scale height at higher altitudes compared to the lower ones. In addition, due to the comparatively lower densities of Nitrogen molecules [N_2], the quenching effect on the $O(^1D)$ state is negligible at these altitudes. All these factors thus contribute to a higher yield of OI 630.0 nm emissions during daytime. As seen from Figure-3.2d, the enhanced density caused three peaks I, II, and III in the dayglow and there is a good match between the measured and estimated magnitudes of 630.0 nm dayglow for II and III, however, the dayglow peak (I) is underestimated in the model emissions. This occurs because, as illustrated in Figure-3.3 (rightmost panel), the electron density measured by ISR exhibited a saturation within the altitude range of 400–600 km. During this period, the actual electron densities are significantly higher compared to other time intervals, including those at II and III, where no similar saturation was detected. Consequently, despite the absence of corresponding indications in the model estimated emissions, the redline emissions observed by HIRISE during peak I are indeed attributed to the increased electron density due to SED phenomena.

Therefore, the important changes in ionospheric parameters obtained using ISR measured altitude profiles and in OI 630.0 nm VER profile obtained by GLOW between 8 and 9 November 2004 are summarized in Table-3.1 during 15-16 LT.

Ionospheric Parameter	8 November, 2004	9 November, 2004	Respective change on 9 November 2004
hmF_2 (km)	~300	400-500	1.5 x increase
NmF_2 (m^{-3})	2 x 10^{11}	~6 x 10^{11}	3.0 x increase
Electron temperature at 500 km (K)	~3500	~700	5.0 x decrease
Upward ion velocity (m s^{-1})	50	200	8.0 x increase
Peak emission (photons cm^{-2} s^{-1})	200	300	1.5 x increase
Peak emission altitude (km)	~250	~450	1.8 x increase

Table 3. 1: *Change in the ionospheric parameters obtained using altitude profiles from ISR and GLOW during 15-16 LT.*

3.3.6 Small-scale fluctuation in 630.0 nm Dayglow and TEC

Though the observed and modeled dayglow emissions show the similar diurnal variations with electron density variations, to ascertain this even further, spectral analysis was carried out of dayglow emissions along with those of TEC. The residuals, acquired through the subtraction of the 3-hour running mean from both dayglow and TEC data, were subjected to Lomb-Scargle spectral analysis (section-2.4). The associated fluctuations, along with their residuals, are depicted in Figure-3.13. The top and middle panels display the dayglow measurements obtained from HIRISE and the GLOW model, respectively, while the bottom panel illustrates the IGS-TEC data retrieved from a co-located GPS receiver in Westford (USA) on 9 November 2004. To mitigate the influence of TEC from slant angles, the analysis was restricted on data corresponding to elevation angles exceeding 60° and within the ±3° range centered at Boston's

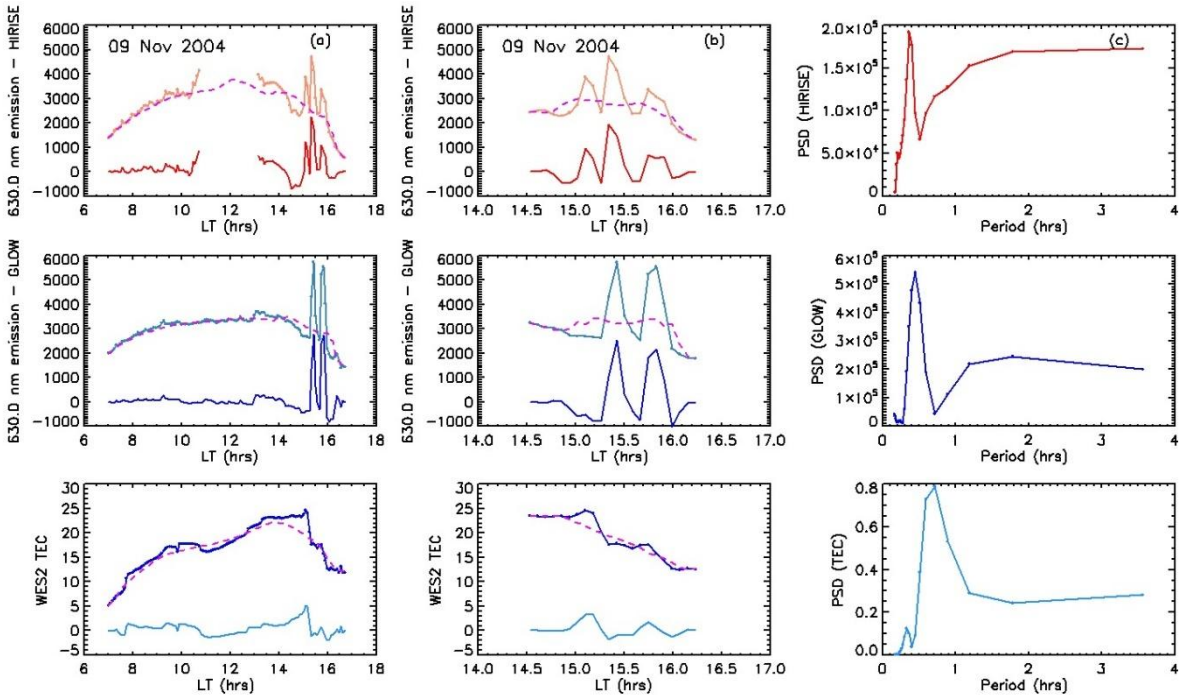

Figure 3. 13: *HIRISE observed dayglow (top row), GLOW estimated dayglow (middle row), and TEC (bottom row) are shown. The 3-hr running average was taken (dashed line) and the residuals thus obtained (with zero mean) are also shown in these panels. The left column shows the diurnal profile of these parameters, middle column shows the variation of these parameters near one hour of major disturbances (15–16 LT ± 0.5 hr), and the right column shows the presence of periodicity of about 30 min in both dayglow (observed, estimated) and TEC for same period.*

latitude. The reanalyzed dayglow, featuring increased temporal resolution (depicted in Figure-3. 2d) for 9 November, was utilized for this investigation. The middle column (b) represents these data for the specific time-duration of about one hour of major disturbances (15–16 L T ± 0.5 hour). Therefore, the resultant power spectral densities (PSDs) from spectral analysis are shown in rightmost column (c) which reveal small fluctuations with periodicities of approximately 24–36 minutes to be present simultaneously across all parameters. It is striking to note that all these independent data products match well during 15–16 LT on 9 November 2004. This further strengthens the identification of observed enhancements in the OI 630.0 nm dayglow emissions in this duration to be an optical signature of SED relating to F-region ionospheric dynamics. These findings outlined and elucidated in this study represent the first report of measurements of storm-enhanced densities over mid-latitude in the red line airglow emissions during daytime.

3.4 Summary

In this chapter, an anomalous enhancement observed in the red line dayglow emission intensities was presented and the cause was explored using various complementary datasets and models. The investigations reveal that on 9 November 2004, a region of SED was formed in the overhead ionosphere during the main phase of the storm which was produced mainly by the expanded convection and SAPS electric field during drastic IMF southward excursion at 15 LT. The passage of such an SED enabled the study of the variations in ionospheric F-region characteristics during disturbed times over the observation location. The altitudinal profiles from Millstone Hill radar during SED reveal both an elevated hmf_2 and enhanced electron density in the topside ionosphere on 9 November. Therefore, a comparison between the dayglow observed by HIRISE and the GLOW estimated emissions revealed that the observed enhancement in 630.0 nm dayglow was primarily attributed to the increase in electron density during dusk hours. The observed quantitative changes in ionospheric parameters include a reduction in plasma temperature by approximately fivefold at altitudes greater than 300 km, alongside an elevation in the peak emission altitude of 630.0 nm dayglow to around 450 km, subsequently accompanied by an increase in hmF_2. Also, the upward ion drift was found to be due to the vertical component of $E \times B$ drift, which indicated the imbalanced local production and loss mechanism during SED as opposed to the downward diffusion. The observed

enhanced density lasted for about an hour during 15 – 16 LT, as IMF Bz turned northward after 16 LT. The enhancement in peak electron density around 15 LT over the zenith at Millstone Hill clearly signaled the onset of SED over the observation location. In conclusion, around 2.5 kR intensity enhancement of OI 630.0 nm dayglow observed during the dusk hours was identified as an optical signature of Storm Enhanced Density (SED) phenomena, potentially representing the first reported impact of SED on airglow emissions during daylight hours.

Chapter: 4

Daytime SAR arcs in red line emission

4.1 Introduction

The history of auroral photography is a fascinating journey through time and technology. Starting with Martin Brendel's pioneering work in 1892, the field has evolved significantly (Eather, 1980). The International Geophysical Year of 1957-58 marked a significant milestone with the deployment of all-sky camera systems globally, allowing for comprehensive horizon-to-horizon documentation of the aurora. This era saw the transition from simple photographic film to the use of image intensifiers, greatly enhancing the sensitivity of detectors. Such advancements made it possible to capture the elusive stable auroral red (SAR) arcs, first discovered in the late 1950s in Europe by Barbier (1958, 1960). These arcs, often less bright than 1000 Rayleighs, are subtle yet critical components of the upper atmosphere, offering insights into the complex interactions between the magnetosphere and ionosphere. Today's all-sky imagers continue this legacy, recording both the vibrant auroras and the faint intensity of airglow, providing continuous observation, and contributing to the understanding of Earth's atmospheric phenomena.

SAR arcs are a notable optical phenomenon mostly observed during nighttime in the mid-latitude ionosphere (e.g., Cole, 1965; Kozyra et al., 1982; Mendillo et al., 2016). These arcs are dominated by atomic oxygen emissions at 630.0 nm produced by the transition of an oxygen atom from its excited O(^{1}D) state, which requires ~2 eV, to the ground energy state O(^{3}P), as a consequence of magnetosphere-ionosphere (MI) coupling. They are produced by the interaction of high-energy plasma in the ring current heating the low-energy plasma in the plasmasphere, which subsequently falls into the ionosphere along the magnetic field lines. This precipitation of heat flux from the near plasmapause region heats F-region electrons at altitudes of ~400 km to temperatures greater than around 3,000 K and thus causes the excitation of the O(^{1}D) state by collisions between ambient O atoms and ionospheric heated electrons.

Therefore, SAR arcs are mostly spectrally pure 'red line' emissions, as collisions that excite the O(^{1}D) state do not have sufficient energy to produce any other emissions. Only one work exists that reported the presence of the green line emissions at 557.7 nm, which requires 4.17 eV of energy for excitation (Mendillo et al., 2016). SAR arcs have typical emission intensity of around 500 ± 270 Rayleigh, however on occasions, very bright emissions also have been reported reaching ~10 kilo-Rayleigh (Baumgardner et al., 2007). These arcs exhibit distinct characteristics, being 50-200 km narrow in latitude and 1000's km broad in longitude, and have been described using all sky imagers and satellite measurements (Craven et al., 1982; Mendillo et al., 1987). Figure-4.1 shows the unwrapped images of OI 630.0 nm (red line) and OI 557.7 nm (green line) emissions in the top (a, b) and bottom (c, d) panels, respectively, during a night on 28 December 2003 between 05:00-06:00 UT (LT = UT-5 hr) captured by an all-sky imager at Millstone Hill. For each individual image, the top and bottom parts indicate geographic north

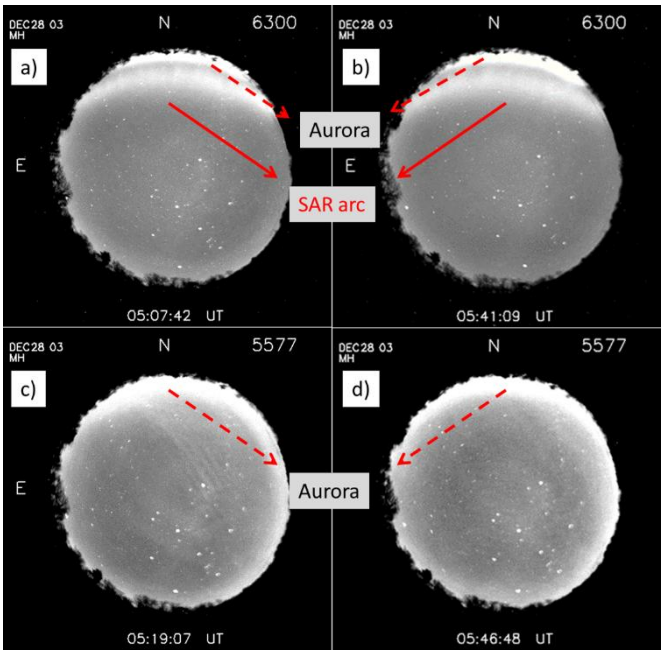

Figure 4. 1: *Examples of SAR Arcs seen at Millstone Hill, Westford, MA. Each panel shows unwrapped all-sky images at Millstone Hill captured between 05:00-06:00 UT (LT=UT-5 hr) on the night of 28 December 2003. The OI 630.0 nm (red line) and 557.7 nm (green line) emissions are represented in top panels (a and b), and bottom panels (c and d), respectively. For each image, N and E represents the geographic north and east directions, respectively. The bright northern most part in each image is aurora (marked by dashed arrow), whereas, to the equatorward of aurora, a SAR arc is seen in the red line (solid arrow), which is clearly absent in the green line emission, representing their spectral purity. From Optical Aeronomy at Boston University (buimaging.com).*

and south, while the left and right parts indicate geographic east and west directions, respectively. In the North most of each image, the bright part represents the aurora in both wavelengths as indicated by dashed arrows. Interestingly, from top panels, a latitudinally narrow and zonally elongated region of enhanced 630.0 nm brightness can be seen equatorward of aurora, which is clearly absent in the green line emission in bottom panel. This increased 630.0 nm brightness region represents the SAR arc, indicated by solid arrow, and the absence of such region in green line emission shows the spectral purity of SAR arcs.

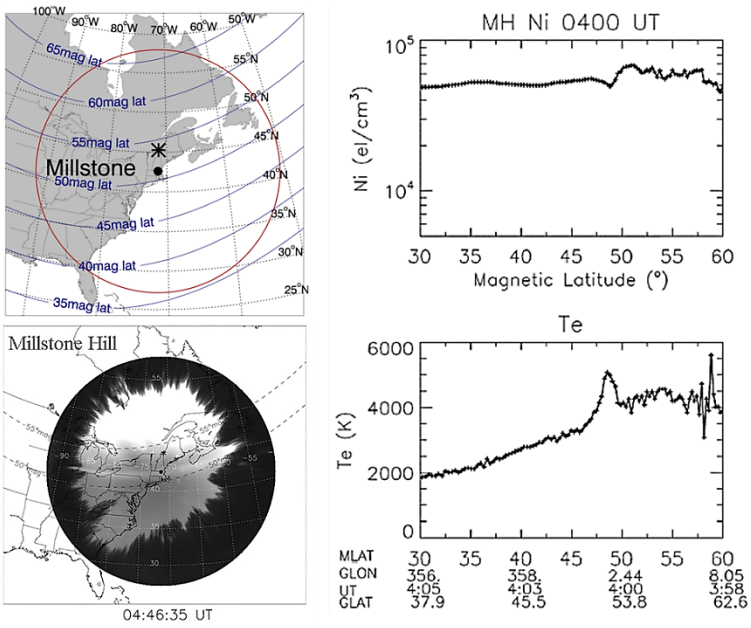

Figure 4. 2: *Observation of SAR arc during nighttime over Millstone Hill on 1 June, 2013 (left column) along with the latitudinal variation of DMSP measured ionospheric ion density (Ni) and electron temperature (Te) (right column). The enhanced Te peak corresponds to the region of SAR arc. After Martinis et al. (2019).*

The formation of SAR arcs provides direct evidence of magnetosphere-ionosphere coupling in the subauroral upper atmosphere as SAR arcs are typically observed in the low electron density (Ne) region of ionospheric trough at mid-latitudes, where the footprint of plasmapause connects with the ionosphere. Therefore, increased electron temperature (Te > 3,000 K) and reduced Ne become two key ionospheric signatures associated with SAR arcs, as evidenced by in-situ measurements (Foster et al., 1994, also as shown in Figure-4.2 during nighttime observed SAR arc. The left column in Figure-4.2 shows a nighttime observation of SAR arc measured over the zenith of Millstone Hill (marked by dot in geographical map) using an all-sky imager while, the right column shows the corresponding ionospheric variation of Te and Ni (≈Ne) measured

by DMSP at ~800 km altitude (Martinis et al., 2019). The enhanced Te peak collocated with reduced density feature corresponds to the latitudinal structure of SAR arc. SAR arc emissions occur during the recovery phase of geomagnetic storms and can be related to storm time substorms. The theoretical framework for SAR arc generation is given in the review paper by Rees and Roble (1975), and their status within the context of magnetosphere-ionosphere coupling is summarized in Kozyra et al. (1997). During periods of high geomagnetic activity, SAR arc features are enhanced and their spatial extent can reach towards lower latitudes (Fok et al., 1991). Therefore, depending on the strength of geomagnetic disturbance, location of occurrence of SAR arcs can vary in the region of L-value ranging from around L=2 to 5. Shiokawa et al. (2009) reported a SAR arc detachment from the main auroral oval during non-storm time substorms, which may relate to the characteristics of ring current particle injection in the inner magnetosphere and could be an important tool to monitor the state of high-energy plasma in the inner magnetosphere. The nighttime studies also have demonstrated the large temporal coverage of SAR arcs using all-sky imagers, showing the occurrence of an arc during 24 consecutive hours (Mendillo et al., 2013). Recent studies, including those by Inaba et al. (2020, 2021), have utilized ground-based all-sky cameras at subauroral latitudes and satellite data to investigate SAR arc generation mechanisms, emphasizing the role of Coulomb collisions and wave activities. They concluded that the Coulomb collision between ring current

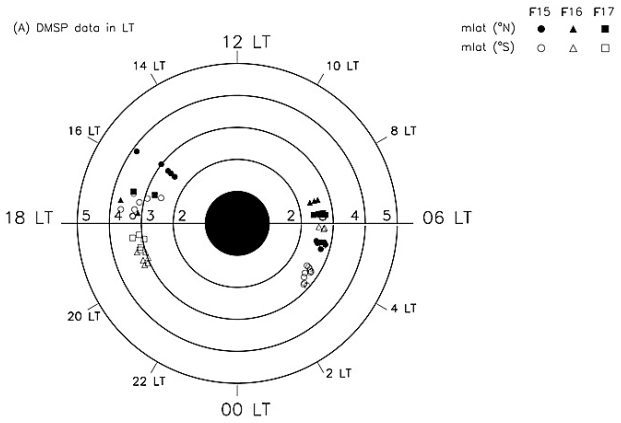

Figure 4. 3: *Locations of Te enhancements (≥ 5000 K) at the lowest sub-auroral latitudes (represented by L value) versus Local Time, as observed from all DMSP passes on 26–27 Sep 2011. Different symbols indicate the different satellites and the hemisphere where the observations were made. The in-situ measured Te peak between L=2-4 and 06-18 LT suggest the presence of SAR in dayside. After Mendillo et al., 2013.*

ions and plasmaspheric dense low-energy plasma is the cause of the detached SAR arcs, while some wave activities may also contribute to the generation of freshly detached SAR arcs. However, comprehensive statistical analyses using conjugate measurements with ionospheric satellites remain to be conducted. Additionally, observations of SAR arcs using ground-based optical measurements have been reported during nighttime only, to date. There have been no reports of ground-based optical measurements of SAR arcs in daytime thereby preventing a comprehensive understanding of their behavior. Nevertheless, considering the mechanisms involved in SAR arc production and heat conduction in the ionosphere from near plasmapause region, SAR arcs can be anticipated to form in dayside (Kozyra et al., 1997). Recent observations (Mendillo et al. 2013) using the DMSP measured electron temperature peak at subauroral latitudes suggested the LT occurrence of SAR arcs on both dayside and nightside. DMSP Te Data from different satellites and hemispheres were merged to form the single composite image in the LT and L-value format, as shown in the Figure-4.3. The locations of in-situ measured Te peaks between L=2-4 and 06-18 LT suggest the presence of SAR in the Earth's dayside. As the alignment of DMSP satellite was in dawn-dusk orbit, no Te Peak is seen near local noon. However, such measurement suggested the presence of daytime SAR arcs. Although the daytime optical airglow measurements are challenging, it has now become a reality with the advent of ground-based dayglow optical techniques (Pallamraju et al., 2002, 2013). Further, the measurement of SAR arcs in the daytime seems particularly promising in view of the fact that the OI 630.0 nm, O(^{1}D), dayglow emissions from Sondrestrom have been used to investigate the daytime cusps (Pallamraju et al., 2004) and both of these processes involve enhancement in the Te for occurrence of the red-line emissions. Therefore, this chapter presents the first reported optical measurements of SAR arcs in daytime using OI 630.0 nm emissions.

4.2 Datasets used

In this chapter, ground-based optical observations of red line emissions over zenith obtained using HIRISE are utilized. In addition to these daytime airglow emissions, the collocated Millstone Hill based digisonde data were also used to acquire the Ne information from the ionograms. These Ne profiles as a function of altitudes were further used as inputs into the GLOW model (section 2.5) to obtain column integrated O(^{1}D) emissions that are required to compare with those measured by HIRISE. On occasions, when Millstone Hill ISR data were

available, additional information on electron and ion temperatures (Te, Ti) were used for obtaining a greater understanding of the ionospheric conditions and to confirm the findings.

4.3 Results and discussions

4.3.1 Observations of optical and ionospheric signature of SAR arcs in daytime

The local daytime variations in the HIRISE measured OI 630.0 nm emissions obtained after following the dayglow extraction procedure (described in section-2.3.2) are represented by red-filled circles line in Figure-4.4. Each point also shows a ±1σ error bar, which ranges from 5% to 18% depending on the signal and background brightness (Pallamraju et al., 2002, 2013). The missing data around local noon is due to the saturation in CCD counts caused by direct

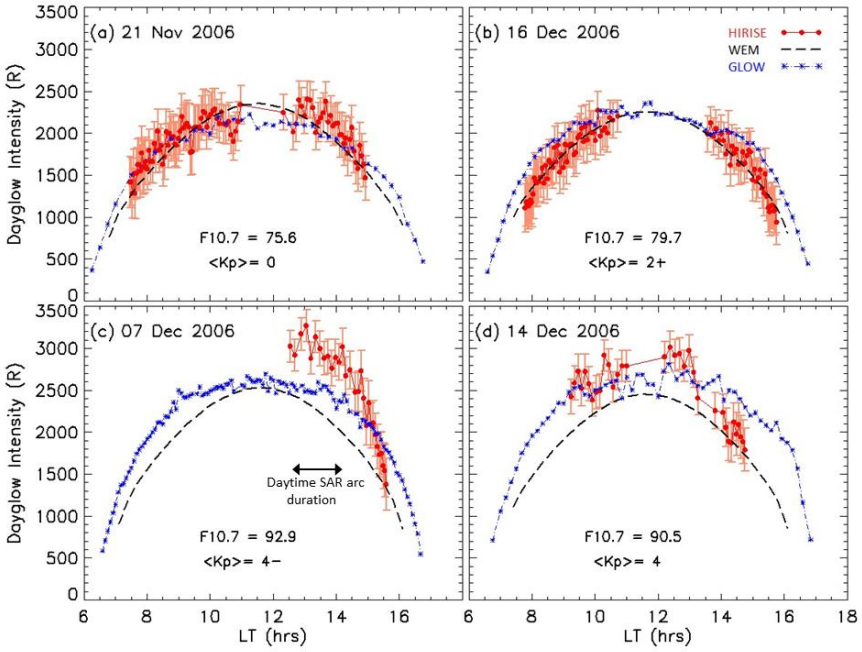

Figure 4. 4: *The daytime OI 630.0 nm airglow emissions on geomagnetically quiet (a, b) and disturbed (c, d) days are shown: HIRISE measurements (red filled circles with ±1σ uncertainties), WEM estimates (black dashed line), and GLOW estimates (blue asterisks). The measured and estimated emissions match well during quiet conditions. The enhancements in measured emissions on 7 December 2006 (panel c), are due to a stable auroral red arc event observed during the daytime for the first time.*

sunlight/solar glare entering through the slit of HIRISE, rendering the image unusable. There are total four days of OI 630.0 nm emission data during daytime shown in Figure-4.4. Of these, two days (a, b) are geomagnetically quiet (daily averaged Kp index, ⟨Kp⟩ < 3) and the other two days (c, d) are geomagnetically disturbed (⟨Kp⟩ ≥ 3). On the forenoon of 7 December 2006, the measurements of daytime airglow emissions were prevented due to clouds in the sky. The solar flux variation during these observation periods was small, ranging from 75 to 93 sfu. The WEM predictions are represented by black dashed lines for all four days. Since WEM estimated emissions are independent of any neutral or electrodynamic changes in the upper atmosphere (discussed in section 2.6.2), the HIRISE O(^{1}D) observations match well with the WEM emissions on geomagnetically quiet days (Figures 4.4a and 4.4b). However, on geomagnetically disturbed days (Figures 4.4c and 4.4d), there is a notable discrepancy between the measured emission magnitudes and WEM estimates. This significant increase in the observed emissions indicates considerable changes in ionospheric behavior on both the disturbed days. To analyze the effect of plasma parameters on O(^{1}D) emission brightness, electron densities measured by the Millstone Hill digisonde were input into the GLOW model. The O(^{1}D) emissions estimated using the GLOW model for all quiet and disturbed days are also depicted in Figure-4.4 by the blue asterisk line. For quiet days, the HIRISE measured O(^{1}D) emissions, GLOW estimates, and WEM predictions all match well in both temporal

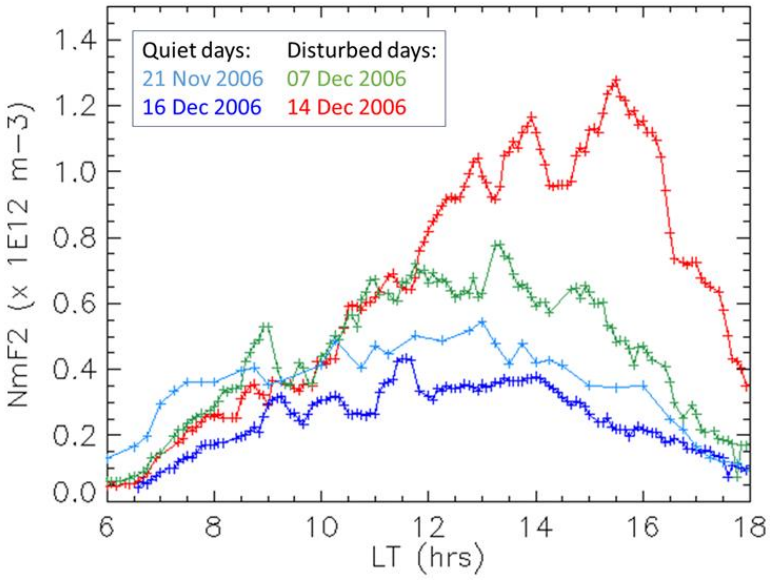

Figure 4. 5: *Digisonde obtained NmF_2 comparison for each day shown in Figure-4.4, representing the largest enhancement in densities on 14 December 2006 as reflected in HIRISE measured and GLOW estimated larger emission intensities.*

behavior and emission magnitudes. On 14 December 2006 (⟨Kp⟩ = 4), WEM underestimates the measured emissions, which is not unexpected since the effects of geomagnetic disturbance in the ionospheric variations are not included in these empirical estimates. However, the GLOW model values match well with the HIRISE measured emissions within measurement uncertainties, as the digisonde measured Ne was incorporated into the model. The ambient plasma densities are known to vary due to changes in electrodynamics, in addition to that in the solar zenith angle and the small time-scale temporal variations are primarily thus shown to be attributed to the DR mechanism. Previous studies also have demonstrated that changes in F-layer Ne are clearly reflected in the variability of O(^{1}D) dayglow emission intensity (e.g., Pallamraju et al., 2001; Upadhyay et al., 2023). Therefore, to validate the variations in electron densities, NmF_2 data from digisonde were compared during these intervals as well, which is shown in Figure-4.5. During the disturbed day of 07 December, NmF_2 was indeed found to be the largest compared with other days. Therefore, the observed enhancement in O(^{1}D) emissions affirms that the increase in electron density (Ne) resulting from the geomagnetic storm on 14 December 2006, led to higher emissions. However, on 7 December (⟨Kp⟩ = 4−), HIRISE measurements significantly exceeded the estimated emissions from the GLOW model despite incorporating the Ne measurements from the digisonde. This suggests that factors other than Ne variations contribute to these enhancements. Such temporal variations in the brightness of daytime O(^{1}D) emissions can also be brought out due to changes in electron temperature as in the case of magnetospheric cusps (Pallamraju et al., 2004). Fortuitously, Millstone Hill ISR was in operation on both these disturbed days (7 and 14 December 2006), and thus, the ISR

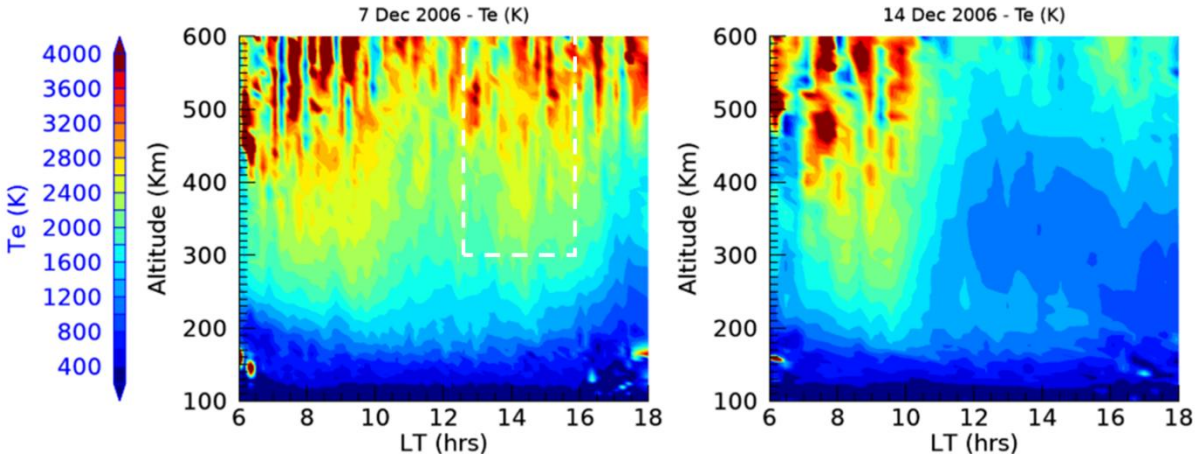

Figure 4. 6: *Millstone Hill ISR measured electron temperature (Te) profiles on 7 and 14 December 2006 in the altitude range 100–600 km. Increased values of Te can be noted on 7 December during similar interval of measured larger emissions, marked by the white-dashed lines.*

measured diurnal variations in electron temperature were examined, as shown in Figure-4.6. The Figure-4.6 clearly indicates an increase in electron temperature (Te > 3,000 K) at altitudes above 300 km on 7 December during the period of enhanced 630.0 nm emissions (13–14 LT). However, this enhancement in Te is not observed on 14 December. Consequently, the HIRISE measured enhancement in red line emissions during daytime on 7 December can be attributed to the significant role played by the larger Te values, which serve as a clear signature of the formation of the SAR arc. Such high electron temperatures trigger the excitation of the 630.0 nm emission by photoelectron-impact mechanism.

4.3.2 Dayside signature of SAR

The increase in Te at high altitudes, which produces the red glow of SAR arcs, results from heating of the topside ionosphere due to the precipitation of low-energy electrons (< 10 eV) from the inner-magnetosphere. Such detection of increased electron flux at energies about 10 eV with coincident increased in Te as observed by the Dynamics Explorer (DE) 2 spacecraft were reported by Kozyra et al. (1997), both in the dayside and the nightside, as shown in Figure-4.7. The spectrogram in Figure-4.7 represents the energy spectrum of precipitating electrons during a long-lived SAR arc event where optical observations were being made in the nightside. The characteristics of enhanced electron fluxes were observed in lowest energy channels at the similar invariant latitudes (ILAT) for both dayside (during 22:48 UT and 22:51 UT) and the

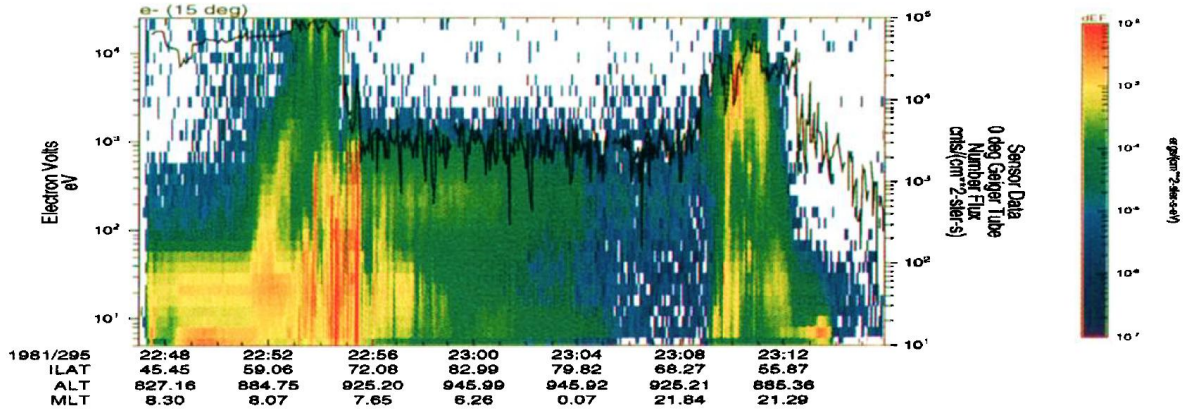

Figure 4. 7: *The Dynamics Explorer (DE)-2 spacecraft observed precipitating electrons in the lowest energy channels in dayside during 22:48 UT and 22:51 UT. (Adapted from Kozyra et al., 1997.)*

nightside (during 23:12 UT and 23:14 UT). These observations therefore not only validated the theory of soft electron precipitation, but also the dayside to nightside extension of SAR arcs. However, as DMSP measures the earth-ward precipitating electrons in the energy range from 30 eV to 30 keV using SSJ/4/5 electrostatic analyzer (Hardy et al., 1984), and the lowest energy detection is thus higher than the energies of soft electron precipitation. Therefore, in-situ measurements of low-energy electrons during the daytime SAR arc measured on 7 December 2006 were not possible by DMSP. Different passes of DMSP satellite data have been used to verify the presence of SAR arcs by their characteristic ionospheric signatures of enhanced Te and reduced ion density, Ni, in the region of their formation (e.g., Baumgardner et al., 2013; Foster et al., 1994; Martinis et al., 2019). Thus, to further validate that the enhanced brightness originated from the SAR arc, the latitudinal behavior of Te/Ne/Ni was investigated during the dayside (06–18 MLT) using high-resolution (~4 s) observations from DMSP-F13 satellite at

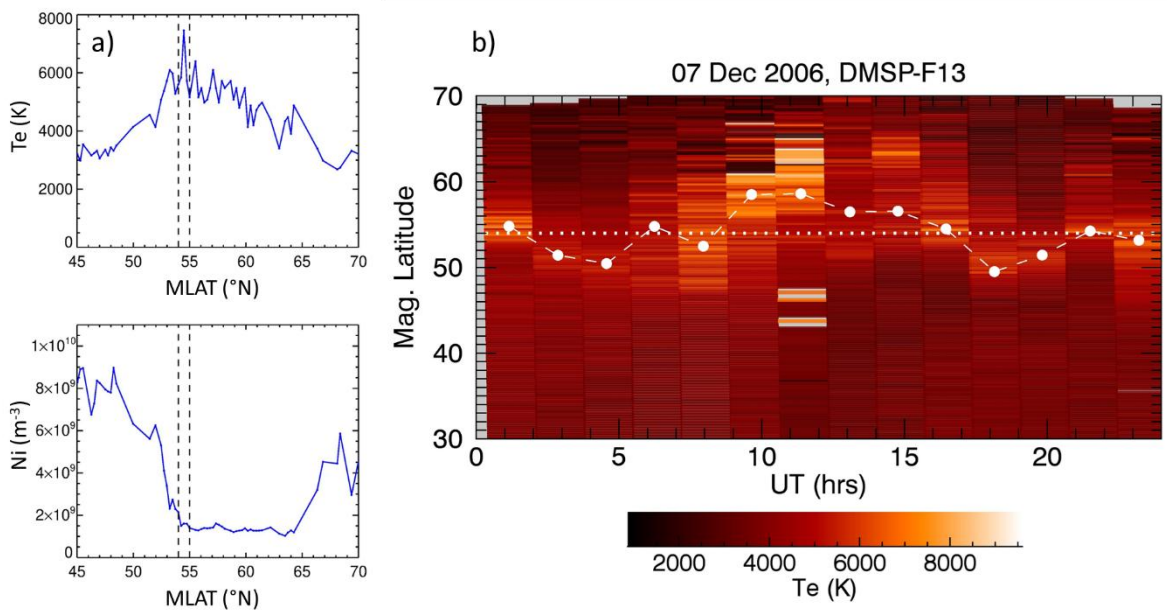

Figure 4. 8: a) *DMSP measured Te and Ni latitudinal variations are shown in top and bottom panel, respectively between 45°–70°N magnetic latitude range near 16.4 UT (11.4 LT) at ~850 km altitude. The dashed vertical lines correspond to 54°–55°N MLAT, overlapping with the latitudinal location of Boston (54.35°N MLAT). A peak in Te close to the equatorward boundary of mid-latitude trough (bottom panel) can be seen.* ***b)*** *The latitudinal Te variation for all dayside DMSP passes covering 30° and 70°N MLAT range is shown, which reveals a region of enhanced Te between 50° and 60°N MLAT globally. White filled-circle line represents the temporal movement of Te peak, reaching below 54°N MLAT (dotted line) during the observational period between 17 to 19 UT.*

an altitude of about 850 km in the topside ionosphere. To remove any ambiguity in DMSP data, only points with flag values ≤ 2 were used, as these are considered reliable (Hairston, 2018).

Since there was no DMSP pass directly over the observation location during the time when the peak enhancement in dayglow emissions was observed, the closest pass (65°W) in proximity and time (16 UT, 6.6 MLT) to the observed red line emission enhancement was considered for further investigation. Consequently, Te/Ne variations within the magnetic latitude (MLAT) range of 45°–70°N were examined (Figure 4.8a). The top and bottom panels of Figure-4.8a display the latitudinal variations in Te and Ni (ion density) around 16.5 UT, respectively. The two dashed vertical lines indicate the 54°–55°N MLAT region, including the location over Boston, at the DMSP orbit altitude (54.35° MLAT). Notably, a peak enhancement in Te was observed near 54° MLAT, falling in to the equatorward region of the mid-latitude trough (characterized by reduced Ni in bottom panel). The location of SAR arc is identified by the position of Te peak falling in low density region of ionospheric trough and the interaction region between the plasmapause and the inner ring current (Fok et al., 1991), as seen in Figure-4.8a. The observation of SAR arcs using optical brightness is difficult in daytime across the globe due to very limited number of observation sites covering a specific magnetic latitude. Therefore, to identify its nature in dayside on 7 December 2006, the temporal and spatial variations of peak Te confined in the 30° to 70°N MLAT

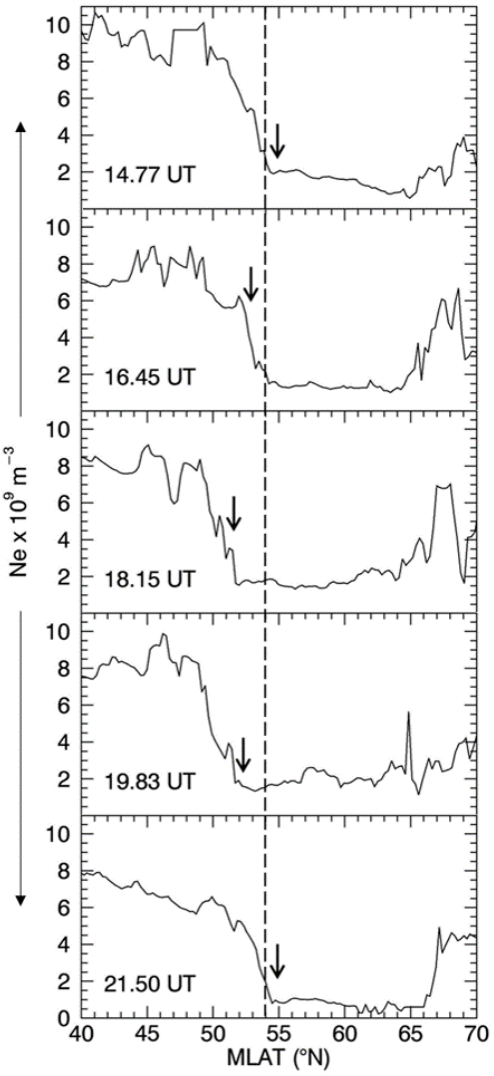

Figure 4. 9: *Latitudinal variation of equatorward boundary of ionospheric trough in 40-70°N MLAT range using DMSP measured Ne. Dashed line marks the observation magnetic latitude. The vertical arrows represent the temporal movement of trough.*

range were examined for all DMSP passes, creating a composite view shown in Figure-4.8b. A white filled-circle line connects all the MLATs corresponding to peak Te within 40°–60°N MLAT, while a horizontal dotted line indicates the observation location's MLAT. Strikingly, a narrow region of enhanced electron temperature between 50° and 60° MLAT was visible on 7 December during each dayside pass of DMSP (Figure-4.8b). The consistently observed Te peak thus reinforces the behavior of SAR arc as a global phenomenon.

The mid-latitude ionospheric trough is associated with the outer boundary of the plasmasphere, commonly referred to as the plasmapause (Weygand et al., 2021). At this boundary, the plasmapause interacts with the inner ring current region, leading to heat transfer via Coulomb collisions to ionospheric altitudes, thereby increasing the electron temperature (Kozyra et al., 1997). Therefore, the behavior of trough was examined using DMSP measured latitudinal Ni variation in the 40-70°N MLAT range, as shown in Figure-4.9 for period of 9-18 LT (14-21 UT). The magnetic latitude of equatorward boundary of trough is indicated by the downward pointing arrow. The dashed vertical line marks the observation location's magnetic latitude (54°N). It was found that a clear reduced density region or the mid-latitude ionospheric trough moved to lower latitudes and further poleward with time and reached below 54° during 16-19 UT. This is the same duration when increased brightness in red line emissions were observed. Therefore, this measurement of enhancement in the O(^{1}D) emissions attributed to daytime subauroral Te peak, makes this the first reported measurements of SAR arcs in the daytime.

4.3.3 Impact of increased electron temperature on 630.0 nm production

As discussed earlier, the OI 630.0 nm emissions depend on both electron density and electron temperature variations. However, in the GLOW model estimates shown earlier in Figure-4.4, only digisonde measured Ne profiles were provided as input to the model to be consistent in the analysis as these data are mostly available in conjunction with dayglow observations, as compared to ISR which has scheduled operational days. Since Te profiles can be measured only by ISR, so the IRI predicted Te profiles were used. However, as mentioned above, ISR was operational on 7 December 2006 and so the Ne, Te profiles were available, the daytime intensity of 630. nm emissions were further estimated using GLOW model by first providing only ISR measured Ne and then both Ne, Te profiles as inputs. Thus, estimated emissions are

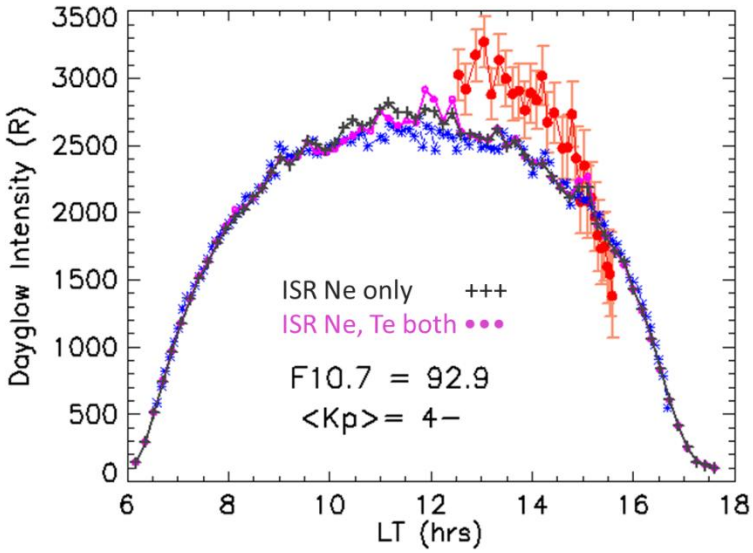

Figure 4. 10: *A comparison of digisonde Ne obtained output of GLOW model with the output obtained after providing first 'ISR Ne only' and then 'ISR Ne, Te both'. The HIRISE observed dayglow emissions are also overplotted (red dots).*

shown in Figure-4.10 superposed with those HIRISE measured and GLOW estimates presented earlier using digisonde Ne profiles in Figure-4.4c. It can be seen that model estimated emission obtained after using ISR and digisonde measured Ne both matched well with each other during the period of HIRISE observations. Consequently, no effect of electron density variation in observed brightness is noticed. The model estimates, once supplemented with additional measured Te profiles, showed that just before the HIRISE measurements began (around 12.5 LT), it predicted the highest emission values (indicated by magenta open circles). These peak emissions were calculated as a consequence of larger Te and suggest that higher electron temperature values were predominant over the Ne variations. However, the model's estimated emissions after this time period again underestimate the emission intensities. This could be due to the reason that ISR has a narrow field-of-view and HIRISE obtained 630.0 nm is a result of column integration of dayglow emissions over zenith. Further, the HIRISE location, Boston, is about 50 km away in the south-east direction of Millstone ISR. Due to dynamic nature of phenomena, especially for highly spatially structured and temporally varying ionospheric features that are usually present during geomagnetic disturbances, exact agreement in the magnitudes of the resulting dayglow with those derived by ISR are not expected. Also, using these two optical and radar datasets, the movement of auroral features towards north-east was inferred (Pallamraju et al., 2011). Therefore, although the HIRISE zenith might have larger Te

magnitudes than ISR measured Te values, the enhancement in Te in topside ionosphere measured by ISR still serves as a good indicator of additional heat deposition. As the enhancement in Te is greater at higher altitudes (Evans, 1973; Fok et al., 1991), an assessment of this variation was made by comparing the ISR Te over higher altitudes (Te_high_alt; averaged in 520–540 km altitude) and lower altitudes (Te_low_alt; averaged in 320–340 km) with the HIRISE measured 630.0 nm emission variability, as shown in Figure-4.11.

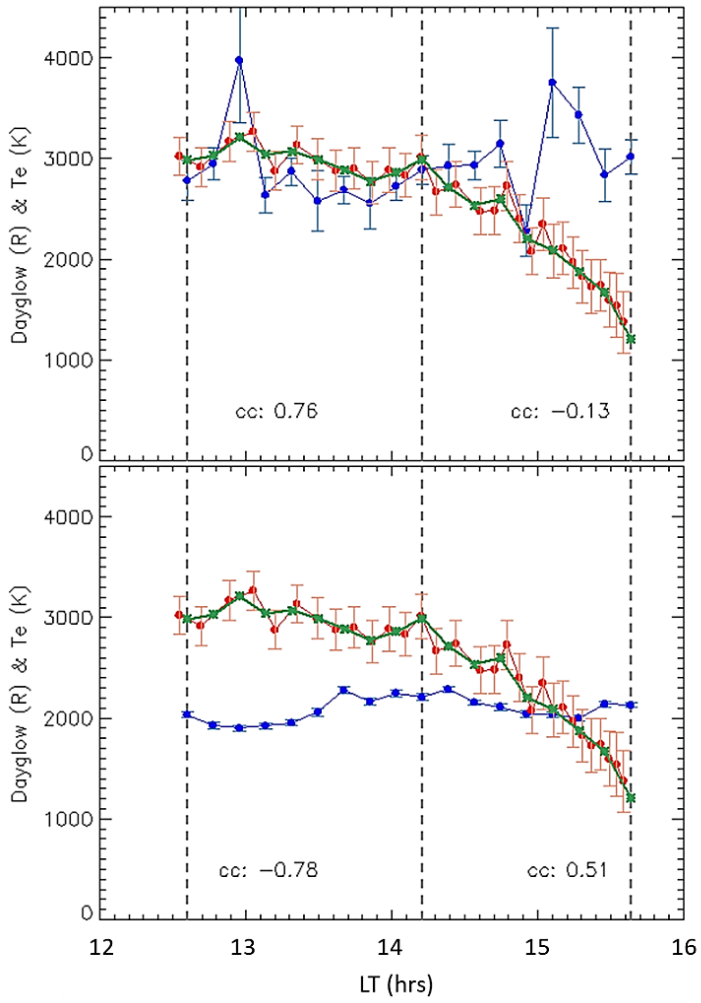

Figure 4. 11: *ISR measured averaged Te in the altitude range of 520–540 km (Te_high_alt) and 320–340 km altitude (Te_low_alt) is shown by blue dots in top and bottom panels, respectively, along with the 630.0 nm emissions on 7 December 2006. The green-asterisks represent the interpolated emissions with respect to the times of ISR measurement. In the top panel, a strong positive correlation of 0.76 can be seen between Te_high_alt and dayglow during 12.6 and 14.2 LT, while the emissions were strongly anti-correlated with bottomside Te during the same period (bottom panel).*

During 12.42–14.21 LT (17.42–19.21 UT), a strong positive correlation (cc = 0.76) was found between dayglow and Te_high_alt (top panel) and unusually a strong anti-correlation with Te_low_alt (cc = − 0.78) (bottom panel). This positive agreement between two independent measurements of Te_high_alt and observed 630.0 nm emissions indicates that SAR arc emissions due to precipitated heat flux were present for about 1 hr 47 min over the observation location. Again, as shown in Figure-4.8b, a region of enhanced Te below 54°N MLAT during the observational period from 17 to 19 UT was visible. Interestingly, this duration is similar when the observed enhancement in brightness showed a strong positive correlation with that of Te_high_alt during 17.42–19.21 UT. Thus, from yet another independent measurement, it can be concluded that the observed enhancement in brightness during 17.42–19.21 UT (12.42–14.21 LT) was indeed due to SAR arc emissions. After this time, as the region of enhanced Te (around 20 UT/15 LT) moved poleward and out of the HIRISE field of view, O(^{1}D) emissions returned to those estimated by the models (Figure-4.4c).

4.3.4 Estimation of electron temperature using forward modeling

As, the earlier discussion suggested, the thermal excitation of O(^{1}D) leading to enhanced 630.0 nm emissions is strongly positively correlated with topside Te variations. Electron density was found to have the least impact on increased brightness measured on 7 December. However, the GLOW model estimated emissions do not show this increase because it considered IRI Te as an input, as mentioned above. The IRI Te does not reflect the effects of heat transfer that results in larger Te values in SAR arc region. Also, the SAR arcs show non-uniform spatial structure with larger temperature at the center than at the edges (e.g., Foster et al., 1994; Rees & Roble, 1975). Further, due to mismatch of co-volume between the HIRISE view directions and ISR scans, as mentioned above, and about 50 km distance between the two observational locations, there could be differences in the values of Te corresponding to that measured by HIRISE than that of ISR. Therefore, this detection of SAR arc in the daytime brings a unique opportunity to delve deeper into assessing the magnitude of Te variation that would have contributed to this SAR arc formation. This assessment of electron temperature was obtained by performing the forward modeling using the GLOW model. To address this issue, the difference in brightness between the observed emissions from HIRISE (I_{obs}) and the estimated intensities from the GLOW model (I_{GLOW}) were analyzed. The forward modeling approach involved iteratively

adjusting the Te by a constant fraction at each altitude above 200 km within the GLOW model to minimize the differences between these two quantities, ultimately yielding a quantitative estimate of Te. This is shown in Figure-4.12, where left figure shows the earlier used Te values as predicted by IRI while the right side shows the Te obtained after performing the forward modeling. A clear enhancement in estimated Te values in the altitude range of 200-650 km can be seen, with much larger magnitudes in the topside of the ionosphere, as compared to those predicted earlier by IRI.

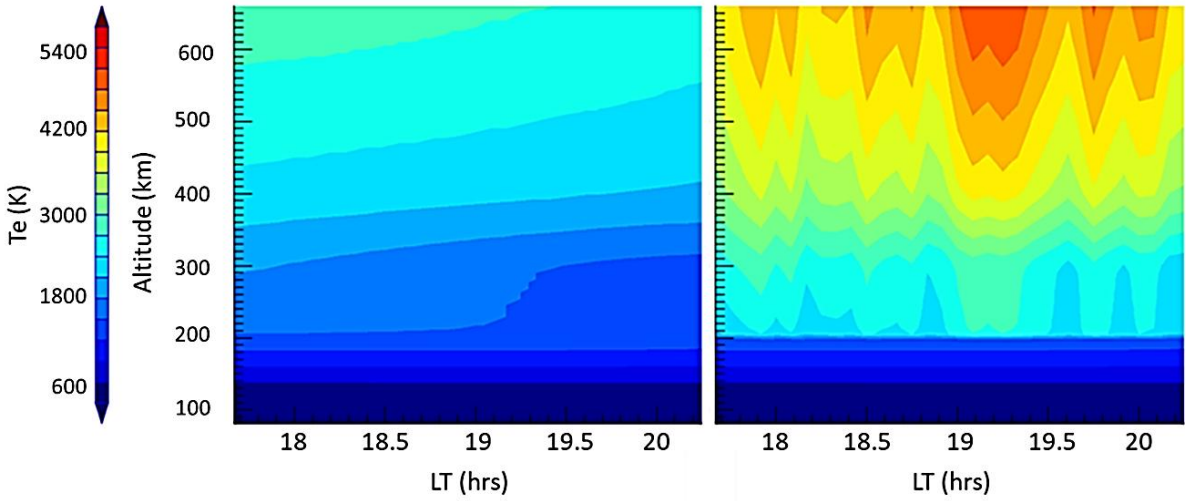

Figure 4. 12: *The left plot shows the IRI predicted usual Te profiles in 100-650 km altitude range on 7 December 2006, while the right plot shows the forward modeling (FM) obtained Te at each altitude above 200 km. Larger Te values obtained by FM can be seen clearly at higher altitudes, which were absent in those predicted by the IRI.*

The larger Te values at higher altitudes are again a signature of downward heat flux deposition in the topside ionosphere. Therefore, the corresponding increase in brightness of $O(^1D)$ emissions obtained through FM is shown in the top panel of Figure-4.13 by green asterisks for 7 December, along with the superposition of HIRISE (red dots) and GLOW (blue asterisks) emissions. The right-side y-axis corresponds to Te and the FM estimated values are shown by sky-blue dots. Through FM, it was found that the minimum Te required to match the model emissions with the observed 630.0 nm emission intensities was 3,503 K, while the maximum Te required was 4,391 K. These elevated Te values align with those previously reported for SAR arcs during nighttime. Interestingly, the percentage enhancements in Te during both night and daytime SAR arcs exhibit similarity. The bottom panel of Figure-4.13 compares the FM estimated Te with the ISR_Te_high and ISR_Te_low. Due to relatively low Te values measured by ISR than those estimated by FM using GLOW model caused an underestimation

of emission intensities. Therefore, forward modeling approach provides a more accurate description of Te variation and magnitudes compared to those at a given altitude (as depicted in top panel). Consequently, daytime O(^{1}D) emission measurements can be used to determine electron temperature in the ionospheric altitudes during SAR arc events, offering insights into magnetospheric-ionospheric coupling during geomagnetic disturbances.

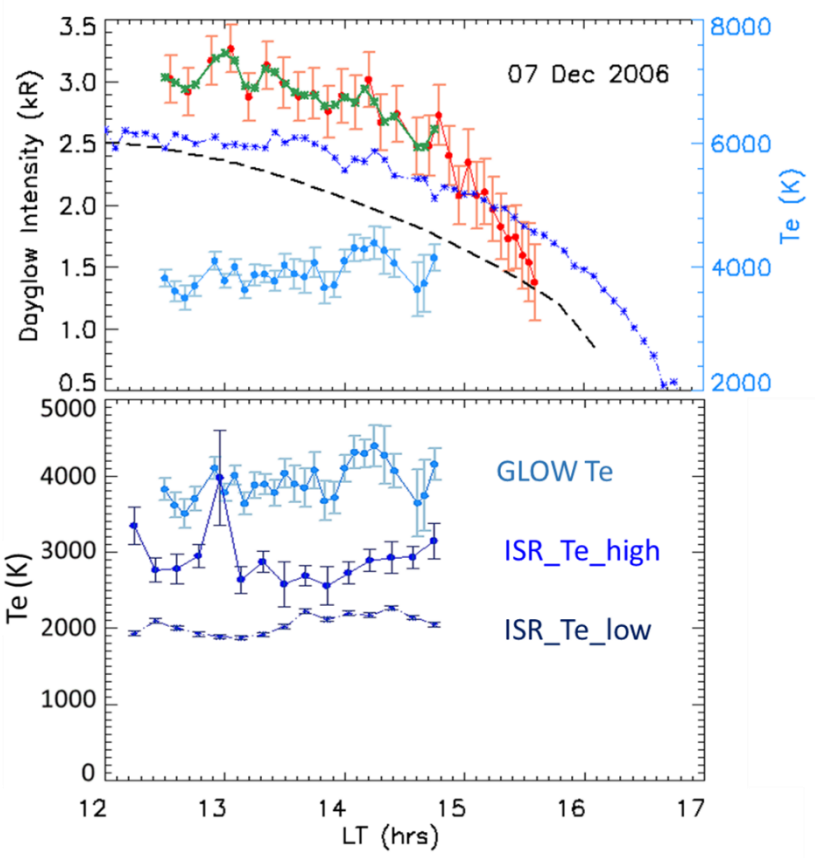

Figure 4. 13: *In top panel, HIRISE (red dots) and GLOW (blue asterisks) emissions are shown. The green-asterisks present the GLOW emissions obtained after performing the forward modeling (FM). The right-side y-axis shows the FM estimated Te (sky-blue dots) in GLOW model to match the model estimates with the observed emissions during the period of 12.5–14.75 LT. The bottom panel compares the FM estimated Te with ISR_Te_high and ISR_Te_low. It is clearly evident that electron temperature values were larger corresponding to that measured by HIRISE than that of ISR.*

The key point here was to examine the quantitative estimate of dominant variable, namely, the Te, which may define a threshold when thermal excitation of O(^{1}D) is effective and it was found that the electron temperature values typically greater than at least 3000 K during daytime can trigger the SAR arc emissions. Therefore, this illustrates that, in practice, when the electron

temperature exceeds 3000–3500 K, a thermal component emerges, and such occurrences should be frequent on other days. During the period when HIRISE data were available in the years 2003-2008, as mentioned in Chapter 2, there were other days when HIRISE measured emissions were beyond the model estimated emissions, as shown in Figure-4.14. It can be seen that such occurrences were observed during the winter months of different years and correspond to the low solar activity, as indicated by the solar flux F10.7 index, while the Kp-index ≥ 3 suggests them to be due to geomagnetically disturbed-time related SAR arcs during daytime. For each of the days shown in Figure-4.14, the red color represents the HIRISE measured emissions along with ±1σ uncertainties, sky-blue dots represent the GLOW estimates

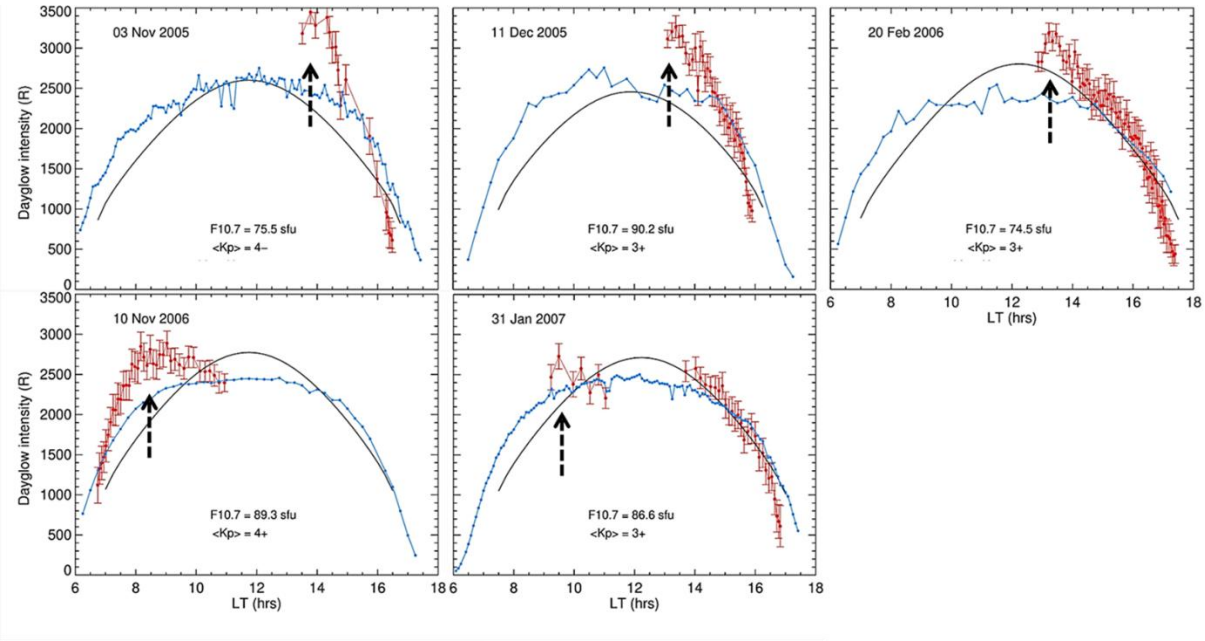

Figure 4. 14: *Other days showing larger brightness of HIRISE measured OI 630.0 nm emissions than the modeled brightness at different local times (indicated by dashed-black vertical arrow), similar to 7 December 2006.*

obtained using digisonde Ne profiles, and the black solid line represents the WEM output. The dashed-black vertical arrow in each panel indicates the time of occurrence of maximum brightness in red line emission intensities, which lasted from few minutes to a few hours and after some time, the measured emission intensity matched with those estimated by the model. The characteristics of these days in terms of time of measured peak brightness, emission intensity, and other geophysical activities are summarized in Table-5.1 All these days described above were further analyzed to identify the impact of electron temperature and additionally, the role of electron heat flux during daytime SAR arcs was determined to cause such Te enhancements associated with SAR arcs, which is discussed in the next chapter.

Date of O(^{1}D) emission enhancement due to daytime SAR arcs.	Local time of peak occurrence in brightness (hours)	Approximate brightness difference between HIRISE measured and GLOW model estimates (Rayleigh)	Daily averaged solar flux F10.7 (sfu)	Daily averaged three hourly Kp-value	Three hourly Kp-value at the time of peak occurrence in brightness
03 November, 2005	13.78	981	75.5	4$^-$	4
11 December, 2005	13.37	825	90.2	3+	4+
20 February, 2006	13.22	828	74.5	3+	3+
10 November, 2006	09.00	559	89.3	4+	4
31 January, 2007	09.50	433	86.6	3+	3

Table 4. 1: *The corresponding characteristics of daytime O(^{1}D) emission enhancement shown in Figure-4.14, similar to 7 December 2006.*

4.4 Summary

In this chapter, the first report of ground-based optical OI 630.0 nm emissions measurements of stable auroral red (SAR) arcs over mid-latitudes during daytime are presented. Previous theoretical understanding suggested that SAR arcs are predominantly linked to post-midnight to dawn sector processes, where ring current energy dissipation via Coulomb collisions is maximized. However, detecting SAR arcs during the daytime has provided new insights into upper atmospheric and magnetospheric dynamics, demonstrating that ring current energy dissipation is not limited to nighttime but also occurs under sunlit conditions. This finding suggests that storm-time plasmasphere heating exhibits distinct characteristics on the dayside. Concurrent measurements of ionospheric parameters from ISR confirmed that the daytime electron temperature (Te) was significantly enhanced on 7 December at higher altitudes,

coinciding with the observed enhancement in the red line emissions. DMSP measurements of Te, showing enhancement in the 50°–60°N MLAT region across the longitudes, supported these findings on SAR arcs. It was also shown that this is a global phenomenon. These independent datasets corroborate the HIRSIE observations suggesting that the 630.0 nm emission enhancement during daytime observed on 7 December 2006, was indeed due to the formation of a SAR arc. Furthermore, forward modeling indicated that the enhancement in Te occurred within the altitude range of 200–650 km, with temperatures ranging from 3,500 to 4,400 K. Consequently, the results presented here introduce new possibilities for quantifying the effects and/or consequences of magnetosphere-ionosphere coupling by using the daytime ground-based high temporal resolution investigations of the optical airglow emissions.

Chapter: 5

Estimation of electron heat flux at ionospheric altitude during SAR arcs

5.1 Introduction

The thermal properties of the upper atmosphere and the ionosphere are significantly influenced during geomagnetic disturbances. The in-situ observation of very large electron temperatures during daytime SAR arcs in the subauroral region, discussed in Chapter 4, indicates the presence of other energy sources causing additional non-local heating apart from usual local daytime heating by solar extreme ultraviolet (EUV) radiation. One such mechanism responsible for non-local heating is the electron heat flux or soft particle precipitation from near plasmapause, which involves the transfer of thermal energy carried by electrons from hotter regions in the inner magnetosphere to cooler ionospheric regions at mid-latitudes. This heat flux precipitation occurs along the closed geomagnetic field lines and impacts the balance of heat gain and loss in the ionosphere (Schun and Nagy, 1978). Several processes have been suggested for the formation of thermal electron fluxes associated with SAR arcs. For instance, Cole (1965) proposed collisional interactions between thermal electrons and ring current protons as a heating mechanism, and Cornwall et al. (1971) discussed the Landau damping of electromagnetic ion cyclotron (EMIC) waves on magnetospheric thermal electrons. Kozyra et al. (1987) introduced the importance of ring current O+ in generating electron heat fluxes. Furthermore, the effective heating of thermal electrons in the ring current region has been demonstrated through nonlinear coupling with lower hybrid waves (Mishin, 2013; Mishin & Burke, 2005). The various aforementioned energy sources related to SAR arcs are localized and are mostly observed during geomagnetic disturbances and thus give rise to localized enhancements in electron temperature as Te peak (Kozyra et al., 1987).

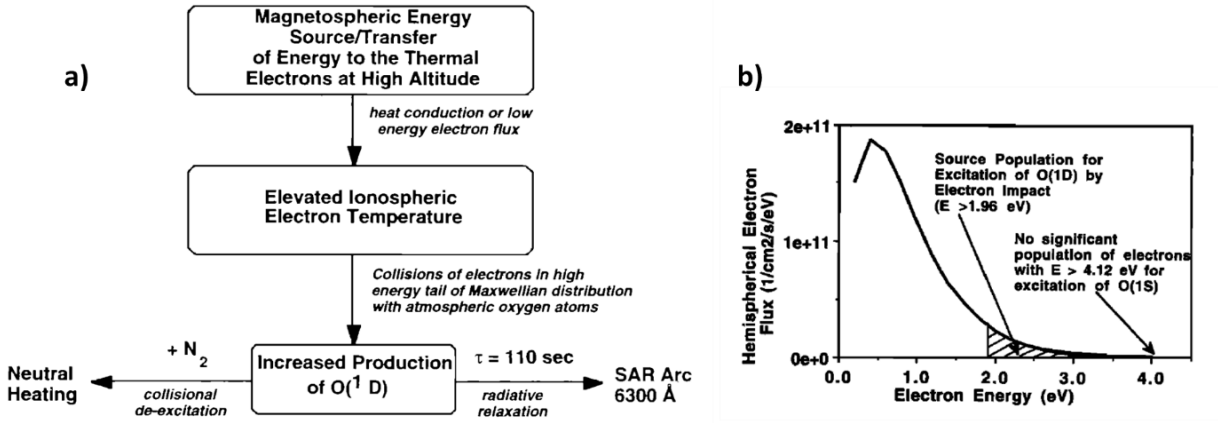

Figure 5. 1: a) *A flow chart representing the process of downward heat flux responsible for the formation of SAR arcs.* ***b)*** *A typical thermal electron Maxwellian distribution within a SAR arc region. The shaded region represents the population of thermal electrons responsible for SAR arc emissions. (Adapted from Kozyra et al., 1997).*

A flow chart depicting the summary process of heat flow to cause the formation of SAR arc is reproduced in Figure-5.1 (Kozyra et al., 1997). As it can be seen from the flow chart in panel (a), the excited O(^{1}D) state that is responsible for the 630.0 nm emissions with a relaxation time of ~110 seconds can also undergo quenching by colliding with Nitrogen molecules (N_2). But, since the neutral densities of N_2 at the heights of generation of SAR arcs are very small in amount (~3 orders of magnitude smaller than plasma densities), therefore, quenching is negligible. Thus, the de-excitation of O(^{1}D) significantly leads to the enhanced 630.0 nm brightness. Also, it can be noted that the precipitating low-energy electrons tend to follow the Maxwellian distribution. From the energy distribution of thermal electrons shown in Figure-5.1b, the population of heated electrons with a low energy range of about 1.96 eV creates the thermal component of SAR arcs. The lack of a sufficient population of electrons at a higher energy range of ~4.17 eV in the energy distribution, as required for the green line (557.7 nm) emission, results in the spectral purity of SAR arcs, as it only contains the redline emission. The energy distribution of precipitated electrons, which drive the electron heat flux along field lines, is isotropic and follows a Maxwellian energy distribution. The role of the isotropic Maxwellian distribution of precipitated electron density (n_M) that could have contributed to the total estimated heat flux at the ionospheric level has been calculated using Equation-5.1.

$$\Phi_M(E) = \frac{n_M \pi E}{(2\pi^3 m E_M^3)^{1/2}} \exp\left(-\frac{E}{E_M}\right) \tag{5.1}$$

In Equation-5.1, Φ_M is the downward electron number flux (e.g., unit of electrons cm^{-2} sec^{-1} keV^{-1}), E represents energy, m is electron mass, and E_M is the characteristic energy. This deposition of electron heat flux in the topside ionosphere influences the thermal properties of the ambient electron gas and serves as a crucial upper boundary condition in models that simulate electron temperature profiles.

5.1.1 Electron thermal balance equation and the electron heat flux in upper F-region

The equation of thermal balance depends on various heating (Q_e) and cooling (L_e) processes, which act as the source and loss of electron energy. The heating during daytime occurs primarily by solar extreme ultraviolet (EUV) radiation or by photoelectrons in the form of local heating, and additionally the non-local plasmaspheric heating as electron heat flux. The energy loss mechanism responsible for the cooling is a complex process, which includes factors such as excitation of the fine structure levels of the Oxygen atom (O), vibrational excitation of N_2, elastic collisions with ambient O^+ ions, and excitation of $O(^1D)$. The electron energy loss rate due to the excitation of $O(^1D)$ state acts as the source of SAR arc emissions (Rees and Roble, 1975). Thus, under steady-state conditions, the electron energy balance equation in the ionosphere, accounting for the sum of energy heating rates (ΣQ_e) and cooling loss rates (ΣL_e) from collisions with other species, can be specified using the electron continuity equation as:

$$\frac{3}{2}N_e k\left(\frac{\partial T_e}{\partial t}\right) = -N_e k T_e \nabla . u_e - \frac{3}{2}N_e k u_e . \nabla T_e - \nabla . q_e + \Sigma Q_e - \Sigma L_e \qquad (5.2)$$

In Equation-5.2, *Ne*, *Te*, and u_e represent the electron density, electron temperature, and the drift velocity of the electron, respectively, while k denotes Boltzmann's constant, and q_e is the electron heat flux. Apart from various source and loss terms of energy mentioned in Equation-5.2, the first, second, and third terms on right-side indicate the adiabatic expansion, advection, and the divergence of heat flow, respectively. The electron drift velocity (u_e) and electron heat flux (Q_e) terms are given as equations-5.3 and 5.4, respectively.

$$u_e = -\frac{J}{eN_e} \qquad (5.3)$$

$$q_e = -K^e \nabla T_e - \beta_e J \tag{5.4}$$

In equations-5.3 and 5.4, J and K^e represent the ionospheric current and electron thermal conductivity, respectively, while β_e indicates the thermoelectric transport coefficient. From Equation-5.3, it can be understood that the ionospheric current is carried by the electrons, and Equation-5.4 suggests that the heat flow is caused by the temperature gradients (ΔT_e) and currents. It is assumed that temperature gradients are in the vertical direction. Thus, in the case of $J=0$, i.e., if field-aligned currents are absent, Equation-5.2 can also be written as Equation-5.5 using these equations, where I is the inclination angle.

$$\frac{3}{2} N_e k \frac{\partial T_e}{\partial t} = \sin^2 I \frac{\partial}{\partial z}\left(K^e \frac{\partial T_e}{\partial z}\right) + \Sigma Q_e - \Sigma L_e \tag{5.5}$$

As the variation in Te at F-region heights occurs rapidly in response to the perturbed conditions, therefore, by considering this assumption for simplification, the left side of Equation-5.5 becomes trivial, and the Equation-5.5 can be written as:

$$\sin^2 I \frac{\partial}{\partial z}\left(K^e \frac{\partial T_e}{\partial z}\right) + \Sigma Q_e - \Sigma L_e = 0 \tag{5.6}$$

The Equation-5.6 is the form of the electron energy balance equation for ionospheric altitudes. Yet again, the divergence of heat flow is represented by the 1st term on the left side and expresses the vertical heat conduction. Therefore, heat conduction through the closed geomagnetic field lines becomes important in regulating the thermal balance in the ionosphere. It is clear that the electron energy balance is dependent on altitudes. At lower heights (below around 300 km), local heating and cooling rates have much influence, which leads to:

$$\Sigma Q_e = \Sigma L_e \tag{5.7}$$

while at higher heights, energy transport dominates. Mostly, at heights greater than 500 km, the heat conduction dominates due to their high mobility of electrons, and thus the Equation-5.6 becomes as:

$$\frac{\partial}{\partial z}\left(K^e \frac{\partial T_e}{\partial z}\right) = 0 \tag{5.8}$$

In this chapter, downward electron heat flux is one of the parameters of interest, which is caused by the currents and temperature gradients, as discussed above. Due to a lack of knowledge of ionospheric currents, this work avoids the current flow term for further simplification, while regarding the temperature gradients, the thermal conductivity of electron gas is examined. Therefore, the classical formula of the electron heat flux (Φ, in units of eV-cm^{-2}-s^{-1}) in the form of Fourier's Law, represented as Equation-5.9, has been used further for the estimation of electron heat flux during daytime SAR arcs, which remains pertinent at ionospheric altitudes.

$$\Phi = 7.7 \times 10^5 \times Te^{\frac{5}{2}} \times \frac{dTe}{dh} \times sin^2 I \tag{5.9}$$

Attempts have been made using the above Equation-5.9 in past studies for the estimation of electron heat flux [e.g., Evans, 1973; Titheridge, 1976; Brace and Theis, 1981]. This non-local heating due to downward heat flow drives high values of electron temperature in the subauroral topside ionosphere (Prölss, 2006). This relation between increased *Te* associated with ionospheric trough and O(^{1}D) emission enhancement causing SAR arc has been shown in various studies for nighttime studies (e.g., Baumgardner et al., 2013; Mendillo et al., 2016; Martinis et al., 2019) and recently, for the first time in the daytime conditions (Upadhyay and Pallamraju, 2024).

Direct measurement of the electron heat flux, which significantly impacts the electron energy balance in the ionosphere, is not feasible by current experimental space plasma techniques, unlike the measurement of electron temperatures. Instead, the electron heat flux is typically inferred through the analysis of variations in electron temperature. Most studies of ionospheric heat flow related to mid-latitude SAR arcs have remained theoretical, primarily focusing on nighttime conditions (e.g., Rees and Roble, 1975; Fok et al., 1991; Kozyra et al., 1987; Inaba et al., 2021). These studies presented the dependence of OI 630.0 nm emission intensities on precipitated heat flux. Also, in the study of the daytime cusp, the increased 630.0 nm dayglow emissions were directly found to be accompanied by enhanced Te due to particle precipitation (Pallamraju et al., 2004).

Therefore, this chapter presents results obtained on the OI 630.0 nm emission enhancements in simultaneity with the enhancements in Te and focuses on quantitatively analyzing the thermal electron fluxes associated with both day and nighttime SAR arcs that are strongly connected to plasmapause heights. To estimate the heat flux, different approaches have been used for

different conditions of day and nighttime depending on the other available ionospheric information, and is discussed in subsequent sections further.

5.2 Datasets used

In this chapter, the zenith measurements of daytime ground-based observations of atomic oxygen 630.0 nm airglow emissions are used primarily for the estimation of daytime electron heat flux during the low solar activity period (September 2005 to April 2007) of solar cycle 23. Due to the unavailability of simultaneous ISR data during these observation days, information on variation in local electron density was utilized from Millstone Hill digisonde. These Ne profiles were used as inputs to the GLOW model to estimate the OI 630.0 nm volume emission rates, which were further integrated to obtain column-integrated OI 630.0 nm emission intensities for comparison with the HIRISE measured emissions under different times and geomagnetic activity conditions. Moreover, to consider the variations in the topside ionosphere, the in-situ measurements of plasma parameters at around 840 km height were obtained from DMSP satellites. This chapter considers the latitudinal variations in Te and Ne to examine the role of Te enhancement as the primary feature since the two important ionospheric signatures associated with SAR arcs of Te peak and decreased electron density are not only observed during nighttime (Baumgardner et al., 2013; Foster et al., 1994) but also during daytime as reported recently (Upadhyay and Pallamraju, 2024). In addition to the variations in bottomside Ne from digisonde and topside Ne from DMSP, the column-integrated TEC acquired from Westford has also been utilized to obtain greater information on plasma density variations covering the entire F-region.

5.3 Results and discussions

5.3.1 Observations of enhanced 630.0 nm emission and electron temperature

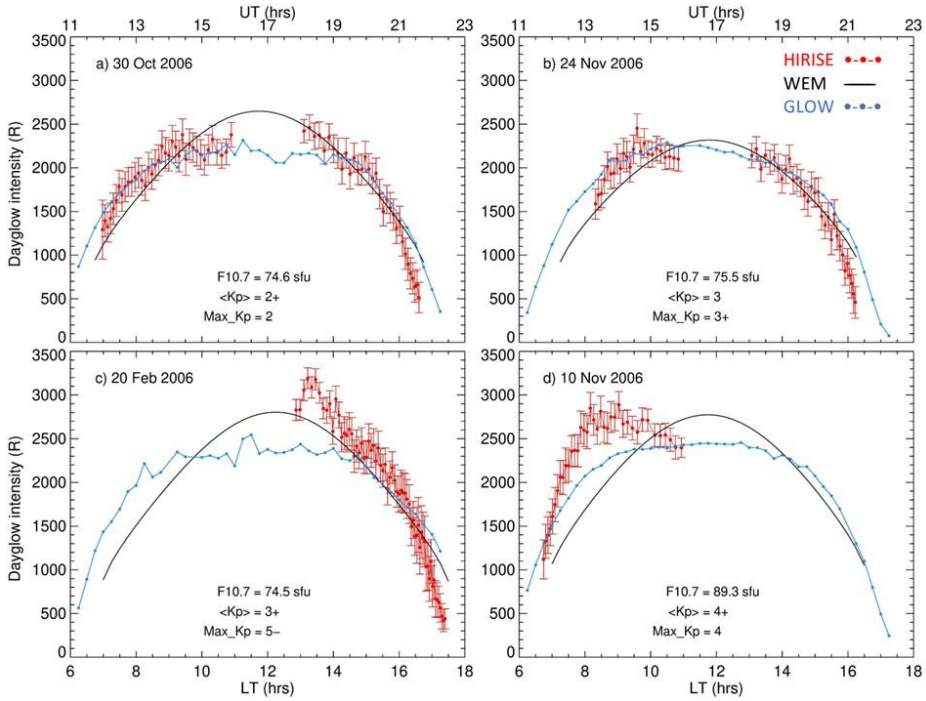

Figure 5. 2: *630.0 nm dayglow temporal variations are shown for four days. Bottom and top x-axes represent the local and universal time (LT=UT-5 hr). The red-color shows the HIRISE measured dayglow emissions over Boston, black line and blue color represents the WEM and GLOW estimates, respectively. The panel-a (30 October2006) shows a geomagnetically quiet day with daily average, <Kp>=2 and maximum Kp (Max_Kp) during daytime hours as 2+. Panels-(b,c,d) show three disturbed days with <Kp> and Max_Kp ≥ 3 and 3+, respectively. The F10.7 for each of the days is also shown. Larger measured emissions by HIRISE on 20 February and 10 November 2006 are due to SAR arcs in the daytime.*

The OI 630.0 nm dayglow emission variations are shown in Figure-5.2 with respect to local time (LT=UT-5 hrs). The solar flux for all these days was low and found to vary between 70-90 sfu. Out of the four days, Figure-5.2a represents the 630.0 nm emission behavior on a geomagnetically quiet day (30 October 2006) with daily averaged <Kp>=2+. As discussed earlier, the variations in the dayglow emissions respond dynamically with regard to the variations in ionospheric characteristics, the maximum Kp (Max_Kp) during the observation period was also examined for each day. On 30 October 2006, the Max_Kp was 2. The other three days shown in Figure-5.2 (b, c, d) represent the behavior of 630.0 nm emission on disturbed days (24 November, 20 February, and 10 November 2006), wherein <Kp> values were 3, 3+, 4+, and the Max_Kp during the observation period reached 3+, 5-, 4, respectively.

For all days shown in Figure-5.2, the diurnal variations of HIRISE measured 630.0 nm emissions are denoted by a dotted red line along with the ± 1σ uncertainties. Around local noon, the direct sunlight enters the instrument, causing CCD saturation and rendering the data collected during this period unusable. Also, data from the forenoon of 20 February 2006, and the afternoon of 10 November 2006, were excluded due to cloud cover. The WEM output of O(^{1}D) dayglow intensity is indicated by black-solid line in Figure-5.2, which matches well with HIRISE measured emissions on quiet day 30 October 2006 (Figure-5.2a). On the disturbed days (figure 5.2b-5.2d), HIRISE emissions show larger intensity than WEM estimates on various occasions. As previously discussed, the 630.0 nm emission intensity is sensitive to the variations in electron density and temperature, which can fluctuate over short time periods in the subauroral latitude ionosphere under disturbed conditions. Hence, firstly to identify the effect of electron density variations, the GLOW model was used to calculate emission intensities using electron density measurements from the collocated digisonde for all days. The GLOW estimated emissions are shown by blue dot line in Figure-5.2, along with the HIRISE measured and WEM calculated emissions. Again, on the quiet day 30 October 2006 (Figure-5.2a), the GLOW estimated emissions also match well with the diurnal variation of emissions measured by HIRISE. On the other hand, the GLOW estimates are larger than those of WEM On the disturbed day 24 November 2006 (Figure-5.2b), but are in good agreement with the HIRISE observed emissions. This indicates that the increased brightness of HIRISE emissions on this day and time correlates with larger electron densities during geomagnetically disturbed periods which were captured by the digisonde electron density measurements. However, on 20 February and 10 November 2006 (Figure-5.2c and 2d), HIRISE measured emissions were even beyond the GLOW predictions at several times, which clearly indicates that the potential cause for observed increased brightness was due to variations of some factors other than, or in addition to, variations in electron density. Another significant parameter that can influence the intensity of 630.0 nm emissions in the subauroral ionosphere is the electron temperature, as previously discussed. Such O(^{1}D) emission enhancements have been reported in the literature for both nighttime and daytime conditions (e.g., Baumgardner et al., 2013; Martinis et al., 2019; Mendillo et al., 2016; Upadhyay and Pallamraju, 2024). These enhanced emissions at F-region altitudes have been attributed to thermal emissions resulting from increased electron temperature (Te) and are considered as a plausible source for SAR arc formation (e.g., Nagy et al., 1970; Kozyra et al., 1997 and reference therein).

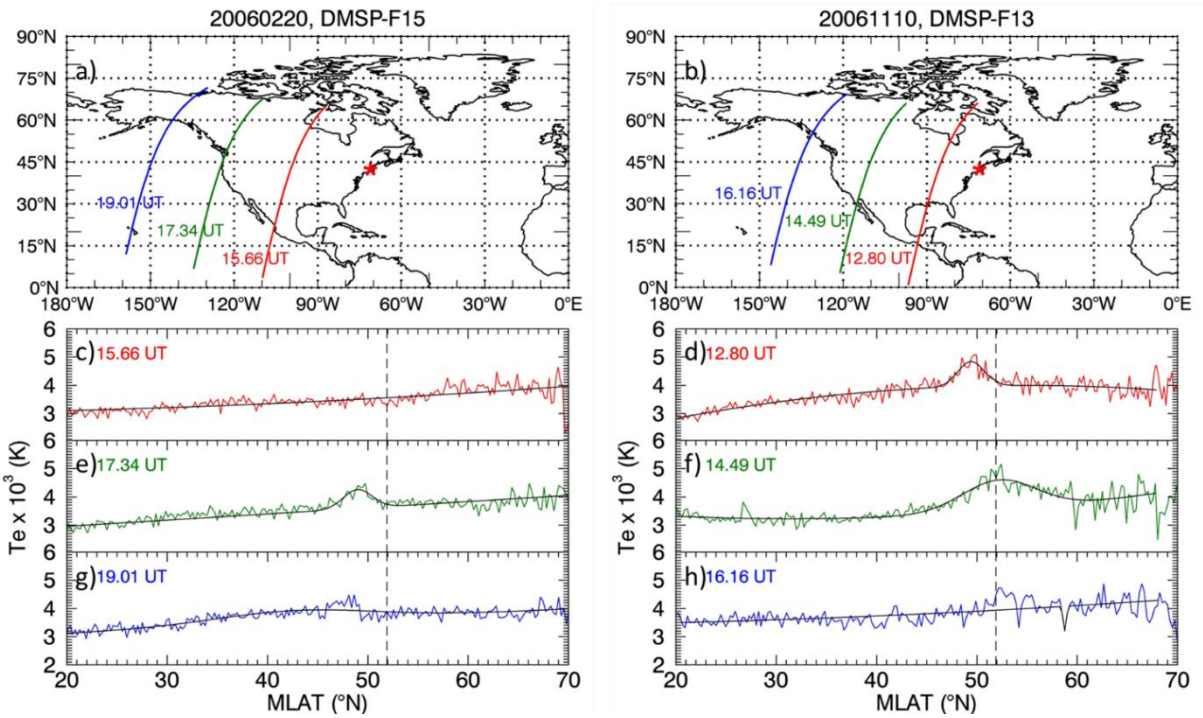

Figure 5. 3: *Panels a and b show ground-tracks of three different DMSP passes on 20 February 2006 and 10 November 2006, respectively, with dayglow observation location, Boston indicated by red star. The panels-c,e,g show the latitudinal Te variation for three passes on 20 February (shown in panel-a) in 20-70° N MLAT range. Similarly, panels-d,f,h represent Te variation on 10 November. The times of DMSP pass over ~52° N MLAT (marked by dashed vertical line) are indicated next to each Te profile. The black-solid line shows the polynomial fits for each Te variations. A sharp Te peak can be seen at 17.34 UT corresponding to observed enhancement in dayglow on 20 February near 13 LT (18 UT) and another Te peak on 10 November from 12.80-14.89 UT, in conjunction with the observed emission brightness duration around 7.2-10 LT (12.2-15 UT).*

To ascertain whether the enhancement in Te led to increased emissions on 20 February and 10 November 2006, in-situ Te data measured by DMSP during the periods of enhanced OI 630.0 nm emissions during daytime were analyzed. From Figure-5.2, it can be noted that the local time of enhancement in emission intensities on 20 February was in the time of 12.5-14.5 LT (17.5-19.5 UT) and on 10 November 2006 between 7.5-10.5 LT (12.5-15.5 UT). Although there were no DMSP passes directly over the observation location during these periods, three passes occurred on the dayside within these intervals of enhanced daytime red line emissions. Ground-tracks of DMSP-F15 on 20 February, with passes over 52° MLAT at 15.66 (red), 17.34 (green), and 19.01 UT (blue) are shown in Figure-5.3 (top left panel-3a). The red star symbol

indicates the location of Boston, where daytime OI 630.0 nm emission measurements were being conducted using HIRISE. The lower panels (Figure-5.3c, 3e, and 3g) depict the corresponding latitudinal Te variation within the magnetic latitude range from 20°N to 70°N at respective times indicated in Figure-5.3a. Similarly, the top right panel-3b shows the ground-track of DMSP-F13 passes on 10 November 2006 at 12.80, 14.49, 16.16 UT, while the lower panels (3d, 3f, 3h) present the Te variations. For each of these latitudinal Te variations, polynomial fits were carried out for clear identification of Te peak, as shown by black line. On 20 February 2006 (Figure-5.3 left panel), initially no Te enhancement was noted during the DMSP-pass at 15.66 UT, but interestingly a sharp Te peak arises at 50° MLAT during the pass at 17.34 UT. This Te peak then started to fade away during the next pass at 19.01 UT. The peak electron temperature at 17.34 UT was noticeably increased by around 1000 K than the previous pass at 15.66 UT, attaining the value of ~4300 K UT during this 1.68-hour interval. This time duration and MLAT of appearance of Te peak at 17.34 UT coincides with that of HIRISE measured dayglow emissions enhancements (17.5-19.5 UT/12.5-14.5 LT). After this period, the HIRISE emissions agree well with the model emissions (Figure-5.2c), which is also consistent the with vanishing of the Te peak in DMSP data in the subsequent pass (Figure-5.3g). On 10 November (Figure-5.3 right panel), a clear sharp Te peak is visible during the pass at 12.80 UT (50° MLAT, Figure-5.3d). This peak in Te moved around 2° poleward from 50° to 52° MLAT by the next pass at 14.49 UT (Figure-5.3f). The maximum brightness of daytime 630.0 nm emissions on 10 November 2006 was measured throughout the time of same period (8-9 LT/13-14 UT, Figure-5.2d). The maximum brightness in the emission intensity near 9 LT (14

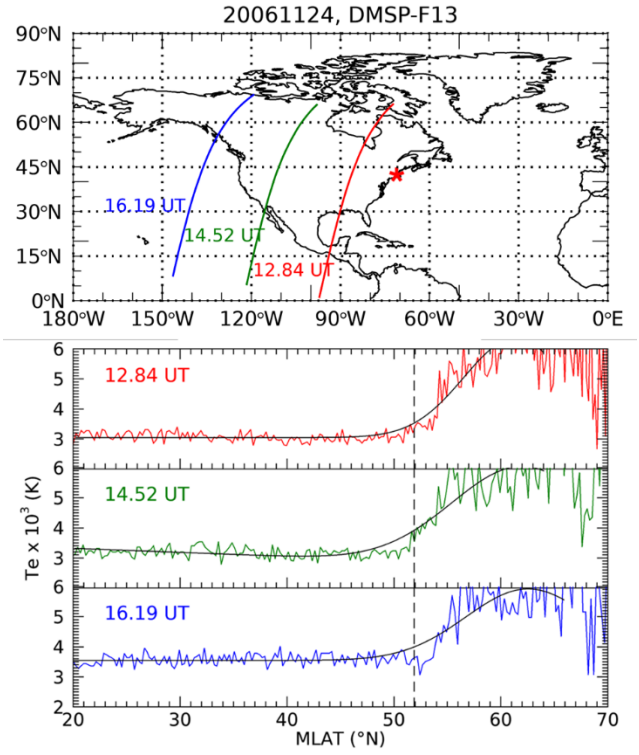

Figure 5. 4: *Similar to Figure-5.3 but for 630.0 nm daytime airglow emission observations on 24 November 2006.*

UT) corresponds to peak Te of around 5000 K at 52.43° MLAT. Therefore, the appearance of this Te peak and its poleward movement during 12.80–14.49 UT were found to be concurrent with the observed enhancement in daytime 630.0 nm emissions by HIRISE. After this duration, as the Te peak diminished at 16.16 UT (Figure-5.3h), the emission brightness started to reduce and followed the GLOW estimated emissions near 11 LT (16 UT). Interestingly, no such Te enhancements were observed on disturbed day 24 November 2006 for three consecutive DMSP passes during the observation period (right panels of Figure-5.4), which yet confirms the variation in emissions to be due to change in Ne on 24 November. However, the temporal enhancements observed on 20 February, and 10 November 2006 in the diurnal variation of the 630.0 nm emissions during daytime agrees well with the time development of the Te peak observed by DMSP, and thus attributed to electron temperature variations.

From the dayglow dataset that corresponds to the years 2005-2007, out of the clear sky days of data obtained, such enhancements in the measured emissions due to Te variations were noted on a few occasions (some of them are shown in Figure-5.5 left column). The observed 630.0 nm emission intensities were found to be greater than the model estimated emissions at those times. The HIRISE measured emissions for disturbed days 03 November, 11 December 2005, 07 December 2006, and 31 January 2007 are represented by red dots in figures 5.5a, 5.5d, 5.5g, and 5.5j respectively, together with WEM and GLOW calculated emissions, similar to Figure-5.2. The <Kp> was found to be 3+ or higher each day, while a daytime maximum Kp of 5⁻ during observation period, with the largest disturbance on 11 December 2005. Figure-5.5(a, d, g, j) reveals that HIRISE measured emissions exceeded the GLOW estimates for a duration of one to two hours. The peak brightness occurred at approximately 14.00, 13.50, 13.01, and 09.50 local times, respectively, on those four days. Similar to what was shown in Figure-5.3, the DMSP measured latitudinal variation in Te is considered corresponding to the time-period of observed brightness in 630.0 nm emissions and for the pass just before or after this duration on these days, as shown in the middle column of Figure-5.5 (panel-b, e, h, k). The column on the right in Figure-5.5 (panels c, f, i, l) displays the corresponding ground track of DMSP satellite for these passes. The red line in middle column represents the Te corresponding to the duration when enhanced brightness was observed in the daytime emissions shown in left column, while the black line represents the Te variation measured just before/after this pass. The black-dotted and red-dashed vertical arrows denote the magnetic latitude of the observation location and the peak Te locations (within the 40°-60°N MLAT range), respectively. The polynomial fit for latitudinal measurements of Te by DMSP is represented by bold red and black lines for the two

passes. it is noteworthy that for each time when peak brightness was observed (Figure-5.5 left column), a region of Te peak exists in the vicinity (within around ±2°) of the observation's magnetic latitude. Of all days, the maximum increase in electron temperature can be seen on

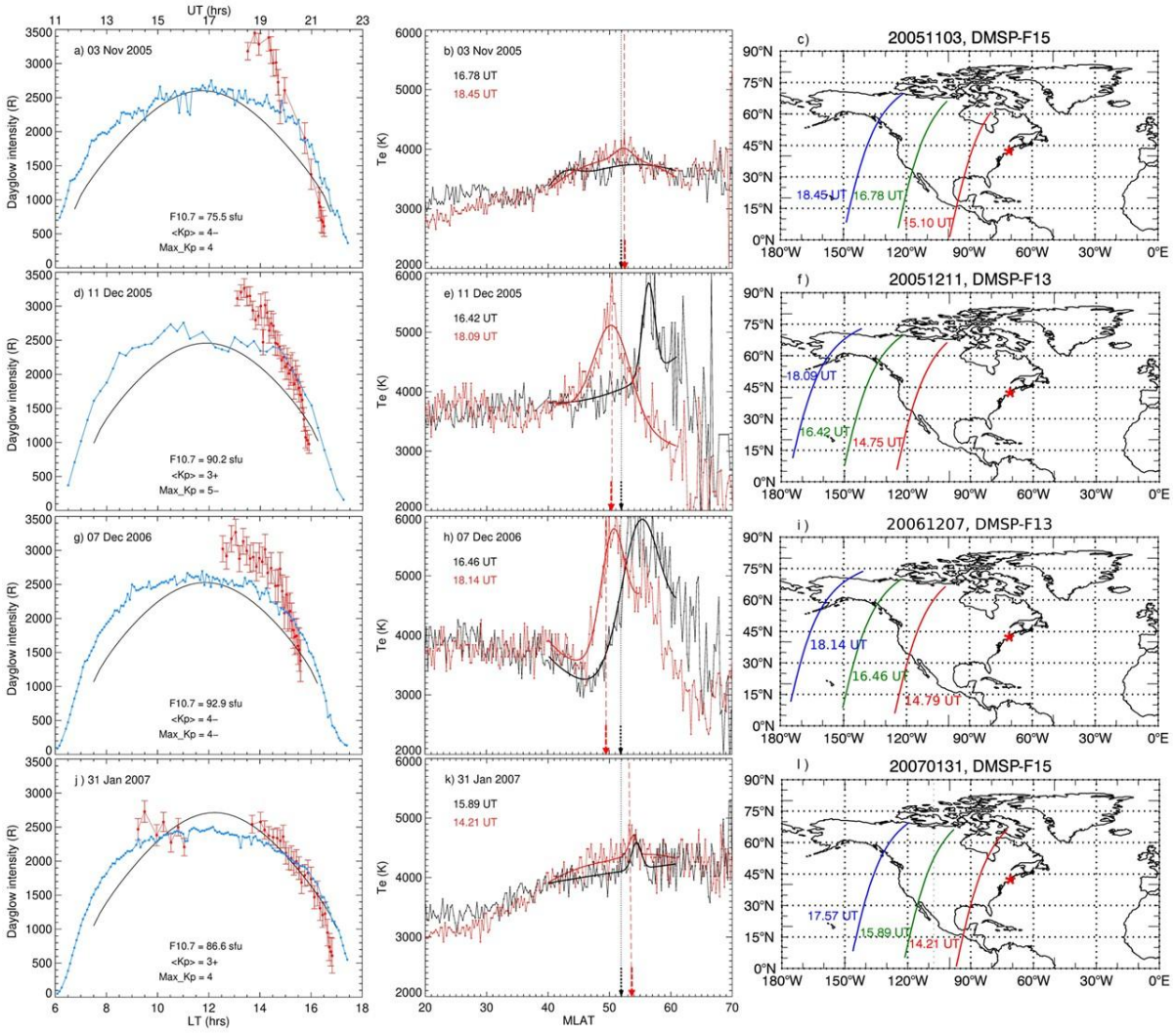

Figure 5. 5: *The left columns show four disturbed days of dayglow observation, similar to Figure-5.2c and 2d. The middle column shows respective DMSP measured latitudinal Te variation for two different passes- one during the time of observed enhancement in 630.0 nm emissions (red-color) and other just before/after this duration (black-color). The dotted-black and red-dashed arrow corresponds to the MLATs of observation of enhanced emission and maximum in Te in 40-60° MLAT range for the first pass. For each profile, a polynomial fit was performed in the 40-60° MLAT range to show Te peak clearly. The right column shows the corresponding DMSP ground-tracks. The poleward shift or disappearance of Te peak can be seen before/after the duration of observed enhancement in emissions by black-colored Te variation.*

07 December 2006 (Figure-5.5h) due to larger disturbances that occurred during daytime. Furthermore, the Te variations for the adjacent passes (indicated by the black lines) demonstrate that the Te enhancement is either absent or the Te peak is situated further poleward beyond the HIRISE field of view at that time. Accordingly, no increase in brightness was observed in the HIRISE measured emissions at these times. Thus, it can be seen that the DMSP measured Te increase correspond well with the observed enhancements in 630.0 nm red line emission intensities during geomagnetically disturbed periods, thereby representing the optical signature of SAR arc emissions in the daytime. The red line emission brightness and electron temperature characteristics attained for these days are summarized in Table-5.1

Date of O(^{1}D) emission enhancement due to SAR arcs.	Time of peak occurrence in brightness (UT; LT=UT-5 hours)	Approximate brightness difference between HIRISE measured and GLOW model estimates (Rayleigh)	Time of DMSP pass crossing over the MLAT of observation location (~52°N) (UT)	Peak Te measured by DMSP in 40-60°N MLAT range (Kelvin)	Latitudinal separation of Te Peak observed by DMSP from that of HIRISE operating from Boston (42.35°N, 71.10°W) (degree)
03 Nov, 2005	18.78	981	18.45	5240	0.5° N
11 Dec, 2005	18.37	825	18.09	5980	1.5° S
20 Feb, 2006	18.22	828	17.34	4480	2.15° S
10 Nov, 2006	14.00	559	14.49	5160	0.53° N
07 Dec, 2006	18.01	800	18.14	6290	2.4° N
31 Jan, 2007	14.50	433	14.21	4880	1.27° N

Table 5. 1: *The observed characteristics of daytime O(^{1}D) emission enhancement measured by HIRISE and DMSP measured peak Te variations.*

Since greater red line emissions during the day can result from both an increase in electron temperature and an increase in electron density, these measurements have been examined in greater details. While, digisondes are a useful tool for measuring electron density increase in the bottomside ionosphere, the incoherent scatter radars also capture topside density variations. This enables information in detecting and investigating phenomena, such as SEDs (e.g., Zou et al., 2013). Since the OI 630.0 nm dayglow emissions are column-integrated in nature and

thus can capture the SED (Upadhyay et al., 2023), as also discussed in Chapter 3. The important aspect about density variations during SEDs is that the enhancement in electron density occurs mainly in topside, and thus causes a rise in the TEC, as shown in Chapter 3. Since the presence of SEDs can be informed in the TEC as well (e.g., Foster et al., 2002), for each of the days shown in Table-5.1, the TEC variations obtained from a collocated GPS-station Westford have been analyzed, which are shown in Figure-5.6a. The times at which enhanced brightness in emissions were observed are indicated by the dashed vertical lines for each day. It can be noticed that there was a noticeable decline in TEC on 3 November 2005, 20 February 2006, 7 December 2006, and 31 January 2007 during the times of observed enhancement in the OI 630.0 nm emissions. On 10 November 2006, and 11 December 2005, there was neither a notable augmentation nor a decrease in TEC during those times that could result in the observed larger brightness from topside ionospheric densities. Consequently, this eliminates the possibility that the observed higher brightness is the result of variations in bottomside or topside electron concentrations and confirms that the greater Te effects are the cause of the

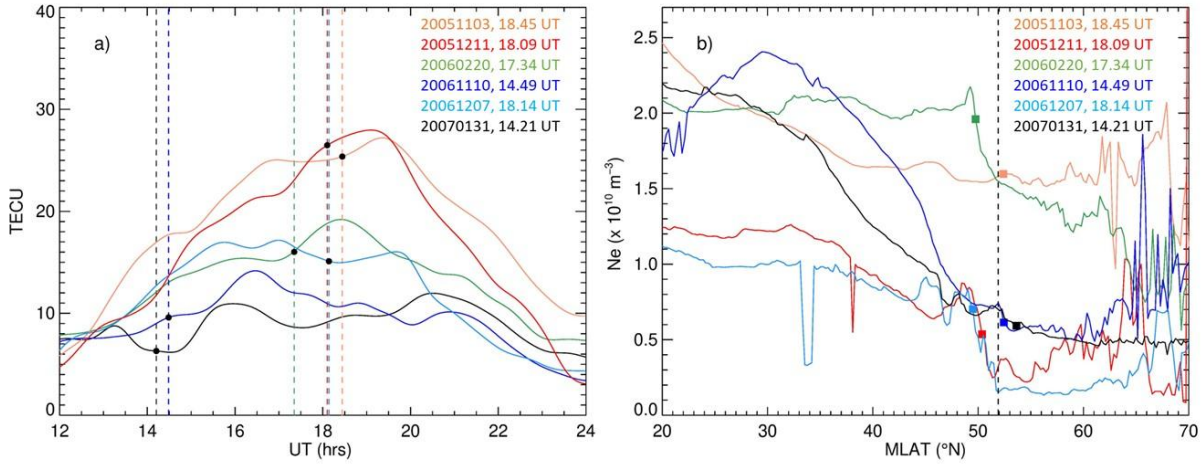

Figure 5. 6: ***a)*** *Diurnal variations in GPS-TEC for all days listed in Table-5.1. The vertical lines correspond to the time of observed increase in the 630.0 nm emission brightness on each day. A clear reduction with no remarkable increase in plasma density can be seen during the period of enhanced emissions on these days, which rules out the in the observed increase in brightness due to the topside density variation* ***b)*** *DMSP measured latitudinal Ne variations between 20-70°N MLAT range corresponding to the time of peak Te occurrence for each day. The dashed line corresponds to the MLAT of observational location, while squares represent the location of Te peak for each latitudinal Ne.*

observed increase in emission intensities. Te enhancements during SAR arcs are known to fall in the reduced density region of the mid-latitude ionospheric trough, as discussed earlier. Consequently, DMSP measured latitudinal Ne variations were taken into consideration in order to investigate the behavior of electron density corresponding to the time of peak Te occurrence (listed in Table-5.1) as illustrated in Figure-5.6b. The MLAT of the observational location is represented by the dashed vertical line in Figure-5.6b, and the Te peak position is indicated by square symbols for each latitudinal Ne. It is evident that the DMSP observed Te peak is located in the lower density area of the ionospheric trough on each given day. The Te peak on 11 December, 20 February, and 7 December were close to the equatorward edge of the trough and were linked to a sharp decline in plasma density. On 3 November 2005, however, there appears to have been a modest rise in plasma density in the vicinity of the Te peak position. The existence of a Te peak accompanied by a slight increase in Ne indicates that on 3 November, in addition to the extra downward heat deposition, plasma from the inner magnetosphere was also provided to ionospheric heights. This instance of elevated Ne during SAR arcs is comparable to that reported by Inaba et al. (2020), when an elevated Te peak was found in the SAR arc region along with an elevated electron density. Thus, these daytime variations in latitudinal Ne suggest that the region of Te peak and the ionospheric trough were collocated, thereby providing the conditions that were conducive for the formation of SAR arcs which resulted in increased brightness in red line emissions during daytime. Table-5.1 shows that the localized Te peak was within a ±2° range, centered at ~52°N MLAT, and that the peak enhancement in Te was substantially larger, ranging between 5000 ± 1000 K. Larger OI 630.0 nm emission intensities are observed when O atoms are excited to their O(^{1}D) state during such high Te values (Kozyra et al., 1997; Rees and Roble, 1975). Pallamraju et al. (2004) observed a direct correlation between greater Te (>4000 K) and increased OI 630.0 nm dayglow emissions in their studies of daytime cusps over high-latitudes. Moreover, as discussed in Chapter 4, the determined high Te values approximately 4400 K were needed to generate the SAR arc emissions during daytime.

It is important to note that higher electron temperatures were observed each day, as mentioned in Table-5.1, which caused an increase in the observed OI 630.0 nm emissions. However, the increased emissions, as measured by HIRISE during these periods, were not reflected in the GLOW estimations. This is again because GLOW utilized Te profiles that were generated using the IRI-model, which does not account for this change during geomagnetic storms. Furthermore, a study by Araujo-Pradere et al. (2003) showed that during geomagnetically

disturbed times, the IRI Te profiles may produce erroneous Te values. Thus, forward modeling (FM) has been carried out to provide a more accurate estimate of the changes in electron temperature on such occasions. In order to carry out FM, the IRI Te was raised iteratively by a constant fraction from the model value at each altitude in the 200–650 km range. The electron density profiles so obtained were used in the GLOW model to obtain volume emission rates, which were integrated to obtain the column integrated dayglow emissions. These were matched with the HIRISE measured emissions to an accuracy of 1% for all the days listed in Table-5.1, as discussed in section-4.4 earlier. The modeling was carried out for all those times where the HIRISE emissions exceeded the GLOW model estimations and at times when ionosonde observed Ne values were available. The results have been presented in Figure-5.7. In Figure-5.7, the blue asterisks represent the GLOW estimations that were derived using FM, and the right-side y-axis indicates the maximum Te value in the altitude range of 200–650 km. These enhanced Te values obtained by FM, ranging between 3000-4500 K, were needed to explain the observed brightness.

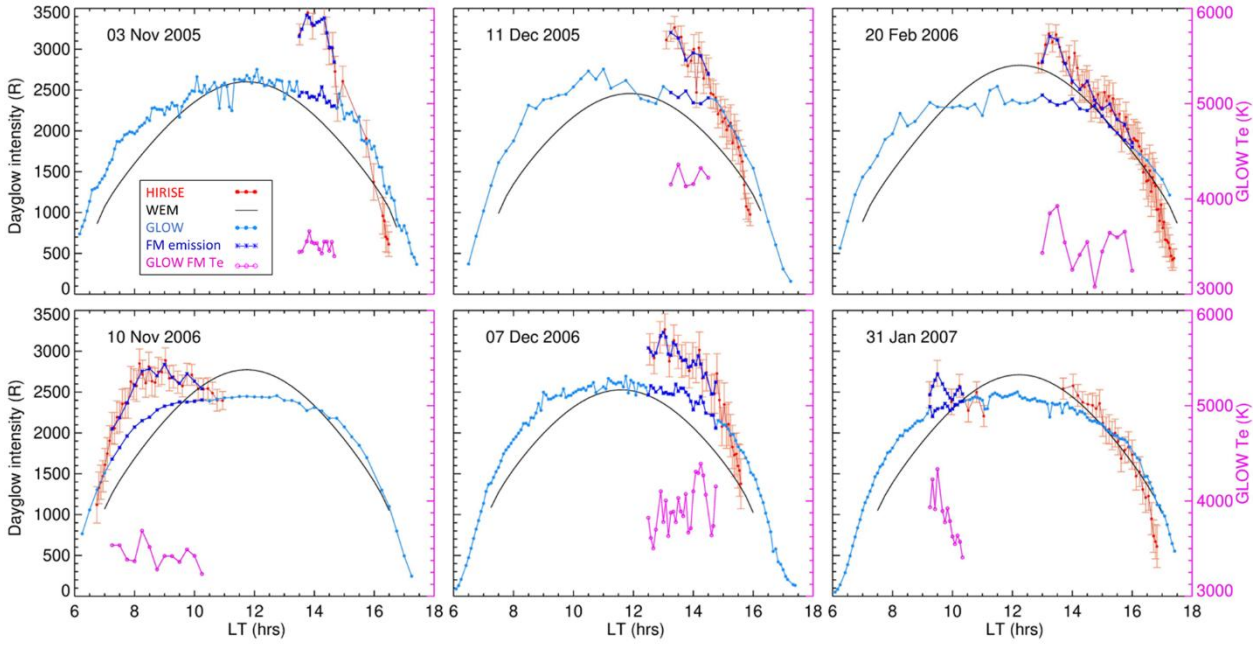

Figure 5. 7: *Emission rates obtained by forward modeling (FM) are shown by blue-asterisks for all days listed in Table-5.1. FM was performed during the period when HIRISE observed emissions were larger than the Model estimates. The FM estimated emissions match well with the HIRISE observed emissions. The right-side y-axis shows the FM estimated maximum Te (in 200-650 km) required to produce higher magnitudes of O(^{1}D) emissions that match with the observed emissions.*

An important conclusion drawn from the larger estimated values of Te by FM and the latitudinally narrow Te peak measured by DMSP is that, apart from local heating caused by solar extreme ultraviolet (EUV) radiation, additional heating due to downward heat deposition occurred in the daytime ionosphere during such disturbed times. The magnetospheric heat can be transferred to ionospheric thermal electrons along the field lines, causing a dramatic enhancement in Te at subauroral ionosphere. Among earlier suggested possible sources responsible for this heat generation, such as, Cornwall et al., 1971; Kozyra et al., 1987; Prölss, 2006, the instabilities generated in the ring current during geomagnetic disturbances work as the main source for this heating, which takes place near the equatorial plane in the inner-magnetosphere. To identify the role of low energy plasma populations, recently, Van Allen Probes (VAP) data were combined with ground-based observation of SAR arcs in the nighttime subauroral ionosphere. Utilizing the plasma measurements from Helium, Oxygen, Proton, and Electron (HOPE) instrument, the population of H+, O+, and He+ ions were found to be enhanced in the equatorial region connected to SAR arcs via closed field lines (Gallardo-Lacourt, et al., 2021). These enhanced ion fluxes are shown in Figure-5.8 along with the variations of low energy density calculated from upper hybrid wave measurements. The shaded

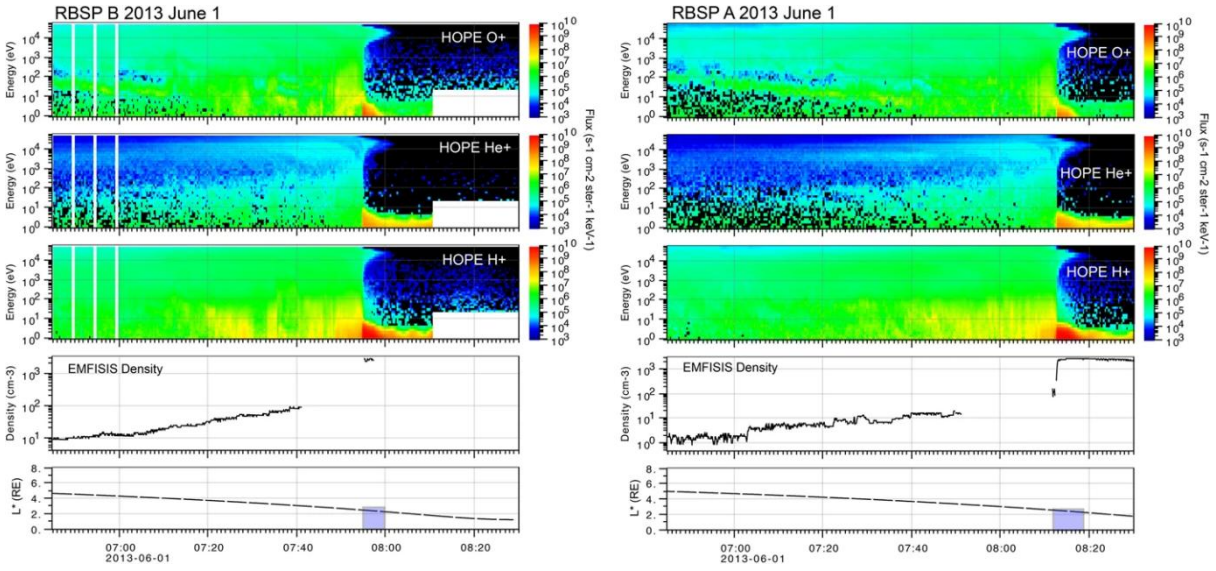

Figure 5. 8: *Van Allen Probe (VAP)- B (left) and VAP A (right) data from HOPE and EMFSIS instruments is shown. The location of the plasmapause associates with enhanced fluxes in the O, He and H ion species during ~08:00 - 08:20 UT. The field lines data obtained by both probes connect to region of SAR arc being measured by the Millstone Hill ASI (shaded blue region). After Gallardo-Lacourt, et al., 2021.*

regions in bottom most panels indicate the mapped position of SAR arc observed from ground, which can be seen to spatially overlap with the plasmapause location.

The heating in these regions occurs in simultaneity with the increased ion fluxes in the low-energy range. The process of energy transfer primarily has been suggested to be through Coulomb collisions between cold plasmaspheric electrons with hot ring current ions and wave-particle interactions from equatorial plane to subauroral ionosphere. Thus, the major source for the heat generation in this study that enhanced the Te was considered to be due to the Coulomb collisions between hot ring current ions and cold plasmaspheric electrons (Fok et al., 1995; Kozyra et al., 1997). There are studies that have reported Te enhancement in subauroral latitudes (e.g., Foster et al., 1994; Baumgardner et al., 2013; Martinis et al., 2019), but there are no reports of measurements of heat flux associated with enhanced Te during daytime SAR arcs, to date. The DMSP Te peak and stronger gradients at higher altitudes indicate that the downward flow of energy due to heat conduction causes considerable variation in Te (Schunk & Nagy, 1978). As a result, the required downward heat flow or electron heat flux causing the observed F-region Te enhancement was estimated into the mid-latitude ionosphere.

5.3.2 Determination of electron heat flux during daytime observation of SAR arc

To estimate the downward electron heat flux (Φ) associated with enhanced Te in the ionosphere, the earlier mentioned Equation-5.9 was used. The heat flux, Φ, was estimated at 300 and 500 km altitudes with corresponding Te magnitudes and a finite average of temperature gradients (dTe/dh) between 250-350 km and 450-550 km. These heights were considered since Te variations are not linear with altitude. The Te variations attributed to solar flux changes are more pronounced near 300-350 km, while the 500-550 km heights show a greater degree of variability through the heat conduction from the inner magnetosphere or plasmasphere (Upadhyay and Pallamraju, 2024). The heat conduction occurs primarily due to fast-moving electrons as compared to ions or neutrals which have low mobility due to their heavier mass. The non-local heating in topside ionosphere due to downward heat flux from plasmasphere regulates the ambient electron temperature, and larger Te gradients can be seen at higher heights above the altitude of SAR arcs. Also, the enhancements observed in $O(^1D)$ emission intensities were found to be attributed to the SAR arc emissions in daytime. Since, it is shown in the previous chapter that red line emission intensity during SAR arcs is strongly

correlated with topside Te variations (at around 500 km) with correlation coefficient of 0.7. Therefore, 300 km is considered as the lower altitudinal region until which the effects of heat flux can be seen and 500 km as the upper regions of heat flux incidence during SAR arc events.

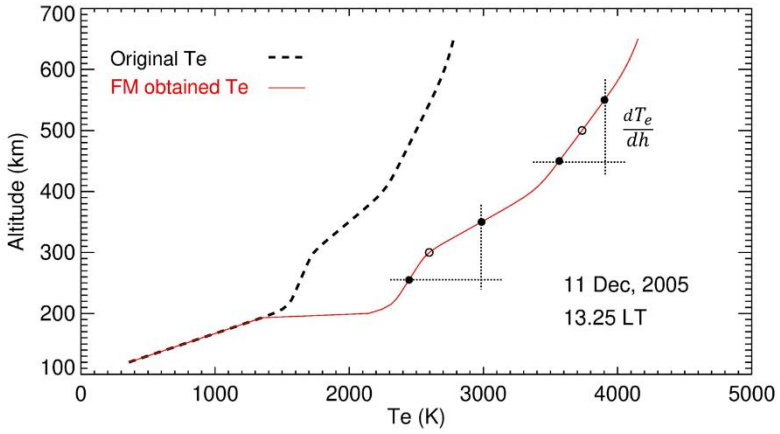

Figure 5. 9: *An example of forward modeling (FM) obtained Te profile to estimate the electron heat flux at 300 and 500 km altitudes.*

The method of temperature gradient can be visualized using an example on 11 December 2005 at 13.25 LT, as shown in Figure-5.9. The dashed black line in Figure-5.9 represents the original IRI calculated Te, while the solid red line indicates the FM computed Te profile (increased in 200-650 km) required to match the GLOW estimates with HIRISE observed emission intensities. The open circle denotes the altitudes of 300 and 500 km at which Φ is estimated, while the filled circles mark the altitudes used to obtain the temperature gradients at those respective altitudes.

The electron heat flux values thus obtained are shown in Figure-5.10 with corresponding electron gas temperatures. A non-linear variation can be seen in the heat flux values inferred from FM computed Te values. It is worth noticing that larger temperatures (Te>3000 K) are mostly present at higher altitudes (500 km), and Te≈3000 K acts as a threshold for rapid increase in the heat flux. A third-order polynomial fit is obtained for the Te resulting from the FM and to the corresponding electron heat flux, Φ, which is:

$$\Phi_{Fit} = 2\,Te^3 - 9 \times 10^3\,Te^2 + 10^7\,Te + 8 \times 10^9 \qquad eV\,cm^{-2}sec^{-1} \tag{5.10}$$

Figure-5.10 shows a fast-reducing heat flux towards lower altitudes corresponding to smaller temperatures, which yield an appreciably good fit. The analytical expression given in Equation-

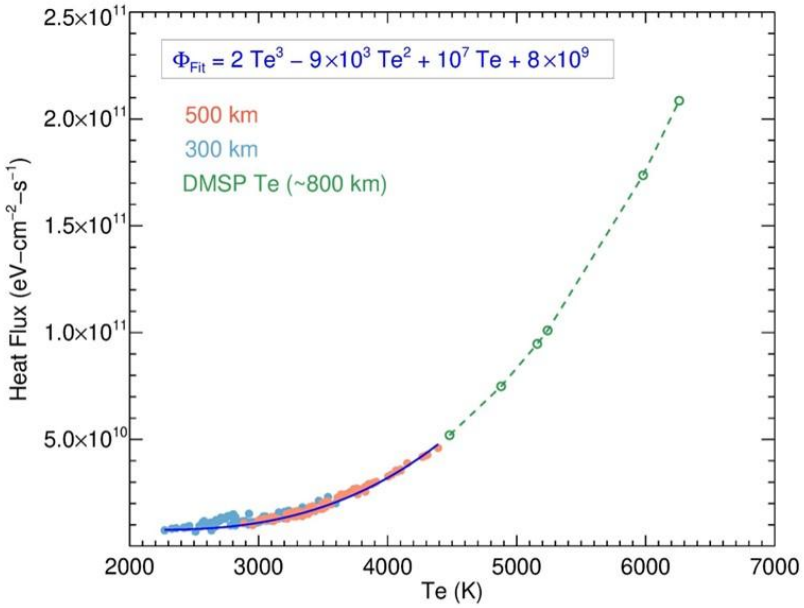

Figure 5. 10: *The estimated heat-flux at 300 (blue dots) and 500 km (red-dots) altitudes using the FM computed Te profiles. The solid-blue line represents the best polynomial fit (Φ_{Fit}) through the measured data points. The obtained relation has been used to calculate the heat flux associated with DMSP peak Te as shown by green dashed line. A non-linear behavior between the estimated heat flux and Te can be seen.*

5.10 above also gives an indication of the heat flux that would have been generated for the temperatures measured by DMSP at ~800 km, as depicted by the green-dashed line in Figure-5.10. The perfect fit also confirms that most of the heat deposition occurs at higher altitudes (>500 km), and it decreases as one moves to lower altitudes, as the heat energy is gradually lost due to conduction by Coulomb collisions. As all the inputs that have gone into the generation of this analytical expression (Eq. 10), it can potentially be used to assess the electron heat flux incident into the ionosphere over other regions of similar inclination angles as well for a given electron temperature.

5.3.2.1 Comparison of the results obtained in the present study with results obtained earlier

Due to difficulty in the measurements of electron heat flux directly, no report exists for comparison of this quantity during the daytime condition till date. However, indirect calculations have been performed to estimate this parameter, both in the daytime and nighttime.

In the work by Evans (1970), the heat flux values were obtained over Millstone Hill in daytime using ISR measured F-region electron temperature profiles which showed a large deposition of downward heat flux ~10^{10} eV-cm^{-2}-sec^{-1} during a disturbed day. A detailed model study (Rees and Roble, 1975) suggested a large variation in the heat flux ranging from ~10^{9} to 10^{11} eV-cm^{-2}-sec^{-1}. The large heat flux values reported in their study were attributed to the calculations performed at a height of 1000 km. A modeling study performed for the peak Te at subauroral latitudes during nighttime to investigate the seasonal variation found the heat flux to be varying between ~0.4 to ~8 x 10^{10} eV-cm^{-2}-sec^{-1} at 500 km during winters (Fok et al., 1991). Such earlier studies were based on theoretical simulations wherein various heat flux values were provided at the topside of the ionosphere to deduce Te and model the resulting SAR arc emissions. However, in this study, a bottom-up approach is presented wherein the actually measured daytime SAR arc emission intensities were used as the base and, through forward modeling, an estimate has been made on the quantity of electron heat flux that would yield the measured red line emission brightness. From Figure-5.6, the estimated electron heat flux can be noted to be varying in the range of 1.0 to 4.6 x 10^{10} eV-cm^{-2}-sec^{-1} at 500 km altitude, which is in the range reported by model studies earlier (Evans, 1970; Fok et al., 1991). The method of energy transfer was considered as Coulomb collisions. The relative effects of other pathways of generation of heat flux and their relative contribution to the O(^{1}D) would be a subject matter of different study, although earlier studies indicate a minor role of other mechanisms (Fok et al., 1991; Kozyra et al., 1993; Inaba et al., 2021). However, based on SAR arc modeling studies, the heat flux of about ~10^{9}-10^{10} eV-cm^{-2}-sec^{-1} is considered sufficient to produce elevated Te and SAR arcs (Kozyra et al., 1993; Rees and Roble, 1975) and the measured heat flux obtained for observed intensities in daytime in this study is close to these values. Even though no direct measurements of heat flux during daytime exist, the heat flux was estimated during nighttime SAR arc events using direct plasma measurements by the Radiation Belt Storm Probes recently rather than using theoretical simulations (Inaba et al., 2021). Their heat flux was found to vary as 2.5 x10^{9} and 5 x10^{9} eV-cm^{-2}-s^{-1} i.e., of the order of ~10^{9} eV-cm^{-2}-s^{-1} as sufficient to cause observed SAR arcs during nighttime. The results presented here on the estimated heat flux show the magnitude of the order of ~10^{10} eV-cm^{-2}-s^{-1} during daytime. Therefore, the magnitude appears to be higher during daytime by about an order of magnitude than that of the nighttime SAR arcs events. The results also confirm that the Te enhancements at subauroral latitudes can also occur during daytime as a consequence of plasmasphere-ionosphere coupling and simultaneously may affect the O(^{1}D) emission intensities. Thus, the results presented here in this study on the quantitative estimation of the electron heat flux are the first reports to the best

of our knowledge associated with the observed daytime SAR arcs as measured by the ground-based OI 630.0 nm red line emission.

5.3.3 Determination and variation of electron heat flux during nighttime SAR arc

As discussed in the previous section, the SAR arc red line emission intensity and corresponding electron temperature can be utilized as the two important ionospheric candidates for the estimation of electron heat flux during daytime. Consequently, an estimate has been made on the electron heat flux in the topside ionosphere using the same parameters for the nighttime

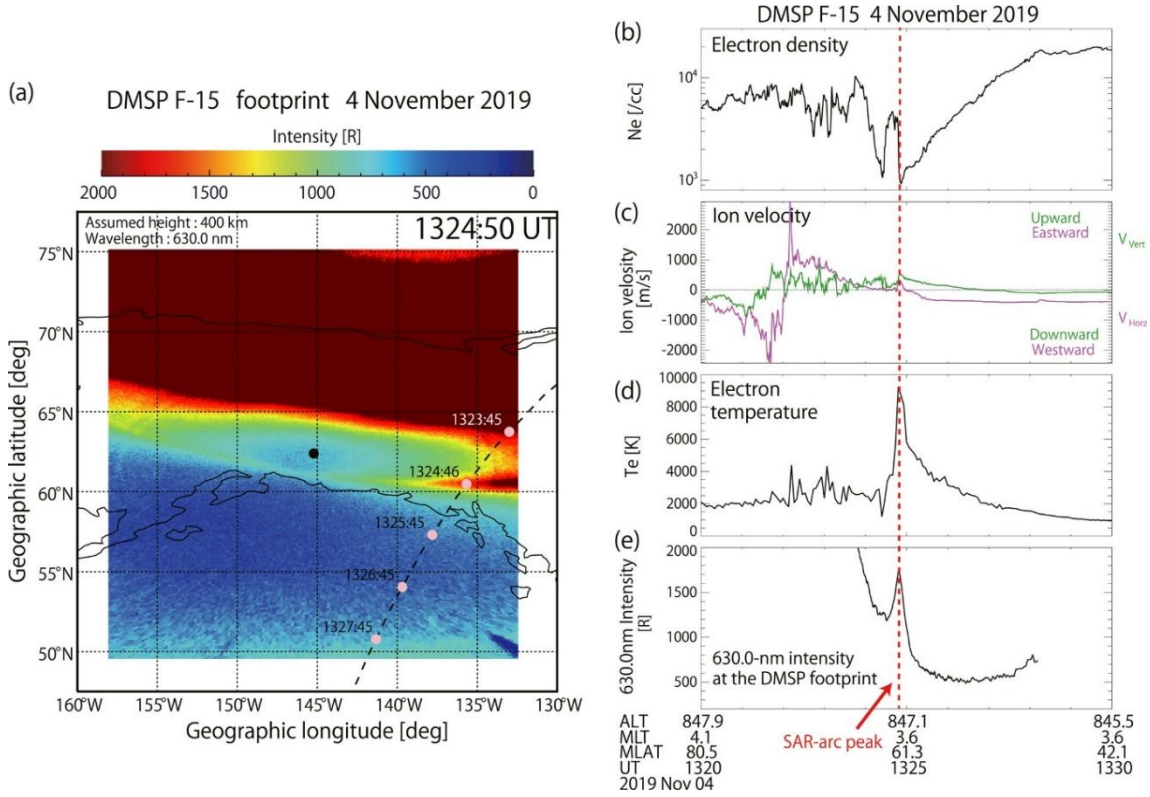

Figure 5. 11: *ASI captured nocturnal 630.0 nm image at Gakona on 4 November 2019 (a), along with DMSP-F15 measured electron density (b), ion velocity (c), and electron temperature (d) are shown. Panel-(e) represents the nighttime red line emission intensity observed at Athabasca close to the footprint of DMSP satellite. The Gakona station is marked by black dot at the center of the image. DMSP pass is shown by black dashed line crossing the SAR arc at 13:24:50 UT mapped to altitude of 400 km. The SAR arc emission intensity can be seen aligned directly with the Te peak indicated by red vertical dashed line. After Inaba et al., 2021.*

SAR arcs. For the study of nighttime electron heat flux, several conjunction events of SAR arcs observed by ground-based all-sky imagers during nighttime at subauroral latitudes have been taken into consideration along with the in-situ measurements of Te from the published literature during the years 2012-2020 of solar cycle (SC) 24.

One such example of SAR arc conjunction event is shown in Figure-5.11, where a SAR arc was observed during nighttime using all sky imager (ASI) at Gakona, Alaska (62.39°N, 214.78°E; MLAT: 63.6°N) on 4 November 2019 (Inaba et al., 2021). The panel-a in Figure-5.11 shows the geographical map of nighttime auroral/airglow emission intensity of red line emission by assuming the emission height at 400 km. The DMSP-F15 satellite crossing mapped to 400 km using IGRF model is also shown by dashed black line at respective times, while the ASI imager location is shown by black dot at the center of the image. The right panels b, c, and d show the variation in Ne, vertical/horizontal ion velocity, and Te, respectively. The panel-e represents the 630.0 nm emission intensity observed at Athabasca near the satellite footprint. The vertical dashed arrow in the right panels clearly marks the location of SAR arc emission in conjunction with enhanced Te peak. Therefore, Table-5.2 lists the specifics of all other occurrences, including the year of the event, the number of conjunction events acquired for every year, the satellites involved, the altitude of the in-situ plasma measurement, and the corresponding reference(s) used.

Event Year	SAR arc observation location	Number of SAR arc conjunction events observed	Satellite and the approximate altitude of in-situ plasma measurement	Reference
2013	Millstone Hill, Westford (42.6°N, 70.5°W); Rothera (67.5°S, 68.1°W)	2	DMSP at 840 km	Mendillo et al., 2016; Martinis et al., 2019
2015	Athabasca (Canada) (54.6°W, 246.36°E)	6	DMSP at 840 km	Gololobov et al., 2023
2017	Nyrölä, Finland (62.34°N, 25.51°E)	1	Swarm-A at 450 km	Inaba et al., 2020
2018	Athabasca (Canada) (54.6°W, 246.36°E)	7	DMSP at 840 km	Gololobov et al., 2023
2019	Gakona, Alaska (62.39°N, 214.78°E)	2	DMSP at 840 km	Inaba et al., 2021

Table 5. 2: *Event List of SAR arc conjunction events during years of Solar Cycle-24 Observed by previous studies.*

The different conjunction events of SAR arc used in this study were observed by ground-based all-sky imager located at subauroral latitudes as listed in Table-5.2 with the simultaneous electron temperature, electron density observation by satellite measurements. The details of these all-sky imagers and satellite measurements can be found in their referenced works, here we focus on the measured SAR arc emission intensity, electron temperature and electron densities during these events for further analysis.

5.3.3.1 Response of model estimated number flux to low-energy particle precipitation

As discussed, the best approach that can be used to estimate the electron heat flux involves the measured Te profiles accompanied with conductivity K^e of thermal electrons using Equation-5.9. During the listed nighttime SAR arc events in Table-5.2, as no vertical Te profile data were available, this temperature gradient method could not be used. In addition, another approach was performed using GLOW model.

The GLOW model consists of an auroral feature to estimate the emissions due to the heat flux precipitation, wherein the parameters of constant integrated electron monoenergetic flux ($\equiv \Phi$) and mean characteristic energy (E_M) are specified as input to the model. These input parameters result in the generation of an incident Maxwellian spectrum in the energy range of 0 eV to 50 keV and thus reflect its impact on modeled airglow emission rates. Therefore, an information of Φ corresponding to the thermal energy (E_M) can be obtained, in addition to the airglow emission intensities affected by this heat flux using the auroral feature of GLOW. The precipitation of electron heat flux on the topside ionosphere is assumed to be isotropic with the Maxwellian energy distribution.

Given that SAR arcs are formed due to low energy particle precipitation (< 10 eV) and necessitate an adequate population of hemispherical electron flux with energies exceeding ~2 eV required to excite the O(^{1}D) state, the model's sensitivity to determine the thermal population at these low energy levels was first examined. Therefore, the profile of downward electron flux at low energies accounted by the GLOW is shown in Figure-5.12. The Figure-5.12 represents the variation in hemispherical electron flux for two different solar activity conditions at nearly same characteristic energy of E_M = 0.41 eV. The red and blue squares represent the profiles during high solar activity (year 2015, T_e= 4720 K) and low solar activity

period (year 2018, T_e= 4733.70 K) of SC-24, respectively. Due to the larger energy bins of 0.5 eV used by GLOW model, the maximum enhancement in the electron flux profile was not recognized in agreement with E_M. Therefore, Equation-5.1 was further utilized to calculate the hemispherical flux at finer energy intervals of 0.1 eV, using a random value of precipitating electron density (n_M) as a scaling parameter. The dashed curve thus demonstrates the scaled hemispherical flux, analogous to the one used by the GLOW model, and exhibits a maximum value at the specified characteristic energy, E_M, marked by the vertical line.

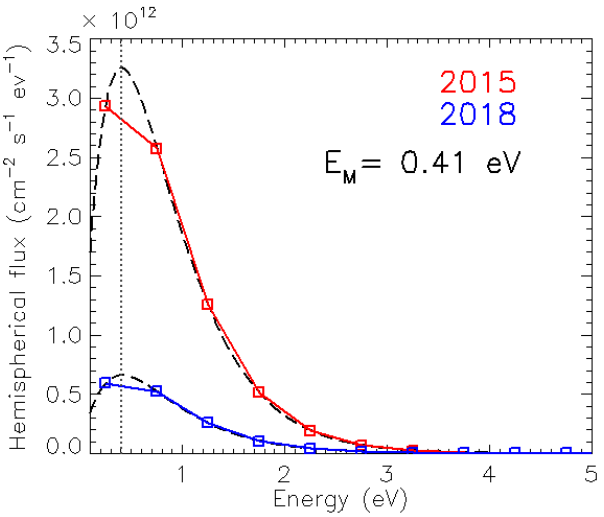

Figure 5. 12: *The hemispherical electron flux obtained from GLOW model (square symbols) and by using the Maxwellian distribution function (black dashed curves) at nearly the same characteristic energy (E_M = 0.41 eV), marked by dotted vertical line. Red and blue color indicates the variations corresponding to high and low solar activity periods i.e., 2015 (HSA) and 2018 (LSA), respectively.*

Based on the two distribution functions presented in Figure-5.12, it is evident that there exists a sufficient quantity of flux in the lower electron population above 1.96 eV energy. This electron flux is due to the downward heat conduction and is responsible for the thermally excited component of the O(^{1}D) state and, consequently, the generation of SAR arcs. Given enough population of thermal electrons available at around 2 eV during both periods of high and low solar activity, the GLOW model is deemed to effectively incorporate the influence of downward electron heat flux on SAR arcs emissions.

5.3.3.2 Electron density, temperature, and estimated heat flux

The in-situ variations of electron density (Ne) and electron temperature (Te) measured during SAR arc conjunction events shown in Figure-5.13a and 13b using black filled circles, respectively, whereas the corresponding solar flux (F10.7) for each event is shown by red color open circles, with the values indicated on right-side y-axis. The Figure-5.13a shows a positive

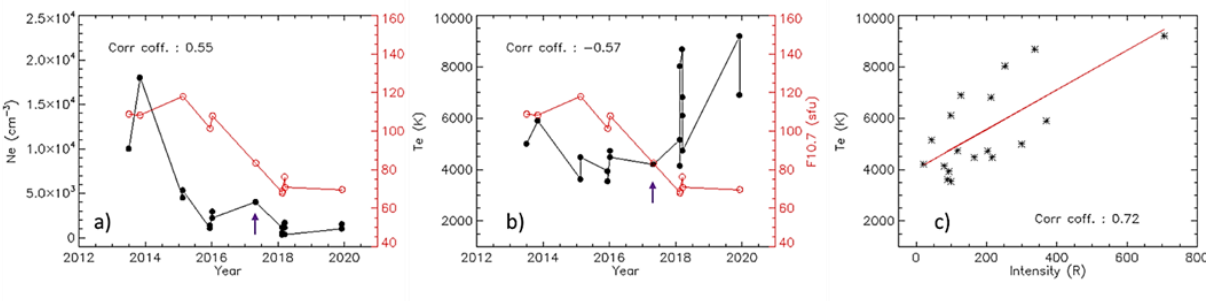

Figure 5. 13: ***a)*** *In-situ measured electron density (Ne), and* ***b)*** *electron temperature (Te) variations (black dots) in conjunction with each SAR arc observation between the year 2012 and 2020 for solar cycle-24 are shown with respect to solar activity index F10.7 (red open circles). A direct and inverse relation of electron density and electron temperature enhancements with solar flux can be seen. Panel* ***c)*** *shows the strong dependence of measured SAR arc intensity with respect to simultaneous electron temperature measurements with a correlation coefficient of 0.72.*

correlation (correlation coefficient, R=0.55) between Ne and F10.7, on the other hand, an anti-correlation exits with correlation coefficient of -0.57 between Te and F10.7 from Figure-5.13b. The observation that Te enhancements do not correlate with solar activity variations strongly indicates that the Te increase was driven by additional energy input, specifically electron heat flux precipitation, which resulted in the heating of ionospheric electrons rather than by solar EUV radiation. Moreover, the ground-based measured nighttime SAR intensity and in-situ measured Te were found to have a strong positive correlation with R=0.72, as displayed in Figure-5.13c, and no relation was found of SAR arc intensity with Ne variations (R= 0.2).

Therefore, such a high dependence of nighttime SAR arc intensities on increased electron temperatures can be understood to be due to the ionospheric electron heating caused by the downward heat flow. As discussed above, GLOW model uses the parameters of electron Maxwellian flux (Φ) and characteristic electron monoenergetic energy (E_M) to generate the Maxwellian electron spectrum and calculate its effect on airglow emissions. Consequently, the associated electron heat flux was estimated using the auroral feature of GLOW.

Therefore, in order to obtain the associated electron heat flux, firstly the typical brightness of OI 630.0 nm nightglow emissions without electron heat flux was calculated for each of the events as background emissions (I_0) using the GLOW model. Then, the observed SAR arc

intensity (I_{obs}) was taken from the previous literatures listed in Table-5.2. The value of I_{obs} was obtained by subtracting ambient 630.0 nm nightglow intensity observed in airglow images from the observed peak intensity at the SAR arc. Then, the modeled background emission intensity I_0 were added to I_{obs} for corresponding events to obtain a resultant emission value (I_{res}; $I_{res} = I_0 + I_{obs}$), which should be reproduced by the GLOW model with a given electron heat flux. The amount of Maxwellian electron heat flux for the observed characteristic energy ($E_M = k_B T_e$) was changed, until the 630.0 nm intensity estimated by the GLOW model matches with I_{res}. In this calculation, the measured electron temperature T_e was used for E_M. Thereby, the values of electron heat lux were obtained as required to produce the observed SAR arc emission intensities during nighttime.

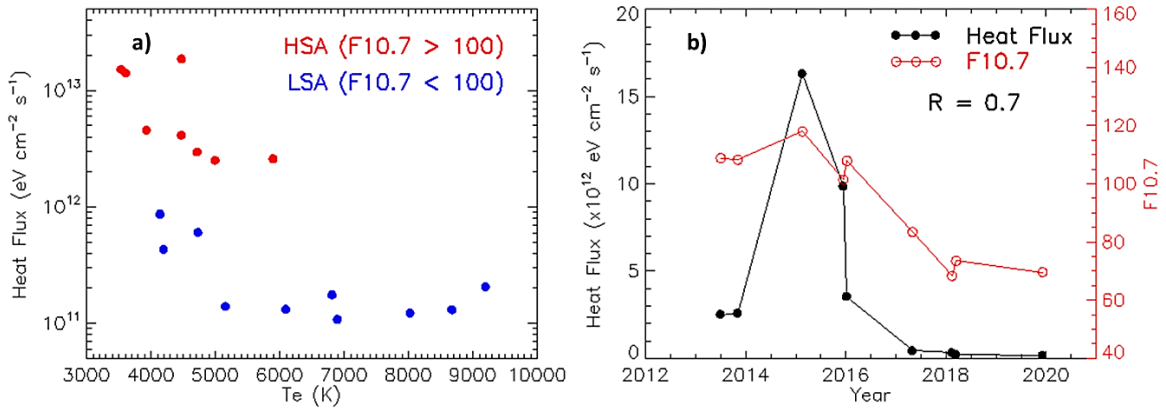

Figure 5. 14: ***a)*** *The estimated electron heat flux at 650 km altitude using measured SAR arc emissions and corresponding Te enhancement is shown. The red and blue dots indicate the variations in the obtained electron heat flux during HSA and LSA periods, respectively. Panel* ***b)*** *shows the estimated heat flux (black dots) variation with solar flux F10.7 (red open circles). The positive correlation of 0.7 between heat flux and F10.7 suggest the strong dependence of downward energy input with solar activity.*

The estimated electron heat flux for each of the individual events is thus shown in Figure-14a along with the associated in-situ measured electron temperatures, where the red and blue filled circles indicate the variation of nighttime heat flux obtained during high solar activity (HSA) and low solar activity (LSA) of SC-24, respectively. The heat flux can be seen to vary between 10^{11} to 10^{13} eV-cm^{-2}-sec^{-1} for these events. It is usually anticipated that a greater enhancement in electron temperature for a given SAR arc would necessitate a larger deposition of heat flux. However, no such correlation between heat flux variation and the corresponding electron

temperature is observed in Figure-5.14a. This lack of correlation may be due to the fact that the events analyzed in this study occurred under diverse seasonal, locational, and geophysical conditions. These varying conditions result in different ambient upper atmospheric characteristics, which the model could not adequately account for, as all remaining neutral and plasma parameters were taken from the MSIS and IRI models. Despite that from Figure-5.14a, during periods of LSA, the estimated electron heat flux during low solar activity was continuing to be nearly same of the order of ~10^{11}. The average value of heat flux during LSA is 2.89 x 10^{11} eV-cm^{-2}-sec^{-1}, while during periods of HSA, the average values of estimated electron heat flux is 8.05 x 10^{12} eV-cm^{-2}-sec^{-1} with a maximum of 1.85 x 10^{13} eV-cm^{-2}-sec^{-1}. In the study by Kozyra et al. (1997), the electron heat flux was found to vary between 5x10^{9} – 3x10^{11} eV cm^{-2} sec^{-1} at 500 km and one order larger during winter of solar maximum than the fall of solar minimum for a SAR arc of ~100 R intensity. Therefore, the magnitude of estimated heat flux during LSA still shows a good agreement with the values reported by Kozyra et al. (1997), although the variations during HSA are larger than their suggested range and around one order larger than LSA.

To more effectively evaluate the differences between high and low solar activity, the calculated heat flux was compared with F10.7, as depicted in Figure-5.14b where, the black filled circles indicate the calculated heat flux, while the red open circles denote the F10.7, plotted against the right-side y-axis. Instead of displaying each data point shown in Figure-5.14a, this representation aggregates the monthly averages for each year. The figure reveals a strong positive correlation between the estimated heat flux and solar activity variations, quantified by the R-value of 0.7. As of now, no studies have examined the solar activity variation in relation to the electron heat flux. Nonetheless, significant seasonal variations have been observed at high latitudes of Alaska, with an increase in heat flux during the summer months relative to winter (Fallen and Watkins, 2013). As a result, in the case of SAR arcs observed at subauroral latitudes, the calculated electron heat flux in this study suggests its solar activity dependence. Notably, a significant positive correlation between the in-situ measured electron densities and the estimated heat flow with solar activity (Figures-5.13b and 5.14a) suggests that the electron densities in the ionospheric region play a significant role in determining the downward electron heat flux. In addition, Equation-5.1 also denotes that the ionospheric electron density (n_M) serves as a crucial element in controlling the electron heat flux.

However, from Figure-5.15a, the scatter between estimated heat flux and in-situ measured Ne (shown by open squares) does not show any correlation between them. Therefore, the number

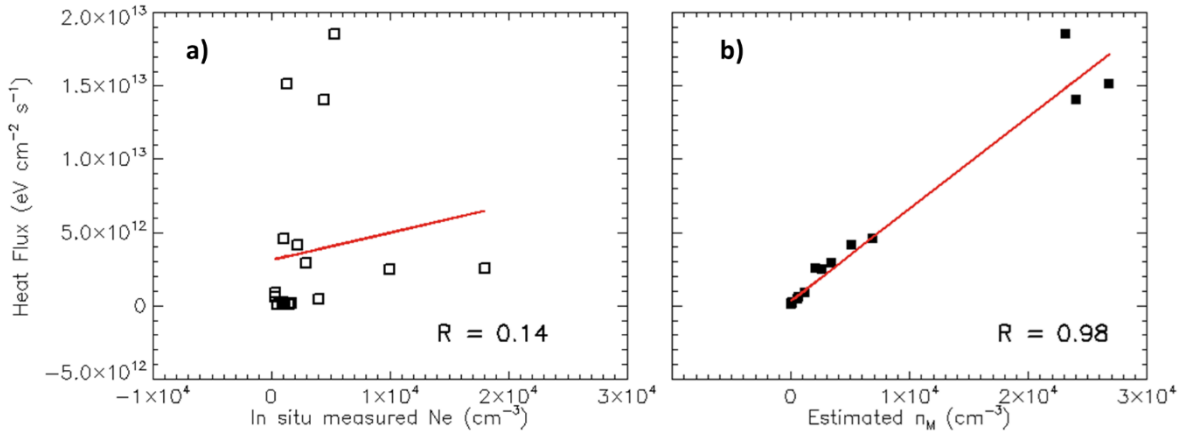

Figure 5. 15: ***a)*** *The estimated heat flux does not show any correlation with respect to in-situ measured electron density (Ne) at ~800 km altitude.* ***b)*** *The heat flux has a strong positive correlation with the estimates of precipitated electron densities Ne at 650 km altitude obtained by using Maxwellian energy distribution function. This indicates the major influence of ambient electron densities in governing the magnitude of downward heat flux.*

of precipitated electron densities in the topside ionosphere *(n_M)* were further estimated using Equation-5.1 to identify their dependence on the heat flux. For doing so, during each of the event, an electron energy flux *Φ(E)* equal to that estimated by GLOW model was obtained using Equation-5.1 by modifying the parameter n_M. Therefore, the estimated n_M is also shown with the associated heat fluxes in Figure-5.15b as filled squares. An almost linear dependence of estimated heat flux with the estimated densities can be seen with an improved correlation of 0.9 in comparison to earlier in-situ measured Ne from Figure-5.15a. In Equation-5.1, the amount of heat flux *Φ(E)* is proportional to value of n_M. Thus, this nearly linear relation between *Φ(E)* and n_M in Figure-5.15b suggests that the effect of E_M does not much contribute to control the amount of electron heat flux. This independence of electron heat flux to E_M can be also seen in Figure-5.14a. This clearly demonstrates that the impact of electron heat flux on ionospheric heating is largely governed by the amount of precipitated electron densities in the medium.

Additionally, not only the role of ionospheric electron densities but also that of the plasmaspheric densities have been found to affect the Te enhancement in the ionosphere during SAR arcs. Kozyra et al. (1997) found double-peaked Te enhancement in the ionosphere to be simultaneously associated with the double-peaked structure in the plasmaspheric ion densities during a SAR arc observation. The typical energies of ion and electrons in the plasmasphere

are less than 1 eV, while the densities are around 1-1000 cm^{-3}. So far, there are no specific measurements on the variation of cold electron density in the plasmasphere during SAR arc events, however the source region of SAR arc has been identified to lie in the overlap region of outer plasmasphere with the inner ring current region (Chu et al., 2019; Inaba et al., 2020; 2021). The outer plasmasphere region, also called the plasmapause, connects to the underlying ionosphere at subauroral latitudes through closed geomagnetic field lines, which generally vary between L=2.5 to 5.5 (Carpenter and Anderson, 1992). The events investigated in this work also correspond to L-values between L = 2.3 to 5. Therefore, by considering the dipolar approximation of the geomagnetic field, the calculated parameter n_M was used to investigate the electron densities in the equatorial region of the plasmapause at L=4. The distribution of densities in the high altitude plasmasphere or inner-magnetosphere (n_{mag}) along the closed magnetic field lines can be assumed to be proportional to the geomagnetic field (i.e., $n_{mag} \propto B$) by considering the conservation of electron flux through the magnetic flux tube. By following the geomagnetic strength near plasmapause at L=4 of around 500 nT and in the ionosphere at subauroral latitudes of about ~50,000 nT, a factor of 1/100 times the estimated ionospheric densities (n_M) will yield the contribution of thermal densities near plasmapause heights. Consequently, the calculated electron density in the closed field line region of inner-magnetosphere was found to vary in the range of around 0.6-12 cc^{-1} and ~21-268 cc^{-1} during low and high solar activities, respectively. The very low electron densities (less than 100 cc^{-1}) estimated here may indicate that the electron heating by the Coulomb collision does not occur at the equatorial plane of the magnetosphere but at the middle altitudes between the equatorial plane and the ionosphere. Actually, the electron density monotonically increases from high to low altitudes along a geomagnetic field line. The density distribution of ring-current high-energy ions along a geomagnetic field line depends on the pitch-angle distribution of the ions, but the density will decrease from high to low altitudes along the geomagnetic field line. The present result may suggest that the Coulomb collision between ring-current ions and plasmaspheric electrons occur at middle altitudes where the product of these two densities provide a local maximum.

5.3.3.3 Behavior of altitude profile of OI 630.0 nm during SAR arcs

Due to the predominantly monochromatic nature of SAR arcs' OI 630.0 nm emissions, analyzing the volume emission rate (VER) of these emissions can provide insights into the

variations of peak height resulting from additional heat deposition. To determine if the GLOW model's physical processes adequately explain the altitude dependent response of SAR arcs due to the input heat flux, the model derived 630.0 nm VER profiles were examined. Figure-5.16a illustrates the two modeled altitude profiles of 630.0 nm VER for the solar maximum year 2015 (indicated by red filled circles) and the solar minimum year 2018 (indicated by blue filled circles), both using a characteristic energy of 0.41 eV and an electron flux distribution shown in Figure-5.12. Additionally, VER profiles for typical 630.0 nm nightglow emissions, in the absence of any downward heat flux, are depicted with open circles for both years. The solar flux during 2015 was 1.5 times higher than 2018, and Table-5.3 summarizes the variations in other observed and estimated parameters for these cases. As shown in Figure-5.16a, the peak VER was similar for both years, but the peak emission altitude was higher at 350 km during the solar maximum and was lower at 281 km during the solar minimum. Additionally, during both solar maximum and minimum periods, the peak altitude of typical 630.0 nm nightglow emissions was approximately 260 km, which is close to the usual altitude of approximately 250

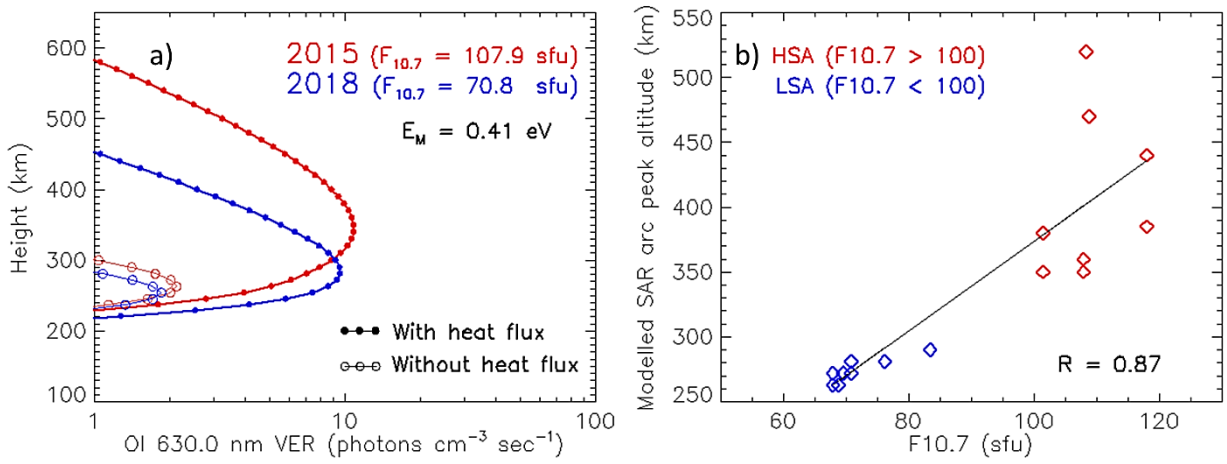

Figure 5. 16: ***a)*** *The modeled volume emission rates (VER; photons cm^{-3} sec^{-1}) for typical OI 630.0 nm nightglow (without heat flux) and SAR arc case (with heat flux) are shown by open and filled dots respectively. Red and blue color indicates the solar activity maximum and minimum durations, as represented by F10.7 index, respectively. Both profiles were derived at nearly same characteristic energy (E_M=0.41 eV). The variation in VER profile for SAR arc case can be seen due to additional heat input, as compared to the typical nightglow profile.* ***b)*** *The variation in peak altitude of modeled SAR arc emissions with respect to solar activity variation is shown. During low periods of solar activity, SAR arc emissions can originate at lower heights as compared with HSA.*

km. Consequently, for the same characteristic energy (0.41 eV), SAR arc emissions peaked below 300 km during periods of low solar activity and above 300 km during high solar activity.

Year	Estimated Heat Flux (eV cm^{-2} sec^{-1})	Solar Flux (sfu)	DMSP Te (K)	DMSP Ne (cm^{-3})	Estimated ionospheric Ne (cm^{-3})	Estimated magnetospheric Ne (cm^{-3})	Modeled Peak emission height (km)
2015	2.94×10^{12}	107.9	4720.00	2939.40	3387.00	33.870	350.0
2018	5.99×10^{11}	70.80	4733.70	358.560	687.050	6.8705	281.0

Table 5. 3: *Variation in the measured and estimated parameters for the two SAR arc events shown in Figure-5.16a.*

To evaluate the altitude distribution of SAR arc emissions for all individual events, the peak emission altitudes of modeled VER were compared with the solar flux variations, represented by the F10.7 index, as depicted in Figure-5.16b. In this figure, red symbols correspond to peak heights during periods of high solar activity (HSA), while blue symbols indicate peak heights during low solar activity (LSA). It is evident that during periods of high solar activity, the peak emission heights are observed in the higher altitude range of 350-450 km, whereas during low solar activity periods, the peak altitude shifts to the lower range of approximately 260-290 km. A strong positive correlation of 0.96, derived from a linear fit, reveals the significant influence of solar activity on the modeled peak emission heights of SAR arcs. Prior studies have reported the peak emission altitude of SAR arcs within the 350-450 km range (Roach and Roach, 1963; Rees and Roble, 1975; Kozyra et al., 1997). Furthermore, calculations of the 630.0 nm VER using complete electron density and temperature profiles from incoherent scatter radar identified the peak emission height to be around 400 km during nighttime SAR arcs (Foster et al., 1994). It is crucial to note that all these height measurements were conducted for nighttime SAR arcs observed near the solar maximum phase of their respective solar cycles. Here, the modeled peak emission heights for HSA are consistent with previous findings. Conversely, during periods of low solar activity, the SAR arc emission height decreases to lower altitudes (below 300 km). Recently, using triangulation of simultaneous measurements from two all-sky cameras and DMSP satellites, the lower edge of the SAR arc emission was found to be in the range of 240-290 km during LSA (2018-2020) and 350-370 km during HSA (2015) for the 24^{th}

solar cycle (Ievenko et al., 2023). The results obtained in the present study are in good agreement with those reported earlier on SAR arc height measurements.

As discussed earlier, SAR arcs are atomic oxygen 630.0 nm emissions which are formed by the collision between heated ambient electrons and the oxygen atoms. Therefore, the altitude profiles of SAR arc will primarily depend on two factors: a) the neutral composition of atomic oxygen, and b) changes in ionospheric electron densities. For the first case of oxygen density variation, during solar maximum, the large thermospheric temperatures will cause the atmospheric heating and increase the scale height of neutral species, which will lead to the upward expansion of atmosphere. On the other hand, lower thermospheric temperature during solar minimum results in contraction of the atmosphere towards lower heights. Hence, the lower heights during solar minimum will encounter larger mass density of atomic oxygen as compared to higher heights. The situation will be opposite during solar maximum. For the second case of electron density variations, during HSA, larger atmospheric density will create shallow depth for precipitated heat flux, resulting in faster cooling by Coulomb collisions with ambient ions at higher altitudes. While due to lower values of Ne above 250 km during LSA, thermal conduction may extend deeper into the ionosphere, resulting in heating at around 300 km to produce the SAR arc. For this reason, out of these ambient parameters, the contribution of atmosphere (and thereby oxygen atom density) to lower altitudes and a deeper penetration of heat flux resulting from reduced electron densities, leads to the formation of SAR arc at lower heights during low solar activity periods.

5.4 Summary

This Chater discusses the role of downward electron heat flux in the mid-latitude ionosphere by making use of information on measured enhancement in $O(^1D)$ emission intensity and corresponding Te enhancements during both day and nighttime and for different solar activity periods. For the electron heat flux during the daytime, along with the ground-based measurements of SAR arc red line emissions, complementary information form empirical, photochemical-models, digisonde, and DMSP measurements were utilized. The larger emission intensities are validated to be due to increased Te, as evidenced by a narrow latitude region of Te peak from DMSP observations at subauroral latitudes during the observed brightness in red line emissions.

As the model calculations underestimated the emission intensities during such periods, a forward modeling approach was carried out to estimate the Te required for a larger yield of observed O(^{1}D) emissions. Furthermore, by using altitude gradient from the estimated Te profiles, a quantitative assessment of electron heat flux precipitation was made during the daytime, as varying in the range of around 1.0 to 4.6 x 10^{10} eV-cm^{-2}-sec^{-1} at an altitude of 500 km. The daytime estimated electron heat flux was found to follow a non-linear increase with electron temperatures. It should be noted that based on the direct measurements of electron heat flux during both day and nighttime, the daytime electron heat flux was found to be larger by around one order of magnitude as compared to the nighttime values.

On the other hand, the downward electron heat flux during nighttime was obtained by utilizing the SAR arc conjunction events data with the in-situ measured ionospheric electron temperature measurements from earlier published literature. The ambient ionospheric information was taken from the model values. The nighttime estimated electron heat flux using model calculations was found to vary between 2.5 x 10^{12} and 1.8 x 10^{13} eV-cm^{-2}-sec^{-1} during periods of high solar activity, and vary from 1.1 to 8.6 x 10^{11} eV-cm^{-2}-sec^{-1} during low solar activity period. Results from this study on the nighttime estimated thermal heat flux agree well with the theoretically estimated heat flux (~10^{10}-10^{11} eV-cm^{-2}-sec^{-1}) presented in past studies during solar minimum. However, as compared to daytime estimated electron heat flux, wherein more realistic values of ionospheric variations were provided from measured Ne profiles, the nighttime heat flux is larger due to consideration of point measurements of Te and Ne and appears quantitatively larger due to the unrealistic model values of the ambient ionosphere during disturbed periods.

However, significant variation in the measured electron heat flux was found between periods of low and high solar activity. The average electron heat flux during the solar maximum is around one order of magnitude larger than that in the solar minimum, as also reported in earlier studies based on theoretical calculations. We have further calculated the precipitating electron densities in the ionosphere using an isotropic Maxwellian distribution and in the near plasmapause heights associated with the SAR arc region. The source electron densities in the inner-magnetosphere at L=4 were found to vary from 0.6-12 cc^{-1} and ~21-268 cc^{-1} during solar minimum and maximum, respectively. It is supposed that the electron heating by the Coulomb collision does not occur at the equatorial plane of the magnetosphere but rather at intermediate heights located between the equatorial plane and the ionosphere along the closed geomagnetic field lines.

In addition, the vertical profiles of OI 630.0 nm VER for modeled SAR arcs were also analyzed, and it was found that the peak emission height of SAR arcs is expected to have solar activity dependence in response to the atomic oxygen variability in the upper atmosphere. Although SAR arcs are widely considered to peak at around 400-450 km altitude, but during low solar activity periods, modeled VER suggests that SAR arc can originate at lower altitudes of around 260-290 km altitude also. The peak emission altitude shows a strong positive correlation with solar activity variation.

As the thermal heat flux is important to explain the formation of SAR arcs and other high and mid-latitude auroral emission intensities, the work presented in this chapter on the estimation of electron heat flux using two major candidates ($O(^1D)$ emission observations and modeled Te) provides a good opportunity to investigate this parameter from ground. The results presented here will also help in understanding the influence of different solar activity periods during nighttime SAR arcs and the complex nature of heat flow due to magnetosphere-ionosphere coupling, which is mostly unknown. Therefore, this work offers new insights for a better understanding of the day and nighttime plasmasphere-ionosphere coupling processes at mid-latitudes, especially during geomagnetically disturbed times.

Chapter: 6

Effect of geomagnetic activity on gravity wave dynamics over mid-latitudes

6.1 Introduction

In the previous chapters, we discussed the effects of magnetosphere-ionosphere and plasmasphere-ionosphere coupling over mid-latitudes during daytime using the measured OI 630.0 nm emission intensities. These effects were investigated during the main phase and recovery phase of the storms, wherein ionospheric features such as the presence of daytime SAID/SAPS electric field and dayside low-energy particle precipitation, among others, were found to act as the required energy source, causing more significant 630.0 nm emissions. However, on geomagnetically quiet days, no drastic change was observed in the variabilities of HIRISE measured 630.0 nm emissions, and the measured emissions matched well with those estimated by the models. A good agreement between the observed measured and calculated emissions resembles no significant perturbations in the ionospheric parameters. Therefore, apart from the ionospheric changes, we investigated the neutral dynamics in the thermosphere during such quiet times. The neutral dynamics are majorly associated with wind perturbations during quiet periods. The atmospheric winds affect both the neutrals and plasma in the upper atmosphere (Rishbeth, 1972), which in turn perturb the airglow emissions. Consequently, their effect can be seen in temporal/spatial variations of airglow emissions (e.g., Teitelbaum et al., 1981; Pallamraju et al., 2010).

There are different types of wave motions, also known as *atmospheric waves*, in the Earth's upper atmosphere. Prevailing winds, thermospheric winds, planetary waves, tidal oscillations, and internal gravity waves are examples of such wave motions. Depending on their prorogation directions, these atmospheric waves have been mainly classified as (i) longitudinal waves, (ii) vertical transverse waves, and (iii) horizontal transverse waves, as shown in Figure-6.1. The

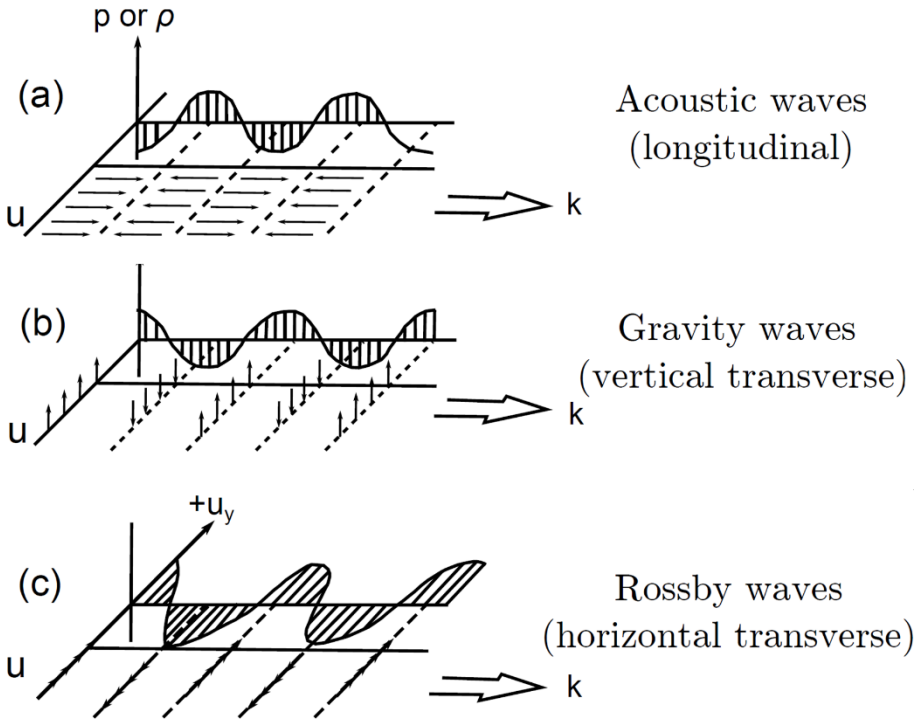

Figure 6. 1: *The three classes of atmospheric waves are shown. The waves can oscillate in three different directions. The variation of magnitudes is not to scale. (After Beer, 1974)*

amalgam of these waves further gives rise to other possible waves present in the atmosphere (Beer, 1974). Therefore, in this chapter, the primary intent is to investigate the variations in the measured OI 630.0 nm emission intensities on geomagnetically quiet days by using the large field-of-view (FOV) data from HIRISE, available on different occasions during the data availability period. These variations are analyzed in the domain of Gravity Waves, an important aspect of upper atmospheric motion affecting the ionosphere.

The *gravity waves* in the upper atmosphere are a specific class of different atmospheric wave motions, as discussed by Hines (1960). Gravity waves are generated by various sources, including topographical features like mountains, wind shear, convective processes in the lower atmosphere, and sudden geophysical events such as tsunamis and volcanic eruptions (e.g., Davis & Peltier, 1979; Smith & Lyjak, 1985; Sato, 1993; Alexander, 1996; Dewan et al., 1998; Farmer & Armi, 1999; Makela et al., 2011; Pallamraju et al., 2014; Singh & Pallamraju, 2016). A schematic of gravity wave propagation due to the effect of mountains is shown in Figure-6.2 (Andrews, 2010). Gravity waves can also be generated by various auroral and equatorial processes over high and low-latitudes, respectively (Pallamraju et al., 2001, 2004, 2010).

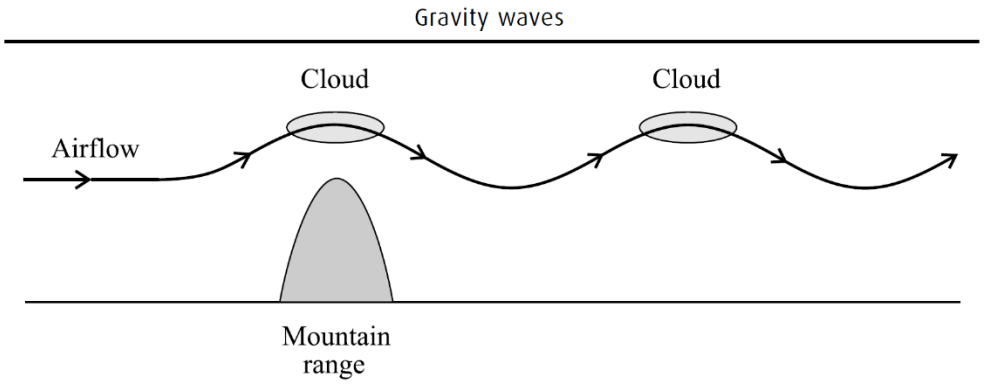

Figure 6. 2: *An illustration of a mountain wave (Lee wave) depicting an internal gravity wave generated by airflow over a mountain range. (After Andrews, 2010)*

Gravity waves, also called *buoyancy waves*, result from the displacement of air parcels in a stable atmospheric layer, where gravity acts as the restoring force. When an air parcel is displaced vertically, the restoring force of gravity pulls it back toward its equilibrium position, resulting in oscillations that propagate through the atmosphere. Therefore, for a disturbed air parcel from its stable state under the influence of buoyancy, the frequency of oscillation in the vertical direction is represented as *Brunt-Vaisala (BV) frequency* (*N*), which is given as:

$$N^2(z) = \frac{g}{T(z)}\left[\frac{g}{C_p} + \frac{dT(z)}{dz}\right] \tag{6.1}$$

where, z is the altitude, T is the temperature, g is the gravitational acceleration, and Cp represents the specific heat of molecules at constant pressure. Gravity wave periods are usually constrained by the Brunt-Väisälä frequency (N), the Coriolis effect (f), and wave dispersion properties. The Brunt-Väisälä frequency sets the lower limit, with typical periods ranging from ~5 to 15 minutes depending on the altitude and the ambient temperature. Whereas, the Coriolis effect limits the upper bound, as waves with periods longer than a few hours begin transitioning into other wave modes. Beyond ~6 hours, gravity waves tend to dissipate or transform into inertial oscillations or planetary waves rather than remaining classical gravity waves. In atmospheric observations, gravity waves with periods exceeding ~6 hours are rarely detected, as they often evolve into inertial gravity waves (~6 hours), planetary (Rossby waves (days to weeks), or atmospheric tides (12-hour and 24-hour periods). Therefore, gravity waves have typical time periods of as low as 15 min (Brunt-Vaisala period) to less than 6 hours. The vertical wavelengths can vary typically between 10-20 km in the mesosphere to a couple of hundred km in the thermosphere, and the horizontal scale sizes vary in the range of 100-1000 km (Oliver

et al., 1997; Mandal et al., 2019, 2020). The vertical and horizontal wavelength of gravity waves can be expressed by the dispersion relation (Hines, 1960):

$$k_z^2 = \frac{N^2}{(u - c_h)^2} - k_h^2 - \frac{1}{4H^2} \tag{6.2}$$

where, k_z and k_h denote the vertical and horizontal wave number ($k = 2\pi/\lambda$; λ: wavelength), respectively, u is the background wind speed, c_h is the horizontal phase speed, and H is the scale height. Therefore, from above Equation-6.2, a stronger ambient wind, directed oppositely to the phase propagation, will enhance the vertical wavelength.

The energy density of gravity waves is directly proportional to ρA^2, where ρ is the atmospheric air density, and A is the wave's amplitude. Therefore, as these waves propagate upward, the decreasing air density with altitude allows gravity waves to grow in amplitude (Figure-6.3), influencing the large-scale atmospheric circulation patterns. Due to a large continuous increase in the amplitude at higher heights, the wave becomes unstable and eventually breaks (Hecht et al., 1997; Fritts et al., 1997), consequently depositing the energy at respective altitudes. This breaking of the gravity wave is particularly significant in the upper atmosphere, as they deposit the energy from their originating region to different parts of the thermosphere.

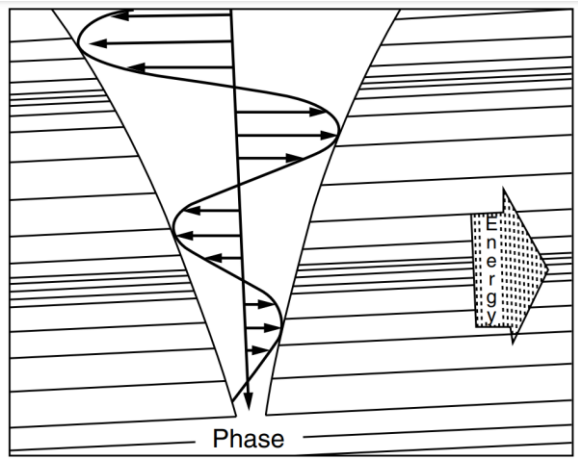

Figure 6. 3: *Schematic representation of internal gravity waves with downward phase propagation and instantaneous velocity vectors. Energy flow is obliquely upward. (Kelley, 2009)*

The gravity wave breaking can be understood in terms of BV frequency (N). From Equation-6.1, when $N^2(z)$ becomes negative at altitudes where temperature gradient $dT(z)/dz$ becomes negative, it gives rise to *convective instability*. Therefore, favorable conditions for gravity wave breaking will occur whenever the term $g/C_p + dT(z)/dz$ becomes negative. Such breaking of gravity waves was also observed using OH nightglow emissions (Yamada et al., 2001). The

atmospheric gravity waves have also been observed in several studies using different airglow emissions (e.g., Taylor & Hapgood, 1988; Fritts & Alexander, 2003; Suzuki et al., 2007).

Investigations of gravity waves can be carried out using ground-based radio and optical techniques (e.g., Pallamraju et al., 2016; Karan & Pallamraju, 2017, 2018; Mandal et al., 2019). Gravity waves exist in a variety of scale sizes and periodicities, and understanding their behavior and effects is essential, as these waves contribute to the redistribution of energy and momentum throughout the atmosphere. Furthermore, their influence on the ionosphere highlights their importance in space weather studies, which are critical for maintaining the functionality of satellite communication and navigation systems. Their importance has been discussed in the literature (e.g., Hocke & Schlegel, 1996; Chakrabarty et al., 2004; Pallamraju et al., 2014). This work reports the results on variabilities observed in the gravity wave dynamics at mid-latitudes during daytime.

6.2 Datasets used

In this work, the primary dataset includes OI 630.0 nm daytime airglow emissions, which are instrumental in examining the dynamics of gravity waves in the thermosphere over mid-latitudes. This study utilizes daytime airglow emission data obtained over Boston (42.36°N, 71.05°W) using the large field-of-view of HIRISE, covering the geographic latitude range of approximately 39-47°N (48-56°N MLAT) from 2005 to 2007, providing substantial temporal and spatial coverage for detailed analysis. The solar flux index (F10.7) and geomagnetic indices (Kp and AE) were utilized to account for day-to-day geophysical variations during dayglow measurements, ensuring that the analysis accurately reflects variability on quiet days ($Kp<3$). Only days with a minimum of 4 hours of clear all-sky data of HIRISE observed dayglow emissions were considered for scale-size calculations.

6.3 Results and Discussions

So far, in the previous chapters, we have discussed the behavior of dayglow emissions over the zenith. HIRISE slit was aligned in the meridional (North-South) direction, so this provided an additional opportunity to image the sky across different latitudes on different occasions. Therefore, apart from the temporal behavior of the OI 630.0 nm dayglow emissions, the

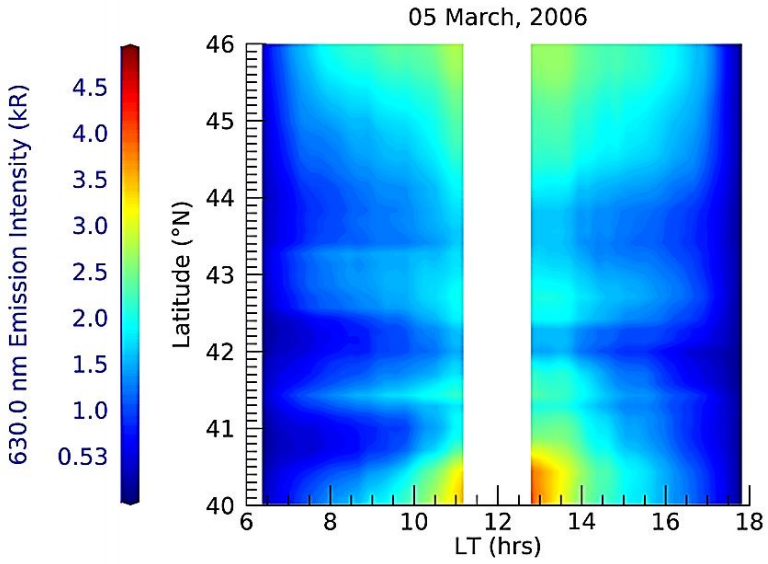

Figure 6. 4: *Diurnal and spatial variation of 630.0 nm airglow emission intensities during daytime is shown on a geomagnetically quiet day of 05 March 2006 (<Kp>=0+). The noon time missing data is due to the saturation of CCD.*

corresponding spatial variation was also obtained over the FOV of HIRISE during such times. The dayglow emission variability as a function of latitude was obtained by following a procedure similar to the dayglow extraction over the zenith mentioned in section 2.3.2 at different latitudes. Therefore, information on both the diurnal and spatial variation of dayglow emissions was obtained.

One typical example of spatially and diurnally varying behavior of OI 630.0 nm emission intensities on a geomagnetically quiet day of 05 March 2006 (<Kp>=0+) is shown in Figure-6.4. The x-axis represents the local time in hours, and the y-axis represents the different latitude information between 40° to 46° geographic North. The color scale represents the dayglow brightness in Rayleighs. The noon time missing data is because of the saturation due to the direct incidence of sunlight through the slit onto the CCD. It can be seen that the diurnally varying emission intensities show a maximum near local noon and a decrease in the afternoon hours at all latitudes. This temporal variation of daytime atomic oxygen 630.0 nm emission intensities represents the solar zenith angle dependence on a quiet day. Further, the spatial direction along the y-axis also shows fluctuations in the variability of dayglow emissions. There are different bright and less intense regions in emission intensity successively in the north-south direction at different local times, which is an indicator of dynamics operative at

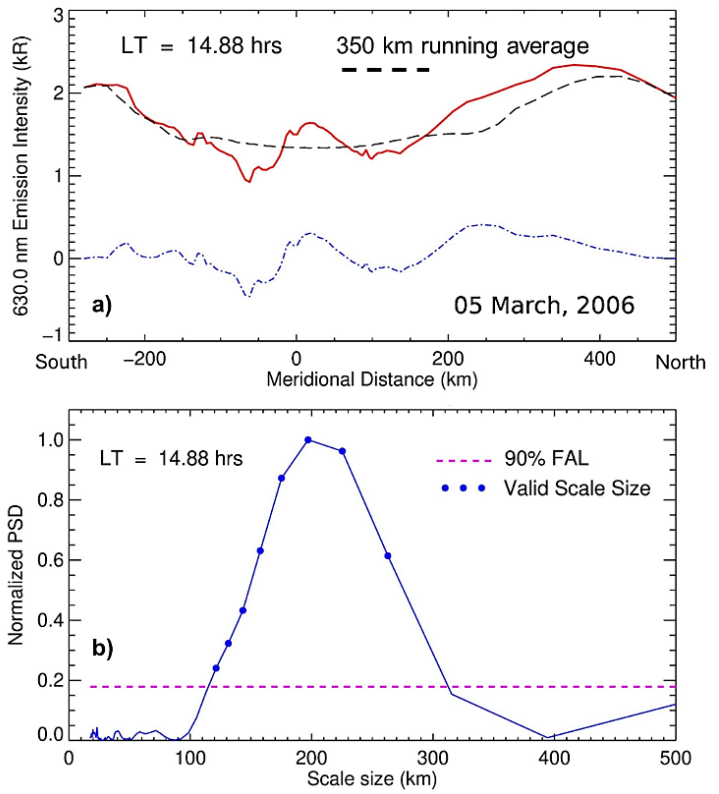

Figure 6. 5: a) *The 15-minute averaged spatial variation of 630.0 emission intensity in meridional direction at 14.88 LT is shown by a red solid line on 05 March 2006. The 350 km running average is shown by a black dashed line. The Residual (difference between running average and dayglow) is shown by a blue dash-dot line.* ***b)*** *The Lomb-Scargle periodogram analysis of the residual is shown by the solid blue line. The horizontal dashed line represents the 90% false alarm limit (FAL). The significant scale sizes with normalized power spectral density (PSD) above FAL are shown by blue dots.*

that time and location. The latitudes with bright and subdued emissions features are due to the gravity waves (e.g., Pallamraju et al., 2016; Kumar et al., 2022).

Such spatial variation of 630.0 nm dayglow emissions over a large scale is a result of the linear superposition of various wave propagations in the medium, which can be related to different scale sizes of GW. Therefore, to obtain the scale sizes corresponding to the gravity wave domain, which can have 10s-1000s km horizontal wavelength, the Lomb-Scargle (LS) analysis, as discussed in section 2.6.3, has been carried out using the measured emission intensities.

6.3.1 Meridional scale-size calculation

To obtain the meridional wave features, the emission intensities were temporally integrated over each 15-minute time interval throughout the day, corresponding to the BV period at the altitude of 630.0 nm emission. This integration eliminates the random small-scale fluctuations from the dayglow variability.

Panel-(a) in Figure-6.5 represents the spatial variation of 630.0 nm dayglow at 14.88 LT (15-minute average between 14.75 and 15.00 LT) on 05 March 2006 by red color solid line. The dayglow intensity is shown on the y-axis, and the meridional distance is shown on the x-axis, where positive and negative distances indicate the poleward and equatorward direction from the center latitude of Boston. Wave-like structures can be seen in the variability of dayglow emission along the meridional direction. To smooth out such variations from the dayglow and extract the fluctuations due to gravity waves, a 350 km running average of spatially distributed emissions in a meridional direction was obtained, as shown by the black dashed line. Therefore, a residual was obtained after taking the running average, indicated by a blue dashed-dot line. From the residual variation, various small- and large-scale intensity fluctuations of different scale sizes appear to be present in the medium. Therefore, wave number analysis was carried out using LS periodogram analysis to identify the significant scale sizes, and the corresponding Lomb-Scargle periodogram is shown in panel-(b) of Figure-6.5. In panel (b), the x-axis

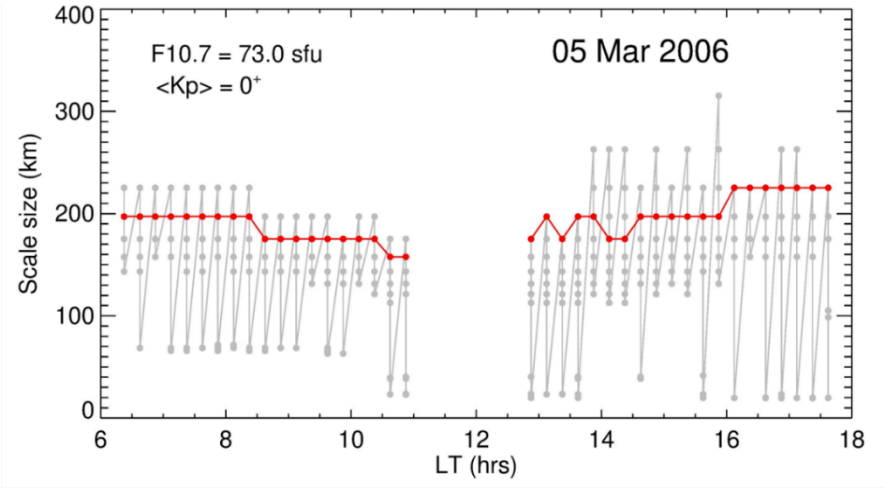

Figure 6. 6: *The diurnal variation of valid scale sizes as obtained from the spectral analysis on 05 March 2006 is shown by gray dots. The red dots indicate the corresponding scale sizes with maximum (PSD) at a given time.*

represents a range of scale size (km), and the y-axis indicates the normalized power spectral density (PSD). The magenta dashed horizontal line represents the 90% false alarm limit (FAL).

The spectral peak at a scale size of 198 km has the maximum PSD above the FAL, marking it as a significant one. In addition, all individual scale sizes satisfying this criterion of having PSD above the FAL at 14.88 LT are shown by blue-filled dots. The gravity wave components below FAL are not considered. This method provides information on different dominant meridional scale sizes (λ_y; km) of gravity waves for each integrated period on a given day at 15 minutes data cadence. Therefore, the local time variation of valid scale sizes thus obtained from the spectral analysis on 05 March 2006 is shown in Figure-6.6. The gray dots indicate the multiple significant scale sizes at different local times, while the red dots mark the scale size with the maximum PSD at each time, as shown above in the case of 198 km at 14.88 LT.

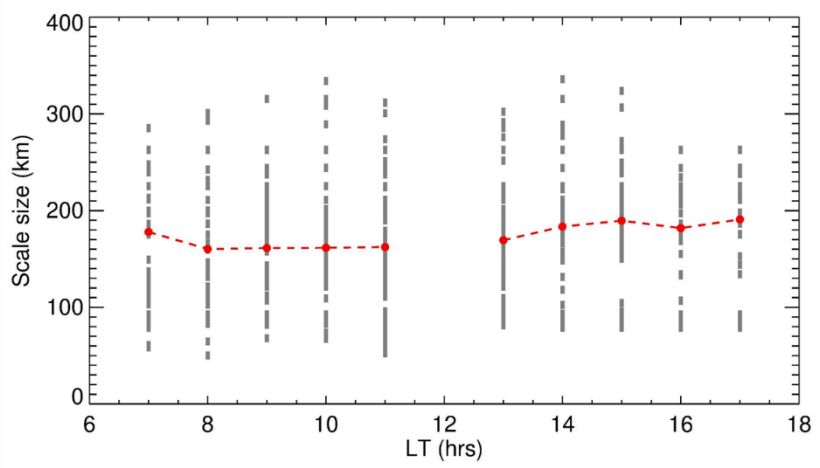

Figure 6. 7: *The calculated scale size with maximum PSD above 90% FAL for each day during data availability from 2005-2007 is shown by a gray dash with respect to local time. The data is binned at one hour time resolution. The red dots indicate the average of scale sizes at individual times.*

The wave number spectral analysis, as described above, was repeated for different geomagnetically quiet days to obtain the temporal variation of valid scale sizes in the meridional direction. Significant day-to-day variabilities of calculated scale sizes were observed in each month. The local time variation of scale sizes calculated for each available day with clear all-sky conditions is shown in Figure-6.7. The calculated scale sizes at a 15-minute data cadence were binned at a 1-hour temporal resolution. The dashed gray vertical dash represents the individual scale sizes associated with maximum power above 90% FAL,

whereas the red-filled dots connected by the dashed lines indicate their weighted average mean at each time. Therefore, the calculated gravity wave scale sizes in the meridional direction were found to range from 50 km to 335 km.

6.3.2 Seasonal variation in calculated scale sizes

As mentioned earlier, the dynamics of thermospheric winds may be influenced by various factors, such as solar heating, joule heating at high latitudes, and topographical features, among others. The scale size of gravity waves, along with their propagation direction, are affected by the role played by thermospheric winds (Hines, 1960; Pallamraju et al., 2016; Mandal et al., 2019). Therefore, the day-to-day variabilities obtained in the calculated GW scale sizes over mid-latitudes were further investigated in terms of the role played by the energetics of high-latitude upper atmosphere. It is well known that the neutral dynamics get perturbed during geomagnetically disturbed periods. However, the focus of this study is to investigate the behavior of GW scale sizes during geomagnetic quiet times. The large FOV data available during 2005-2007 presents us with an opportunity to identify if the high-mid latitude coupling

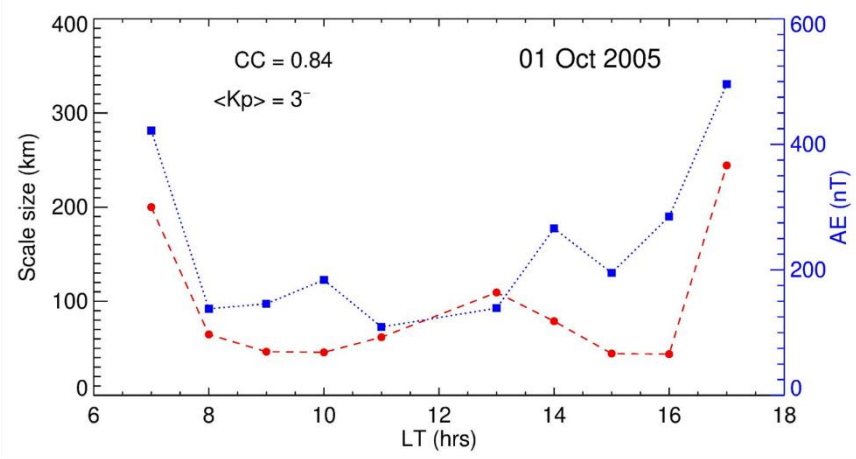

Figure 6. 8: *The calculated scale sizes binned at 1-hour temporal resolution with respect to local time are shown by red filled dots (connected by dashed line) on a quiet day 01 October 2005, with daily averaged Kp=3–. The corresponding AE index variation at the same time intervals is shown by blue-filled squares (connected by a dotted line). The AE values are shown on the right-side y-axis. A correlation coefficient (cc) of 0.84 can be seen between the calculated scale size and AE index variation.*

is also effective in the neutral dynamics for geomagnetic quiet times. For doing so, the 1-hourly binned values of calculated scale sizes on each day were compared with the temporal variation of the AE index, which is closely correlated with auroral activity and is used to indicate the nature of high-latitude phenomena. Further, the AE index has also been shown to be correlated with vertical propagation in GW over low latitudes during disturbed periods (Mandal & Pallamraju, 2020).

In this work, as the data correspond to mid-latitudes, it was explored whether the meridional scale sizes, λ_y (km), at these latitudes respond to the effects of high latitudes. Figure-6.8 shows one such example of a comparison of gravity wave scale sizes with AE index during the daytime on a quiet day, 01 October 2005, with daily averaged Kp = 3^-. The red-filled dots represent the hourly values of scale sizes, connected by the dashed lines, while the AE index values are represented by blue-filled squares, connected by dotted lines. The AE index values are shown on the right-side y-axis. It is very striking to note that a positive correlation of 0.84 between the diurnal variation of scale sizes and the AE index was seen, indicating an influence of high latitude effects on mid-latitude neutral dynamics, even during geomagnetic quiet times. This encouraged us to carry out such analyses on various other quiet days. The correlation coefficient varied from 0.2 to 0.9.

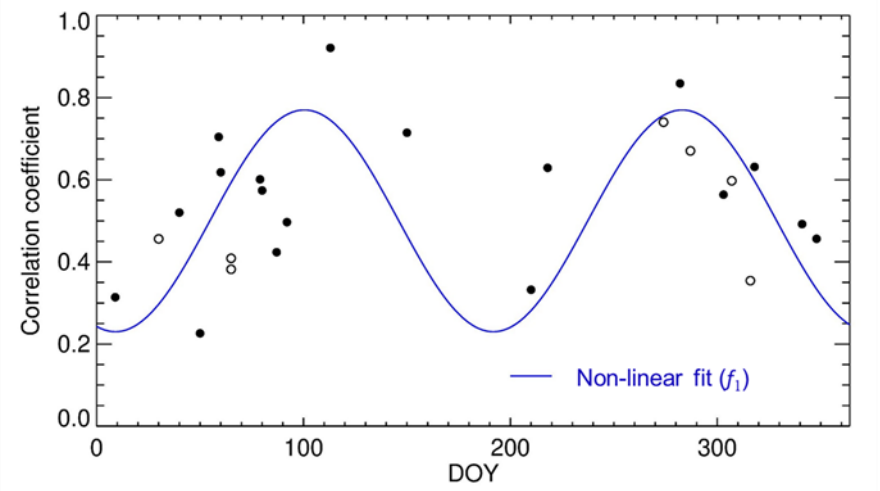

Figure 6. 9: *The variation of the correlation coefficient between GW meridional scale size and AE index is shown with respect to the day of the year (DOY) during 2005-2007. The filled (open) circles represent the variation on quiet (disturbed) days. The solid blue line is the non-linear fit to the quiet time values, given by Equation-6.3. The blue curve indicates a semi-annual variation in the influence of the AE index on gravity wave dynamics at mid-latitudes.*

To identify the influence of high-latitude activity on meridional gravity waves over mid-latitudes, such correlation values between scale sizes and AE values were plotted for each analyzed day, as shown by the filled circles in Figure-6.9. The presence of frequent clouds during the summer months prevented the dayglow observations, resulting in a lack of data. However, more days of data were available during winter and equinox months. It can be seen that the correlation between AE and scale sizes is low in winter months and is higher towards the equinox. Also, from the available data for summer months, the correlation again appears to be low, as compared to the equinoctial months. A non-linear fit was applied to the data points to illustrate the variation as a function of the day of the year. This fit, denoted as f_1, models the relationship between the correlation coefficient and the day of the year, d, as described by Equation-6.3 (where, T=365.25 and d_0 = 4.4), and is represented by the blue solid line.

$$f_1 = 0.5 + 0.27 \times \sin\left[\frac{2\pi}{(T/2)} \times d + d_0\right] \tag{6.3}$$

A double-humped structure can be seen peaking on days near March–April (day=100) and September–October (day=280) during the equinoxes. In addition, we also examined the correlation values for disturbed days with such all-sky data, which is shown by open circles. Although there were fewer data points during disturbed times, the correlation values intriguingly appeared to follow a similar pattern to that of the quiet time variation. It is interesting to note that in an earlier study by Mandal and Pallamraju (2020; hereafter M&P), the calculated scale sizes of GW in the vertical direction from a low-latitude location, Ahmedabad (23°N, 72.5°E) during geomagnetic quiet times were also shown to have a double-humped pattern with two peaks near the equinox. Figure-6.10 shows the results from that study on vertical scale sizes (λ_z; km) in the top panel obtained during 2012-2014, while the bottom panel represents the total number of days of data availability corresponding to each month during the two years. The daily averaged values of calculated vertical scale sizes are shown by black dots with respect to the day of the year, while the red diamonds show the monthly mean in the top panel of Figure-6.10.

$$< \lambda_z > = 269.11 - 67.32 \sin\left[\left(\frac{2\pi}{148.93}\right) d + 0.19\right] \tag{6.4}$$

where, d is the day of the year and $< \lambda_z >$ represents the quiet time annual variation in vertical wavelengths of gravity waves (Mandal & Pallamraju, 2020).

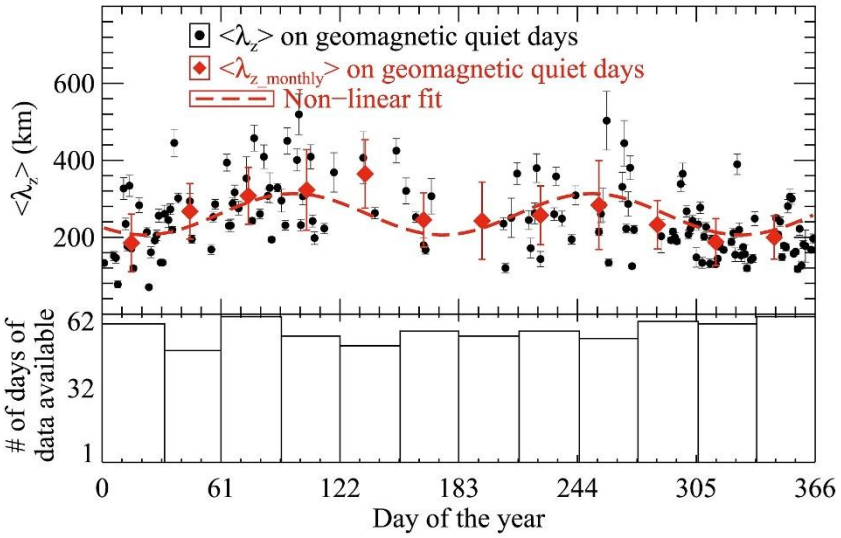

Figure 6. 10: *The vertical scale sizes were calculated over a low-latitude location, Ahmedabad (23°N, 72.5°E), under quiet times during 2012-2014. The top panel shows the daily averaged scale size values by black dots. The red diamonds show their monthly mean. The bottom panel shows the number of days with data availability for each month during these two years. A semi-annual variation in vertical scale sizes can be seen by the red-dashed curve in the top panel (Mandal & Pallamraju, 2020).*

The annual variation of vertical scale sizes was represented by performing a non-linear fit, as given by Equation-6.4, and is shown by the red dashed curve. Since, if the flow direction is the same for both winds and wave propagation, it results in an increase in horizontal scale sizes and a corresponding decrease in vertical scale sizes. The effect of wind flow direction on wave propagation can be understood using the (a) relationship between horizontal wavelength of GW and background wind using dispersion relation for GW, and (b) Annual variation of background wind as below-

(a) Relationship Between Horizontal Wavelength of Gravity Waves and Background Wind Using the Dispersion Relation:

GWs in the upper atmosphere are influenced by the background wind through the dispersion relation, which describes the relationship between wave frequency, wavenumber, and atmospheric parameters. The general form of the dispersion relation for a gravity wave under the effect of buoyancy and rotation is given by Equation-6.5 as below:

$$\omega^2 = N^2 \frac{k_h^2}{m^2} + f^2 \qquad (6.5)$$

where, ω is the intrinsic frequency of the wave, N is the Brunt-Väisälä frequency, k_h is horizontal wave number given by sum of zonal (k_z) and meridional (k_m) wavenumbers ($k_h^2 = k_z^2 + k_m^2$), m is the vertical wavenumber, and f is the Coriolis parameter due to Earth's rotation, which depends on latitude. At mid-latitudes, the Coriolis parameter is moderate, meaning rotational effects significantly influence wave propagation. When a background wind (say U, assumed to be in meridional direction) is present, the observed (Doppler-shifted) frequency (ω_{obs}) is related to the intrinsic frequency by following relation:

$$\omega_{obs} = \omega + k_m U \;\Rightarrow\; \omega = \omega_{obs} - k_m U \tag{6.6}$$

The horizontal wavelength λ_h is related to the horizontal wavenumber k_h as:

$$\lambda_h = \frac{2\pi}{k_h}$$

Therefore, using the dispersion relation, we get the horizontal wavenumber given by:

$$k_h^2 = \frac{(\omega^2 - f^2)m^2}{N^2} \tag{6.7}$$

Substitution of $\omega = \omega_{obs} - k_m U$ in above relation modifies the horizontal wavenumber as:

$$k_h^2 = \frac{((\omega_{obs} - k_m U)^2 - f^2)m^2}{N^2} \tag{6.8}$$

Since $k_h^2 = k_z^2 + k_m^2$, the effective horizontal wavenumber depends on the background wind U, leading to the modification of the intrinsic wave properties, as described by Equation-6.8. This Doppler shifting effect implies that the observed frequency varies depending on the wind direction. The impact of positive or negative wind speeds on wave propagation can be understood as follows:

Case-I: For positive wind speeds (U>0, wind moving in the direction of wave propagation):

From above relation, the intrinsic frequency ω decreases for positive wind speeds (U>0), leading to a decrease in k_h (larger horizontal wavelength λ_h) and the wave stretches in the horizontal direction.

Case-II: For negative wind speeds (U<0, wind moving opposite to the direction of wave propagation):

For negative wind speeds (U<0), the intrinsic frequency ω increases, leading to an increase in k_h (smaller horizontal wavelength λ_h) and the wave becomes more compressed in the horizontal direction.

Therefore, when the background wind is aligned with the wave propagation direction, the intrinsic frequency decreases due to Doppler shifting, leading to a reduction in horizontal wavenumber and an increase in horizontal wavelength. Conversely, when the background wind opposes the wave propagation, the intrinsic frequency increases, resulting in a higher horizontal wavenumber and a shorter horizontal wavelength.

(b) Annual Variation of Background Meridional Winds in the Thermosphere Over Mid-Latitudes:

The background winds in the thermosphere at mid-latitudes also exhibit significant annual variation, driven by several key factors. One of the primary influences on meridional winds in the thermosphere is global-scale circulation, where solar heating in the lower thermosphere (100–200 km) generates pressure gradients that drive winds from the summer hemisphere toward the winter hemisphere. During summer and winter, strong temperature and pressure gradients, resulting from differential solar heating between the hemispheres, produce intense trans-hemispheric winds, forming a pole-to-pole circulation. During equinoxes, when both hemispheres receive nearly equal solar heating, the meridional winds weaken due to the reduced pressure gradient. Therefore, this meridional circulation varies annually as solar heating shifts between hemispheres, altering wind patterns, and the global meridional winds, primarily modulated by solar heating and associated pressure gradients, undergo systematic seasonal changes in response to variations in the distribution of solar energy.

Thus, background winds significantly modify the horizontal wavelength of gravity waves at mid-latitudes through Doppler shifting, while Coriolis effects and wave filtering influence their propagation. The thermal balance, governed by large-scale temperature gradients, determines the strength and direction of meridional winds. The annual variation of background winds shapes large-scale atmospheric circulation by modulating wave propagation, momentum transfer, and heat redistribution.

Therefore, in the work by Mandal & Pallamraju (2020), it was explained that the variation in the propagation of horizontal winds over the low latitude location caused such semi-annual variation of vertical scale sizes.

Figure-6.11 represents the non-linear fits obtained from these two diverse latitudes throughout the year, as described by equations-6.3 and 6.4. The red dashed curve shows the fit derived for vertical scale sizes over low latitudes (given by M&P), while the blue solid line represents the non-linear fit derived for the variation of correlation coefficients over mid-latitudes, shown in Figure-6.9. The left and right-side y-axis show the corresponding λ_z and correlation values, respectively. It is striking to note that there is a good match between the phases of these two variations, although with a small offset of 24 days in the equinox months. It is to be noted that these two datasets are separated in latitudes, longitudes, duration of data, and parameters (λ_z in low-latitudes and correlation-coefficient between λ_y and AE-index), but for geomagnetically quiet days. This emphasizes that this double humped distribution is geophysical in nature on a global scale.

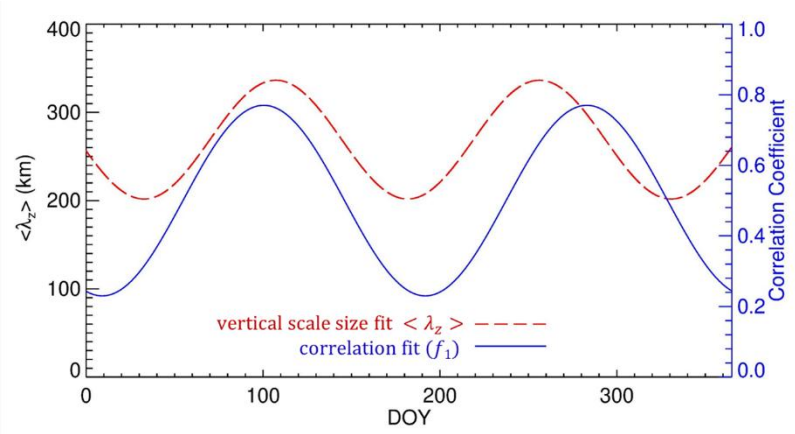

Figure 6. 11: *A comparison of semi-annual variation obtained for vertical scale sizes (λ_z) and correlation-coefficient between λ_y and AE-index, from Equations-6.3 and 6.4 is shown by red-dashed and solid blue curves, respectively, with respect to the day of the year.*

To explain the cause of such semi-annual variation on the impact of the AE index on GW scale sizes at mid-latitudes, the AE index was further examined. The AE-index is made up of AU (auroral upper) and AL (auroral lower) indices, which are associated with the eastward and

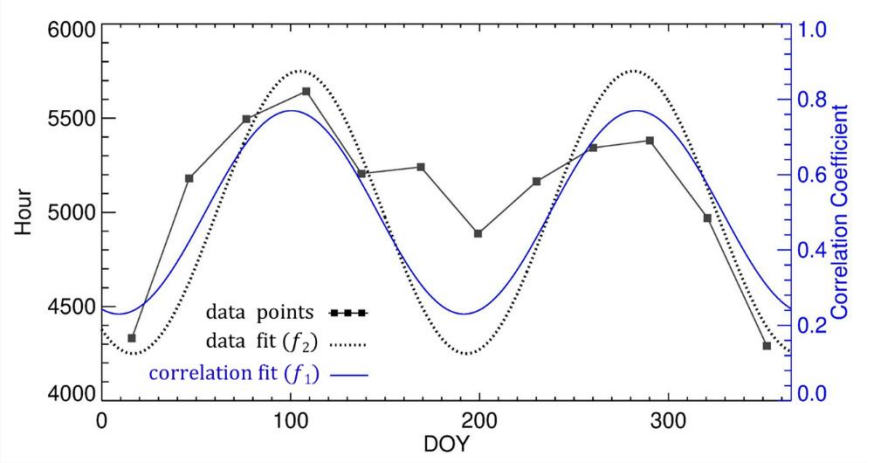

Figure 6. 12: *The distribution of the occurrence frequency during disturbed periods with AL index less than -135 nT, based on 20 years of datasets is shown by black squares (Adapted from Ahn & Moon, 2003). The non-linear fit f_2 to the monthly data points is shown by black dotted curve. The correlation fit f_1 is also overplotted by solid blue curve. No significant difference can be seen between the maxima of these two curves, which lie near day 100 and 275 during the spring and fall equinox, respectively.*

westward auroral electrojets, respectively. These auroral electrojets are mostly the Hall currents flowing in a zonal direction (Araki et al., 1989). Therefore, the AE index provides the composite effect of auroral activity as the combination of these two indices. The strength of these electrojets is largely governed by the conductivity and electric field at auroral latitudes. The Hall conductivity is controlled by the solar ultraviolet intensity, which results in the variation of eastward electrojet, i.e., Hall conductivity, thus affecting the AU index. Since the solar intensity is maximum during summer months, this will yield the largest possible AU values during summer months. The AL index is mostly measured from the stations located in post-midnight or near-dawn regions (Allen & Kroehl, 1975). On the darker side of Earth, the major contribution to westward electrojets on the dawn side comes from the perturbation of the electric field. This electric field clearly has been shown to have seasonal dependence with a maximum during the equinox, also known as the R-M effect (Russell & McPherron, 1973). Consequently, the AL index has also been found to show semi-seasonal variations. Such semi-annual variations of occurrence frequency of AL are shown in Figure-6.12, showing the maxima near the equinox (Ahn & Moon, 2003).

As the AL-index is thus dominated mainly by the electric fields, it also serves as a good indicator of the substorm's intensity. In the case of different substorms, the onset of the main

or expansion phase may not necessarily require the southward IMF Bz, and the already stored energy in the magnetotail may get released into the ionosphere (McPherron et al., 1973) and may precipitate over high-latitudes. Therefore, even though the Kp-index, a 3-hourly planetary geomagnetic activity index, shows the global quiet time conditions, the high-latitude upper atmosphere can undergo several energetic changes. The streaming of charged particles in the high latitude upper atmosphere from magnetotail or plasma sheet region during substorms can cause thermospheric heating. This heat can be subsequently circulated equatorward, affecting the composition of the upper atmosphere.

Similar to the non-linear fit f_1, carried out in Figure-6.9, we have obtained a sinusoidal fit, f_2, to the Ahn and Moon (2003) data, as described by Equation-6.9 below:

$$f_2 = 5000 + 750 \times \sin[0.0356 \times d + 4.12] \tag{6.9}$$

where, d is the day of the year. This non-linear fit is also shown by the black dotted line in Figure-6.12. Based on this fit, we can see that the amplitude of the variation is maximum at day 104 and 282 during equinoctial months, which is quite similar to the non-linear fit obtained in our data shown in Figure-6.9. To aid the eye, we have re-plotted this non-linear fit of correlation values in Figure-6.12 by blue solid curve. From this blue curve, the maxima are also found to correspond to days 100 and 280 during equinoxes. Therefore, no significant difference was obtained between these two curves. Nevertheless, it is striking to note that even during such quiet conditions, the meridional scale sizes seem to respond to the AE variations, as the mid-latitudes region is closer to the auroral zone, which can still be captured by the variability of OI 630.0 nm emissions.

6.4 Summary

This chapter discusses the variation of thermospheric gravity waves over mid-latitudes using the large field-of-view data of OI 630.0 nm emissions during daytime. The scale sizes were calculated in the meridional direction using the Lomb-Scargle analysis for geomagnetically quiet days. The typical calculated meridional scale size variation in the mid-latitude region varies from around 50 to 335 km, depending on the day-to-day ambient atmospheric background variations. It was found that the diurnal behavior of scale sizes correlates well with

the hourly measured AE-index compared to the 3-hourly Kp values. Therefore, different responses to the AE index were investigated to identify the day-to-day seasonal variability of GW scale sizes. The influence of AE values, representing the strength of substorm, was seen to dominate during equinoxes, while the effects were suppressed during winter and summer. Thus, a semi-annual variation was observed in the variation of gravity wave dynamics, influenced by the high-latitude auroral activity, which has been quantified by a non-linear fit as a function of the day of the year. This non-linear behavior of the relationship between meridional winds and the AE index during geomagnetic quiet conditions matches well with the 20-year averaged AL index variation, wherein geomagnetic disturbances played a significant role. Such influence of quiet-time auroral activity on seasonal variations on neutral dynamics is important for the further investigation of ionospheric responses affected by the winds and/or electric field perturbations in future studies.

Chapter: 7

Summary and Future Scope

7.1 Summary

The Earth's mid-latitude region experiences significant changes during disturbance times. The upper atmosphere at mid-latitudes is a critical region of various coupling effects, such as magnetosphere-plasmasphere-ionosphere coupling and thermosphere-ionosphere coupling, which results in several large-scale space-weather phenomena. This thesis investigates the impact of these coupling processes on the mid-latitude upper atmosphere during daytime conditions. The necessary background information related to such effects over mid- and high-latitudes is presented in Chapter 1. Also, some of the mid-latitude phenomena and the role of multiple airglow emissions are discussed in this chapter.

Several mid-latitude phenomena are associated with airglow emissions and can be traced using high-resolution multi-wavelength observations. This study primarily used the daytime atomic oxygen (OI) 630.0 nm emissions to investigate the mid-latitude phenomena. These optical data were obtained during the daytime from Boston, a mid-latitude location, using a ground-based high-resolution imaging spectrograph using Echelle grating (HIRISE). Detailed information about the instrument, the production mechanisms of daytime OI 630.0 nm emissions, and the procedure of dayglow extraction is provided in Chapter 2. In addition to the optical measurements, this chapter also discusses the various datasets (e.g., radar and in-situ measurements), physics-based and empirical models, and the data analyses techniques used in this work.

The results obtained from the data analysis of these multiple datasets are discussed in Chapters 3-6. These Chapters discuss the first reported results of mid-latitude thermospheric-ionospheric phenomena as seen in OI 630.0 nm airglow during daytime under varying levels of

geomagnetic activity. The schematic in Figure-7.1 illustrates the phases of geomagnetic activity addressed in each chapter and the observed coupling effects.

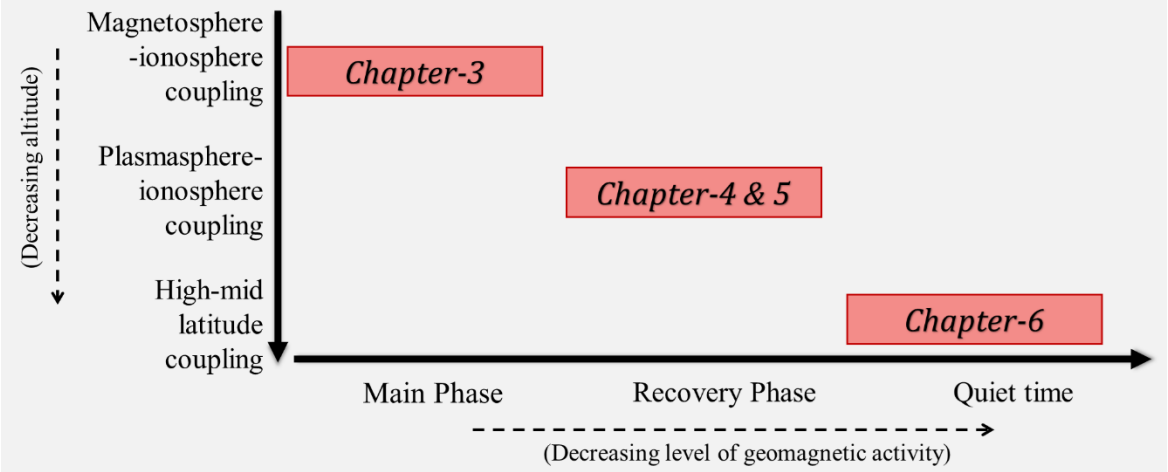

Figure 7. 1: *A schematic illustration of the work discussed in the thesis chapters over mid-latitudes during daytime conditions.*

The measured intensity of daytime airglow emissions at 630.0 nm wavelength for different geophysical conditions was investigated in this regard. The measured emission intensities during the daytime period were found to exceed those estimated by the models on several disturbed days. The influence of energy sources from high altitudes of magnetosphere and plasmasphere regions into the mid-latitude ionosphere was investigated, which revealed new and exciting results. It is shown that the large upward ion flow due to the daytime eastward electric field results in larger electron densities, Ne, in the topside ionosphere, consequently increasing peak height of 630.0 nm dayglow emissions to 450 km altitude. While the observed daytime SED is associated with a strong upward flow of plasma during the storm's main phase, the role of downward precipitation of soft particles can also happen on the dayside of the Earth during a recovery phase. The downward electron flux increases ambient topside electron temperature, Te, which led to the first reported observations of daytime SAR arc. Interestingly, such plasma perturbation during disturbed times can also occur under quiet periods. However, these effects may be limited to high latitudes associated with the substorm activity. Based on our optical measurements, their impact can be observed in the gravity wave dynamics over mid-latitudes due to the reorganization in the thermospheric winds.

Here, we present a concise summary of our findings, addressing the questions outlined in Chapter 1, Section 1.5, with a focus on the dynamics of the daytime upper atmosphere over mid-latitudes.

a) What are the optical consequences of storm-enhanced densities?

Storm-enhanced densities (SEDs) are formed because of magnetosphere-ionosphere (M-I) coupling. SED usually correlates with significant increases in Ne above 300-400 km. The 630.0 nm airglow emission peaks around 230 km. Consequently, higher Ne at greater altitudes and reduced Ne in the bottomside ionosphere typically can be considered to decrease 630.0 nm emissions during SED events. However, the HIRISE measurements revealed contrasting results. As demonstrated in Chapter 3, during the SED event on 9 November 2004, the interaction of the overhead ionosphere with the electric field (~10 mV m^{-1}) of magnetospheric origin led to a stronger $E \times B$ drift perpendicular to the local magnetic field. The vertical component of this $E \times B$ drift resulted in a stronger upward ion drift (> 200 m s^{-1}), including O_2^+ and other ions, causing an uplift of the entire ionosphere. Therefore, the increased O_2^+ and Ne and reduced loss rate at higher heights resulted in an enhanced 630.0 nm brightness at that altitude through the dissociative recombination mechanism. The altitudinal variation of Ne measured by ISR showed a larger increase (around five times) above 350 km, wherein the electron temperature was reduced drastically. To determine whether the 630.0 nm emissions originated from similar altitudes, volume emission rate (VER) profiles were calculated using the GLOW model. The modeled VER indicated a shift in the peak altitude of 630.0 nm emissions to higher altitudes, mirroring the Ne variations. The corresponding quantification of variation in different parameters is presented in Table-3.1. The role of the electric field in causing such drastic variations in 630.0 nm emission and Ne was investigated using ROTI variation, which showed the expansion of the high-latitude cell pattern to the overhead ionosphere. The rapid expansion persisted for an hour, in accordance with the southward IMF during the main phase, and the enhancement in Ne and HIRISE measured OI 630.0 nm emissions was consistent with this duration, as presented in Upadhyay et al., 2023.

b) Can SAR arc be observed during daytime? If so, what will the role of thermal enhancements be in producing daytime SAR arcs?

The previous chapter discussed the role of M-I coupling effects in the topside ionosphere. However, on occasions when there was no role of such larger Ne, measured 630.0 nm emissions

were still found to peak at different local times. Further investigation led to the study of another ionospheric permeameter, Te, which is responsible for larger emissions, as in the case of SAR arcs, which were mostly observed during nighttime. Using the high-resolution daytime OI 630.0 nm airglow emissions, representing the spectral purity of SAR arcs as red line emissions, we present the first-ever detection of daytime SAR arcs in Chapter 4. The larger red line emissions on 7 December 2006 were indeed found to be attributed to increased Te at higher heights above 350 km measured by ISR. DMSP Te measurements further verified a latitudinally narrow region of enhanced Te peak at around 840 km altitude. Using multiple passes of DMSP on the dayside, the location of the Te peak in 50°-60° N MLAT and the observed larger brightness of red line emissions were found to be in good agreement. Therefore, in the absence of visible optical signatures in daytime, satellite observations of electron temperature enhancements and plasma density reductions can serve as a key indicator of previously undetected SAR arc activity. Furthermore, daytime SAR arc detection has enabled the first investigation of estimating the corresponding electron temperature enhancements and electron heat flux variations using measured emission intensities. It was shown that during SAR arcs, downward heat deposition mostly occurs in the topside ionosphere, and correspondingly, the measured emission intensity was found to correlate strongly with topside Te at around 520 km altitude. We further performed the forward modeling (FM) to investigate the role of thermal enhancements due to downward electron heat flux causing the larger intensity of 630.0 nm emissions. The estimated Te required to produce the measured daytime SAR arcs was found to vary between 3500-4400 K. Thus, the detection of SAR arcs in the daytime significantly advances our understanding of dayside plasmasphere-ionosphere interactions. Such results on daytime SAR arcs and their dayside occurrence were presented in Upadhayay and Pallamraju, 2024.

c) How can an electron heat flux be quantified using 630.0 nm emissions for daytime SAR arcs?

In the earlier chapter, the role of downward electron heat flux was identified using simultaneous increased red line emission intensity and Te during daytime. The quantification of required daytime electron heat flux to increase the ambient Te as a consequence of plasmasphere–ionosphere coupling was carried out in Chapter 5. The best way to obtain the electron heat flux is to use the thermal conductivity from the Te profile. This work calculated the electron heat

flux at 300 and 500-km altitudes. To do so, the FM computed Te profiles were analyzed. The estimated daytime electron heat flux was found to be of the order of 10^{10} eV cm^{-2} s^{-1} and varies non-linearly with Te. An analytic expression for electron heat flux was obtained using a measured 630.0 nm emission intensity, and Te values were also presented in equation 5.10. The results reveal altitude-dependent heat flux variations, with higher magnitudes observed during daytime than nighttime. Such variations had previously been discussed only in theoretical models and nighttime studies. This work therefore not only provided the first direct observational confirmation of SAR arcs in the daytime conditions but also enabled the estimation of electron heat flux in the daytime at those altitude regions, accurate information on which is otherwise not possible to be obtained by any other method.

In addition to calculating daytime electron heat flux, using measured 630.0 nm emission intensity and Te as the two important candidates, the nighttime heat flux was also calculated. However, due to the absence of full Te profiles, the GLOW model was used to calculate the required electron heat flux for several nighttime SAR arc conjunction events listed in Table-5.2. Using the large solar cycle data, it was found that electron heat flux is dependent on the solar cycle and is mostly governed by ionospheric densities. It was found that the electron heat flux and the peak altitude of the SAR arc vary with respect to the solar cycle. So far, studies have only considered SAR arcs to peak at 400-450 km. However, our results suggested that SAR arcs can also occur below 300 km altitude for periods of low solar activity. The two important factors were elucidated as the compressed thermospheric atomic oxygen variation and reduced electron densities due to low solar ionization. These findings on electron heat flux and SAR arc peak altitude variation provide new insights to understand the influence of plasmasphere–ionosphere coupling during both day and nighttime. These results on the dynamics of electron heat flux variations in the mid-latitude ionosphere are presented in Upadhyay et al., 2024a; 2024b.

d) Apart from the dramatic ionospheric changes during geomagnetic disturbances, how do the thermospheric neutral dynamics vary in the mid-latitude upper atmosphere during quiet times?

The disturbed time ionospheric perturbations were discussed in the previous chapters. Chapter 6 discusses the complex interactions between ionospheric and thermospheric processes during quiet time periods in terms of variations in gravity waves (GW). Using large field-of-view data

from HIRISE from 2005-2007, the meridional scale sizes were calculated using wave number analysis. A day-to-day variability was found in the scale size variation, typically varying from about 50 to 335 km depending on the background conditions. As mid-latitude regions are closer to the high latitudes, the influence of auroral activity in the meridional scale sizes was investigated using the AE index. The calculated scale sizes are found to be seasonally dependent on auroral activity, which peaks near equinoctial months. The investigation of such seasonal variation was found to be due to the variation of AL-index or westward auroral electrojet. It was interpreted that larger transhemispheric winds during winter months may also suppress the impact of auroral activity on mid-altitude GW dynamics due to a larger temperature gradient between two hemispheres than during equinoxes. The results mentioned above on the thermosphere-ionosphere coupling suggest that enhanced auroral activity, typically associated with high-latitude regions, can influence the dynamics of the upper atmosphere over mid-latitudes during quiet times as well. Therefore, these results on the mid-latitude region improve our understanding of the different coupling processes between the atmospheric layers, plasmasphere-ionosphere coupling, and M-I coupling, enabling the transfer of energy and momentum into the upper atmosphere.

7.2 Future Scope

The primary findings in this thesis are based on the coupling effects over mid-latitudes during daytime conditions. These results were obtained using the variability of OI 630.0 nm emission intensities. Several of these coupling phenomena have a pronounced impact on the variability of plasmas, either in the ionospheric or magnetospheric regions. These findings open new avenues for further research, including refining the SAR arc models about M-I coupling, exploring potential differences in heating mechanisms, and understanding how ring current decay processes evolve over an entire 24-hour cycle, where the background ionospheric densities, conductivities, electric fields, neutral wind magnitude and their direction– all of them vary as a function of solar zenith angle. Therefore, the present thesis brings out several newer aspects that need to be investigated in the future. Some of these are listed below:

i) The role of ion outflow due to large upward vertical drifts through ionospheric storm-enhanced densities (SEDs) under different solar activities and its effect on

the ring current plasma density distribution needs investigation as a consequence of plasmasphere-ionosphere coupling.

ii) Ring current instabilities act as a source for SAR arc formation. In this work, the formation of the SAR arc has been only considered to be due to the Coulomb collisions. The validity and efficacy of other proposed mechanisms of the SAR arc formation for nighttime conditions can be revisited for SAR arc formation on the dayside.

iii) As these mid-latitude phenomena impact plasma distribution, any associated ionospheric or plasmaspheric irregularities must be investigated not only to advance our understanding of fundamental plasma physics processes that drive these phenomena but also to quantify the adverse effect that can be posed by them during disturbed space weather conditions.

iv) Improving the algorithms that incorporate ionospheric correction for GNSS applications. For this effort, the quantified effects of electron density, electron temperature, and electron heat flux for multiple times of disturbance required to be ingested in the model.

v) Exploring the energy transfer mechanisms between the high latitude ionosphere and magnetotail or plasma sheet in both hemispheres, especially during geomagnetically quiet periods, will enable a greater understanding of the exact cause and effects of quiet time auroral heating and particle precipitation and their impact on the global wind circulation.

vi) Assessing the impact of ring current and plasmapause dynamics on satellites and spacecraft due to SED plumes or heat generation during SAR arcs, particularly regarding radiation exposure and surface charging, in the context of their influence on the space weather.

References

Ahn, B. H., & Moon, G. H. (2003). Seasonal and universal time variations of the AU, AL and Dst indices. Journal of The Korean Astronomical Society, vol. 36, issue spc1, pp. 93-99, 36, 93-99.

Alexander, M. J. (1996). A simulated spectrum of convectively generated gravity waves: Propagation from the tropopause to the mesopause and effects on the middle atmosphere. Journal of Geophysical Research: Atmospheres, 101(D1), 1571-1588.

Alge, E., Adams, N. G., & Smith, D. (1983). Measurements of the dissociative recombination coefficients of O2+, NO+ and NH4+ in the temperature range 200-600K. Journal of Physics B: Atomic and Molecular Physics, 16(8), 1433–1444.

Allen, J. H., & Kroehl, H. W. (1975). Spatial and temporal distributions of magnetic effects of auroral electrojets as derived from AE indices. Journal of Geophysical Research, 80(25), 3667-3677.

Akasofu, S. I. (1981). Auroral arcs and auroral potential structure. Physics of auroral arc formation, 25, 1-14.

Anderson, P. C. (2004). Subauroral electric fields and magnetospheric convection during the April, 2002 geomagnetic storms. Geophysical Research Letters, 31(11), L11801.

Andrews, D. G. (2010), An Introduction to Atmospheric Physics, Cambridge University Press.

Anderson, P. C., Hanson, W. B., Heelis, R. A., Craven, J. D., Baker, D. N., & Frank, L. A. (1993). A proposed production model of rapid subauroral ion drifts and their relationship to substorm evolution. Journal of Geophysical Research: Space Physics, 98(A4), 6069-6078.

Araki, T., Schlegel, K., & Lühr, H. (1989). Geomagnetic effects of the Hall and Pedersen current flowing in the auroral ionosphere. Journal of Geophysical Research: Space Physics, 94(A12), 17185-17199.

Archer, W. E., St.-Maurice, J. P., Gallardo-Lacourt, B., Perry, G. W., Cully, C. M., Donovan, E., ... & Eurich, D. (2019). The vertical distribution of the optical emissions of a Steve and Picket Fence event. Geophysical Research Letters, 46(19), 10719-10725.

Araujo-Pradere, E. A., Fuller-Rowell, T. J., & Bilitza, D. (2003). Validation of the STORM response in IRI2000. Journal of Geophysical Research, 108(A3), 1120.

Bailey, S. M., C. A. Barth, and S. C. Solomon (2002), A model of nitric oxide in the thermosphere, J. Geophys. Res., 107(A8), 1205.

Baker, D. N., Pulkkinen, T. I., Hones Jr, E. W., Belian, R. D., McPherron, R. L., & Angelopoulos, V. (1994). Signatures of the substorm recovery phase at high-altitude spacecraft. Journal of Geophysical Research: Space Physics, 99(A6), 10967-10979.

Baker, D. N., Kanekal, S. G., Hoxie, V. C., Henderson, M. G., Li, X., Spence, H. E., ... & Claudepierre, S. G. (2013). A long-lived relativistic electron storage ring embedded in Earth's outer Van Allen belt. Science, 340(6129), 186-190.

Balan, N., & Rao, P. B. (1990). Dependence of ionospheric response on the local time of sudden commencement and the intensity of geomagnetic storms. Journal of atmospheric and terrestrial physics, 52(4), 269-275.

Balan, N., Shiokawa, K., Otsuka, Y., Kikuchi, T., Vijaya Lekshmi, D., Kawamura, S., et al. (2010). A physical mechanism of positive ionospheric storms at low latitudes and midlatitudes. Journal of Geophysical Research, 115(A2).

Banks, P. (1966). Charged particle temperatures and electron thermal conductivity in the upper atmosphere. Annales Geophysicae, 22, 557–587.

Banks, P. M., & Nagy, A. F. (1970). Concerning the influence of elastic scattering upon photoelectron transport and escape. Journal of Geophysical Research, 75, 1902.

Barbier, D. (1958). L'activité aurorale aux basses latitudes. Publications of the Observatoire Haute-Provence, 4(21), 2745.

Barbier, D. (1960). L'arc auroral stable. In Annales Geophysicae (Vol. 16, p. 544).

Barmore, F. E. (1977). High resolution observations of the 6300 Å oxygen line in the day airglow. Planetary and Space Science, 25(2), 185-191.

Baumgardner, J., Wroten, J., Semeter, J., Kozyra, J., Buonsanto, M., Erickson, P., & Mendillo, M. (2007). A very bright SAR arc: Implications for extreme magnetosphere-ionosphere coupling. Annales Geophysicae, 25(12), 2593–2608.

Baumgardner, J., Wroten, J., Mendillo, M., Martinis, C., Barbieri, C., Umbriaco, G., et al. (2013). Imaging space weather over Europe. SpaceWeather, 11(2), 69–78.

Beer, T. (1974), Atmospheric Waves, Wiley.

Bens, A. R., Cogger, L. L., & Shepherd, G. G. (1965). Upper atmospheric temperatures from Doppler line widths—III: Observation of the OI dayglow emission at 6300 Å. Planetary and Space Science, 13(6), 551-563.

Bilitza, D. (1990). International reference ionosphere: IRI-90. The National Space Science Data Center, 90–22.

Bilitza, D. (2009). Evaluation of the IRI-2007 model options for the topside electron density. Advances in space research, 44(6), 701-706.

Borovsky, J. E., & Denton, M. H. (2008). A statistical look at plasmaspheric drainage plumes. Journal of Geophysical Research: Space Physics, 113(A9).

Brice, N. M. (1967). Bulk motion of the magnetosphere. Journal of Geophysical Research, 72(21), 5193-5211.

Brace, L. H., and R. F. Theis (1981), Global empirical models of ionospheric electron temperature in the upper F-region and plasmasphere based on in situ measurements from the Atmospheric Explorer-C, ISIS-1 and ISIS-2 satellites, J. Atmos. Terr. Phys., 43, 1317–1334.

Brady, M., & Legge, G. E. (2009). Camera calibration for natural image studies and vision research. JOSA A, 26(1), 30-42.

Broadfoot, A. L., & Hunten, D. M. (1966). N2+ emission in the twilight. Planetary and Space Science, 14(12), 1303-1319.

Broadfoot, A. L. (1967). Twilight Ca+ emission from meteor trails up to 280 km. Planetary and Space Science, 15(3), 503-514.

Burton RK, McPherron RL, Russell CT (1975) An empirical relationship between interplanetary conditions and Dst. J Geophys Res 80:4204–4214.

Buonsanto, M. J. (1999). Ionospheric storms—a review. Space Science Reviews, 88(3), 563-601.

Carpenter, D. L. (1963). Whistler evidence of a 'knee'in the magnetospheric ionization density profile. Journal of Geophysical Research, 68(6), 1675-1682.

Carpenter, D. L. (1966). Whistler studies of the plasmapause in the magnetosphere: 1. Temporal variations in the position of the knee and some evidence on plasma motions near the knee. Journal of Geophysical Research, 71(3), 693-709.

Carpenter, D. L., & Anderson, R. R. (1992). An ISEE/whistler model of equatorial electron density in the magnetosphere. Journal of Geophysical Research: Space Physics, 97(A2), 1097-1108.

Chamberlain, J.W., 1961. Physics of the Aurora and Airglow. Academic Press, New York.

Chamberlain, J. W. (1995). Physics of the aurora and airglow. Washington DC: American Geophysicsl Union.

Chapman, S., & Ferraro, V. C. (1933). A new theory of magnetic storms. Terrestrial Magnetism and Atmospheric Electricity, 38(2), 79-96.

Chakrabarti, S. (1998). Ground based spectroscopic studies of sunlit airglow and aurora. Journal of atmospheric and solar-terrestrial physics, 60(14), 1403-1423.

Chakrabarti, S., Pallamraju, D., Baumgardner, J., & Vaillancourt, J. (2001). HiTIES: A High Throughput Imaging Echelle Spectrogragh for ground-based visible airglow and auroral studies. Journal of Geophysical Research: Space Physics, 106(A12), 30337-30348.

Chakrabarty, D., Sekar, R., Narayanan, R., Pant, T. K., & Niranjan, K. (2004). Thermospheric gravity wave modes over low and equatorial latitudes during daytime. Journal of Geophysical Research: Space Physics, 109(A12).

Chakrabarty, D., Sekar, R., Narayanan, R., Devasia, C. V., & Pathan, B. M. (2005). Evidence for the interplanetary electric field effect on the OI 630.0 nm airglow over low latitude. Journal of Geophysical Research: Space Physics, 110(A11).

Chu, X., Malaspina, D., Gallardo-Lacourt, B., Liang, J., Andersson, L., Ma, Q., ... & MacDonald, E. A. (2019). Identifying STEVE's magnetospheric driver using conjugate observations in the magnetosphere and on the ground. Geophysical Research Letters, 46(22), 12665-12674.

Cocks, T. D., & Jacka, F. (1979). Daytime thermospheric temperatures, wind velocities and emission intensities derived from ground based observations of the OIλ630 nm airglow line profile. Journal of Atmospheric and Terrestrial Physics, 41(4), 409-415.

Cocks, T. D., Creighton, D. F., & Jacka, F. (1980). Application of a dual Fabry-Perot spectrometer for daytime airglow studies. Journal of Atmospheric and Terrestrial Physics, 42(5), 499-511.

Cole, K. D. (1965). Stable auroral red arcs, sinks for energy of D st main phase. Journal of Geophysical Research, 70(7), 1689-1706.

Conde, M., Greet, P., & Jacka, F. (1992). The Ring effect in the sodium D2 Fraunhofer line of day skylight over Mawson, Antarctica. Journal of Geophysical Research: Atmospheres, 97(D11), 11561-11565.

Cornwall, J., F. Coroniti, and R. Thorne (1970), Turbulent loss of ring current protons, J. Geophys. Res., 75, 4699.

Cornwall, J., F. Coroniti, and R. Thorne (1971), Unified theory of SAR arc formation at the plasmapause, J. Geophys. Res., 76, 4428.

Coster, A., & Foster, J. (2007). Space-weather impacts of the subauroral polarization stream. URSI Radio Science Bulletin, 2007(321), 28-36.

Coster, A., & Skone, S. (2009). Monitoring storm-enhanced density using IGS reference station data. Journal of Geodesy, 83, 345-351.

Craven, J. D., Frank, L. A., & Ackerson, K. L. (1982). Global observations of a SAR arc. Geophysical Research Letters, 9(9), 961–964.

Culot, F., Lathuillere, C., & Lilensten, J. (2005). Influence of geomagnetic activity on the OI 630.0 and 557.7 nm dayglow. Journal of Geophysical Research: Space Physics, 110(A1).

Das, U., Pallamraju, D., & Chakrabarti, S. (2010). Effect of an X-class solar flare on the OI 630 nm dayglow emissions. Journal of Geophysical Research, 115(A8), A08302.

Davis, T. N., & Sugiura, M. (1966). Auroral electrojet activity index AE and its universal time variations. Journal of Geophysical Research, 71(3), 785-801.

Davis, P. A., & Peltier, W. R. (1979). Some characteristics of the Kelvin-Helmholtz and resonant overreflection modes of shear flow instability and of their interaction through vortex pairing. Journal of Atmospheric Sciences, 36(12), 2394-2412.

De Abreu, A. J., Fagundes, P. R., Sahai, Y., De Jesus, R., Bittencourt, J. A., Brunini, C., ... & Pimenta, A. A. (2010). Hemispheric asymmetries in the ionospheric response observed in the American sector during an intense geomagnetic storm. Journal of Geophysical Research: Space Physics, 115(A12).

Deeming, T. J., Fourier analysis with unequally-spaced data, Astrophys. Space Sci., 36, 137–158, 1975.

Dessler AJ, Parker EN (1959) Hydromagnetic theory of geomagnetic storms. J Geophys Res 64:2239–2252.

Delbouille, L., Roland, G., & Neven, L. (1973). Photometric atlas of the solar spectrum from 3000 to 10,000 Å. Institute d'Astrophysique de l'Universite de Liege, B4200 Cointe-Ougre.

Dewan, E. Á., Picard, R. H., O'Neil, R. R., Gardiner, H. A., Gibson, J., Mill, J. D., ... & Gallery, W. O. (1998). MSX satellite observations of thunderstorm-generated gravity waves in mid-wave infrared images of the upper stratosphere. Geophysical Research Letters, 25(7), 939-942.

Doering, J. P. (1992). Absolute differential and integral electron excitation cross sections for atomic oxygen: 9. Improved cross section for the $^3P \rightarrow {}^1D$ transition from 4.0 to 30 eV. Journal of Geophysical Research: Space Physics, 97(A12), 19531-19534.

Doherty, P., Coster, A. J., & Murtagh, W. (2004). Space weather effects of October–November 2003. GPS Solutions, 8, 267-271.

Doornbos, E. (2012). Thermospheric density and wind determination from satellite dynamics. Springer Science & Business Media.

Dungey, J. W. (1961). Interplanetary magnetic field and the auroral zones. Physical Review Letters, 6(2), 47.

Ebihara, Y., & Fok, M. C. (2004). Post-midnight storm-time enhancement of tens-of-keV proton flux. Journal of Geophysical Research: Space Physics, 109(A12).

Egeland A, Burke WJ (2012) The ring current: a short biography. Hist Geo Space Sci 3:131–142.

Ejiri, M. K., Shiokawa, K., Ogawa, T., Igarashi, K., Nakamura, T., & Tsuda, T. (2003). Statistical study of short-period gravity waves in OH and OI nightglow images at two separated sites. *Journal of Geophysical Research: Atmospheres*, *108*(D21).

Evans, J. V. (1969). Theory and practice of ionosphere study by Thomson scatter radar. Proceedings of the IEEE, 57(4), 496-530.

Evans, J. V. (1970). F-region heating observed during the main phase of magnetic storms. Journal of Geophysical Research, 75(25), 4815–4823.

Evans, J. V. (1973), Seasonal and sunspot cycle variations of F region electron temperature and protonospheric heat fluxes, J. Geophys. Res., 78, 2344–2349.

Fairfield DH (1971) Average and unusual locations of the Earth's magnetopause and bow shock. J Geophys Res 76:6700–6716

Farmer, D., & Armi, L. (1999). Stratified flow over topography: The role of small-scale entrainment and mixing in flow establishment. Proceedings of the Royal Society of London. Series A: Mathematical, Physical and Engineering Sciences, 455(1989), 3221-3258.

Field, P. R., Rishbeth, H., Moffett, R. J., Wenden, D. W., Fuller-Rowell, T. J., Millward, G. H., & Aylward, A. D. (1998). Modelling composition changes in F-layer storms. Journal of Atmospheric and Solar-Terrestrial Physics, 60(5), 523-543.

Fejer, B. G., Spiro, R. W., Wolf, R. A., & Foster, J. C. (1990, June). Latitudinal variation of perturbation electric fields during magnetically disturbed periods-1986 Sundial observations and model results. In Annales Geophysicae (Vol. 8, pp. 441-454).

Floyd, L., Newmark, J., Cook, J., Herring, L., & McMullin, D. (2005). Solar EUV and UV spectral irradiances and solar indices. Journal of Atmospheric and Solar-Terrestrial Physics, 67(1-2), 3-15.

Fok, M. C., Kozyra, J. U., Warren, M. F., & Brace, L. H. (1991). Seasonal variations in the subauroral electron temperature enhancement. Journal of Geophysical Research, 96(A6), 9773–9780.

Fok, M. C., Craven, P. D., Moore, T. E., & Richards, P. G. (1995). Ring current-plasmasphere coupling through Coulomb collisions. Cross-scale coupling in space plasmas, 93, 161–171.

Foster, J. C. (1989). Plasma transport through the dayside cleft: A source of ionization patches in the polar cap. In P. Sandholt & A. Egeland (Eds.), Electromagnetic coupling in the polar clefts and caps (pp. 343–354).

Foster, J. C. (1993). Storm time plasma transport at middle and high latitudes. Journal of Geophysical Research, 98(A2), 1675–1689.

Foster, J. C., Buonsanto, M. J., Mendillo, M., Nottingham, D., Rich, F. J., & Denig, W. (1994). Coordinated stable auroral red arc observations: Relationship to plasma convection. Journal of Geophysical Research, 99(A6), 11429–11439.

Foster, J. C., & Burke, W. J. (2002). SAPS: A new categorization for sub-auroral electric fields. Eos, Transactions American Geophysical Union, 83(36), 393-394.

Foster, J. C., & Vo, H. B. (2002). Average characteristics and activity dependence of the subauroral polarization stream. Journal of Geophysical Research: Space Physics, 107(A12), SIA-16.

Foster, J. C., Erickson, P. J., Coster, A. J., Goldstein, J., & Rich, F. J. (2002). Ionospheric signatures of plasmaspheric tails. Geophysical Research Letters, 29(13), 1-1.

Foster, J. C., Coster, A. J., Erickson, P. J., Holt, J. M., Lind, F. D., Rideout, W., et al. (2005). Multiradar observations of the polar tongue of ionization. Journal of Geophysical Research, 110(A9), A09S31

Foster, J. C., Rideout, W., Sandel, B., Forrester, W. T., & Rich, F. J. (2007). On the relationship of SAPS to storm-enhanced density. Journal of Atmospheric and Solar-Terrestrial Physics, 69(3), 303–313.

Foster, J. C. (2008). Ionospheric-magnetospheric-heliospheric coupling: Storm-time thermal plasma redistribution. Mid-Latitude Dynamics and Disturbances. Geophysical Monograph Series, 181, 121–134.

Fritts, D. C., Isler, J. R., Hecht, J. H., Walterscheid, R. L., & Andreassen, Ø. (1997). Wave breaking signatures in sodium densities and OH nightglow: 2. Simulation of wave and instability structures. Journal of Geophysical Research: Atmospheres, 102(D6), 6669-6684.

Fritts, D. C., & Alexander, M. J. (2003). Gravity wave dynamics and effects in the middle atmosphere. Reviews of Geophysics, 41(1), 1003.

Fuller-Rowell, T. J., Codrescu, M. V., Roble, R. G., & Richmond, A. D. (1997). How does the thermosphere and ionosphere react to a geomagnetic storm?. Geophysical monograph series, 98, 203-225.

Galkin, I. A., Khmyrov, G. M., Kozlov, A. V., Reinisch, B. W., Huang, X., Paznukhov, V. V., et al. (2008). The ARTIST 5, in radio sounding and plasma physics. AIP Conference Proceedings, 974(1), 150–159.

Galperin, Y.I., Ponomarev, V.N. and Zosimova, A.G. (1974.): Plasma convection in polar ionosphere. Ann. Geophys., 30, 1-7

Goldstein, J. (2007). Plasmasphere response: Tutorial and review of recent imaging results. Solar dynamics and its effects on the heliosphere and Earth, 203-216.

Grainger, J. F., & Ring, J. (1962). Anomalous Fraunhofer line profiles. Nature, 193(4817), 762-762.

Greenspan, M. E., Anderson, P. B., & Pelegatti, J. M. (1986). Characteristics of the thermal plasma monitors (SSIES) for the defence meteorological satellite program (DMSP) spacecraft S8 through F10. Tech. Rep. AFGL-TR-86-0227. Air Force Geophysics Laboratory.

Guberman, S. L. (1988). The production of O (1D) from dissociative recombination of O2+. Planetary and space science, 36(1), 47-53.

Gordon, W. E. (1958). Incoherent scattering of radio waves by free electrons with applications to space exploration by radar. Proceedings of the IRE, 46(11), 1824-1829.

Gurubaran, S., & Sridharan, R. (1993). Effect of meridional winds and neutral temperatures on the F layer heights over low latitude. *Journal of Geophysical Research*, 98(A7), 11629–11635.

Gurubaran, S., Sridharan, R., & Raghavarao, R. (1995). Effects of neutral temperature on meridional winds estimated from ionospheric data. Journal of Atmospheric and Terrestrial Physics, 57(10), 1095-1101.

Hairston, M. (2018). Madrigal SSIES-2 manual. Center for Space Sciences, University of Texas at Dallas.

Hardy, D. A., L. K. Schmitt, M. S. Gussenhoven, F. J. Marshall, H. C. Yeh, T. L. Shumaker, A. Hube, & J. Pantazis (1984). Precipitating electron and ion detectors (SSJ/4) for the block 5D/flights 6-10 DMSP Satellites: Calibration and data presentation, Rep. AFGL-TR-84-0317, Air Force Geophys. Lab., Hanscom Air Force Base, Mass.

Hargreaves, J. K. (1992). The solar-terrestrial environment: an introduction to geospace-the science of the terrestrial upper atmosphere, ionosphere, and magnetosphere. Cambridge university press.

Hasegawa, A., & Mima, K. (1978). Anomalous transport produced by kinetic Alfvén wave turbulence. Journal of Geophysical Research: Space Physics, 83(A3), 1117-1123.

Hays, P. B., & Sharp, W. E. (1973). Twilight airglow: 1. Photoelectrons and [OI] 5577-Angstrom radiation. Journal of Geophysical Research, 78(7), 1153-1166.

Hays, P. B., Rusch, D. W., Roble, R. G., & Walker, J. C. G. (1978). The OI (6300 Å) airglow. Reviews of Geophysics, 16(2), 225-232.

Hecht, J. H., Walterscheid, R. L., Fritts, D. C., Isler, J. R., Senft, D. C., Gardner, C. S., & Franke, S. J. (1997). Wave breaking signatures in OH airglow and sodium densities and temperatures: 1. Airglow imaging, Na lidar, and MF radar observations. Journal of Geophysical Research: Atmospheres, 102(D6), 6655-6668.

Heelis, R. A., Sojka, J. J., David, M., & Schunk, R. W. (2009). Storm time density enhancements in the middle-latitude dayside ionosphere. Journal of Geophysical Research, 114(A3), A03315.

Heelis, R. A. (2016). Longitude and hemispheric dependencies in storm-enhanced density. Ionospheric space weather: Longitude and hemispheric dependences and lower atmosphere forcing, 59-70.

Hines, C. O. (1960). Internal atmospheric gravity waves at ionospheric heights. Canadian Journal of Physics, 38(11), 1441-1481.

Hernandez, G., & Roble, R. G. (1976). Direct measurements of nighttime thermospheric winds and temperatures, 2. Geomagnetic storms. Journal of Geophysical Research, 81(28), 5173-5181.

Hocke, K., & Schlegel, K. (1996, September). A review of atmospheric gravity waves and travelling ionospheric disturbances: 1982–1995. In Annales geophysicae (Vol. 14, No. 9, p. 917).

Horne, J. H., & Baliunas, S. L. (1986). A prescription for period analysis of unevenly sampled time series. Astrophysical Journal, Part 1 (ISSN 0004-637X), vol. 302, March 15, 1986, p. 757-763. Research, supported by the National Geographic Society and, the Smithsonian Institution., 302, 757-763.

Horvath, I., & Lovell, B. C. (2021). Investigating the coupled magnetosphere-ionosphere-thermosphere (M-I-T) system s responses to the 20 November 2003 Superstorm. Journal of Geophysical Research: Space Physics, 126(9), e2021JA029215.

Hosokawa, K., Taguchi, S., Shiokawa, K., Otsuka, Y., Ogawa, Y., & Nicolls, M. (2014). Global imaging of polar cap patches with dual airglow imagers. Geophysical Research Letters, 41(1), 1–6.

Huang, C.-S., Foster, J. C., Goncharenko, L. P., Erickson, P. J., Rideout, W., & Coster, A. J. (2005). A strong positive phase of ionospheric storms observed by the Millstone Hill incoherent scatter radar and global GPS network. Journal of Geophysical Research, 110(A6), A06303.

Hultqvist B, Øieroset M, Paschmann G, Treumann R (eds) (1999) Magnetospheric plasma sources and losses, space sciences series of ISSI, vol 6. Kluver Academic Publishers, Dordrecht, Holland.

Ievenko, I. B., Parnikov, S. G., & Sokolnikov, A. V. (2023). Relationship of the Stable Auroral Red Arc Height to Solar Activity: Observation Results at the Yakutsk Meridian. Bulletin of the Russian Academy of Sciences: Physics, 87(2), 220-227.

Inaba, Y., Shiokawa, K., Oyama, S.-I., Otsuka, Y., Oksanen, A., Shinbori, A., et al. (2020). Plasma and field observations in the magnetospheric source region of a stable auroral red (SAR) arc by the Arase satellite on 28 March 2017. Journal of Geophysical Research: Space Physics, 125(10), e2020JA028068.

Inaba, Y., Shiokawa, K., Oyama, S. I., Otsuka, Y., Connors, M., Schofield, I., et al. (2021). Multi-event Analysis of plasma and field variations in Source of Stable Auroral Red (SAR) arcs in inner magnetosphere during non-storm-time substorms. Journal of Geophysical Research: Space Physics, 126(4), e2020JA029081.

Jee, G. (2023). Fundamentals of numerical modeling of the mid-latitude ionosphere. Journal of Astronomy and Space Sciences, 40(1), 11-18.

Jordanova, V. K., R. Torbert, R. Thorne, H. Collin, J. Roeder, and J. Foster (1999), Ring current activity during the early Bz < 0 phase of the January 1997 magnetic cloud, J. Geophys. Res., 104, 24,895.

Kamide, Y., & Akasofu, S. I. (1976). The location of the field-aligned currents with respect to discrete auroral arcs. Journal of Geophysical Research, 81(22), 3999-4003.

Karan, D. K., & Pallamraju, D. (2017). Small-scale longitudinal variations in the daytime equatorial thermospheric wave dynamics as inferred from oxygen dayglow emissions. Journal of Geophysical Research: Space Physics, 122(6), 6528-6542.

Karlsson, T., Marklund, G. T., Blomberg, L. G., & Mälkki, A. (1998). Subauroral electric fields observed by the Freja satellite: A statistical study. Journal of Geophysical Research: Space Physics, 103(A3), 4327-4341.

KELLEY, M. C., & HEELIS, R. A. (1989). The Earth's ionosphere: plasma physics and electrodynamics. International geophysics series, 43.

Kelley, M. C. (2009), The Earth's Ionosphere: Plasma Physics & Electrodynamics, vol. 96, Academic press.

Kelley, M. C., Vlasov, M. N., Foster, J. C., & Coster, A. J. (2004). A quantitative explanation for the phenomenon known as storm-enhanced density. Geophysical Research Letters, 31(19), L19809.

Kelley, M. C., J. J. Makela, J. L. Chau, and M. J. Nicolls (2003), Penetration of the solar wind electric field into the magnetosphere/ionosphere system, Geophys. Res. Lett., 30(4), 1158.

Kikuchi, T., K. K. Hashimoto, and K. Nozaki (2008), Penetration of magnetospheric electric fields to the equator during a geomagnetic storm, J. Geophys. Res., 113, A06214.

Kivelson, M. G., & Russell, C. T. (Eds.). (1995). Introduction to space physics. Cambridge university press.

Klobuchar, J. A. (1996). Global positioning system: Theory and applications. Ionospheric Effects in GPS, 1, 485-515.

Kokubun S (1972) Relationship of interplanetary magnetic field structure with development of substorm and storm main phase. Planet Space Sci 20:1033–1049.

Kozyra, J. U., Brace, L. H., Cravens, T. E., & Nagy, A. F. (1986). A statistical study of the subauroral electron temperature enhancement using Dynamics Explorer 2 Langmuir probe observations. Journal of Geophysical Research, 91(A10), 11270–11280.

Kozyra, J., E. Shelley, R. Comfort, L. Brace, T. E. Cravens, and A. Nagy (1987), The role of ring current O+ in the formation of stable auroral red arcs, J. Geophys. Res., 92, 7487.

Kozyra, J. U., Chandler, M. O., Hamilton, D. C., Peterson, W. K., Klumpar, D. M., Slater, D. W., et al. (1993). The role of ring current nose events in producing stable auroral red arc intensifications during the main

phase: Observations during the September 19–24, 1984 equinox transition study. Journal of Geophysical Research, 98(A6), 9267–9283.

Kozyra, J. U., Nagy, A. F., & Slater, D. W. (1997). High-altitude energy source(s) for stable auroral red arcs. Reviews of Geophysics, 35(2), 155–190.

Kosch, M. J., Pedersen, T., Mishin, E., Oyama, S. L., Hughes, J., Senior, A., ... & Bristow, B. (2007). Coordinated optical and radar observations of ionospheric pumping for a frequency pass through the second electron gyroharmonic at HAARP. *Journal of Geophysical Research: Space Physics*, *112*(A6).

Kubota, M., Shiokawa, K., Ejiri, M. K., Otsuka, Y., Ogawa, T., Sakanoi, T., ... & Saito, A. (2000). Traveling ionospheric disturbances observed in the OI 630-nm nightglow images over Japan by using a Multipoint Imager Network during the FRONT Campaign. *Geophysical research letters*, *27*(24), 4037-4040.

Kulkarni, P. V. (1976). Rocket study of 5577-Å OI emission at night over the magnetic equator. Journal of Geophysical Research, 81(22), 3740-3744.

Kumar, S., Pallamraju, D., Suryawanshi, P., Vijayalakshmi, T., & Seemala, G. K. (2022). On the latitudinal variation in OI 630.0 nm dayglow emissions in response to the equatorial electrodynamic processes and neutral winds. Advances in Space Research, 69(2), 926-938.

Johnson, C. Y. (1969). Ion and neutral composition of the ionosphere. Annals of the IQSY, 5, 197-213.

Lakshmi Narayanan, V., Gurubaran, S., & Emperumal, K. (2010). Airglow imaging observations of small-scale structures driven by convective instability in the upper mesosphere over Tirunelveli (8.7°N). *Journal of Geophysical Research: Atmospheres*, 115(D19), D19119.

Laskar, F. I., & Pallamraju, D. (2014). Does sudden stratospheric warming induce meridional circulation in the mesosphere thermosphere system?. Journal of Geophysical Research: Space Physics, 119(12), 10-133.

Le, G., Slavin, J. A., & Strangeway, R. J. (2010). Space Technology 5 observations of the imbalance of regions 1 and 2 field-aligned currents and its implication to the cross-polar cap Pedersen currents. Journal of Geophysical Research: Space Physics, 115(A7).

Lemaire, J. F., & Gringauz, K. I. (1998). The Earth's plasmasphere (p. 372).

Liemohn, M., J. Kozyra, P. Richards, G. Khazanov, M. Buonsanto, and V. Jordanova (2000), Ring current heating of the thermal electrons at solar maximum, J. Geophys. Res., 105, 27,767.

Liu, Y., & Xiong, C. (2020). Morphology evolution of the midlatitude ionospheric trough in nighttime under geomagnetic quiet conditions. Journal of Geophysical Research: Space Physics, 125(8), e2019JA027361.

Lobzin, V. V., & Pavlov, A. V. (1999, June). Correlations between SAR arc intensity and solar and geomagnetic activity. In Annales Geophysicae (Vol. 17, pp. 770-781). Springer-Verlag.

Lomb, N. R. (1976). Least-squares frequency analysis of unequally spaced data. Astrophysics and space science, 39, 447-462.

López-González, M. J., et al. (2007), Ground-based mesospheric temperatures at mid-latitude derived from O2 and OH airglow SATI data: Comparison with SABER measurements, J. Atmos. Sol. Terr. Phys., 69, 2379–2390.

Lu, G., Goncharenko, L., Nicolls, M. J., Maute, A., Coster, A., & Paxton, L. J. (2012). Ionospheric and thermospheric variations associated with prompt penetration electric fields. Journal of Geophysical Research: Space Physics, 117(A8).

Lui ATY, McEntire RW, Krimigis SM (1987) Evolution of the ring current during two geomagnetic storms. J Geophys Res 92:7459–7470.

MacDonald, E. A., Donovan, E., Nishimura, Y., Case, N. A., Gillies, D. M., Gallardo-Lacourt, B., ... & Schofield, I. (2018). New science in plain sight: Citizen scientists lead to the discovery of optical structure in the upper atmosphere. Science advances, 4(3), eaaq0030.

Makela, J. J., Ledvina, B. M., Kelley, M. C., & Kintner, P. M. (2004, September). Analysis of the seasonal variations of equatorial plasma bubble occurrence observed from Haleakala, Hawaii. In *Annales Geophysicae* (Vol. 22, No. 9, pp. 3109-3121). Göttingen, Germany: Copernicus Publications.

Makela, J. J., Meriwether, J. W., Huang, Y., & Sherwood, P. J. (2011). Simulation and analysis of a multi-order imaging Fabry–Perot interferometer for the study of thermospheric winds and temperatures. Applied Optics, 50(22), 4403-4416.

Makela, J. J., Fisher, D. J., Meriwether, J. W., Buriti, R. A., & Medeiros, A. F. (2013). Near-continual ground-based nighttime observations of thermospheric neutral winds and temperatures over equatorial Brazil from 2009 to 2012. *Journal of Atmospheric and Solar-Terrestrial Physics*, *103*, 94-102.

Makela, J. J., Kelley, M. C., González, S. A., Aponte, N., & McCoy, R. P. (2001). Ionospheric topography maps using multiple-wavelength all-sky images. *Journal of Geophysical Research: Space Physics*, *106*(A12), 29161-29174.

Mandal, S., & Pallamraju, D. (2020). Thermospheric gravity wave characteristics in the daytime over low-latitudes during geomagnetic quiet and disturbed conditions. Journal of Atmospheric and Solar-Terrestrial Physics, 211, 105470.

Mandal, S., Pallamraju, D., Karan, D. K., Phadke, K. A., Singh, R. P., & Suryawanshi, P. (2019). On deriving gravity wave characteristics in the daytime upper atmosphere using radio technique. Journal of Geophysical Research: Space Physics, 124(8), 6985-6997.

Mandal, S., Pallamraju, D., & Suryawanshi, P. (2020). Changes in the daytime thermospheric gravity wave propagation characteristics over low-latitudes in response to the variation in solar flux. Journal of Atmospheric and Solar-Terrestrial Physics, 209, 105414.

Mannucci, A. J., Tsurutani, B. T., Iijima, B. A., Komjathy, A., Saito, A., Gonzalez, W. D., et al. (2005). Dayside global ionospheric response to the major interplanetary events of October 29–30, 2003 “Halloween Storms”. Geophysical Research Letters, 32(12), L12S02.

Mantas, G. P., & Carlson, H. C. (1991). Reexamination of the O (3P→ 1D) excitation rate by thermal electron impact. Geophysical Research Letters, 18(2), 159-162.

Martinis, C., Baumgardner, J., Wroten, J., & Mendillo, M. (2010). Seasonal dependence of MSTIDs obtained from 630.0 nm airglow imaging at Arecibo. *Geophysical Research Letters*, *37*(11).

Martinis, C., Baumgardner, J., Mendillo, M., Taylor, M. J., Moffat-Griffin, T., Wroten, J., et al. (2019). First ground-based conjugate observations of stable auroral red (SAR) arcs. Journal of Geophysical Research: Space Physics, 124(6), 4658–4671.

Maynard, N. C. (1978). On large poleward-directed electric fields at sub-auroral latitudes. Geophysical Research Letters, 5(7), 617-618.

Mayr, H. G., Harris, I., & Spencer, N. W. (1978). Some properties of upper atmosphere dynamics. Reviews of Geophysics, 16(4), 539-565.

McIlwain, C. E. (1961). Coordinates for mapping the distribution of magnetically trapped particles. Journal of Geophysical Research, 66(11), 3681–3691.

McPherron, R. L., Russell, C. T., & Aubry, M. P. (1973). Satellite studies of magnetospheric substorms on August 15, 1968: 9. Phenomenological model for substorms. Journal of Geophysical Research, 78(16), 3131-3149.

Mende, S. B., & Turner, C. (2019). Color ratios of subauroral (STEVE) arcs. Journal of Geophysical Research: Space Physics, 124(7), 5945-5955.

Mende, S. B., Harding, B. J., & Turner, C. (2019). Subauroral green STEVE arcs: Evidence for low-energy excitation. Geophysical Research Letters, 46(24), 14256–14262.

Mendillo, M., Papagiannis, M. D., & Klobuchar, J. A. (1970). Ionospheric storms at midlatitudes. Radio Science, 5(6), 895–898.

Mendillo, M., & Baumgardner, J. (1982). Airglow characteristics of equatorial plasma depletions. Journal of Geophysical Research: Space Physics, 87(A9), 7641-7652.

Mendillo, M., Baumgardner, J., Nottingham, D., Aarons, J., Reinisch, B., Scali, J., & Kelley, M. (1997). Investigations of thermospheric-ionospheric dynamics with 6300-Å images from the Arecibo Observatory. Journal of Geophysical Research: Space Physics, 102(A4), 7331-7343.

Mendillo, M., Meriwether, J., & Biondi, M. (2001). Testing the thermospheric neutral wind suppression mechanism for day-to-day variability of equatorial spread F. Journal of Geophysical Research: Space Physics, 106(A3), 3655-3663.

Mendillo, M. (2006). Storms in the ionosphere: Patterns and processes for total electron content. Reviews of Geophysics, 44(4).

Mendillo, M., & Narvaez, C. (2010, July). Ionospheric storms at geophysically-equivalent sites–Part 2: Local time storm patterns for subauroral ionospheres. In Annales Geophysicae (Vol. 28, No. 7, pp. 1449-1462). Göttingen, Germany: Copernicus Publications.

Mendillo, M., Baumgardner, J., Wroten, J., Martinis, C., Smith, S., Merenda, K. D., et al. (2013). Imaging magnetospheric boundaries at ionospheric heights. Journal of Geophysical Research: Space Physics, 118(11), 7294–7305

Mendillo, M., Finan, R., Baumgardner, J., Wroten, J., Martinis, C., & Casillas, M. (2016a). A stable auroral red (SAR) arc with multiple emission features. *Journal of Geophysical Research: Space Physics*, *121*(10), 10-564.M.

Mendillo, M., Baumgardner, J., & Wroten, J. (2016b). SAR arcs we have seen: Evidence for variability in stable auroral red arcs. *Journal of Geophysical Research: Space Physics*, *121*(1), 245-262.Nagy, A. F., & Banks, P. M. (1970). Photoelectron fluxes in the ionosphere. Journal of Geophysical Research, 75, 6260.

Mendillo, M., & Wroten, J. (2019). Modeling stable auroral red (SAR) arcs at geomagnetic conjugate points: Implications for hemispheric asymmetries in heat fluxes. Journal of Geophysical Research: Space Physics, 124(7), 6330-6342.

Meredith, N. P., Horne, R. B., Glauert, S. A., & Anderson, R. R. (2007). Slot region electron loss timescales due to plasmaspheric hiss and lightning-generated whistlers. Journal of Geophysical Research: Space Physics, 112(A8).

Meriwether Jr, J. W., Moody, J. W., Biondi, M. A., & Roble, R. G. (1986). Optical interferometric measurements of nighttime equatorial thermospheric winds at Arequipa, Peru. Journal of Geophysical Research: Space Physics, 91(A5), 5557-5566.

Meriwether, J. W. (2006). Studies of thermospheric dynamics with a Fabry–Perot interferometer network: A review. Journal of Atmospheric and Solar-Terrestrial Physics, 68(13), 1576-1589.

Mishin, E. V., & Burke, W. J. (2005). Stormtime coupling of the ring current, plasmasphere, and topside ionosphere: Electromagnetic and plasma disturbances. Journal of Geophysical Research: Space Physics, 110(A7).

Mishin, E., Nishimura, Y., & Foster, J. (2017). SAPS/SAID revisited: A causal relation to the substorm current wedge. *Journal of Geophysical Research: Space Physics*, *122*(8), 8516-8535.

Miyoshi, Y., Morioka, A., & Misawa, H. (2000). Long term modulation of low altitude proton radiation belt by the Earth's atmosphere. Geophysical Research Letters, 27(14), 2169-2172.

Moldwin, M. B., Zou, S., & Heine, T. (2016, December). The story of plumes: The development of a new conceptual framework for understanding magnetosphere and ionosphere coupling. In Annales Geophysicae (Vol. 34, No. 12, pp. 1243-1253). Göttingen, Germany: Copernicus Publications.

Moore, C. E., Minnaert, M. G. J., & Houtgast, J. (1966). The Solar Spectrum 2935 Å to 8770 Å, U.S. NBS Monogr., 61, 98–101.

Mostefaoui, T., Laubé, S., Gautier, G., Rebrion-Rowe, C., Rowe, B. R., & Mitchell, J. B. A. (1999). The dissociative recombination of NO+: The influence of the vibrational excitation state. Journal of Physics B: Atomic, Molecular and Optical Physics, 32(22), 5247.

Mukherjee, G. K., Parihar, N., Niranjan, K., & Manju, G. (2006). Signature of midnight temperature maximum (MTM) using OI 630 nm airglow.

Nagy, A. F., & Banks, P. M. (1970). Photoelectron fluxes in the ionosphere. Journal of Geophysical Research, 75(31), 6260-6270.

Nagy, A. F., Roble, R. G., & Hays, P. B. (1970). Stable mid-latitude red arcs: Observations and theory. Space Science Reviews, 11(5), 709–727.

Narayanan, R., J. N. Desai, N. K. Modi, R. Raghavarao, and R. Sridharan (1989), Dayglow photometry: a new approach, Appl. Opt., 28, 2138-2142.

Narayanan, V. L., Gurubaran, S., Emperumal, K., & Patil, P. T. (2013). A study on the night time equatorward movement of ionization anomaly using thermospheric airglow imaging technique. Journal of Atmospheric and Solar-Terrestrial Physics, 103, 113-120.

Nishida A (2000) The Earth's dynamic magnetotail. Space Sci Rev 91:507–577.

Nishimura, Y., Gallardo-Lacourt, B., Zou, Y., Mishin, E., Knudsen, D. J., Donovan, E. F., ... & Raybell, R. (2019). Magnetospheric signatures of STEVE: Implications for the magnetospheric energy source and interhemispheric conjugacy. Geophysical Research Letters, 46(11), 5637-5644.

Noxon, J. F. (1968). Day airglow. Space Science Reviews, Volume 8, Issue 1, pp. 92-134, 8, 92-134.

Noxon, J. F., Whipple Jr, E. C., & Hyde, R. S. (1979). Stratospheric NO2: 1. Observational method and behavior at mid-latitude. Journal of Geophysical Research: Oceans, 84(C8), 5047-5065.

Obayashi, T. (1964), Morphology of storms in the ionosphere, Research in Geophysics, vol. 1, edited by H. Odishaw, pp. 335–366, MIT Press, Cambridge, Mass.

Oliver, W. L., Otsuka, Y., Sato, M., Takami, T., & Fukao, S. (1997). A climatology of F region gravity wave propagation over the middle and upper atmosphere radar. Journal of Geophysical Research, 102(A7), 14,499–14,512.

Otsuka, Y., Shiokawa, K., Ogawa, T., & Wilkinson, P. (2002). Geomagnetic conjugate observations of equatorial airglow depletions. *Geophysical Research Letters*, *29*(15), 43-1.

Pallamraju, D., Errors in airglow & auroral emission measurements, 2003

Pallamraju, D. (1996), Studies of daytime upper atmospheric phenomena using ground-based optical techniques, Ph.D. thesis, Devi Ahilya Vishwa Vidyalaya of Indore.

Pallam Raju, D., R. Sridharan, R. Narayanan, N. K. Modi, R. Raghavarao, and B. H. Subbaraya (1995), Ground-based optical observations of daytime auroral emissions from Antarctica, Journal of Atmospheric and Terrestrial Physics, 57(13), 1591-1597.

Pallam Raju, D., R. Sridharan, S. Gurubaran, and R. Raghavarao (1996), First results from ground-based daytime optical investigation of the development of the equatorial ionization anomaly, Ann. Geophys., 14 (2), 238-245.

Pallamraju, D., & Sridharan, R. (1998a). Ground-based optical measurements of daytime auroral emissions: A new means of investigating space-weather related processes. Proceedings of the Indian Academy of Sciences-Earth and Planetary Sciences, 107, 203-211.

Pallam Raju, D., & Sridharan, R. (1998b). High resolution 2-D maps of OI 630.0 nm thermospheric dayglow from equatorial latitudes. In Annales Geophysicae (Vol. 16, No. 8, pp. 997-1006). Copernicus GmbH.

Pallamraju, D., Baumgardner, J., & Chakrabarti, S. (2000). A multiwavelength investigation of the Ring effect in the day sky spectrum. Geophysical Research Letters, 27(13), 1875–1878.

Pallamraju, D., Baumgardner, J., Chakrabarti, S., & Pedersen, T. R. (2001). Simultaneous ground-based observations of an auroral arc in daytime/twilighttime OI 630.0 nm emission and by Incoherent Scatter Radar. Journal of Geophysical Research, 106(A4), 5543–5549.

Pallamraju, D., Baumgardner, J., & Chakrabarti, S. (2002). HIRISE: A ground-based high-resolution imaging spectrograph using echelle grating for measuring daytime airglow/auroral emissions. Journal of Atmospheric and Solar-Terrestrial Physics, 64(12–14), 1581–1587.

Pallamraju, D., Chakrabarti, S., & Valladares, C. E. (2004, September). Magnetic storm-induced enhancement in neutral composition at low latitudes as inferred by O (1 D) dayglow measurements from Chile. In Annales Geophysicae (Vol. 22, No. 9, pp. 3241-3250). Göttingen, Germany: Copernicus Publications.

Pallamraju, D., Chakrabarti, S., Doe, R., & Pedersen, T. (2004). First ground-based OI 630 nm optical measurements of daytime cusplike and F-region auroral precipitation. Geophysical Research Letters, 31(8), L08807.

Pallamraju, D., & Chakrabarti, S. (2005). First ground-based measurements of OI 6300 A daytime aurora over Boston in response to the 30 October 2003 geomagnetic storm. Geophysical Research Letters, 32(3), L03S10.

Pallamraju, D., Das, U., & Chakrabarti, S. (2010). Short-and long-timescale thermospheric variability as observed from OI 630.0 nm dayglow emissions from low latitudes. Journal of Geophysical Research: Space Physics, 115(A6).

Pallamraju, D., Chakrabarti, S., & Solomon, S. C. (2011). On deriving incident auroral particle fluxes in the daytime using combined ground-based optical and radar measurements. Journal of Geophysical Research: Space Physics, 116(A4).

Pallamraju, D., Laskar, F. I., Singh, R. P., Baumgardner, J., & Chakrabarti, S. (2013). MISE: A multiwavelength imaging spectrograph using echelle grating for daytime optical aeronomy investigations. Journal of Atmospheric and Solar-Terrestrial Physics, 103, 176–183.

Pallamraju, D., Baumgardner, J., Singh, R. P., Laskar, F. I., Mendillo, C., Cook, T., ... & Chakrabarti, S. (2014). Daytime wave characteristics in the mesosphere lower thermosphere region: Results from the Balloon-borne Investigations of Regional-atmospheric Dynamics experiment. Journal of Geophysical Research: Space Physics, 119(3), 2229-2242.

Pallamraju, D., Karan, D. K., & Phadke, K. A. (2016). First three-dimensional wave characteristics in the daytime upper atmosphere derived from ground-based multiwavelength oxygen dayglow emission measurements. Geophysical Research Letters, 43(11), 5545-5553.

Pallamraju, D., Karan, D. K., Laskar, F. I., Lakshmi, T. V., & Chakrabarti, S. (2020). Effect of solar flux versus compositional variations on the variability of daytime oxygen optical emission rates over low-and mid-latitudes. Journal of Atmospheric and Solar-Terrestrial Physics, 205, 105293.

Palmer, Christopher. (2020). Diffraction Grating Handbook, eighth edition.

Pedersen, T., Gustavsson, B., Mishin, E., Kendall, E., Mills, T., Carlson, H. C., & Snyder, A. L. (2010). Creation of artificial ionospheric layers using high-power HF waves. *Geophysical Research Letters*, *37*(2).

Peymirat, C., Richmond, A. D., & Kobea, A. T. (2000). Electrodynamic coupling of high and low latitudes: Simulations of shielding/overshielding effects. Journal of Geophysical Research: Space Physics, 105(A10), 22991-23003.

Pi, X., Mannucci, A. J., Lindqwister, U. J., & Ho, C. M. (1997). Monitoring of global ionospheric irregularities using the worldwide GPS network. Geophysical Research Letters, 24(18), 2283–2286.

Picone, J. M., Hedin, A. E., Drob, D. P., & Aikin, A. C. (2002). NRLMSISE-00 empirical model of the atmosphere: Statistical comparisons and scientific issues. Journal of Geophysical Research, 107(A12), SIA15-1–SIA15-16.

Pimenta, A. A., Sahai, Y., Bittencourt, J. A., & Rich, F. J. (2007). Ionospheric plasma blobs observed by OI 630 nm all-sky imaging in the Brazilian tropical sector during the major geomagnetic storm of April 6–7, 2000. Geophysical Research Letters, 34(2), L02820.

Pirog, O. M., Polekh, N. M., Tashchilin, A. V., Romanova, E. B., & Zherebtsov, G. A. (2006). Response of ionosphere to the great geomagnetic storm of September 1998: Observation and modeling. Advances in Space Research, 37(5), 1081-1087.

Prölss, G. W., & Von Zahn, U. (1974). Esro 4 Gas Analyzer results 2. Direct measurements of changes in the neutral composition during an ionospheric storm. Journal of Geophysical Research, 79(16), 2535-2539.

Prölss, G. W., Roemer, M., & Slowey, J. W. (1988). Dissipation of solar wind energy in the Earth's upper atmosphere: The geomagnetic activity effect. Advances in space research, 8(5-6), 215-261.

Prölss, G. W. (1991). Thermosphere-ionosphere coupling during disturbed conditions. Journal of geomagnetism and geoelectricity, 43(Supplement1), 537-549.

Prölss, G. (1993), Common origin of positive ionospheric storms at middle latitudes and the geomagnetic activity effect at low latitudes, J. Geophys. Res., 98, 5981–5991.

Prölss, G. W. (1995). Ionospheric F-region storms. In Handbook of Atmospheric Electrodynamics (1995) (pp. 195-248). CRC press.

Prölss, G. W. (1997). Magnetic storm associated perturbations of the upper atmosphere. Geophysical Monograph Series, 98, 227-241.

Prölss, G. W., & Craven, J. D. (1998). Perturbations of the FUV dayglow and ionospheric storm effects. Advances in Space Research, 22(1), 129-134.

Prölss, G. W. (2006). Subauroral electron temperature enhancement in the nighttime ionosphere. Annales Geophysicae, 24(7), 1871–1885.

Rama Rao, P. V. S., Niranjan, K., Prasad, D. S. V. V. D., Gopi Krishna, S., & Uma, G. (2006, September). On the validity of the ionospheric pierce point (IPP) altitude of 350 km in the Indian equatorial and low-latitude sector. In Annales Geophysicae (Vol. 24, No. 8, pp. 2159-2168). Göttingen, Germany: Copernicus Publications.

Rees, M. H., & Roble, R. G. (1975). Observations and theory of the formation of stable auroral red arcs. Reviews of Geophysics, 13(1), 201–242.

Reinisch, B. W., & Xueqin, H. (1983). Automatic calculation of electron density profiles from digital ionograms: 3. Processing of bottomside ionograms. Radio Science, 18(3), 477–492.

Reinisch, B. W., & Huang, X. (2001). Deducing topside profiles and total electron content from bottomside ionograms. Advances in Space Research, 27(1), 23–30.

Rich, F. J., & Hairston, M. (1994). Large-scale convection patterns observed by DMSP. Journal of Geophysical Research, 99(A3), 3827–3844.

Rishbeth, H. (1977). Dynamics of the equatorial F-region. Journal of Atmospheric and Terrestrial Physics, 39(9–10), 1159–1168.

Rishbeth, H., & Garriott, O. K. (1969). Introduction to ionospheric physics. Introduction to ionospheric physics.

Rishbeth, H. (1998). How the thermospheric circulation affects the ionospheric F2-layer. Journal of Atmospheric and Solar-Terrestrial Physics, 60(14), 1385-1402.

Regi, M. (2016). ULF power fluctuations in the solar-wind parameters and their relationship with the relativistic electron flux at the geosynchronous orbit. Il Nuovo Cimento, 100(285), 39.

Rees, M. H. (1989). *Physics and chemistry of the upper atmosphere*. Cambridge University Press..

Rich, F. J., & Hairston, M. (1994). Large-scale convection patterns observed by DMSP. Journal of Geophysical Research, 99(A3), 3827–3844.

Rich, F. J., Burke, W. J., Kelley, M. C., & Smiddy, M. (1980). Observations of field-aligned currents in association with strong convection electric fields at subauroral latitudes. Journal of Geophysical Research: Space Physics, 85(A5), 2335-2340.

Richards, P. G., Fennelly, J. A., & Torr, D. G. (1994). EUVAC: A solar EUV flux model for aeronomic calculations. Journal of Geophysical Research, 116(A8), 8981.

Rideout, W., and Coster, A. (2006). Automated GPS Processing for Global Total Electron Content Data. GPS Solut. 10 (3), 219–228.

Rishbeth, H., & Barron, D. W. (1960). Equilibrium electron distributions in the ionospheric F2-layer. Journal of Atmospheric and Terrestrial Physics, 18(2-3), 234-252.

Roach, F. E., & Roach, J. R. (1963). Stable 6300 Å auroral arcs in mid-latitudes. Planetary and Space Science, 11(5), 523-540.

Roederer, J. G. (1970). Dynamics of Geomagnetically Trapped Radiation. Physics and Chemistry in Space, 46.

Rowland, D. E., & Wygant, J. R. (1998). Dependence of the large-scale, inner magnetospheric electric field on geomagnetic activity. Journal of Geophysical Research: Space Physics, 103(A7), 14959-14964.

Russell, C. T. (2003). The structure of the magnetopause. Planetary and Space Science, 51(12), 731-744.

Russell, C. T., & McPherron, R. (1973). Semiannual variation of geomagnetic activity. Journal of geophysical research, 78(1), 92-108.

Safrankova J, Nemecek Z, Dusik S, Prech L, Sibeck DG, Borodkova NN (2002) Ann Geophys 30:301–309

Šafránková, J., Němeček, Z., Dušík, Š., Přech, L., Sibeck, D. G., & Borodkova, N. N. (2002). The magnetopause shape and location: A comparison of the Interball and Geotail observations with models. In *Annales Geophysicae* (Vol. 20, No. 3, pp. 301-309). Copernicus GmbH.

Sato, K. (1993). Small-scale wind disturbances observed by the MU radar during the passage of Typhoon Kelly. Journal of Atmospheric Sciences, 50(4), 518-537.

Scargle, J. D. (1982). Studies in astronomical time series analysis. II-Statistical aspects of spectral analysis of unevenly spaced data. Astrophysical Journal, Part 1, vol. 263, Dec. 15, 1982, p. 835-853., 263, 835-853.

Schunk, R. W., and A. F. Nagy (1978), Electron temperatures in the F region of the ionosphere: Theory and observations, Rev. Geophys., 16(3), 355–399.

Schunk, R. W., and A. F. Nagy (2009), Ionospheres, 2nd ed., Cambridge Univ. Press, New York.

Sckopke N (1966) A general relation between the energy of trapped particles and the disturbance field near the Earth. J Geophys Res 71:3125–3130.

Seaton, M. J. (1956), A possible explanation of the drop in F-region critical densities accompanying major ionospheric storms, J. Atmos. Sol. Terr. Phys., 8, 122–124.

Seemala, G. K., & Valladares, C. E. (2011). Statistics of total electron content depletions observed over the South American continent for the year 2008.Radio Science, 46, RS5019.

Seo, Y., Horwitz, J. L., & Caton, R. (1997). Statistical relationships between high-latitude ionospheric F region/topside upflows and their drivers:DE 2 observations. Journal of Geophysical Research, 102(A4), 7493–7500

Shepherd, G. G. (1979). Dayside cleft aurora and its ionospheric effects. Reviews of Geophysics, 17(8), 2017-2033.

Shepherd, G. G., Winningham, J. D., Bunn, F. E., & Thirkettle, F. W. (1980). An empirical determination of the production efficiency for auroral 6300-Å emission by energetic electrons. *Journal of Geophysical Research: Space Physics*, *85*(A2), 715-721.

Shepherd, G. G., Thuillier, G., Gault, W. A., Solheim, B. H., Hersom, C., Alunni, J. M., ... & Wimperis, J. (1993a). WINDII, the wind imaging interferometer on the upper atmosphere research satellite. Journal of Geophysical Research: Atmospheres, 98(D6), 10725-10750.

Shepherd, G. G., Thuillier, G., Solheim, B. H., Chandra, S., Cogger, L. L., Duboin, M. L., ... & Vial, F. (1993b). Longitudinal structure in atomic oxygen concentrations observed with WINDII on UARS. Geophysical research letters, 20(12), 1303-1306.

Shepherd, G. G., McLandress, C., & SOLDHEIM, B. (1995). Tidal influence of O (1S) airglow emission rate distributions at the geographic equator as observed by WINDII. *Geophysical research letters*, *22*(3), 275-278.

Shepherd, G. G., Siddiqi, N. J., Wiens, R. H., & Zhang, S. (1997). Airglow measurements of possible changes in the ionosphere and middle atmosphere. *Advances in Space Research*, *20*(11), 2127-2135.

Shepherd, G. G., & Cho, Y. M. (2021). On the Relationship of the O (1D) 630.0 nm dayglow emission to the F10. 7 cm solar flux and the solar zenith angle. Journal of Geophysical Research: Space Physics, 126(3), e2020JA028715.

Shiokawa, K., Katoh, Y., Satoh, M., Ejiri, M. K., Ogawa, T., Nakamura, T., ... & Wiens, R. H. (1999). Development of optical mesosphere thermosphere imagers (OMTI). Earth, Planets and Space, 51, 887-896.

Shiokawa, K., Kadota, T., Otsuka, Y., Ogawa, T., Nakamura, T., & Fukao, S. (2003a). A two-channel Fabry-Perot interferometer with thermoelectric-cooled CCD detectors for neutral wind measurement in the upper atmosphere. Earth, planets and space, 55, 271-275.

Shiokawa, K., Ihara, C., Otsuka, Y., & Ogawa, T. (2003b). Statistical study of nighttime medium-scale traveling ionospheric disturbances using midlatitude airglow images. Journal of Geophysical Research, 108(A1), 1052.

Shiokawa, K., Otsuka, Y., & Ogawa, T. (2006). Quasiperiodic southward moving waves in 630-nm airglow images in the equatorial thermosphere. Journal of Geophysical Research: Space Physics, 111(A6).

Shiokawa, K., Otsuka, Y., & Ogawa, T. (2009). Propagation characteristics of night-time mesospheric and thermospheric waves observed by optical mesosphere thermosphere imagers at middle and low latitudes. *Earth Planets and Space*, **61**, 479–491.

Shiokawa, K., Miyoshi, Y., Brandt, P. C., Evans, D. S., Frey, H. U., Goldstein, J., & Yumoto, K. (2013). Ground and satellite observations of low-latitude red auroras at the initial phase of magnetic storms. Journal of Geophysical Research: Space Physics, 118(1), 256-270.

Shprits, Y. Y., Subbotin, D. A., Meredith, N. P., & Elkington, S. R. (2008). Review of modeling of losses and sources of relativistic electrons in the outer radiation belt II: Local acceleration and loss. Journal of atmospheric and solar-terrestrial physics, 70(14), 1694-1713.

Sigernes, F., Dyrland, M., Brekke, P., Chernouss, S., Lorentzen, D. A., Oksavik, K., & Deehr, C. S. (2011). Two methods to forecast auroral displays. Journal of Space Weather and Space Climate, 1(1), A03.

Singh, A. K., Siingh, D., & Singh, R. P. (2010). Space weather: physics, effects and predictability. Surveys in geophysics, 31, 581-638.

Singh, R. P., & Pallamraju, D. (2015). On the latitudinal distribution of mesospheric temperatures during sudden stratospheric warming events. Journal of Geophysical Research: Space Physics, 120(4), 2926-2939.

Singh, R. P., & Pallamraju, D. (2016). Effect of cyclone Nilofar on mesospheric wave dynamics as inferred from optical nightglow observations from Mount Abu, India. Journal of Geophysical Research: Space Physics, 121(6), 5856-5867.

Singh, R. P., and D. Pallamraju, (2017), Near Infrared Imaging Spectrograph (NIRIS) for ground-based mesospheric OH (6-2) and O2(0-1) intensity and temperature measurements, J. Earth Syst. Sci. 126:88.

Smiddy, M., Kelley, M. C., Burke, W., Rich, F., Sagalyn, R., Shuman, B., ... & Lai, S. (1977). Intense poleward-directed electric fields near the ionospheric projection of the plasmapause. Geophysical Research Letters, 4(11), 543-546.

Smith, A. K., & Lyjak, L. V. (1985). An observational estimate of gravity wave drag from the momentum balance in the middle atmosphere. Journal of Geophysical Research: Atmospheres, 90(D1), 2233-2241.

Solomon, S. C., Hays, P. B., & Abreu, V. J. (1988). The auroral 6300 Å emission: Observations and modeling. Journal of Geophysical Research: Space Physics, 93(A9), 9867-9882.

Solomon, S. C., & Abreu, V. J. (1989). The 630 nm dayglow. Journal of Geophysical Research, 94(A6), 6817–6824.

Solomon, S. C. (2017). Global modeling of thermospheric airglow in the far ultraviolet. Journal of Geophysical Research: Space Physics, 122(7), 7834-7848.

Southwood, D. J., & Wolf, R. A. (1978). An assessment of the role of precipitation in magnetospheric convection. Journal of Geophysical Research: Space Physics, 83(A11), 5227-5232.

Spiro, R. W., Heelis, R. A., & Hanson, W. B. (1978). Ion convection and the formation of the mid-latitude F region ionization trough. Journal of Geophysical Research: Space Physics, 83(A9), 4255-4264.

Spiro, R., Heelis, R., & Hanson, W. (1979). Rapid subauroral ion drifts observed by Atmospheric Explorer C. Geophysical Research Letters, 6(8), 657–660.

Spiro, R. W., Wolf, R. A., & Fejer, B. G. (1988, February). Penetrating of high-latitude-electric-field effects to low latitudes during SUNDIAL 1984. In Annales Geophysicae (Vol. 6, pp. 39-49).

Sridharan, R., Raghavarao, R., Gurubaran, S., & Narayanan, R. (1991). First results of OI 630.0 nm dayglow measurements from equatorial latitudes. Journal of atmospheric and terrestrial physics, 53(6-7), 521-528.

Sridharan, R., R. Narayanan, and N. K. Modi (1992), Improved chopper mask for the dayglow photometer., Appl. Opt., 31 (4), 425-6.

Sridharan, R., Haider, S. A., Gurubaran, S., Sekar, R., & Narayanan, R. (1992b). OI 630.0-nm dayglow in the region of equatorial ionization anomaly: Temporal variability and its causative mechanism. Journal of Geophysical Research: Space Physics, 97(A9), 13715-13721.

Sridharan, R., Sekar, R., & Gurubaran, S. (1993a). Two-dimensional high-resolution imaging of the equatorial plasma fountain. Journal of atmospheric and terrestrial physics, 55(13), 1661-1665.

Sridharan, R., R. Narayanan, N. K. Modi, and D. P. Raju (1993), Novel mask design for multiwavelength dayglow photometry., Appl. Opt., 32 (22), 4178-80.

Sridharan, R., Raju, D. P., Narayanan, R., Modi, N. K., Subbaraya, B. H., & Raghavarao, R. (1995). Daytime measurements of optical auroral emissions from Antarctica. Current science, 830-834.

Sridharan, R., N. K. Modi, D. P. Raju, R. Narayanan, T. K. Pant, A. Taori, and D. Chakrabarty (1998), A multiwavelength daytime photometer - a new tool for the investigation of atmospheric processes, Meas. Sci. Technol., 9 (4), 585.

Sugiura, M. (1963). Hourly values of equatorial Dst for the IGY (No. NASA-TM-X-55238).

Sumod, S. G., Pant, T. K., Vineeth, C., & Hossain, M. M. (2014). On the ionospheric and thermospheric response of solar flare events of 19 January 2005: An investigation using radio and optical techniques. Journal of Geophysical Research: Space Physics, 119(6), 5049–5059

Sun, Y. Y., Matsuo, T., Araujo-Pradere, E. A., & Liu, J. Y. (2013). Ground-based GPS observation of SED-associated irregularities over CONUS. Journal of Geophysical Research: Space Physics, 118(5), 2478-2489.

Suzuki, S., Shiokawa, K., Otsuka, Y., Ogawa, T., Nakamura, K., & Nakamura, T. (2007). A concentric gravity wave structure in the mesospheric airglow images. Journal of Geophysical Research: Atmospheres, 112(D2).

Swift, W. R., Torr, D. G., Torr, M. R., Hamilton, C., Dougani, H., Richards, P. G., & Sivjee, G. G. (1990). A procedure for the extraction of airglow features in the presence of strong background radiation. Journal of Geophysical Research: Space Physics, 95(A9), 15227-15241.

Takagi, Y., Shiokawa, K., Otsuka, Y., Connors, M., & Schofield, I. (2018). Statistical analysis of SAR arc detachment from the main oval based on 11-year, all-sky imaging observation at Athabasca, Canada. Geophysical Research Letters, 45(21), 11-539.

Tanaka T (2007) Magnetosphere–ionosphere convection as a compound system. Space Sci Rev 133:1–72

Tascione T. F., Introduction to the space environment (Krieger Publishing Company, Malabar FL) 1988.

Taylor, M. J., & Hapgood, M. A. (1988). Identification of a thunderstorm as a source of short period gravity waves in the upper atmospheric nightglow emissions. Planetary and Space Science, 36(10), 975-985.

Taylor, M. J., Bishop, M. B., & Taylor, V. (1995). All-sky measurements of short period waves imaged in the OI(557.7 nm), Na(589.2 nm) and near infrared OH and O2(0, 1) nightglow emissions during the aloha-93 campaign. Geophysical Research Letters, 22(20), 2833–2836.

Teitelbaum, H., Massebeuf, M., Fellous, J. L., Petitdidier, M., Christophe, J., & Blanco, F. (1981). Simultaneous measurements of meteor winds and green line intensity variations: Gravity waves and planetary waves. Journal of Geophysical Research: Space Physics, 86(A9), 7767-7770.

Tepley, C. A., Meriwether Jr, J. W., Walker, J. C. G., & Mathews, J. D. (1981). Observations of neutral iron emission in twilight spectra. Journal of Geophysical Research: Space Physics, 86(A6), 4831-4835.

Thomas, E. G., Baker, J. B., Ruohoniemi, J. M., Clausen, L. B., Coster, A. J., Foster, J. C., & Erickson, P. J. (2013). Direct observations of the role of convection electric field in the formation of a polar tongue of ionization from storm enhanced density. Journal of Geophysical Research: Space Physics, 118(3), 1180–1189.

Titheridge, J. E. (1976), Plasma temperatures from Alouette electron density profiles, Planet. Space Sci., 24, 247–259.

Torr, D. G., Torr, M. R., Walker, J. C. G., Nier, A. O., Brace, L. H., & Brinton, H. C. (1976). Recombination of O2+ in the ionosphere. Journal of Geophysical Research, 81(31), 5578–5580.

Torr, M. R., & Torr, D. G. (1982). The role of metastable species in the thermosphere. Reviews of Geophysics, 20(1), 91-144.

Torr, M. R., Torr, D. G., & Hinteregger, H. E. (1980). Solar flux variability in the Schumann-Runge continuum as a function of solar cycle 21. Journal of Geophysical Research: Space Physics, 85(A11), 6063-6068.

Tsagouri, I., Belehaki, A., Moraitis, G., & Mavromichalaki, H. (2000). Positive and negative ionospheric disturbances at middle latitudes during geomagnetic storms. Geophysical Research Letters, 27(21), 3579-3582.

Tsurutani, B. T. (2000). Solar/interplanetary plasma phenomena causing geomagnetic activity at Earth. In *Plasmas in the Universe* (pp. 273-286). IOS Press.

Tsurutani, B. T., Gonzalez, W. D., Lakhina, G. S., & Alex, S. (2003). The extreme magnetic storm of 1–2 September 1859. Journal of Geophysical Research: Space Physics, 108(A7).

Upadhyay, K., Pallamraju, D., & Chakrabarti, S. (2023). Imprint of storm enhanced density in ground-based OI 630.0 nm dayglow measurements. Journal of Geophysical Research: Space Physics, 128(9), e2023JA031409.

Upadhyay, K., & Pallamraju, D. (2024). First daytime red-line emission measurements of the stable auroral red (SAR) arcs. *Geophysical Research Letters*, *51*(3), e2023GL106292.

Upadhyay, K., Pallamraju, D., & Chakrabarti, S. (2024a). Estimation of downward heat flux into the F region from the inner magnetosphere during Stable Auroral Red (SAR) arc events in the daytime obtained using OI 630.0 nm red line emissions, Journal of Geophysical Research - Space Physics, 129(7), e2024JA032694.

Upadhyay, K., Shiokawa, K., Pallamraju, D., & Gololobov, A. (2024b). Determination of electron heat flux in the topside ionosphere and its impact on the vertical profile of OI 630.0 nm emission rate during nighttime SAR arcs for different solar activity conditions. Advances in Space Research, 75(6), 4731-4739.

Vegabd, L. (1939). Hydrogen showers in the auroral region. Nature, 144(3661), 1089-1090.

Van Allen, J. A., & Frank, L. A. (1959). Survey of radiation around the earth to a radial distance of 107,400 kilometers (Vol. 59, No. 2). Department of Physics, State University of Iowa.

Voiculescu, M., Nygrén, T., Aikio, A., & Kuula, R. (2010). An olden but golden EISCAT observation of a quiet-time ionospheric trough. Journal of Geophysical Research: Space Physics, 115(A10).

Wallace, L. (1961). An attempt to observe the day airglow. Journal of Geophysical Research, 66(5), 1585-1586.

Wallace, L., & McElroy, M. B. (1966). The visual dayglow. Planetary and Space Science, 14(8), 677-708.

Walt, M. (1994). Introduction to geomagnetically trapped radiation. Camb. Atmos. Space Sci. Ser, 10.

Walsh, B. M., Phan, T. D., Sibeck, D. G., & Souza, V. M. (2014). The plasmaspheric plume and magnetopause reconnection. Geophysical Research Letters, 41(2), 223-228.

Weimer DR (2005) Improved ionospheric electrodynamic models and application to calculating Joule heating rates. J Geophys Res 110(A05306):1–21

Welling DT, Andre M, Dandouras I, Delcourt D, Fazakerley A, Fontaine D, Foster J, Ilie R, Kistler L, Lee JH, Liemohn MW, Slavin JA, Wang CP, Wiltberger M, Yau A (2015) The Earth: plasma sources, losses, and transport processes. Space Sci Rev 192:145–208

Weygand, J. M., Zhelavskaya, I., & Shprits, Y. U. R. I. (2021). A comparison of the location of the mid-latitude trough and plasmapause boundary. Journal of Geophysical Research: Space Physics, 126(4), e2020JA028213.

Wickwar, V. B., & Kofman, W. (1984). Dayside red auroras at very high latitudes: The importance of thermal excitation. Geophysical research letters, 11(9), 923-926.

Witasse, O., Lilensten, J., Lathuillere, C., & Blelly, P. L. (1999). Modeling the OI 630.0 and 557.7 nm thermospheric dayglow during EISCAT-WINDII coordinated measurements. Journal of Geophysical Research: Space Physics, 104(A11), 24639-24655.

Yadav, S., Shiokawa, K., Otsuka, Y., Connors, M., & St Maurice, J. P. (2021). Multi-wavelength imaging observations of STEVE at Athabasca,Canada. Journal of Geophysical Research: Space Physics, 126(2), 2020JA028622.

Yamada, Y., Fukunishi, H., Nakamura, T., & Tsuda, T. (2001). Breaking of small-scale gravity wave and transition to turbulence observed in OH airglow. Geophysical research letters, 28(11), 2153-2156.

Yeh, H. C., & Foster, J. C. (1990). Storm time heavy ion outflow at mid-latitude. Journal of Geophysical Research: Space Physics, 95(A6), 7881-7891.

Yeh, H. C., Foster, J. C., Rich, F. J., & Swider, W. (1991). Storm time electric field penetration observed at mid-latitude. Journal of Geophysical Research: Space Physics, 96(A4), 5707-5721.

Yuan, Z.-G., Deng, X.-H., Zhang, S.-R., Wan, W.-X., & Reinisch, B. W. (2009). F region behavior in the SED plume during a geomagnetic superstorm: A case study. Journal of Geophysical Research, 114(A8), A08303.

Zhao, H., & Zong, Q. G. (2012). Seasonal and diurnal variation of geomagnetic activity: Russell-McPherron effect during different IMF polarity and/or extreme solar wind conditions. Journal of Geophysical Research: Space Physics, 117(A11).

Zou, S., Ridley, A. J., Moldwin, M. B., Nicolls, M. J., Coster, A. J., Thomas, E. G., & Ruohoniemi, J. M. (2013). Multi-instrument observations of SED during 24–25 October 2011 storm: Implications for SED formation processes. Journal of Geophysical Research: Space Physics, 118(12), 7798–7809.

Zou, S., Moldwin, M. B., Ridley, A. J., Nicolls, M. J., Coster, A. J., Thomas, E. G., & Ruohoniemi, J. M. (2014). On the generation/decay of the storm-enhanced density plumes: Role of the convection flow and field-aligned ion flow. Journal of Geophysical Research: Space Physics, 119(10), 8543-8559.

List of Publications

1. **Upadhyay, K.**, Pallamraju, D., & Chakrabarti, S. (2023), Imprint of storm enhanced density in ground-based OI 630.0 nm dayglow measurements, Journal of Geophysical Research: Space Physics, 128, e2023JA031409. https://doi.org/10.1029/2023JA031409

2. **Upadhyay, K.**, & Pallamraju, D. (2024). First daytime red-line emission measurements of the stable auroral red (SAR) arcs. Geophysical Research Letters, 51(3), e2023GL106292. https://doi.org/10.1029/2023GL106292

3. **Upadhyay, K.,** Pallamraju, D., & Chakrabarti, S. (2024). Estimation of downward heat flux into the F-region from the inner-magnetosphere during stable auroral red (SAR) arc events in the daytime obtained using OI 630.0 nm red-line emissions. Journal of Geophysical Research: Space Physics, 129(7), e2024JA032694. https://doi.org/10.1029/2024JA032694

4. **Upadhyay, K.**, Shiokawa, K., Pallamraju, D., & Gololobov, A. (2024). Determination of electron heat flux in the topside ionosphere and its impact on the vertical profile of OI 630.0 nm emission rate during nighttime SAR arcs for different solar activity conditions. Advances in Space Research, 75(6), 4731-4739. https://doi.org/10.1016/j.asr.2024.12.046

5. **Upadhyay, K.**, & Pallamraju, D., Effect of high latitude processes on mid latitude wave dynamics during geomagnetic quiet times. (Manuscript under preparation.)

Presentations at Conferences

1. **Kshitiz Upadhyay**, and Duggirala Pallamraju, "Quantification of sub-auroral electron temperature enhancements affecting the brightness of O(^{1}D) emissions under the influence of plasmasphere-ionosphere coupling in the dayside of the Earth," 3rd Indian Space Weather Conference (ISWC-2024), 05 - 09 October, 2024 held at Indian Institute of Technology (IIT), Roorkee. [Oral]

2. **Duggirala Pallamraju** and Kshitiz Upadhyay, "First ground-based daytime red line observations of stable auroral red arcs and storm enhanced densities — signatures of plasmasphere-ionosphere interactions in the daytime" 45th COSPAR General Assembly, 14 -20 July, 2024, held at Busan, South Korea. (Invited talk; Session C1.1)

3. **Kshitiz Upadhyay** and Duggirala Pallamraju, "Estimation of the downward heat flux in subauroral ionosphere using O(^{1}D) dayglow emissions," National Space Science Symposium (NSSS-2024), 26 February-01 March, 2024 held at Goa University, Goa. [Oral].

4. **Kshitiz Upadhyay**, "Investigations of the Earth's Mid- and High- Latitude Ionospheric processes using science payloads on-board the DISHA-H Aeronomy Satellite Mission," 2nd Indian Space Weather Conference (ISWC-2023), 19-20 October, 2023 held at PRL, Ahmedabad, Gujarat. [Oral]

5. **Kshitiz Upadhyay**, Duggirala Pallamraju, and Supriya Chakrabarti, "Imprint of storm enhanced density in ground-based OI 630.0 nm dayglow measurements," 28th General Assembly of the International Union of Geodesy and Geophysics (IUGG), 11-20 July, 2023 held at Berlin, Germany. [Oral]

6. **Kshitiz Upadhyay** and Duggirala Pallamraju, “Investigation of M-I coupling generated mid-latitude phenomena using ground-based OI 630.0 nm dayglow measurements,” National Conference on Polar Sciences (NCPS)-2023, 16-19 May, 2023 held at National Centre for Polar and Ocean Research (NCPOR), Vasco da Gama, Goa. [Poster]

7. **Kshitiz Upadhyay** and Duggirala Pallamraju, “Neutral Gravity Wave Dynamics Over Mid-Latitudes”, International Symposium on Equatorial Aeronomy (ISEA-16), 12-16 September 2022. [poster]

8. **Kshitiz Upadhyay** and Duggirala Pallamraju, “The O(^{1}D) 630.0 nm dayglow emission variability over Midlatitudes,” 15th Quadrennial Solar-Terrestrial Physics Symposium (STP-15), 21st February – 25th February, 2022. [Oral]

9. **Kshitiz Upadhyay** and Duggirala Pallamraju, “Investigations of mid-latitude upper atmosphere,” 21st National Space Science Symposium (NSSS-2022), 31st January – 4th February, 2022. [Poster]

Recognitions

1. Awarded by the **Young Polar Scientist Award** for the best poster presentation under the theme *'Space Weather and Meteorology'* in the *'National Conference on Polar Sciences*' organized by the National Center for Polar and Ocean Research, held from 16-19 May 2023.

2. Awarded by the **SCOSTEP Visiting Scholar (SVS)-2023** award to visit the '*Institute for Space Earth Environmental Research (ISEE), Nagoya University, Japan*' during the period of October - December 2023.

Publications attached with the thesis

1. **Upadhyay, K.**, Pallamraju, D., & Chakrabarti, S. (2023), Imprint of storm enhanced density in ground-based OI 630.0 nm dayglow measurements, Journal of Geophysical Research: Space Physics, 128, e2023JA031409. https://doi.org/10.1029/2023JA031409

2. **Upadhyay, K.**, & Pallamraju, D. (Jan, 2024). First daytime red-line emission measurements of the stable auroral red (SAR) arcs. Geophysical Research Letters, 51(3), e2023GL106292. https://doi.org/10.1029/2023GL106292

3. **Upadhyay, K.,** Pallamraju, D., & Chakrabarti, S. (2024). Estimation of downward heat flux into the F-region from the inner-magnetosphere during stable auroral red (SAR) arc events in the daytime obtained using OI 630.0 nm red-line emissions. Journal of Geophysical Research: Space Physics, 129(7), e2024JA032694. https://doi.org/10.1029/2024JA032694

4. **Upadhyay, K.**, Shiokawa, K., Pallamraju, D., & Gololobov, A. (2024). Determination of electron heat flux in the topside ionosphere and its impact on the vertical profile of OI 630.0 nm emission rate during nighttime SAR arcs for different solar activity conditions. Advances in Space Research, 75(6), 4731-4739. https://doi.org/10.1016/j.asr.2024.12.046

Check for updates

JGR Space Physics

RESEARCH ARTICLE
10.1029/2023JA031409

Imprint of Storm Enhanced Density in Ground-Based OI 630.0 nm Dayglow Measurements

Kshitiz Upadhyay[1,2], Duggirala Pallamraju[1], and Supriya Chakrabarti[3]

[1]Physical Research Laboratory, Ahmedabad, India, [2]Indian Institute of Technology, Gandhinagar, India, [3]University of Massachusetts, Lowell, MA, USA

Key Points:

- Anomalous enhancement in OI 630.0 nm dayglow emissions was observed during superstorm over mid-latitude location, Boston
- This enhanced dayglow intensity is in simultaneity with increased electron density possibly making it the first daytime storm enhanced density (SED) observations
- Model estimates show the peak emission altitude of dayglow emission shifted to higher altitudes during the SED observation duration

Supporting Information:

Supporting Information may be found in the online version of this article.

Correspondence to:

D. Pallamraju,
raju@prl.res.in

Citation:

Upadhyay, K., Pallamraju, D., & Chakrabarti, S. (2023). Imprint of storm enhanced density in ground-based OI 630.0 nm dayglow measurements. *Journal of Geophysical Research: Space Physics*, *128*, e2023JA031409. https://doi.org/10.1029/2023JA031409

Received 15 FEB 2023
Accepted 14 AUG 2023

Author Contributions:

Conceptualization: Duggirala Pallamraju
Formal analysis: Kshitiz Upadhyay
Funding acquisition: Duggirala Pallamraju, Supriya Chakrabarti
Investigation: Kshitiz Upadhyay, Duggirala Pallamraju
Methodology: Kshitiz Upadhyay, Duggirala Pallamraju
Project Administration: Duggirala Pallamraju
Resources: Duggirala Pallamraju, Supriya Chakrabarti
Software: Kshitiz Upadhyay
Supervision: Duggirala Pallamraju
Writing – original draft: Kshitiz Upadhyay
Writing – review & editing: Kshitiz Upadhyay, Duggirala Pallamraju, Supriya Chakrabarti

© 2023 American Geophysical Union. All Rights Reserved.

Abstract The mid-latitude upper atmosphere is directly affected by the inner magnetosphere through the interactions at the closed geomagnetic field line boundary. Several space weather phenomena associated with magnetospheric-plasmaspheric exchanges can be mapped to mid-latitudes. One such phenomena that occurs over mid-latitudes during geomagnetic storms is the storm enhanced density (SED). So far, storm time ionospheric features have been studied primarily using radar, GPS and in situ measurements. We present high spectral resolution ground-based measurements of OI 630.0 nm dayglow emissions obtained from Boston to investigate thermospheric behavior during both geomagnetic quiet and disturbed times, as these are very sensitive to changes in the ionospheric plasma temperatures, and densities. During a geomagnetic storm on 7–9 Nov 2004 (Kp = 9-), an anomalous enhancement in brightness (>1 kR) was observed in the dayglow for about an hour duration near local sunset (dusk hours), which was not seen on other neighboring days. This enhancement in OI 630.0 nm dayglow observed on 9 Nov 2004 is confirmed to be a SED event as seen from the complimentary datasets, the Millstone Hill incoherent scatter radar (ISR), Defence Meteorological Satellite Program satellite and GPS total electron content. Further, model estimates of OI 630.0 nm dayglow intensities using ISR measured electron/ion temperature and electron densities as inputs show good agreement with our measurements. These results make this study possibly the first report on the daytime optical signatures of SED.

1. Introduction

The Earth's magnetosphere-ionosphere-thermosphere system undergoes various changes during strong geomagnetic disturbances, wherein, the upper atmosphere at high-latitudes experiences most of the changes. The mid-latitude ionosphere also witnesses several space-weather phenomena during geomagnetic disturbances such as, stable auroral red (SAR) arcs (e.g., Baumgardner et al., 2007; Kozyra et al., 1997), Strong Thermal Emission Velocity Enhancements (STEVEs; e.g., MacDonald et al., 2018; Mende et al., 2019; Yadav et al., 2021), sub-auroral ion drift (SAID; e.g., Spiro et al., 1979; Mishin et al., 2017) and storm enhanced density (SED; e.g., Foster, 1993). These phenomena exhibit unique features in plasma density (SED), plasma temperature (SAR, STEVE), and plasma velocity (SAID) etc., which are due to the magnetosphere-ionosphere coupling through closed geomagnetic field lines. Also, the expansion of high-latitude convection cell to sub-auroral latitudes sometimes creates a strong polarization electric field (e.g., Yeh et al., 1991) across the sub-auroral ionosphere. Different energy sources in the upper atmosphere such as, solar EUV radiation, particle precipitation, etc. excite various photochemical reactions, which results in airglow emissions through photoelectron impact, photodissociation, three-body mechanism, and radiative recombination processes (Solomon & Abreu, 1989). The airglow emissions that originate at higher altitudes become good tracers to investigate the ionospheric changes, as these OI 630.0 nm dayglow emissions are very sensitive to any changes in the electron density (e.g., Pallamraju et al., 2001), electron temperature (e.g., Pallamraju et al., 2004), and particle precipitation of varying flux (e.g., Pallamraju et al., 2011), etc. The OI 630.0 nm nightglow emissions have been used in many previous studies of upper atmospheric features during storm times such as, traveling ionospheric disturbances (TIDs) (e.g., Shiokawa et al., 2003), ionospheric plasma blobs (Pimenta et al., 2007), polar cap patches (Hosokawa et al., 2014). With the advent of ground based daytime airglow emission measurements, the observations carried out over middle- and high-latitudes have revealed several new results on the daytime upper atmospheric phenomena, which include, the detection of daytime auroral arcs and magnetospheric cusps (Pallamraju et al., 2001, 2004), daytime aurora over Boston (Pallamraju & Chakrabarti, 2005), and the retrieval of fluxes and energies of particles that produced daytime aurora (Pallamraju et al., 2011). Photochemically produced (without any dynamics) OI 630.0 nm dayglow emissions typically originate at around 230–250 km altitude and, in general, show an increase (decrease)

21699402, 2023, 9, Downloaded from https://agupubs.onlinelibrary.wiley.com/doi/10.1029/2023JA031409 by Physical Research Laboratory, Wiley Online Library on [02/02/2024]. See the Terms and Conditions (https://onlinelibrary.wiley.com/terms-and-conditions) on Wiley Online Library for rules of use; OA articles are governed by the applicable Creative Commons License

in emission intensity from dawn to local noon (local noon to dusk) with a maximum at local noon. We report on a sudden anomalous enhancement in O(^{1}D) dayglow emissions over Boston around dusk for about an hour during a super-geomagnetic storm during 7–9 Nov 2004, as observed by the High-Resolution Imaging Spectrograph using Echelle grating (HIRISE). This sudden enhancement in dayglow emissions appears to be an optical signature of SED during the daytime.

SED is a pre-midnight mid-latitude phenomenon in which the electron density is suddenly increased by a large amount in the topside ionosphere (Foster, 1989) and the peak height of F-layer (hmF_2) is shifted to higher altitudes (Yuan et al., 2009; Zou et al., 2013). These SEDs occur during the initial phase of a geomagnetic storm and are generally associated with a strong polarization electric field and a strong sunward ion velocity (≈1,000 ms^{-1}) (Foster et al., 2002). To understand the evolution and formation of SED, various mechanisms have been proposed. Foster (1993) suggested that the interaction of the expanded equatorward boundary of the high latitude convection cell with the ionosphere over mid-latitudes can produce a SED plume region. Kelley et al. (2004) suggested that the observed enhancement in the plasma density during SED can be due to the plasma flow form pre-midnight region to noon-side by sunward convection. A super fountain effect was also suggested by Mannucci et al. (2005) to be responsible for the SED formation over mid-latitudes. Foster et al. (2007) presented that subauroral polarization electric field interaction over mid-latitudes can take the enhanced SED plasma in poleward direction, and thus forms the poleward streaming SED plume. The SED plumes sometimes can reach to polar regions by forming a tongue of ionisation (TOI) and the formation of TOI in association with convection electric field was investigated by Thomas et al. (2013) for two different SEDs. The SED plumes are suggested to be a signature of the erosion of outer layers of plasmasphere due to subauroral polarization stream (SAPS; Foster & Vo, 2002) electric fields by Foster and Burke (2002). Albeit different mechanisms of SED formation are proposed, these are in some ways associated with the role of ExB drift provided by expanded convection cell (e.g., Heelis et al., 2009; Thomas et al., 2013). The SED structures during geomagnetic storms have been investigated mainly using the GPS-TEC observations (e.g., Foster, 2008, and references therein). In this work, using simultaneous radio datasets from collocated Millstone Hill Incoherent Scatter Radar (ISR) and GPS-TEC, the observed anomalous enhancement in the optical OI 630.0 nm emissions is investigated as a possible signature of SED phenomena over mid-latitudes during daytime. Physics based photochemical GLOW model (Solomon, 2017; Solomon et al., 1988) estimation of the total brightness of OI 630.0 nm emissions, with measured ISR ionospheric values as inputs, show a good match with those observed by the HIRISE.

2. Data

2.1. Optical (OI 630.0 nm Dayglow Emission) Measurements

The OI 630.0 nm (red line) daytime airglow emissions are the primary optical data used in this study and have been obtained using a ground-based instrument called the High-Resolution Imaging Spectrograph using Echelle grating (HIRISE, Pallamraju et al., 2002). Observations were carried out during 7–9 Nov 2004 from Boston (42.36°N, 71.05°W, invariant latitude (Λ) ≈ 53°), a mid-latitude location. HIRISE provided spectral images centered around zenith with field of view (FOV) of about 6°. OI 630.0 nm dayglow emissions from the spectral images of HIRISE have been obtained using the extraction procedure described in detail in Pallamraju et al. (2000, 2002), wherein, the difference between solar and sky spectra obtained at 630.0 nm wavelength region yields the dayglow emission intensity by appropriately estimating the contribution of scattering (or Ring) effect (Pallamraju et al., 2002). The diurnal behavior of dayglow was obtained with 5 min data cadence.

2.2. Millstone Hill ISR/digisonde

The collocated Millstone Hill incoherent scatter radar (ISR) observations of local ionospheric plasma parameters are available at http://millstonehill.haystack.mit.edu/. The ISR data that are available at an interval of around 6.5 min have been used to provide independent information on the ionospheric conditions during the observed anomalous enhancement in the red line dayglow. The location of Millstone Hill ISR has an L-value of around 2.7 (McIlwain parameter; McIlwain, 1961), and sometimes plasmapause comes closer to it during large geomagnetic storms (e.g., Foster et al., 2002). The ISR was operated in the ionospheric mode on 8 and 9 Nov 2004 wherein, vertical profiles of electron density (Ne), electron temperature (Te), ion temperature (Ti) among other ionospheric parameters were available for zenith. Since, ISR data were not available on 7 Nov 2004, the electron

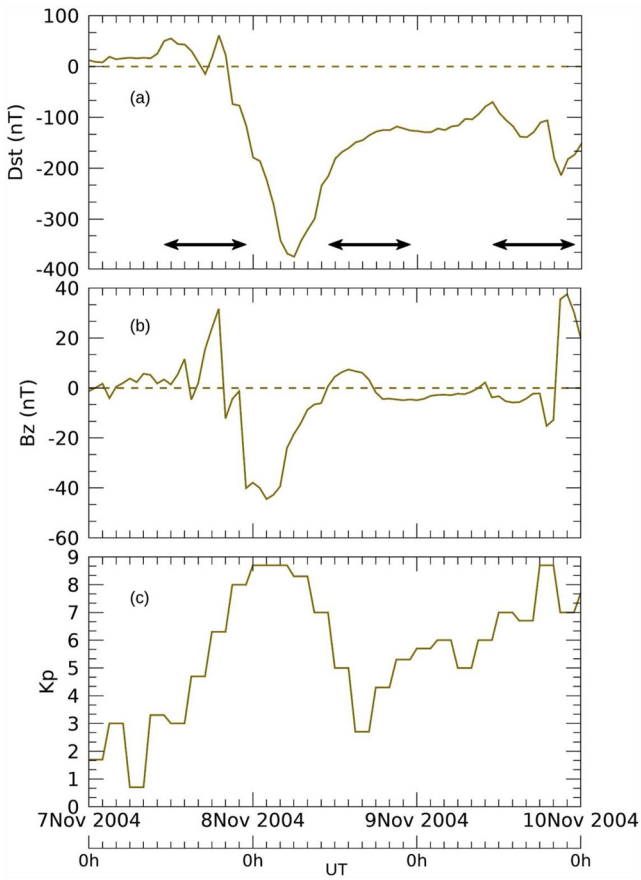

Figure 1. The panels (a)–(c) show the variations in Dst-index, IMF- Bz component, and 3-hourly Kp-index values for the duration of the observation period (7–9 Nov 2004). The horizontal arrows represent the daytime (6–18 LT) on each day. The strong geomagnetic disturbances of Kp = 9- can be seen on 8 Nov (∼1 UT) and 9 Nov (∼20 UT); LT = UT-5 hr.

density data from a Millstone Hill based digisonde have been used. The inversion of digisonde ionograms into electron density profiles were performed using the ARTIST software (Galkin et al., 2008; Reinisch & Xueqin, 1983). The digisonde ionograms are available at a data cadence of 15 min.

2.3. Radio Measurements (GPS/TEC)

To examine the large-scale latitudinal variation in total electron content (TEC) on 9 Nov 2004, we have used the world-wide distributed GNSS (global navigation satellite system) receiver obtained total electron content (TEC) data from Institute for Space-Earth Environmental Research (ISEE), Nagoya University website (https://stdb2.isee.nagoya-u.ac.jp/GPS/shinbori/AGRID2/nc/2004/314/) at 5 min time interval and 0.5° × 0.5° geographic longitude and latitude grid. As SED is usually observed to be generated in the lower mid-latitude regions (Foster, 1993), in this study, a range of 45°N–55°N magnetic latitude (MLAT) has been considered for analysis to ascertain its large-scale temporal evolution over 90°W to 60°W geographic longitude (GLON). For doing so, the longitudinal average of TEC at each corresponding magnetic latitude has been considered.

For obtaining specific variation in diurnal TEC over Boston during the period of interest, a collocated GPS station at Westford, Massachusetts (USA) (42.6°N, 71.4°W, GPS code = WES2) is also used. The GPS station data were obtained from NASA CDDIS website (https://cddis.nasa.gov/Data_and_Derived_Products/GNSS/GNSS_data_and_product_archive.html). The characteristics of GPS TEC and Millstone Hill ISR obtained profiles of electron density have been found to be similar.

2.4. In Situ Satellite Observations

The Defence Meteorological Satellite Program (DMSP) satellites are high-inclination near-polar orbit satellites which provide ionospheric electron temperature, electron density, horizontal and vertical plasma drifts, and precipitating particle information at around 840 km altitude. This space-borne data set was used to provide plasma convection velocities in topside ionosphere.

2.5. Geomagnetic Indices

For the solar-geophysical conditions during 7–9 Nov 2004, the IMF-Bz component, geomagnetic indices (Kp-index, Dst) at 1 hr time interval and the daily-averaged solar flux (F10.7 cm wavelength) measured as 10^{-22}Wm^{-2} Hz^{-1} (sfu; solar flux unit) were obtained from high-resolution OMNI-web (https://omniweb.gsfc.nasa.gov/ow.html) and their variations are shown in Figure 1.

3. Model Emissions

The GLOW model (Solomon, 2017; Solomon et al., 1988) was used to provide the estimates of OI 630.0 nm redline dayglow emission rate. The metastable state O(^{1}D) of atomic oxygen is produced by (a) Photoelectron impact on atomic oxygen (PE), (b) Photo-dissociation of molecular oxygen (PD), and (c) Dissociative recombination of molecular oxygen ions (DR). The radiative lifetime of O(^{1}D) metastable state is ∼110 s where, it can either produce dayglow by emitting radiation at 630.0 nm wavelength or get lost by quenching with nitrogen (N_2), oxygen atom (O) or molecules (O_2). Therefore, under photochemical equilibrium, both production and loss rates are considered to derive the volume emission rate of OI 630.0 nm dayglow ($VER_{630.0}$). The formula to estimate $VER_{630.0}$ at any given height (h) is based on the following equation-

$$\mathrm{VER}_{630.0} = A_{630.0}\left[\frac{P_{\mathrm{PE}}(h) + P_{\mathrm{PD}}(h) + P_{\mathrm{DR}}(h)}{A_{1_D} + \left(k_{N_2}[N_2(h)] + k_{O_2}[O_2(h)] + k_O[O(h)]\right)}\right]. \quad (1)$$

21699402, 2023, 9, Downloaded from https://agupubs.onlinelibrary.wiley.com/doi/10.1029/2023JA031409 by Physical Research Laboratory, Wiley Online Library on [02/02/2024]. See the Terms and Conditions (https://onlinelibrary.wiley.com/terms-and-conditions) on Wiley Online Library for rules of use; OA articles are governed by the applicable Creative Commons License

21699402, 2023, 9, Downloaded from https://agupubs.onlinelibrary.wiley.com/doi/10.1029/2023JA031409 by Physical Research Laboratory, Wiley Online Library on [02/02/2024]. See the Terms and Conditions (https://onlinelibrary.wiley.com/terms-and-conditions) on Wiley Online Library for rules of use; OA articles are governed by the applicable Creative Commons License

where, P denotes the production of O(^{1}D) for different aforementioned production mechanisms, $A_{630.0}$ is the Einstein's transition coefficient for O(^{1}D) state, k_x denotes quenching rates by atmospheric species ($x = N_2$, O_2 and O), and A_{1D} is Einstein transition probability to account for branching. The details of various coefficients can be found in GLOW model (Solomon, 2017). By providing the height dependent plasma and neutral densities, the $VER_{630.0}$ is calculated. For neutral gas profiles in the thermosphere, GLOW model uses the Naval Research Laboratory Mass Spectrometer Incoherent Scatter (NRLMSIS-00) atmosphere (Picone et al., 2002) as inputs, whereas the International Reference Ionosphere (IRI-90) (Bilitza, 1990) model for the ionospheric electron and ion densities and electron/ion temperatures.

In our study, altitude profiles of the IRI estimated Ne, Te, and Ti were replaced with those measured by ISR during the times when ISR data were available. Using these altitude profiles, vertical profiles of volume emission rates (VER) of 630.0 nm emissions were obtained using the estimation described above (Equation 1). These volume emission rates are vertically integrated to obtain the total column brightness of 630.0 nm emissions which were then compared with the ground-based column integrated dayglow emission measurements by HIRISE.

An empirical model given by Shepherd and Cho (2021) developed using the OI 630.0 nm dayglow data obtained from WIND imaging interferometer (WINDII) on board the Upper Atmospheric Research Satellite (UARS) is also used. WEM predicts the 630.0 nm dayglow emission intensity (I) for a given day using the following equation:

$$\ln(I) = 5.237 + 0.212 \times \mathrm{Cos}^2\chi + 1.664 \times \mathrm{Cos}^{0.5}\chi + 0.072 \times (\ln F10.7)^2. \quad (2)$$

where, F10.7 is the solar flux on that day and χ is solar zenith angle (in degrees) a given time at a given location. Therefore, WEM (Equation 2) predicts the temporal behavior of O(^{1}D) dayglow emissions for a given location.

4. Observation and Results

It can be seen from the production mechanisms for the red line dayglow described in Section 3 that the PD and PE mechanisms are dominant contributors during daytime and are solely solar flux and solar zenith angle dependent, whereas the DR mechanism depends on the electron and O_2^+ densities. Therefore, any temporal variation in plasma density (greater than ~12 min; Brunt–Väisälä period) in the ionosphere-thermosphere region gets imprinted in the variability of dayglow emission rates. The height of the peak electron density during geomagnetic quiet-times typically lies in the range of 230–250 km in daytime. During storms, perturbations in the electric field or/and winds can lift the plasma to higher (lower) altitudes, resulting in a decrease (increase) in the electron density in the bottom side ionosphere. Therefore, if the electron density decreases, it can be considered that the OI 630.0 nm emission intensity will also decrease. In this work, we report on an anomalous enhancement in the observed dayglow intensity during storm-time that was caused by a significant increase in electron density at altitudes above 300 km. We also present the corresponding associated ionospheric features with their diurnal variation, which show a clear relationship with storm enhanced electron density over mid-latitudes.

Figure-1 shows the geomagnetic conditions during the 7–9 Nov 2004, with Dst, IMF Bz, and Kp indices. The solar flux on these days varied in the range of 120–140 sfu (1 sfu = 10^{-22}Wm^{-2} Hz^{-1}). A strong full halo coronal mass ejection (CME) occurred on 7 Nov 2004 at 1726 UT (LT = UT-5 hr), as observed by SOHO/LASCO. The interaction of CME sheath plasma with magnetopause caused a huge perturbation in Earth's geomagnetic field. A sudden storm commencement was observed on 7 Nov 2004 at around 19 UT (14 LT) with the Dst reaching +60 nT, as shown in Figure 1a, followed by the onset of the main phase of the storm with the Dst minimum dropping to around −370 nT at 6 UT (1 LT) on 8 Nov 2004, making this event into a category of superstorm. Another major disturbance was noted on 9 Nov 2004, when a sudden strong negative excursion in IMF Bz at 20 UT (15 LT), as shown in Figure 1b, caused a large decrease in the induced magnetic field on the ground with the Dst again dropping down to a value of around −210 nT. From Figure 1c, it can be noted that the maximum value of Kp-index was 9- during 2–4 UT on 8 Nov 2004 and 18–20 UT (13–15 LT) on 9 Nov 2004, indicating the severity of the storm. The IMF Bz was −12 nT at 20 UT (15 LT) and turned to 35 nT after an hour at 21 UT (16 LT) on 9 Nov 2004. This northward turning of the IMF Bz after 21 UT on 9 Nov 2004 reduced the geoeffectiveness of the storm.

HIRISE images provide dayglow intensity in arbitrary data unit/Analog to Digital units (ADU). To convert the emission intensity from ADU to Rayleigh, WEM model predicted emissions are used. During geomagnetically

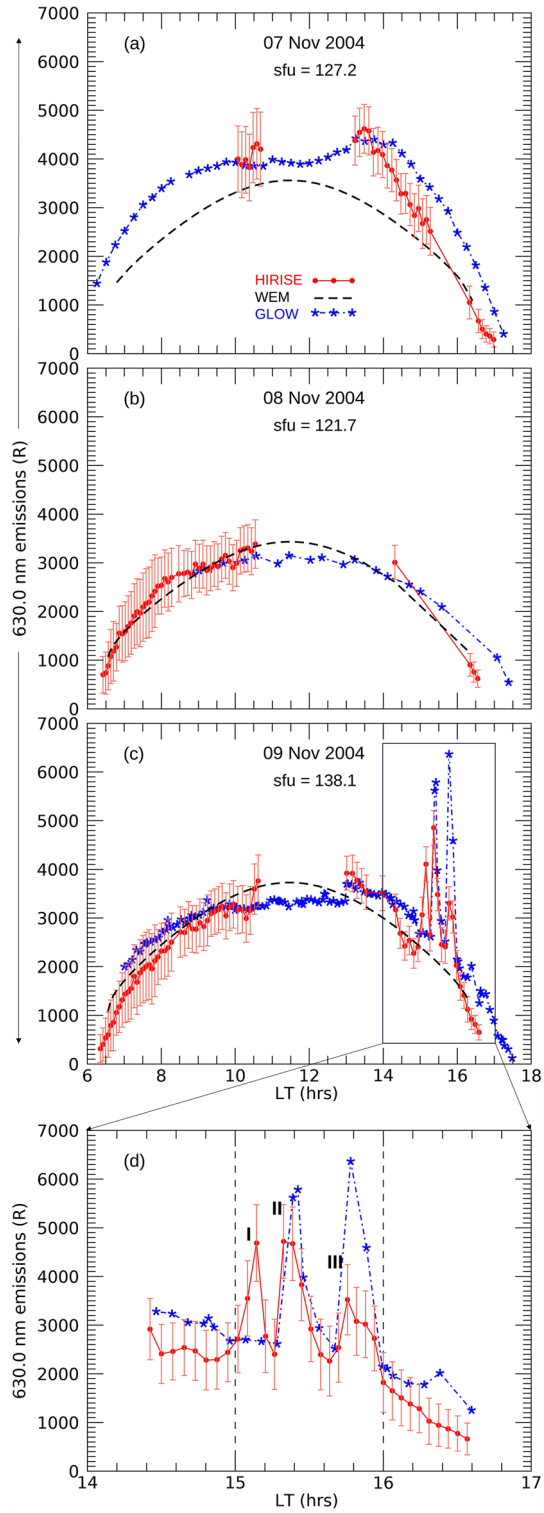

Figure 2. Diurnal variation of observed OI 630.0 nm dayglow emission intensity (along with ±1σ values) as measured by HIRISE (red dots) over zenith (FOV ≈ 6°), estimated by GLOW-model estimates (blue asterisks), and by WEM predictions (black dashed line) are shown. Panels (a)–(c) show the variations corresponding to 7, 8, and 9 Nov 2004. Panel (d) shows the zoomed-in plot of dayglow variation for 9 Nov during 14–17 LT at a higher data cadence of ∼4 min.

quiet times, the diurnal behavior of WEM estimates, which consider only the solar flux and solar zenith angle values as inputs, match well with that of the ground-based measurements. Thus, in this work, the intensity (ADU) obtained by HIRISE have been scaled with the WEM predictions for geomagnetically quiet periods, when the dayglow emissions are considered to be governed only by photo chemistry, to obtain the dayglow emission rates in Rayleighs. Thus, the three panels (a)–(c) in Figure 2 show the HIRISE measured O(^{1}D) dayglow emissions in Rayleighs (red dots) along with ±1σ values for 7, 8, and 9 Nov 2004. On 9 Nov, due to larger signal strength near 15 hr, the dayglow variations were reanalyzed at a slightly higher data cadence (∼4 min, exposure: 200 s) for specific period of 14–17 LT, as shown in Figure 2d. The missing data before 10 LT and during 14–16.2 LT on 7 and 8 Nov are due to the presence of clouds in the field of view of HIRISE. The noon time dayglow data were not available, as the presence of direct sunlight overhead causes saturation in HIRISE images. The WEM O(^{1}D) emission estimates for all the days corresponding to their solar flux values are also shown in Figure 2 as black dashed line along with the observed O(^{1}D) emissions. It may be noted that on 8 and 9 Nov the measured values match well with those of WEM until 14.5 LT. On 7 Nov, the measurements show larger values than the WEM estimates. Such differences can occur if the electron densities are larger on this geomagnetically disturbed day. Therefore, on this day we considered the measured electron densities from a collocated digisonde and corresponding ionic composition as predicted by the IRI model for the given values of measured electron density, as inputs to the GLOW model. The resulting output is shown in Figure 2 as the line joining blue asterisks. It can be noted that the GLOW model output matches better with the measurements as compared to the WEM estimates, indicating that indeed the larger electron densities on this day contributed significantly in increasing the red line dayglow emission intensities. The agreement is not perfect, however, which could be due to approximations in the estimation in altitude profile of electron density above peak F_2 height of the F-region. Incidentally, as also mentioned above, on 8 and 9 Nov Millstone Hill ISR data were available and so altitude profiles of the measured plasma parameters in the range of 90–800 km have been used as inputs into the GLOW model. It can be seen that, on all these days the GLOW model estimates match well with the HIRISE measured emissions, except during 14.5–16 LT on 9 Nov, when sharp excursions are seen in both the measured and estimated emissions (although with some differences in magnitudes). The ISR data used corresponds to the mean azimuth and elevation angles of 178° and 88°, which are very close to the zenith of HIRISE field of view. Nevertheless, there could be a mismatch in the co-volume corresponding to both these measurements, which can contribute to the small differences in the magnitudes of HIRISE measured, and estimated emissions using ISR data. A clear enhanced emission peak of intensity of more than 1 kR in the O(^{1}D) dayglow emissions is observed near the dusk time (at ∼15 LT) for about an hour. Note that there are three peaks I, II, and III in the HIRISE observations at 15.16, 15.37, and 15.78 LT, respectively. The model emissions match with the measurements at two peaks (II and III).

In order to identify the cause for such sudden enhancements in the dayglow, the altitude profiles of Ne, Te, and Ti on 9 Nov 2004 as a function of time were investigated (Figure 3). The top, middle and the bottom rows show the variations of Te, Ti, and Ne, respectively. The left two columns show the diurnal variation of all profiles of 8 and 9 Nov 2004. The rightmost column shows the comparison in these parameters (Te, Ti, and Ne) for these two

21699402, 2023, 9, Downloaded from https://agupubs.onlinelibrary.wiley.com/doi/10.1029/2023JA031409 by Physical Research Laboratory, Wiley Online Library on [02/02/2024]. See the Terms and Conditions (https://onlinelibrary.wiley.com/terms-and-conditions) on Wiley Online Library for rules of use; OA articles are governed by the applicable Creative Commons License

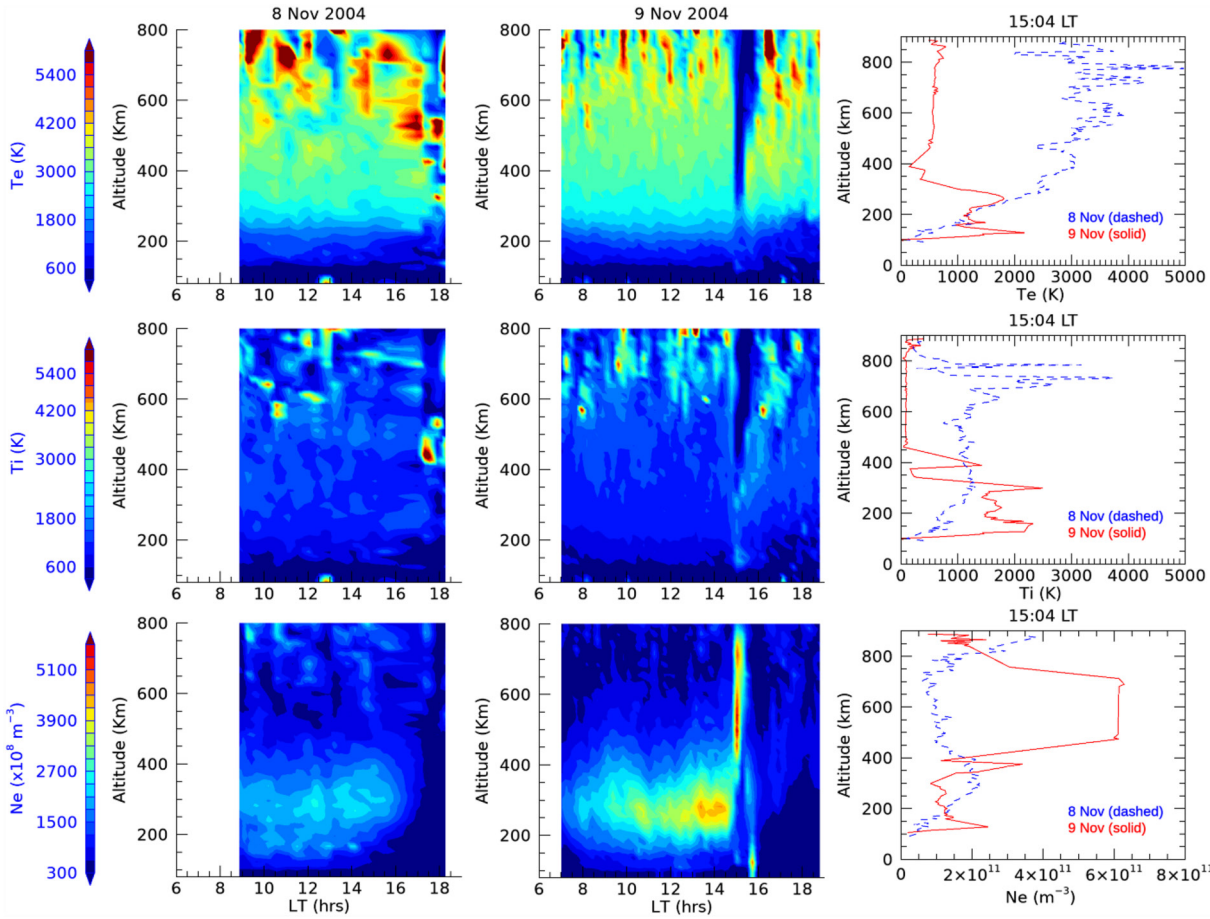

Figure 3. The left two columns show the local time variation of altitude profiles of Te (top), Ti (middle) and Ne (bottom), as measured by the Millstone Hill ISR on 8 and 9 Nov 2004. The third column shows the comparision of these parameters at 15:04 LT, which is the time of major geomagnetic disturbance observed on the 9 Nov 2004.

days, around 15 LT when large enhancements were observed in the OI 630.0 nm dayglow measurements (shown in Figure 2). A decrease by a factor of 1.2 in electron density was observed in the altitude region of 200–400 km on 9 Nov in comparison with that of 8 Nov, whereas, at altitudes greater than 400 km, an increase by a factor of 4–5 is seen. This indicates a shift in the peak of F-layer to higher altitudes (400–700 km). Similarly, a large reduction in electron and ion temperature at altitudes greater than 400 km can be seen on 9 Nov in comparison to that on 8 Nov at 15 LT.

The F-layer plasma height can change (increase/decrease) dramatically, depending on the strength of the electric field (eastward/westward) which causes ExB drift (Rishbeth, 1977). Also, mid-latitude phenomena like SAR arcs can cause an enhancement in Te which can results in enhancements in the O(^{1}D) emission magnitudes in the altitudes around 400 km during geomagnetic disturbances. In order to investigate that, an average of Ne, Te, and Ti in the altitude range of 200–450 km, has been considered for further study (Figure S1 in Supporting Information S1). It has been noted that at 15 LT there is a sudden decrease in the average electron density and electron temperature, while there is an increase in the average ion temperature up to 3000 K on this day. The average electron temperature decreased by a factor of 2, while the ion temperature was enhanced by about the same factor. Simultaneous reduction in electron density, a decrease in electron temperature, and an increase in ion temperature in the bottom side ionosphere– all of them indicate to an upward lift in the F-region plasma, which can be due to wind and/or eastward electric field. However, as the effect of winds on the F-layer height is expected to be gradual in nature in comparison to the sudden enhancement observed in this case, the role of eastward electric field has been investigated. It is known that during geomagnetic disturbances, high latitude electric fields may penetrate promptly into the sub-auroral ionosphere. To examine the role of this effect, we reviewed the electric field based on the simultaneous ISR measurements. A strong eastward electric field of ~10 mV-m^{-1} was

21699402, 2023, 9, Downloaded from https://agupubs.onlinelibrary.wiley.com/doi/10.1029/2023JA031409 by Physical Research Laboratory, Wiley Online Library on [02/02/2024]. See the Terms and Conditions (https://onlinelibrary.wiley.com/terms-and-conditions) on Wiley Online Library for rules of use; OA articles are governed by the applicable Creative Commons License

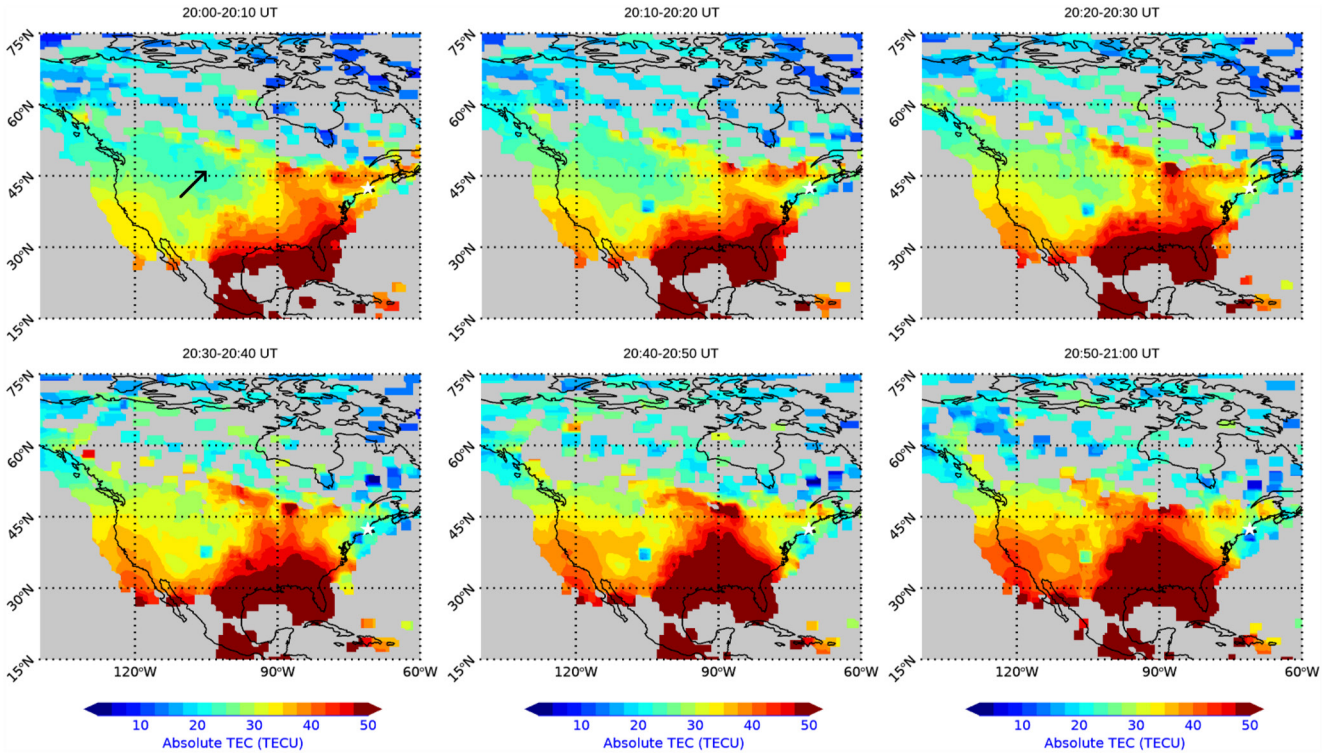

Figure 4. The TEC maps involving 5-min integration during the period of observed enhancement in dayglow that is, 20–21 UT (15–16 LT) on 9 Nov TEC from Movie S1. White star indicates the observation location, Boston (42.36°N, 71.05°W). The black arrow at 20 UT (15 LT) signals the onset of enhanced density plume.

detected at 15 LT on 9 Nov 2004, which was the strongest on that day. Therefore, it is inferred that the prompt penetration of high latitude electric field in the sub-auroral ionosphere provided the strong ExB drift that lifted the plasma up, resulting in an increase in the peak height of the F-region. Further, a strong upward ion velocity during 15–16 LT at all altitudes was observed by ISR, causing a reduction in the plasma density at altitudes below 300 km. The thermal conduction among fast moving ions most likely caused an increase in the ion temperature. The magnitudes of ion temperature are generally lower than the electron temperatures in the F-region altitudes due to their heavier mass, but in this case, a strong upward ion velocity provided sufficient kinetic energy to the ions that raised their temperatures to values greater than those in the bottom side F-region. However, unlike electron temperature ion temperatures do not play any role in the production of 630.0 nm emission rates (e.g., Torr et al., 1976; Alge et al., 1983). Since there was a significant reduction in the electron temperature at all altitudes above 300 km (Figure 3), the enhancements in the dayglow intensities observed during 15–16 LT are inferred to be directly caused by the enhancements in the observed electron densities in the ionosphere above 400 km. A sudden enhancement in the electron density at higher altitudes and an increase in hmF_2 associated with strong sunward convection, are some of the characteristics of the mid-latitude phenomenon SED (Foster et al., 2005; Huang et al., 2005). In earlier studies, mainly GPS-TEC data were used to study the SED over the mid-latitudes (e.g., Foster, 2008; Zou et al., 2014). Therefore, in order to verify the same in this study as well, the variations in TEC over North America during the observation period were examined using 2D TEC maps. The absolute TEC variations on 9 Nov 2004 with 5 min temporal resolution is shown by Movie S1. Here, we present the TEC maps on 9 Nov involving 5-min integration (Figure 4) during the period of observed enhancement in dayglow that is, 15–16 LT (20–21 UT). It can be noted from top row of Figure 4 that an enhanced density plume (shown by an arrow) is formed at 20 UT over Boston (white star) and undergoing a sunward movement under the influence of the 2-cell pattern over the magnetosphere which had expanded until mid-latitude at this time. In addition to the SED plume, the bottom row of Figure 4 clearly depicts a large increase in TEC with time over mid-latitudes. Since, due to sparse GPS receivers at high latitudes, TEC maps do not contain enough data points at those latitudes. Therefore, data of half hour duration 20:00–20:30 UT (15:00–15:30 LT) is combined to give a comprehensive picture of the SED structure, as shown in Figure 5 (Note the change in the colorbar range from that used in Figure 4). From Figure 5, it can be seen clearly that the observation location (white star symbol) is in

21699402, 2023, 9, Downloaded from https://agupubs.onlinelibrary.wiley.com/doi/10.1029/2023JA031409 by Physical Research Laboratory, Wiley Online Library on [02/02/2024]. See the Terms and Conditions (https://onlinelibrary.wiley.com/terms-and-conditions) on Wiley Online Library for rules of use; OA articles are governed by the applicable Creative Commons License

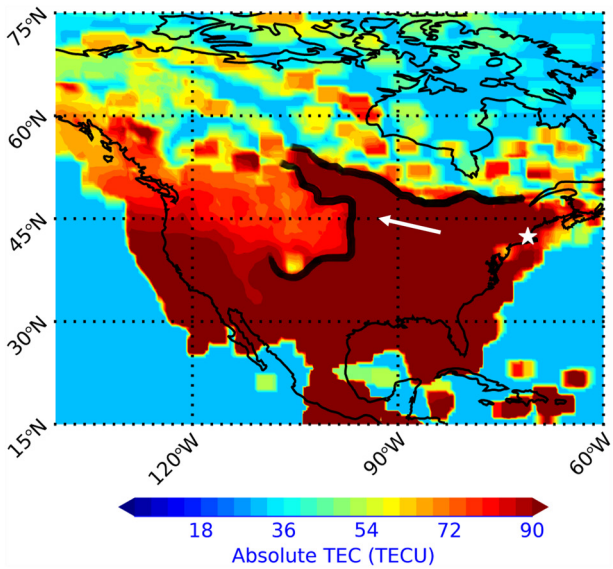

Figure 5. 2D TEC map for 9 Nov obtained by integrating the TEC for a half hour duration (15:00–15:30 LT). The white arrow represents the direction of motion of SED plume, which is sunward. The white star indicates the observation location, Boston.

the midst of the structure associated with the SED. A sharp gradient in SED plume formed over mid-latitudes is indicated by white arrow and thick black lines. Zou et al. (2014) showed that the SED plumes can attain various range of TEC enhancements from ∼1.4 to 5.5 times than their quiet time values. Therefore, the local time variation in the absolute TEC over mid-latitudes on 9 Nov along with those of quiet days (5–6 Nov, 13–14 Nov) as obtained in the 45°N to 55°N magnetic latitude range has been shown in Figure 6. The black dash-dot lines show the variations in TEC on four quiet days at each degree magnetic latitude from 45° to 55°N. The solid red lines represent the variations in TEC for 9 Nov 2004 (disturbed day). It can be seen that until 10 LT, the temporal TEC variation on 9 Nov (solid red), was almost similar to those seen on the quiet days but was lower than those on the quiet days from 10 to 15 LT. However, after 15 LT, a clear enhancement in the TEC in ∼45°–55°N magnetic-latitude range can be seen on 9 Nov 2004, which is in clear contrast to those on the quiet days. Such sudden increase in TEC after 15 LT that is, during dusk hours associated with IMF southward Bz component has been observed during geomagnetic storms. This storm enhanced TEC over mid-latitude during the dusk hours has been referred to as the "dusk effect" (Evans, 1970; Mendillo et al., 1970). The comparison of TEC on 9 Nov with other quiet days (5–6 Nov, 13–14 Nov) shows ∼1.25 times increase, which is close to the lower end of the range of 1.4 times that Zou et al. (2014) reported.

5. Discussion

To interpret the effect of high-mid latitude coupling, we investigated the variation in the rate of change of TEC index (ROTI; 10^{16} electrons m^{-2} min^{-1}; Pi et al., 1997) over North America on 9 Nov. This is shown by Movie S2 and the stills from Movie S2 during 14–17 LT (19–22 UT) at half an hour interval are shown here in Figure 7. During the period of 15–16 LT, a large increase in ROTI extending over all longitudes of North America and reaching observation location (Boston; white star) at 15 LT (20 UT) can be seen. This enhanced region remained persistent for about an hour (20–21

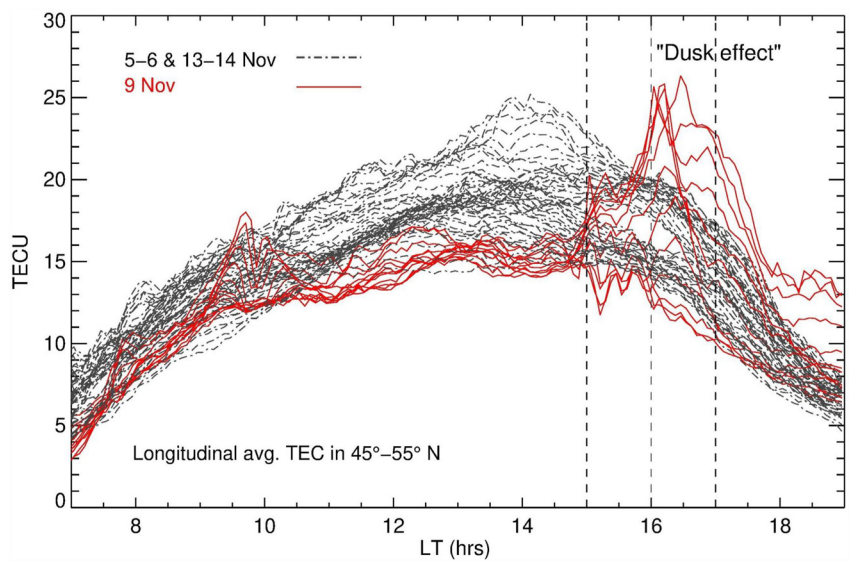

Figure 6. The GPS-TEC temporal variation in the mid-latitude range 45°–55° MLAT within 90°W to 60°W geographic longitude. Different lines represent the TEC variation for different magnetic latitudes separated by 1° in the range of 45°N–55°N. The black dashed lines represent the two quiet days before (5–6 Nov) and after (13–14 Nov) the storm day (9 Nov), while the solid red lines correspond to the variation on the storm day. A clear enhancement in TEC in the 45°–55°N MLAT range can be seen in evening hours (15–17 LT), which illustrates the "dusk effect."

21699402, 2023, 9, Downloaded from https://agupubs.onlinelibrary.wiley.com/doi/10.1029/2023JA031409 by Physical Research Laboratory, Wiley Online Library on [02/02/2024]. See the Terms and Conditions (https://onlinelibrary.wiley.com/terms-and-conditions) on Wiley Online Library for rules of use; OA articles are governed by the applicable Creative Commons License

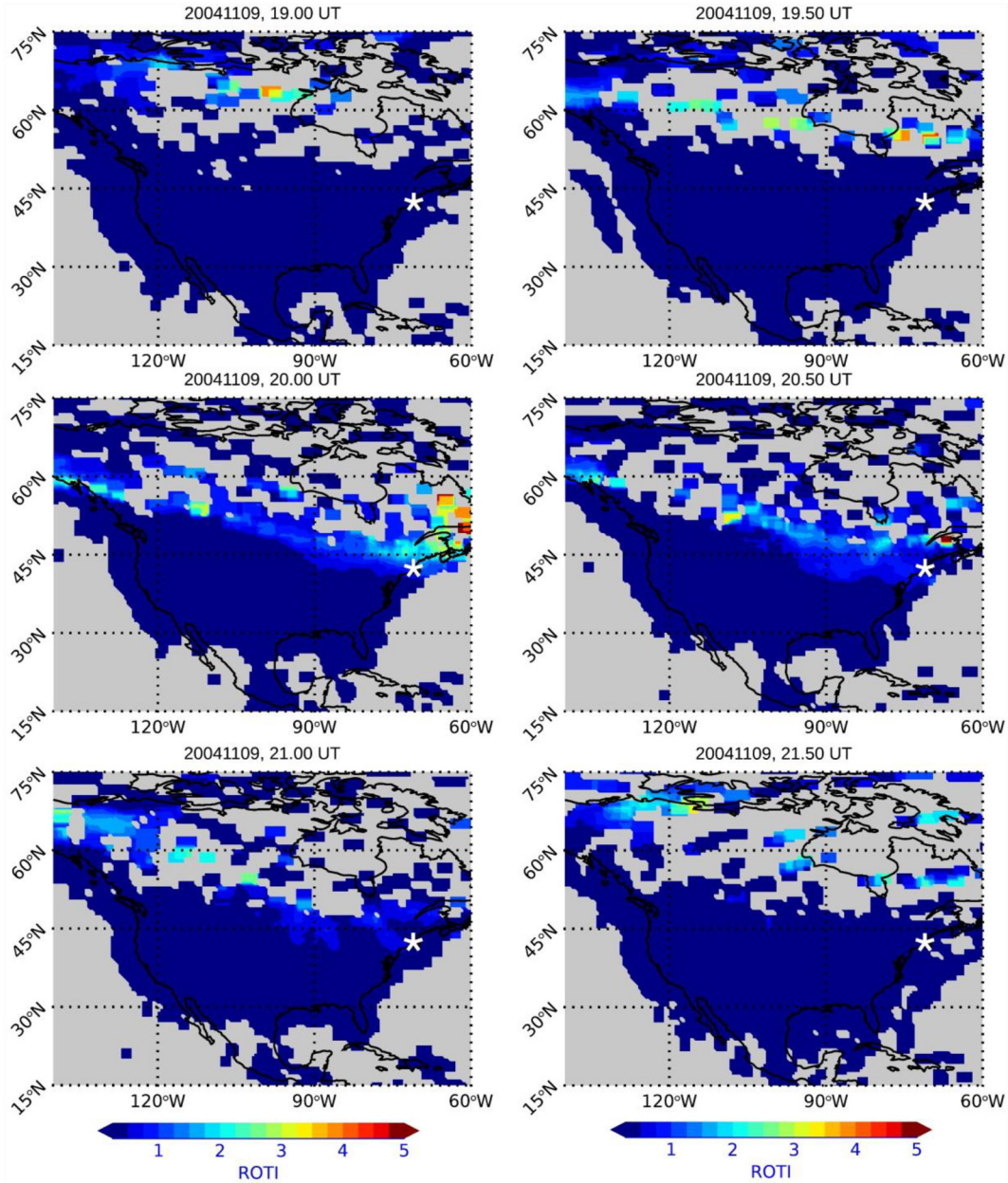

Figure 7. ROTI maps over North America on 9 Nov 2004 during 19–22 UT at half an hour interval. The white star symbol represents the observation location, Boston.

UT) over observation location in association with the second main phase of the storm. This region manifests the expansion of equatorward boundary of two cell pattern to lower latitudes, which is associated with SAPS (sub-auroral polarization streams) electric fields. Therefore, it is inferred that high latitude convection cell pattern was expanded to mid-latitudes. The rapid equatorward movement from high to mid latitudes was in association with southward IMF Bz during 20–21 UT (15–16 LT) and was thereby present over the observation field of view for an hour. To examine the flow of plasma convection, we considered DMSP data during 20–21 UT. The Figure 8a shows the closest DMSP-F14 pass (thick red line) at 21.09 UT (16.09 LT) over enlarged ROTI map at 21.08 UT (16.08 LT). The two dashed white lines represent the 40° and 60°N MLAT and intersect the F14 pass at point P1 and P2. A fast horizontal ion drift (Vy) of ∼1 km-s^{-1} in sunward direction was observed by DMSP (Figure 8b) between P1 and P2 region (marked by black dashed line). As SAPS are also associated with sunward moving fast ions, thus the presence of SAPS electric field in the overhead ionosphere is found to be responsible

21699402, 2023, 9, Downloaded from https://agupubs.onlinelibrary.wiley.com/doi/10.1029/2023JA031409 by Physical Research Laboratory, Wiley Online Library on [02/02/2024]. See the Terms and Conditions (https://onlinelibrary.wiley.com/terms-and-conditions) on Wiley Online Library for rules of use; OA articles are governed by the applicable Creative Commons License

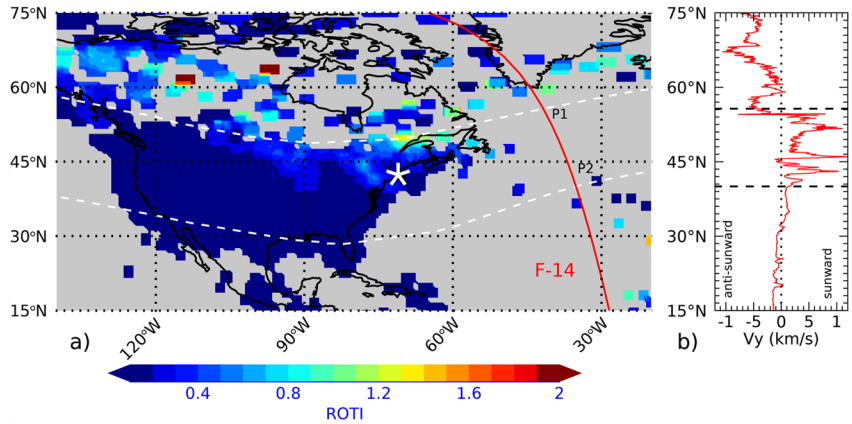

Figure 8. (a) The enlarged ROTI map (with changed colorbar to highlight the variation) upto 20°W showing the ground track of DMSP-F14 (red line) at 21.08 UT (16.08 LT). The two white dashed line represent the 40° and 60° N MLAT which intersect the DMSP pass at P1 and P2. (b) DMSP observed horizontal ion velocities (positive is sunward) between P1 and P2 region (black dashed line). This region can be seen having fast plasma flow (~1 km-s^{-1}) in sunward direction.

in providing the ExB vertical drift and therefore, the increased hmf_2, as observed in the ISR measured altitude profiles of electron density during the storm main phase on 9 Nov.

If we consider the altitude variation in Ne, Te, and Ti (Figure 3), we find that in the case of 8 Nov, these parameters do not show any abnormal behavior. However, on 9 Nov, a striking change from the general temporal behavior is observed for around 1 hr near dusk. An elevated height of hmF_2 causes enhancement in the electron density (~by a factor of 4–5) at higher altitudes (Figure 3). The F-peak was in the altitude range 250–300 km, which suddenly increased in about 15 min to 450–550 km altitude around 15 LT, during the period of main phase of the storm on 9 Nov. As discussed, this shift in hmF_2 by around 200 km to higher altitudes is found to be associated with the SAPS electric field. The F region maximum electron density (N_mF_2) was found to be 2.3×10^{11} m^{-3} at 15 LT on 8 Nov and 6.28×10^{11} m^{-3} on 9 Nov around same local time, indicating an enhancement by a factor of about 2.7. The enhanced density caused the peaks I, II, and III in the dayglow. There is a good match between the measured and estimated magnitudes of the red line dayglow for II and III, however, the dayglow peak (I) is underestimated in the model emissions. This is because, as seen in Figure 3 (rightmost panel), the ISR measured electron density showed a saturation in the altitude region of 400–600 km. The true values of electron densities at this time are much larger than the other times, including those at II and III, as no such saturation was observed at other times. Thus, although the model estimates do not show it, the redline emissions as observed in HIRISE at the time of peak I are indeed due to SED phenomena. From the altitude profile of electron temperature, it can be seen that there was a decrease in Te by more than 2000 K above 300 km in the F-region during the period of enhanced emissions on 9 Nov in comparison with 8 Nov, while the ion temperature shows an enhancement (~700 K) in the bottom side F-region only. However, at higher altitudes (above 300 Km) Ti shows a reduction. Earlier studies (e.g., Seo et al., 1997) have shown that energetic particle precipitation (<200 eV) can increase ionospheric electron temperature by 1000 K or more. The electron temperature measured on 9 Nov was only around 700 K, thereby, indicating no effects of particle precipitation of low energies. We therefore, conclude that the elevated TEC values observed are due to the transport of plasma convected from the post-dusk sector to the dayside associated with the strong sunward convection (Foster et al., 2002). The ROTI variations show that as the storm progressed, the convection cell expanded equatorward and reached latitude of Boston during 15–16 LT. The interaction of the overhead ionosphere with sunward and equatorward convecting plasmaspheric density resulted in a greater build-up of total electron content after 15 LT. Increased hmF_2, reduced electron temperature, large convection cell pattern and increased TEC over mid-latitudes in the afternoon sector, are some of the characteristics of the SED (Foster et al., 2007; Zou et al., 2014, and references therein). The effect of altitude variation in electron temperature during SED phenomena is found to be different, which could be, either a reduction or enhancement of Te in topside ionosphere (Zou et al., 2013) and all of these are seen in the present case. Figure 3 shows similar Te variation as described in Zou et al. (2013), however, ion temperature typically shows the same altitude variation as electron temperature, but with a drastic drop at higher altitudes (>400 km). The GPS-TEC and Millstone Hill ISR data together affirm the observed anomalous enhancements in the dayglow

21699402, 2023, 9, Downloaded from https://agupubs.onlinelibrary.wiley.com/doi/10.1029/2023JA031409 by Physical Research Laboratory, Wiley Online Library on [02/02/2024]. See the Terms and Conditions (https://onlinelibrary.wiley.com/terms-and-conditions) on Wiley Online Library for rules of use; OA articles are governed by the applicable Creative Commons License

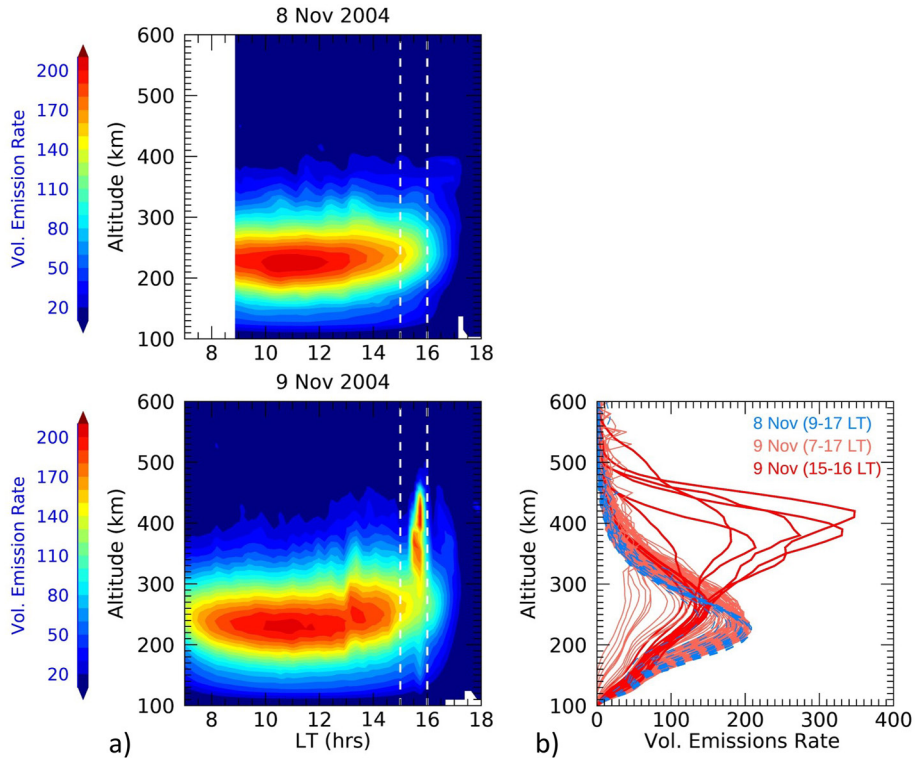

Figure 9. (a)The OI 630.0 nm volume emission rates (VER) as a function of time, as estimated by the GLOW model using as inputs the ISR measured Ne, Te, and Ti data. The 9 Nov VER in panel (b) clearly shows a shift in peak emissions to higher altitudes (up to 420 km) during 15–16 LT (thick red lines).

brightness to be a consequence of storm enhanced density phenomena over mid-latitudes. The enhanced dayglow brightness near dusk time (15–16 LT) was due to an increased N_mF_2, as O(^{1}D) dayglow emission intensity variations are shown to be in accordance with those of F-region electron density (Pallamraju et al., 1996, 2004, 2010). To investigate the altitudinal effects of ionospheric parameters on O(^{1}D) dayglow emissions, we used the ISR measured Ne, Te, Ti profiles and estimated volume emission rates as a function of altitude and local time in the GLOW model for 8 and 9 Nov (Figure 9a). Figure 9b shows the VER as a function of altitude for the two days at different times. It is clearly seen that during 15–16 LT the emissions enhance up to 1.5 times of the peak production of ~200 photons-cm^{-2}-sec^{-1}. Further, during the period of observed enhancements in emissions, the peak production altitude of 630.0 nm emission is shifted to greater than 300 km, similar to the ISR measured electron density (Figure-3). It is to be appreciated that the mechanism of dissociative recombination of O_2^+ is of two stages process, wherein first there is a charge exchange between O^+ and O_2 to form O_2^+. As in the present case, Ne increases at higher altitudes, charge conservation demands that there is a corresponding enhancement in O^+. These enhanced densities of O^+ and Ne by the power of 2 compensate more than enough for the decrease in O_2 by a factor of 1/*e* for about a scale height at higher altitudes compared to those at the lower ones. Further, due to relatively smaller densities of Nitrogen molecules [N_2], the quenching of the O(^{1}D) state is negligible at these altitudes. All of these factors contribute in a higher yield of OI 630.00 nm emissions. Hence, all the discussions above confirm that the observed enhancement in the dayglow is primarily due to the storm enhanced electron density. Furthermore, to ascertain this even further, we carried out spectral analysis on observed and modeled dayglow emissions along with those of TEC. The residuals obtained by subtracting the 3-hr running average from dayglow and TEC were subjected to Lomb-Scargle spectral analysis. The corresponding variations are shown in Figure 10a with their residuals. The dayglow measurements from HIRISE and GLOW model are shown in top and middle panels, while the IGS-TEC data from a collocated GPS receiver at Westford (USA) on 9 Nov is shown in the bottom panel of Figure-10a. In order to avoid the TEC contribution from slant angles, the data considered were restricted to elevation angles greater than 60° and in the ±3° range centered at the latitude of Boston. The reanalyzed dayglow with higher data cadence (Figure 2d), on 9 Nov was used for this analysis.

21699402, 2023, 9, Downloaded from https://agupubs.onlinelibrary.wiley.com/doi/10.1029/2023JA031409 by Physical Research Laboratory, Wiley Online Library on [02/02/2024]. See the Terms and Conditions (https://onlinelibrary.wiley.com/terms-and-conditions) on Wiley Online Library for rules of use; OA articles are governed by the applicable Creative Commons License

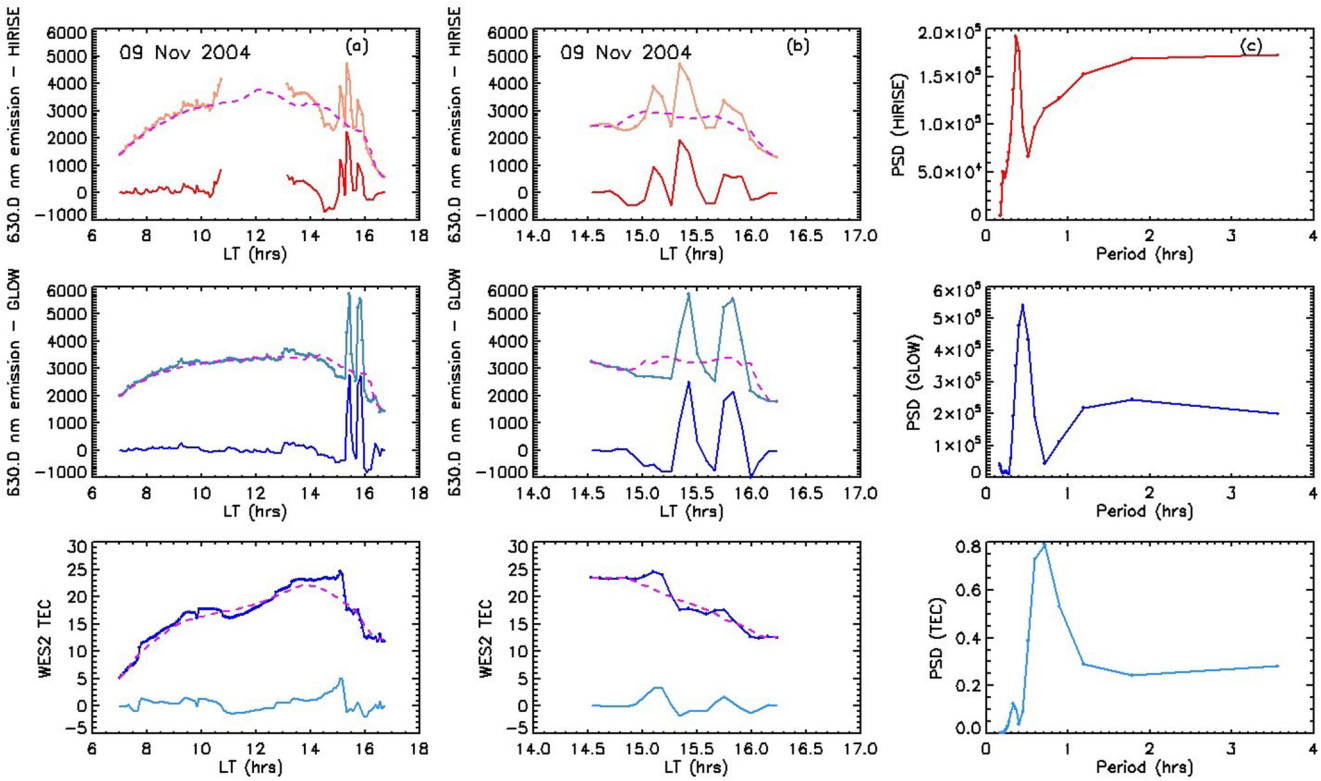

Figure 10. HIRISE observed dayglow (top row), GLOW estimated dayglow (middle row), and TEC (bottom row) are shown. The 3-hr running average was taken (dashed line) and the residuals thus obtained (with zero mean) are also shown in these panels. The left column shows the diurnal profile of these parameters, middle column shows the variation of these parameters near one hour of major disturbances (15–16 LT ± 0.5 hr), and the right column shows the presence of periodicity of about 30 min in both dayglow (observed, estimated) and TEC during the same period.

Figure 10b shows these data during the period of 14–17 LT. The resulting PSD are shown in Figure 10c, wherein small fluctuations of periodicities ∼24–36 min seem to be present in all these parameters, thereby reinforcing the detection of the SED signature in the 630.0 nm dayglow.

It is striking to note that all these independent data products match well during 15–16 LT on 9 Nov 2004. The observed enhancements in the OI 630.0 nm dayglow emissions in this duration affirm this to be an optical signature of SED relating to F-region ionospheric characteristics. The result as presented and described in this work is the first report of measurements of storm enhanced densities in the daytime red line airglow emissions, to the best of our knowledge.

6. Summary

In this work, we have presented an anomalous enhancement observed in the red line dayglow emission intensities and explored its cause using various complementary datasets and models. The investigations reveal that on 9 Nov 2004, a strong convection of magnetospheric origin expanded from high latitudes to sub auroral latitudes and interacted with the corotating magnetic field at the boundary of plasmasphere. A comparison in dusk hours between HIRISE observed dayglow and GLOW estimated emissions indicated that the observed enhancement in 630.0 nm dayglow is due primarily to the increase in electron density. The corresponding quantitative changes as observed in the ionospheric parameters include a reduction in plasma temperature by around a factor of 5 and a 6-fold increase in the electron density at altitudes greater than 300 km. The observed enhanced density is confined to around 1 hr as the IMF Bz turned northward after 16 LT. The enhancement in peak electron density around 15 LT over zenith at Millstone Hill clearly signaled the onset of SED over the observation location. A strong electric field penetration of magnetospheric origin into sub auroral latitudes appears as the possible cause for the formation of SED over mid-latitudes. The observed 1 kR intensity enhancement of OI 630 nm dayglow during the dusk hours is found to be associated with a large increase in electron density, making it possibly the first reported dayglow signature of SED phenomena.

21699402, 2023, 9, Downloaded from https://agupubs.onlinelibrary.wiley.com/doi/10.1029/2023JA031409 by Physical Research Laboratory, Wiley Online Library on [02/02/2024]. See the Terms and Conditions (https://onlinelibrary.wiley.com/terms-and-conditions) on Wiley Online Library for rules of use; OA articles are governed by the applicable Creative Commons License

Data Availability Statement

The hourly geomagnetic indices data and daily averaged solar flux data are obtained from the GSFC/SPDF OMNIWeb interface at (https://omniweb.gsfc.nasa.gov/ow.html) (King & Papitashvili, 2005). The observed and modeled optical OI 630.0 nm emission data obtained at Boston are available at https://osf.io/uv2zq/ and can be publicly accessed. The Millstone Hill ISR data are obtained from cedar madrigal database (Erickson, 2004; http://cedar.openmadrigal.org/) and are available at http://millstonehill.haystack.mit.edu/list. The TEC data to construct 2D maps are obtained from the website of the Institute for Space-Earth Environmental Research (ISEE) at Nagoya University and available at https://stdb2.isee.nagoya-u.ac.jp/GPS/shinbori/AGRID2/nc/2004/314/. The DMSP data product are downloaded from the cedar madrigal database and available at https://w3id.org/cedar?experiment_list=experiments3/2004/dms/09nov04&file_list=dms_20041109_14s1.001.hdf5. The GNSS TEC daily data at Westford station are available from Crustal Dynamics Data Information System (CDDIS) (Noll, 2010) at https://cddis.nasa.gov/Data_and_Derived_Products/GNSS/GNSS_data_and_product_archive.html. The GLOW model source code is available at https://www2.hao.ucar.edu/modeling/glow.

Acknowledgments
The authors acknowledge the CEDAR madrigal database to access the Millstone Hill observatory data. The work at the University of Massachusetts, Lowell was supported by Lowell Center for Space Science & Technology (LoCSST). This work is supported by the Department of Space, Government of India.

References

Alge, E., Adams, N. G., & Smith, D. (1983). Measurements of the dissociative recombination coefficients of O_2^+, NO^+ and NH_4^+ in the temperature range 200-600K. *Journal of Physics B: Atomic and Molecular Physics*, *16*(8), 1433–1444. https://doi.org/10.1088/0022-3700/16/8/017

Baumgardner, J., Wroten, J., Semeter, J., Kozyra, J., Buonsanto, M., Erickson, P., & Mendillo, M. (2007). A very bright SAR arc: Implications for extreme magnetosphere-ionosphere coupling. *Annales Geophysicae*, *25*(12), 2593–2608. https://doi.org/10.5194/angeo-25-2593-2007

Bilitza, D. (1990). *International reference ionosphere: IRI-90* (pp. 90–22). Natl. Space Sci. Data Cent. Rep. Retrieved from https://ntrs.nasa.gov/archive/nasa/casi.ntrs.nasa.gov/19910021307.pdf

Erickson, MIT/Haystack Observatory. (2004). Data from the CEDAR madrigal database [Dataset]. Haystack. Retrieved from http://millstonehill.haystack.mit.edu/list

Evans, J. V. (1970). The June 1965 magnetic storm: Millstone hill observations. *Journal of Atmospheric and Terrestrial Physics*, *32*(10), 1629–1640. https://doi.org/10.1016/0021-9169(70)90169-8

Foster, J. C. (1989). Plasma transport through the dayside cleft: A source of ionization patches in the polar cap. In P. Sandholt & A. Egeland (Eds.), *Electromagnetic coupling in the polar clefts and caps* (pp. 343–354). Kluwer Acad.

Foster, J. C. (1993). Storm time plasma transport at middle and high latitudes. *Journal of Geophysical Research*, *98*(A2), 1675–1689. https://doi.org/10.1029/92ja02032

Foster, J. C. (2008). Ionospheric-magnetospheric-heliospheric coupling: Storm-time thermal plasma redistribution. Mid-Latitude Dynamics and Disturbances. *Geophysical Monograph Series*, *181*, 121–134. https://doi.org/10.1029/181GM12

Foster, J. C., & Burke, W. J. (2002). SAPS: A new categorization for sub-auroral electric fields. *Eos, Transactions American Geophysical Union*, *83*(36), 393–394. https://doi.org/10.1029/2002eo000289

Foster, J. C., Coster, A. J., Erickson, P. J., Holt, J. M., Lind, F. D., Rideout, W., et al. (2005). Multiradar observations of the polar tongue of ionization. *Journal of Geophysical Research*, *110*(A9), A09S31. https://doi.org/10.1029/2004JA010928

Foster, J. C., Erickson, P. J., Coster, A. J., Goldstein, J., & Rich, F. J. (2002). Ionospheric signatures of plasmaspheric tails. *Geophysical Research Letters*, *29*(13), 1-1–1-4. https://doi.org/10.1029/2002GL015067

Foster, J. C., Rideout, W., Sandel, B., Forrester, W. T., & Rich, F. J. (2007). On the relationship of SAPS to storm-enhanced density. *Journal of Atmospheric and Solar-Terrestrial Physics*, *69*(3), 303–313. https://doi.org/10.1016/j.jastp.2006.07.021

Foster, J. C., & Vo, H. B. (2002). Average characteristics and activity dependence of the subauroral polarization stream. *Journal of Geophysical Research*, *107*(A12), SIA16-1–SIA16-10. https://doi.org/10.1029/2002ja009409

Galkin, I. A., Khmyrov, G. M., Kozlov, A. V., Reinisch, B. W., Huang, X., Paznukhov, V. V., et al. (2008). The ARTIST 5, in radio sounding and plasma physics. *AIP Conference Proceedings*, *974*(1), 150–159. https://doi.org/10.1063/1.2885024

Heelis, R. A., Sojka, J. J., David, M., & Schunk, R. W. (2009). Storm time density enhancements in the middle-latitude dayside ionosphere. *Journal of Geophysical Research*, *114*(A3), A03315. https://doi.org/10.1029/2008JA013690

Hosokawa, K., Taguchi, S., Shiokawa, K., Otsuka, Y., Ogawa, Y., & Nicolls, M. (2014). Global imaging of polar cap patches with dual airglow imagers. *Geophysical Research Letters*, *41*(1), 1–6. https://doi.org/10.1002/2013gl058748

Huang, C.-S., Foster, J. C., Goncharenko, L. P., Erickson, P. J., Rideout, W., & Coster, A. J. (2005). A strong positive phase of ionospheric storms observed by the Millstone Hill incoherent scatter radar and global GPS network. *Journal of Geophysical Research*, *110*(A6), A06303. https://doi.org/10.1029/2004JA010865

Kelley, M. C., Vlasov, M. N., Foster, J. C., & Coster, A. J. (2004). A quantitative explanation for the phenomenon known as storm-enhanced density. *Geophysical Research Letters*, *31*(19), L19809. https://doi.org/10.1029/2004gl020875

King, J. H., & Papitashvili, N. E. (2005). Solar wind spatial scales in and comparisons of hourly Wind and ACE plasma and magnetic field data [Dataset]. Journal of Geophysical Research, *110*(A2), A02209. https://doi.org/10.1029/2004JA010649

Kozyra, J. U., Nagy, A. F., & Slater, D. W. (1997). High-altitude energy source(s) for stable auroral red arcs. *Reviews of Geophysics*, *35*(2), 155–190. https://doi.org/10.1029/96RG03194

MacDonald, E. A., Donovan, E., Nishimura, Y., Case, N. A., Gillies, D. M., Gallardo-lacourt, B., et al. (2018). New science in plain sight: Citizen Scientists lead to the discovery of optical structure in the upper atmosphere. *Science Advances*, *4*(3), 16–21. https://doi.org/10.1126/sciadv.aaq0030

Mannucci, A. J., Tsurutani, B. T., Iijima, B. A., Komjathy, A., Saito, A., Gonzalez, W. D., et al. (2005). Dayside global ionospheric response to the major interplanetary events of October 29–30, 2003 "Halloween Storms". *Geophysical Research Letters*, *32*(12), L12S02. https://doi.org/10.1029/2004gl021467

McIlwain, C. E. (1961). Coordinates for mapping the distribution of magnetically trapped particles. *Journal of Geophysical Research*, *66*(11), 3681–3691. https://doi.org/10.1029/JZ066i011p03681

21699402, 2023, 9, Downloaded from https://agupubs.onlinelibrary.wiley.com/doi/10.1029/2023JA031409 by Physical Research Laboratory, Wiley Online Library on [02/02/2024]. See the Terms and Conditions (https://onlinelibrary.wiley.com/terms-and-conditions) on Wiley Online Library for rules of use; OA articles are governed by the applicable Creative Commons License

Mende, S. B., Harding, B. J., & Turner, C. (2019). Subauroral green STEVE arcs: Evidence for low-energy excitation. *Geophysical Research Letters*, *46*(24), 14256–14262. https://doi.org/10.1029/2019GL086145

Mendillo, M., Papagiannis, M. D., & Klobuchar, J. A. (1970). Ionospheric storms at midlatitudes. *Radio Science*, *5*(6), 895–898. https://doi.org/10.1029/rs005i006p00895

Mishin, E., Nishimura, Y., & Foster, J. (2017). SAPS/SAID revisited: A causal relation to the substorm current wedge. *Journal of Geophysical Research: Space Physics*, *122*(8), 8516–8535. https://doi.org/10.1002/2017ja024263

Noll, C. E. (2010). The crustal dynamics data information system: A resource to support scientific analysis using space geodesy [Dataset]. Advances in Space Research, *45*(12), 1421–1440. https://doi.org/10.1016/j.asr.2010.01.018

Pallamraju, D., Baumgardner, J., & Chakrabarti, S. (2000). A multiwavelength investigation of the Ring effect in the day sky spectrum. *Geophysical Research Letters*, *27*(13), 1875–1878. https://doi.org/10.1029/1999gl010961

Pallamraju, D., Baumgardner, J., & Chakrabarti, S. (2002). HIRISE: A ground-based high-resolution imaging spectrograph using echelle grating for measuring daytime airglow/auroral emissions. *Journal of Atmospheric and Solar-Terrestrial Physics*, *64*(12–14), 1581–1587. https://doi.org/10.1016/s1364-6826(02)00095-0

Pallamraju, D., Baumgardner, J., Chakrabarti, S., & Pedersen, T. R. (2001). Simultaneous ground-based observations of an auroral arc in daytime/twilighttime OI 630.0 nm emission and by Incoherent Scatter Radar. *Journal of Geophysical Research*, *106*(A4), 5543–5549. https://doi.org/10.1029/2000ja000244

Pallamraju, D., & Chakrabarti, S. (2005). First ground-based measurements of OI 6300 A daytime aurora over Boston in response to the 30 October 2003 geomagnetic storm. *Geophysical Research Letters*, *32*(3), L03S10. https://doi.org/10.1029/2004GL021417

Pallamraju, D., Chakrabarti, S., Doe, R., & Pedersen, T. (2004). First ground-based OI 630 nm optical measurements of daytime cusplike and F-region auroral precipitation. *Geophysical Research Letters*, *31*(8), L08807. https://doi.org/10.1029/2003gl019173

Pallamraju, D., Chakrabarti, S., & Solomon, S. C. (2011). On deriving incident auroral particle fluxes in the daytime using combined ground-based optical and radar measurements. *Journal of Geophysical Research*, *116*(A4), A04309. https://doi.org/10.1029/2010JA015934

Pallamraju, D., Das, U., & Chakrabarti, S. (2010). Short- and long-timescale thermospheric variability as observed from OI 630.0 nm dayglow emissions from low-latitudes. *Journal of Geophysical Research*, *115*(A6), A06312. https://doi.org/10.1029/2009JA015042

Pallam Raju, D., Sridharan, R., Gurubaran, S., & Raghavarao, R. (1996). First results from ground-based daytime optical investigation of the development of the equatorial ionization anomaly. *Annales de Geophysique*, *14*(2), 238–245. https://doi.org/10.1007/s00585-996-0238-9

Pi, X., Mannucci, A. J., Lindqwister, U. J., & Ho, C. M. (1997). Monitoring of global ionospheric irregularities using the worldwide GPS network. *Geophysical Research Letters*, *24*(18), 2283–2286. https://doi.org/10.1029/97gl02273

Picone, J. M., Hedin, A. E., Drob, D. P., & Aikin, A. C. (2002). NRLMSISE-00 empirical model of the atmosphere: Statistical comparisons and scientific issues. *Journal of Geophysical Research*, *107*(A12), SIA15-1–SIA15-16. https://doi.org/10.1029/2002JA009430

Pimenta, A. A., Sahai, Y., Bittencourt, J. A., & Rich, F. J. (2007). Ionospheric plasma blobs observed by OI 630 nm all-sky imaging in the Brazilian tropical sector during the major geomagnetic storm of April 6–7, 2000. *Geophysical Research Letters*, *34*(2), L02820. https://doi.org/10.1029/2006gl028529

Reinisch, B. W., & Xueqin, H. (1983). Automatic calculation of electron density profiles from digital ionograms: 3. Processing of bottomside ionograms. *Radio Science*, *18*(3), 477–492. https://doi.org/10.1029/rs018i003p00477

Rishbeth, H. (1977). Dynamics of the equatorial F-region. *Journal of Atmospheric and Terrestrial Physics*, *39*(9–10), 1159–1168. https://doi.org/10.1016/0021-9169(77)90024-1

Seo, Y., Horwitz, J. L., & Caton, R. (1997). Statistical relationships between high-latitude ionospheric F region/topside upflows and their drivers: DE 2 observations. *Journal of Geophysical Research*, *102*(A4), 7493–7500. https://doi.org/10.1029/97ja00151

Shepherd, G. G., & Cho, Y. M. (2021). On the Relationship of the O (1D) 630.0 nm dayglow emission to the F10. 7 cm solar flux and the solar zenith angle. *Journal of Geophysical Research: Space Physics*, *126*(3), e2020JA028715. https://doi.org/10.1029/2020ja028715

Shiokawa, K., Ihara, C., Otsuka, Y., & Ogawa, T. (2003). Statistical study of nighttime medium-scale traveling ionospheric disturbances using midlatitude airglow images. *Journal of Geophysical Research*, *108*(A1), 1052. https://doi.org/10.1029/2002ja009491

Solomon, S. C. (2017). Global modeling of thermospheric airglow in the far ultraviolet. *Journal of Geophysical Research: Space Physics*, *122*(7), 7834–7848. https://doi.org/10.1002/2017ja024314

Solomon, S. C., & Abreu, V. J. (1989). The 630 nm dayglow. *Journal of Geophysical Research*, *94*(A6), 6817–6824. https://doi.org/10.1029/JA094iA06p06817

Solomon, S. C., Hays, P. B., & Abreu, V. J. (1988). The auroral 6300 Å emission: Observations and modeling. *Journal of Geophysical Research*, *93*(A9), 9867–9882. https://doi.org/10.1029/ja093ia09p09867

Spiro, R. W., Heelis, R. A., & Hanson, W. B. (1979). Rapid subauroral ion drifts observed by Atmosphere Explorer C. *Geophysical Research Letters*, *6*(8), 657–660. https://doi.org/10.1029/gl006i008p00657

Thomas, E. G., Baker, J. B., Ruohoniemi, J. M., Clausen, L. B., Coster, A. J., Foster, J. C., & Erickson, P. J. (2013). Direct observations of the role of convection electric field in the formation of a polar tongue of ionization from storm enhanced density. *Journal of Geophysical Research: Space Physics*, *118*(3), 1180–1189. https://doi.org/10.1002/jgra.50116

Torr, D. G., Torr, M. R., Walker, J. C. G., Nier, A. O., Brace, L. H., & Brinton, H. C. (1976). Recombination of O_2+ in the ionosphere. *Journal of Geophysical Research*, *81*(31), 5578–5580. https://doi.org/10.1029/ja081i031p05578

Yadav, S., Shiokawa, K., Otsuka, Y., Connors, M., & St Maurice, J. P. (2021). Multi-wavelength imaging observations of STEVE at Athabasca, Canada. *Journal of Geophysical Research: Space Physics*, *126*(2), 2020JA028622. https://doi.org/10.1029/2020ja028622

Yeh, H.-C., Foster, J. C., Rich, F. J., & Swider, W. (1991). Storm time electric field penetration observed at mid-latitude. *Journal of Geophysical Research*, *96*(A4), 5707–5721. https://doi.org/10.1029/90JA02751

Yuan, Z.-G., Deng, X.-H., Zhang, S.-R., Wan, W.-X., & Reinisch, B. W. (2009). F region behavior in the SED plume during a geomagnetic superstorm: A case study. *Journal of Geophysical Research*, *114*(A8), A08303. https://doi.org/10.1029/2008JA013841

Zou, S., Moldwin, M. B., Ridley, A. J., Nicolls, M. J., Coster, A. J., Thomas, E. G., & Ruohoniemi, J. M. (2014). On the generation/decay of the storm-enhanced density plumes: Role of the convection flow and field-aligned ion flow. *Journal of Geophysical Research: Space Physics*, *119*(10), 8543–8559. https://doi.org/10.1002/2014ja020408

Zou, S., Ridley, A. J., Moldwin, M. B., Nicolls, M. J., Coster, A. J., Thomas, E. G., & Ruohoniemi, J. M. (2013). Multi-instrument observations of SED during 24–25 October 2011 storm: Implications for SED formation processes. *Journal of Geophysical Research: Space Physics*, *118*(12), 7798–7809. https://doi.org/10.1002/2013JA018860

21699402, 2023, 9, Downloaded from https://agupubs.onlinelibrary.wiley.com/doi/10.1029/2023JA031409 by Physical Research Laboratory, Wiley Online Library on [02/02/2024]. See the Terms and Conditions (https://onlinelibrary.wiley.com/terms-and-conditions) on Wiley Online Library for rules of use; OA articles are governed by the applicable Creative Commons License

Check for updates

Geophysical Research Letters

RESEARCH LETTER
10.1029/2023GL106292

First Daytime Red-Line Emission Measurements of the Stable Auroral Red (SAR) Arcs

Kshitiz Upadhyay[1,2] and Duggirala Pallamraju[1]

[1]Physical Research Laboratory, Ahmedabad, India, [2]Indian Institute of Technology, Gandhinagar, India

Key Points:

- Ground-based measurements of O(^{1}D) dayglow showed enhancement in emissions on a geomagnetically disturbed day at a mid-latitude location
- Complementary data sets revealed the increase in optical emissions to be stable auroral red (SAR) arcs, which are associated with elevated electron temperatures
- This study presents the first ground-based detection of daytime SAR arcs in OI 630.0 nm red-line emissions

Supporting Information:

Supporting Information may be found in the online version of this article.

Correspondence to:

D. Pallamraju,
raju@prl.res.in

Citation:

Upadhyay, K., & Pallamraju, D. (2024). First daytime red-line emission measurements of the stable auroral red (SAR) arcs. *Geophysical Research Letters*, *51*, e2023GL106292. https://doi.org/10.1029/2023GL106292

Received 7 SEP 2023
Accepted 19 JAN 2024

© 2024 The Authors.
This is an open access article under the terms of the Creative Commons Attribution-NonCommercial-NoDerivs License, which permits use and distribution in any medium, provided the original work is properly cited, the use is non-commercial and no modifications or adaptations are made.

Abstract We present the first ground-based measurements of daytime stable auroral red (SAR) arc using OI 630.0 nm emissions. SAR arc is a direct consequence of heat conduction from the inner-magnetosphere to the ionospheric regions characterized by increased electron temperatures and low electron density in the region of mid-latitude trough. So far, SAR arc emissions have only been reported for nighttime conditions. For the present study, daytime optical measurements were enabled using a high-resolution imaging echelle spectrograph from Boston (42.36°N, 71.05°W, MLAT ≈ 53°). Simultaneous Millstone Hill Incoherent Scatter Radar and Defense Meteorological Satellite Program measurements of electron density and temperature confirm our findings. Forward modeling approach enabled estimation of daytime electron temperatures in 200–650 km altitude during this SAR arc event to be varying between 3,500 and 4,400 K. These observations open numerous possibilities of optical investigations of magnetospheric-ionospheric interactions during daytime, when the upper atmosphere is dynamic with large gradients in ionospheric conductivities, temperatures, and winds.

Plain Language Summary A latitudinally narrow and zonally elongated channel consisting of enhanced red-line emissions are known to be present, on occasions, in the optical measurements in the sub-auroral latitudes and are referred to as the stable auroral red (SAR) arcs. These are now known to be caused by the conduction of heat from the Ring current region into the ionosphere. Earlier studies suggested an increased electron temperature (above ∼300 km altitude) collocated with the low electron density region of ionospheric trough. So far, observations of SAR arcs have only been reported for the night time. In the daytime, due to the presence of sunlight the atmospheric conditions are different, so also are the upper atmospheric dynamics. The measurements of SAR arcs in the daytime are also challenging as the background solar brightness is very large. In this work, by making use of high spectral resolution optical measurements in the daytime, we present the first measurements of daytime SAR arcs and perform model calculations to estimate the values of electron temperature in the 200–650 km altitude range to be varying in the range of 3,500–4400 K.

1. Introduction

Sun-Earth interactions give rise to various space weather phenomena in which auroral displays at high latitudes are one of the prominent ones. A phenomenon called stable auroral red (SAR) arc (Barbier, 1958) is formed equatorward in the sub-auroral latitudes. SAR arc emissions occur at optical region and are monochromatic at 630.0 nm (red-line). These emissions originate due to the excitation of oxygen atoms (OI) in the topside of the F-region ionosphere (300–500 km in altitude). SAR arcs are global in nature, covering ∼100° longitudinally (Mendillo et al., 2013), but are narrow in latitude (1°–2° wide) and mostly formed during geomagnetic storms. Possible mechanisms for its production (Kozyra et al., 1997 and references therein), morphology, characteristics in terms of brightness and longevity have been reported in the literature (e.g., Baumgardner et al., 2007; Mendillo et al., 2016). These link SAR arc occurrence to the plasmapause in the inner magnetosphere. The plasmapause typically lies at $L = 3$–5 (McIlwain, 1961; L-value defines the distance from the Earth's surface in terms of Earth's radius, R_E, where a particular geomagnetic field line crosses the geomagnetic equator). However, it can also reach to lower L-values (corresponding to lower latitudes) during large geomagnetic disturbances (Fok et al., 1991). Therefore, depending on the strength of geomagnetic disturbance, location of occurrence of SAR arcs can vary in the region of $L = 2$ to $L = 4$. SAR arcs can persist for a few hours to a few days as observed by ground-based optical and satellite-based plasma measurements (Craven et al., 1982; Mendillo et al., 2016). An elevated electron temperature, Te, is shown to be the main diagnostic for the generation of SAR arcs (Rees & Roble, 1975). During geomagnetic storms, ring current energetic ions, electrons and cold plasmaspheric electrons near the plasmapause boundary come close enough which enables interaction through Coulomb collisions. The heat energy generated by Coulomb collisions at ring-current and plasmapause interaction region is transferred to

19448007, 2024, 3, Downloaded from https://agupubs.onlinelibrary.wiley.com/doi/10.1029/2023GL106292 by Physical Research Laboratory, Wiley Online Library on [02/02/2024]. See the Terms and Conditions (https://onlinelibrary.wiley.com/terms-and-conditions) on Wiley Online Library for rules of use; OA articles are governed by the applicable Creative Commons License

ionospheric altitudes via conduction along geomagnetic field lines resulting in heating the ambient electrons to several thousands of degrees (Prölss, 2006). It has been shown that the soft electron flux (<10 eV) in the Maxwellian tail of electron distribution consists of enough electron population with energies required to excite oxygen atoms to O(^{1}D) state which radiates the 630.0 nm emission (Kozyra et al., 1997). These emissions have been observed typically in the mid-latitude trough region where electron density, Ne, is reduced. Thus, an elevated Te (>3,000 K) and depleted Ne are the two important signatures that characterize a SAR arc as seen in the in-situ measurements (Foster et al., 1994). Thus, formation of SAR arcs is a direct evidence of magnetosphere-ionosphere coupling in the sub-auroral latitude upper atmosphere. SAR arcs have been observed during weak geomagnetic disturbed periods as well (Dst > −30 nT; Kp < 3) (e.g., Inaba et al., 2021; Kozyra et al., 1997), which indicates that there exist sources other than heat conduction through Coulomb collisions for the formation of SAR arcs. Such observations are understood to be due to the energy stored in the magnetosphere at an earlier time being released and transferred to the sub-auroral ionosphere later. This energy can also be generated by wave-particle interaction, however the SAR arcs formed in such scenario may be less intense (Kozyra et al., 1997). Though various sources and mechanisms have been suggested for SAR arc formation, all these eventually result in increasing the Te. SAR arc brightness has been observed to vary from 50 R to ∼10 kR, typically lying in the range of ∼500 ± 270 R (Baumgardner et al., 2007). Observations of SAR arcs have been made using ground-based optical measurements during nighttime, but, to the best of our knowledge, there have been no reports of ground-based measurements of daytime SAR arcs. They can, however, be expected in the daytime considering the nature of production of SAR arcs and the process of heat conduction in the ionosphere from near plasmapause region (Kozyra et al., 1997; Mendillo et al., 2013). Although the daytime optical airglow measurements are challenging, it has now become a reality with the advent of ground-based dayglow optical techniques (Pallamraju et al., 2002, 2013). Further, the measurement of SAR arcs in the daytime seems particularly promising in view of the fact that the OI 630.0 nm, O(^{1}D), dayglow emissions from Sondrestrom have been used to investigate the daytime cusps (Pallamraju et al., 2004) and both of these processes involve enhancement in the Te for occurrence of the red-line emissions. For the present study, these O(^{1}D) emissions were obtained from Boston, a mid-latitude location, using a High-Resolution Imaging Spectrograph using Echelle grating (HIRISE).

2. Data Used and Methodology

2.1. Daytime O(^{1}D) Emission Measurements

The O(^{1}D) dayglow emissions used in this study have been obtained using HIRISE (Pallamraju et al., 2002). HIRISE measured sky spectrum is compared with the solar spectrum in order to obtain the information corresponding to O(^{1}D) dayglow emission intensity. The sky spectrum is different from the solar spectrum in terms of the telluric absorptions, airglow emissions, and scattering. Therefore, the dayglow extraction procedure has been used, as discussed in detail earlier (Pallamraju et al., 2000, 2002), to properly account for such differences and obtain the contribution due to daytime emissions alone. The temporal behavior of O(^{1}D) emission variability was obtained with a data cadence of 5 min.

2.2. Ionospheric Parameters From Digisonde and Incoherent Scatter Radar (ISR)

Millstone Hill based digisonde data were used to acquire the Ne information from the ionograms obtained periodically. The bottomside ionograms obtained are used to deduce topside profiles based on the R-H method (Reinisch & Huang, 2001) and these profiles are made available at the Digital Ionogram DataBase. These values as a function of altitudes were used as inputs into the GLOW model (discussed below) to obtain altitude profiles of volume emission rates. These were then used to obtain column integrated values of O(^{1}D) emissions in order to compare them with those measured by HIRISE. On occasions, when Millstone Hill Incoherent Scatter Radar (ISR) (42.6°N, 71.5°W, $\Lambda \approx 53.3°$) data are available, additional information on electron and ion temperatures (Te, Ti) can be used for obtaining a greater understanding of the ionospheric conditions and confirm the findings.

2.3. Model Emissions

O(^{1}D) emission is a forbidden transition with a radiative lifetime of around 120 s. During daytime, the O(^{1}D) state is produced mainly due to (a) photoelectron impact (PEI; $O + e^* \rightarrow O(^1D) + e$), (b) Photodissociation in Schumann-Range continuum (PD; $O_2 + hv \rightarrow O(^1D) + O$), and (c) Dissociative recombination (DR; $O_2 + e^- \rightarrow O(^1D) + O$). This excited O(^{1}D) returns to the ground state by emitting a photon at 630.0 nm wavelength

19448007, 2024, 3, Downloaded from https://agupubs.onlinelibrary.wiley.com/doi/10.1029/2023GL106292 by Physical Research Laboratory, Wiley Online Library on [02/02/2024]. See the Terms and Conditions (https://onlinelibrary.wiley.com/terms-and-conditions) on Wiley Online Library for rules of use; OA articles are governed by the applicable Creative Commons License

(Pallamraju et al., 1996; Solomon & Abreu, 1989). For SAR arcs, the mechanism O + e* gives rise to O(^{1}D) to yield a red-line photon (Rees & Roble, 1975). In addition to the HIRISE measurements of O(^{1}D) emissions, a physics-based (GLOW) model estimation (Solomon, 2017) has been used to predict dayglow intensity based on aforementioned production mechanisms. The GLOW model uses Naval Research Laboratory Mass Spectrometer Incoherent Scatter (NRLMSIS-00) model atmosphere (Picone et al., 2002) and International Reference Ionosphere model (Bilitza, 1990) as inputs to estimate the O(^{1}D) column emissions rates. The IRI predicted Ne profiles are replaced with Millstone Hill digisonde Ne profiles as inputs to the GLOW model to consider the day-to-day variation in electron densities, and thereby increase the accuracy of the estimations. Further, an empirical model, WEM (WINDII empirical model; Shepherd & Cho, 2021) has been used to estimate the diurnal variability of O(^{1}D) emissions. WEM uses solar flux (F10.7, sfu = 10^{-22} Wm^{-2} Hz^{-1}) and solar zenith angle (χ) as inputs to Equation 1 for predicting the O(^{1}D) emission intensity (I) for a given day.

$$\ln(I) = 5.237 + 0.212 * \mathrm{Cos}^2\chi + 1.664 * \mathrm{Cos}^{0.5}\chi + 0.072 * (\ln F10.7)^2 \quad (1)$$

2.4. In Situ Satellite Observations

The Defense Meteorological Satellite Program (DMSP) provides information on ionospheric electron temperature, electron (≈ion) density, horizontal and vertical plasma drifts, and precipitating particle flux at an altitude of around 850 km (Greenspan et al., 1986; Rich & Hairston, 1994). DMSP data have been used earlier for identification of SAR arcs (e.g., Baumgardner et al., 2007; Martinis et al., 2019; Mendillo et al., 2016). Different passes of DMSP satellite data were used to verify the presence of SAR arcs by their characteristic signatures of enhanced Te and reduced ion density, Ni, in the region of their formation (Baumgardner et al., 2013; Foster et al., 1994).

3. Observations and Results

Out of the production mechanisms for dayglow described above, the PEI and PD mechanisms depend on the neutral densities (O and O_2) and photoelectron and solar EUV flux that are incident at a given location at a given time, and therefore the dayglow emissions generated through these two mechanisms are expected to vary as a function of solar zenith angle. Whereas, the DR mechanism also depends on the ambient electron and ion densities present at a given time. It is known that the ambient plasma densities show variations due to changes in electrodynamics, in addition to that of the solar zenith angle. Therefore, small time-scale temporal variation has been shown to be mainly due to the DR mechanism. Thus, it has been shown in earlier studies that variations in the F-layer Ne can be readily noticed in the O(^{1}D) dayglow emission intensity variability (e.g., Pallamraju et al., 2001; Upadhyay et al., 2023). Shorter duration temporal variations can also be brought out due to changes in energetic electron flux through the PEI mechanism as in the case of magnetospheric cusps (Pallamraju et al., 2004) or solar flares (Das et al., 2010).

In this work, ground-based optical observations of O(^{1}D) emissions over zenith obtained using HIRISE are presented. In order to quantify the variations (in Rayleighs) during geomagnetic disturbed times, the dayglow measurements made by HIRISE have been first scaled with the WEM model estimates during quiet times. The temporal variations in the HIRISE measured 630.0 nm emissions thus obtained are shown by red-colored filled-circles line in Figure 1 along with the $\pm 1\sigma$ error bar at each point, which varies in the range of 5%–18% depending on the signal and background brightness (Pallamraju et al., 2002, 2013). The missing data around local noon is because of the saturation in CCD counts due to entry of direct sunlight/solar glare through the slit of the HIRISE, thereby rendering the image unusable.

Four days of dayglow data are shown in Figure 1. Out of them, two (a, b) are geomagnetically quiet (daily averaged Kp index, $\langle \mathbf{Kp} \rangle < 3$) and the remaining two (c, d) are disturbed days ($\langle \mathbf{Kp} \rangle \geq 3$). The presence of clouds in the forenoon on 7 December 2006, prevented the dayglow measurements. The solar flux variation was found to be small (in the range of 75–93 sfu). The WEM predictions are shown in black-dashed lines for all these 4 days. Since the WEM estimated emissions are independent of any neutral or electrodynamic changes in the upper atmosphere, the HIRISE O(^{1}D) observations and WEM emissions match well with each other as expected for geomagnetically quiet days (Figures 1a and 1b). However, on geomagnetically disturbed days (Figures 1c and 1d), there is a distinct difference in the measured emission magnitudes and WEM estimates. This significant increase in the observed emissions suggests that on both these disturbed days, there were considerable changes in

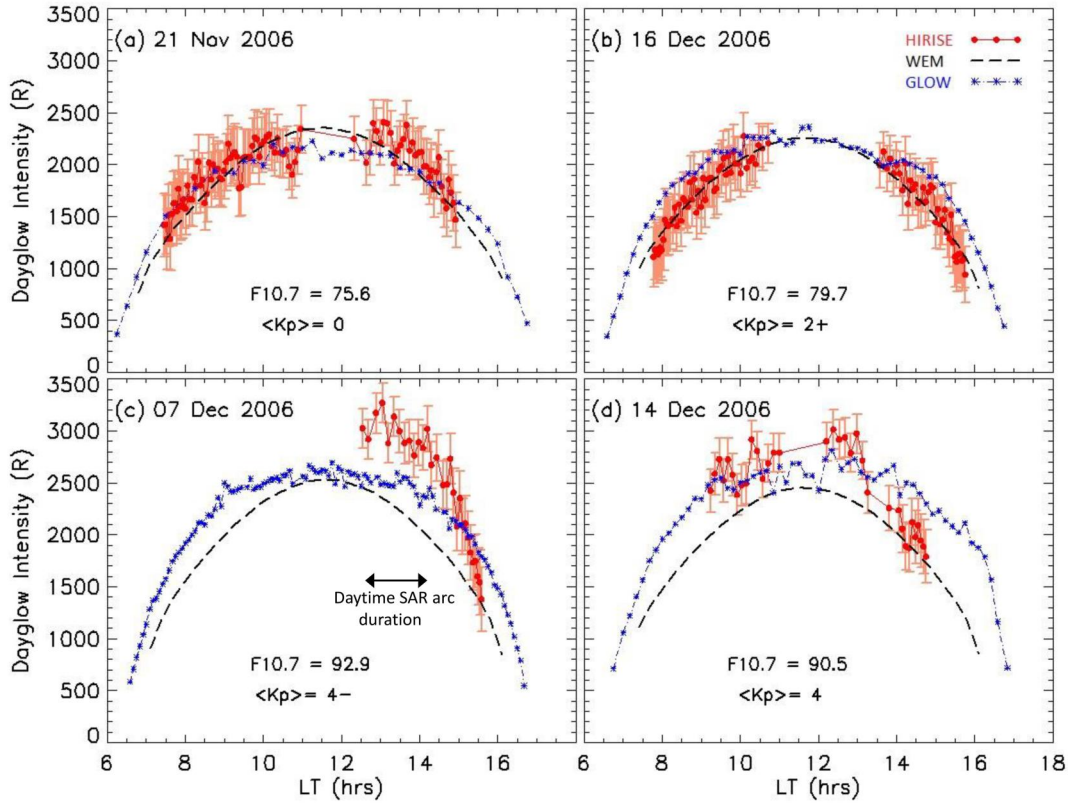

Figure 1. Temporal variations in the 630.0 nm dayglow emissions on geomagnetically quiet (a, b) and disturbed (c, d) days are shown: High-Resolution Imaging Spectrograph using Echelle grating (HIRISE) measured emissions (red filled-circles line) along with $\pm 1\sigma$ uncertainties, WEM estimates (black-dashed line) and GLOW estimated emissions (blue-asterisk line). All the dayglow values match well with one another during geomagnetic quiet conditions. The enhancements in the measured emission values on 7 December 2006 (panel c) are due to the stable auroral red arc event in the daytime that are being reported for the first time.

the ionospheric behavior. To investigate the effect of plasma parameters on the O(^{1}D) emission magnitudes, the measured electron densities by Millstone Hill digisonde were considered as inputs into the GLOW model. The O(^{1}D) emissions estimated using GLOW model, for all quiet and disturbed days thus obtained are also shown in Figure 1 by the blue-asterisk line. It can be seen that for quiet days, the HIRISE measured O(^{1}D) emissions, GLOW estimated emissions, and WEM estimates, all match well with each other, both in diurnal behavior and in magnitudes. On 14 December 2006 ($\langle \mathbf{Kp} \rangle = 4$), WEM underestimates the measured emissions, which is not unexpected as the variations due to geomagnetic disturbances are not represented in these empirical estimates. However, the GLOW model values match well with the HIRSE measured emissions within measurement uncertainties as the digisonde measured Ne, has been used as an input into the GLOW model. This indicates that the enhancement in Ne due to the geomagnetic storm on 14 December 2006 resulted in an enhancement in the O(^{1}D) emissions. Whereas, on 7 December ($\langle \mathbf{Kp} \rangle = 4^-$), HIRISE measured emissions significantly exceed the GLOW model estimated emissions, despite the digisonde measured Ne being incorporated into the calculations, indicating that the cause of observed enhancements is some factor(s) other than the Ne variations. Fortuitously, on both these disturbed days (7 and 14 December 2006), Millstone Hill ISR was in operation, and thus, the diurnal variation in Te were available. As electron temperature affects the daytime O(^{1}D) emissions (e.g., Pallamraju et al., 2004), the ISR measured Te were examined (Figure 2). The Figure 2 clearly shows an enhancement in Te (>3,000 K) at higher altitudes (>300 km) on 7 December during the period of enhanced 630.0 nm emissions (13–14 LT) which is clearly absent on 14 December. Therefore, it can be considered that the daytime enhancement in the red-line emissions on 7 December were due to a significant role played by enhanced Te, which forms a clear signature of the formation of SAR arc.

19448007, 2024, 3, Downloaded from https://agupubs.onlinelibrary.wiley.com/doi/10.1029/2023GL106292 by Physical Research Laboratory, Wiley Online Library on [02/02/2024]. See the Terms and Conditions (https://onlinelibrary.wiley.com/terms-and-conditions) on Wiley Online Library for rules of use; OA articles are governed by the applicable Creative Commons License

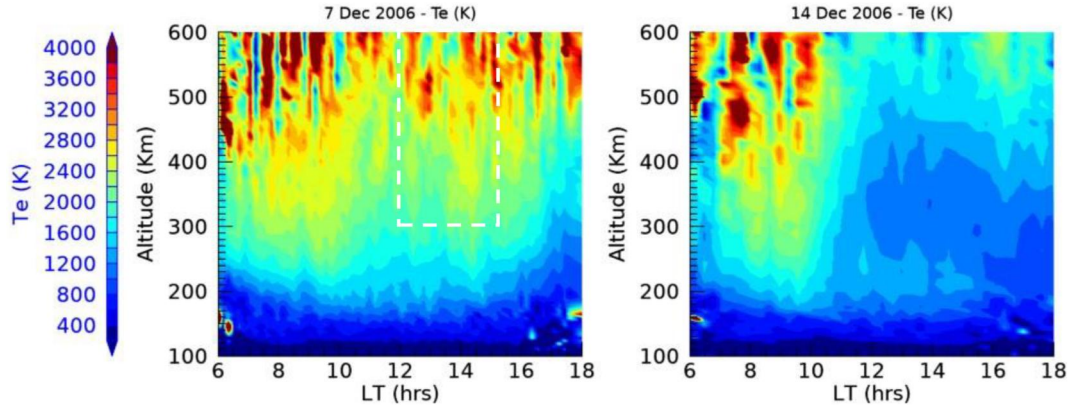

Figure 2. Millstone Hill Incoherent Scatter Radar measured electron temperature (Te) on 7 and 14 December in the altitude range 100–600 km. Enhanced values of Te can be noted on 7 December 2006 in our observation duration, as marked by the white-dashed lines.

The nighttime airglow studies have shown elevated Te and reduced Ne during SAR arc events with 1°–2° latitudinal width (e.g., Baumgardner et al., 2013; Foster et al., 1994). Therefore, to further confirm that the observed emissions are due to the SAR arc, the latitudinal Te/Ne/Ni ionospheric behavior was examined using the DMSP-F13 satellite measured high-resolution (~4 s) observations of Te and Ni in topside ionosphere (~850 km altitude) in dayside (06–18 MLT). To remove any ambiguity in the DMSP data, the points with flag values ≤2 were used, as they are considered to be reliable (Hairston, 2018). As there exists no pass of DMSP directly over our observation location during the time of peak enhancement observed in dayglow emissions, the pass that was closest (65°W) to our location and nearest in time (16 UT, 6.6 MLT) to the observed time of red-line emission enhancement has been considered for further investigation. Therefore, the Te/Ne variations measured in the magnetic latitude (MLAT) range of 45°–70°N are examined (Figure 3a). The top (bottom) panel of Figure 3a presents the latitudinal Te (Ni) variation around 16.5 UT. The two dashed vertical lines mark the region of 54°–55°N MLAT, which includes the location over Boston, corresponding to the altitude of DMSP orbit (54.35° MLAT). The Figure 3a clearly shows a peak enhancement in Te near 54° MLAT, which corresponds to the

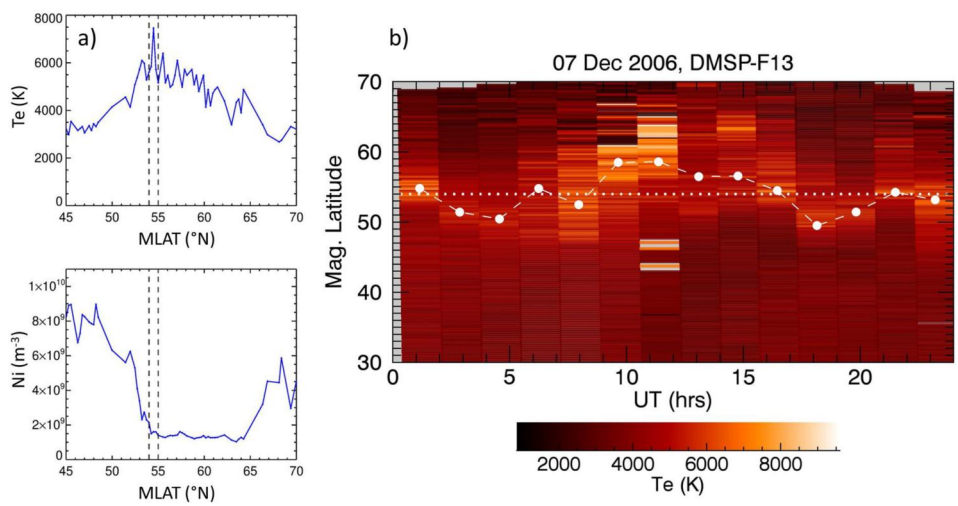

Figure 3. (a) Defense Meteorological Satellite Program (DMSP) Te and Ni variations (at ~850 km) are shown in the top and bottom panels for the 45°–70°N magnetic latitude (MLAT) range around 16.4 UT (11.4 LT). The dashed vertical lines mark the 54°–55°N MLAT, which overlaps with the latitudinal location of Boston (54.35°N MLAT). A peak in electron temperature can be seen close to the equatorward boundary of midlatitude trough. (b) Latitudinal Te variation for all DMSP passes between 30° and 70°N MLAT range is shown. White filled-circle line represents the temporal movement of Te peak. Horizontal-dashed line marks the MLAT of observational location. A region of enhanced Te can be clearly seen between 50° and 60°N MLAT range throughout the globe and reaching below 54°N during the observational period 17–19 UT.

19448007, 2024, 3, Downloaded from https://agupubs.onlinelibrary.wiley.com/doi/10.1029/2023GL106292 by Physical Research Laboratory, Wiley Online Library on [02/02/2024]. See the Terms and Conditions (https://onlinelibrary.wiley.com/terms-and-conditions) on Wiley Online Library for rules of use; OA articles are governed by the applicable Creative Commons License

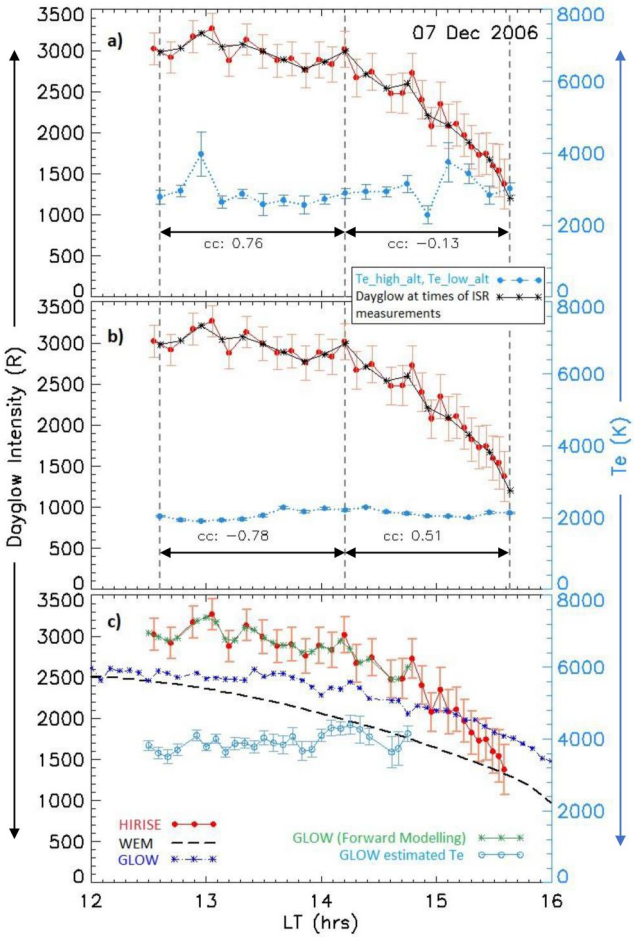

Figure 4. Incoherent Scatter Radar (ISR) measured averaged Te in the altitude range of 520–540 km (Te_high_alt) and 320–340 km altitude (Te_low_alt) is shown by sky-blue dotted line in panels (a) and (b), respectively, along with the 630.0 nm emissions on 7 December 2006. The black-asterisk line presents the interpolated emissions with respect to the times of ISR measurement. In panel (a), a strong positive correlation of 0.76 can be seen between Te_high_alt and dayglow during 12.6 and 14.2 LT. Panel (c) represents the 7 December High-Resolution Imaging Spectrograph using Echelle grating (HIRISE) (red) and GLOW (blue) emissions. The green-asterisk line presents the GLOW emissions obtained after performing the forward modeling. The right-side *y*-axis shows the estimated Te (sky-blue) obtained after carrying out forward modeling in GLOW model to match with the observed emissions during the period of 12.5–14.75 LT.

equatorward region of mid-latitude trough (reduced Ni). It is known that the mid-latitude ionospheric trough is connected with the outer boundary of plasmasphere, also known as plasmapause (Weygand et al., 2021). At this boundary, plasmapause interacts with the inner ring current region and thus the heat generated by Coulomb collision is conducted to ionospheric altitudes which increases the Te (Kozyra et al., 1997). This measurement of enhancement in the O(^{1}D) emissions, thus, makes this the first reported measurements of SAR arcs in the daytime.

As SAR arc location is determined by the position of Te peak and the location of interaction region between plasmapause and the inner ring current region (Fok et al., 1991), we investigated the peak variation in Te in the 30° to 70°N MLAT region for all passes of DMSP, on 7 December 2006 and a composite picture has been made as shown in Figure 3b. A white filled-circle line joins all the MLAT corresponding to peak Te in the latitude range of 40–60°N MLAT, and the horizontal dotted-line marks the MLAT of the observation location. The striking feature that can be seen in all passes (Figure 3b) is a narrow region of elevated Te between 50° and 60° MLAT on 7 December. The Te peak observed in each pass once again affirms the characteristic of the SAR arc being a global phenomenon.

4. Discussion and Conclusions

This detection of SAR arc in the daytime encourages us to delve deeper into assessing the magnitude of Te variation that would have contributed to this SAR arc formation. As the enhancement in Te is greater at higher altitudes (Evans, 1973; Fok et al., 1991), we made an assessment of this variation by comparing the ISR Te over higher altitude (Te_high_alt; averaged in 520–540 km altitude) and lower altitudes (Te_low_alt; averaged in 320–340 km) with the HIRISE measured 630.0 nm emission variability. During 12.42–14.21 LT (17.42–19.21 UT), a strong positive correlation (cc = 0.76) was found between dayglow and Te_high_alt (Figure 4a) and surprisingly a strong negative correlation with Te_low_alt (cc = −0.78) (Figure 4b). This agreement between two independent measurements of Te_high_alt and observed dayglow indicates that SAR arc emissions due to precipitated heat flux were present for about 1 hr 47 min over the observation location.

From white filled-circles in Figure 3b, it can be noticed that the region of enhanced Te at 18 UT reached to a latitude closer to 50°N MLAT before moving poleward after 20 UT. This time duration (17.42–19.21 UT) is similar to the period (shown in Figure 4a), wherein the observed SAR arc emissions showed a strong positive correlation with that of Te_high_alt. For the sake of consistency, the Te and Ne derived by different DMSP passes for all the four days shown in Figure 1 were considered (Figure S1), and it is apparent that 7 December shows largest values of Te and smallest Ne. Thus, from yet another independent measurement, it can be concluded that the observed enhancement in brightness as compared to the estimated values using the measured Ne as inputs during 17.42–19.21 UT (12.42–14.21 LT) was indeed due to SAR arc emissions. After this time, as the region of enhanced Te (around 20 UT/15 LT) moved poleward and out of the HIRISE field of view, the O(^{1}D) emissions returned to those estimated by the models (Figure 1c).

Based on all the experimental evidences presented, it is clear that the measured increase in 630.0 nm emissions is indeed due to the enhancement in Te. However, the GLOW modeled emission does not show this increase because it considered IRI Te as an input, as mentioned above. The IRI Te does not reflect the effects of heat transfer that results in larger Te values in SAR arc region. Also, the SAR arcs show non-uniform spatial structure with larger temperature at the center than at the edges (e.g., Foster et al., 1994; Rees & Roble, 1975). Further, due to issues such as correspondence of co-volume between the HIRISE view directions and ISR scans (Pallamraju

19448007, 2024, 3, Downloaded from https://agupubs.onlinelibrary.wiley.com/doi/10.1029/2023GL106292 by Physical Research Laboratory, Wiley Online Library on [02/02/2024]. See the Terms and Conditions (https://onlinelibrary.wiley.com/terms-and-conditions) on Wiley Online Library for rules of use; OA articles are governed by the applicable Creative Commons License

19448007, 2024, 3, Downloaded from https://agupubs.onlinelibrary.wiley.com/doi/10.1029/2023GL106292 by Physical Research Laboratory, Wiley Online Library on [02/02/2024]. See the Terms and Conditions (https://onlinelibrary.wiley.com/terms-and-conditions) on Wiley Online Library for rules of use; OA articles are governed by the applicable Creative Commons License

et al., 2011) and about 50 km distance between the two observational locations, there could be differences in the values of Te corresponding to that measured by HIRISE than that of ISR. Therefore, this presents us with a unique opportunity to make a quantitative estimate of the integrated values of Te through forward modeling that would have contributed to the observed emission enhancement due to SAR arc. To address this issue, the brightness difference between GLOW estimated intensities (I_{GLOW}) and HIRISE observed emissions (I_{obs}) were considered and different magnitudes of Te were supplied iteratively to the GLOW model to minimize their differences to obtain a quantitative estimate of Te. Figure 4c presents the observed O(^{1}D) emissions (red) along with GLOW estimates (blue) and the emissions obtained by forward modeling (green-asterisks) for 7 December. Here, the right-side *y*-axis corresponds to Te. The minimum Te required to match the model emissions with those of the observed dayglow emissions was 3,503 K and maximum was 4,391 K. Such high Te values seem to be consistent with those reported for SAR arcs during night time. This is particularly interesting as their percentage enhancements from the usual values of Te in the night and day are similar. These Te values, thus obtained by the forward modeling, are expected to describe both the variation and magnitudes of Te more accurately in comparison with those at a given altitude (Figure 4a). Thus, the daytime O(^{1}D) emission measurements can be used to obtain the Te in the ionospheric altitudes during SAR arc events. Such studies can yield further insights into the magnetospheric-ionospheric coupling that takes place during geomagnetic storms.

5. Summary

In this study, we present the first ground-based measurements of SAR arc emissions using OI 630.0 nm dayglow. The observations were carried out from a mid-latitude location, Boston, during geomagnetic disturbance ($\langle$**Kp**$\rangle$ = 4$^-$) on 7 December 2006. Simultaneous measurements of ISR confirm that Te was significantly enhanced on this day during the times of the observed enhancement in the red-line emissions. As SAR arcs are a global phenomenon, DMSP measurements of Te were investigated which did show an enhanced Te in the region of 50°–60°N MLAT throughout the longitudes. All these independent data, add credence to the HIRSIE observations that the dayglow emission enhancement seen on 7 December 2006 to be due to the formation of SAR arc on this day. Further, forward modeling revealed that in 200–650 km altitude, the enhancement in Te was in the range of 3,500–4,400 K. Thus, this study presents new possibilities in quantifying the effects and/or consequences of the magnetosphere-ionosphere coupling using the daytime ground-based high temporal resolution investigations of the optical airglow emissions.

Data Availability Statement

The daily geomagnetic indices data and solar flux data are obtained from the GSFC/SPDF OMNIWeb interface at https://omniweb.gsfc.nasa.gov/ow.html (King & Papitashvili, 2005). The observed and modelled optical OI 630.0 nm emission data obtained at Boston are available in Pallamraju (2023). The Digisonde data used in this work were obtained from the Digital Ionogram DataBase (DIDBase; Reinisch & Galkin, 2011, https://giro.uml.edu/didbase/), using Global Ionosphere Radio Observatory (GIRO) portal. The authors acknowledge S. Solomon for providing the GLOW model code available at https://www2.hao.ucar.edu/modeling/glow. Millstone Hill ISR data were obtained from http://millstonehill.haystack.mit.edu/list using cedar madrigal database (Phil Erickson, 2004). The DMSP data product are downloaded from the cedar madrigal database and are available at https://w3id.org/cedar?experiment_list=experiments3/2006/dms/07dec06&file_list=dms_20061207_13e.001.hdf5.

Acknowledgments
HIRISE operation at Boston was supported, in part, by NSF Grant 0437100. This work is supported by the Department of Space, Government of India.

References

Barbier, D. (1958). L'activité aurorale aux basses latitudes. *Publications of the Observatoire Haute-Provence*, *4*(21), 2745.

Baumgardner, J., Wroten, J., Mendillo, M., Martinis, C., Barbieri, C., Umbriaco, G., et al. (2013). Imaging space weather over Europe. *Space Weather*, *11*(2), 69–78. https://doi.org/10.1002/swe.20027

Baumgardner, J., Wroten, J., Semeter, J., Kozyra, J., Buonsanto, M., Erickson, P., & Mendillo, M. (2007). A very bright SAR arc: Implications for extreme magnetosphere-ionosphere coupling. *Annales Geophysicae*, *25*(12), 2593–2608. https://doi.org/10.5194/angeo-25-2593-2007

Bilitza, D. (1990). *International reference ionosphere: IRI-90-22*. National Space Science Data Center Report. Retrieved from https://ntrs.nasa.gov/archive/nasa/casi.ntrs.nasa.gov/19910021307.pdf

Craven, J. D., Frank, L. A., & Ackerson, K. L. (1982). Global observations of a SAR arc. *Geophysical Research Letters*, *9*(9), 961–964.

Das, U., Pallamraju, D., & Chakrabarti, S. (2010). Effect of an X-class solar flare on the OI 630 nm dayglow emissions. *Journal of Geophysical Research*, *115*(A8), A08302. https://doi.org/10.1029/2010JA015370

Evans, J. V. (1973). Seasonal and sunspot cycle variations of F region electron temperatures and protonospheric heat fluxes. *Journal of Geophysical Research*, *78*(13), 2344–2349. https://doi.org/10.1029/ja078i013p02344

Fok, M. C., Kozyra, J. U., Warren, M. F., & Brace, L. H. (1991). Seasonal variations in the subauroral electron temperature enhancement. *Journal of Geophysical Research*, *96*(A6), 9773–9780. https://doi.org/10.1029/91ja00791

Foster, J. C., Buonsanto, M. J., Mendillo, M., Nottingham, D., Rich, F. J., & Denig, W. (1994). Coordinated stable auroral red arc observations: Relationship to plasma convection. *Journal of Geophysical Research*, *99*(A6), 11429–11439. https://doi.org/10.1029/93ja03140

Greenspan, M. E., Anderson, P. B., & Pelagatti, J. M. (1986). Characteristics of the thermal plasma monitor (SSIES) for the defense meteorological satellite program (DMSP) spacecraft S 8 through S 10(report, for 19 June 1984–30 Sepetember 1986).

Hairston, M. (2018). *Madrigal SSIES-2 manual*. Center for Space Sciences, University of Texas at Dallas. Retrieved from http://cedar.openmadrigal.org/static/siteSpecific/UT_Dallas_DMSP_Description.pdf

Inaba, Y., Shiokawa, K., Oyama, S. I., Otsuka, Y., Connors, M., Schofield, I., et al. (2021). Multi-event Analysis of plasma and field variations in Source of Stable Auroral Red (SAR) arcs in inner magnetosphere during non-storm-time substorms. *Journal of Geophysical Research: Space Physics*, *126*(4), e2020JA029081. https://doi.org/10.1029/2020ja029081

King, J. H., & Papitashvili, N. E. (2005). Solar wind spatial scales in and comparisons of hourly Wind and ACE plasma and magnetic field data [Dataset]. Journal of Geophysical Research, *110*(A2), A02209. https://doi.org/10.1029/2004JA010649

Kozyra, J. U., Nagy, A. F., & Slater, D. W. (1997). High-altitude energy source (s) for stable auroral red arcs. *Reviews of Geophysics*, *35*(2), 155–190. https://doi.org/10.1029/96rg03194

Martinis, C., Baumgardner, J., Mendillo, M., Taylor, M. J., Moffat-Griffin, T., Wroten, J., et al. (2019). First ground-based conjugate observations of stable auroral red (SAR) arcs. *Journal of Geophysical Research: Space Physics*, *124*(6), 4658–4671. https://doi.org/10.1029/2018ja026017

McIlwain, C. E. (1961). Coordinates for mapping the distribution of magnetically trapped particles. *Journal of Geophysical Research*, *66*(11), 3681–3691. https://doi.org/10.1029/jz066i011p03681

Mendillo, M., Baumgardner, J., & Wroten, J. (2016). SAR arcs we have seen: Evidence for variability in stable auroral red arcs. *Journal of Geophysical Research: Space Physics*, *121*(1), 245–262. https://doi.org/10.1002/2015ja021722

Mendillo, M., Baumgardner, J., Wroten, J., Martinis, C., Smith, S., Merenda, K. D., et al. (2013). Imaging magnetospheric boundaries at ionospheric heights. *Journal of Geophysical Research: Space Physics*, *118*(11), 7294–7305. https://doi.org/10.1002/2013JA019267

Pallamraju, D. (2023). SAR_Arcs_in_Daytime [Dataset]. OSF. https://doi.org/10.17605/OSF.IO/NKARQ

Pallamraju, D., Baumgardner, J., & Chakrabarti, S. (2000). A multiwavelength investigation of the Ring effect in the day sky spectrum. *Geophysical Research Letters*, *27*(13), 1875–1878. https://doi.org/10.1029/1999gl010961

Pallamraju, D., Baumgardner, J., & Chakrabarti, S. (2002). HIRISE: A ground-based high-resolution imaging spectrograph using echelle grating for measuring daytime airglow/auroral emissions.

Pallamraju, D., Baumgardner, J., Chakrabarti, S., & Pedersen, T. R. (2001). Simultaneous ground-based observations of an auroral arc in daytime/twilighttime OI 630.0 nm emission and by Incoherent Scatter Radar. *Journal of Geophysical Research*, *106*(A4), 5543–5549. https://doi.org/10.1029/2000ja000244

Pallamraju, D., Chakrabarti, S., Doe, R., & Pedersen, T. (2004). First ground-based OI 630 nm optical measurements of daytime cusplike and F-region auroral precipitation. *Geophysical Research Letters*, *31*(8), L08807. https://doi.org/10.1029/2003gl019173

Pallamraju, D., Chakrabarti, S., & Solomon, S. C. (2011). On deriving incident auroral particle fluxes in the daytime using combined ground-based optical and radar measurements. *Journal of Geophysical Research*, *116*(A4), A04309. https://doi.org/10.1029/2010JA015934

Pallamraju, D., Laskar, F. I., Singh, R. P., Baumgardner, J., & Chakrabarti, S. (2013). MISE: A multiwavelength imaging spectrograph using echelle grating for daytime optical aeronomy investigations. *Journal of Atmospheric and Solar-Terrestrial Physics*, *103*, 176–183. https://doi.org/10.1016/j.jastp.2012.12.003

Pallamraju, D., Sridharan, R., Gurubaran, S., & Raghavarao, R. (1996). First results from ground-based daytime optical investigation of the development of the equatorial ionization anomaly. *Annales Geophysicae*, *14*(2), 238. https://doi.org/10.1007/s005850050285

Phil Erickson, MIT/Haystack Observatory. (2004). Data from the CEDAR madrigal database [Dataset]. MIT. Retrieved from http://millstonehill.haystack.mit.edu/list

Picone, J. M., Hedin, A. E., Drob, D. P., & Aikin, A. C. (2002). NRLMSISE-00 empirical model of the atmosphere: Statistical comparisons and scientific issues. *Journal of Geophysical Research*, *107*(A12), 1468. https://doi.org/10.1029/2002JA009430

Prölss, G. W. (2006). Subauroral electron temperature enhancement in the nighttime ionosphere. *Annales Geophysicae*, *24*(7), 1871–1885. https://doi.org/10.5194/angeo-24-1871-2006

Rees, M. H., & Roble, R. G. (1975). Observations and theory of the formation of stable auroral red arcs. *Reviews of Geophysics*, *13*(1), 201–242. https://doi.org/10.1029/rg013i001p00201

Reinisch, B. W., & Galkin, I. A. (2011). Global ionospheric radio observatory (GIRO) [Dataset]. Earth Planets and Space, *63*(4), 377–381. https://doi.org/10.5047/eps.2011.03.001

Reinisch, B. W., & Huang, X. (2001). Deducing topside profiles and total electron content from bottomside ionograms. *Advances in Space Research*, *27*(1), 23–30. https://doi.org/10.1016/s0273-1177(00)00136-8

Rich, F. J., & Hairston, M. (1994). Large-scale convection patterns observed by DMSP. *Journal of Geophysical Research*, *99*(A3), 3827–3844. https://doi.org/10.1029/93ja03296

Shepherd, G. G., & Cho, Y. M. (2021). On the relationship of the O (1D) 630.0 nm dayglow emission to the F10. 7 cm solar flux and the solar zenith angle. *Journal of Geophysical Research: Space Physics*, *126*(3), e2020JA028715. https://doi.org/10.1029/2020ja028715

Solomon, S. C. (2017). Global modeling of thermospheric airglow in the far ultraviolet. *Journal of Geophysical Research: Space Physics*, *122*(7), 7834–7848. https://doi.org/10.1002/2017JA024314

Solomon, S. C., & Abreu, V. J. (1989). The 630 nm dayglow. *Journal of Geophysical Research*, *94*(A6), 6817–6824. https://doi.org/10.1029/JA094iA06p06817

Upadhyay, K., Pallamraju, D., & Chakrabarti, S. (2023). Imprint of storm enhanced density in ground-based OI 630.0 nm dayglow measurements. *Journal of Geophysical Research: Space Physics*, *128*(9), e2023JA031409. https://doi.org/10.1029/2023JA031409

Weygand, J. M., Zhelavskaya, I., & Shprits, Y. U. R. I. (2021). A comparison of the location of the mid-latitude trough and plasmapause boundary. *Journal of Geophysical Research: Space Physics*, *126*(4), e2020JA028213. https://doi.org/10.1029/2020ja028213

19448007, 2024, 3, Downloaded from https://agupubs.onlinelibrary.wiley.com/doi/10.1029/2023GL106292 by Physical Research Laboratory, Wiley Online Library on [02/02/2024]. See the Terms and Conditions (https://onlinelibrary.wiley.com/terms-and-conditions) on Wiley Online Library for rules of use; OA articles are governed by the applicable Creative Commons License

Check for updates

JGR Space Physics

RESEARCH ARTICLE
10.1029/2024JA032694

Key Points:

- Enhancements were observed in daytime O(^{1}D) red-line emissions during geomagnetically disturbed days over Boston, a mid-latitude location
- Direct measurement of electron temperature (Te) by DMSP showed increased brightness accompanied by increased Te at mid-latitudes
- The downward heat flux associated with larger Te in the daytime using O (^{1}D) emissions has been obtained for the first time

Correspondence to:
D. Pallamraju,
raju@prl.res.in

Citation:
Upadhyay, K., Pallamraju, D., & Chakrabarti, S. (2024). Estimation of downward heat flux into the F-region from the inner-magnetosphere during stable auroral red (SAR) arc events in the daytime obtained using OI 630.0 nm red-line emissions. *Journal of Geophysical Research: Space Physics*, *129*, e2024JA032694. https://doi.org/10.1029/2024JA032694

Received 28 MAR 2024
Accepted 18 JUN 2024

© 2024. American Geophysical Union. All Rights Reserved.

Estimation of Downward Heat Flux Into the F-Region From the Inner-Magnetosphere During Stable Auroral Red (SAR) Arc Events in the Daytime Obtained Using OI 630.0 nm Red-Line Emissions

Kshitiz Upadhyay[1,2], Duggirala Pallamraju[1], and Supriya Chakrabarti[3]

[1]Physical Research Laboratory, Ahmedabad, India, [2]Indian Institute of Technology, Gandhinagar, India, [3]University of Massachusetts, Lowell, MA, USA

Abstract Stable Auroral Red (SAR) arcs are enhanced OI 630.0 nm emissions formed due to an increased electron temperature (Te) near the equatorward wall of mid-latitude trough during geomagnetic disturbances. The Te enhancement associated with SAR arcs is driven by electron heating through heat flux precipitation from near plasmapause region to ionospheric F-region via heat conduction. Although Te enhancements have been reported by radar/satellite measurements along with increased 630.0 nm brightness during SAR arc events, measurements of corresponding heat flux are sparse, and almost none in the daytime. This work presents the results on the estimation of electron heat flux incident during SAR arcs formed during daytime obtained by a comprehensive suite of measurements, and forward modeling. We present observations of several SAR arc events when the ground-based OI 630.0 nm emissions were larger than the model values during disturbed periods and were found to be existing in conjunction with increased Te at the altitude of DMSP (~840 km). Forward modeling was carried out to determine the values of Te that would cause an enhancement in these emissions during daytime at much lower altitudes (~400–500 km). These values of Te were used to estimate the required electron heat flux varying in the range of ~1.0–4.6 $\times 10^{10}$ eV-cm^{-2}-s^{-1}. These results present the first estimates of F-region heat flux enabled using ground-based OI 630.0 nm emissions and open a new approach in the investigations of energy released into the ionosphere through heat conduction for daytime conditions during geomagnetically disturbed periods.

Plain Language Summary Stable Auroral Red (SAR) arcs are atomic oxygen redline (630.0 nm) emissions observed in the mid-latitude ionosphere. These are optical manifestations of direct energy transfer from high-altitude regions of inner-magnetosphere to the ionospheric altitudes. The process of energy transfer occurs in the form of electron heat flux or soft particle precipitation (<10 eV) along closed geomagnetic field lines. Downward heat flux increases the ambient electron temperature in the topside ionosphere, which contributes in imparting energy to the Oxygen atoms and exciting them to higher energy states. The return of excited atoms to ground-state results in the formation of SAR arcs. Although the electron temperature can be measured at high-altitudes by satellites during SAR arc events, the corresponding electron heat flux cannot be measured directly using existing experimental space plasma techniques. Therefore, model calculations are preferred. Important to this study is the estimation of required heat flux that caused enhancements in the measured daytime redline emissions from the ground, which were beyond the model estimates. This study finds the daytime energy flux required for producing SAR arcs is larger than that for the nighttime SAR arcs. Such findings are being reported for the first time.

1. Introduction

The mid-latitude upper atmosphere remains a favorable source for plasmasphere-ionosphere interactions at the edge of the poleward boundary of closed geomagnetic field lines. The geomagnetic storms give rise to several features over mid latitudes, such as, ionospheric storms during the expansion phase (e.g., Balan et al., 2010; Huang et al., 2005), sub-auroral ion drifts (SAID) reaching ~1 km-s^{-1} (Anderson, 2004; Foster, 1993) and increased dawn side electric fields (Horvath & Lovell, 2021), etc. Moreover, the electron density and electron temperature in the mid-latitude ionosphere are also greatly affected during geomagnetic disturbances. The depletion in plasma density at mid-latitudes forms the ionospheric trough. Sometimes during geomagnetic disturbances, this trough region coincides with a latitudinally narrow region (1–3°) of increased electron temperature

21699402, 2024, 7, Downloaded from https://agupubs.onlinelibrary.wiley.com/doi/10.1029/2024JA032694 by Physical Research Laboratory, Wiley Online Library on [05/07/2024]. See the Terms and Conditions (https://onlinelibrary.wiley.com/terms-and-conditions) on Wiley Online Library for rules of use; OA articles are governed by the applicable Creative Commons License

(Te) as observed in satellite measurements (Prölss, 2006). Large elevation scans by incoherent scatter radars also show enhanced electron temperature associated with trough region (e.g., Foster et al., 1994) over mid-latitudes. The night time observations suggest that sufficiently high enhancements in Te (>3,000°K) enable the excitation of atomic oxygen to its O(^{1}D) state and produces OI 630.0 nm red-line emissions in the form of stable auroral red (SAR) arcs (e.g., Kozyra et al., 1997; Rees & Roble, 1975). This relation between increased Te associated with ionospheric trough and O(^{1}D) emission enhancement causing SAR arc has been shown in various studies for nighttime (e.g., Baumgardner et al., 2013; Martinis et al., 2019; Mendillo et al., 2016) and recently, for the first time in daytime conditions (Upadhyay & Pallamraju, 2024).

Specific causes for sudden mid-latitude electron temperature enhancements are not completely understood yet. Various possible explanations have been suggested for increased electron temperature during geomagnetically disturbed times, such as, Coulomb collisions between low energy plasmaspheric particles and hot ring current ions (e.g., Kozyra et al., 1997 and references therein), Landau damping of electromagnetic ion cyclotron (EMIC) waves (Cornwall et al., 1971), and wave particle interactions (e.g., Mishin & Burke, 2005 and references therein), among others. These theories suggest a downward flow of heat by thermal conduction (or low-energy electrons) from the vicinity of outer plasmaspheric boundary having electron gas with even higher temperatures. This energy transfer from the inner-magnetosphere is considered to be the most probable source of ionospheric electron heating (Kozyra et al., 1997). Since the downward electron heat flux affects the thermal balance in the ionospheric F-region during storms, the resulting enhancement in Te can serve as a good proxy to understand the energy distribution by heat conduction in the mid-latitude ionosphere.

No technique exists to directly measure the electron heat flux precipitation from plasmasphere in to the topside ionosphere throughout. However, attempts have been made to derive precipitated heat flux using different ionospheric observations. One classic approach was performed by Evans (1973) using altitude profiles of Te at Millstone Hill for both day and nighttime conditions during different seasons and solar activity. In that work, it was found that daytime heat fluxes are larger in winters than in summers. In another work (Rees & Roble, 1975), modeling study was used to calculate the heat flow for low and high electron density values at the topside of the ionosphere and assessed that this heat contribution was responsible for enhancement in the OI 630.0 nm emission intensities during SAR arcs. Fok et al. (1991) estimated the night time electron temperatures as a function of heat flux using an ionospheric "storm model" for different seasons. These studies presented the dependence of OI 630.0 nm emission intensities on precipitated heat flux. Also, in the study of daytime cusp, the increased 630.0 nm dayglow emissions were directly found to be accompanied by enhanced Te due to particle precipitation (D. Pallamraju et al., 2004, 2011). Recently, Inaba et al. (2021) estimated the plasmaspheric heat flux using satellite measurements considering coulomb collisions as most reasonable process of energy transfer during night time.

Due to the sensitivity of OI 630.0 nm airglow emissions to Te variations as discussed above, these emissions become good tracers to investigate the associated ambient plasma characteristics from the ground during both day and night times. In this work, we aim to estimate the electron heat flux precipitated from near plasmapause region in mid-latitude upper ionosphere during daytime conditions, when SAR arcs were measured by ground-based high resolution imaging spectrograph from Boston.

2. Data

2.1. OI 630.0 nm Dayglow Observations

The daytime ground-based observations of atomic oxygen 630.0 nm airglow were carried out using High-Resolution Imaging Spectrograph using Echelle grating (HIRISE, D. Pallamraju et al., 2002) from Boston (42.36°N, 71.05°W, magnetic latitude (MLAT)≈51.90°N), a mid-latitude location. The available data from HIRISE were considered during September-2005 to April-2007 over zenith. The HIRISE obtained spectral images were used to extract the dayglow emission brightness at 630.0 nm wavelength at a cadence of 5-min by following the dayglow extraction procedure as given in detail by D. Pallamraju et al. (2000, 2002), and is briefly described here. Firstly, the HIRISE obtained sky spectra was compared with the solar spectra (Delbouille et al., 1973) in wavelengths and continuum regions around the 630.0 nm using the least-squares technique, and their difference was obtained. Since the sky spectrum contains airglow emissions, telluric absorptions, and scattering contributions, the difference that is obtained at 630.0 nm corresponds to the contributions from the optical emissions and scattering (Ring effect). To remove the scattering contribution from 630.0 nm emission region, a neighboring Fraunhofer absorption region separated by just ~0.035 nm which has an equivalent

21699402, 2024, 7, Downloaded from https://agupubs.onlinelibrary.wiley.com/doi/10.1029/2024JA032694 by Physical Research Laboratory, Wiley Online Library on [05/07/2024]. See the Terms and Conditions (https://onlinelibrary.wiley.com/terms-and-conditions) on Wiley Online Library for rules of use; OA articles are governed by the applicable Creative Commons License

absorption line strength (normalized depth × FWHM) with that of the 630.0 nm region was considered. As this region does not consists of any telluric lines, the difference between the contributions from the sky and the scaled solar spectra corresponds to the contribution of the Ring effect. As it has been shown that the scattering contribution in two neighboring absorption regions of equivalent absorption line strengths is equal (D. Pallamraju et al., 2000), the difference in contributions between these two regions suitably accounts for the contributions of scattering and hence yields the information on the 630.0 nm dayglow emissions alone (D. Pallamraju et al., 2002).

2.2. Millstone Hill Digisonde

For the information on variation in local electron density, the data from a collocated Millstone Hill based digisonde (42.60°N, 71.50°W) were used. The vertical profiles of electron density were obtained from digisonde ionograms using the R-H method (Reinisch & Huang, 2001). These were used as inputs to the GLOW model to estimate the OI 630.0 nm volume emission rates at a given time, as detailed in section-3 below. The model estimated emission profiles were then used to obtain the column integrated OI 630.0 nm emission intensities to enable comparison with the HIRISE measured emissions for different local times and geomagnetic activity conditions.

2.3. Satellite Plasma Measurements

The in situ measurements of plasma parameters (electron density, Ne, and electron temperature, Te) were obtained from different passes of Defense Meteorological Satellite Program (DMSP) satellites. DMSP provides information on ionospheric plasma at an altitude of around 840 km. As, increased Te peak and reduced Ne are the two important ionospheric signatures of the presence of SAR arcs (Baumgardner et al., 2013; Foster et al., 1994), several studies have used DMSP measured nighttime Ne, and Te variations to identify SAR arcs over mid-latitudes (e.g., Martinis et al., 2019; Mendillo et al., 2016). In addition, a few earlier studies have reported an increased Te in both nighttime (e.g., Mendillo et al., 2013) and daytime (Upadhyay & Pallamraju, 2024) as measured by DMSP corresponding to the presence of SAR arcs. In this study, we have used daytime (6–18 magnetic local time, MLT) DMSP latitudinal measurements at 4-s resolution to examine the presence of peak Te along with its location.

In addition to the variations in bottomside Ne from digisonde and topside Ne from DMSP, the column integrated plasma density, (Total Electron Content, TEC) as obtained from collocated GPS-station Westford (42.6°N, 71.4°W, GPS code = WES2) are also used in this study.

2.4. Geomagnetic Indices

To describe the geophysical conditions, daily averaged solar flux (F10.7) values measured in solar flux unit (sfu; 1sfu = 10^{-22}Wm^{-2} Hz^{-1}) and the hourly geomagnetic indices (Dst, Kp) attained from SPDF OMNIWeb were used. Geomagnetically quiet and disturbed periods were segregated with Kp < 3 and Kp ≥ 3. Geomagnetic Coordinates were obtained for a given year using the OMNIWeb service at https://omniweb.gsfc.nasa.gov/vitmo/cgm.html.

3. Model Emissions

The OI 630.0 nm airglow emissions are produced by the de-excitation of atomic oxygen from its excited state O(^{1}D) to its ground state O(^{3}P). O(^{1}D) in daytime is formed by the collision of O(^{3}P) with thermal and photo electrons (photoelectron impact; PEI), photo-dissociation (PD) of Oxygen molecule (O_2), and dissociative recombination of O_2^+ (DR) production mechanisms (D. P. Pallamraju et al., 1996; Solomon & Abreu, 1989). The photochemical model, GLOW, (Solomon, 2017) provides the column integrated emission intensity at 630.0 nm by considering the neutral and ionospheric parameters as inputs. For thermospheric neutral densities and temperatures, GLOW model uses Naval Research Laboratory Mass Spectrometer Incoherent Scatter (NRLMSIS-00) atmosphere (Picone et al., 2002) and International Reference Ionosphere (IRI-90) for ionospheric plasma (electron/ion) densities and their temperatures (Bilitza, 1990). In this work, the digisonde measured values of electron densities are fed instead of IRI electron densities to improve the accuracy of the GLOW model predicted emissions, while the positive ion densities are taken in proportion to maintain the charge-neutrality condition at each altitude. This apportionment is carried out as described in the IRI. The comparison of GLOW estimates with the HIRISE measured dayglow emissions will provide greater insights into the dynamics of ionosphere-thermosphere regions, especially during geomagnetic disturbances, as discussed in the next section. In

21699402, 2024, 7, Downloaded from https://agupubs.onlinelibrary.wiley.com/doi/10.1029/2024JA032694 by Physical Research Laboratory, Wiley Online Library on [05/07/2024]. See the Terms and Conditions (https://onlinelibrary.wiley.com/terms-and-conditions) on Wiley Online Library for rules of use; OA articles are governed by the applicable Creative Commons License

addition, based on the global OI 630.0 nm measurements by WINDII (Wind Doppler Imaging Interferometer) on board UARS (Upper Atmospheric Research Satellite), a WINDII empirical model (WEM) has been developed (Shepherd & Cho, 2021). WEM predicts the OI 630.0 nm emissions using the values of solar flux and solar zenith angle at any given time. The estimated dayglow emissions from these two models are used to compare with our HIRISE measured dayglow emission variability. WEM predictions have been shown to match well with the HIRISE measured OI 630.0 nm dayglow during geomagnetically quiet days (D. Pallamraju et al., 2020, Shepherd & Cho, 2021). Upadhyay et al. (2023) showed that by applying the scaling factor between HIRISE data and WEM predictions obtained during geomagnetically quiet days, the dayglow brightness values can be obtained during geomagnetic disturbances. The same approach has been applied in this study as well.

4. Observation and Results

From the aforementioned OI 630.0 nm dayglow production mechanisms, it can be noted that the contribution to the OI 630.0 nm dayglow by photoelectron impact and photodissociation mechanisms is primarily dependent on solar flux and solar zenith angle. The dayglow production rate due to dissociative recombination depends on ambient electron densities (Ne) at a given time, and their variation can be quite dynamic (of the order of a few minutes), especially during geomagnetic storms. Also, positive and negative ionospheric storms can alter the ionospheric electron densities from their mean quiet time behavior at a given latitude. Therefore, in several earlier studies, small time scale variations in Ne during geomagnetic disturbances have been shown to affect the 630.0 nm dayglow intensity variability at all latitudes (e.g., Pallamraju & Chakrabarti, 2005; D. Pallamraju et al., 1996, 2001, 2010; Upadhyay et al., 2023). Temporal variations in the dayglow emissions can also occur through the photoelectron impact mechanism on occasions, such as, occurrence of solar flares (e.g., Das et al., 2010; Sumod et al., 2014). Also, during some geomagnetically disturbed periods, when additional deposition of heat from inner-magnetosphere in the mid-latitude ionosphere increases the ambient electron temperature (Te) to more than 3000 K, such enhanced Te also causes production of O(^{1}D) emissions through the PEI mechanism and thereby produces SAR arcs (Rees & Roble, 1975; Upadhyay & Pallamraju, 2024).

This work presents results obtained on the daytime OI 630.0 nm emission enhancements measured during geomagnetically disturbed days. The observed intensities were larger than the model estimated emissions. Complementary data from in situ satellite measurements ascertain that the HIRISE measured dayglow emissions were collocated and in simultaneity with the enhancements in Te. In this work, electron heat flux precipitated from near the plasmapause region at F-region heights is estimated during such periods of observed enhancement in OI 630.0 nm brightness.

Figures 1a–1d shows 4 days of HIRISE measured dayglow emission variations with respect to local time (LT = UT-5 hrs). The solar flux for all these days was low and close to 80 sfu. Figure 1a shows a geomagnetically quiet day (30-October 2006) with daily averaged <Kp> = 2+. Due to the dynamic nature of dayglow emission variability associated with ionospheric variations during the disturbed periods, the maximum Kp (Max_Kp) during the observation period was also examined for each day. For 30-October 2006, the Max_Kp was 2. On the other hand, for the three disturbed days (24-November, 20-February, and 10-November 2006) the <Kp> values were 3, 3+, 4+, and the maximum Kp (Max_Kp) during observation period were 3+, 5−, 4 respectively, as shown in Figures 1b–1d. For each day in Figure 1, temporal variations of HIRISE measured O(^{1}D) dayglow emission intensities (along with ±1σ) are shown by dotted-red line. Due to direct entry of sunlight into the instrument around local-noon, CCD gets saturated and thus, the data during that period are not useful. Also, due to the presence of clouds in the forenoon of 20-February 2006 and afternoon of 10-November 2006, those data were not considered. The black-solid line in Figure 1 represents the WEM estimated O(^{1}D) dayglow intensity which match well with HIRISE measured emissions on the quiet day 30-October 2006 (Figure 1a). On the disturbed days (Figures 1b–1d), HIRISE emissions show larger intensity than WEM estimates on various occasions. As discussed above, the O(^{1}D) dayglow intensity is sensitive to the variation in electron density and temperature which can change over small time-periods in subauroral-latitude ionosphere during geomagnetically disturbed periods. Therefore, firstly to identify the effect of electron density variations, GLOW model was used to calculate emission intensities using measured electron density from collocated digisonde for each day. The GLOW estimated emissions are shown by blue-dot line in Figure 1. It can be seen that on the quiet day 30-October 2006 (Figure 1a), the GLOW estimated emissions too match well with the diurnal variation of emissions measured by HIRISE. On the disturbed day 24-November 2006 (Figure 1b), the GLOW estimates are larger than those of WEM, but are in good agreement with the HIRISE observed emissions. This suggests that brighter HIRISE

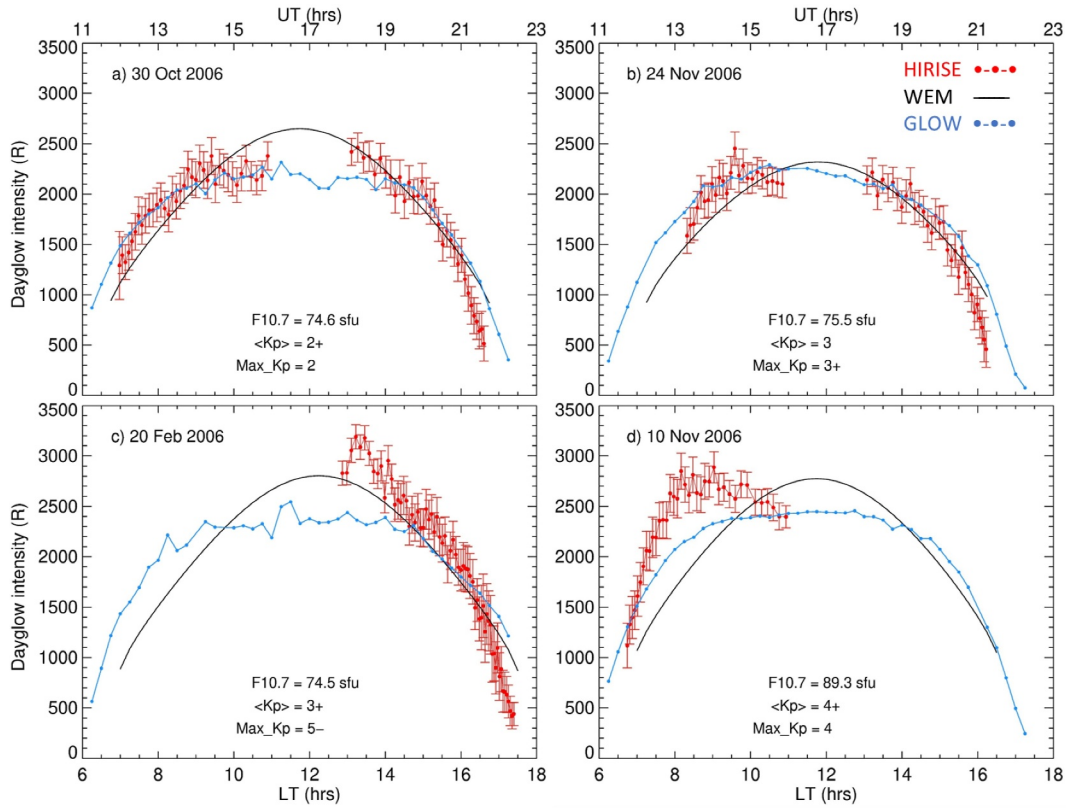

Figure 1. Dayglow temporal variations are shown for 4 days. Bottom and top *x*-axes represent the local and universal time (Local time, LT = UT-5 hrs). The red-dots show the HIRISE measured dayglow emissions over Boston, black-solid line represents the WEM calculated emissions and the blue-dots show the GLOW model output obtained by using as inputs the ionosonde measured electron densities at Millstone Hill. The panel-a (30-October 2006) shows a geomagnetically quiet day with daily average, <Kp> = 2 and maximum Kp (Max_Kp) during daytime hours as 2+. Panels-(b–d) show three geomagnetically disturbed days with <Kp> and Max_Kp ≥ 3 and 3+. The daily averaged solar flux represented by F10.7 for each of the days is also shown. Larger measured emissions by HIRISE on 20-February and 10-November 2006 are due to SAR arcs in the daytime.

emissions on this day and time were associated with higher electron densities during disturbed times which were captured in the digisonde electron density data. However, on 20-February and 10-November 2006 (Figures 1c and 1d), HIRISE measured emissions were even larger than the GLOW predictions. This clearly indicates the potential cause for this enhancement to be something other than (or in addition to) the electron density variations. Another important parameter that can affect O(^{1}D) emissions is the electron temperature in subauroral ionosphere as discussed in Section 3. Such O(^{1}D) 630.0 nm emission enhancements have been reported in the literature for both night time and daytime conditions (e.g., Baumgardner et al., 2013; Martinis et al., 2019; Mendillo et al., 2016; Upadhyay & Pallamraju, 2024). These larger emissions at F-region heights have been described by thermal emissions due to increased Te and as a plausible source for SAR arc formation (e.g., Nagy et al., 1970; Kozyra et al., 1997 and reference therein). To ascertain if the Te enhancement caused larger emissions on 20-February and 10-November 2006, DMSP measured in situ Te data during the period of enhanced emissions observed in the OI 630.0 nm dayglow were considered. From Figure 1, it can be noted that the local time of enhancement in dayglow on 20-February was during 12.5–14.5 LT (17.5–19.5 UT) and on 10-November 2006 during 7.5–10.5 LT (12.5–15.5 UT). There were no DMSP passes over the observation location in these durations, however, there were three passes in the dayside during these intervals of enhanced daytime red-line emissions. Ground-tracks of DMSP-F15 on 20-February 2006 with passes over 52°N MLAT at 15.66 (red), 17.34 (green), and 19.01 UT (blue) are shown in Figure 2 (top left panel-2a). The red star symbol points to the location of Boston, from where the OI 630.nm emission measurements were made during daytime using HIRISE. The bottom panels (2c, 2e, 2g) in Figure 2 show the corresponding Te variation in the magnetic latitude range from 20°N to 70°N at the times indicated in Figure 2a. Similarly, the top right panel-2b shows the DMSP-F13 passes on

21699402, 2024, 7, Downloaded from https://agupubs.onlinelibrary.wiley.com/doi/10.1029/2024JA032694 by Physical Research Laboratory, Wiley Online Library on [05/07/2024]. See the Terms and Conditions (https://onlinelibrary.wiley.com/terms-and-conditions) on Wiley Online Library for rules of use; OA articles are governed by the applicable Creative Commons License

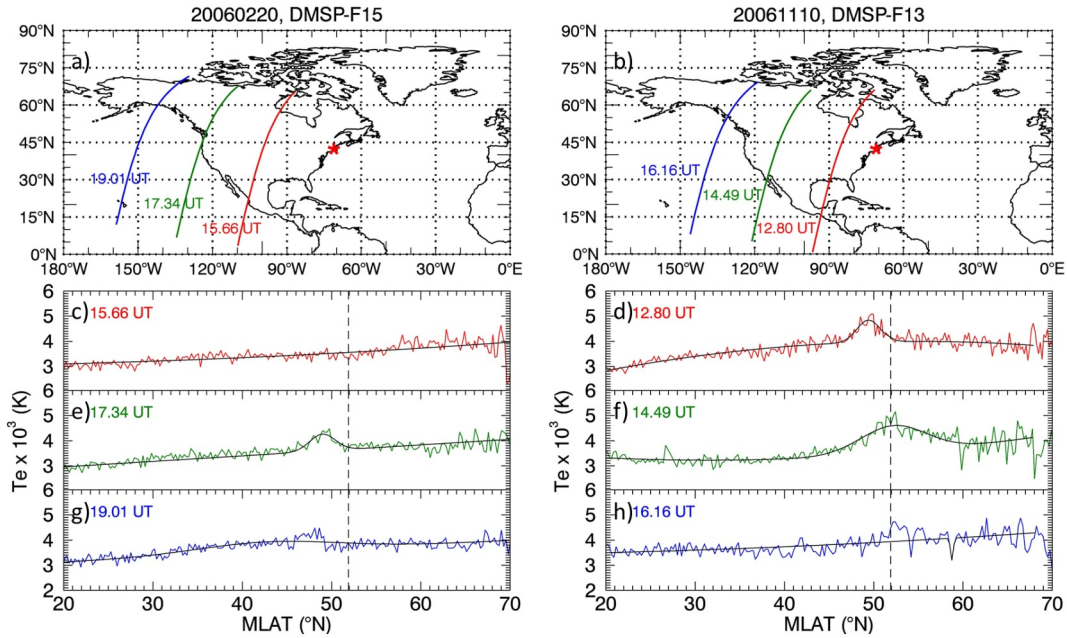

Figure 2. The panels-a and b show ground-tracks of three different DMSP passes on 20-February 2006 and 10-November 2006, respectively. The red star depicts the dayglow observation location, Boston. The panels-(c, e, g) show the DMSP measured Te variation for three passes on 20-February (shown in panel-a) in 20–70°N MLAT range. Similarly, panels-(d, f, h) represents the latitudinal Te variation on 10-November 2006 measured by DMSP. The times of DMSP pass over ~52°N MLAT (marked by dashed vertical line) are indicated next to each Te profile. The black-solid line in each of the DMSP Te values show the polynomial fits. A sharp Te peak can be seen at 17.34 UT corresponding to observed enhancement in dayglow near 13 LT (18 UT) on 20-February and another Te peak from 12.80 to 14.89 UT on 10-November 2006, in conjunction with the observed dayglow enhancement duration ~7.2–10 LT (12.2–15 UT).

10-November 2006 at 12.80, 14.49, 16.16 UT and the bottom panels (2d, 2f, 2h) present the corresponding Te variations. For each of these latitudinal Te variations, polynomial fits were carried out, as shown by black line. On 20-February 2006 (Figure 2 left panel), initially no Te enhancement was noted during the DMSP-pass at 15.66 UT, but interestingly a sharp Te peak arises at 50° MLAT during the 17.34 UT pass. This Te peak then started to fade away during the next pass at 19.01 UT. The peak electron temperature at 17.34 UT was noticeably increased by around 1,000 K than the previous pass at 15.66 UT attaining the value of ~4,300 K UT during this 1.68-hr interval. This time duration and MLAT of appearance of Te peak at 17.34 UT coincides with that of HIRISE measured dayglow emissions enhancements (17.5–19.5 UT/12.5–14.5 LT). These emissions match with model emissions after this duration (Figure 1c), which is also consistent with the disappearance of the Te peak in the DMSP data in the following pass (Figure 2g). On 10-November 2006 (Figure 2 right panel), a clear sharp Te peak can be seen during the pass at 12.80 UT (50° MLAT, Figure 2d). This peak in Te moved ~2° poleward from 50° to 52° MLAT by the next pass at 14.49 UT (Figure 2f). The maximum intensity in dayglow on 10-November 2006 was observed during the same period (8–9 LT/13–14 UT, Figure 1d). The maximum brightness in dayglow near 9 LT (14 UT) corresponds to peak Te of ~5,000 K at 52.43° MLAT. Therefore, the appearance of this Te peak and its poleward movement during 12.80–14.49 UT were found to be concurrent with the observed enhancement in dayglow emissions by HIRISE. Subsequent to this duration as the Te peak diminished at 16.16 UT (Figure 2h), the emissions started to decrease and follow the GLOW estimated emissions near 11 LT (16 UT). The time evolution of DMSP observed Te-peak on 20-February and 10-November 2006 show a good agreement with temporal enhancements observed in the diurnal variation of the 630.0 nm emissions during daytime.

From the dayglow data set that corresponds to years 2005–2007, out of the clear sky days of data obtained, we noted enhancements in the measured emissions on a few occasions (some of them are shown in Figure 3 left column) that were beyond the GLOW model estimates on that day. The HIRISE observed emissions on disturbed days 03-November 2005, 11-December 2005, 07-December 2006, and 31-January 2007 are shown by red dots in Figures 3a, 3d, 3g, and 3j respectively, similar to Figure 1 along with WEM and GLOW estimated emissions. The <Kp> was found to be 3+ or more on each day, while the maximum Kp during daytime reached 5−, with the

21699402, 2024, 7, Downloaded from https://agupubs.onlinelibrary.wiley.com/doi/10.1029/2024JA032694 by Physical Research Laboratory, Wiley Online Library on [05/07/2024]. See the Terms and Conditions (https://onlinelibrary.wiley.com/terms-and-conditions) on Wiley Online Library for rules of use; OA articles are governed by the applicable Creative Commons License

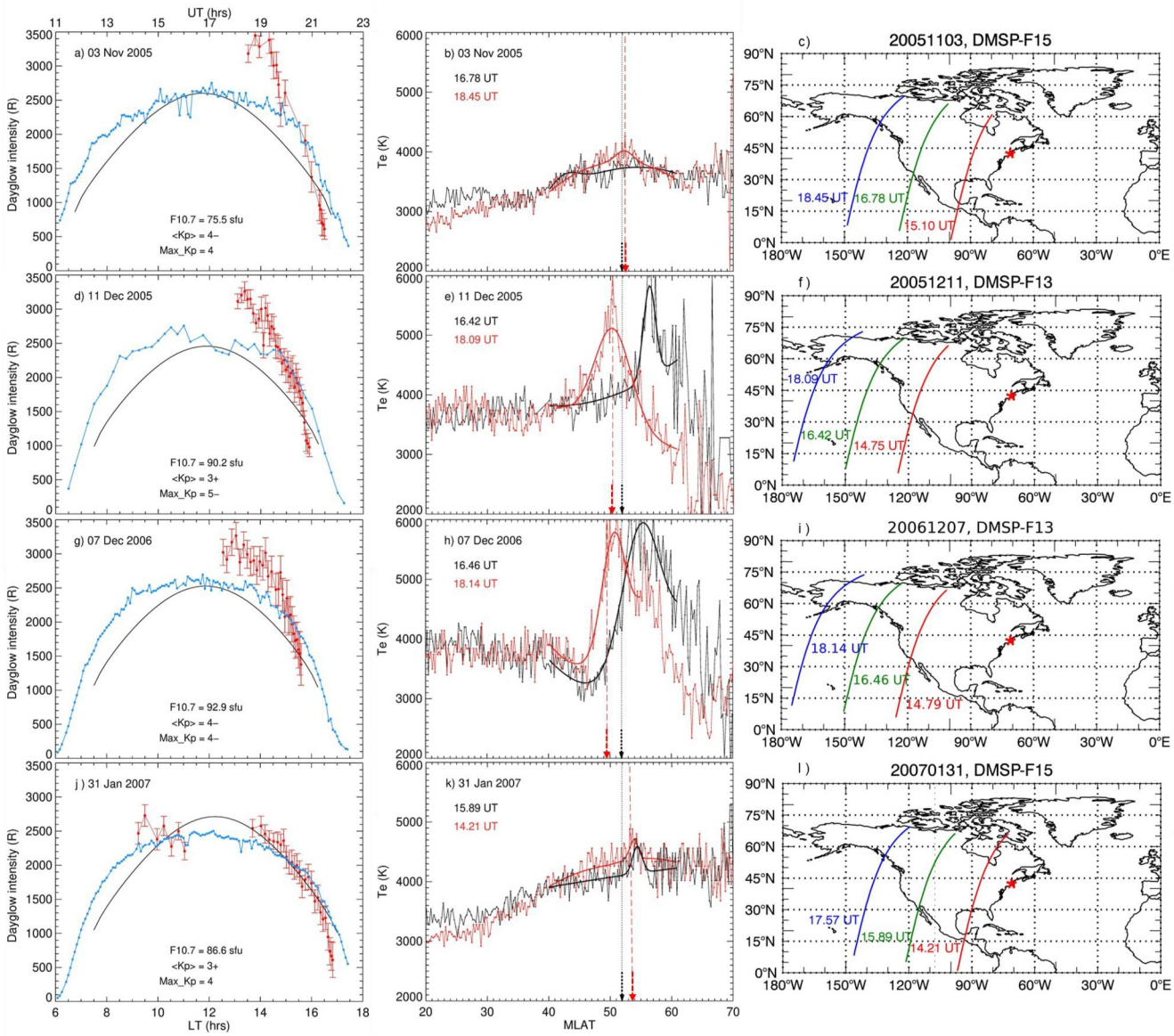

Figure 3. The left column (panel-a, d, g, j) shows four disturbed days of dayglow observation, similar to Figures 1c and 1d. The bottom and top *x*-axes represent LT and UT, respectively. The middle column (panel-b, e, h, k) shows respective DMSP measured latitudinal Te variation for two different passes-one during the time of observed enhancement in 630.0 nm emissions (red-color) and other just before/after this duration (black-color). The dotted-black and red-dashed arrow corresponds to the MLATs of observation of enhanced emission and maximum in Te in 40–60° MLAT range for the first pass. For each profile, a polynomial fit was performed in the 40–60° MLAT range to show Te peak clearly. The right column shows the corresponding DMSP ground-tracks for measured Te variations (middle-panel). The poleward shift or disappearance of Te peak can be seen before/after the duration of observed enhancement in emissions by black-colored Te variation.

largest disturbance being on 11-December 2005. It can be seen from Figures 3a, 3d, 3g, and 3j that HIRISE observed emissions were beyond the model estimates for 1–2 hr. The peak brightness was observed around 14.00, 13.50, 13.01, and 09.50 LT, respectively, on these 4 days. Similar to what was presented in Figure 2, here, we focus on the DMSP measured latitudinal variation in Te corresponding to the time-period of observed emission brightness and for the pass just before or after this duration on these days, as shown in Figure 3 panel-b, e, h, k (middle column). The corresponding ground-track of the DMSP satellite for these passes is shown in Figure 3 panel-c, f, i, l (right column). The red-line in middle column represents the Te corresponding to the duration when enhanced brightness was observed in the daytime emissions shown in left column, while the black line represents the Te variation measured just before/after this pass. The black-dotted and the red-dashed vertical arrows indicate the magnetic latitude of the observation and peak Te (in the 40–60°N MLAT range) locations. The polynomial fit

21699402, 2024, 7, Downloaded from https://agupubs.onlinelibrary.wiley.com/doi/10.1029/2024JA032694 by Physical Research Laboratory, Wiley Online Library on [05/07/2024]. See the Terms and Conditions (https://onlinelibrary.wiley.com/terms-and-conditions) on Wiley Online Library for rules of use; OA articles are governed by the applicable Creative Commons License

21699402, 2024, 7, Downloaded from https://agupubs.onlinelibrary.wiley.com/doi/10.1029/2024JA032694 by Physical Research Laboratory, Wiley Online Library on [05/07/2024]. See the Terms and Conditions (https://onlinelibrary.wiley.com/terms-and-conditions) on Wiley Online Library for rules of use; OA articles are governed by the applicable Creative Commons License

Table 1
The Observed Characteristics of Daytime O(^{1}D) Emission Enhancement Measured by HIRISE and DMSP Measured Peak Te Variations

Date of O(^{1}D) emission enhancement due to SAR arcs.	Time of peak occurrence in brightness (UT; LT = UT-5 hours)	Approximate brightness difference between HIRISE measured and GLOW model estimates (Rayleigh)	Time of DMSP pass crossing over the MLAT of observation location (~52°N) (UT)	Peak Te measured by DMSP in 40–60°N MLAT range (Kelvin)	Latitudinal separation of Te Peak observed by DMSP from that of HIRISE operating from Boston (42.36°N, 71.05°W) (degree)
03-November 2005	18.78	981	18.45	5,240	0.5°N
11-December 2005	18.37	825	18.09	5,980	1.5°S
20-February 2006	18.22	828	17.34	4,480	2.15°S
10-November 2006	14.00	559	14.49	5,160	0.53°N
07-December 2006	18.01	800	18.14	6,290	2.4°N
31-January 2007	14.50	433	14.21	4,880	1.27°N

for DMSP measured Te is shown by thick red/black lines for the two passes. It is interesting to note that, for each time when maximum brightness was observed (Figure 3 left column), a region of Te peak exists in the vicinity of latitude (MLAT) of dayglow observations within ±2°. Of all days, the maximum enhancement in Te can be seen on 07-December 2006 (Figure 3h) corresponding to greater geomagnetic disturbances during daytime. Moreover, the Te variations for the other neighboring passes (black-line) show that enhancement in Te is either absent or that the peak in Te is located further poleward and away from the HIRISE field of view at that time. Consequently, no enhancement was observed in the HIRISE measured emissions at these times. Therefore, DMSP measured Te enhancements complement well with the observed increase in O(^{1}D) emission intensities during such disturbed periods, and thus correspond to the optical signature of SAR arc emissions in the daytime. The O(^{1}D) emission brightness and Te characteristics obtained for these days are summarized in Table 1.

5. Discussion

As not only an increase in electron temperature, but also the electron density enhancement can give rise to enhanced red-line emissions during daytime, it is required that this aspect needs a closer inspection. While the bottomside electron density enhancements can be measured by digisondes, the enhancements in the densities in the topside, as in case of storm enhanced density (SED) can be captured clearly by the Incoherent Scatter Radars (e.g., Zou et al., 2013). Being column-integrated in nature, the OI 630.0 nm dayglow emissions can and do capture the SED. In one of our recent works, we had reported the first measurements of SED in the daytime using the HIRISE measurements from Boston (Upadhyay et al., 2023). As SEDs can cause an enhancement in TEC as well (e.g., Foster et al., 2002), an assessment has been made of TEC variation on all these days listed in Table 1, as shown in Figure 4a. The dashed-vertical lines for each day correspond to the times when enhanced brightness were observed. A clear dip in TEC was present notably on 03-November 2005, 20-February 2006, 07-December 2006, and 31-January 2007. Neither a dip nor any noteworthy enhancement was noted in TEC on 11-December 2005 and 10-November 2006 that could contribute to any of the observed increase in emission intensities from topside ionospheric densities. Therefore, this clearly rules out the possibility of observed increased brightness to be due to the variation in either bottomside or topside electron densities and further leads to the confirmation on enhanced Te effects to be responsible for the observed enhancement in the brightness.

As Te enhancements during SAR arcs are known to fall in the reduced density region of mid latitude ionospheric trough (Baumgardner et al., 2013; Prölss, 2006), therefore, to examine the behavior of electron density corresponding to the time of peak Te occurrence (listed in Table 1) DMSP measured latitudinal Ne variations were considered, as shown in Figure 4b. In Figure 4b, dashed vertical line corresponds to the MLAT of observation location, while square symbols for each latitudinal Ne represent the location of Te peak. It can be seen that for each day the location of DMSP measured Te peak is in the reduced density region of ionospheric trough. The Te peaks on 11-December, 20-February, and 07-December were associated with rapid fall of plasma density and located in close proximity of equatorward edge of trough. However, on 03-November 2005, the Te peak location seems to be associated with a slight increase in plasma density in its vicinity. The presence of Te peak in

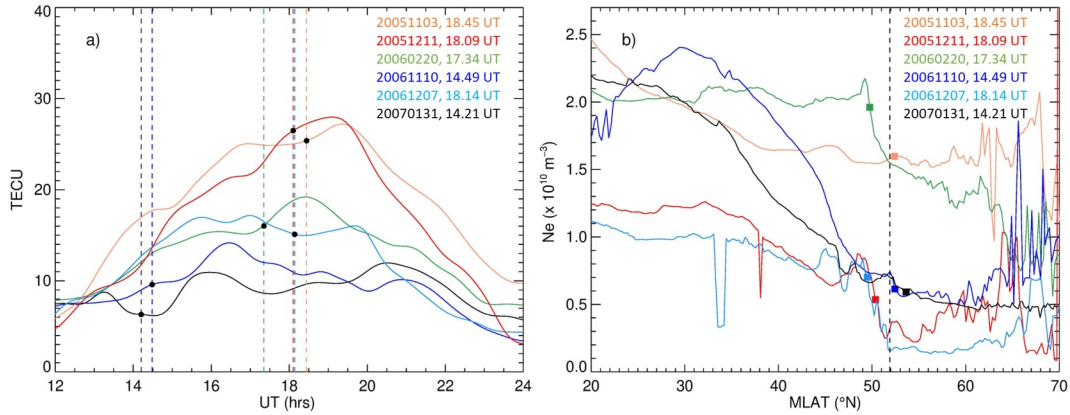

Figure 4. (a) Diurnal variations in GPS-TEC for all days listed in Table 1. The dashed-vertical lines correspond to the time of observed increase in the 630.0 nm emission brightness on each day. A clear reduction with no remarkable increase in plasma density can be seen during the period of enhanced emissions on these days, which rules out the topside electron density enhancements, such as SEDs, if any as the cause for the redline emission enhancement. (b) DMSP measured latitudinal Ne variations between 20 and 70°N MLAT range corresponding to the time of peak Te occurrence for each day. The dashed-vertical line corresponds to the MLAT of observational-location, while square symbols represent the location of Te peak for each latitudinal Ne.

association with a small Ne increase suggests that on 03-November, not only did the additional downward heat deposition occur but also the plasma was supplied from the inner-magnetosphere. This case of increased Ne resulting in SAR arcs is similar to that observed by Inaba et al. (2020), wherein enhanced Te peak was collocated with increased electron density in SAR arc region. Therefore, these latitudinal Ne variations suggest that the presence of enhanced Te peak was collocated with the ionospheric trough, providing the conducive conditions for SAR arc formation, and reflected as enhanced brightness in daytime red-line emissions.

Table 1 depicts that maximum enhancement in Te was much greater and was varying between 5,000 ± 1,000 K with the localized Te peak within around ±2° range centered at ~52°N MLAT. Such high Te values are found to be sufficient enough to excite O atoms to their O(^{1}D) state and cause larger OI 630.0 nm emission intensities (Kozyra et al., 1997; Rees & Roble, 1975). In the study of high-latitude daytime cusps by D. Pallamraju et al. (2004), the enhanced OI 630.0 nm dayglow emissions were found to be directly associated with increased Te (>4,000 K). Furthermore, the recent work by Upadhyay and Pallamraju (2024) estimated the sufficiently high Te values (reaching approximately 4,400 K) required to produce the daytime SAR arc emissions. It is worth noting that all days listed in Table 1 with observed enhancements in the OI 630.0 nm emissions were associated with increased electron temperatures. The GLOW estimates, however, did not reflect large emissions as measured by HIRISE during these time intervals. This is due to the fact that the IRI-model generated Te profiles were used in GLOW, which do not reflect this change. Also, study by Araujo-Pradere et al. (2003) found that the IRI Te-profiles might provide inaccurate Te values during geomagnetically disturbed periods. Therefore, to obtain a better estimation of electron temperature variations on these occasions, forward modeling (FM) has been carried out. To perform FM, we have iteratively increased Te at each altitude in the 200–650 km range by a constant fraction from the model value to match GLOW estimates within 1% of HIRISE measured emission brightnesses for all the days listed in Table 1. The modeling was carried out for all times when ionosonde measured Ne values were available and HIRISE emissions were larger than the GLOW estimates. Thus, the GLOW estimates obtained after forward modeling are shown in Figure 5 by blue-asterisks, wherein, the maximum Te value in the range of 200–650 km required to satisfy this enhancement is given in the right-side *y*-axis. It may be noted that the maximum temperature obtained by FM varies in the range from 3,000 to 4,500 K, which are consistent with earlier estimates of Te (Upadhyay & Pallamraju, 2024) for daytime SAR arcs. Such high electron temperatures trigger the excitation of the 630.0 nm emission by photoelectron impact mechanism. Furthermore, an important finding from the latitudinally narrow Te peak measured by DMSP and the larger estimated values of Te by FM suggests that during disturbed times, additional heating due to downward heat deposition may occur in the daytime ionosphere apart from the local heating by solar extreme ultraviolet (EUV) radiation. Such sudden enhancement in Te during periods of geomagnetic disturbances in subauroral ionosphere can result from deposition of magnetospheric heat to thermal electrons. The various possible sources responsible for this heat inflow

21699402, 2024, 7, Downloaded from https://agupubs.onlinelibrary.wiley.com/doi/10.1029/2024JA032694 by Physical Research Laboratory, Wiley Online Library on [05/07/2024]. See the Terms and Conditions (https://onlinelibrary.wiley.com/terms-and-conditions) on Wiley Online Library for rules of use; OA articles are governed by the applicable Creative Commons License

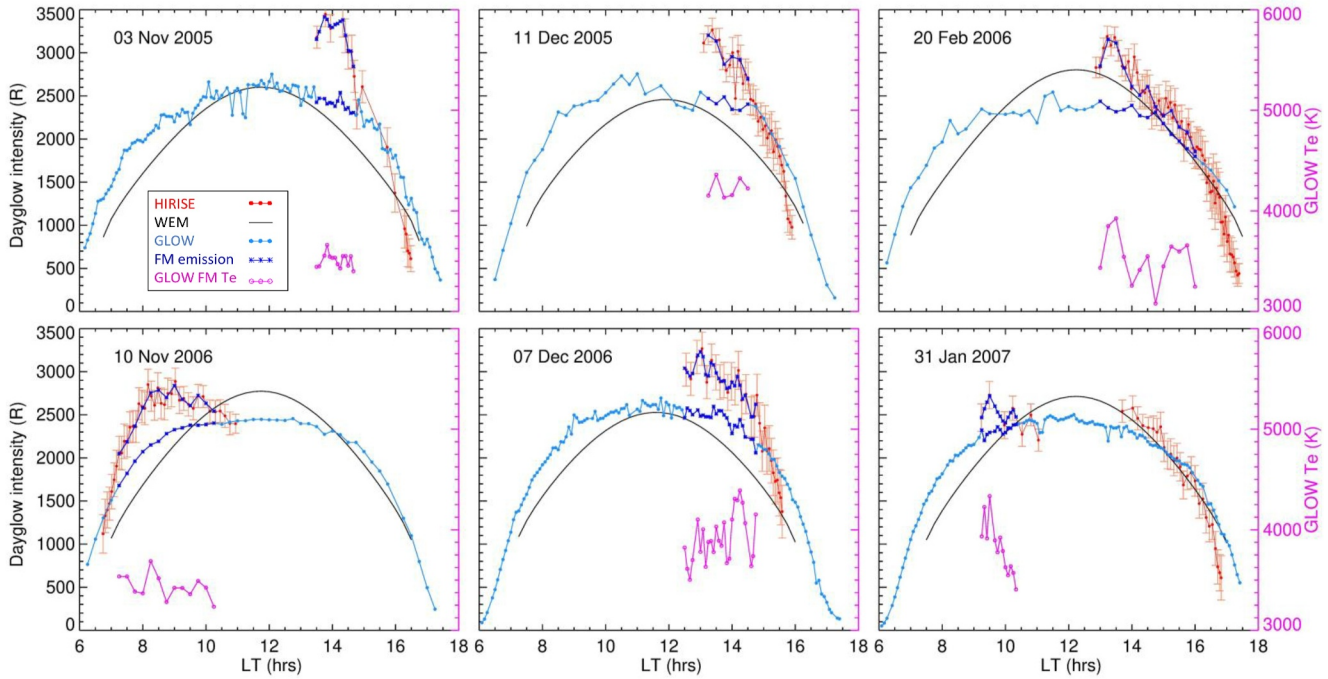

Figure 5. Emission rates obtained by forward modeling (FM) are shown by blue-asterisks for all days listed in Table 1. FM was performed during the period when HIRISE observed emissions were larger than the Model estimates. The FM estimated emissions match well with the HIRISE observed emissions. The right-side *y*-axis for each day shows the FM estimated maximum electron temperature (in 200–650 km) required to produce higher magnitudes of O(^{1}D) emissions that match with the observed emissions.

include (a) energy transfer from near plasmapause caused by strengthened ring current during storm-time over the equator, and (b) very low-energy particle precipitation, with the former suggested to be the major contributor (Cornwall et al., 1971; Kozyra et al., 1987; Prölss, 2006). The instabilities generated in the ring current during geomagnetic disturbances work as the main source for this heating, which takes place near the equatorial plane. Energy transfer mechanisms such as, Coulomb collisions and wave-particle interactions are suggested from equatorial plane to subauroral ionosphere following the closed geomagnetic field lines. Here, we consider the major source for the heat generation that enhances the Te to be the Coulomb collisions between hot ring current ions and cold plasmaspheric electrons (Fok et al., 1995; Kozyra et al., 1997). The downward heat flow from near plasmapause heights during geomagnetic disturbances is also the root cause for high electron temperatures and SAR arcs formation, dominated by 630.0 nm emissions (Kozyra et al., 1986). There are studies that have reported Te enhancement in sub-auroral latitudes that produce SAR arcs (e.g., Baumgardner et al., 2013; Foster et al., 1994; Martinis et al., 2019), but there are no reports of measurements of heat flux associated with enhanced Te, to the best of our knowledge. The downward flow of energy by heat conduction through closed field lines causes major variation in Te at high-altitudes (Schunk & Nagy, 1978), as evidenced by DMSP Te peak and larger gradients at higher heights. Therefore, main part of this study focuses on the downward heat flow into mid-latitude ionosphere during daytime, which was required to elevate the F-region Te. In order to estimate the downward heat flux (Φ) associated with enhanced Te in the ionosphere, we use Te computed by the FM as input into the following thermal Equation 1.

$$\Phi = 7.7 \times 10^5 \times \mathrm{Te}^{5/2} \times \frac{\mathrm{dTe}}{\mathrm{dh}} \times \sin^2 \mathrm{I} \quad \mathrm{eV/cm^2/sec} \tag{1}$$

where, Te is the electron temperature, $\frac{\mathrm{dTe}}{\mathrm{dh}}$ is the temperature gradient and I is the geomagnetic inclination angle. Φ was estimated at 300 and 500 km altitudes with corresponding Te magnitudes and finite average of gradients between 250 and 350 km, and 450–550 km. These heights were considered since Te variations are not linear with altitude. The Te variations attributed to solar flux changes are more pronounced near 300–350 km, while the 500–550 km heights show a greater degree of variability through the heat conduction from the inner magnetosphere or

21699402, 2024, 7, Downloaded from https://agupubs.onlinelibrary.wiley.com/doi/10.1029/2024JA032694 by Physical Research Laboratory, Wiley Online Library on [05/07/2024]. See the Terms and Conditions (https://onlinelibrary.wiley.com/terms-and-conditions) on Wiley Online Library for rules of use; OA articles are governed by the applicable Creative Commons License

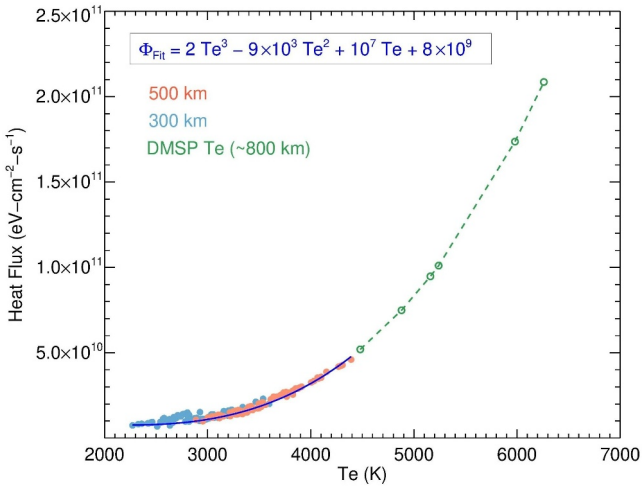

Figure 6. The estimated heat-flux at 300 (blue dots) and 500 km (red-dots) altitudes using the FM computed Te profiles. The solid-blue line represents the best polynomial fit (Φ_{Fit}) through the measured data points. The obtained relation has been used to calculate the heat flux associated with DMSP peak Te as shown by green dashed line. A non-linear behavior between the estimated heat flux and Te can be seen.

plasmasphere. The non-local heating in topside ionosphere due to downward electron heat flux from plasmasphere regulates the ambient electron temperature, and larger Te gradients can be seen at higher heights above the altitude of SAR arcs. Also, the enhancements observed in O(^{1}D) emission intensities were found to be attributed to the SAR arc emissions in daytime. In the recent study by Upadhyay and Pallamraju (2024), it is shown that O(^{1}D) emission intensity during SAR arcs is strongly correlated with topside (at around 500 km) Te variations with a correlation coefficient of 0.7. Therefore, 300 km is considered as the lower altitudinal region until which the effects of heat flux can be seen and the 500 km to be the upper regions of heat flux incidence, during SAR arc events. The heat flux values thus obtained are shown in Figure 6 with corresponding electron gas temperatures. A non-linear variation can be seen in the heat flux values inferred from FM computed Te values. It is worth noticing that larger temperatures (Te > 3,000 K) are mostly present at higher altitudes (500 km) and Te ≈ 3,000 K acts as a threshold for rapid increase in the heat-flux. A third order polynomial fit is obtained for the Te resulting from the FM and to the corresponding estimated heat flux, Φ, which is:

$$\Phi_{Fit} = 2\,Te^3 - 9\times10^3\,Te^2 + 10^7\,Te + 8\times10^9 \quad eV/cm^2/sec \qquad (2)$$

Figure 6 shows a fast-reducing heat flux toward lower heights corresponding to smaller temperatures which yields an appreciably good fit. The analytical expression given in Equation 2 above also gives an indication of the heat flux that would have been generated for the temperatures measured by DMSP at ~800 km, as depicted by the green-dashed line in Figure 6. This again confirms that most of the heat deposition occurs at higher altitudes (>500 km) and it decrease as one moves to lower altitudes, as the heat energy is gradually lost due to conduction by Coulomb collisions. As all the inputs that have gone into the generation of this analytical expression (Equation 2), it can potentially be used to assess the electron heat flux incident into the ionosphere over other regions of similar inclination angles for a given electron temperature.

6. Comparison of Heat Flux Estimated With Previous Results

Due to difficulty of direct measurement of electron heat flux, no report exists for direct comparison of this quantity during the daytime condition till date, however, indirect calculations have been performed to estimate this parameter, both in the daytime and night time. In the work by Evans (1970), the heat flux values were obtained over Millstone Hill in daytime using F-region electron temperature profiles which showed a large deposition of downward heat flux ~10^{10} eV-cm^{-2}-sec^{-1} during a disturbed day. A detailed model study (Rees & Roble, 1975) suggested a large variation in the heat flux ranging from ~10^9 to 10^{11} eV-cm^{-2}-sec^{-1}. Their large heat flux values reported were attributed to the calculations performed at a height of 1,000 km. A modeling study performed for the peak Te at subauroral latitudes during night time to investigate the seasonal variation found the heat flux to be varying between ~0.4 and ~8 × 10^{10} eV-cm^{-2}-sec^{-1} at 500 km during winters (Fok et al., 1991). Such earlier studies were based on theoretical simulations wherein various heat flux values were provided at the topside of the ionosphere to deduce Te and model the resulting SAR arc emissions. However, in this study, we present a bottom-up approach wherein we actually use the measured daytime SAR arc emission intensities as the base and through forward modeling estimate as to what quantity of heat flux would yield the measured red-line emission brightness. From Figure 6, the estimated heat flux can be noted to be varying in the range of 1.0–4.6 × 10^{10} eV-cm^{-2}-sec^{-1} at 500 km altitude, which is in the range reported by model studies earlier (Evans, 1970; Fok et al., 1991). The method of energy transfer was considered as Coulomb collisions. The relative effects of other pathways of generation of electron heat flux and their relative contribution to the O(^{1}D) would be a subject matter of different study, although earlier studies indicate a minor role of other mechanisms (Fok et al., 1991; Kozyra et al., 1993). However, based on SAR arc modeling studies, the electron heat flux of about ~10^9–10^{10} eV-cm^{-2}-sec^{-1} is considered sufficient to produce elevated Te and SAR arcs (Kozyra et al., 1993; Rees & Roble, 1975) and the measured heat flux obtained for observed intensities in daytime in our study is close to these values. Even though no direct measurements of heat flux during daytime exist, the heat flux was estimated

21699402, 2024, 7, Downloaded from https://agupubs.onlinelibrary.wiley.com/doi/10.1029/2024JA032694 by Physical Research Laboratory, Wiley Online Library on [05/07/2024]. See the Terms and Conditions (https://onlinelibrary.wiley.com/terms-and-conditions) on Wiley Online Library for rules of use; OA articles are governed by the applicable Creative Commons License

21699402, 2024, 7, Downloaded from https://agupubs.onlinelibrary.wiley.com/doi/10.1029/2024JA032694 by Physical Research Laboratory, Wiley Online Library on [05/07/2024]. See the Terms and Conditions (https://onlinelibrary.wiley.com/terms-and-conditions) on Wiley Online Library for rules of use; OA articles are governed by the applicable Creative Commons License

during night time SAR arc events using direct plasma measurements by the Radiation Belt Storm Probes recently rather than theoretical simulations (Inaba et al., 2021). Their heat flux was found to vary as 2.5×10^9 and 5×10^9 eV-cm^{-2}-s^{-1}, that is, of the order of $\sim 10^9$ eV-cm^{-2}-s^{-1} as sufficient to cause the observed SAR arcs during night time. The results presented here on the estimated heat flux show the magnitude of the order of $\sim 10^{10}$ eV-cm^{-2}-s^{-1} during daytime. Therefore, using estimated electron heat flux from direct measurements, the magnitude appears to be higher during daytime by about an order of magnitude than that of the night time SAR arcs events. The results also confirm that the Te enhancements at subauroral latitudes can also occur during daytime as a consequence of plasmasphere-ionosphere coupling and simultaneously may affect the O(^{1}D) emission intensities. Thus, the results presented here in this study on the quantitative estimation of the heat flux associated with the observed daytime SAR arcs as measured by the ground-based OI 630.0 nm red-line emission are the first reports to the best of our knowledge.

7. Summary

This work demonstrates the measured enhancement in O(^{1}D) emission intensity during daytime to be associated with Te enhancements over mid-latitudes. The brightness enhancements measured in 630.0 nm emissions are investigated using complementary information from empirical, photochemical-models, digisonde, and DMSP measurements. Since the DMSP measured high-altitude (~800 km) Te peak in 50°–54°N MLAT range during the disturbed periods are symptomatic of energy transfer from near the plasmapause region, variations in Te were used to provide an independent information. The larger emission intensities are validated to be due to increased Te, as evidenced by a narrow latitude region of Te peak from DMSP observations at subauroral latitudes during the observed larger brightness in red-line emissions. However, the model calculations underestimated the emission intensities during such periods. Therefore, a forward modeling approach was carried out to estimate the required Te that could contribute to a greater yield of O(^{1}D) emissions to match with the HIRISE measured SAR arc emissions in the daytime. Therefore, in this study, we made the first quantitative assessment on electron heat flux precipitation in the daytime using estimated Te values and found it to be in the range of around 1.0 to 4.6×10^{10} eV-cm^{-2}-sec^{-1} at an altitude of 500 km. It was found that the electron heat flux follows a non-linear increase with electron temperatures. As the thermal heat flux is important to explain the formation of SAR arcs and other high-latitude auroral emission intensities, the work presented in this study on the estimation of heat flux using two major candidates (O(^{1}D) emission observations and modeled Te) provides a good opportunity to investigate this parameter from ground and offers new insights for a better understanding of the daytime plasmasphere-ionosphere coupling processes.

Data Availability Statement

The daily solar geophysical indices data are obtained from the GSFC/SPDF OMNIWeb interface at https://omniweb.gsfc.nasa.gov/form/dx1.html (King & Papitashvili, 2005). The daytime observed and modelled optical OI 630.0 nm emission data obtained at Boston are available in D. Pallamraju (2024). The Digisonde data used in this work were obtained through the public access portal of Digital Ionogram DataBase (DIDBase; Reinisch & Galkin, 2011, https://giro.uml.edu/didbase/), using the SAO Explorer software tool (https://ulcar.uml.edu/SAO-X/SAO-X.html). The DMSP data product are downloaded from the cedar madrigal database (Erickson, 2004; http://cedar.openmadrigal.org/). The data from Madrigal can be accessed for the first-time user by providing brief user information. The GNSS TEC daily data at Westford station are downloaded from Crustal Dynamics Data Information System (CDDIS) (Noll, 2010) at https://cddis.nasa.gov/archive/gnss/data/daily/ which requires a log-in credentials. The GLOW model source code is available at https://www2.hao.ucar.edu/modeling/glow.

Acknowledgments
This work is supported by the Department of Space, Government of India. Work at UML was carried out under Massachusetts Technology Collaborative.

References

Anderson, P. C. (2004). Subauroral electric fields and magnetospheric convection during the April, 2002 geomagnetic storms. *Geophysical Research Letters*, *31*(11), L11801. https://doi.org/10.1029/2004GL019588

Araujo-Pradere, E. A., Fuller-Rowell, T. J., & Bilitza, D. (2003). Validation of the STORM response in IRI2000. *Journal of Geophysical Research*, *108*(A3), 1120. https://doi.org/10.1029/2002JA009720

Balan, N., Shiokawa, K., Otsuka, Y., Kikuchi, T., Vijaya Lekshmi, D., Kawamura, S., et al. (2010). A physical mechanism of positive ionospheric storms at low latitudes and midlatitudes. *Journal of Geophysical Research*, *115*(A2). https://doi.org/10.1029/2009ja014515

Baumgardner, J., Wroten, J., Mendillo, M., Martinis, C., Barbieri, C., Umbriaco, G., et al. (2013). Imaging space weather over Europe. *Space Weather*, *11*(2), 69–78. https://doi.org/10.1002/swe.20027

Bilitza, D. (1990). International reference ionosphere: IRI-90. *The National Space Science Data Center*, 90–22. Retrieved from https://ntrs.nasa.gov/archive/nasa/casi.ntrs.nasa.gov/19910021307.pdf

Cornwall, J. M., Coroniti, F. V., & Thorne, R. M. (1971). Unified theory of SAR arc formation at the plasmapause. *Journal of Geophysical Research*, *76*(19), 4428–4445. https://doi.org/10.1029/JA076i019p04428

Das, U., Pallamraju, D., & Chakrabarti, S. (2010). Effect of an X-Class solar flare on the OI 630 nm dayglow emissions. *Journal of Geophysical Research*, *115*(A8). https://doi.org/10.1029/2010ja015370

Delbouille, L., Roland, G., & Neven, L. (1973). *Photometric atlas of the solar spectrum from 3000 to 10,000 Å*. Institute d'Astrophysique de l'Universite de Liege, B4200 Cointe-Ougre.

Erickson, P., & MIT/Haystack Observatory. (2004). Data from the CEDAR madrigal database [Dataset]. *Haystack*, Retrieved from http://millstonehill.haystack.mit.edu/list

Evans, J. V. (1970). F-region heating observed during the main phase of magnetic storms. *Journal of Geophysical Research*, *75*(25), 4815–4823. https://doi.org/10.1029/ja075i025p04815

Evans, J. V. (1973). Seasonal and sunspot cycle variations of F region electron temperatures and protonospheric heat fluxes. *Journal of Geophysical Research*, *78*(13), 2344–2349. https://doi.org/10.1029/ja078i013p02344

Fok, M. C., Craven, P. D., Moore, T. E., & Richards, P. G. (1995). Ring current-plasmasphere coupling through Coulomb collisions. Cross-scale coupling in space plasmas, *93*, 161–171.

Fok, M. C., Kozyra, J. U., Warren, M. F., & Brace, L. H. (1991). Seasonal variations in the subauroral electron temperature enhancement. *Journal of Geophysical Research*, *96*(A6), 9773–9780. https://doi.org/10.1029/91ja00791

Foster, J. C. (1993). Storm time plasma transport at middle and high latitudes. *Journal of Geophysical Research*, *98*(A2), 1675–1689. https://doi.org/10.1029/92JA02032

Foster, J. C., Buonsanto, M. J., Mendillo, M., Nottingham, D., Rich, F. J., & Denig, W. (1994). Coordinated stable auroral red arc observations: Relationship to plasma convection. *Journal of Geophysical Research*, *99*(A6), 11429–11439. https://doi.org/10.1029/93JA03140

Foster, J. C., Erickson, P. J., Coster, A. J., Goldstein, J., & Rich, F. J. (2002). Ionospheric signatures of plasmaspheric tails. *Geophysical Research Letters*, *29*(13), 1-1–1-4. https://doi.org/10.1029/2002GL015067

Horvath, I., & Lovell, B. C. (2021). Investigating the coupled magnetosphere-ionosphere-thermosphere (M-I-T) system s responses to the 20 November 2003 Superstorm. *Journal of Geophysical Research: Space Physics*, *126*(9), e2021JA029215. https://doi.org/10.1029/2021JA029215

Huang, C. S., Foster, J. C., Goncharenko, L. P., Erickson, P. J., Rideout, W., & Coster, A. J. (2005). A strong positive phase of ionospheric storms observed by the Millstone Hill incoherent scatter radar and global GPS network. *Journal of Geophysical Research*, *110*(A6). https://doi.org/10.1029/2004ja010865

Inaba, Y., Shiokawa, K., Oyama, S. I., Otsuka, Y., Connors, M., Schofield, I., et al. (2021). Multi-event Analysis of plasma and field variations in Source of Stable Auroral Red (SAR) arcs in inner magnetosphere during non-storm-time substorms. *Journal of Geophysical Research: Space Physics*, *126*(4), e2020JA029081. https://doi.org/10.1029/2020ja029081

Inaba, Y., Shiokawa, K., Oyama, S.-I., Otsuka, Y., Oksanen, A., Shinbori, A., et al. (2020). Plasma and field observations in the magnetospheric source region of a stable auroral red (SAR) arc by the Arase satellite on 28 March 2017. *Journal of Geophysical Research: Space Physics*, *125*(10), e2020JA028068. https://doi.org/10.1029/2020JA028068

King, J. H., & Papitashvili, N. E. (2005). Solar wind spatial scales in and comparisons of hourly Wind and ACE plasma and magnetic field data [Dataset]. *Journal of Geophysical Research*, *110*(A2), A02209. https://doi.org/10.1029/2004JA010649

Kozyra, J. U., Brace, L. H., Cravens, T. E., & Nagy, A. F. (1986). A statistical study of the subauroral electron temperature enhancement using Dynamics Explorer 2 Langmuir probe observations. *Journal of Geophysical Research*, *91*(A10), 11270–11280. https://doi.org/10.1029/JA091iA10p11270

Kozyra, J. U., Chandler, M. O., Hamilton, D. C., Peterson, W. K., Klumpar, D. M., Slater, D. W., et al. (1993). The role of ring current nose events in producing stable auroral red arc intensifications during the main phase: Observations during the September 19–24, 1984 equinox transition study. *Journal of Geophysical Research*, *98*(A6), 9267–9283. https://doi.org/10.1029/92JA02554

Kozyra, J. U., Nagy, A. F., & Slater, D. W. (1997). High-altitude energy source (s) for stable auroral red arcs. *Reviews of Geophysics*, *35*(2), 155–190. https://doi.org/10.1029/96rg03194

Kozyra, J. U., Shelley, E. G., Comfort, R. H., Brace, L. H., Cravens, T. E., & Nagy, A. F. (1987). The role of ring current O+ in the formation of stable auroral red arcs. *Journal of Geophysical Research*, *92*(A7), 7487–7502. https://doi.org/10.1029/JA092iA07p07487

Martinis, C., Baumgardner, J., Mendillo, M., Taylor, M. J., Moffat-Griffin, T., Wroten, J., et al. (2019). First ground-based conjugate observations of stable auroral red (SAR) arcs. *Journal of Geophysical Research: Space Physics*, *124*(6), 4658–4671. https://doi.org/10.1029/2018ja026017

Mendillo, M., Baumgardner, J., & Wroten, J. (2016). SAR arcs we have seen: Evidence for variability in stable auroral red arcs. *Journal of Geophysical Research: Space Physics*, *121*(1), 245–262. https://doi.org/10.1002/2015ja021722

Mendillo, M., Baumgardner, J., Wroten, J., Martinis, C., Smith, S., Merenda, K. D., et al. (2013). Imaging magnetospheric boundaries at ionospheric heights. *Journal of Geophysical Research: Space Physics*, *118*(11), 7294–7305. https://doi.org/10.1002/2013JA019267

Mishin, E. V., & Burke, W. J. (2005). Stormtime coupling of the ring current, plasmasphere, and topside ionosphere: Electromagnetic and plasma disturbances. *Journal of Geophysical Research*, *110*(A7). https://doi.org/10.1029/2005ja011021

Nagy, A. F., Roble, R. G., & Hays, P. B. (1970). Stable mid-latitude red arcs: Observations and theory. *Space Science Reviews*, *11*(5), 709–727. https://doi.org/10.1007/bf00177029

Noll, C. E. (2010). The crustal dynamics data information system: A resource to support scientific analysis using space geodesy [Dataset]. *Advances in Space Research*, *45*(12), 1421–1440. https://doi.org/10.1016/j.asr.2010.01.018

Pallamraju, D. (2024). SAR_Arcs_and_Associated_Electron_Heat_Flux [Dataset]. *OSF*, *554*. https://doi.org/10.17605/OSF.IO/7KN53

Pallamraju, D., Baumgardner, J., & Chakrabarti, S. (2000). A multiwavelength investigation of the Ring effect in the day sky spectrum. *Geophysical Research Letters*, *27*(13), 1875–1878. https://doi.org/10.1029/1999gl010961

Pallamraju, D., Baumgardner, J., & Chakrabarti, S. (2002). HIRISE: A ground-based high-resolution imaging spectrograph using echelle grating for measuring daytime airglow/auroral emissions. *Journal of Atmospheric and Solar-Terrestrial Physics*, *64*(12–14), 1581–1587. https://doi.org/10.1016/s1364-6826(02)00095-0

Pallamraju, D., Baumgardner, J., Chakrabarti, S., & Pedersen, T. R. (2001). Simultaneous ground based observations of an auroral arc in daytime/twilighttime OI 630.0 nm emission and by incoherent scatter radar. *Journal of Geophysical Research*, *106*(A4), 5543–5549. https://doi.org/10.1029/2000ja000244

Pallamraju, D., & Chakrabarti, S. (2005). First ground-based measurements of OI 6300 Å daytime aurora over Boston in response to the 30 October 2003 geomagnetic storm. *Geophysical Research Letters*, *32*(3), L03S10. https://doi.org/10.1029/2004GL021417

Pallamraju, D., Chakrabarti, S., Doe, R., & Pedersen, T. (2004). First ground-based OI 630 nm optical measurements of daytime cusplike and Fregion auroral precipitation. *Geophysical Research Letters*, *31*(8), L08807. https://doi.org/10.1029/2003gl019173

21699402, 2024, 7, Downloaded from https://agupubs.onlinelibrary.wiley.com/doi/10.1029/2024JA032694 by Physical Research Laboratory, Wiley Online Library on [05/07/2024]. See the Terms and Conditions (https://onlinelibrary.wiley.com/terms-and-conditions) on Wiley Online Library for rules of use; OA articles are governed by the applicable Creative Commons License

Pallamraju, D., Chakrabarti, S., & Solomon, S. C. (2011). On deriving incident auroral particle fluxes in the daytime using combined ground-based optical and radar measurements. *Journal of Geophysical Research*, *116*(A4). https://doi.org/10.1029/2010JA015934

Pallamraju, D., Das, U., & Chakrabarti, S. (2010). Short- and long-timescale thermospheric variability as observed from OI 630.0 nm dayglow emissions from low-latitudes. *Journal of Geophysical Research*, *115*(A6), A06312. https://doi.org/10.1029/2009JA015042

Pallamraju, D., Karan, D. K., Laskar, F. I., Vijaya Lakshmi, T., & Chakrabarti, S. (2020). Effect of solar flux versus compositional variations on the variability of daytime oxygen optical emission rates over low- and mid-latitudes. *Journal of Atmospheric and Solar-Terrestrial Physics*, *205*, 105293. https://doi.org/10.1016/j.jastp.2020.105293

Pallamraju, D. P., Sridharan, R., Gurubaran, S., & Raghavarao, R. (1996). First results from ground-based daytime optical investigation of the development of the equatorial ionization anomaly. *Annales Geophysicae*, *14*(2), 238. https://doi.org/10.1007/s005850050285

Picone, J. M., Hedin, A. E., Drob, D. P., & Aikin, A. C. (2002). NRLMSISE-00 empirical model of the atmosphere: Statistical comparisons and scientific issues. *Journal of Geophysical Research*, *107*(A12), SIA15-1–SIA15-16. https://doi.org/10.1029/2002JA009430

Prölss, G. W. (2006). Subauroral electron temperature enhancement in the nighttime ionosphere. *Annals of Geophysics*, *24*(7), 1871–1885. https://doi.org/10.5194/angeo-24-1871-2006

Rees, M. H., & Roble, R. G. (1975). Observations and theory of the formation of stable auroral red arcs. *Reviews of Geophysics*, *13*(1), 201–242. https://doi.org/10.1029/rg013i001p00201

Reinisch, B. W., & Galkin, I. A. (2011). Global ionospheric radio observatory (GIRO) [Dataset]. *Earth Planets and Space*, *63*(4), 377–381. https://doi.org/10.5047/eps.2011.03.001

Reinisch, B. W., & Huang, X. (2001). Deducing topside profiles and total electron content from bottomside ionograms. *Advances in Space Research*, *27*(1), 23–30. https://doi.org/10.1016/s0273-1177(00)00136-8

Schunk, R. W., & Nagy, A. F. (1978). Electron temperatures in the F region of the ionosphere: Theory and observations. *Reviews of Geophysics*, *16*(3), 355–399. https://doi.org/10.1029/RG016i003p00355

Shepherd, G. G., & Cho, Y. M. (2021). On the Relationship of the O (1D) 630.0 nm dayglow emission to the F10. 7 cm solar flux and the solar zenith angle. *Journal of Geophysical Research: Space Physics*, *126*(3), e2020JA028715. https://doi.org/10.1029/2020ja028715

Solomon, S. C. (2017). Global modeling of thermospheric airglow in the far ultraviolet. *Journal of Geophysical Research: Space Physics*, *122*(7), 7834–7848. https://doi.org/10.1002/2017JA024314

Solomon, S. C., & Abreu, V. J. (1989). The 630 nm dayglow. *Journal of Geophysical Research*, *94*(A6), 6817–6824. https://doi.org/10.1029/JA094iA06p06817

Sumod, S. G., Pant, T. K., Vineeth, C., & Hossain, M. M. (2014). On the ionospheric and thermospheric response of solar flare events of 19 January 2005: An investigation using radio and optical techniques. *Journal of Geophysical Research: Space Physics*, *119*(6), 5049–5059. https://doi.org/10.1002/2013JA019714

Upadhyay, K., & Pallamraju (2024). First daytime red-line emission measurements of the Stable Auroral Red (SAR) arcs. *Geophysical Research Letters*, *51*(3). https://doi.org/10.1029/2023GL106292

Upadhyay, K., Pallamraju, D., & Chakrabarti, S. (2023). Imprint of storm enhanced density in ground-based OI 630.0 nm dayglow measurements. *Journal of Geophysical Research: Space Physics*, *128*(9), e2023JA031409. https://doi.org/10.1029/2023JA031409

Zou, S., Ridley, A. J., Moldwin, M. B., Nicolls, M. J., Coster, A. J., Thomas, E. G., & Ruohoniemi, J. M. (2013). Multi-instrument observations of SED during 24–25 October 2011 storm: Implications for SED formation processes. *Journal of Geophysical Research: Space Physics*, *118*(12), 7798–7809. https://doi.org/10.1002/2013JA018860

21699402, 2024, 7, Downloaded from https://agupubs.onlinelibrary.wiley.com/doi/10.1029/2024JA032694 by Physical Research Laboratory, Wiley Online Library on [05/07/2024]. See the Terms and Conditions (https://onlinelibrary.wiley.com/terms-and-conditions) on Wiley Online Library for rules of use; OA articles are governed by the applicable Creative Commons License

Available online at www.sciencedirect.com

ScienceDirect

Advances in Space Research 75 (2025) 4731–4739

ADVANCES IN SPACE RESEARCH (a COSPAR publication)

www.elsevier.com/locate/asr

Determination of electron heat flux in the topside ionosphere and its impact on the vertical profile of OI 630.0 nm emission rate during nighttime SAR arcs for different solar activity conditions

Kshitiz Upadhyay [a,b,*], Kazuo Shiokawa [c], Duggirala Pallamraju [a], Artem Gololobov [d]

[a] Physical Research Laboratory, Ahmedabad, India
[b] Indian Institute of Technology, Gandhinagar, India
[c] Institute for Space-Earth Environmental Research, Nagoya University, Nagoya, Japan
[d] Yu.G. Shafer Institute of Cosmophysical Research and Aeronomy of Siberian Branch of the Russian Academy of Sciences, Yakut Scientific Center of Siberian Branch of the Russian Academy of Sciences, Yakutsk, Russia

Received 1 September 2024; received in revised form 18 November 2024; accepted 19 December 2024
Available online 25 December 2024

Abstract

Electron heat flux in the ionosphere plays a crucial role in altering the electron temperature and thermal balance of the electron population, especially over subauroral- and high-latitudes. The downward flow of electron heat flux in the subauroral-latitude ionosphere through magnetosphere-ionosphere coupling causes an enhancement in the electron temperature, thereby leading to the formation of Stable Auroral Red (SAR) arcs. Understanding the relationship between heat flux and electron temperature is critical, as no technique exists to measure heat flux directly in the SAR arc region. This study primarily reports the characteristics of thermal electron heat flux of SAR arcs in the sub-auroral ionosphere and its influence on the plasma densities in the inner-magnetosphere and the SAR arc peak emission altitude. The downward electron heat flux has been characterized by using measured atomic oxygen red line emission intensity in conjunction with simultaneous enhancements of electron temperature by in-situ measurements for several nighttime SAR arc events reported in the literature for the period of 2012–2020 of solar cycle-24, and by using GLOW, a physics-based model. The present investigation reveals considerable variation in the estimated heat flux and SAR arc emission altitudes due to the influence of solar activity. This study, thus, quantifies the electron heat flux, averaging 2.89×10^{11} eV-cm^{-2}-sec^{-1} near solar minimum and 8.05×10^{12} eV-cm^{-2}-sec^{-1} during solar maximum, associated with ionospheric heating during observations of nighttime SAR arcs and their relevance to space weather phenomena.
© 2024 COSPAR. Published by Elsevier B.V. All rights are reserved, including those for text and data mining, AI training, and similar technologies.

Keywords: Subauroral ionosphere; OI 630.0 nm emissions; Stable Auroral Red (SAR) arcs; Electron heat flux precipitation; Subauroral electron temperature (Te) enhancement; Space weather

1. Introduction

Stable auroral red (SAR) arcs in the mid-latitude ionosphere are formed due to atomic oxygen (OI) 630.0 nm (red line) emissions and are the optical manifestation of direct energy transfer from near plasmapause region to

* Corresponding author at: Physical Research Laboratory, Ahmedabad, India.
E-mail addresses: kshitiz@prl.res.in (K. Upadhyay), shiokawa@nagoya-u.jp (K. Shiokawa), raju@prl.res.in (D. Pallamraju), golart87@gmail.com (A. Gololobov).

https://doi.org/10.1016/j.asr.2024.12.046
0273-1177/© 2024 COSPAR. Published by Elsevier B.V. All rights are reserved, including those for text and data mining, AI training, and similar technologies.

the ionosphere over mid-latitudes (Rees & Roble, 1975; Kozyra et al., 1997). Various sources for the generation of SAR arcs have been found, such as Coulomb collision between hot ring-current ions and cold electrons, wave particle interactions, and Alfven wave dissipation in the plasmasphere, among others (e.g., Kozyra et al., 1987; Fok et al., 1993, Mishin & Burke, 2005; Leonovich et al., 2021). The source of this energy lies in the geomagnetic equatorial plane and is conducted to the mid-latitude ionosphere along the geomagnetic field lines which heat the ambient electrons (Prölss, 2006). These heated electrons undergo collisions with atomic oxygen and thereby excite it to $O(^1D)$ state, which on deexcitation produces 630.0 nm emissions. Therefore, (i) the elevated electron temperature, Te, and (ii) collocated reduced electron density, Ne, are the two important ionospheric signatures of SAR arcs, apart from the optical signature of enhanced red line emissions (Foster et al., 1994; Mendillo et al., 2013; Upadhyay and Pallamraju, 2024; Upadhyay et al., 2024). Several properties of SAR arcs have been described in terms of their brightness, longevity, inhomogeneities in the structure, occurrence during the initial phase of the storm, etc. (e.g., Ievenko et al., 2008; Shiokawa et al., 2013; Mendillo et al., 2016). Occurrence of SAR arcs have also been reported during the daytime using satellite measurement of electron temperature enhancement (Mendillo et al., 2013), and recently for the first time in the ground-based OI 630.0 nm daytime airglow emissions by Upadhyay and Pallamraju (2024). The presence of these daytime SAR arcs was also confirmed by enhanced Te values as measured by the simultaneously operating incoherent scatter radar. Although the Te enhancement during SAR arcs, which serves as a good proxy for the downward heat deposition is observed and reported in several works, studies on the role of low-energy electron heat flux responsible for this heating are sparse. Primarily, theoretical simulations have been performed to measure the heat flux during SAR arcs using an ionospheric model (e.g., Rees and Roble, 1975; Fok et al., 1991; Kozyra et al., 1993). Recently, the heat flux was estimated for three SAR arc events using direct plasma measurements at the conjugate magnetosphere by the Radiation Belt Storm Probes (Inaba et al., 2021). They found that the estimated heat fluxes were sufficient for two events, while the flux was insufficient for the other fresh SAR arc event which is accompanied by a local flux of enhanced energies of electrons (<200 eV) and various electromagnetic waves. Gololobov et al. (2023) reported that the measured brightness of SAR arc emissions was strongly positively correlated with DMSP measured electron temperatures (Te) (correlation coefficient of 0.9) for both solar maxima and minima. Therefore, the magnetospheric heat flux was inferred to be affecting the Te in the topside ionosphere and producing the observed SAR arc emissions. Considering the role of heat flux, which represents the transfer of thermal energy through the ionosphere, its quantification and investigation becomes crucial to understand the governing ionospheric heating processes due to magnetospheric-ionospheric dynamics.

In this background, for the present work, an estimate has been made on the electron heat flux in the topside ionosphere using the measured SAR arc emission intensity and the corresponding enhanced electron temperature as inputs into the physics-based model, GLOW, as discussed in section-2. SAR arcs can be measured using ground-based all-sky imagers, the Te enhancement is mostly measured in-situ by satellites, such as, DMSP and SWARM (e.g., Mendillo et al. 2016; Martinis et al., 2019; Inaba et al., 2020; 2021; Gololobov et al., 2023). Therefore, in this study, several conjunction events of SAR arcs in the nighttime located at sub-auroral latitudes corresponding to solar cycle-24 have been considered from the published literature during the years 2012–2020. The details of these events are listed in Table 1 which include the year of the events, number of conjunction events obtained for each year, satellites, and altitude of in-situ measurement of plasma, along with their reference(s). With a particular focus on heat flux, their impact on the volume emission rates of OI 630.0 nm as a function of altitude have been analyzed for each event of nighttime SAR arcs. The heat flux estimated in this work shows a good agreement with earlier suggested heat flux values associated with SAR arcs. As the events used in this study encompass data during both solar maximum and minimum of solar cycle-24, it provides us with an opportunity to compare their variation for different solar activity levels.

2. Observations and model

2.1. Model description

The different conjunction events of SAR arc used in this study were observed by ground-based all-sky imager located at sub-auroral latitudes as listed in Table 1 with the simultaneous electron temperature, electron density observation by satellite measurements (Mendillo et al., 2016; Martinis et al., 2019; Inaba et al., 2020; Inaba et al., 2021; Gololobov et al., 2023). Here, we focus on the measured SAR arc emission intensity, electron temperature and electron densities during these events. As it is clear from Table 1, these SAR arc events were observed between the years 2013 and 2019, and so correspond to the data for different solar activity levels – with 2015 representing a near solar maximum condition and the years 2013 and 2019 representing the solar minimum of solar cycle-24. The solar radio flux at 10.7 cm wavelength (F10.7; unit = sfu; 1 sfu = 10^{-22}W-m^{-2}-Hz^{-1}) data obtained from OMNI database were used as an indicator of solar activity variation, wherein F10.7 greater than 100 and less than 100 sfu represent the high solar activity (HSA) and low solar activity (LSA) periods, respectively.

In addition to the measured SAR arc parameters, to estimate the heat flux, the GLOW model has been used (Solomon, 2017) to estimate the volume emission rates of

Table 1
Event List of SAR arc conjunction events during years of Solar Cycle-24 Observed by previous studies.

Event Year	SAR arc observation location	Number of SAR arc conjunction events observed	Satellite and the approximate altitude of in-situ plasma measurement	Reference
2013	Millstone Hill, Westford (42.6°N, 70.5° W); Rothera (67.5°S, 68.1°W)	2	DMSP at 840 km	Mendillo et al., 2016; Martinis et al., 2019
2015	Athabasca, Canada (54.6°N, 246.36°E)	6	DMSP at 840 km	Gololobov et al., 2023
2017	Nyrölä, Finland (62.34°N, 25.51°E)	1	Swarm-A at 450 km	Inaba et al., 2020
2018	Athabasca, Canada (54.6°N, 246.36°E)	7	DMSP at 840 km	Gololobov et al., 2023
2019	Gakona, Alaska (62.39°N, 214.78°E)	2	DMSP at 840 km	Inaba et al., 2021

the red line airglow. GLOW model includes the two-stream electron transport technique given by Nagy and Banks (1970) to model the electron transport through the atmosphere and provide dayglow/nightglow emission intensities. The model considers 650 km height as top of the atmosphere and the altitude profiles of airglow emission rates are calculated by considering the variation of neutral atmospheric composition from Naval Research Laboratory Mass Spectrometer Incoherent Scatter (NRLMSIS-00; Picone et al., 2002) and the variations of ionospheric electron/ion densities and temperatures as provided by International Reference Ionosphere model (IRI-90; Bilitza, 1990). GLOW also uses a specified parameter of total electron flux (Φ) and the characteristic energy (E_M) at the top of the atmosphere to generate a Maxwellian spectra of downward electron flux at different energy bins varying from 0 eV to 50 keV and considers its effect on airglow emission rates. We have used this feature of GLOW to estimate the thermal electron flux (heat flux) as required for SAR arc emissions. The precipitation of electron heat flux on the topside ionosphere is assumed to be isotropic with the Maxwellian energy distribution. Additionally, the role of isotropic Maxwellian distribution of precipitated electron density (n_M) that could have contributed to the total estimated heat flux at ionospheric level has been calculated using the equation-1 given below:

$$\Phi_M(E) = \frac{n_M \pi E}{\left(2\pi^3 m E_M^3\right)^{1/2}} \exp\left(-\frac{E}{E_M}\right) \quad (1)$$

In Eq. (1), Φ_M is the downward electron number flux (e.g., in unit of electrons-cm^{-2}-sec^{-1}-keV^{-1}), E represents energies, m is electron mass, and E_M is the characteristic energy.

2.2. Response of model estimated number flux to low-energy particle precipitation

Since SAR arcs are associated with soft-electron precipitation (< 10 eV) and requires sufficient population of hemispherical electron flux with energies greater than 1.96 eV for the excitation of O(^{1}D) state, firstly the sensitivity of the model to detect the thermal population at such low energies was examined. Therefore, the profile of downward electron flux at low energies accounted by GLOW is shown in Fig. 1. In this figure, the hemispherical electron flux is shown for the two SAR arc events during 2015 (solar maximum) and 2018 (solar minimum). These events were

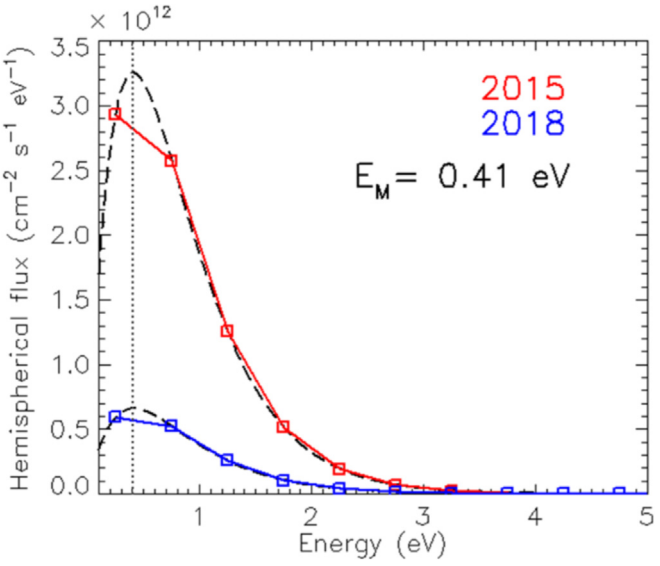

Fig. 1. The hemispherical electron flux obtained from GLOW model (square symbols) and by using the Maxwellian distribution function (black dashed curves) at nearly the same characteristic energy (E_M = 0.41 eV), marked by dotted vertical line. Red and blue color indicates the variations corresponding to high and low solar activity periods i.e., 2015 (HSA) and 2018 (LSA), respectively.

measured at the nearly same characteristic energy of E_M = 0.41 eV, equivalent to T_e = 4720 K for 2015 and T_e = 4733.70 K for 2018, taken from the DMSP measurements by Gololobov et al. (2023), and are represented by red and blue squares, respectively. The different amounts of flux were attributed to the varying SAR arc intensities and downward heat flow during both individual events. Due to the larger energy bins of 0.5 eV used by GLOW model, the peak flux corresponding to E_M was not identified. Therefore, equation-1 was used to obtain the hemispherical flux at much smaller energy bins of 0.1 eV by using an arbitrary value of precipitating electron density (n_M) as the scaling parameter. The black-dashed curve thus represents the scaled hemispherical flux similar to that obtained by GLOW and reflects the maximum peak at a given characteristic energy, E_M, as indicated by vertical dotted line. From both the distribution functions depicted in Fig. 1, it can be seen that there exists a finite amount of flux in the electron population in the tail of this Maxwellian distribution beyond 1.96 eV energy, which is the source for the thermally excited component of O(^{1}D) state due to the

downward heat conduction, and thereby responsible for the production of SAR arcs. Therefore, as sufficient flux is available at 1.96 eV in both the solar activity conditions, the GLOW model is considered to estimate the effect of downward heat flux on SAR arc emissions.

3. Result and discussion

The in-situ measured N_e and T_e variations for each of the SAR arc events is shown by black dots in Fig. 2a and Fig. 2b, respectively. The right-side y-axis represents the F10.7 index by red open circles to indicate the solar activity variation for each event. A positive correlation (R = 0.55) between solar flux F10.7 and electron density can be seen from Fig. 2a, whereas, the in-situ measured electron temperature enhancements show an anti-correlation of R = -0.57 with solar flux variation (Fig. 2b). The fact that the T_e enhancements do not follow the solar activity variation primarily suggests that T_e was increased due to additional energy input i.e., heat flux precipitation that caused the heating of ionospheric electrons rather than by the heating from solar EUV radiation. Although, no significant dependence was found between the SAR arc intensity and electron densities (correlation coefficient = 0.2), a strong positive correlation (correlation coefficient of 0.72) was found between SAR arc intensity and electron temperature, as shown in Fig. 2c.

Such a high dependence of emission intensity with enhanced Te variation is due to the ionospheric electron heating caused by the downward heat flow. Therefore, to quantify the required thermal electron heat fluxes, the auroral feature of GLOW model with inputs of electron Maxwellian flux (eV-cm^{-2}-s^{-1}) and electron Maxwellian characteristic energy (E_M, eV) was used to calculate the measured SAR arc intensities.

3.1. Estimated heat flux

Depending on the ambient background conditions, SAR arc emission intensities can be significantly larger (~20 R or more; Baumgardner et al., 2007) than usual nightglow emissions at these latitudes (~10 R). Therefore, in order to obtain the associated electron heat flux, firstly the typical brightness of OI 630.0 nm nightglow emissions without electron heat flux was calculated for each of the events as background emissions (I_0) using the GLOW model. Then, the observed SAR arc intensity (I_{obs}) was taken from the studies reported in the literature listed (Table 1). The value of I_{obs} was obtained by subtracting ambient 630.0 nm nightglow intensity observed in airglow images from the observed peak intensity at the SAR arc. Then, the modelled background emission intensities I_0 were added to the values of I_{obs} of corresponding events to obtain a resultant emission value (I_{res}; $I_{res} = I_0 + I_{obs}$), which should be reproduced by the GLOW model for a suitable electron heat flux. Therefore, in the model estimations, the amount of Maxwellian electron heat flux for the observed characteristic energy ($E_M = k_B T_e$) was changed until the 630.0 nm intensity estimated by the GLOW model matches with I_{res}. In this calculation, the measured electron temperature T_e was used for E_M.

Thereby, information on the required heat fluxes associated with the measured electron temperatures for individual events were obtained as shown in Fig. 3a. The red and blue dots represent the estimated heat flux variation for periods of high solar activity (HSA) and low solar activity (LSA), respectively. It can be seen that the total electron heat flux values for these events range from approximately 10^{11} –10^{13} eV-cm^{-2}-sec^{-1}, with estimated values varying between 2.5 x 10^{12} –1.8 x 10^{13} eV-cm^{-2}-sec^{-1} during HSA, and 1.1–8.6 x 10^{11} eV-cm^{-2}-sec^{-1} during LSA. Generally, it is expected that for a given SAR arc, larger Te enhancement will require larger amount of deposition of heat flux, yet no such relation is seen between variation of heat flux and corresponding Te from Fig. 3a. This could be due to the fact that the events used in this study occurred during different seasons, locations, and geophysical conditions, and hence, their ambient upper atmospheric characteristics are expected to be different from case to case and therefore, could not be properly accounted for by the model. Nevertheless, from Fig. 3a, the estimated heat flux during low solar activity does not vary signifi-

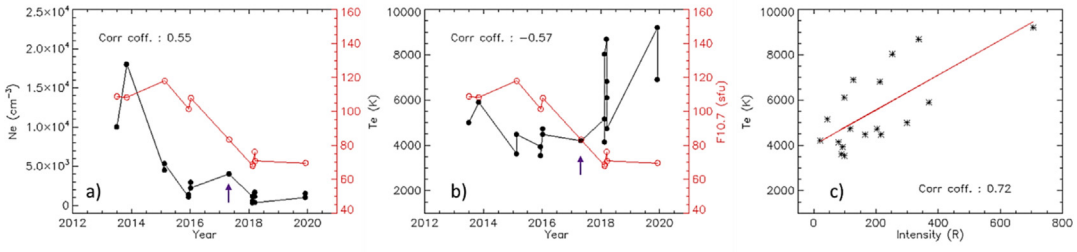

Fig. 2. **a)** DMSP and Swarm satellite measured electron density (Ne), and **b)** electron temperature (Te) variations (black dots) in conjunction with each SAR arc observation between the year 2012 and 2020 for solar cycle-24 are shown with respect to solar activity index F10.7 (red open circles). Vertical magenta arrows in 2017 denote Ne and Te measurements taken by Swarm at ~ 450 km, while the remaining data points are obtained from DMSP at approximately 840 km altitude. A direct and inverse relation of electron density and electron temperature enhancements with solar flux can be seen. Panel **c)** shows the strong dependence of measured SAR arc intensity with respect to simultaneous electron temperature measurements with a correlation coefficient of 0.72.

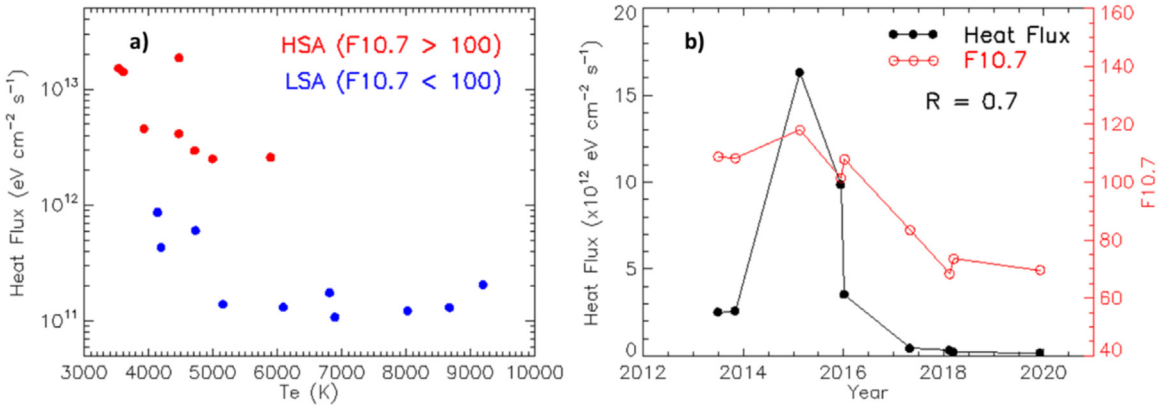

Fig. 3. **a)** The estimated electron heat flux at 650 km altitude using measured SAR arc emissions and corresponding electron temperature enhancement for each event is shown. The red and blue dots indicate the variations in the obtained electron heat flux during HSA and LSA periods, respectively. The panel **b)** shows the monthly averaged values of estimated heat flux (black dots) variation with solar flux F10.7 (red open circles)**.** The positive correlation of 0.7 between heat flux and F10.7 suggest the strong dependence of downward energy input with solar activity.

cantly. The average value of heat flux during LSA is 2.89 x 10^{11} eV-cm^{-2}-sec^{-1}, while during periods of HSA, it is around one order larger, 8.05 x 10^{12} eV-cm^{-2}-sec^{-1} with a maximum of 1.85 x 10^{13} eV-cm^{-2}-sec^{-1}. In the study by Kozyra et al. (1997), the electron heat flux was found to vary between 5x10^{9} – 3x10^{11} eV-cm^{-2}-sec^{-1} at 500 km and one order larger during winter of solar maximum than the fall of solar minimum for a SAR arc of ~ 100 R intensity. Therefore, the magnitude of the estimated heat flux during LSA still shows a good agreement with the values reported by Kozyra et al. (1997), although the variations during HSA are larger than their suggested range.

To better evaluate such differences between high and low solar activity, the estimated heat flux was compared with solar flux F10.7, as shown in Fig. 3b. The black dots represent the estimated heat flux, while the red open circles represent F10.7 variation as indicated by the y-axis on right-side. Here, instead of each individual value as shown in Fig. 3a, the monthly averaged values for each year are presented. It can be seen that the estimated heat flux tends to follow the solar activity variation with a high positive correlation (correlation coefficient of 0.7). To the best of our knowledge, no such solar activity variation of electron heat flux has been reported till date. However, significant seasonal variations were found over high latitudes of Alaska, showing greater heat flux magnitudes during summer than winter (Fallen and Watkins, 2013). Consequently, the electron heat flux estimated here suggests that it follows the solar activity variation in case of SAR arcs observed at sub-auroral latitudes. Interestingly, a good positive correlation of not only estimated heat flux but also the in-situ measured electron densities with solar activity (Fig. 3b and 2a) leads to the inference that the ionospheric electron densities play a notable role in defining the downward electron heat flux. Also, as evident from equation-1, the ionospheric electron density acts as an important parameter to regulate the electron heat flux.

The estimated heat flux and in-situ measured Ne (shown by open squares) does not show any correlation between them (Fig. 4a). Therefore, we further estimated the number densities of electrons that precipitated in the topside ionosphere (n_M) using equation-1 to identify their dependence on the heat flux. For doing so, during each event, an electron energy flux Φ(E) equal to that estimated by GLOW model was obtained using equation-1 by modifying the parameter n_M. The estimated n_M at 650 km altitude associated with heat fluxes by following this procedure are also shown (Fig. 4b as filled squares). An almost linear dependence of estimated heat flux with the precipitated electron densities estimated in topside ionosphere can be seen with an improved correlation of 0.98 in comparison to earlier in-situ measured Ne in Fig. 4a. In equation (1), the amount of heat flux Φ(E) is proportional to value of n_M. Thus, this nearly linear relation between Φ(E) and n_M in Fig. 4b suggests that the effect of E_M does not contribute much to the amount of electron heat flux. This independence of electron heat flux to E_M can be also seen in Fig. 3a.

3.2. Plasmaspheric density

Additionally, not only do the role of ionospheric electron densities but also that of the plasmaspheric densities affect the Te enhancements in the ionosphere during SAR arcs. Kozyra et al. (1997) found double-peaked Te enhancement in the ionosphere to be simultaneously associated with the double-peaked structure in the plasmaspheric ion densities during a SAR arc event. The typical energies of ion and electrons in the plasmasphere are less than 1 eV, while the densities are around 1 to thousands cm^{-3}. So far, there are no specific measurements on the variation of cold electron density in the plasmasphere during SAR arc events, however, the source region of SAR arc has been identified to lie in the overlap region of outer plasmasphere with the inner ring current region (Chu et al.,

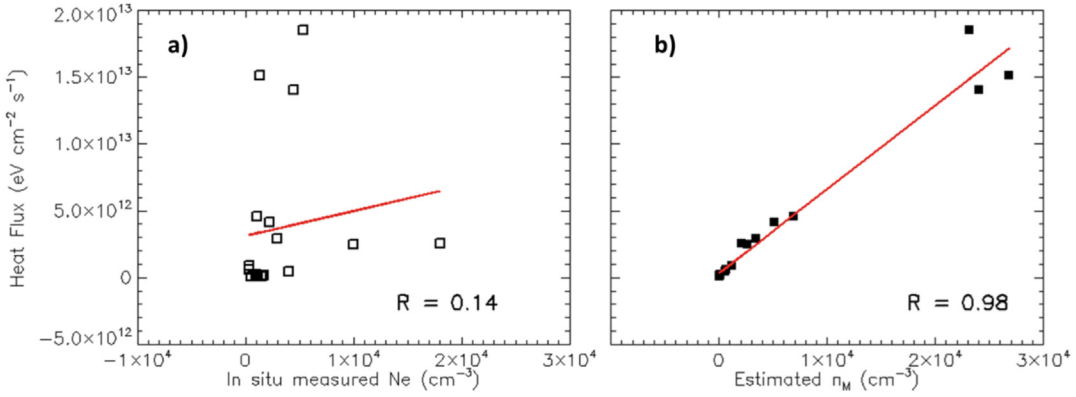

Fig. 4. **a)** The estimated heat flux does not show any correlation with respect to in-situ measured electron density (n_M) at ~ 800 km altitude. **b)** The heat flux has a strong positive correlation with the estimates of precipitated electron densities in the ionosphere at 650 km altitude obtained by using Maxwellian energy distribution function. This indicates the major influence of ambient electron densities in governing the magnitude of downward heat flux.

2019; Inaba et al., 2020; 2021). The outer plasmasphere region, near the plasmapause is connected with the underlying ionosphere at sub-auroral latitudes through closed geomagnetic field lines and generally varies between L = 2.5 to L = 5.5 (Carpenter and Anderson, 1992). The events used in this work also corresponds to L-value between L = 2.3 to L = 5. Therefore, by considering the dipolar approximation of the geomagnetic field we have calculated the electron densities that would be present in the equatorial region of the plasmapause at L = 4. The distribution of densities in the high altitude plasmasphere or inner magnetosphere (n_{mag}) along the closed magnetic field lines can be assumed to be proportional to geomagnetic field (i.e., $n_{mag} \propto B$) by considering the conservation of electron flux through the magnetic flux tube. By following the geomagnetic strength near plasmapause at L = 4 of around 500 nT and in the ionosphere at sub-auroral latitudes of about ~ 50,000 nT, a factor of 1/100 times the estimated ionospheric densities (n_M) have been considered correspond to the thermal densities near the plasmapause heights. Consequently, the calculated electron density in the closed field line region of inner magnetosphere was found to vary in the range of around 0.6–12 cm^{-3} and 21–268 cm^{-3} during the low and high solar activity period, respectively. The very low values of electron densities estimated here may indicate that the electron heating by the Coulomb collisions does not occur at the equatorial plane of the magnetosphere but rather at intermediate heights located between the equatorial plane and the ionosphere along the closed geomagnetic field lines. Actually, the electron density monotonically increases from high to low altitudes along a geomagnetic field line. The density distribution of ring-current high-energy ions along a geomagnetic field line depends on the pitch-angle distribution of the ions, but the density will decrease from high to low altitudes along the geomagnetic field line. The present result may suggest that the Coulomb collision between ring-current ions and plasmaspheric electrons occur at middle altitudes where the product of these two densities provide a local maximum.

3.3. Impact on altitude profile of OI 630.0 nm during SAR arc

SAR arcs are considered to peak at an altitude of around 400–450 km range (Kozyra et al., 1997, Mendillo et al., 2016). Since SAR arcs are predominantly monochromatic OI 630.0 nm emissions, the volume emission rate (VER) of these emissions can yield information on the peak height variation caused by the additional heat deposition. Therefore, in order to identify whether the GLOW model can explain the height-dependent response of SAR arcs due to the input heat flux, model estimated 630.0 nm VER profiles were analyzed. Here, the two modelled altitude profiles of 630.0 nm VER are shown in Fig. 5a corresponding to the same characteristic energy of 0.41 eV as input and electron flux distribution as presented in Fig. 1 for solar maximum year 2015 (filled red dots) and solar minimum 2018 (filled blue dots). The volume emission rate profile for typical 630.0 nm nightglow emission in the absence of any downward heat flux is shown as well for both the cases by open circles. The solar flux for 2015 events were 1.5 times larger, and the variations in other observed and estimated parameters for these two cases are summarized in Table 2. From the filled-dots in Fig. 5a, it can be seen that although the peak volume emission rate was nearly same in both cases, the altitude of peak emission was located at a higher altitude (350 km) during solar maxima, whereas the peak emission height was lower (281 km) during the solar minima. Moreover, during both solar maximum and minimum, the peak altitude of the usual 630.0 nm nightglow was located at ~ 260 km i.e., remained closer to the typical altitude of ~ 250 km. Therefore, for same characteristic energy (0.41 eV), the SAR arc emission was found to peak below 300 km during low solar activity, while the peak was located above 300 km for high solar activity period.

To investigate the altitude distribution of different SAR arc emissions, the peak emission heights of modelled volume emission rates for each of the events were compared with solar flux variation using the F10.7 solar activity

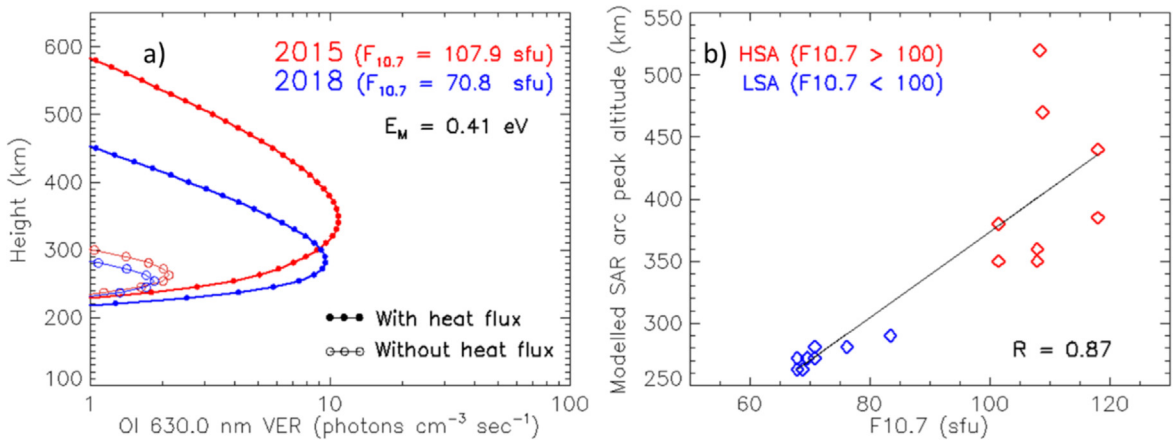

Fig. 5. **a)** The modelled volume emission rates (VER; photons cm^{-3} sec^{-1}) for typical OI 630.0 nm nightglow (without heat flux) and SAR arc case (with heat flux) are shown by open and filled dots, respectively. The red and blue colors indicate the solar activity maximum and minimum durations, as represented by F10.7 index. Both profiles were obtained at nearly the same characteristic energy (E_M = 0.41 eV). The variation in VER profile for SAR arc case can be seen due to additional heat input, as compared to the typical nightglow profile. **b)** The variation in peak altitude of modelled SAR arc emissions with respect to solar activity variation is shown. It can be seen that during low periods of solar activity, SAR arc emissions can originate at lower heights as compared with HSA.

Table 2
Variation in the measured and estimated parameters for the two SAR arc events shown in Fig. 5a.

Year	Solar Flux (sfu)	Estimated Heat Flux (eV-cm^{-2}-sec^{-1})	DMSP Te (K)	DMSP Ne (cm^{-3})	Estimated precipitated n_M (cm^{-3})	Estimated n_M at L = 4 in the inner magnetosphere (cm^{-3})	Modelled Peak emission height (km)
2015	107.9	2.94×10^{12}	4720.00	2939.40	3387.00	33.870	350.0
2018	70.80	5.99×10^{11}	4733.70	358.560	687.050	6.8705	281.0

index, as shown in Fig. 5b. In Fig. 5b, the red and blue symbols represent the peak height of 630.0 nm VER for solar maxima and minima, respectively. It can be seen that, during solar maximum, the peak height lies at a higher altitude range of 350–450 km and shifts to a lower altitude range of ~ 260–290 km during the low solar activity periods. A strong positive correlation of 0.87 from linear fit indicates an influence of solar activity variation on the modelled peak emission height of SAR arcs. Several studies have suggested the peak emission altitude of SAR arc to be in the range of 350–450 km (Roach and Roach, 1963; Rees and Roble, 1975, Kozyra et al., 1997). Also, the model calculated 630.0 nm volume emission rate using full profile of electron density and temperature data from the incoherent scatter radar showed the peak emission height close to 400 km during night time SAR arc (Foster et al., 1994). It is important to note that all these height measurements were performed for the nighttime SAR arcs observed near the solar maximum of that solar cycle. Here, the altitude range of model calculated peak emission height for year 2015 (HSA) agrees very well with the past studies. However, during year 2018 (LSA), the SAR arc emission height is reduced to lower altitudes (below 300 km). Recently, using triangulation of simultaneous measurements from two all-sky cameras and DMSP satellites, the lower edge of the SAR arc emission was found to be in the range of 240–290 km during LSA (2018–2020) and 350–370 km during HSA (2015) for the 24th solar cycle (Ievenko et al., 2023). The results obtained in the present study are in good agreement with those reported earlier on SAR arc height measurements.

As discussed earlier, SAR arcs are atomic oxygen 630.0 nm emissions which are formed by the collision between heated ambient electrons and the oxygen atoms. Therefore, the altitude profiles of SAR arcs will primarily depend on two factors: a) the neutral composition of atomic oxygen and b) changes in ionospheric electron densities. For the first case of oxygen density variation, during solar maximum, the large thermospheric temperatures will cause the atmospheric heating and increase the scale height of neutral species, which will lead to the upward expansion of the atmosphere. On the other hand, lower thermospheric temperature during solar minimum results in contraction of the atmosphere towards lower heights. Hence, the lower heights during solar minimum will encounter a larger mass density of atomic oxygen as compared to higher heights. The situation will be opposite during the solar maximum. For the case of electron density variations, during HSA, larger atmospheric density will create shallow depth for precipitated heat flux, resulting in faster cooling by Coulomb collisions with ambient ions at higher altitudes. While due to lower values of Ne above 250 km during

LSA, thermal conduction may extend deeper into the ionosphere, resulting in heating at around 300 km to produce SAR arcs. For this reason, out of these ambient parameters, the contribution of the atmosphere (and thereby oxygen atom density) to lower altitudes and a deeper penetration of heat flux resulting from reduced electron densities, which leads to the formation of SAR arcs at lower heights during low solar activity periods (Fig. 5b).

4. Summary

In this work, we have estimated the required downward electron heat flux during nighttime by making use of SAR arc measurements reported in the published literature and have compared these values for different solar activity periods. The results of this study can be summarized as follows.

1. The estimated electron heat flux varies from 2.5×10^{12}–1.8×10^{13} eV-cm^{-2}-sec^{-1} during periods of high solar activity, and 1.1–8.6 $\times$ 10^{11} eV-cm^{-2}-sec^{-1} during low solar activity periods. These estimates of electron heat flux were obtained using direct measurements of red line emission intensity of SAR arcs in conjunction with the ionospheric electron temperature measurements from DMSP and Swarm. Results from this study on the nighttime estimated thermal heat flux agree well with the theoretically estimated heat flux ($\sim 10^{10}$-10^{11} eV-cm^{-2}-sec^{-1}) presented earlier for the solar minimum. Also, we found significant variation in the measured heat flux between low and high solar activity. The average heat flux during solar maximum is around one order of magnitude larger than that in the solar minimum, as also reported in earlier studies based on theoretical calculations.
2. We have further calculated the precipitating electron densities in the ionosphere using an isotropic Maxwellian distribution and in the near plasmapause heights associated with the SAR arc region. The source electron densities at L = 4 in the inner magnetosphere were found to vary from 0.6-12 cm^{-3} and $\sim$ 21–268 cm^{-3} during solar minimum and maximum, respectively. It is supposed that the electron heating by the Coulomb collision does not occur at the equatorial plane of the magnetosphere but rather at intermediate heights located between the equatorial plane and the ionosphere along the closed geomagnetic field lines.
3. The vertical profiles of OI 630.0 nm VER for modelled SAR arcs were also analyzed, and it was found that the peak emission height of SAR arcs is expected to have solar activity dependence in response to the atomic oxygen variability in the upper atmosphere. Although SAR arcs are widely considered to peak at around 400–450 km altitude, but during low solar activity periods, modelled VER suggests that SAR arcs can also originate at lower altitudes of around 260–290 km. The peak emission altitude shows a strong positive correlation with solar activity variation.

The results presented in this study will help in the understanding of the complex nature of interaction influenced by incidence of heat flux due to magnetosphere-ionosphere coupling.

Declaration of competing interest

The authors declare that they have no known competing financial interests or personal relationships that could have appeared to influence the work reported in this paper.

Acknowledgments

KU acknowledges the support from the Institute for Space-Earth Environmental Research (ISEE), Nagoya University, Nagoya, Japan during the period of his visit as a SCOSTEP visiting scholar (SVS). KU also acknowledges the travel support to Japan by SCOSTEP under the SVS program. This work at ISEE, Japan is supported by the Japan Society for the Promotion of Science (JSPS) KAKENHI (21H04518; 22K21345) and JSPS core-to-core program (JPJSCCB20210003; JPJSCCB20240003). This work at the Physical Research Laboratory, Ahmedabad is supported by the Department of Space, Government of India.

Data availability

The solar geophysical indices data are utilized from the GSFC/SPDF OMNIWeb interface at https://omniweb.gsfc.nasa.gov/form/dx1.html. The GLOW model source code is available at https://www2.hao.ucar.edu/modeling/glow.

References

Baumgardner, J., Wroten, J., Semeter, J., Kozyra, J., Buonsanto, M., Erickson, P., and Mendillo, M. 2007. A very bright SAR arc: implications for extreme magnetosphere-ionosphere coupling. In Annales Geophysicae (Vol. 25, No. 12, pp. 2593-2608). Göttingen, Germany: Copernicus Publications. https://doi.org/10.5194/angeo-25-2593-2007.

Bilitza, D. 1990. International reference ionosphere: IRI-90-22. National Space Science Data Center Report. https://ntrs.nasa.gov/archive/nasa/casi.ntrs.nasa.gov/19910021307.pdf.

Carpenter, D.L., Anderson, R.R., 1992. An ISEE/Whistler model of equatorial electron density in the magnetosphere. J. Geophys. Res. 97, 1097–1108. https://doi.org/10.1029/91JA01548.

Chu, X., Malaspina, D., Gallardo-Lacourt, B., Liang, J., Andersson, L., Ma, Q., et al., 2019. Identifying STEVE's magnetospheric driver using conjugate observations in the magnetosphere and on the ground. Geophys. Res. Lett. 46, 12665–12674. https://doi.org/10.1029/2019gl082789.

Fallen, C.T., Watkins, B.J., 2013. Diurnal and seasonal variation of electron heat flux measured with the poker flat incoherent-scatter radar. J. Geophys. Res. Space Phys. 118 (8), 5327–5332. https://doi.org/10.1002/jgra.50485.

Fok, M.C., Kozyra, J.U., Warren, M.F., Brace, L.H., 1991. Seasonal variations in the subauroral electron temperature enhancement. J. Geophys. Res. 96 (A6), 9773–9780. https://doi.org/10.1029/91ja00791.

Fok, M.-C., Kozyra, J.U., Nagy, A.F., Ramussen, C.E., Khazanov, V., 1993. Decay of equatorial ring current ions and associated aeronom-

ical consequences. J. Geophys. Res. 98, 19381–19393. https://doi.org/10.1029/93ja01848.

Foster, J.C., Buonsanto, M.J., Mendillo, M., Nottingham, D., Rich, F.J., Denig, W., 1994. Coordinated stable auroral red arc observations: Relationship to plasma convection. J. Geophys. Res. 99 (A6), 11429–11439. https://doi.org/10.1029/93ja03140.

Gololobov, A., Shiokawa, K., Baishev, D., Inaba, Y., Otsuka, Y., Connors, M., 2023. Multi-event conjugate measurements of the SAR arc detachment from the auroral oval using DMSP satellites and an all-sky camera at Athabasca, Canada. J. Geophys. Res. Space Phys. 128. https://doi.org/10.1029/2022JA030544 e2022JA030544.

Inaba, Y., Shiokawa, K., Oyama, S., Otsuka, Y., Oksanen, A., Shinbori, A., et al., 2020. Plasma and field observations in the magnetospheric source region of a stable auroral red (SAR) arc by the Arase satellite on March 28, 2017. J. Geophys. Res. Space Phys. 125. https://doi.org/10.1029/2020ja028068.

Ievenko, I.B., Parnikov, S.G., Alexeyev, V.N., 2008. Relationship of the diffuse aurora and SAR arc dynamics to substorms and storms. Advances in Space Research 41 (8), 1252–1260. https://doi.org/10.1016/j.asr.2007.07.030.

Ievenko, I.B., Parnikov, S.G., Sokolnikov, A.V., 2023. Relationship of the Stable Auroral Red Arc Height to Solar Activity: Observation Results at the Yakutsk Meridian. Bulletin of the Russian Academy of Sciences: Physics 87 (2), 220–227. https://doi.org/10.3103/S1062873822700964.

Inaba, Y., Shiokawa, K., Oyama, S.I., Otsuka, Y., Connors, M., Schofield, I., et al., 2021. Multi-event Analysis of plasma and field variations in Source of Stable Auroral Red (SAR) arcs in inner magnetosphere during non-storm-time substorms. J. Geophys. Res. Space Phys. 126 (4). https://doi.org/10.1029/2020ja029081 e2020JA029081.

Kozyra, J.U., Shelley, E.G., Comfort, R.H., Brace, L.H., Cravens, T.E., Nagy, A.F., 1987. The role of ring current O+ in the formation of stable auroral red arcs. J. Geophys. Res. 92, 7487–7502. https://doi.org/10.1029/ja092ia07p07487.

Kozyra, J.U., Chandler, M.O., Hamilton, D.C., Peterson, W.K., Klumpar, D.M., Slater, D.W., et al., 1993. The role of ring current nose events in producing stable auroral red arc intensifications during the main phase: Observations during the September 19–24, 1984, Equinox Transition Study. J. Geophys. Res. 98, 9267–9283. https://doi.org/10.1029/92ja02554.

Kozyra, J.U., Nagy, A.F., Slater, D.W., 1997. High-altitude energy source (s) for stable auroral red arcs. Rev. Geophys. 35 (2), 155–190. https://doi.org/10.1029/96RG03194.

Leonovich, A.S., Kozlov, D.A., Vlasov, A.A., 2021. Kinetic Alfven waves near a dissipative layer. J. Geophys. Res. Space Phys. 126 (10). https://doi.org/10.1029/2021JA029580 e2021JA029580.

Martinis, C., Baumgardner, J., Mendillo, M., Taylor, M.J., Moffat-Griffin, T., Wroten, J., et al., 2019. First ground-based conjugate observations of stable auroral red (SAR) arcs. J. Geophys. Res. Space Phys. 124 (6), 4658–4671. https://doi.org/10.1029/2018ja026017.

Mendillo, M., Baumgardner, J., Wroten, J., Martinis, C., Smith, S., Merenda, K.D., et al., 2013. Imaging magnetospheric boundaries at ionospheric heights. J. Geophys. Res. Space Phys. 118 (11), 7294–7305. https://doi.org/10.1002/2013JA019267.

Mendillo, M., Baumgardner, J., Wroten, J., 2016. SAR arcs we have seen: Evidence for variability in stable auroral red arcs. J. Geophys. Res. Space Phys. 121 (1), 245–262. https://doi.org/10.1002/2015ja021722.

Mishin, E.V., Burke, W.J., 2005. Stormtime coupling of the ring current, plasmasphere, and topside ionosphere: Electromagnetic and plasma disturbances. J. Geophys. Res. 110 (A7). https://doi.org/10.1029/2005ja011021.

Nagy, A., Banks, P., 1970. Photoelectron fluxes in the ionosphere. J. Geophys. Res. 75 (31), 6260–6270.

Picone, J.M., Hedin, A.E., Drob, D.P., Aikin, A.C., 2002. NRLMSISE-00 empirical model of the atmosphere: Statistical comparisons and scientific issues. J. Geophys. Res. 107 (A12), 1468. https://doi.org/10.1029/2002JA009430.

Prölss, G.W., 2006. Subauroral electron temperature enhancement in the nighttime ionosphere. Ann. Geophys. 24 (7), 1871–1885. https://doi.org/10.5194/angeo-24-1871-2006.

Rees, M.H., Roble, R.G., 1975. Observations and theory of the formation of stable auroral red arcs. Rev. Geophys. 13 (1), 201–242. https://doi.org/10.1029/rg013i001p00201.

Roach, F.E., Roach, J.R., 1963. Stable 6300Å auroral arcs in midlatitudes. Planet. Space Sci. I1, 523–545. https://doi.org/10.1016/0032-0633(63)90076-x.

Shiokawa, K., Miyoshi, Y., Brandt, P.C., Evans, D.S., Frey, H.U., Goldstein, J., Yumoto, K., 2013. Ground and satellite observations of low-latitude red auroras at the initial phase of magnetic storms. J. Geophys. Res. Space Phys. 118, 256–270. https://doi.org/10.1029/2012ja018001.

Solomon, S.C., 2017. Global modeling of thermospheric airglow in the far ultraviolet. J. Geophys. Res. Space Phys. 122 (7), 7834–7848. https://doi.org/10.1002/2017JA024314.

Upadhyay, K., Pallamraju, D., 2024. First daytime red-line emission measurements of the stable auroral red (SAR) arcs. Geophys. Res. Lett. 51. https://doi.org/10.1029/2023GL106292 e2023GL106292.

Upadhyay, K., Pallamraju, D., Chakrabarti, S., 2024. Estimation of downward heat flux into the F-region from the inner-magnetosphere during stable auroral red (SAR) arc events in the daytime obtained using OI 630.0 nm red-line emissions. J. Geophys. Res. Space Phys. 129 (7). https://doi.org/10.1029/2024JA032694 e2024JA032694.